

UNCLASSIFIED

AD 4 2 1 4 8 3

DEFENSE DOCUMENTATION CENTER

FOR

SCIENTIFIC AND TECHNICAL INFORMATION

CAMERON STATION, ALEXANDRIA, VIRGINIA



UNCLASSIFIED

NOTICE: When government or other drawings, specifications or other data are used for any purpose other than in connection with a definitely related government procurement operation, the U. S. Government thereby incurs no responsibility, nor any obligation whatsoever; and the fact that the Government may have formulated, furnished, or in any way supplied the said drawings, specifications, or other data is not to be regarded by implication or otherwise as in any manner licensing the holder or any other person or corporation, or conveying any rights or permission to manufacture, use or sell any patented invention that may in any way be related thereto.

421483
CLASSIFIED BY DDC
AC NO 113

abstracts of the

Thirteenth Annual

SYMPOSIUM

USAF ANTENNA RESEARCH
and
DEVELOPMENT PROGRAM

Sponsored by

AIR FORCE AVIONICS LABORATORY
WRIGHT PATTERSON AIR FORCE BASE, OHIO.

In cooperation with the

UNIVERSITY of ILLINOIS.

October 14, 15, 16, 17, 18, 1963.

Robert Allerton Park, Monticello, Illinois.

UNCLASSIFIED

UNCLASSIFIED

Abstracts of the
THIRTEENTH ANNUAL SYMPOSIUM
ON
THE USAF ANTENNA RESEARCH AND DEVELOPMENT PROGRAM

SPONSORED BY
AIR FORCE AVIONICS LABORATORY
WRIGHT PATTERSON AIR FORCE BASE, OHIO

ROBERT ALLERTON PARK
(University of Illinois)
Monticello, Illinois

14, 15, 16, 17, 18 October, 1963

UNCLASSIFIED

NOTICES

When Government drawings, specifications, or other data are used for any purpose other than in connection with a definitely related government procurement operation, the United States Government thereby incurs no responsibility nor any obligation whatsoever; and the fact that the Government may have formulated, furnished, or in any way supplied the said drawings, specifications, or other data is not to be regarded by implication or otherwise as in any manner licensing the holder or any other person or corporation, or conveying any rights or permission to manufacture, use or sell any patented invention that may in any way be related thereto.

CONTENTS

BROADBAND ANTENNAS

- | | |
|--|---|
| Broadband Antenna Feeds for Aris Telemetry System | E. P. Valkenburg and J. C. Pullara, DYNATRONICS, INC., ORLANDO, FLORIDA |
| A Broadband Conical Scan Automatic Tracking Antenna System | R. L. Young, C. A. Lovejoy, and L. E. Williams, RADIATION, INC., MELBOURNE, FLORIDA |
| A Log-Periodic Cavity Slot Antenna | V. A. Mikenas and P. E. Mayes, UNIVERSITY OF ILLINOIS, URBANA, ILLINOIS |

MUTUAL COUPLING

- | | |
|---|--|
| Mutual Coupling Effects in Phased Array Antennas | Charles C. Allen, GENERAL ELECTRIC COMPANY, SCHENECTADY, NEW YORK |
| Coupling Effects with Slot and Spiral Antennas | R. M. Kalafus, R. B. Harris, Y. K. Kwon, and J.A.M. Lyon,, UNIVERSITY OF MICHIGAN, ANN ARBOR, MICHIGAN |
| Minimum Energy Patterns | H. C. Hiscox, WESTINGHOUSE ELECTRIC CORPORATION, BALTIMORE, MARYLAND |
| Antenna Polarization Analysis by Amplitude Measurement of Multiple Components | J. S. Hollis and L. Clayton, SCIENTIFIC-ATLANTA, INC., ATLANTA, GEORGIA |
| Log-Periodic Helical Dipole Arrays | D. T. Stephenson and P. E. Mayes, UNIVERSITY OF ILLINOIS, URBANA, ILLINOIS |

ARRAYS

- | | |
|--|--|
| Octave Bandwidth Multiple Beam Array | Martin E. Mehron, ADVANCED DEVELOPMENT LABORATORIES, NASHUA, NEW HAMPSHIRE |
| Array Factors with Zone-Plate Spacings | A. J. Mony and R. M. Hoge, NORTH AMERICAN AVIATION, COLUMBUS, OHIO |
-

CONTENTS (Continued)

Planar Array Antenna for Airborne
Surveillance Radar

G. A. Podolski, S. Slampyak,
R. Middlestead, and A. M. Smith,
PHILCO CORPORATION, BLUE BELL,
PENNSYLVANIA

A 500:1 Scale Model of WARLA -
The Wide Aperture Radio Location
Array

J. W. Greiser and G. S. Brown,
UNIVERSITY OF ILLINOIS, URBANA,
ILLINOIS

A Transistorized Beam Control Array

J. R. Copeland, OHIO STATE UNIVERSITY,
COLUMBUS, OHIO

LOADED ANTENNAS

Current Discontinuity Devices

B. J. Bittner, KAMAN-NUCLEAR COMPANY,
COLORADO SPRINGS, COLORADO

Ferrite Loaded-Slot and Traveling
Wave Antenna

A. T. Adams, J.A.M. Lyon, and
J. E. Herman, UNIVERSITY OF MICHIGAN,
ANN ARBOR, MICHIGAN

Analysis and Design of Tunnel Diode
Loaded Dipole Antennas

Kyohar Fujimoto, OHIO STATE UNIVERSITY,
COLUMBUS, OHIO

High Speed Ferrite Phase Shifters

Raymond F. Mix, GENERAL DYNAMICS,
POMONA, CALIFORNIA

Preparation and Submission of
Procurement Proposals

E. M. Turner, RESEARCH AND TECHNOLOGY
DIVISION, WRIGHT PATTERSON AIR FORCE
BASE, OHIO

ENVIRONMENTAL FACTORS

Hardened Antennas for Atlas and
Titan Missile Site Communications

D. L. Holzschuh, COLLINS RADIO
COMPANY, DALLAS, TEXAS

A Progress Report on 2000⁰ Antenna
Elements

John J. Earshen and R. J. Blum,
CORNELL AERONAUTICAL RESEARCH
LABORATORY, BUFFALO, NEW YORK

Dielectrics for Antennas

E. J. Luoma and D. J. Epstein,
EMERSON & CUMING, INC., CANTON,
MASSACHUSETTS

CONTENTS (Continued)

Corona and Breakdown as a Function of Humidity at Low Air Pressure	P. F. Stang, LOCKHEED AIRCRAFT COMPANY, BURBANK, CALIFORNIA
Ionization Enhanced Voltage Breakdown	C. A. Hinrichs, McDONNELL AIRCRAFT CORPORATION, ST. LOUIS, MISSOURI

ANTENNA PROTOTYPES

C-Band Beacon Antenna for Project Apollo	W. O. Puro and F. X. Linder, LITTON INDUSTRIES, INC., COLLEGE PARK, MARYLAND
HF Crossed-Slot Antenna and Applications	W. L. Snow, THE MARTIN COMPANY, DENVER, COLORADO
A Waveguide Resonant Ring Antenna Yielding an Omnidirectional Pattern	T. E. Charlton, E. R. Murphy, and J. W. Pool, MOTOROLA, INC., SCOTTSDALE, ARIZONA
B-70 Antenna System	E. D. Wegner, NORTH AMERICAN AVIATION, LOS ANGELES, CALIFORNIA
Summary of Aircraft Radome Shapes and Electrical Characteristics with Monopulse Antennas	G. M. Randall and D. F. Zemke, NORTH AMERICAN AIRCRAFT CORPORATION, ANAHEIM, CALIFORNIA

PAPERS NOT PRESENTED

An S-Band Conical Spiral Antenna for Space Vehicle Application	R. J. Eckstein, MOTOROLA, INC., WESTERN CENTER, SCOTTSDALE, ARIZONA
Automatic Calibration Systems for Tracking Radars	Leonard Blaisdell, SYLVANIA ELECTRONICS SYSTEMS-EAST, WALTHAM, MASSACHUSETTS
Boresight Errors in the Near Field of a Monopulse Antenna	Peter R. Zuzolo, Stanley J. Jurczak and Joseph A. Castrigno, REPUBLIC AVIATION CORPORATION, ENGINEERING DIVISION, FARMINGDALE, NEW YORK
The Solution for Antenna Array Input Impedance by the Method of Symmetrical Components and an Alternating Current Network Calculator	Jack W. Pool, MOTOROLA, INC., MILITARY ELECTRONICS DIVISION, WESTERN CENTER, SCOTTSDALE, ARIZONA
Hydroacoustic Simulation of Antenna Radiation Characteristics	M. L. Parker, Jr., W. A. Meyer and H. J. Hewitt, MELPAR, INC., FALLS CHURCH, VIRGINIA

BROADBAND ANTENNA FEEDS

FOR

ARIS TELEMETRY SYSTEM

BY

E. P. Valkenburg and J. C. Pullara

Dynatronics, Inc.
Box 2566
Orlando, Florida

Presented at

USAF Antenna Symposium
Monticello Facility
University of Illinois
15-18 October 1963

BROADBAND ANTENNA FEEDS FOR ARIS TELEMETRY SYSTEM

by

E. P. Valkenburg and J. C. Pullara

The antenna feed systems described in this paper were designed and developed to satisfy the broadband telemetry tracking requirements of two Advance Range Instrumentation Ships (figure 1). Each ship is instrumented with tracking and data collection equipment considered by many to be more sophisticated than most existing tracking facilities on the Atlantic Missile Range. The additional ability of the ARIS System to be deployed in support of almost any mission has greatly increased the capabilities of the Atlantic Missile Range.

The ARIS Telemetry Antenna System is capable of auto-tracking and collecting data at any frequency in the bands 215 to 1000 mc and 12.5 to 14.5 gc; thus fulfilling both current and future telemetry requirements. Two independent conically scanned feed systems are provided to illuminate the 30-foot diameter solid reflector ($f/d = 0.29$) as shown in figure 2. The Broadband Feed SF-1 (215-1000 mc) is supported at the focal point of the dish by an octapod spar configuration while the Ku-Band Feed SF-4 (12.5 to 14.5 gc) is located at the vertex of the parabolic reflector. The vertex feed operates on the Cassegrain principle and is functional only when the hyperbolic sub-reflector is mounted between the broadband feed and the main dish. The requirement for circular polarization on each of the feed systems prohibits simultaneous operation in both frequency bands. The sub-reflector is therefore designed to be easily removed and accurately re-positioned.

Both feeds are conically scanned at 1200 rpm to produce a 20-cycle error signal required to provide a tracking performance compatible with the high angular acceleration capability of the telemetry antenna of 30 degrees per second per second. The 20-cycle scan rate also serves to ensure an adequate safety margin between the inherent vibrations of the feed and the natural resonant frequencies of other antenna system components. Each feed is precision balanced to less than 1-mil double deflection as measured at the bearing housing to insure a minimum vibration and a maximum feed operating life.

The conical scan system employed for this program provides two advantages not available in most conventional systems: "spurious modulation cancellation" and "scanning symmetry". The simultaneous dual channel operation of the feeds provides for spurious modulation cancellation by combining the true error signals, which are inherently 180 degrees out of phase, with the spurious modulations which are always in-phase with respect to each feed element. By using special combining techniques the desired error signals are made to reinforce while the unwanted spurious modulations are cancelled.

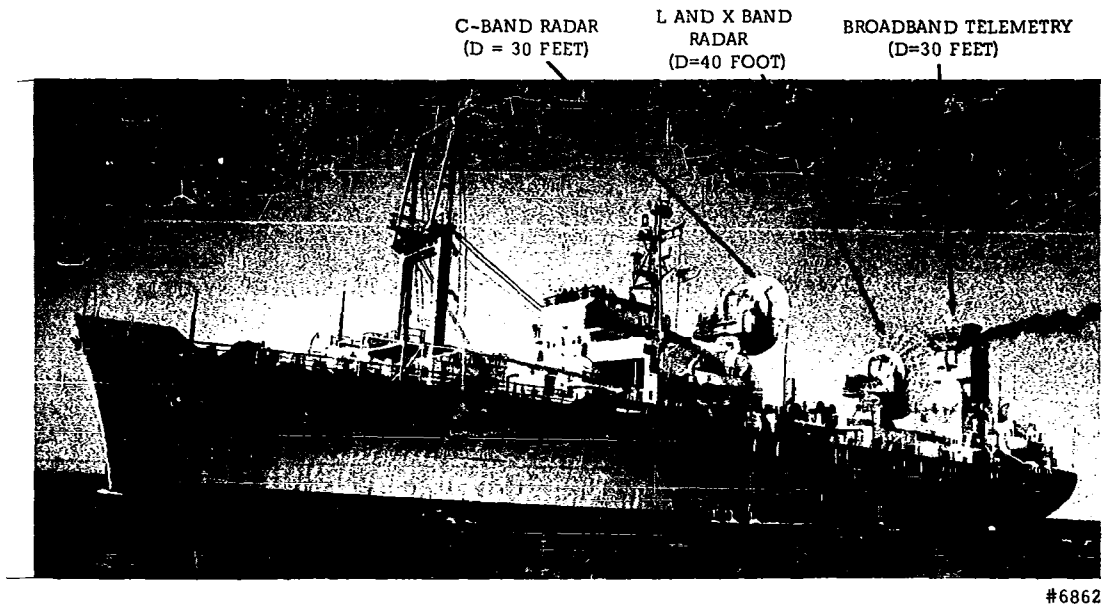


Figure 1. Advance Range Instrumentation Ship

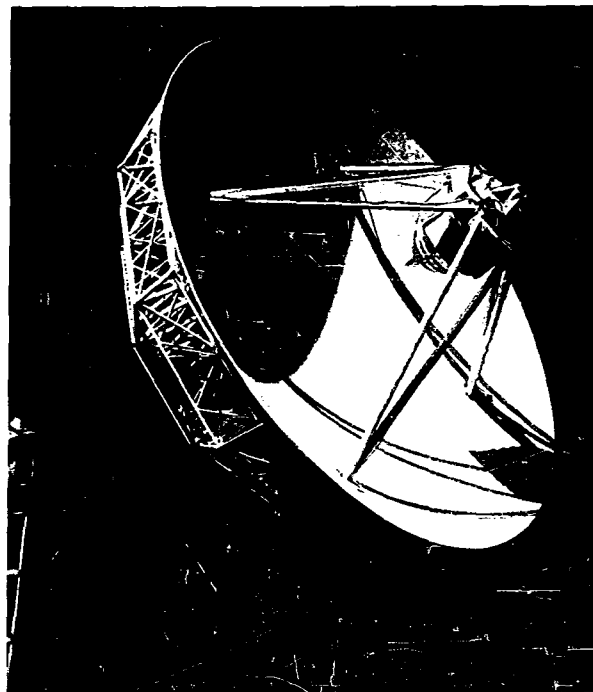


Figure 2. Telemetry Antenna on Test Range
(Without Cassegrain Reflector)

Scanning symmetry, realized by rotating the entire feed structure about its axis of symmetry, reduces the pointing error normally encountered in conventional scan systems, employing offset-waveguide, scanning splash plates and other techniques. Pointing errors in conical scan systems are partially due to nutation noise, i.e., modulation of feed impedance, axial ratio, pattern, etc. produced by the scanning device. Nutation noise of the feed and its rotary joint can therefore be held to a minimum by careful design of mechanical symmetry in both the feed and its environment.

The symmetry and phasing properties of the broadband feed configuration permit increased pointing accuracy as a result of the cancellation of spurious amplitude modulation and other unwanted signals caused by multipath and missile spin. This dual-channel system attains an accuracy comparable to that of a monopulse system without the complexities associated with such a system, and these characteristics are attained over a bandwidth greatly exceeding that of a multi-channel phase coherent receiving system.

This paper describes the design philosophy employed in the r-f development of each of the feeds and presents the performance of each feed when installed in the 30-foot reflector.

Broadband Feed SF-1 (215-1000 mc)

The feed comprises two oppositely wound conical spiral antennas (figure 3) which permit simultaneous reception of left and right circularly polarized waves. The conical spiral antenna belongs to the class of frequency independent antennas and therefore provides essentially constant beamwidth, axial ratio, and impedance over the operating band. The spiral is fed at the tip of the cone with a broadband balun to provide a balanced transformation from the 50-ohm coaxial line impedance at the base of the cone to the 150-ohm characteristic impedance of the antenna. This transformation is realized by a rigid coaxial line whose outer conductor is linearly tapered. Tchebychev and logarithmic taper functions were considered; however, the performance improvements were not sufficient to justify the associated increase in fabrication costs.

The successful operation of the balun depends on the degree of symmetry realized in its fabrication. If balun symmetry is not realized, a substantial increase in VSWR, axial ratio and pattern asymmetry will be experienced.

A 10 db beamwidth of 162 degrees is required of the feed to provide an illumination of the 30-foot reflector ($f/d = .29$) commensurate with the required gain and sidelobe performance. This requirement was fulfilled by a 30-degree cone with a conductor pitch angle of 73 degrees. The length of the cone is dictated by the requirement that the base diameter must be one wavelength in circumference at the lowest operating frequency (215 mc). An additional length (20-30%) is commonly employed to insure a strong and symmetrical radiating current band and to minimize interference caused by current reflection at the end of the conductor. The design parameters of each cone (figure 4) were established on the basis of work performed at the University of Illinois, (references 1 and 2) and experimental measurements conducted at Dynatronics, Inc.



#4714-A

Figure 3. Dual Cone Assembly Without Shroud

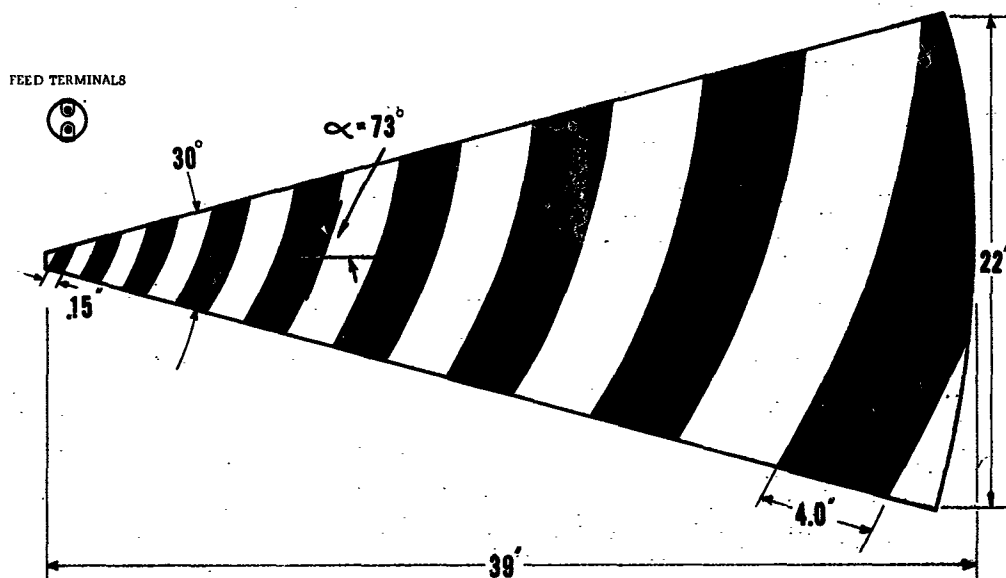


Figure 4. Conical Spiral Parameters

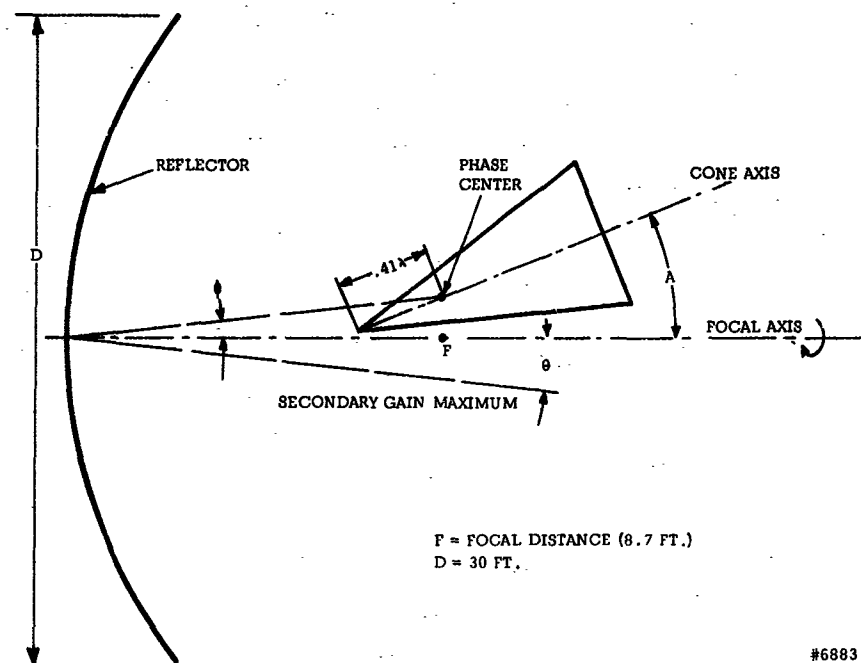


Figure 5. Geometry Employed for Calculating Cone Offset Angle

The two cones are positioned diametrically opposite the reflector focal axis so that each cone axis forms a 22-degree angle with respect to the axis of the rotation. The angle of 22-degrees was predetermined to provide a constant electrical spacing between the phase center and the axis of rotation, independent of the frequency of operation.

The following equations demonstrate that an angle "A" can be found to provide a constant crossover level independent of frequency (figure 5):

$$(1) \quad \theta = k \varnothing; \quad \text{where } k = \text{beam deviation factor} < 1$$

and,

$$(2) \quad \tan \varnothing \approx \varnothing = \frac{.41 \lambda \sin A}{F}; \quad \text{for } \varnothing < 10^\circ$$

where, $.41 \lambda$ is the position of the phase center along the axis of a 30 degree cone with a 73 degree conductor pitch angle; therefore, substituting (2) in (1):

$$(3) \quad \theta = \frac{K .41 \lambda \sin A}{F}$$

For any given aperture illumination; it can be shown that:

$$(4) \quad \frac{BW}{2} = \frac{K \lambda}{2D}; \quad \text{where } BW = \text{beamwidth and } K \text{ is a constant in degrees.}$$

For the special condition when,

$$(5) \quad \frac{K}{2D} = \frac{(k) (.41) \sin A_1}{F}$$

Substituting (5) in (3) produces:

$$\theta = \frac{K \lambda}{2D}$$

And finally from (4):

$$\theta = \frac{BW}{2}$$

This means that for some angle A, where $A = \sin^{-1} \left(\frac{KF}{2(.41) Dk} \right)$,

$\frac{BW}{2}$ will change in proportion to a change in θ to provide a constant crossover level independent of frequency.

For the parameters of the ARIS Program, and crossover at 1 db:

$$D = 30 \text{ feet}$$

$$K = 40^\circ \text{ or } .7 \text{ radians for } BW_{1 \text{ db}} \text{ (reference 3)}$$

$$k = .81 \text{ for } f/d = .29$$

$$F = 8.7 \text{ feet}$$

$$A = \sin^{-1} \frac{(K) F}{2 (.41) D (k)}$$

Therefore:

$$A = 18 \text{ degrees.}$$

It should be noted that the solution for "A" does not account for the beam-broadening which is experienced at the extremes of the band due to defocusing. Nor does the solution account for the change in F, used in the expression:

$$\tan \phi = \frac{.41 \lambda \sin A}{F},$$

which is experienced as the phase center moves along the cone axis as a function of frequency.

The calculated value of A = 18 degrees was used as the starting point of an experimental program designed to establish the optimum value of "A" for a minimum change in crossover as a function of frequency. The experimental program resulted in a value A = 22 degrees.

The dual cone assembly is positioned in the reflector so that the axis of rotation is coincident with the focal axis. The feed is located along the focal axis so that the phase center position associated with the arithmetical mean frequency between 215-960 mc lies in the focal plane of the reflector. This positioning provides a minimum and equal amount of defocusing (.65 db loss in gain) at the extremes of the operational frequency band.

The mechanical design considerations required to produce a feed with the electrical characteristics described above and a strength-to-weight ratio commensurate with the requirement for 1200 rpm rotation, could be the subject of another paper. It should be noted that the 1200 rpm rotation produces a velocity of 185 mph and a force of about 1000 g's at a point on the periphery of the cone assembly at its largest diameter (5 feet). A precision balanced rotating structure is required to ensure the continuing operation of the feed under these extreme conditions. The curve of figure 6 shows the variation of dynamic balance as a function of time for a period of 24 hours. The variation in balance from t = 0 to t = 5 hours is due to the variation of coefficient of expansion of the materials in the feed. Stabilization of balance and temperature is realized after 5 hours of running time.

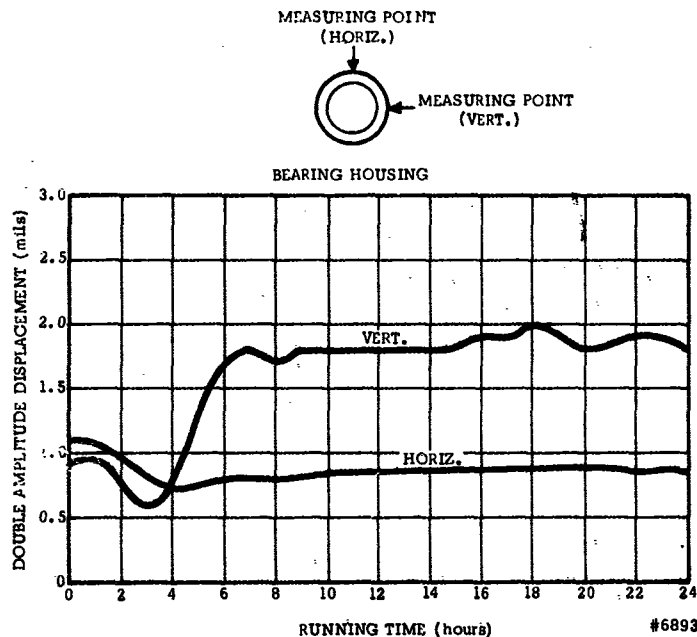


Figure 6. Balance vs Time

The two cones are encased in a conical shroud (5 feet in diameter at the base), (figure 7) which serves to minimize the driving horsepower and to reduce the heat produced by air turbulence within the radome. The rotating cone assembly is coupled to a shaft which is driven at 1200 rpm in the main housing structure. The housing contains the drive motor, reference generator, rotary joint, heaters, and blowers. The conical radome serves to protect the precision balanced assembly from the elements and reduces the wind loading under high speed operation.

The broadband dual channel rotary joint (RT-50) transfers the r-f energy from each of the rotating cones through a constant impedance to fixed transmission lines. The narrow band frequency limitations of most high speed rotary joints has been overcome by replacing the commonly used choke-joint with spring loaded contacting surfaces. The resultant unit provides the required broadband operation with a VSWR of less than 1.5 to insertion loss less than 0.5 db, and WOW less than 1.1 to 1.

The performance of the broadband feed after installation in the 30-foot diameter reflector was measured by ITT Federal Laboratories at the Kennedy Antenna Division Range.

Beamwidth - (3db)

The data presented in figure 8 shows measured beamwidths slightly wider than those calculated using a cosine 1.5θ illumination function. The difference is partly due to the effects of blockage caused by the 5-foot diameter feed and eight 5-inch diameter spars.



#6894

Figure 7. Broadband Feed With Radome Removed

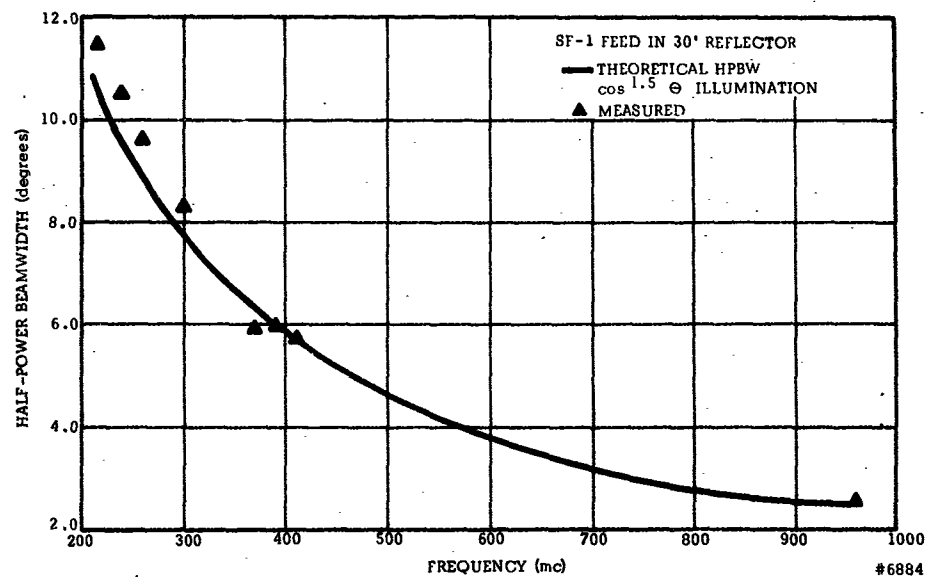


Figure 8. Beamwidth (3 db) vs Frequency

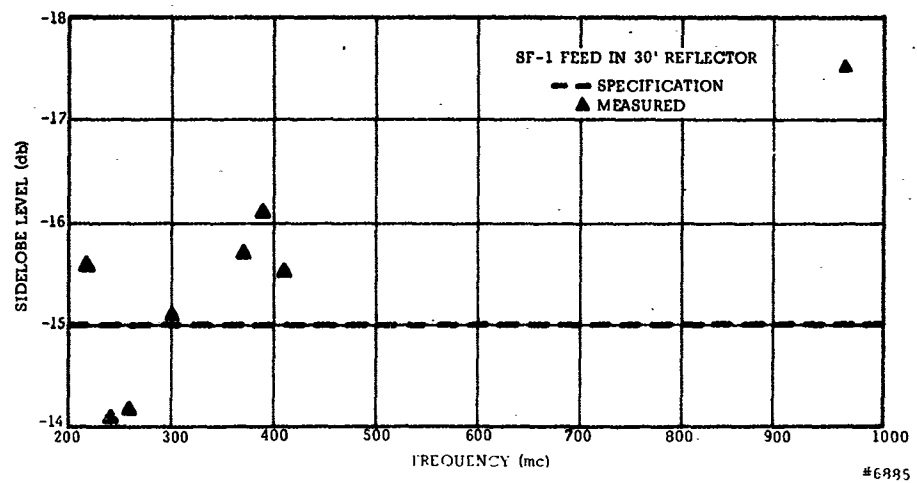


Figure 9. Sidelobe Level vs Frequency

Sidelobe Level

The data presented in figure 9 shows the average sidelobe level at each frequency. A sidelobe variation was experienced as a function of the proximity of spars with respect to the plane of investigation. The 5-inch metallic spars generated a sidelobe level variation of about 2.5 db.

Gain

The solid curve of figure 10 shows the results of a thorough analysis to determine the gain of a 30-foot reflector over the band. The analysis considered all losses to be encountered in the feed including illumination taper, spillover, blockage, beam squint, defocusing, crossover, surface tolerance, rotary joint insertion loss, feed loss, cable loss, and VSWR loss. Most of these parameters are independent of frequency. The average efficiency of the system at the crossover point is 25 percent. If crossover is neglected, the gain increases 1 db, resulting in an efficiency of 32 per cent. It should be noted that the commonly accepted value of reflector efficiency of 55 per cent does not include losses due to beam squint, defocusing, rotary joint, cables and VSWR.

The deviations between the calculated gain and the measured points cannot be fully explained at this time. The close correlation between points in the 215-300 mc range, the sudden drop of 2 db in the range from 350 to 450 mc, and a further drop of 2 db at 960 mc, correspond to changes in reference antennas. Due to delivery commitments, time did not permit recalibration of the reference standard gain antenna and a re-measurement of the gain.

Axial Ratio

The axial ratios presented in figure 11 were measured at the crossover point where the power level is between 1 db and 2 db below the peak of the beam. Based on scale model measurements made at Dynatronics, Inc., axial ratio improvements on the order of 1 db can be expected at the beam maximum.

Crossover Level

The offset of the cones from the focal axis was designed to provide a crossover of 1 ± 0.5 db. The calculations assumed a constant axial ratio across the secondary beam, whereas the measurements have shown a variation of approximately 1 db from the beam maximum to the crossover point. This omission in the calculation is partly responsible for the resultant crossover of 2 ± 0.5 db as shown in figure 12. Another reason for the difference between calculated and measured results is that vertical and horizontal polarizations were used for the measurements instead of circular. The data presented have not been corrected for axial ratio.

VSWR

The VSWR data presented in figure 13 was measured at the feed output terminals with the feed installed in the 30-foot reflector. The measurements include reflections from the cone assembly, parabolic reflector, rotary joint and associated connectors. The VSWR of the cone assembly alone is less than 2 to 1 while the rotary joint exhibits a VSWR of less than 1.5 to 1 over the band from 215 to 1000 mc.

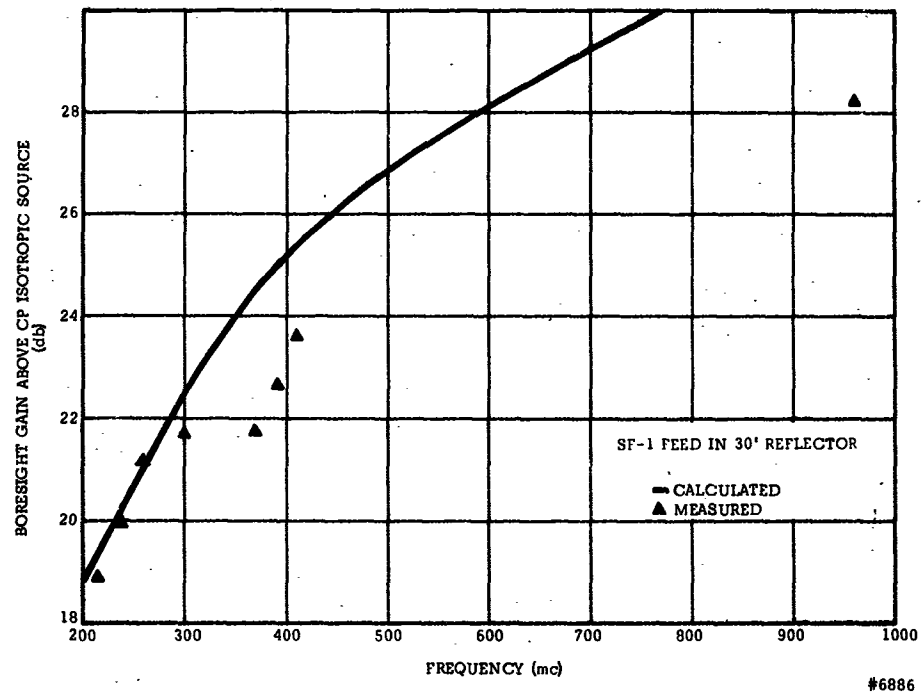


Figure 10. Boresight Gain vs Frequency

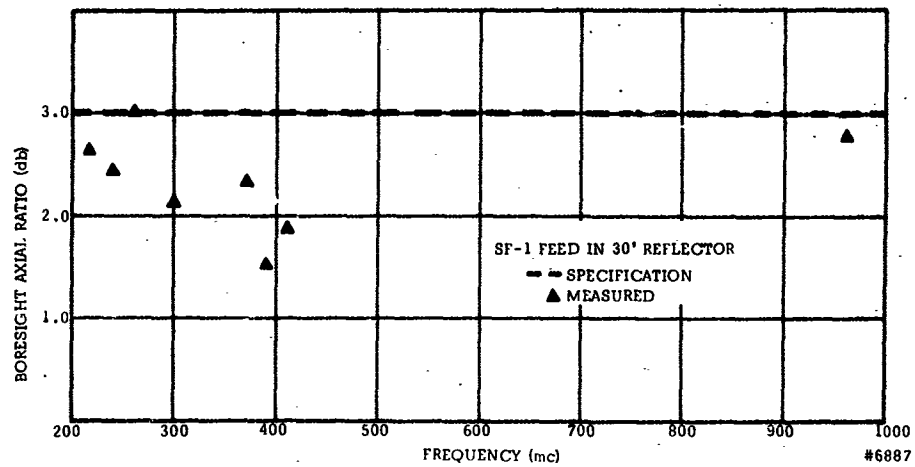


Figure 11. Boresight Axial Ratio vs Frequency

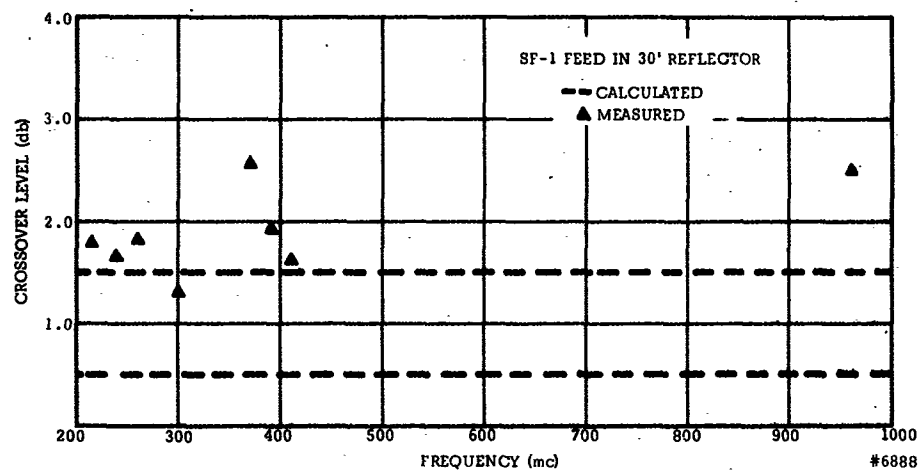


Figure 12. Crossover Level vs Frequency

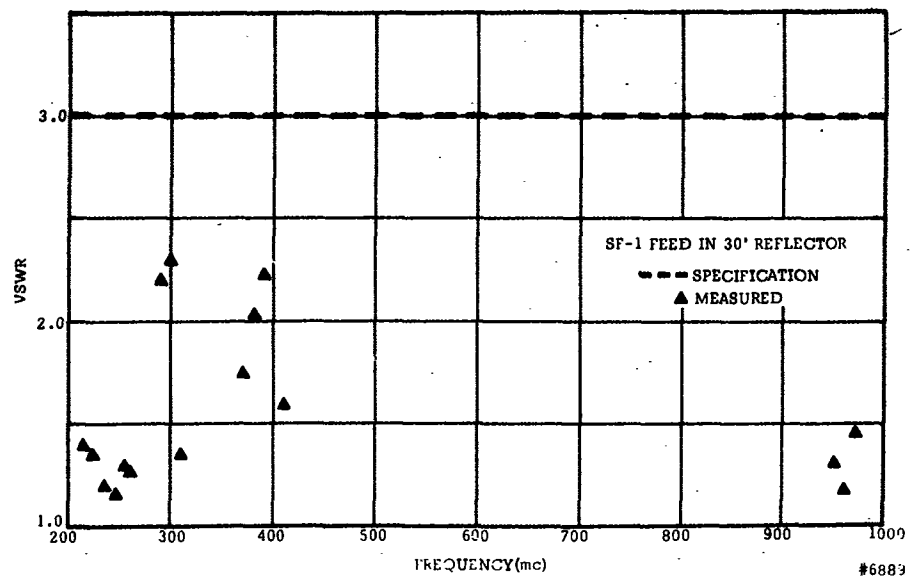
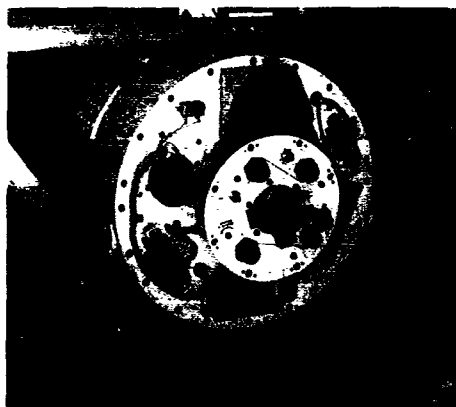
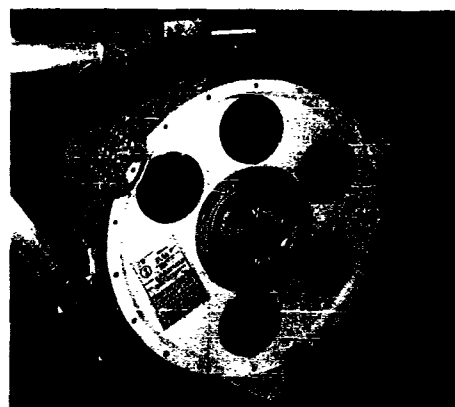


Figure 13. VSWR vs Frequency



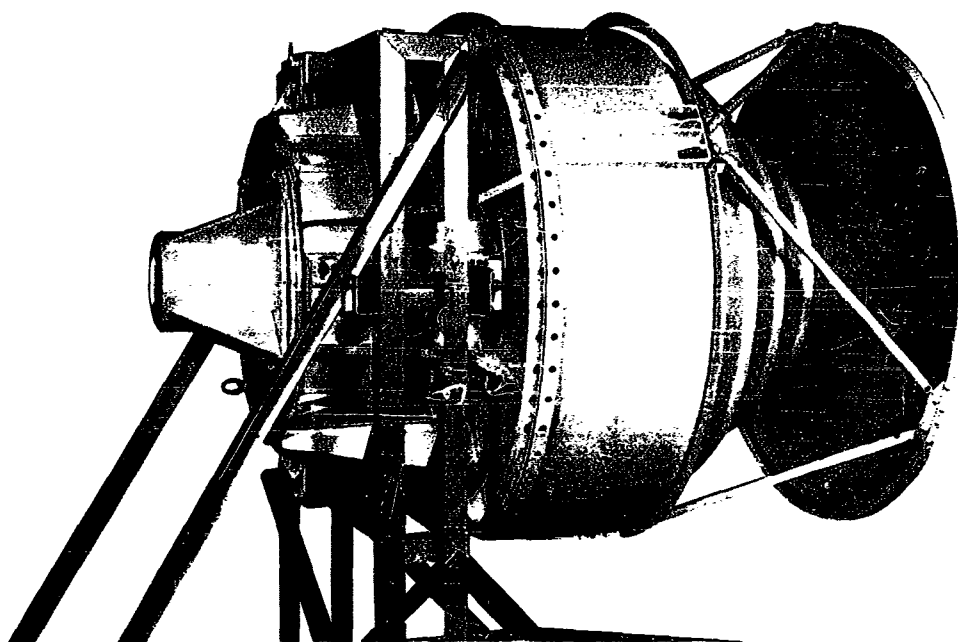
Front View



Rear View

#6895

Figure 14. Front and Rear View of Vertex Feed



#6871

Figure 15. Cassegrain Reflector Mounted on Broadband Feed

Vertex Feed SF-4 (12.5 to 14.5 gc)

The vertex feed employs the same basic operating principles as the broadband feed in that it provides polarization diversity, two independent but simultaneous channels, and scans at a 1200 rpm. The conical spirals are replaced in the SF-4 feed with two circularly polarized horns as shown in figure 14. The waveguide horns operate over the frequency band from 12.5 to 14.5 gc and generate circular polarization through a quarter wave dielectric plate in the circular waveguide at a 45-degree angle with respect to the input rectangular waveguide. This technique of generating circular polarization was first developed at The Naval Research Laboratories and has since become a commonly used technique for producing circularly polarized waveguide antennas.

The 30-foot parabolic reflector is easily converted to receive telemetry signals in the 12.5 to 14.5 gc band by installing a 5-foot diameter hyperbolic reflector immediately in front of the broadband feed as shown in the photograph of figure 15. The resulting Cassegrain system provides a means of using the 30-foot parabolic reflector for telemetry tracking in two greatly separated frequency bands without having to replace the entire feed system. The general design parameters for a Cassegrain antenna are shown in figure 16 (reference 4).

Normally, the feed would provide a well focused system for optimum gain and sidelobe performance. However, a defocused system was desired at 13.5 gc in order to increase the 0.17 degree beamwidth of the 30-foot reflector. The wider beam increased the cone of acquisition and keeps the crossover slope within the tracking capabilities of the servo system.

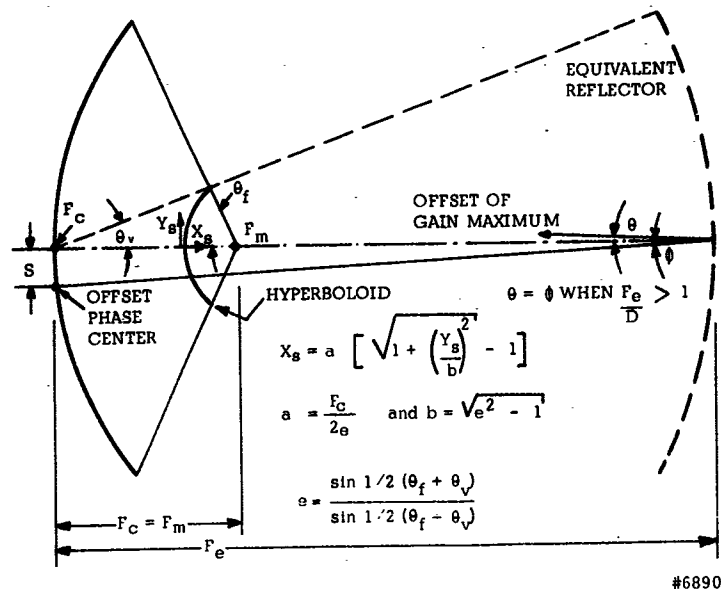


Figure 16. Design Parameters of a Cassegrain System

Movement of the feed from the focal point along the focal axis produces the quadratic phase error needed to generate a wider beam. The amount of feed displacement required can be calculated by comparing the path lengths of all rays incident upon the reflector. The maximum difference in path length will occur between the incoming ray which strikes the edge of the equivalent parabolic reflector and that which strikes the center of the reflector as shown in figure 17. This difference is used to determine beam broadening and gain loss. Calculations were verified by experimental measurements performed at 2200 mcs on a Newtonian system ($f/d = .4$). The results of these measurements shown in the chart of figure 18 illustrate the increase in beamwidth and reduction in gain as a function of feed displacement.

The experimental program showed a very close correlation with the theoretical analysis presented by Lechtrek (reference 5) in the variation of beamwidth as a function of phase error. However, a greater loss in gain was experienced experimentally than was predicted by Lechtrek. It is believed that the complex phenomena of blockage and reflector surface tolerance is responsible for the difference between the predicted and measured gain function.

The design of the defocussed Cassegrain system was based on the experimental measurements. The fact that the measurements and calculations were made for a Newtonian system does not restrict their application since the Cassegrain system can be analysed as an equivalent Newtonian system, as proposed by Hannon. The normalization of phase error to radians makes it possible to apply these results to any f/D system.

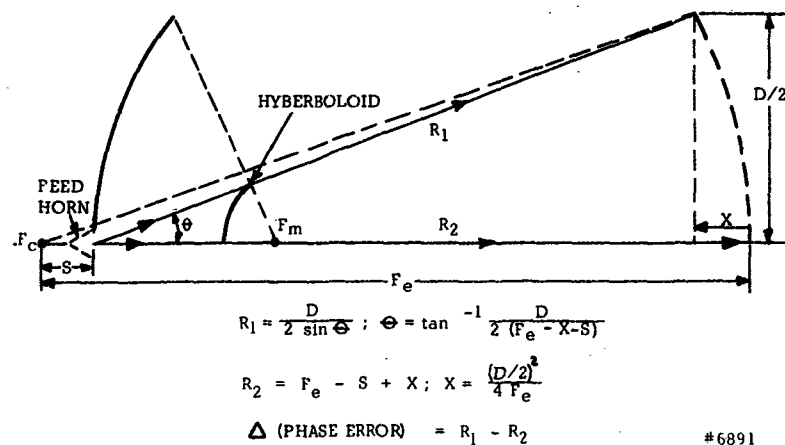
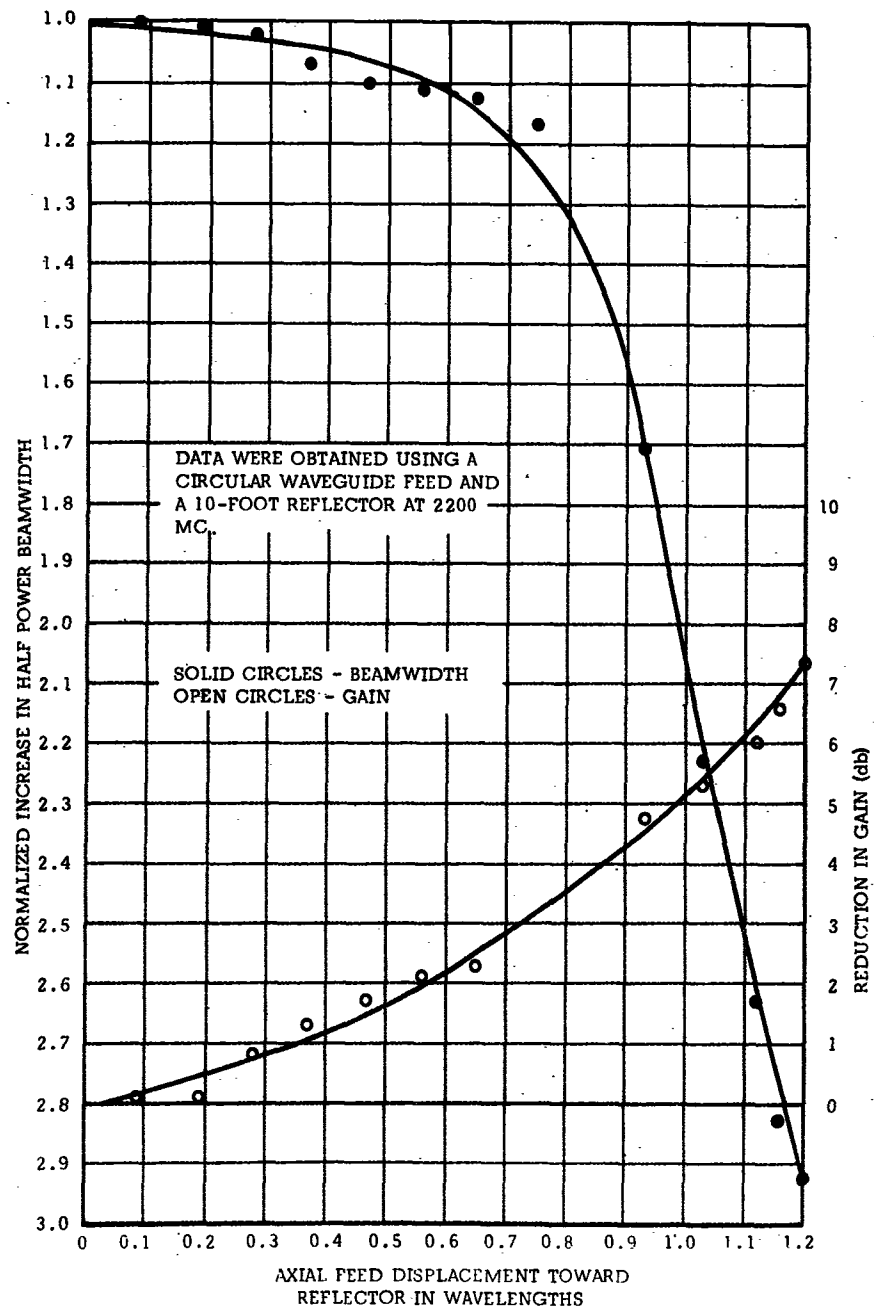


Figure 17. Ray Geometry in Defocussed Cassegrain System



#4564

Figure 18. Effects of Axial Displacement on the Pattern of a Parabola of $F/D = 0.4$

The design objective in defocusing the Cassegrain antenna system was to provide a maximum beamwidth without main beam bifurcation. It can be seen from the curves presented in Lechtrek's article that 5.26 radians of phase error will cause bifurcation of the main beam. In order to provide a reasonable safety margin in defocusing the beam prior to bifurcation, the vertex feed was removed from the focal point by 18 inches to give a phase error of 4.18 radians. This amount of phase error resulted in half power beamwidth broadening from .17 to .47 degrees and a decrease in gain of 6.5 db.

The following table presents a comparison between the feed design specifications and the measured data. In general, differences in measured and calculated data can be explained by the same discussions presented for the Broadband Feed, Model SF-1.

	<u>Specs.</u>	<u>Measurement</u>
Gain	49 db	47.7 db
Sidelobe	-15 db max.	-17.6 db
B.W.	0.45°	0.47°
A.R.	3.0 db max.	1.9 db
Crossover	1.5 ± .5 db	1.2 db
VSWR	2.0 max.	1.6

Summary

The design and development of dual-channel, conically scanned tracking feed systems has provided significant improvements in the utility and performance of tracking and telemetry systems exceeding those previously attained with conical scan auto-track antenna systems currently available. The capability of simultaneous reception of RCP and LCP, frequency diversity capabilities, coherent noise cancellation, and broadband performance are a few of the areas of considerable improvement.

Although the Broadband Feed SF-1 is used in this application to cover the band from 215 to 1000 mc, the basic feed elements are capable of operating continuously to 2300 mc. The factors limiting the operation of the Model SF-1 Feed to the range 215 to 1000 mc are, 1) the location of the feed with respect to the focal point of the dish and, 2) the limited frequency range of the rotary joint. The position of the feed with respect to the dish focal point dictates the amount of loss in gain due to defocusing. The feed is positioned for maximum gain in the 215 to 1000 mc band. The rotary joints (RJ-50T) delivered with the SF-1 feed systems are capable of operating in the center channel from 100 to 2300 mc but are limited in the outer channel from 100 to 1000 mc.

Dynatronics, Inc. has since increased the frequency coverage of the rotary joint and the new Model RJ-51 is currently being used in improved Broadband Feeds SF-2 to cover the frequency range from 100 to 2300 mc.

ACKNOWLEDGEMENT

The authors wish to acknowledge the contributions made by J. E. Lemon in designing the defocussed Cassegrain System. The subject feed systems were designed and developed for ITT Federal Laboratories, Nutley, New Jersey.

REFERENCES

1. Dyson, J. D. and Mayes, P.E. " New Circularly - Polarized Frequency - Independent Antennas with Conical Beam or Omni-Directional Patterns ", PGAP Transactions, July 1961
2. Dyson, J. D. " The Unidirectional Equiangular Spiral Antenna " PGAP Transactions, October 1959
3. ITE Antenna Handbook, pages 4 and 6
4. Hannon, P.W. " Microwave Antennas Derived from the Cassegrain Telescope " PGAP Transactions, March 1961
5. Lehtrek, L. W. " Fresnel Antenna Patterns " PGAP Transactions July 1955

A BROADBAND CONICAL SCAN
AUTOMATIC TRACKING ANTENNA SYSTEM

FOR PRESENTATION AT
THIRTEENTH ANNUAL SYMPOSIUM ON
USAF ANTENNA RESEARCH AND DEVELOPMENT

UNIVERSITY OF ILLINOIS

15 - 18 OCTOBER 1963

- L. R. Young
- C. A. Lovejoy
- L. E. Williams

Radiation Incorporated
Melbourne, Florida

A BROADBAND CONICAL SCAN
AUTOMATIC TRACKING ANTENNA SYSTEM

By: L. R. Young
C. A. Lovejoy
L. E. Williams
Radiation Incorporated
Melbourne, Florida

SUMMARY

At the 12th Annual Symposium on USAF Antenna Research and Development, a broadband antenna system was described which utilized an array of four parabolic reflectors with log periodic feeds. Although designed primarily for phase monopulse operation, two such antenna systems were recently adapted for automatic tracking using conical scan techniques. Variable phase shifters were developed which produce essentially a constant differential phase shift over a frequency band of 2:1 or more. These non-contacting phase shifters consist of a combination of both low- and high-pass constant K filters with variable LC elements. For a given variation in L and C, the relative phase shift of the low-pass filter increases with frequency whereas the high-pass phase shift decreases with frequency in the pass band. With proper design a differential phase shift of about ± 25 degrees can be obtained over a 2:1 frequency band with a VSWR of less than 2:1. Calculated and measured performance data are given for both the phase shifters and the antenna systems utilizing the phase shifters.

INTRODUCTION

A broadband antenna array has been described that is capable of operation over a bandwidth of a decade or more.* The array consists of a cluster of four parabolic reflectors arranged in a diamond and each reflector is fed with a frequency independent feed. When the array is utilized as a monopulse automatic tracking system, it is necessary to provide hybrid comparators and three channel monopulse receivers to cover the entire frequency band and the system becomes complex and expensive. To simplify the system and reduce cost a conical scan technique was developed which utilizes a variable phase shifter in series with each element of the array for error signal generation and a single channel tracking receiver.

Most phase shifters are essentially "line-stretchers" and the phase shift, for a given change in electrical length, varies directly with frequency. To achieve broadband conical scan and maintain a constant crossover depth with the array a constant differential phase shift with frequency is required. For this reason the "line-stretcher" type of phase shifters are limited to frequency bands appreciably less than 2:1. The combination of high-pass and low-pass constant K filter phase shifters described herein have a theoretical differential phase shift that is constant within approximately $\pm 10\%$ over a 3:1 frequency band.

Scanning by means of diode switching or by means of varactor filters tends to be noisy and to introduce more insertion loss than a simple passive noncontacting variable filter.

THE METHOD OF SCAN

The method of producing conical scan by means of variable phase shifters is illustrated in Figure 1. There are four variable phase shifters, one in series with each antenna element, that are driven in the proper electrical phase to squint the secondary pattern of the antenna sequentially around the boresight and produce conical scan. As frequency increases, the beam width of the antenna decreases and the amount of squint required for a particular value of crossover reduces in proportion. The differential phase shift required to maintain a constant crossover level with fixed element spacing is independent of frequency as illustrated in the derivation in Figure 2. In this derivation it is assumed that the phase across the aperture of the antenna is constant over the surface of each reflector. It is also assumed that the two center reflectors have the same relative reference phase while

* Williams, L.E., "A New Broadband Tracking Antenna," 12th Annual Symposium on USAF Antenna Research and Development; October 1962.

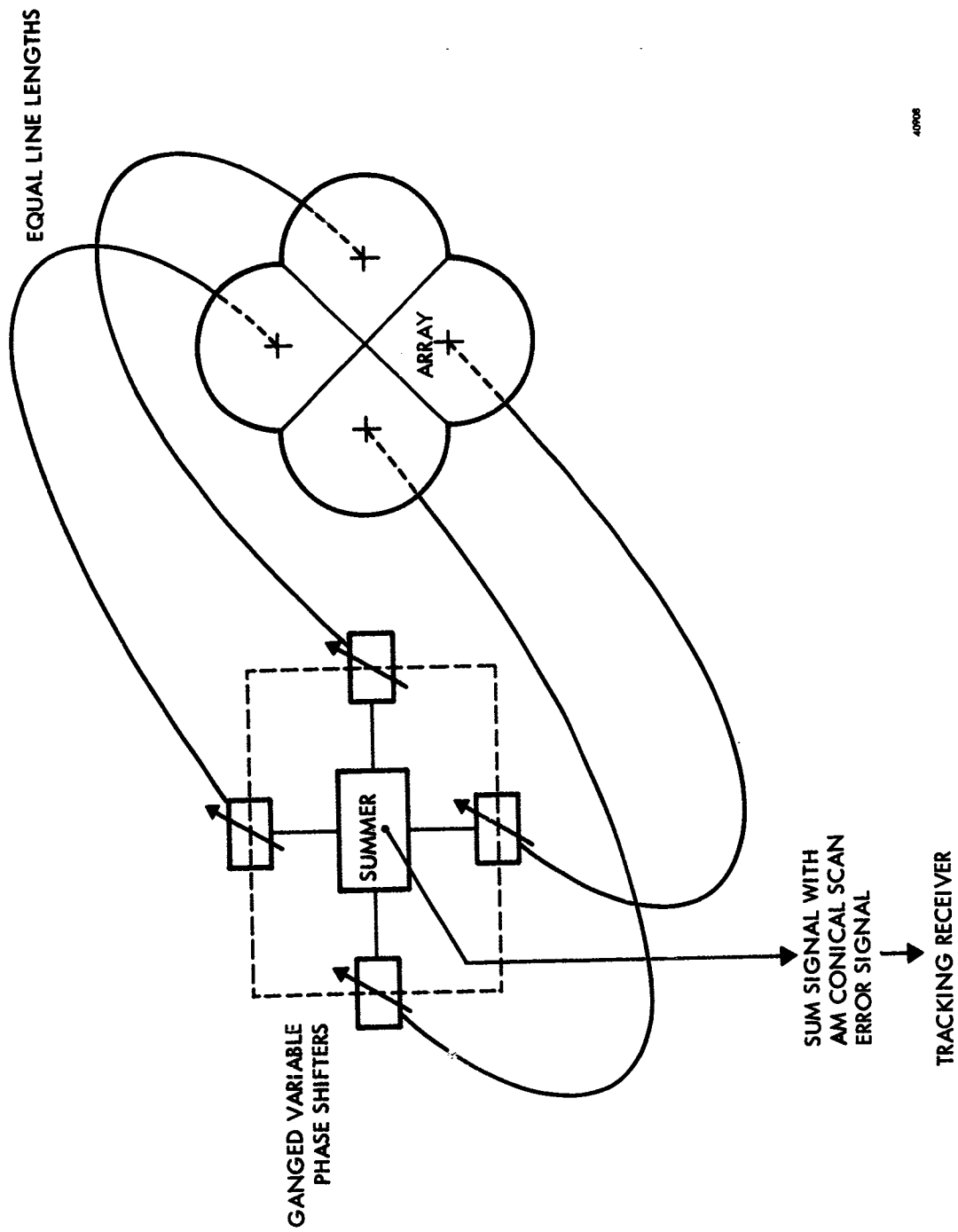
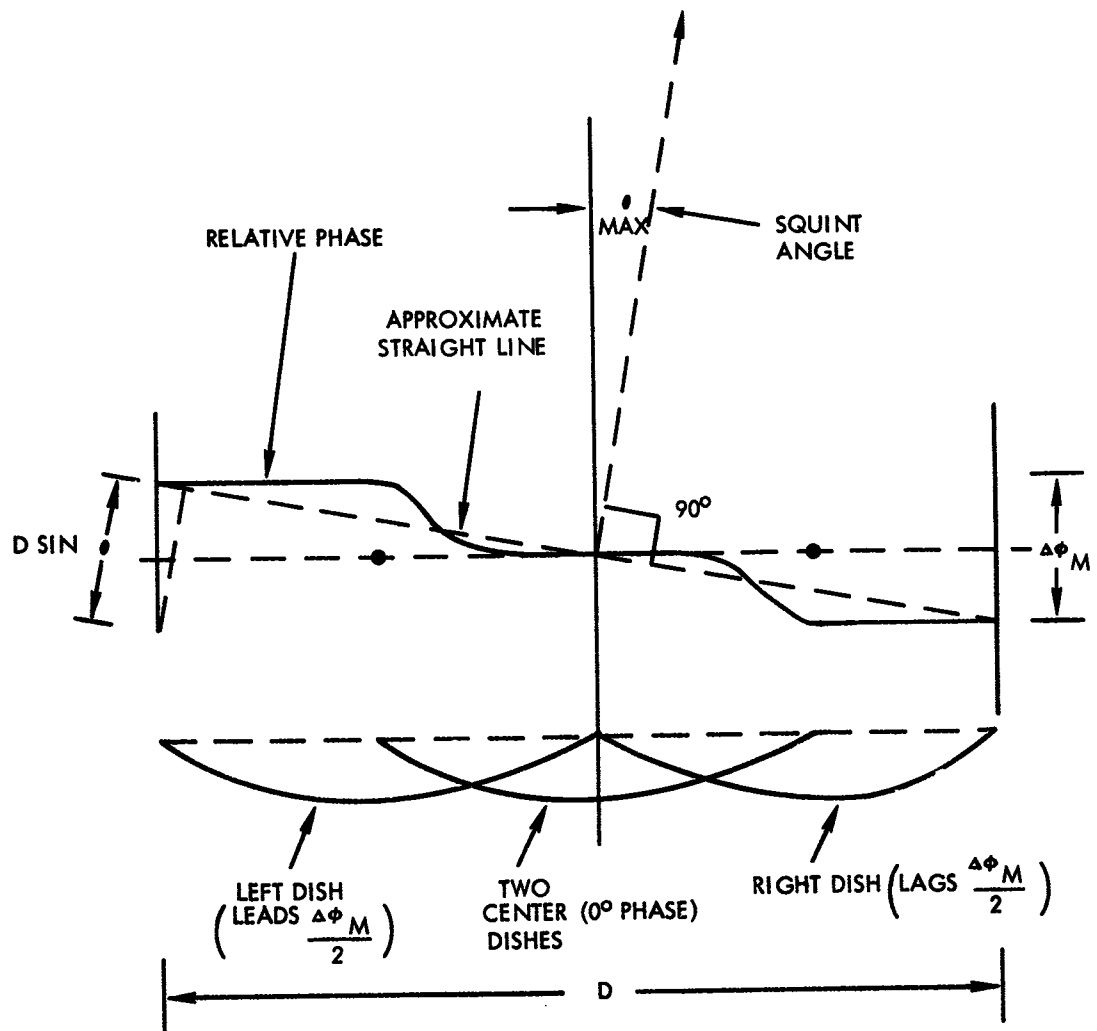


Figure 1. Method of Scan - Block Diagram



$$BW \approx \frac{64\lambda}{D} \text{ DEGREES}$$

$$\text{LET MAXIMUM SQUINT ANGLE} = \theta_{\text{MAX}} = K(BW) = \frac{64\lambda}{D} \text{ DEGREES}$$

$$\text{MAXIMUM DIFFERENTIAL PHASE SHIFT BETWEEN RIGHT AND LEFT ELEMENTS} = \Delta\phi_M = \frac{2\pi D}{\lambda} \sin \theta$$

ASSUME $\sin \theta \approx \theta$ (SMALL ANGLES)

$$\text{NOW, } \Delta\phi_M = \frac{2\pi D}{\lambda} K \frac{64\lambda}{D}$$

$$\text{ON } \approx K 400 \text{ DEGREES AT ALL FREQUENCIES}$$

$$\pm K 200 \text{ DEGREES}$$

40909

Figure 2. Derivation of differential phase shift required for conical scan with a fixed crossover level.

the reflector on one side is advanced in phase and the reflector on the other side is retarded. The effective phase across the entire aperture essentially steps between the three levels and is approximated by means of a straight line as shown in the figure. If the maximum differential phase shift between the opposite reflectors is something less than 65 degrees, the maximum phase error across the aperture, with respect to the assumed linear phase, is less than $1/20$ of a wave length. Phase errors of this order of magnitude do not seriously affect the gain of the antenna. The equation, beam width = $64\lambda/D$, was determined from experimental measurements on similar antennas.

The variable phase shifters are physically small and can be operated at relatively high scan rates compared to the more general nutating feed systems. The feed systems are orthogonally polarized; horizontal and vertical or right and left circular polarizations are available. This feature permits the operator to track with one polarization utilizing conical scan and receive with the orthogonal polarization without conical scan thus realizing the full gain of the antenna. An alternate method of operation is to conically scan both polarizations and select the one with a larger signal level for the tracking signal and also the data channel. Various combining techniques are also possible. For instance, the two polarizations can be scanned 180 degrees out of phase and the error signals combined so as to cancel the effects of amplitude modulation, produced by the source or propagation path, that might fall in the scan frequency band.

Figure 3 is a crossover pattern produced by inserting a relative phase shift of ± 22.5 degrees into the two outside elements.

THE SCANNER

A schematic diagram of a single phase shifter is shown in Figure 4. This particular phase shifter consists of two low-pass " π " sections, and two high-pass "T" sections. Each L and C element of the phase shifter is variable, and all vary together so that they are maximum at the same time and minimum at the same time. The lumped inductances are varied by inserting conductors between the turns of a coil, thus, reducing the self and mutual inductance of the turns.

If the ratio of L/C remains constant, the impedance will remain virtually constant far into the pass band. The cutoff frequency varies inversely as the square root of L times C for both filter sections. The cutoff frequency of the high-pass filter is therefore minimum at the same time the cutoff frequency of low-pass filter is a minimum. The phase shift characteristic of a single T section high-pass filter is negative and varies from $-\pi$ at cutoff toward zero with increasing frequency. The phase shift characteristic of a single π section low-pass filter is π at cutoff and approaches zero with decreasing frequency. Figure 5 is a phase shift plot of a

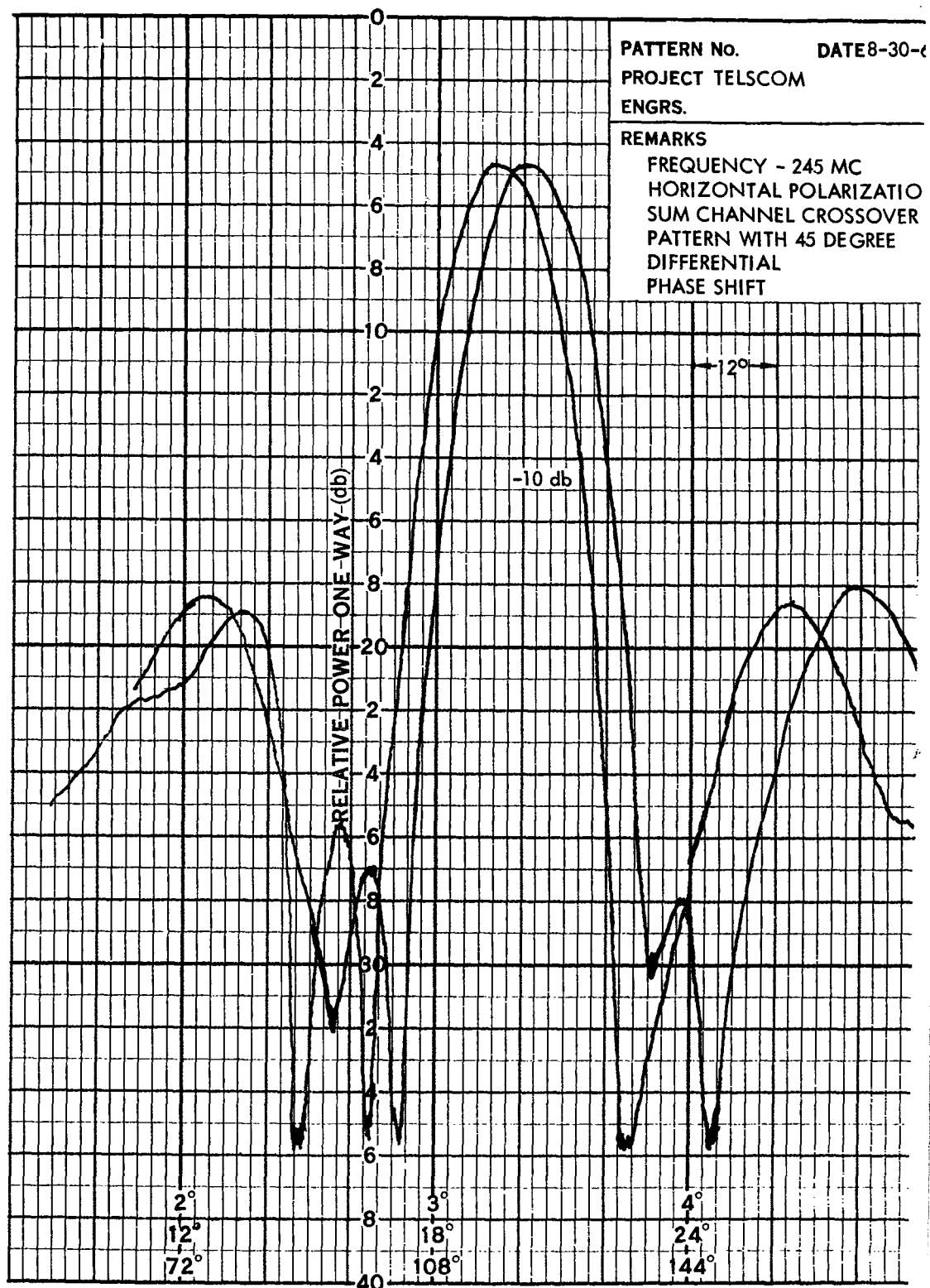


Figure 3. Sum Channel Crossover Pattern with 45° differential phase shift.

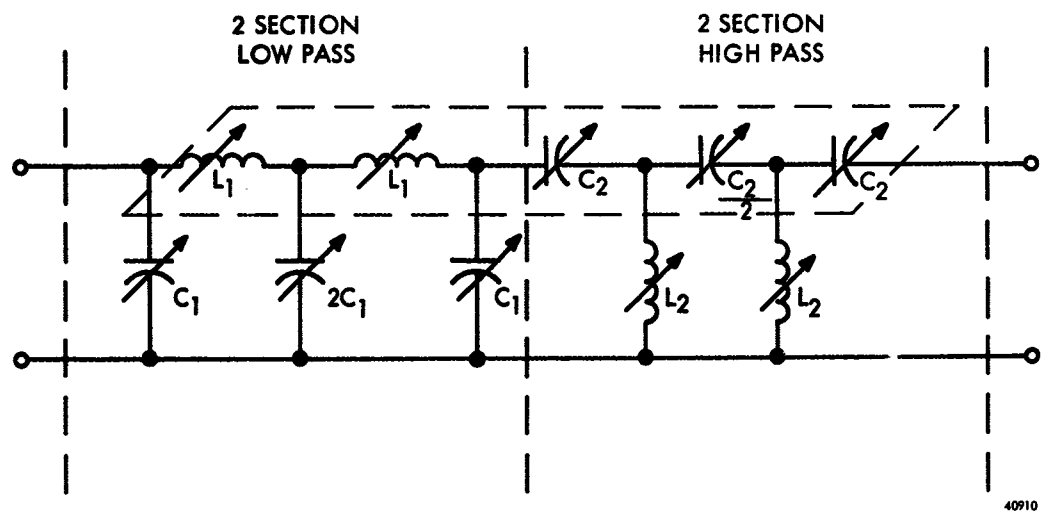


Figure 4. Phase Shift Scanner - Schematic Diagram

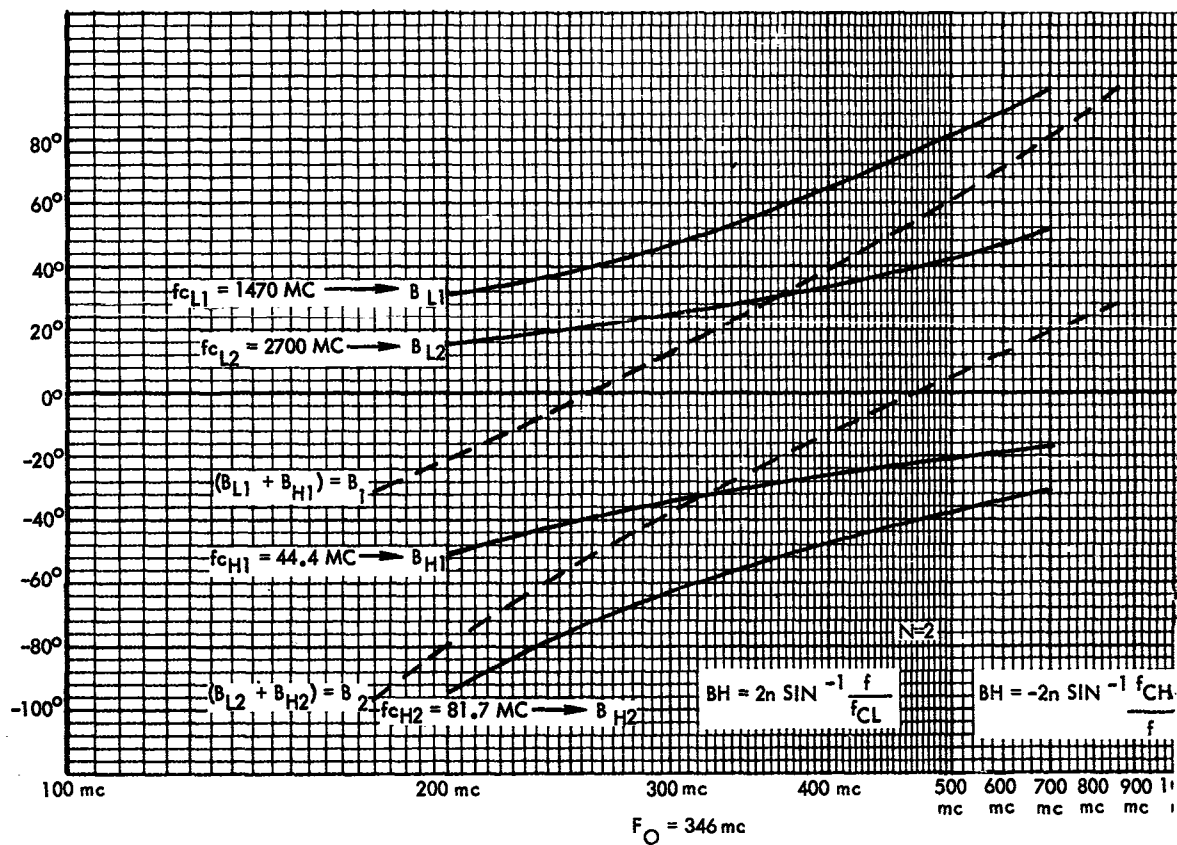


Figure 5. Theoretical maximum and minimum phase shift of the variable filters as a function of frequency.

two section low-pass and two section high-pass phase shifter. The upper curves marked B_{L1} and B_{L2} show the extremes of phase shift across a 3:1 band for a two section low-pass filter when the cutoff varies from 1470 mc to 2700 mc. The lower curves marked B_{H1} and B_{H2} are for the high-pass filter with a variation in cutoff from 81.7 mc to 44.4 mc. The two curves marked B_1 and B_2 are the overall phase shift of the combination showing $B_1 = B_{L1} + B_{H1}$ and $B_2 = B_{L2} + B_{H2}$. The difference between B_1 and B_2 is the differential phase shift across the combination as the two cutoff frequencies are varied. Figure 6 is a plot of the differential phase shift across a greater than 3:1 band. The cutoff frequencies were set so that the band center or minimum differential phase shift was 50 degrees. The total tolerance allowed was 50 to 65 degrees, and it is seen from the curve that this tolerance allows a 3.9:1 band. The experimental points are taken from a phase shifter similar to the one described and it can be seen that the band from 265 to 500 mc is not centered, nor is the minimum at 50 degrees, but the phase shift is easily within the tolerance limits for this relatively narrow band.

A complete scanner consists of four such phase shifters connected through a four-way power divider and adjusted in relative phase so that opposing phase shifters were 180 degrees out of phase and adjacent phase shifters are 90 degrees out of phase.

Figure 7 is a plot of the relative phase shift of a single phase shifter versus shaft rotation. Two views of the 135 to 265 mc phase shifter, with the cover removed, are shown in Figure 8. The complete VHF scanner assembly is shown in Figure 9.

DESCRIPTION OF COMPLETE SYSTEM

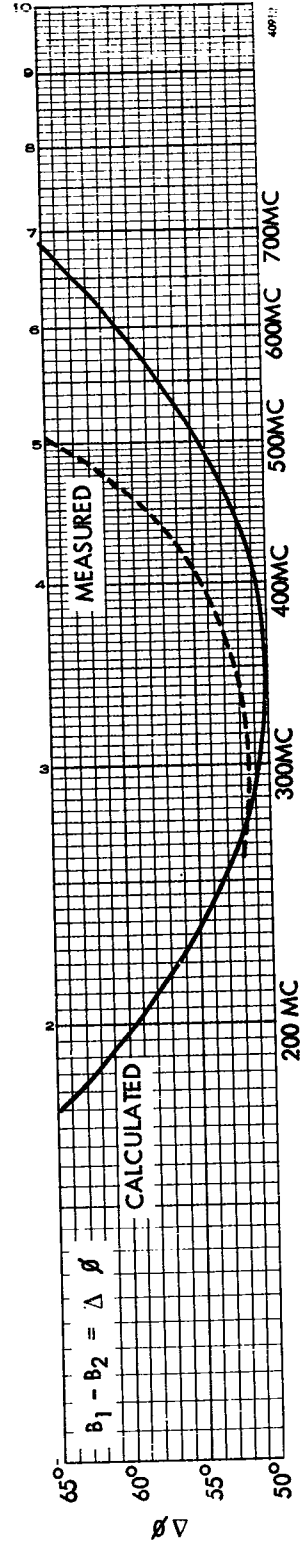
Recently two systems, as described above, were delivered to PMR for use at South Point, Hawaii. Both of these systems utilize four reflectors which are 10 feet in diameter. The first system covered a single frequency band from 135 mc to 265 mc and employed orthogonal log periodic dipole feeds. The operator can select orthogonal linear polarization or orthogonal circular polarization for the outputs. A block diagram of the RF (VHF) subsystem is shown in Figure 10.

The second PMR system covered four frequency bands as follows:

Band 1	265 to 530 mc
Band 2	530 to 1000 mc
Band 3	1400 to 1550 mc
Band 4	2200 to 2300 mc

This system employs orthogonal triangular tooth log periodic feed elements. The block diagram of the RF (UHF) subsystem is shown in Figure 11. Figure 12 is a photo of the UHF antenna.

2 HIGH PASS AND 2 LOW PASS VARIABLE FILTERS



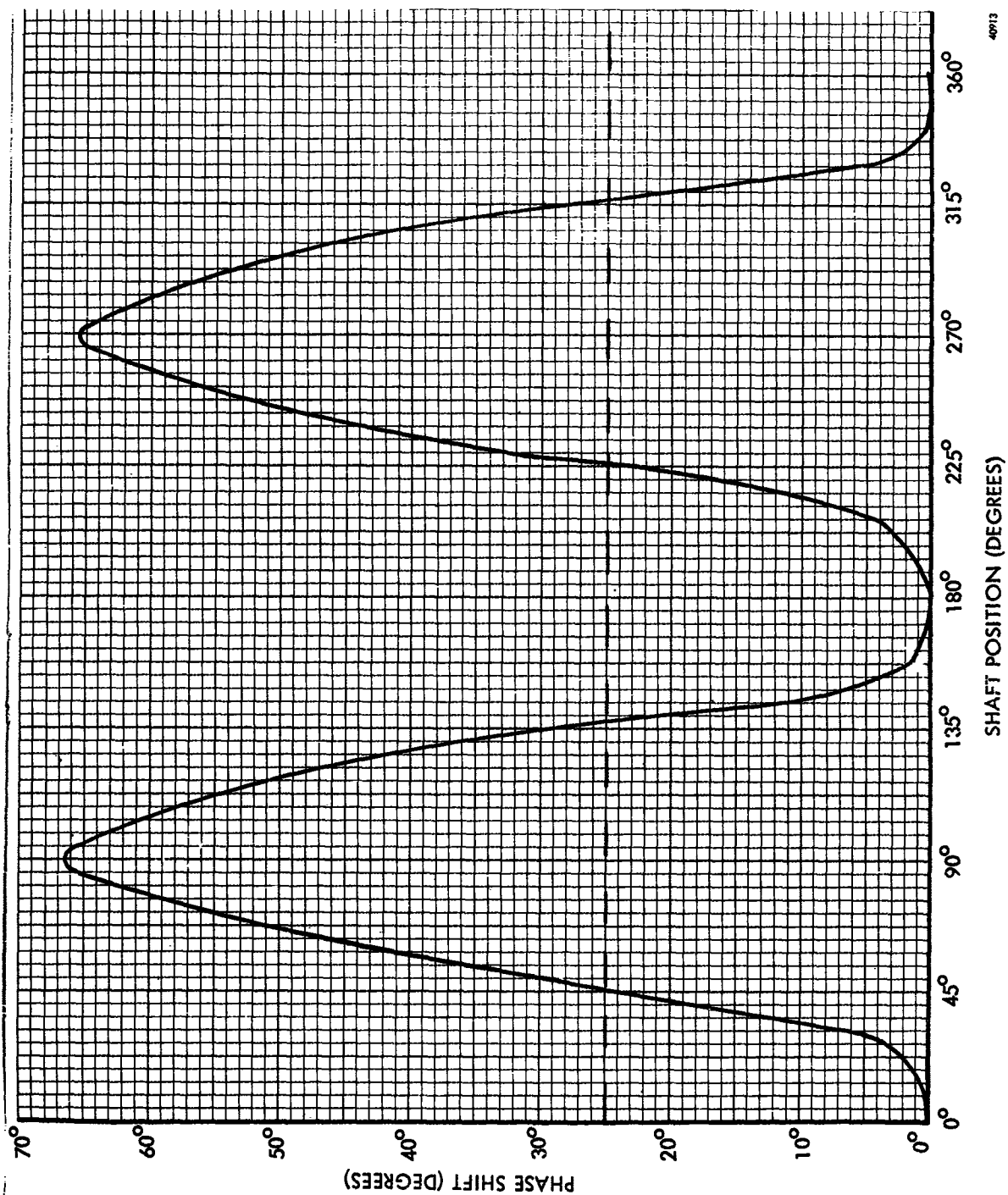


Figure 7. Relative Phase Shift versus Shaft Rotation at 500 mc.

40713

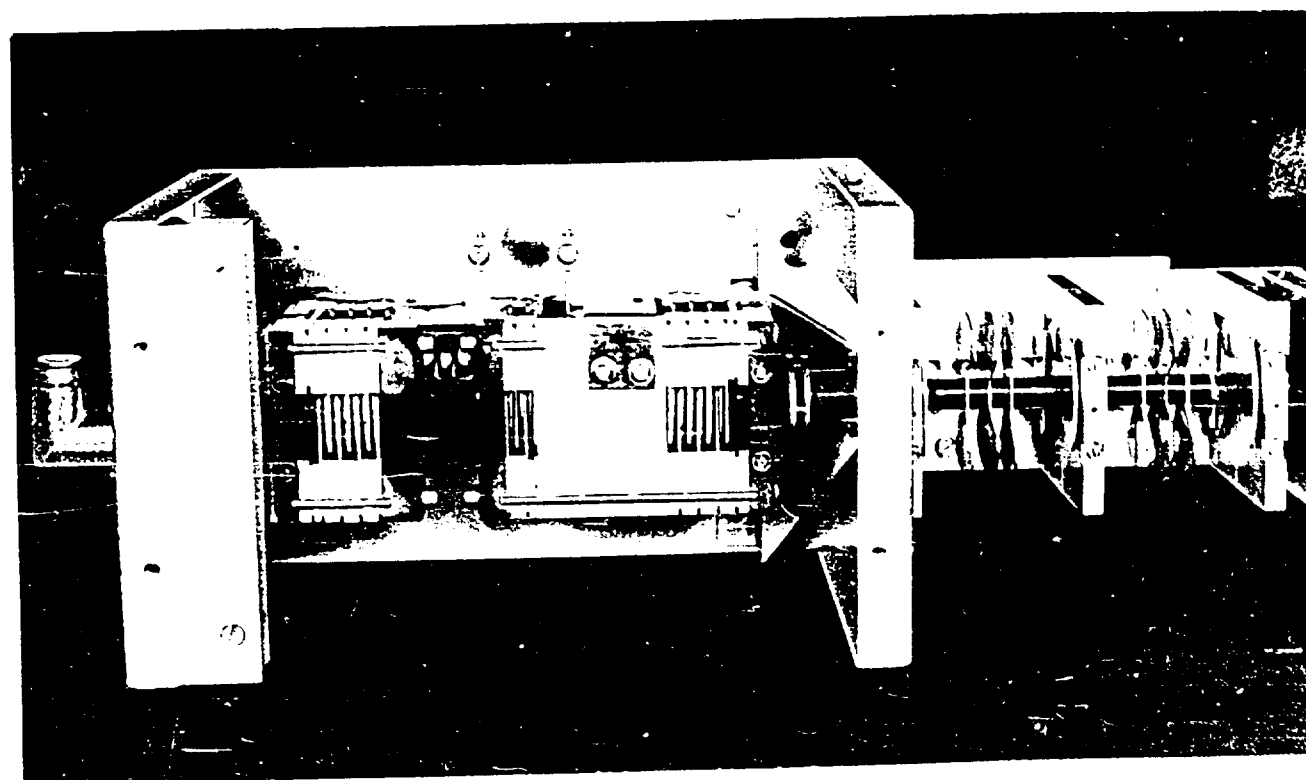
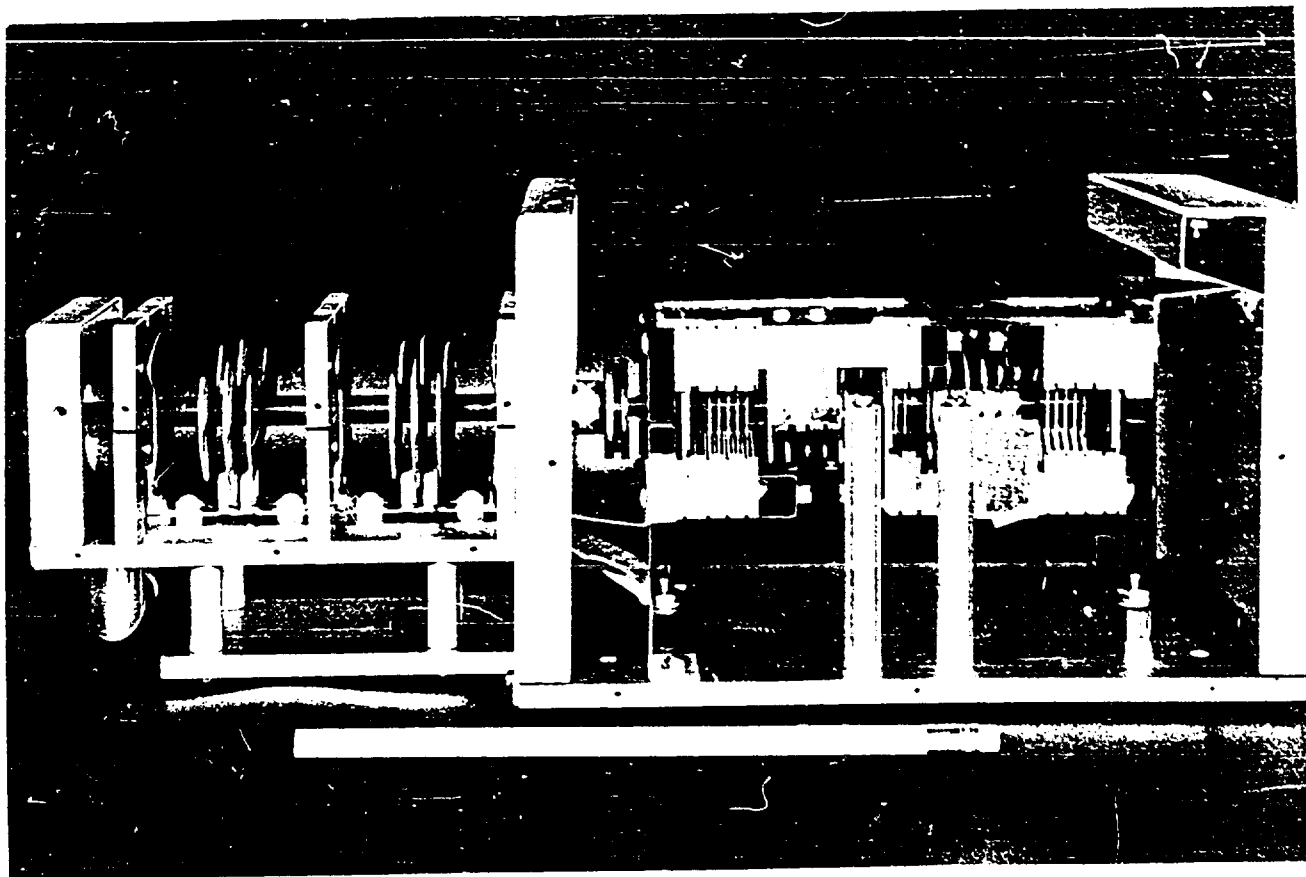
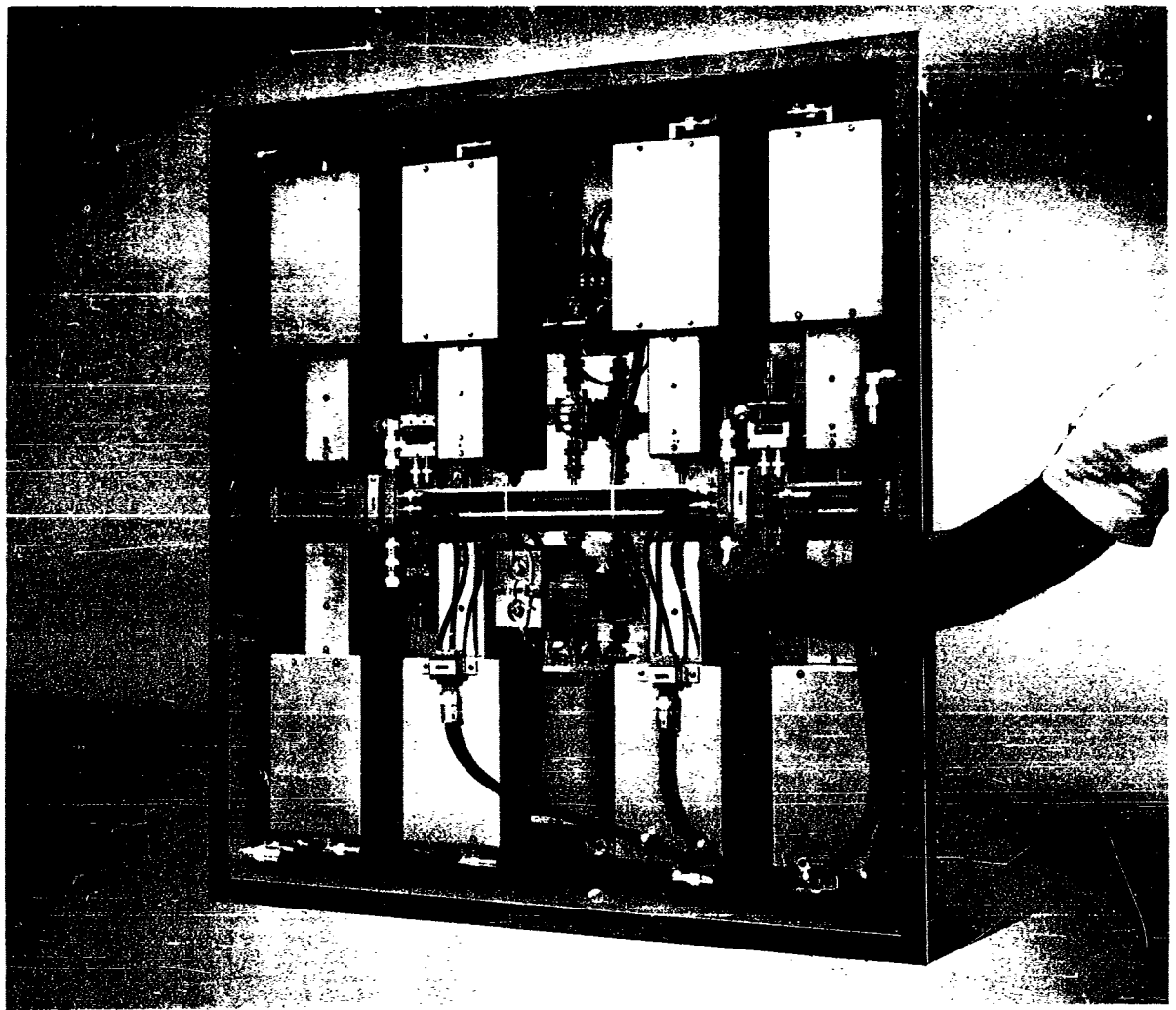
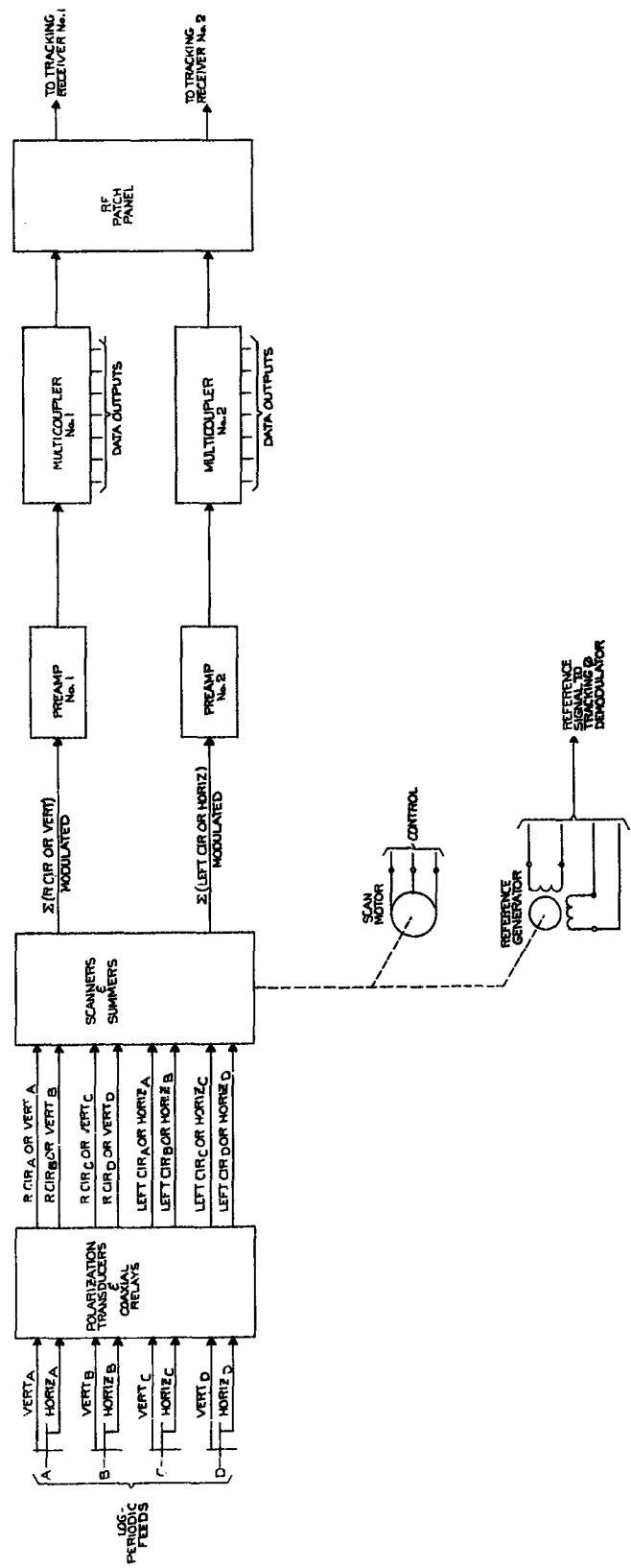


Figure 8. Scanner with cover removed (two views)



1738-36

Figure 9. VHF Scanner Assembly



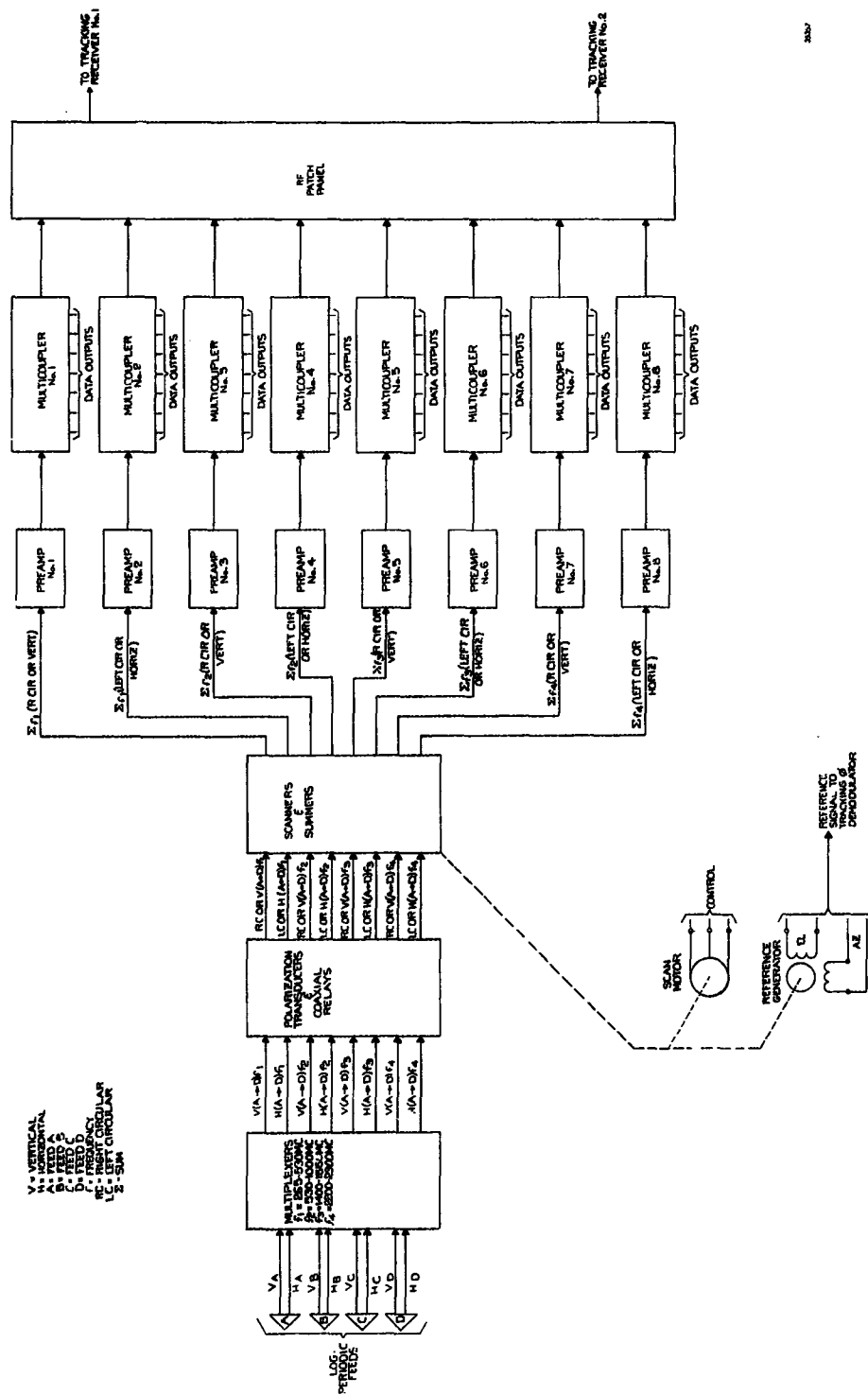


Figure 11. RF Subsystem (UHF) - Block Diagram

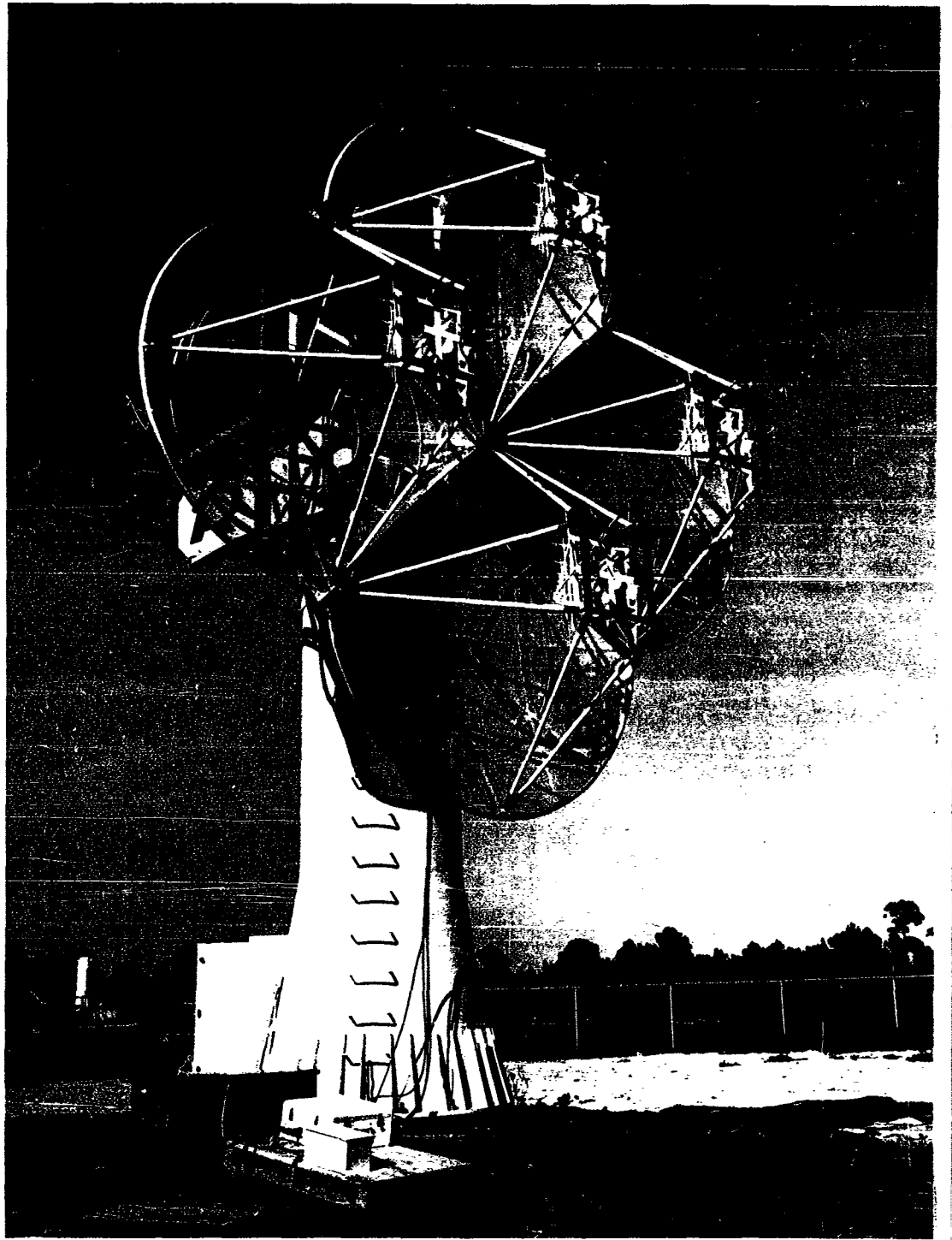


Figure 12. Photograph of UHF System

It was necessary to separate the individual frequency bands by means of a frequency multiplexer so that each polarization transducer and scanner could function independently over a frequency band less than 2:1. The polarization transducers are so connected that the horizontal and vertical polarization can be combined with an approximate 90 degrees phase shift to produce right circular and left circular polarization at the hybrid output parts or the horizontal and vertical can be connected directly to the output. Hybrids are also used to combine the outputs from the individual scanners.

At the time of this writing the systems were still undergoing tests and complete performance data were not available.

CONCLUSIONS

The variable high-pass low-pass filter phase shifter can be used to conically scan a four-element array over a frequency band approaching 4:1 with essentially constant crossover level. Since this scan method utilizes a single channel AM receiver for tracking it is less complex and expensive than the monopulse counterpart. The scanner is physically small and scan rates of 100 cps or more are easily achieved.

ACKNOWLEDGEMENT

The antenna systems described were constructed for PMR under Contract N123(61756)32597A.

LOG-PERIODIC CAVITY-BACKED SLOT ANTENNA

V. A. Mikenas and P. E. Mayes*

1. INTRODUCTION

The past several years have seen the development and wide use of the log-periodic dipole array¹. Extensive investigations have been undertaken and, as a result, many design data now exist for this antenna². The basic requirements for successful performance have been established and thus it is hoped that the key to the successful operation of various other log-periodic structures may be found in the log-periodic dipole array. In particular, the LP dipole array is used in this paper as the starting point for development of a broadband cavity-slot antenna.

2. EQUIVALENT CIRCUITS

Consider the equivalent circuit representation of the log-periodic dipole array shown in Figure 1. The shunt elements on the line represent the dipole self-impedances. To complete the representation the mutual coupling between dipoles must be added. However, the first consideration is to achieve a broadband antenna which can be mounted below, and radiate through, a ground plane. We seek to do this by changing the radiating elements from dipoles to slots. Since it is desired that the radiation shall occur only in the half space above the ground plane, the individual slots are backed with closed waveguide sections to form cavity-slot radiators. The dominant mode can be excited at the base of the rectangular cavities by using a loop or probe. The loop-coupled cavity-slot has input impedance variation similar to the admittance of a dipole. Hence the cavity-slot is the dual of the dipole. The dual of the equivalent circuit of the dipole array (neglecting mutuals) is shown in Figure 2. This equivalent circuit suggests that a series-fed set of cavity-backed slot radiators which are scaled consecutively in a log-periodic manner should operate in a way similar to the log-periodic dipole array. A program of testing of antennas which were designed using

*Antenna Laboratory, University of Illinois, Urbana, Illinois.

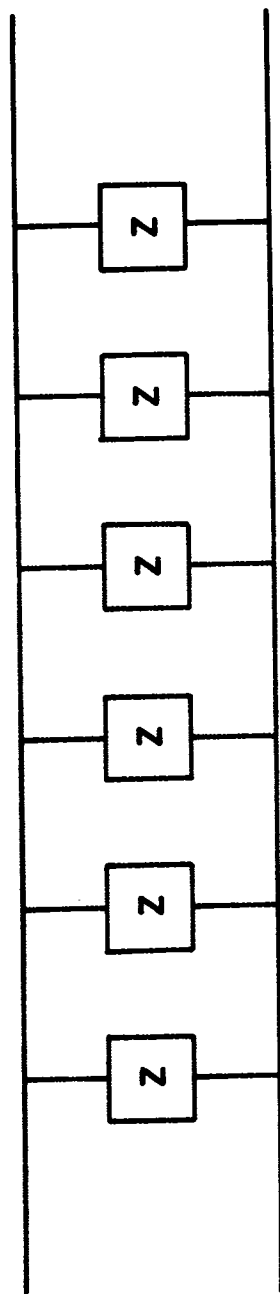


Figure 1. Equivalent circuit of the dipole array.

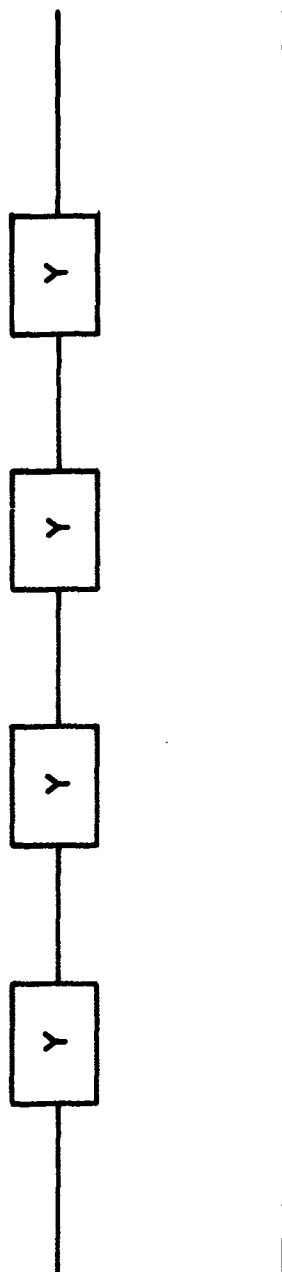


Figure 2. Dual of equivalent circuit of the dipole array.

these considerations has produced promising results, although the data obtained so far are in no measure as complete as has been gathered for the LP dipole.

3. CONSTRUCTION

Since the number of parameters present in the cavity-slot radiator exceeds that of the dipole array, the design of the former is more complicated. However, as far as applicable, the known facts about LP dipole arrays have been used as clues in the proper selection of parameters for the cavity-backed slot antenna. Each cavity was scaled with respect to its larger neighbor by the factor τ to produce a log-periodic design. A value of $\tau = 0.85$ was chosen for the first models. This value corresponds to values commonly found in log-periodic dipole arrays. Performance data will be discussed for a model with a total of 9 cavities which is illustrated in Figure 3. The taper angle α for this antenna was 16.5° . The feed loops were transposed in adjacent cavities to correspond to the transposed feeder of the LP dipole array. The complete antenna and feed system was then placed in a ground screen for impedance and near field measurements. A view of the antenna from under the ground screen is shown in Figure 4.

4. MEASUREMENTS

The first set of measurements was performed with loops constructed using printed circuit techniques. The loops were all scaled by the value τ and inserted into the individual cavities as shown in Figure 5. A few minor changes in the feed point and transmission line were made to achieve better performance. A typical impedance plot is shown in Figure 6. Although the points are scattered, there is a tendency to group on the high impedance side of the Smith Chart.

A number of far field patterns were also taken and a typical set of these is shown in Figure 7. Most of the patterns display the backfire beam which is characteristic of the log-periodic dipole. However, there were a few frequencies where bidirectional patterns were observed. Near field measurements were made which provided useful information with regard to the active region of the antenna and the causes of pattern variation. Several typical results

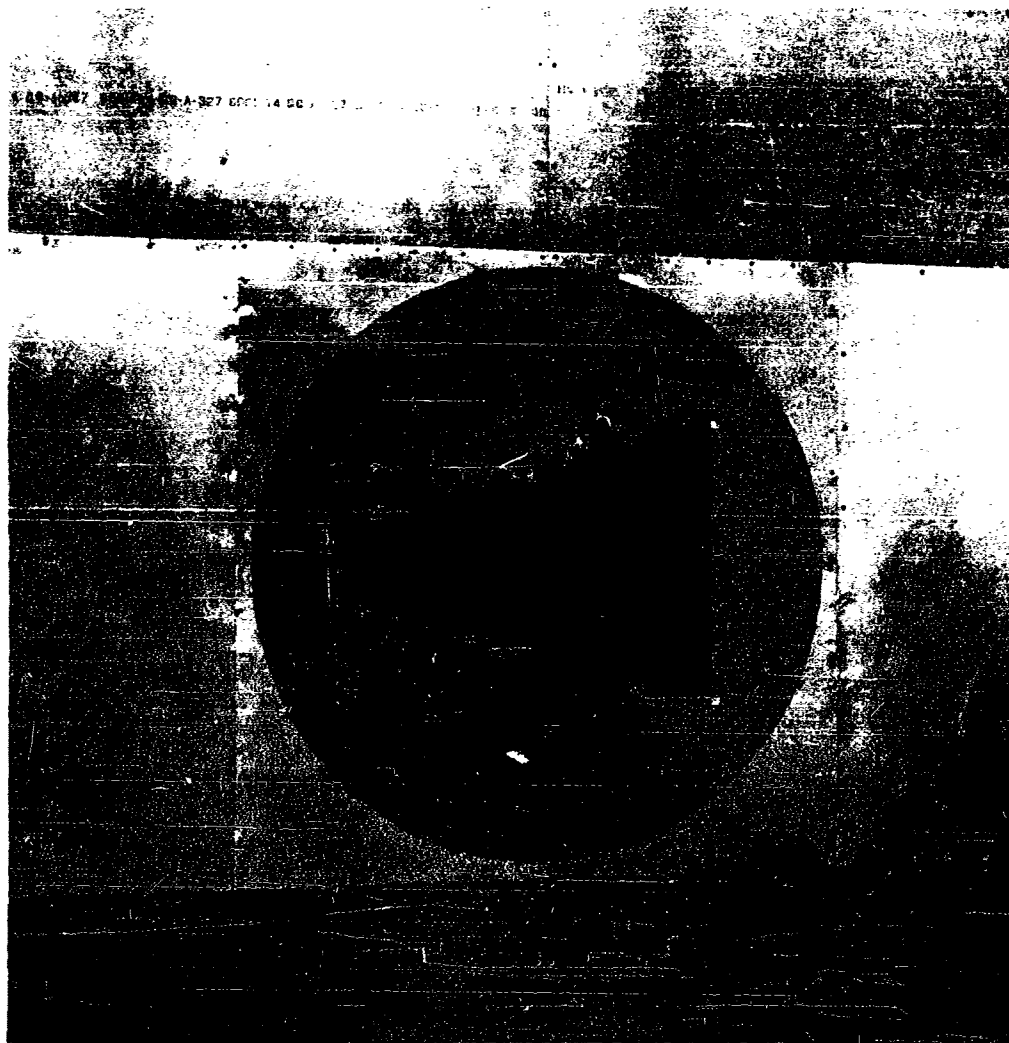


Figure 3. Front view of antenna.

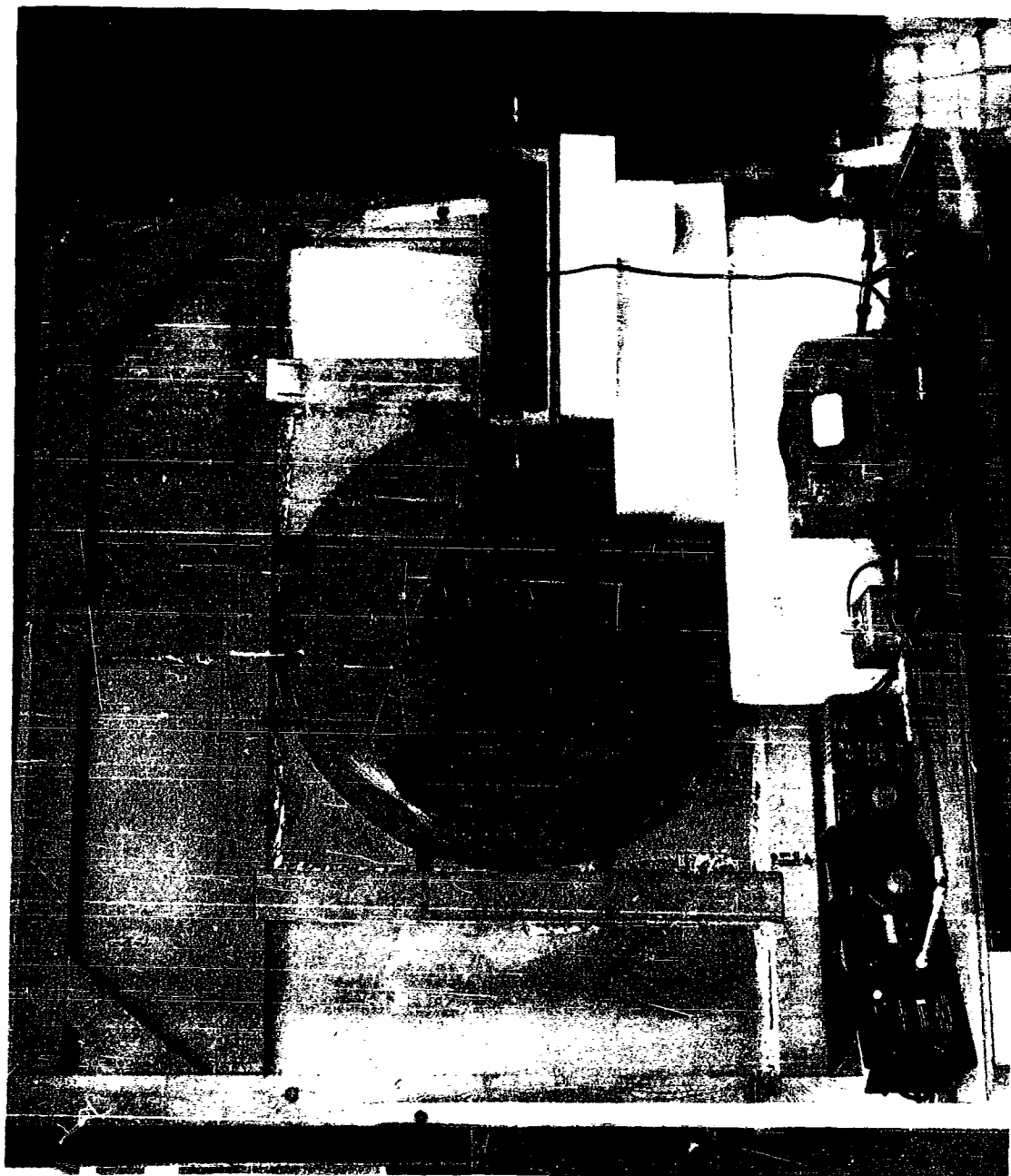


Figure 4. Back view of antenna and measuring apparatus.

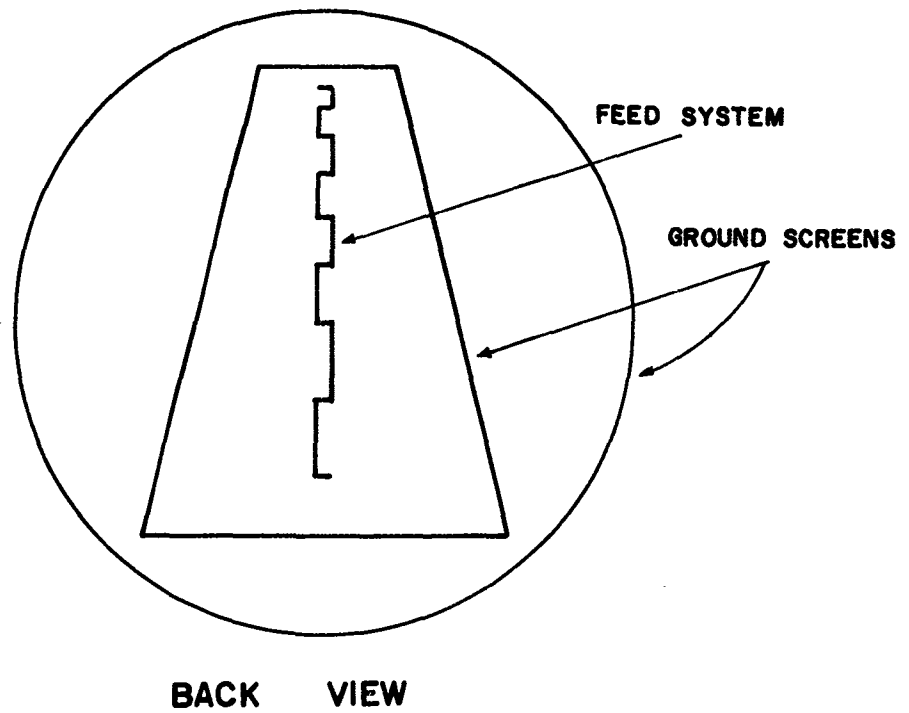
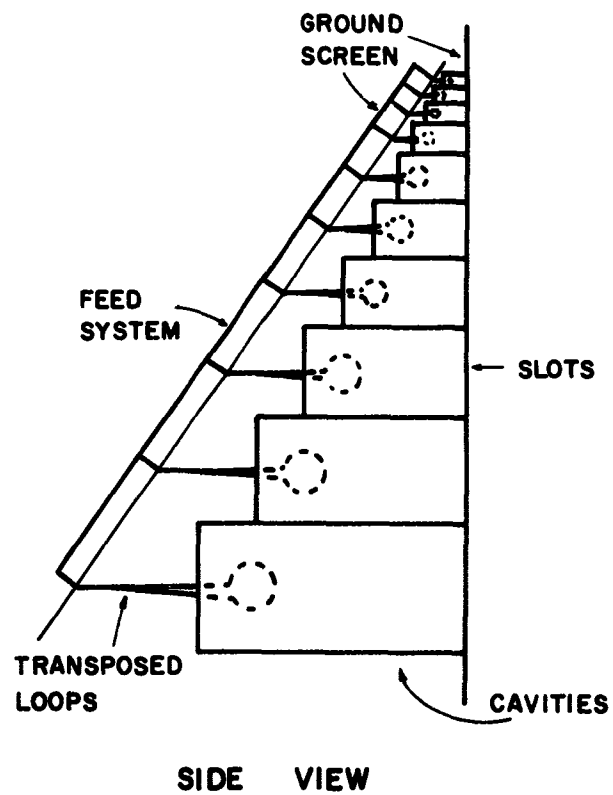


Figure 5. Cavities with loops shown inserted.

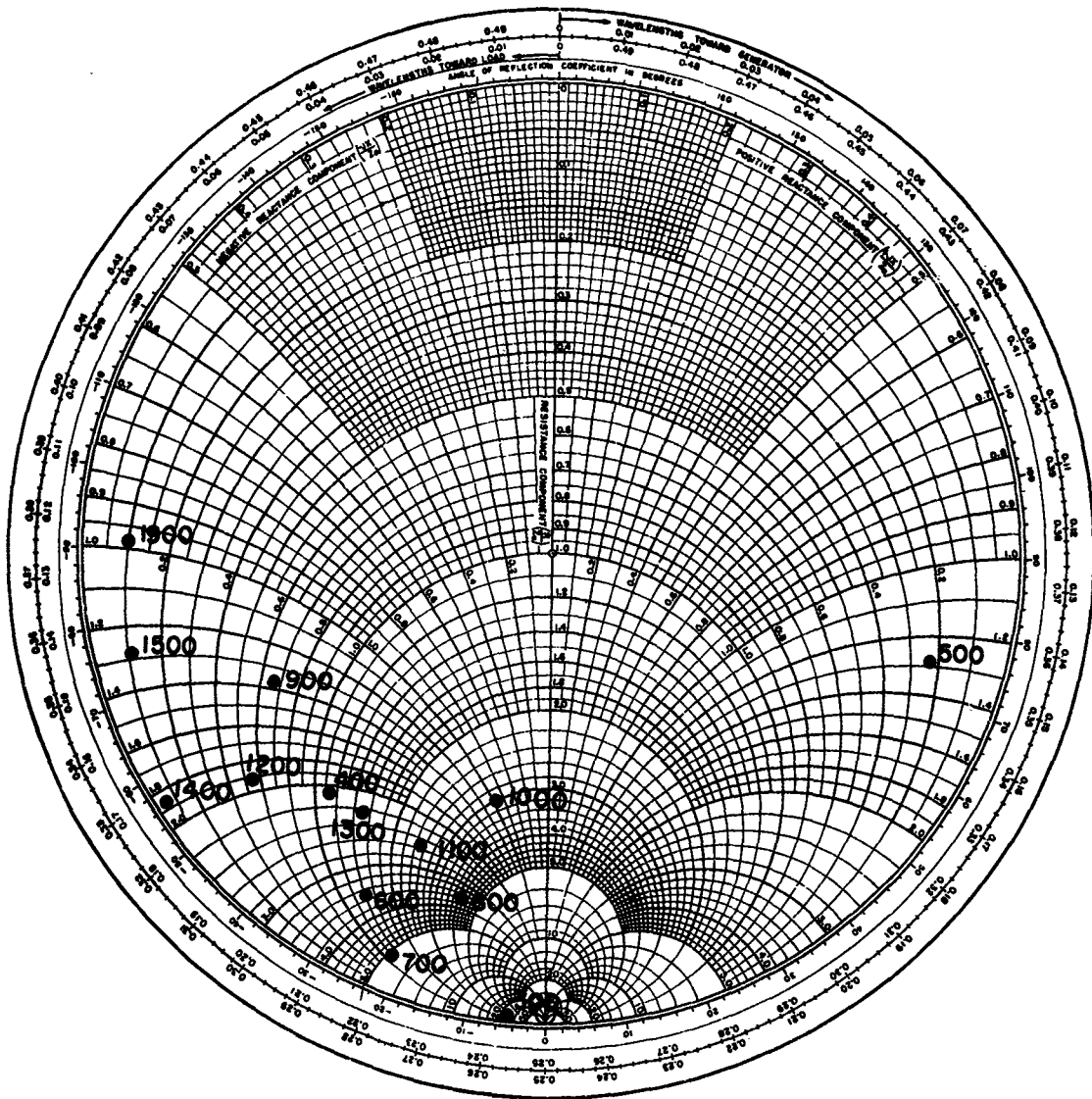


Figure 6. Impedance locus versus frequency in Mc referred to 50 ohms.

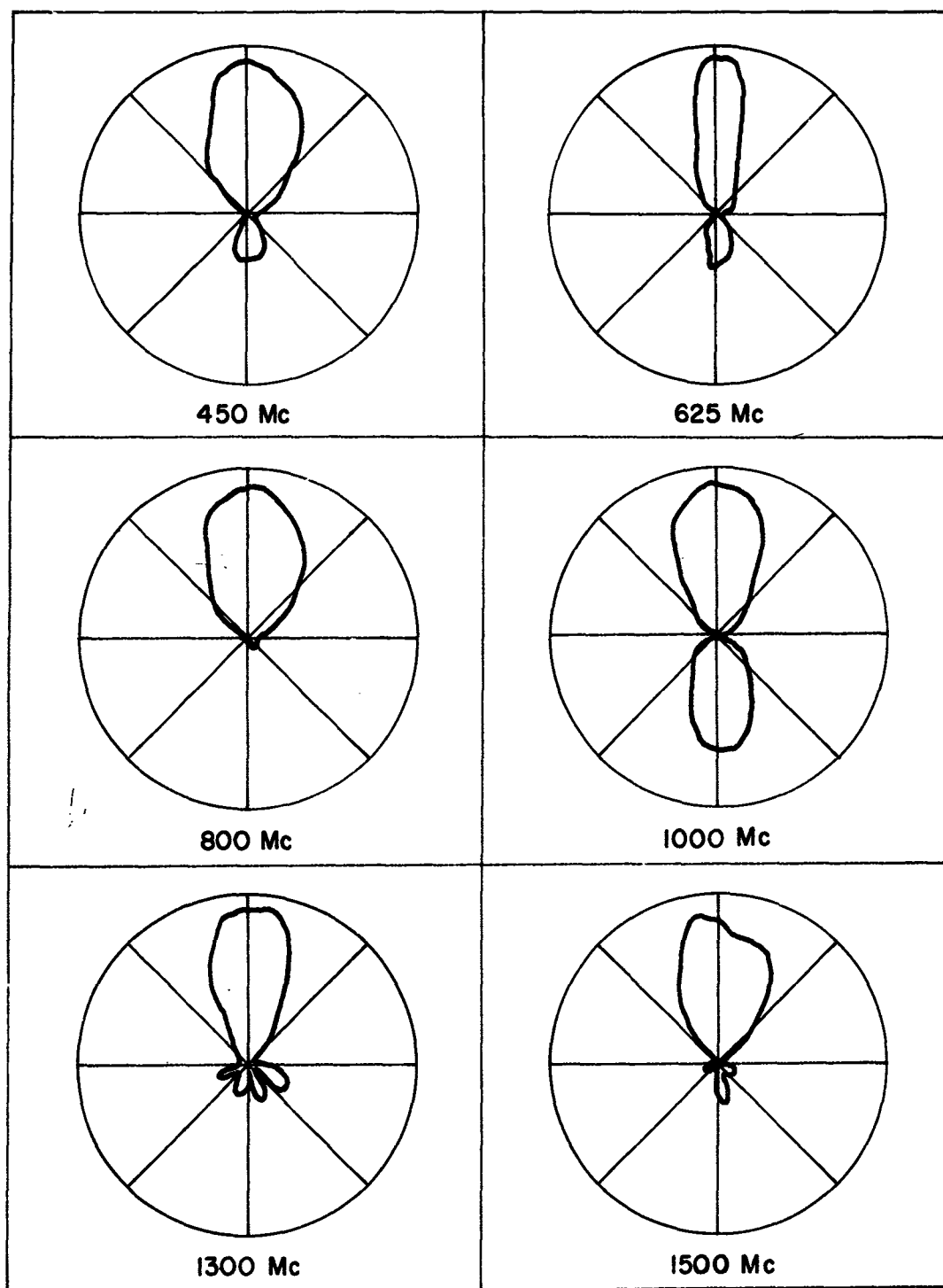


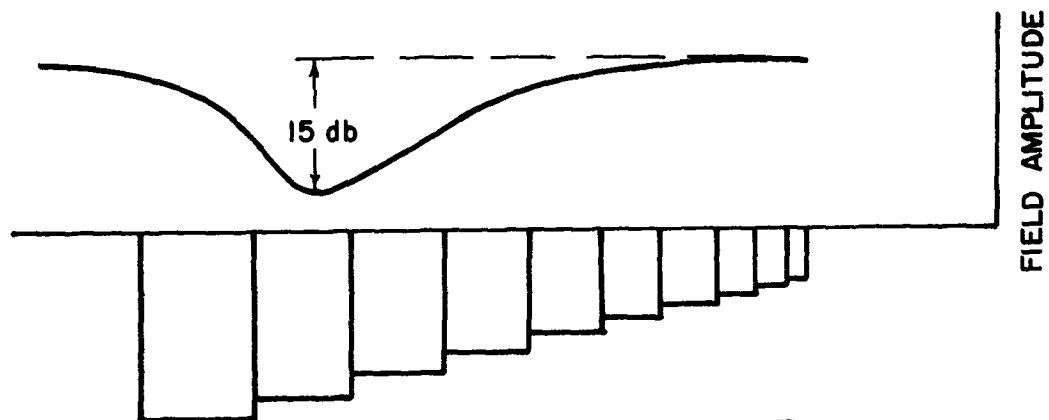
Figure 7. H-plane patterns of the cavity-backed slot antenna.

are shown in Figure 8. Note that there is considerable energy at the large end of the antenna at the frequency where the bidirectional beam occurs; whereas, the active region is well defined and near fields are negligible at the large end at the frequency of the unidirectional backfire beam.

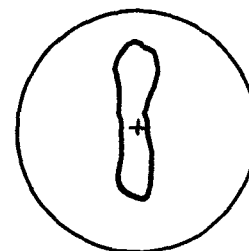
Although the cavity-backed slot antenna was operating in a fairly satisfactory fashion, it seemed necessary to increase the coupling of energy from the loop through the cavity to free space in order to improve the performance. To investigate the coupling between the feed line and free space, a single cavity was constructed with several adjustable parameters to enable the determination of maximum coupling. It was found that maximum coupling was attained when the loop was removed some distance from the bottom of the cavity (approximately one eighth of a wavelength). The feed system of the log-periodic slot antenna was then adjusted in an attempt to increase the coupling of energy to free space. Although the information determined from the single cavity would not be exactly true in the log-periodic array of cavities (due to mutual coupling between adjacent cavities), it would nevertheless give a good indication as to how the coupling of energy to free space might be increased.

Due to the required flexibility, 300 ohm twin lead was used in place of the printed circuit loops in the rearranged feed system. Some accuracy was sacrificed but, from the experimental results, it appeared to be negligible. Indeed, there was a marked improvement in the impedance plot as can be seen in Figure 9. The antenna displayed satisfactory performance over a bandwidth of approximately 2:1 in both impedance characteristics and far field patterns. Some typical far field patterns are shown in Figure 10.

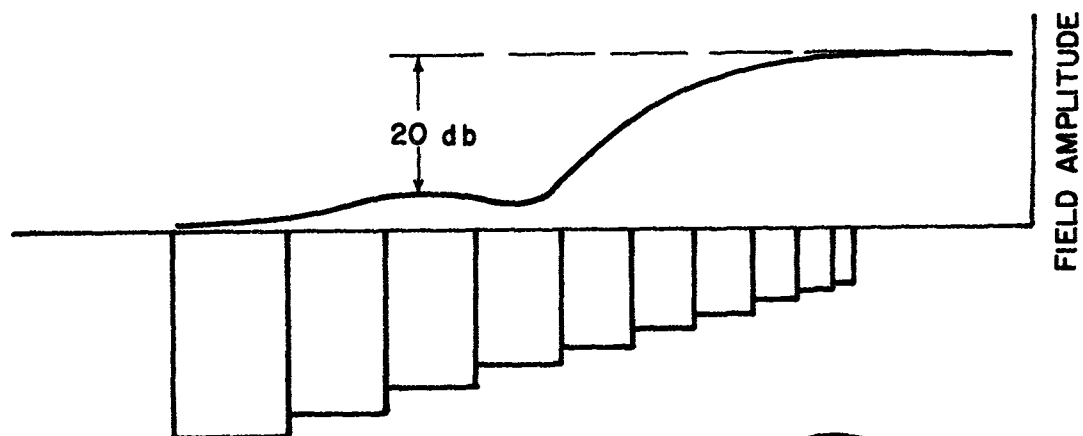
It was noted that the active region was, in all cases, in front of the cavity whose cutoff frequency corresponded to the operating frequency, by approximately 20%. Although it is not possible to operate the cavities at their cutoff frequency, it is desirable, however, to operate at a frequency where reflections from the slot aperture are low. This will insure as good an impedance match as is possible so as to maximize the coupling of energy to free space. The task of operating with the cavities in this condition may be accomplished in one of several ways. One solution is the proper phasing of loops between adjacent cavities to shift the active region toward the larger cavities. Another approach would be to slightly reduce the cavity slot length.



625 Mc



H-PLANE PATTERN



800 Mc

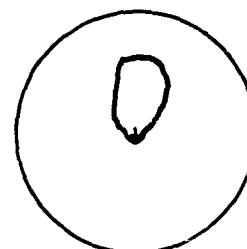


Figure 8. Near field plots for 625 Mc and 800 Mc.

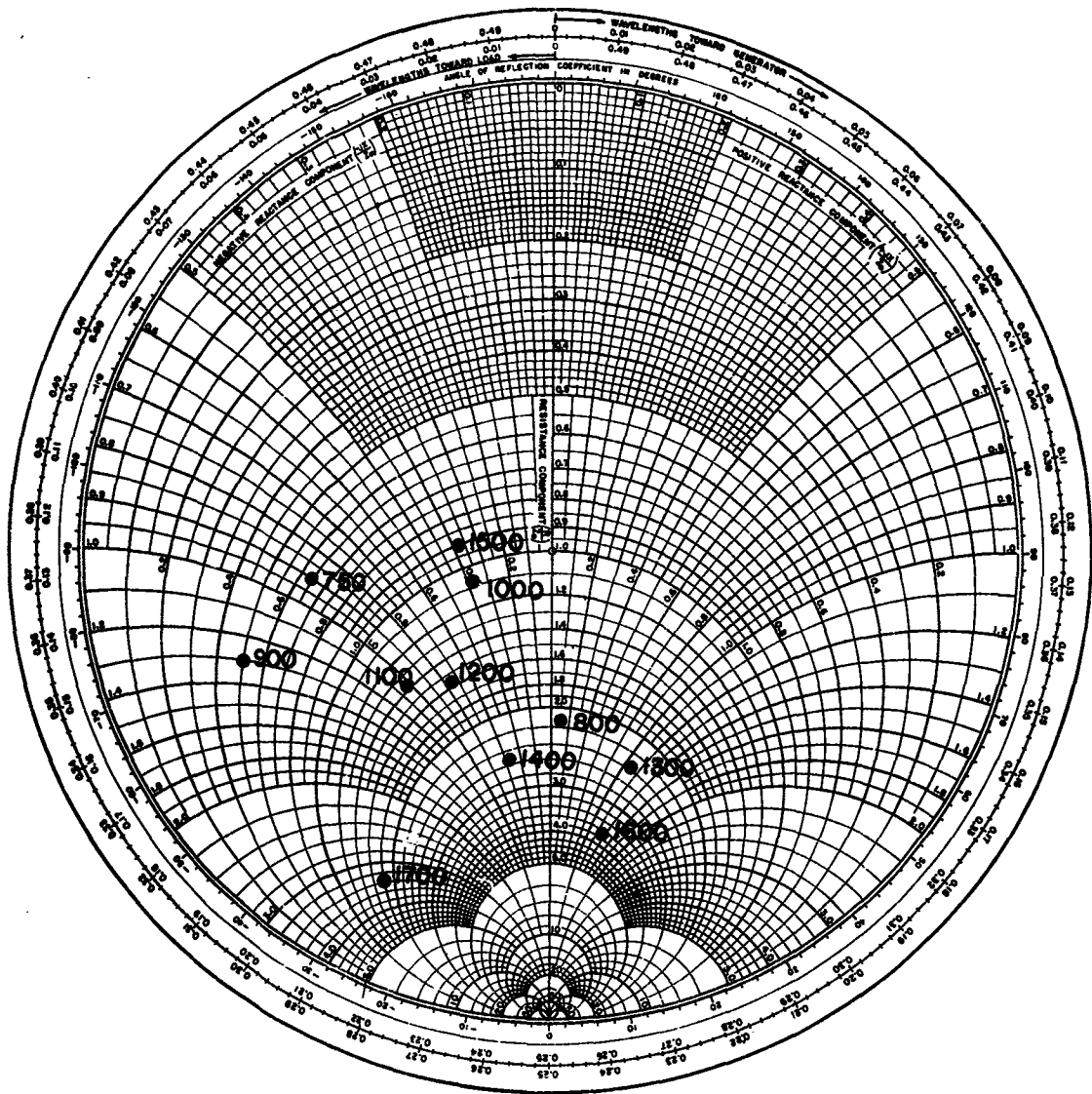


Figure 9. Impedance locus versus frequency in Mc referred to 50 ohms.

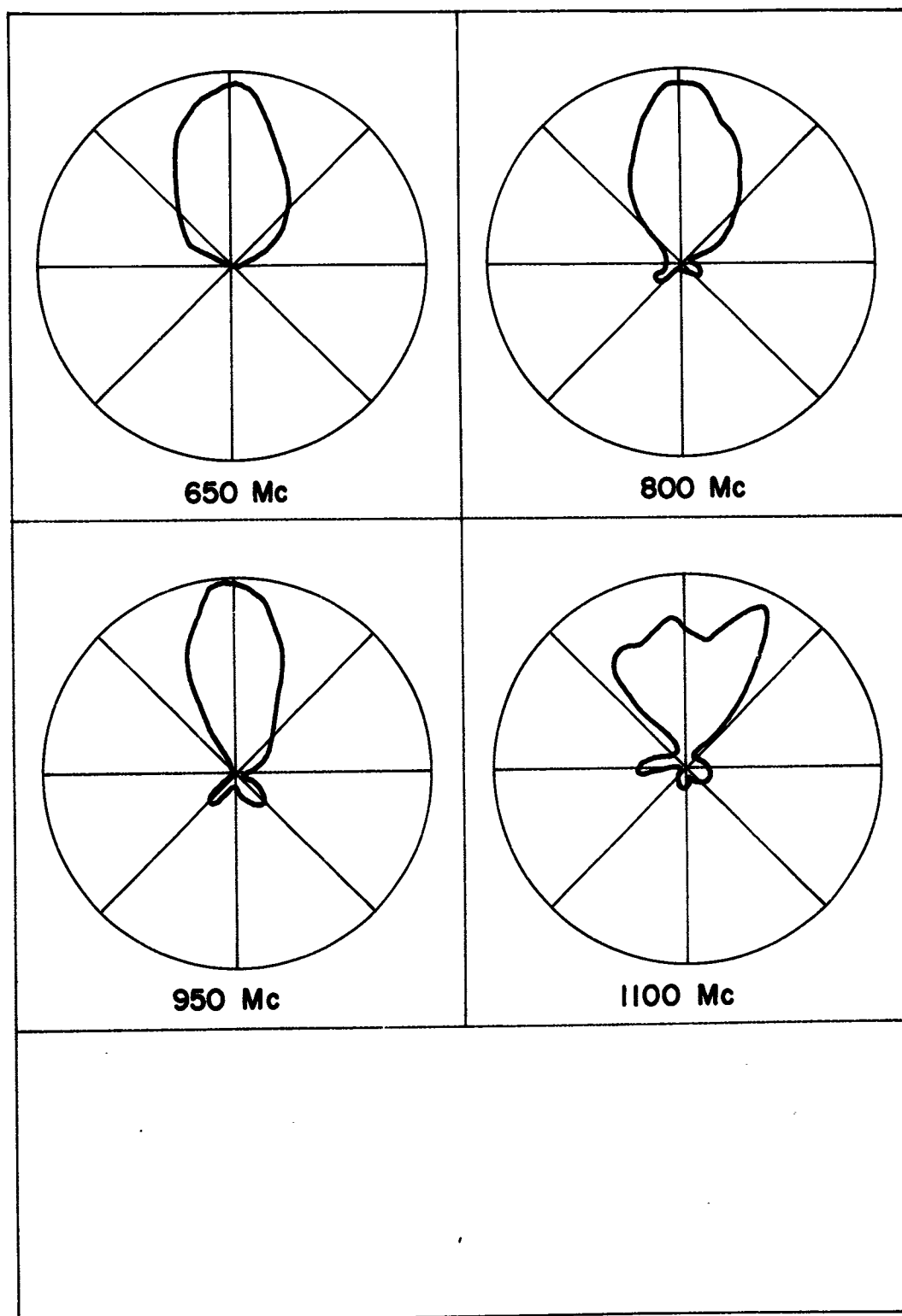


Figure 10a. H-plane patterns of the cavity-backed slot antenna.

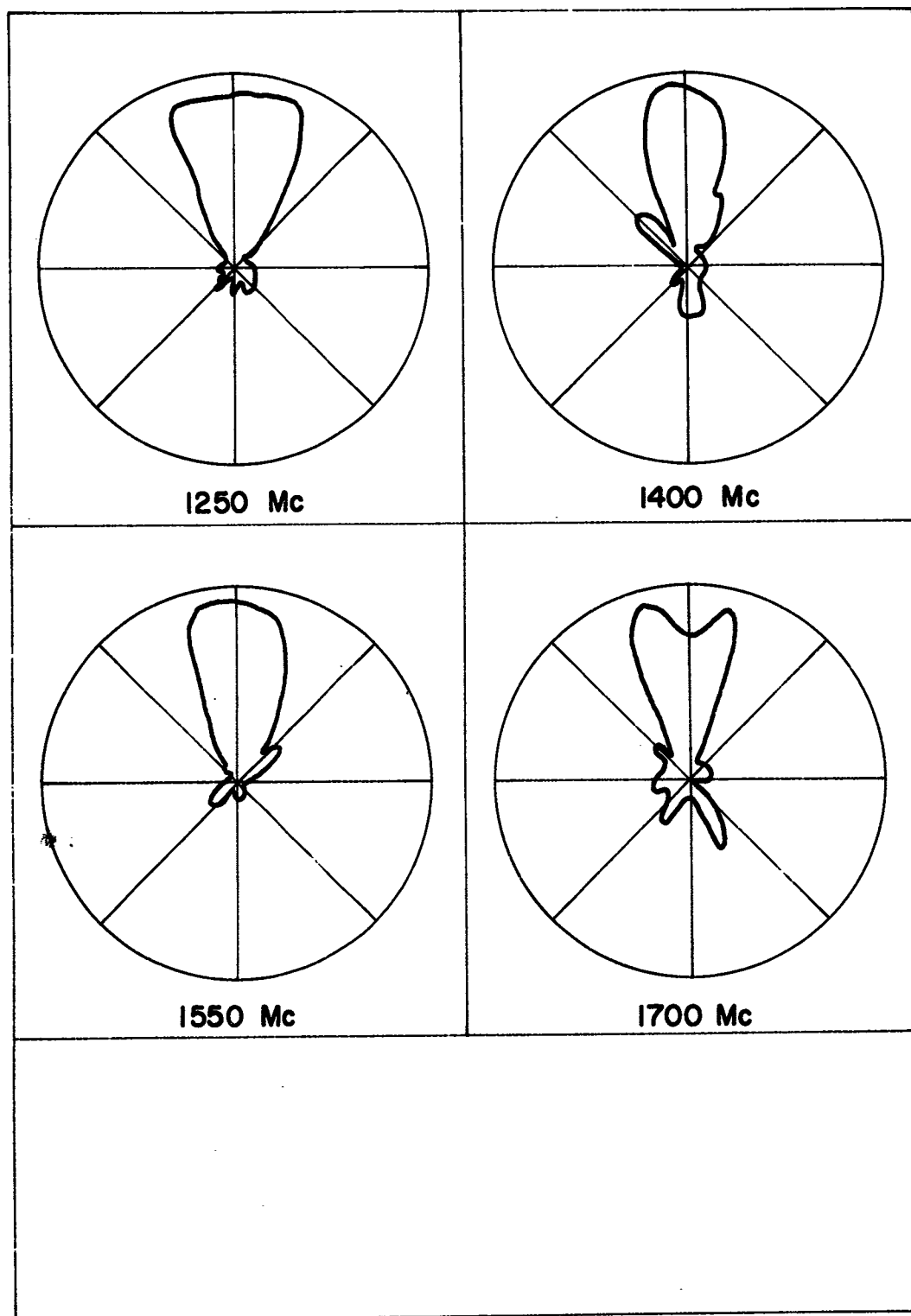


Figure 10b. H-plane patterns of the cavity-backed slot antenna.

5. CONCLUSIONS AND FUTURE PLANS

It was found that the design of a log-periodic cavity-backed slot antenna could be successfully based upon considerations of the dual of the equivalent circuit of the log-periodic dipole array. However, since the duality process gives little or no insight into cavity or cavity-loop-coupling behavior, these latter factors added to the complexity of the design of the total structure. It was, nevertheless, found that properties of a single cavity and loop coupling system could be successfully applied to the cavity array yielding improved performance.

A uniform periodic structure is now being constructed and it is hoped that further information about operation of the log-periodic structure will be obtained from measurements and calculations using the uniform model. Several variations of the present feed are also to be made in an effort to better determine design criteria for the log-periodic cavity-backed slot antenna.

6. REFERENCES

1. D. E. Isbell, "Log-Periodic Dipole Arrays", IRE Transactions on Antennas and Propagation, Vol. AP-8, pp. 260-267; May 1960. Also, Technical Report No. 39, Contract AF33(616)-6079, 1 June 1959, Antenna Laboratory, University of Illinois, Urbana, Illinois.
2. R. L. Carrel, "Analysis and Design of the Log-Periodic Dipole Antenna", Technical Report No. 52, Contract AF33(616)-6079, 1 October 1961, Antenna Laboratory, University of Illinois, Urbana, Illinois.

ACKNOWLEDGMENT

The work described here was supported by Aeronautical Systems Division, USAF, Wright-Patterson AFB under Contract No. AF33(657)-10474.

MUTUAL COURLING

**Mutual Coupling Effects
in
Phased Array Antennas**

by

**Charles C. Allen
General Electric Company
Advanced Technology Laboratories
Schenectady, New York**

Mutual Coupling Effects
in
Phased Array Antennas

by

Charles C. Allen
General Electric Company
Advanced Technology Laboratories
Schenectady, New York

I. Introduction

Mutual coupling effects are of utmost importance in determining the performance of steerable phased array antennas in radar and communications systems. The radiation pattern of an array and the input impedance can both be affected adversely by mutual coupling between the radiating elements. In general, the effects on the pattern and impedance change with scan angle because of the change in relative phase of the element excitations required to steer the beam. Means of reducing and compensating for these effects are essential for the proper design of efficient arrays to meet the advanced requirements of systems currently being planned.

The nature of these effects has been investigated by several persons and the results presented in the literature. The variation in theoretical element driving-point impedance with element location in the array and array scan angle was shown by Carter¹ for both an infinite wire array and a half-wave dipole array with elements spaced one-half wavelength on centers and one-quarter wavelength above a ground plane. Further analytical results for gain variation as well as driving-point impedance were presented by Allen,² with some experimental confirmation, for a planar dipole array with several different element spacings and distances to the ground plane. Experimental measurements of the mutual impedances and the

contribution of each element to the array pattern (based on mutual impedance to a pick-up antenna as a function of angle) were shown by Kurtz, et al,³ for 10 element linear arrays and 5 x 10 element planar arrays of dipoles spaced one-half wavelength on centers and one-quarter wavelength above a ground plane, with special emphasis on edge effects. Means of compensation for mutual coupling effects in dipole arrays were investigated theoretically by Edelberg and Oliner⁴ using the unit cell approach developed by them for analyzing waveguide slot arrays.⁵

This paper presents the initial results of a program for investigating mutual coupling effects, devising means for their reduction, and developing general array design relationships. A 7 x 7 array of dielectrically-loaded circular-waveguide horn radiators with an adjustable ground plane was constructed for operation at S band, and measurements were made of the coupling between radiating elements, the element VSWR, and the element pattern in its array environment as functions of the ground plane position and frequency. The approach used in making these measurements was to excite the central element of the array with all other elements terminated in matched loads. From the data obtained with this approach, the performance of a much larger array of like elements can be determined on a digital computer by a superposition formulation similar to that discussed in Allen's analysis.²

A general discussion of the approach used, the related array concepts, and the aim of the overall program is given in Section II. The results of measurements on the waveguide horn array are presented with discussion in Section III.

II. General Discussion

The approach used in this investigation lends itself directly to the calculation of the driving point and pattern characteristics for any large phased array having an element design and arrangement like that of a small array on which measurements have been made, given a specified distribution of generator excitations. The driving point characteristics are obtained by systematically indexing the matrix for a limited patch of elements, obtained from measurements made on the small array, over the larger array with appropriate weighting equal to the excitation distribution. Edge effects are taken into account by using the different matrices obtained from measurements made at the edges and corners of the small array. The array pattern characteristics are similarly obtained by summing the appropriate element patterns over the array with the corresponding weighting and the proper space phase term.

In general, an array of radiating elements constitutes a linear passive network in which the mutual couplings between the terminals of all elements in the array can be represented by a set of fixed constants expressed as either an impedance, an admittance, or a scattering matrix. In addition to these couplings between the element terminals, each radiating element has distributed coupling to the space surrounding the array. This distributed coupling is also fixed for a given array geometry and corresponds to the radiation pattern of a single excited element in its array environment, thus it includes the effect of any parasitic radiation from neighboring elements. Instead of measuring the mutual impedances between elements, which relate the open circuited voltages of all other elements to the current in an excited element of the array, the coupling coefficients

between elements terminated in generator impedances matched to the connecting transmission lines are measured directly for one element excited at a time (i.e., all other generator voltages equal to zero). The coupling coefficients thus measured are the coupled wave terms of a scattering matrix taken at the terminals of the array elements, and the reflected wave term is obtained by direct measurement of the excited element reflection coefficient. The corresponding patterns of the excited element in its array environment are also measured under these conditions of terminated neighboring elements.

Instead of forming a complete scattering matrix for the small array by measuring all the coupling coefficients, only a partial matrix is formed for the couplings to all elements around the excited element. This partial matrix when indexed over the large array (with different terms substituted near the edges as mentioned above) and weighted by the excitation voltage distribution accounts for all possible couplings between terminals of the large array. The resulting coupled and reflected waves at the element terminals when all elements of the large array are excited, are then the linear superposition of all the individual element contributions. These results can be left in the form of active reflection coefficient versus scan angle for each element in the array, or converted to the corresponding active element impedances.

In calculating the patterns for the large array, care must be taken to properly weight the measured element patterns. Since these are measured with all generator impedances in place, the contribution of any element pattern to the overall array pattern is proportional to its own generator voltage rather than its net voltage or current, in accordance

with linear superposition. In addition to weighting each element pattern by the amplitude and phase of its generator voltage, it must also be multiplied by the relative space phase term corresponding to the pattern angle and the element position in the array. These conditions are equivalent to the array pattern formulation given by Allen,² except that individual generator voltages are used instead of currents for individually excited elements.

For initial measurements aimed at investigating and minimizing mutual coupling effects, it is only necessary to obtain the magnitudes of the coupling coefficients and element patterns, the phases only being required for the final element configuration that is used for large array analysis. In arriving at criteria to serve as guides for such initial measurements, it is helpful to consider the related array concepts. The currents induced over an array when a single element is excited can be considered as equivalent to various modes being excited over the array. Some of these modes can propagate back into the transmission lines connected to the neighboring elements, while others cannot and are therefore parasitically radiated. The modes that propagate into the neighboring transmission lines affect the input impedances of the neighboring elements, while the modes that parasitically radiate contribute to the resultant pattern of the excited element in its array environment. While the space surrounding the array has no single pair of terminals, the distributed coupling of an excited element to that space may be sampled in a given direction, as discussed by Kurtz, et al,³ and is a function of the direction. The pattern of each element in its array environment thus determines the contribution made by that element to the overall array pattern as a function of the pattern angle, when all elements are excited.

The overall array pattern is impaired by differences between the individual element patterns which result from different array environments at different locations in the array (i.e., edge effects). While the input impedance to each element is affected by mutual coupling, this in itself does not affect the overall array pattern for element patterns taken under the conditions discussed above, since the individual generator voltages are not necessarily affected. The exact manner in which mutual coupling affects the overall impedance and pattern of a phased array depends on the nature of the network used to connect the radiating elements to form the array pattern. This may be a passive waveguide network in which case the various element impedances can combine directly, or an active network having amplifiers and/or frequency converters in each element feed line. In either case, the network should present a matched impedance to the individual element feed lines in order to minimize second order effects of mutual coupling. Such second order reflections, if present, can be treated as additional input waves to the array scattering matrix determined for matched generators.

It would be desirable to have no energy coupled back into the transmission lines connected to neighboring elements of a phased array since such coupling not only affects the element input impedances but represents a loss of power that could otherwise be radiated and thus lowers the array efficiency. It can also adversely affect the operation of transmitting tubes connected to the elements and thus result in variation of the element excitations with scan angle. To achieve such a condition, the coupling coefficients from any excited element to all others would have to be zero. Forward coupling to neighboring elements would still occur in this case and contribute to the pattern of an individually excited element, but the element

pattern in its array environment would then be a cosine power pattern, as discussed by Parad,⁶ independent of the particular element design that produced the zero coupling condition. As a result, the array would remain matched with scan angle (if initially matched) and the gain would vary only as the cosine of the scan angle.

The overall aim of this program is to devise means of reducing the mutual coupling of energy into neighboring elements to a minimum while maintaining a satisfactory pattern for an individual element in its array environment. If this can be achieved satisfactorily, a frame of dummy elements can then be placed around the edge of an array to overcome the adverse effects of the edge elements on the array pattern. Since coupling into the dummy elements would be small in that case, their terminations would not be critical and would represent little loss of power. The principal function of the dummy elements would be to provide parasitic radiation for the edge elements similar to that provided by the array environment of the central elements and thus make the patterns of all excited elements more nearly alike.

Edelberg and Oliner⁴ have shown analytically that significant improvement in the E-plane scan characteristic of a dipole array can be obtained by adding baffles. Their analysis is based on an infinite array (or the central portion of a large array) with equal amplitude of excitation for all elements, however, and does not take edge effects into account.⁵ Under those conditions and for a linearly progressive phase difference between elements, they treated the array as a periodic structure and derived a unit cell network. The relation between the approach of Edelberg and Oliner and the one discussed in this paper is that, in their approach all elements are excited and only a resultant dominant mode exists over the array based on the

conditions imposed, whereas in the approach discussed here a single element is excited in its array environment and all the possible modes are present. Once the mutual coupling into neighboring elements has been minimized using the latter approach, it may then be desirable to reduce any remaining variation in active element impedance with scan angle by compensating for the residual coupling in a manner similar to that of Edelberg and Oliner. In any case, it is desirable that the coupling be reduced sufficiently to permit a border of dummy elements to be placed around the array and thus minimize the edge effects on the individual element pattern.

III. Measurements on Waveguide Horn Array

A photograph of the dielectrically-loaded circular-waveguide horn array with flush dielectric radiating elements is shown in Figure 1. This array has forty-nine 1.670-inch diameter circular apertures spaced two inches on centers in both planes. The dielectric filling is of Rexolite #1422. The flush dielectric elements are matched by an annular groove 1.565-inch wide by 0.132-inch radial depth starting 0.257 inch back from the horn mouth. A transverse butt joint in the dielectric filling is located 1.850 inches back from the horn mouth to permit each of these elements to be removed and replaced by an extended shaped element having a 1.850-inch long cylindrical section which is inserted into the waveguide. The results presented here are only for the flush dielectric elements.

A movable ground plane was constructed so as to be adjustable from a position flush with the horn mouths to a position two inches back from the horn mouths. The problem of maintaining adequate contact at the junction of the round waveguide tubing and the ground plane was solved by cutting beveled edges on the back side of the 3/16-inch thick aluminum ground plane around

the holes where the tubes pass through. Tightly wound bronze coil springs 0.080 inch in diameter were then clamped into the bevels by a 1/4-inch aluminum panel which was bolted to the back of the ground plane.

The method of measurement and the element identification system are illustrated in Figure 2. The accuracy of the bolometer detector, amplifier, and voltmeter used was within ± 0.5 db when checked with a precision attenuator over a 40 db range. The coupling measurements were made by exciting the center element (0,0) with all other elements terminated in matched loads and measuring the relative signal level from elements (m,0) along the x axis, elements (0,n) along the y axis, and elements (m=n) along the diagonal. The polarization of the elements was such that the E plane was parallel to the y axis, thus E-plane coupling was measured along the y axis and H-plane coupling along the x axis.

Results obtained in a preliminary investigation on a linear array of six circular-waveguide horns with flush dielectric elements showed that considerable reduction in H-plane coupling could be obtained by moving the ground plane back from the horn mouths. The H-plane couplings for the linear array of six horns are shown in Figure 3a as functions of the distance d from the horn mouths back to the ground plane for a frequency of 3150 Mc. It is seen that the H-plane coupling to the first and second neighboring elements is reduced 14 db and 19 db, respectively, for d = 1.3 inches. The E-plane couplings, obtained by rotating the polarization 90° , are shown in Figure 3b. It is seen that for d = 0 the E-plane couplings are comparable to the H-plane couplings, but as d is increased the E-plane couplings increase as much as 10 db at d = 0.8 inch and then return at d = 1.3 inches to about the same values as for d = 0.

The H-plane, E-plane, and diagonal couplings for the 7 x 7 waveguide horn array are shown in Figures 4a, b, and c, respectively, as functions of the ground plane distance d for a frequency of 3150 Mc. While the couplings measured in the 49-horn planar array are similar in their gross behavior to those measured in the six-horn linear array, the changes in coupling are of lesser magnitude in general and there are more variations with d . Some of these variations tend to form cusps having very low values of coupling. In order to aid in selecting an optimum ground plane position, the values of coupling to the three closest horns were replotted on a single sheet as shown in Figure 4d.

In making these coupling measurements, a matched condition to the excited input horn (0,0) was maintained at all times with a tuner and a matched detector was connected to the coupled horn (m,n) being measured; however, the coupled horn was not tuned to present a matched source to the detector. This was judged the most practical method since the tuner on the excited center element needed to be adjusted only once for each position of the ground plane. On the other hand, if it were attempted to match the coupled elements, not only would an adjustment have to be made for every position of the ground plane but also for every element. Since the coupled element mismatch was less than a 2 to 1 VSWR, the amount of error produced in the coupling measurement should be less than 0.3 db.

The VSWR's of the elements in the 7 x 7 waveguide horn array are shown in Figures 5a, b, and c as functions of the ground plane distance d for a frequency of 3150 Mc. These are the VSWR's of only the horn mouths, since all the reflections up to each horn mouth were matched out by a tuner at each input with a matched load inserted in each horn. The input VSWR's

are seen to change greatly with the ground plane distance d , although the curves are smoother in general than those for the coupling.

The coupling and VSWR data were used together with the element patterns to select a ground plane position of $d = 1.125$ inches for further measurements. The H-plane coupling, Figure 4a, indicated a distance between 1.12 and 1.25 inches while the E-plane coupling, Figure 4b, indicated a distance between 1.00 and 1.12 inches. The diagonal coupling, Figure 4c, indicated a distance between 1.25 and 1.50 inches, but this was given less weight since the values of diagonal coupling are lower. The composite plot in Figure 4d indicates a best overall distance of 1.25 inches, but by itself this does not take account of the 2nd and 3rd element couplings in the E plane for which 1.12 inches is a better distance. The VSWR's are all lower for a distance of 1.25 to 1.50 inches, but are under 1.6 for $d = 1.12$ inches. As will be seen later, the principal E-plane patterns are good over the range from $d = 1.00$ to 1.50 inches, while the principal H-plane patterns are best from $d = 1.00$ to 1.25 inches. Taking all of these factors into account, the value of $d = 1.125$ inches was selected.

The H-plane, E-plane, and diagonal couplings for $d = 1.125$ inches were then measured over the 20 percent band from 2850 Mc to 3450 Mc and are shown in Figures 6a, b, and c, respectively. The corresponding VSWR's are shown in Figures 7a, b, and c. It is apparent from these data that the circular-waveguide horn array with flush dielectric elements and $d = 1.125$ inches works best over the 10 percent band from about 3150 Mc to 3450 Mc. Most of the VSWR's are below 1.5 over the latter band, and the couplings all decrease below their values at 3150 Mc except for the couplings to the 2nd and 3rd elements in the E plane which remain reasonably low. While the

E-plane couplings decrease over the band from 3150 Mc to 2850 Mc and the H-plane and diagonal couplings increase only moderately, the VSWR's exceed 1.5 at 3000 Mc and reach 3 to 1 at 2850 Mc.

In using a phased array for wide angle scanning, however, it is important to consider the variation in electrical spacing of the elements over the frequency band in addition to the coupling and VSWR. A second major lobe will begin to form at $\theta = -90^\circ$ when the element spacing in wavelengths becomes equal to $1/(1 + \sin \theta_m)$ where θ_m is the maximum scan angle. The two-inch element spacing in the 7 x 7 waveguide horn array is equal to 0.483, 0.508, 0.534, 0.559, and 0.585 wavelength at 2850, 3000, 3150, 3300, and 3450 Mc, respectively. The corresponding maximum scan angles, θ_m , are 90° , 75.2° , 60.8° , 52.1° , and 45.2° . The magnitude of the second major lobe which is formed when these values of scan angle are reached and exceeded depends, of course, on the amount of suppression provided by the individual element pattern near $\theta = \pm 90^\circ$. The present array design with flush dielectric elements should be satisfactory over the band from 3150 Mc to 3450 Mc for a $\pm 45^\circ$ scan sector. For a scan sector of $\pm 50^\circ$, however, it would be preferable to use the array over the 10 percent band from 3000 Mc to 3300 Mc and rematch the elements for a better VSWR over that band.

The principal H-plane patterns of the center element in the 7 x 7 waveguide horn array are shown in Figures 8a, b, c, and d for several ground plane positions at 3150 Mc. Similar patterns for the principal E plane are shown in Figures 9a, b, c, and d. These results show that the element patterns are most sensitive to variation of the ground plane distance d in the range from 3/8 inch to one inch. For d from zero to 1/4 inch, there is only minor change in the H-plane pattern and no appreciable change in the

E-plane pattern. From 1.125 inches to 2 inches, the patterns show negligible change in the E plane while there is some fall-off of the H-plane pattern shoulders between 1.25 and 1.50 inches.

The radical pattern changes in the critical region are attributed to the fact that the distance from the edges of the horns back to the ground plane passes through the anti-resonant quarter-wavelength condition. A quarter wavelength at 3150 Mc is about 0.94 inch, and the end loading by the large waveguide horn diameter would foreshorten the anti-resonant length somewhat. If only a simple TEM mode existed between the horns, the ground plane would be one-half wavelength back from the horn mouths at $d = 1.88$ inches and thus behave the same as the flush ground plane. This is seen to be more nearly the case for the coupling and VSWR than for the patterns.

Outside the critical region from $d = 3/8$ inch to one inch, the measured horn patterns show suitable characteristics for use in a wide angle scanned array. The -3 db beamwidth is about 110 degrees in the H plane and about 100 degrees in the E plane with fairly rapid fall off outside these ranges.

Off-axis H-plane patterns were measured at 3150 Mc with a ground plane distance of 1.125 inches for E-plane angles of 20° , 40° and 60° . These patterns are shown in Figure 10 and indicate that good volume coverage is obtained.

Principal-plane patterns were also measured in 150 Mc steps from 2850 Mc to 3450 Mc with a ground plane distance of 1.125 inches. These are shown in Figure 11a for the H plane and in Figure 11b for the E plane. They remain most constant over the 3000 Mc to 3300 Mc band in the H plane and

over the 3150 Mc to 3450 Mc band in the E plane. The H-plane pattern at 3450 Mc is somewhat narrow, while the E-plane patterns at 2850 Mc and 3000 Mc are relatively poor. (Note: The apparent gain advantage at 3000 Mc in the E plane is misleading, since the recorded patterns are not relative to a reference level that remained fixed with frequency.) It is quite possible that the patterns at 2850 Mc in the H plane and at 2850 Mc and 3000 Mc in the E plane would be improved by using a ground plane distance greater than 1.125 inches, since this distance may be too close to the critical region at the longer wavelengths.

IV. Conclusions

Mutual coupling effects on the pattern and impedance characteristics of a large steerable phased array antenna can be readily investigated by a combination of suitable measurements made on a smaller array of like elements and a computer formulation based on superposition. Rather than determining the mutual impedances between elements, terms of an array scattering matrix are obtained by direct measurement in this approach. Edge effects are also taken into account. Effects on the overall array pattern are readily predicted in advance from the measured patterns of elements of the small array when individually excited in their array environment with all other elements terminated, since an element pattern for these conditions contributes in direct proportion to its excitation voltage and includes all mutual coupling effects on that element.

From the results presented here, it is apparent that the coupling, VSWR, and patterns of the radiating elements in a phased array are greatly affected by the position of the ground plane relative to the element apertures. An improper position of the ground plane behind the radiating

elements can have disastrous effects on the VSWR and patterns. Some improvement in these mutual coupling effects can be obtained by proper location of the ground plane, but it appears that major improvement will depend more on the element design and on the placement of devices around the elements to reduce the coupling.

V. Acknowledgements

This work was sponsored by the Heavy Military Electronics Department of the General Electric Company on internal development funds. The measurements were made by Messrs. M. F. Bolster, J. J. Jarek, and F. R. Rakvica.

References

1. P. S. Carter, Jr., "Mutual Impedance Effects in Large Beam Scanning Arrays," IRE Trans. on Antennas and Propagation, vol. AP-8, pp. 276-285; May 1960.
2. J. L. Allen, "Gain and Impedance Variation in Scanned Dipole Arrays," IRE Trans. on Antennas and Propagation, vol. AP-10, pp. 566-572; September 1962.
3. L. A. Kurtz, et al., "Mutual-Coupling Effects in Scanning Dipole Arrays," IRE Trans. on Antennas and Propagation, vol. AP-9, pp. 433-443; September 1961.
4. S. Edelberg and A. A. Oliner, "Mutual Coupling Effects in Large Antenna Arrays II: Compensation Effects," IRE Trans. on Antennas and Propagation, vol. AP-8, pp. 360-367; July 1960.
5. S. Edelberg and A. A. Oliner, "Mutual Coupling Effects in Large Antenna Arrays: Part I - Slot Arrays," IRE Trans. on Antennas and Propagation, vol. AP-8, pp. 286-297; May 1960.
6. L. Parad, "Some Mutual Impedance Effects in Phased Array," Microwave Journal, vol. V, pp. 87-89; June 1962.



WAVEGUIDE HORN ARRAY

Figure 1

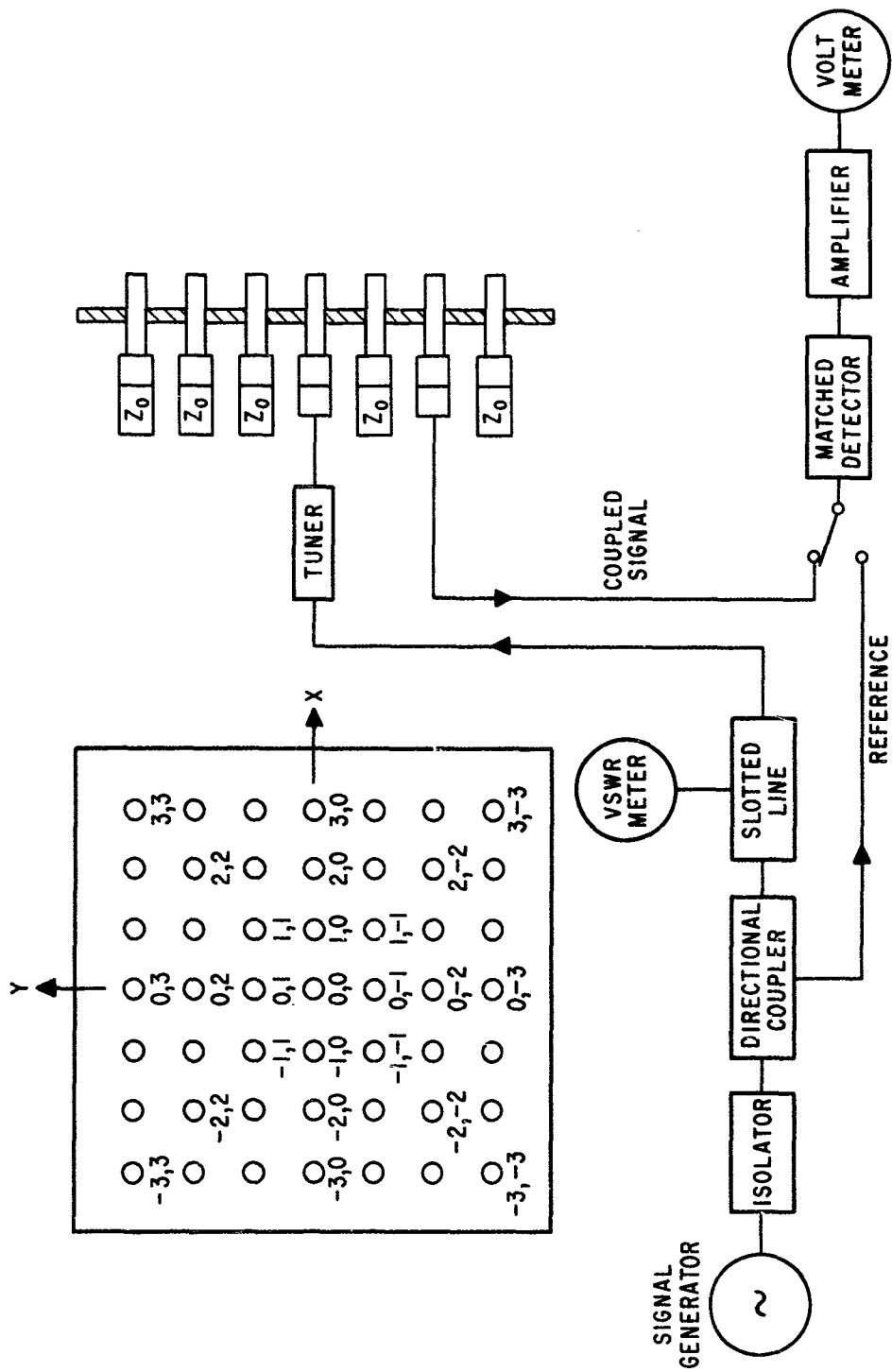


FIG. 2

MUTUAL COUPLING IN 6-HORN LINEAR ARRAY
 VS GROUND PLANE DISTANCE, d
 $f = 3150 \text{ Mc}$
 H-PLANE COUPLING

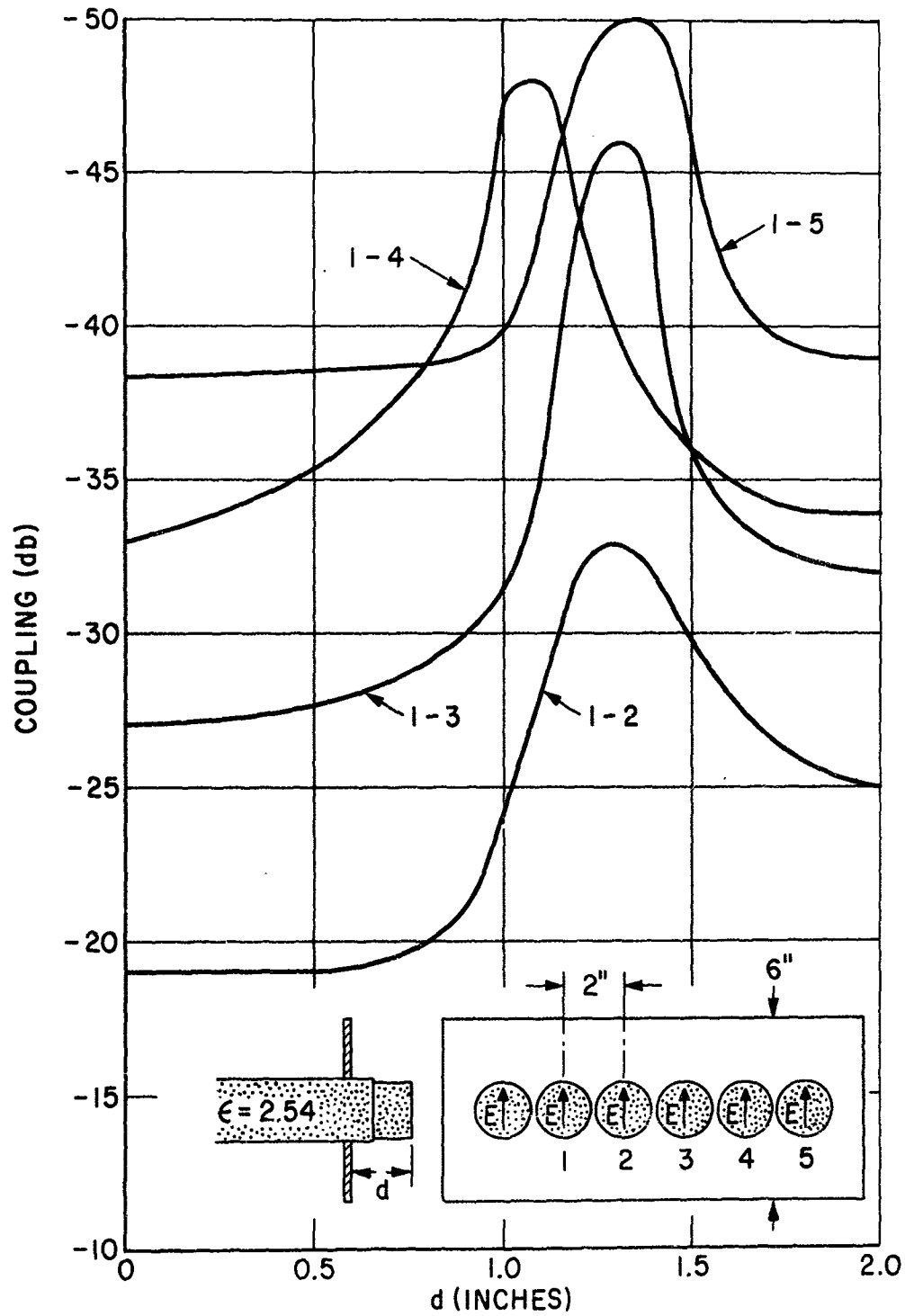


FIG. 3a

MUTUAL COUPLING IN 6-HORN LINEAR ARRAY VS GROUND PLANE DISTANCE, d

$f = 3150 \text{ Mc}$

E - PLANE COUPLING

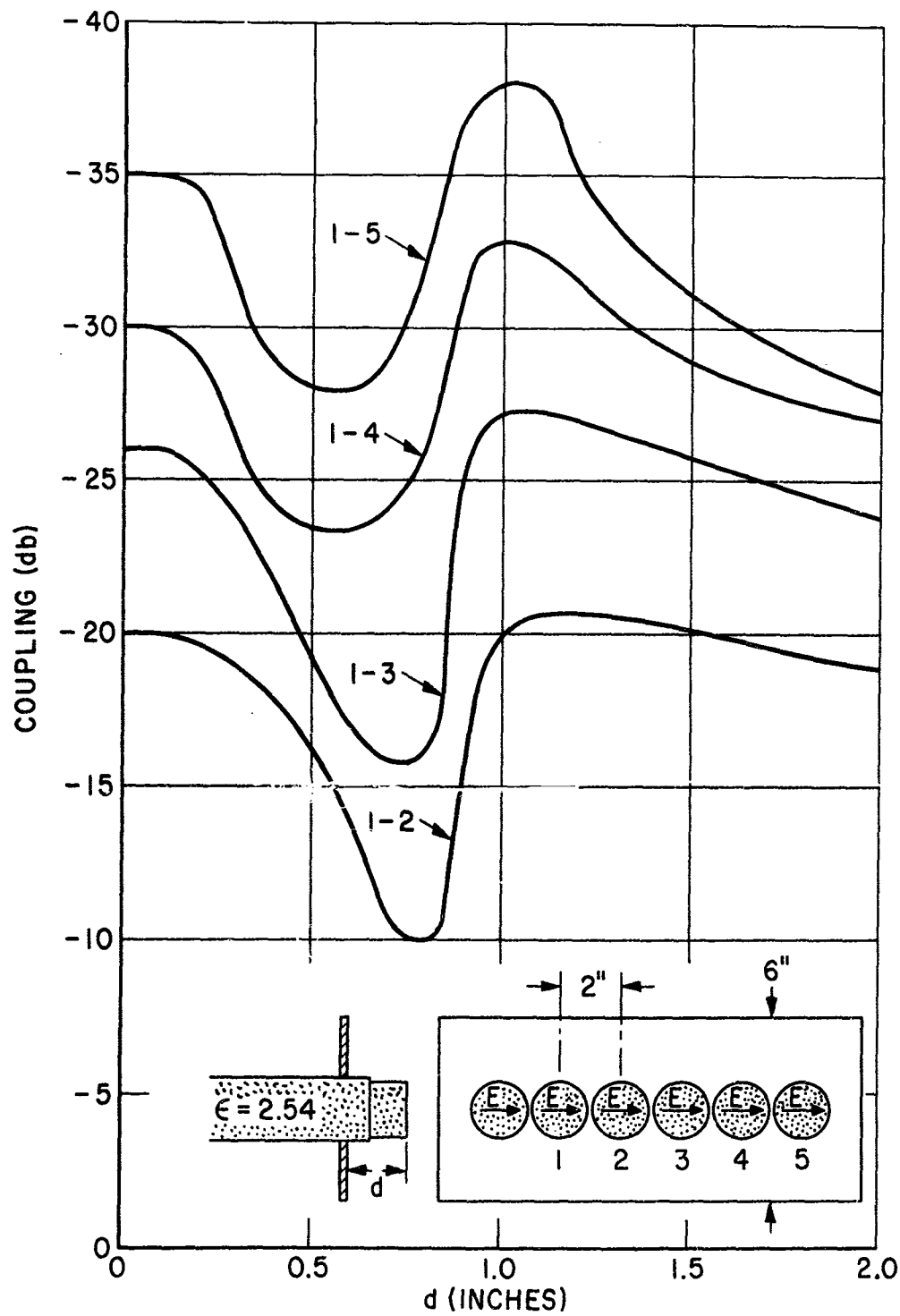


FIG. 3b

MUTUAL COUPLING IN 7 X 7 HORN ARRAY
VS GROUND PLANE DISTANCE, d
 $f = 3150 \text{ Mc}$
H-PLANE COUPLING

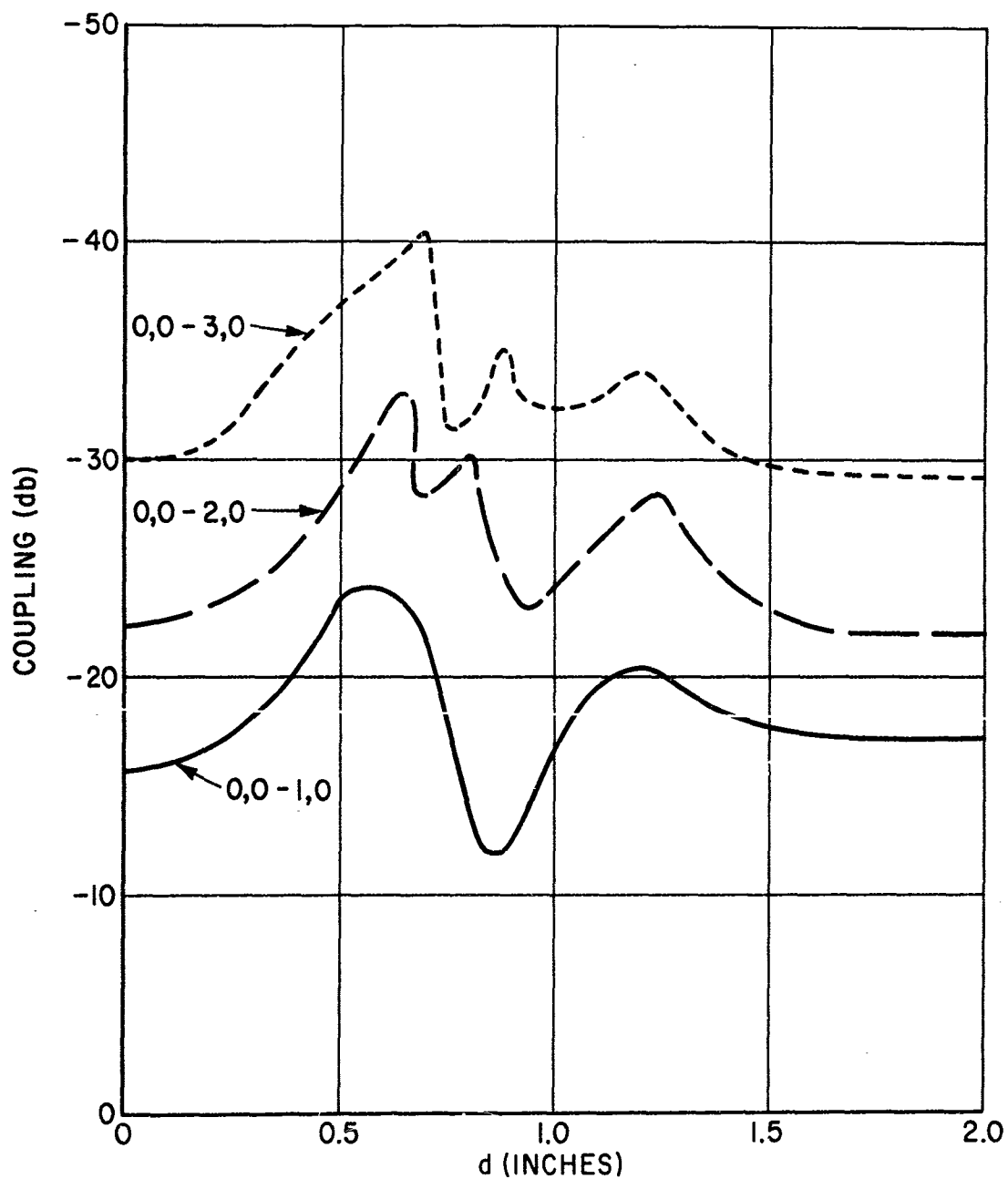


FIG. 4a

MUTUAL COUPLING IN 7 X 7 HORN ARRAY
VS GROUND PLANE DISTANCE, d
 $f = 3150$ Mc
E-PLANE COUPLING

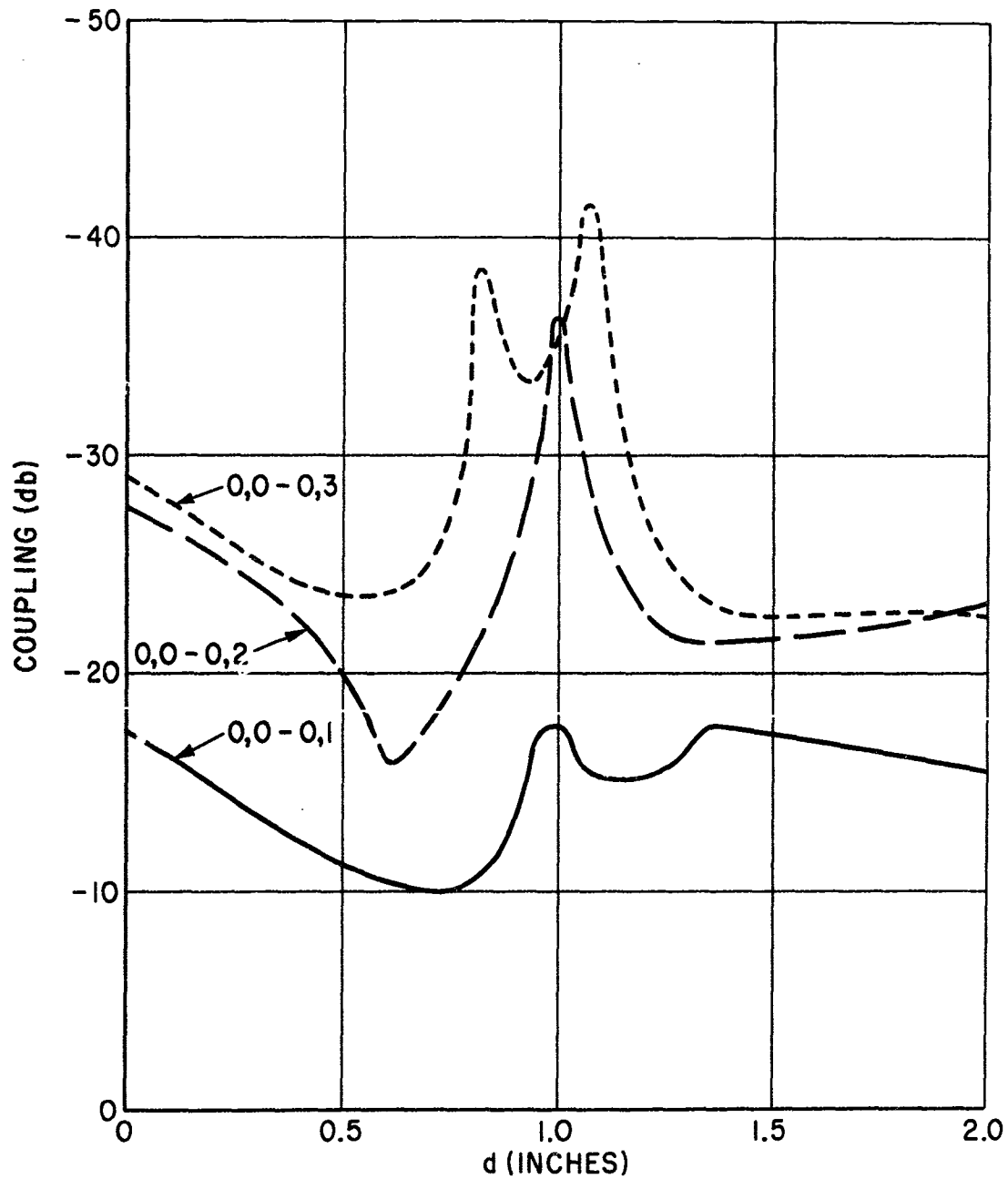


FIG. 4b

MUTUAL COUPLING IN 7 X 7 HORN ARRAY
 VS GROUND PLANE DISTANCE, d
 $f = 3150$ Mc
 THREE NEAREST ELEMENTS

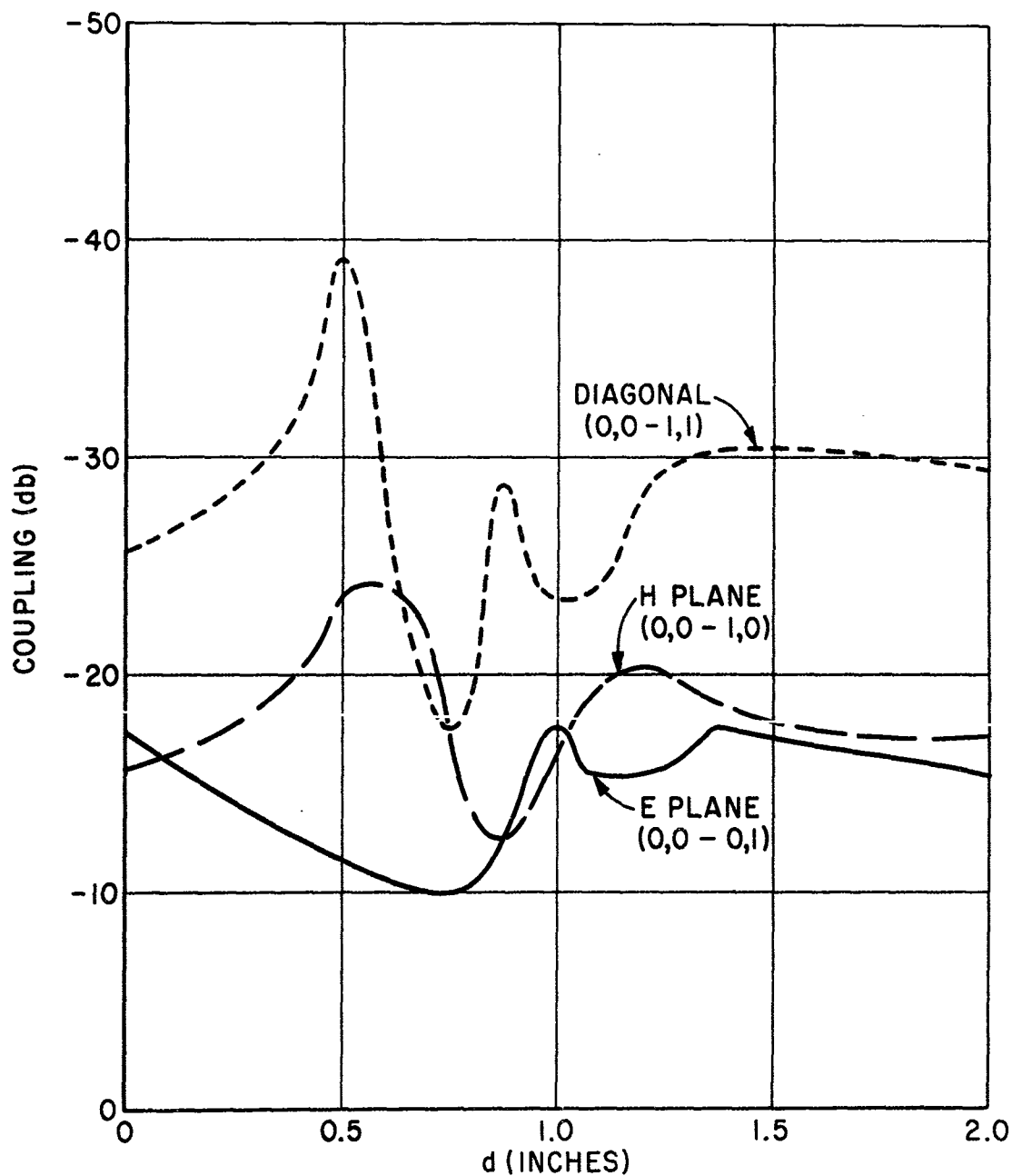


FIG. 4d

INPUT VSWR OF ELEMENT IN 7 X 7 HORN ARRAY
VS GROUND PLANE DISTANCE, d
 $f = 3150 \text{ Mc}$

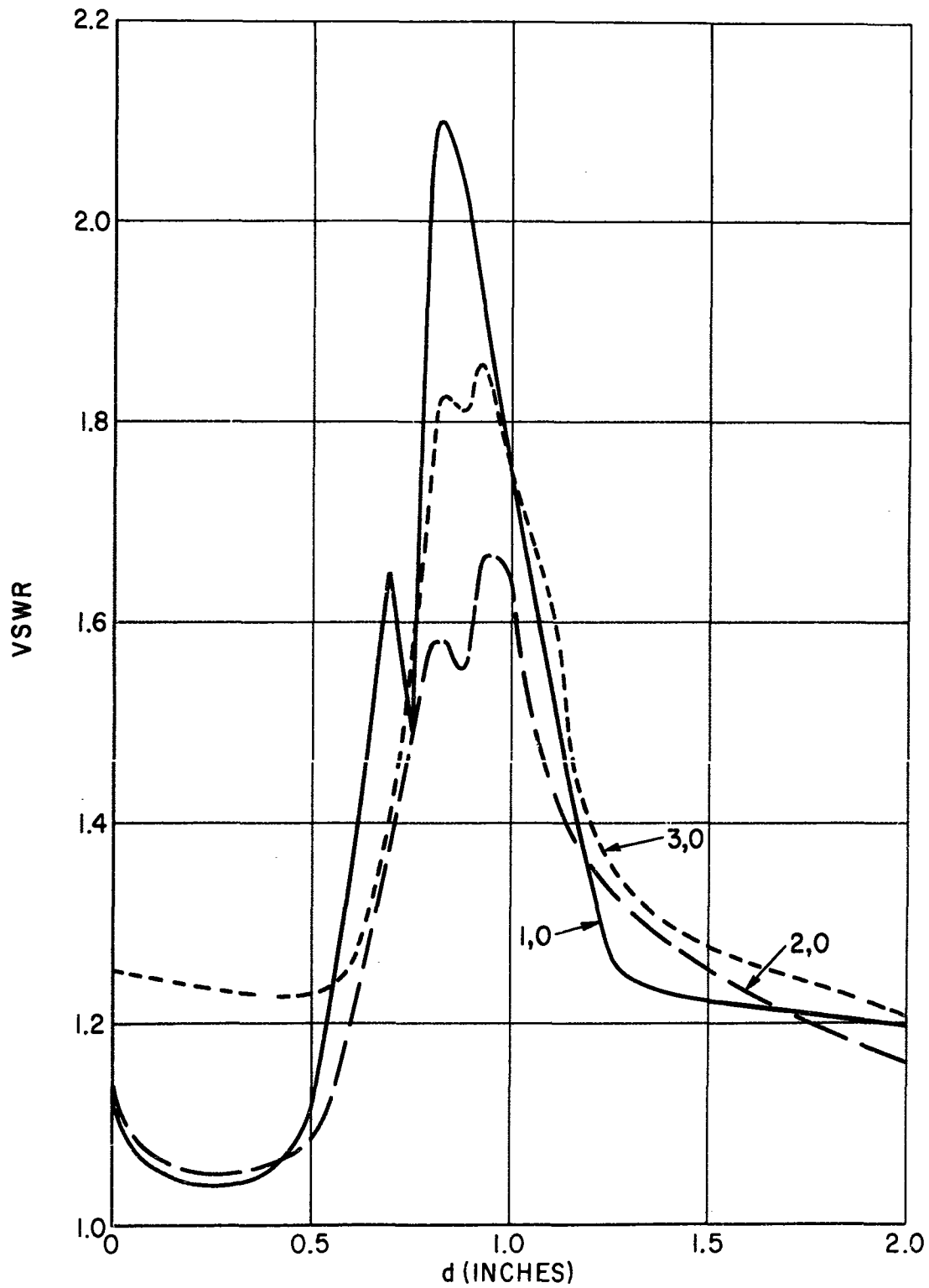


FIG. 5a

INPUT VSWR OF ELEMENT IN 7 X 7 HORN ARRAY
VS GROUND PLANE DISTANCE, d
 $f = 3150 \text{ Mc}$

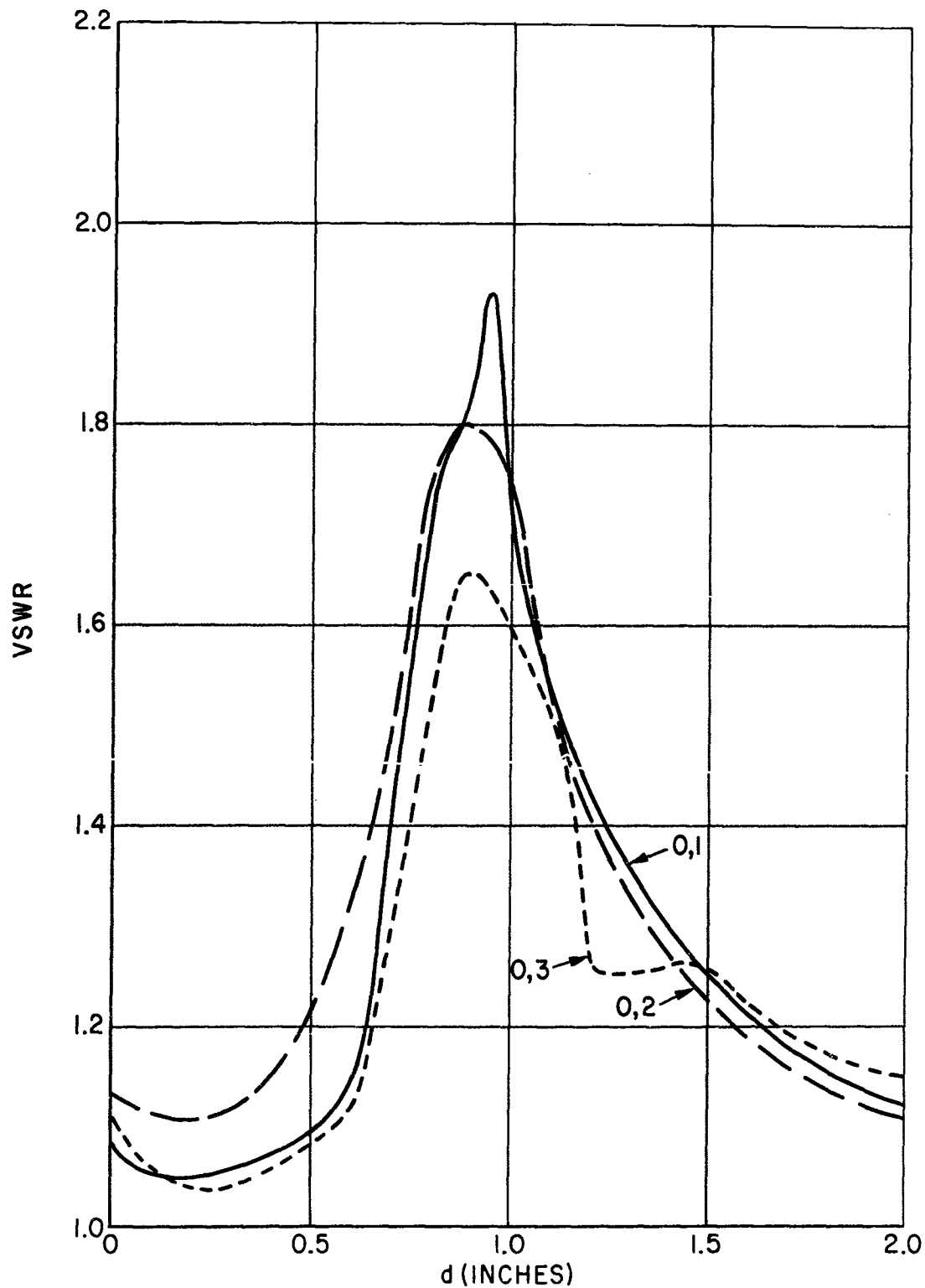


FIG. 5b

INPUT VSWR OF ELEMENT IN 7 X 7 HORN ARRAY
VS GROUND PLANE DISTANCE, d
 $f = 3150 \text{ Mc}$

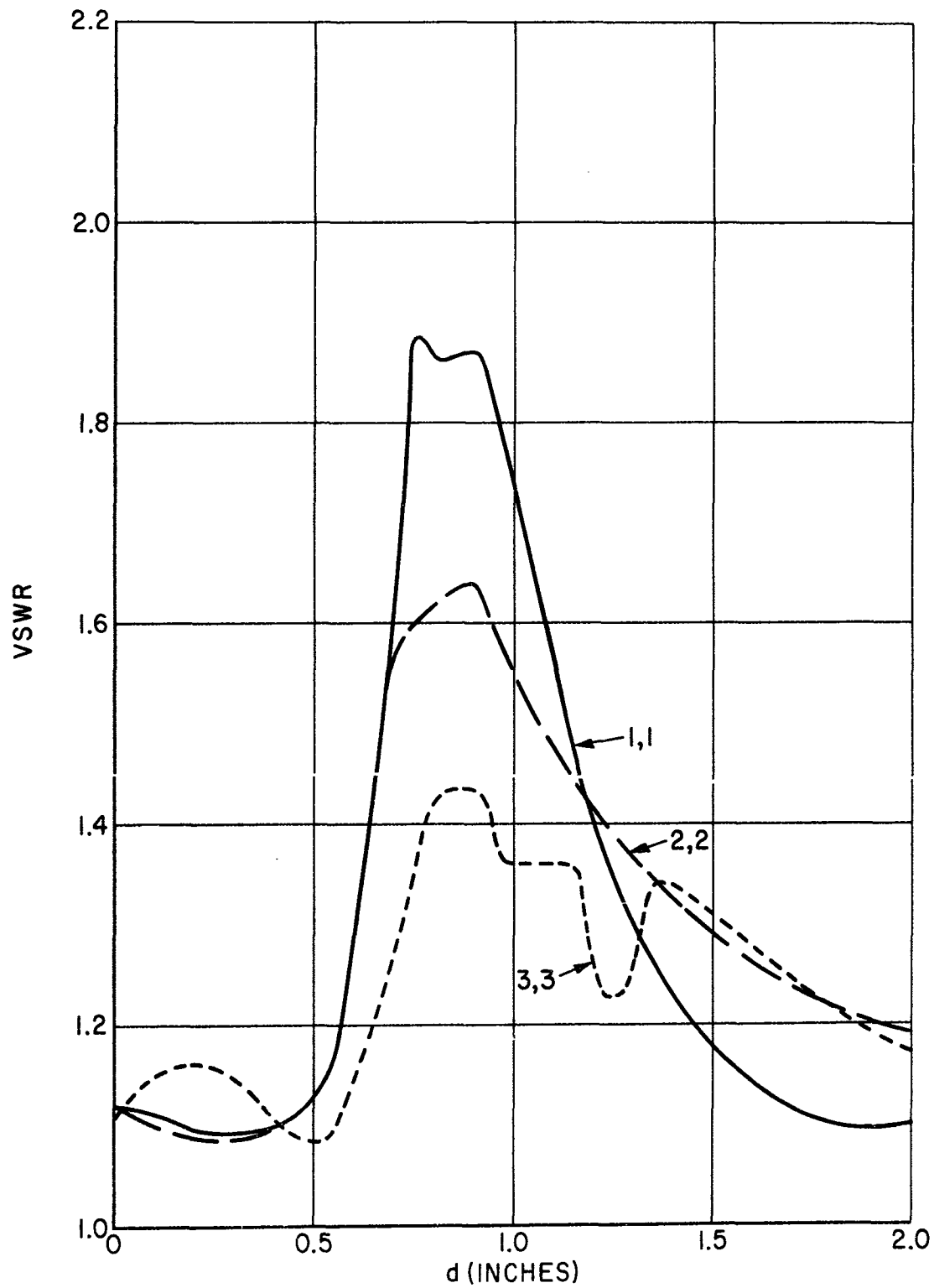


FIG. 5c

MUTUAL COUPLING IN 7 X 7 HORN ARRAY
VS FREQUENCY
 $d = 1.125''$
H-PLANE COUPLING

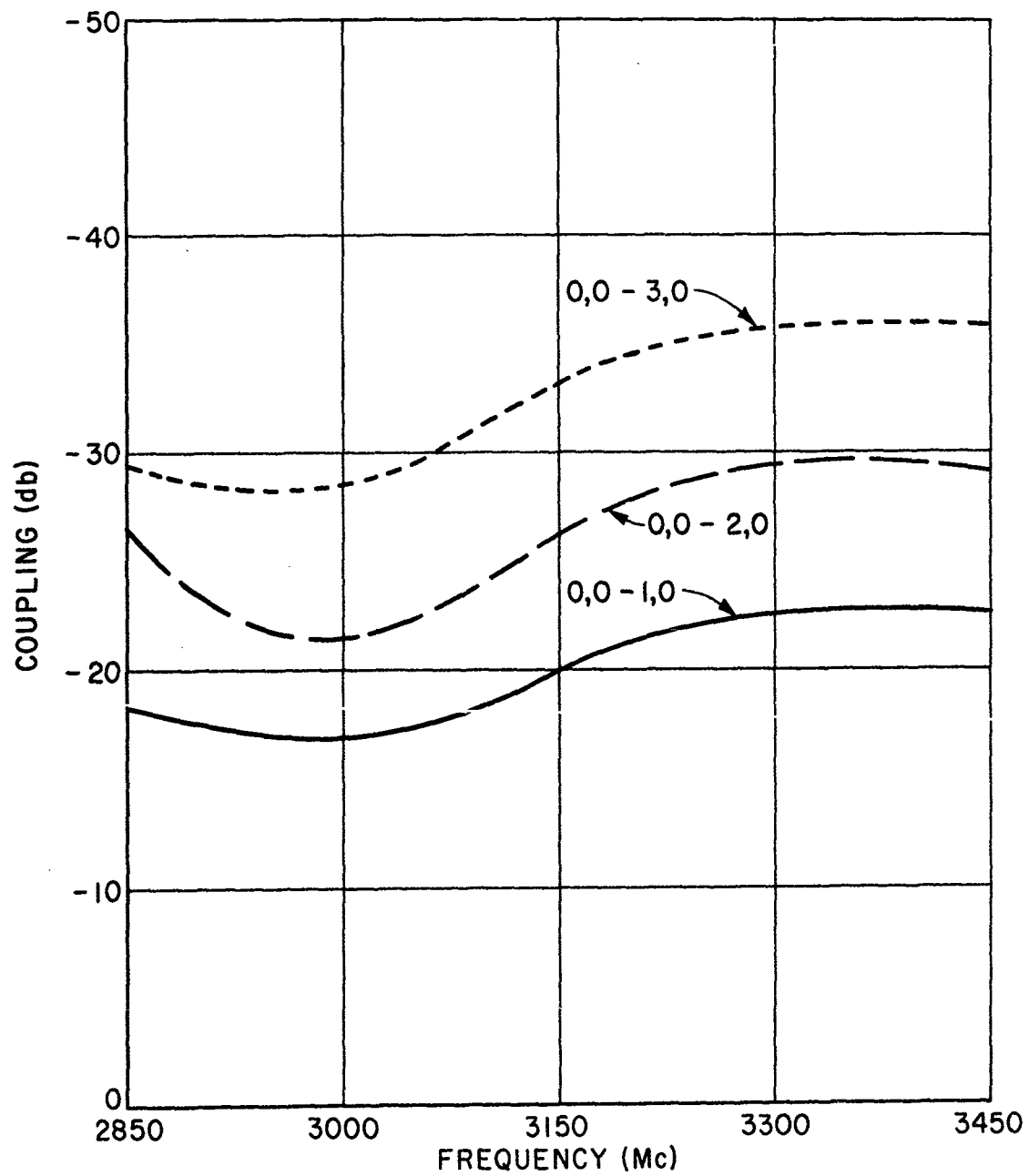


FIG. 6a

MUTUAL COUPLING IN 7 X 7 HORN ARRAY
VS FREQUENCY
 $d = 1.125''$
E - PLANE COUPLING

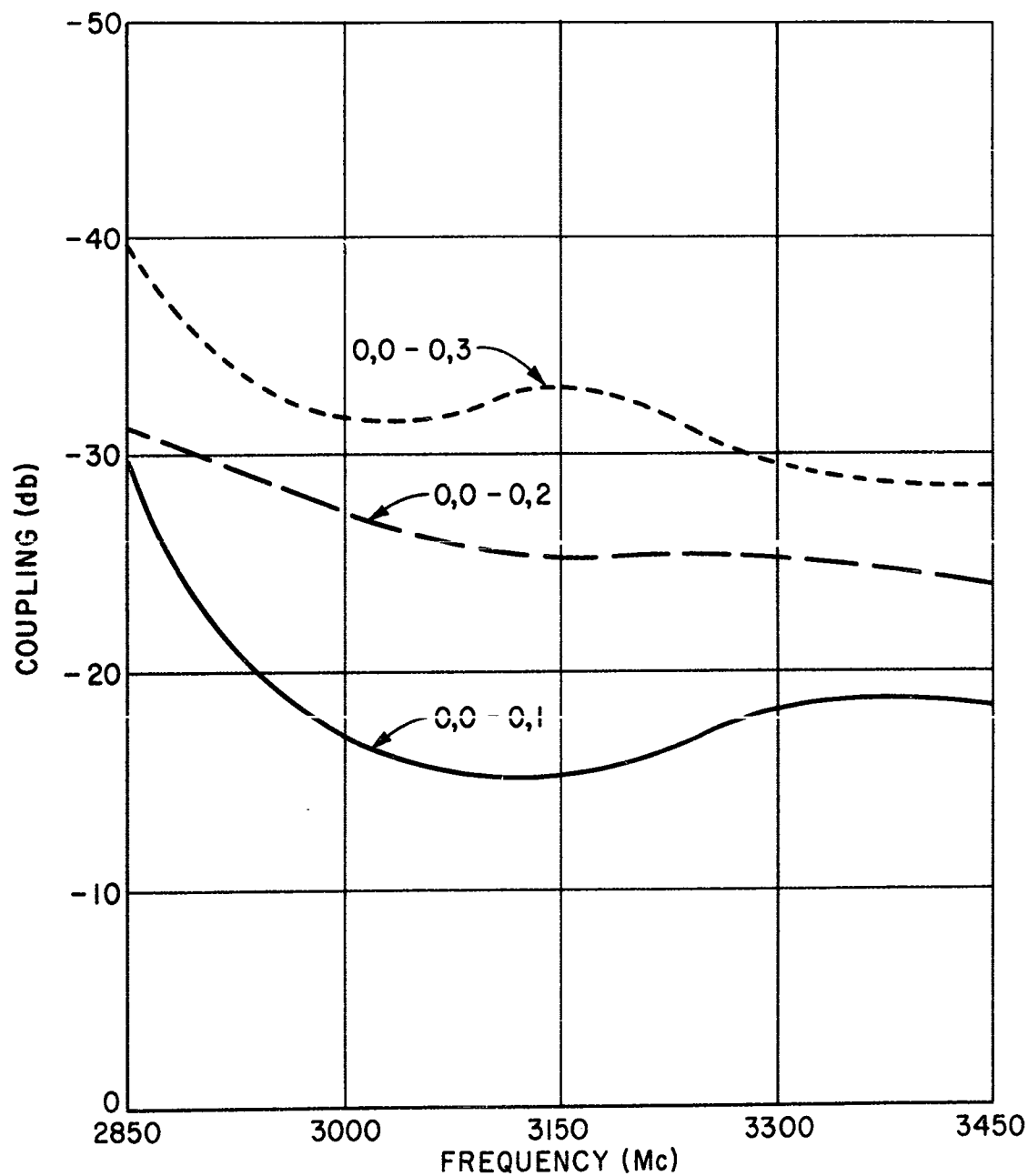


FIG. 6b

MUTUAL COUPLING IN 7X7 HORN ARRAY
VS FREQUENCY
 $d = 1.125''$
DIAGONAL COUPLING

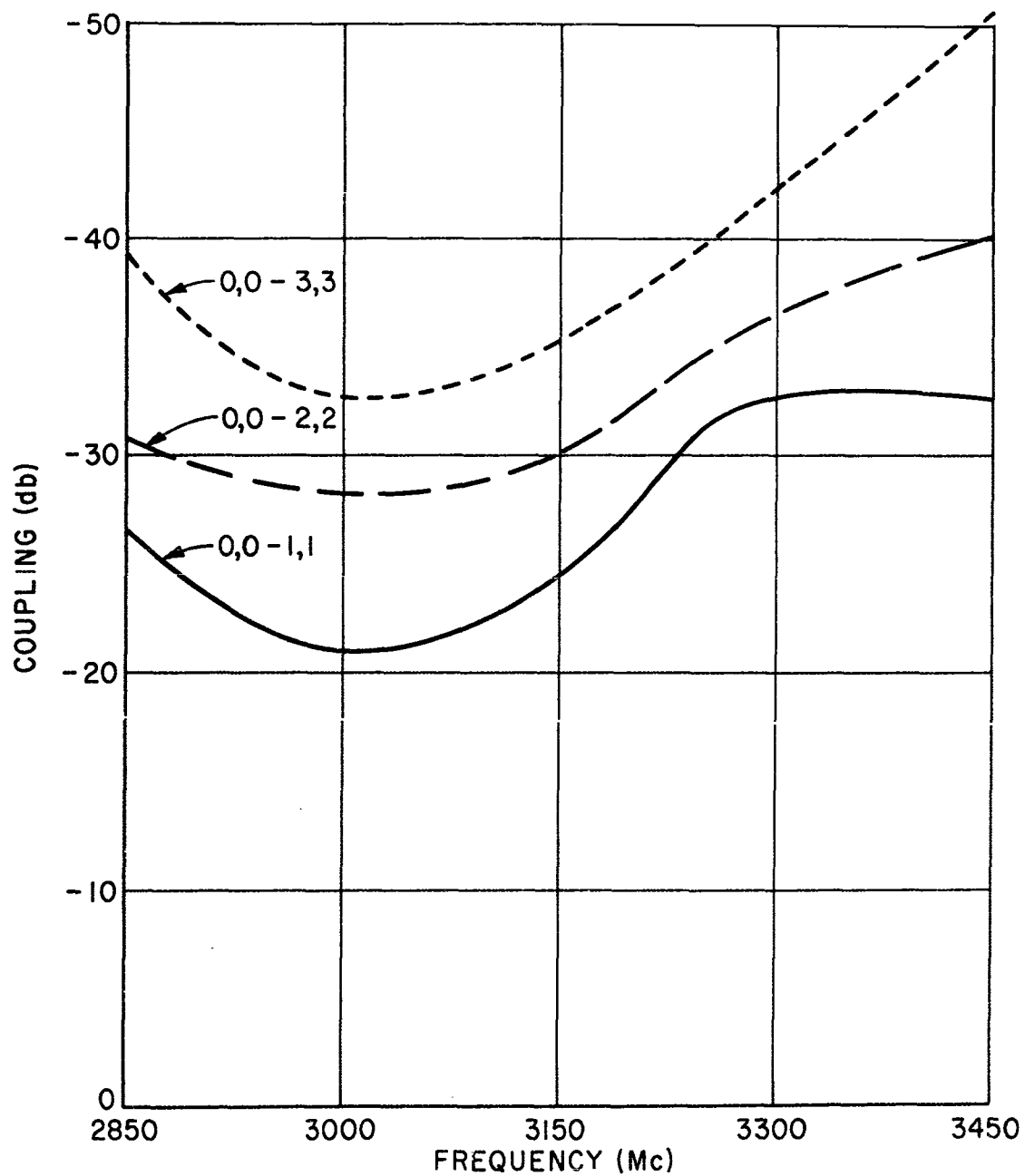


FIG. 6c

INPUT VSWR OF ELEMENT IN 7X7 HORN ARRAY
VS FREQUENCY
 $d = 1.125''$

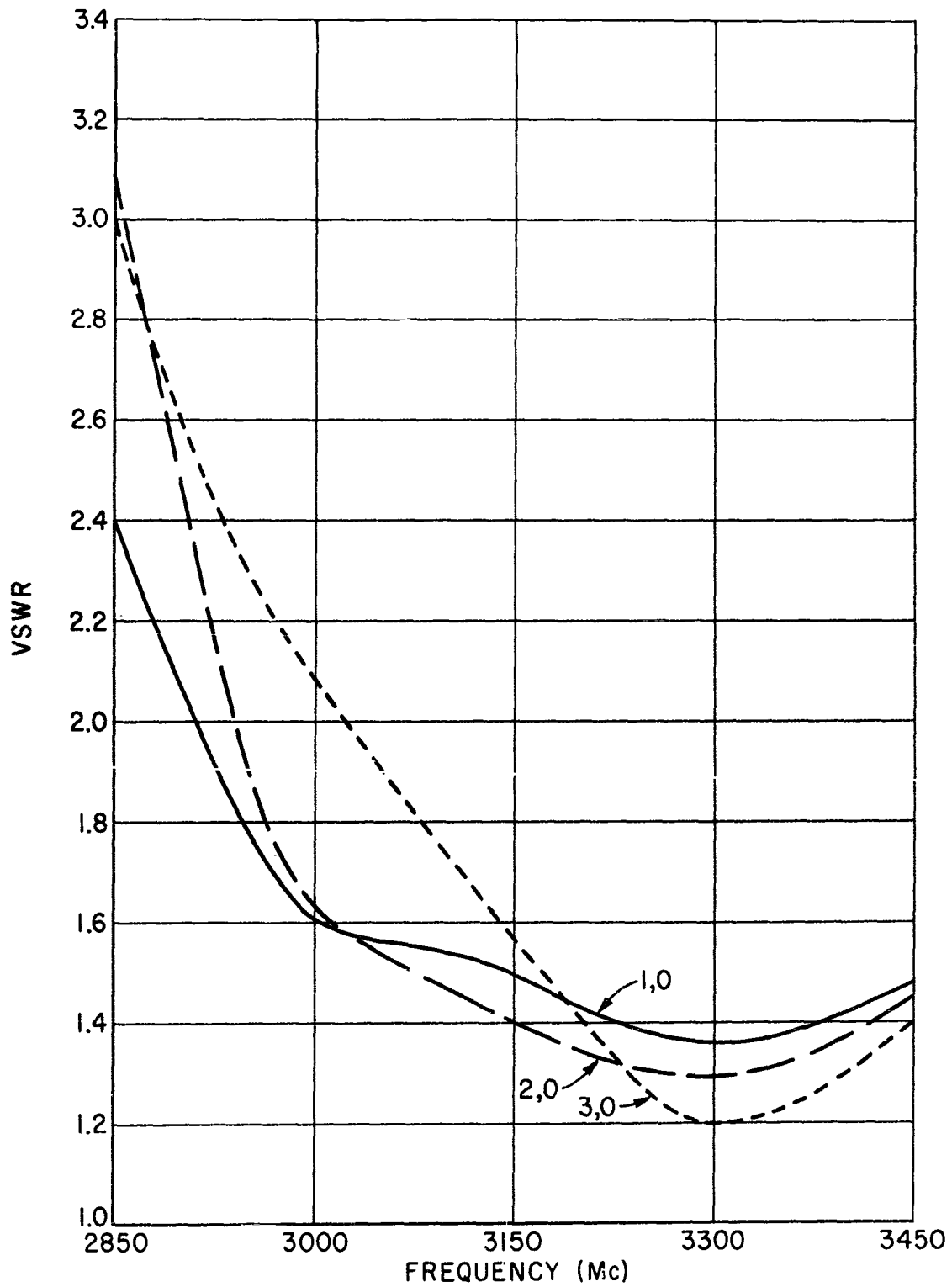


FIG. 7a

INPUT VSWR OF ELEMENT IN 7X7 HORN ARRAY
VS FREQUENCY
 $d = 1.125''$

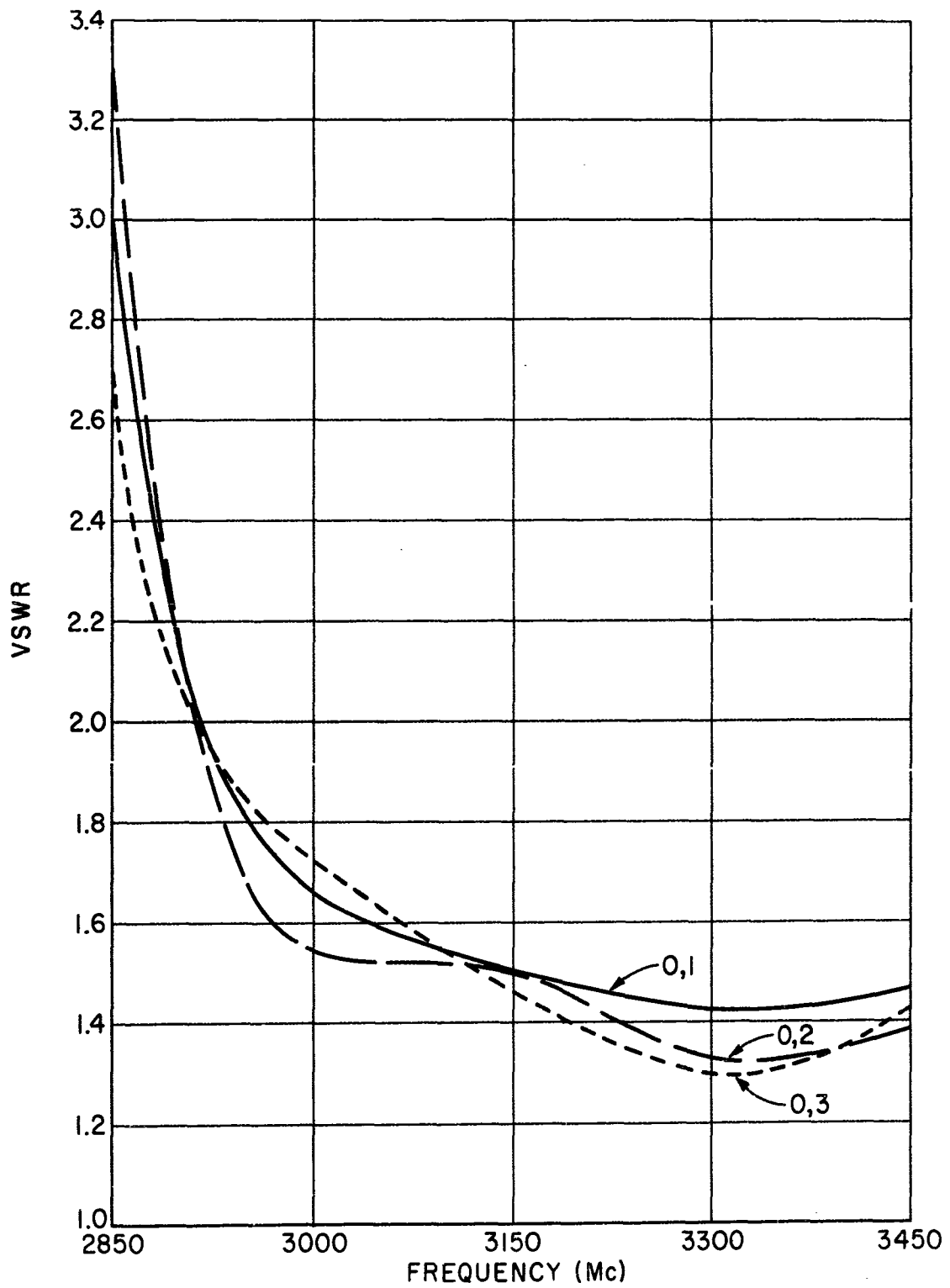


FIG. 7b

INPUT VSWR OF ELEMENT IN 7X7 HORN ARRAY
VS FREQUENCY
 $d = 1.125''$

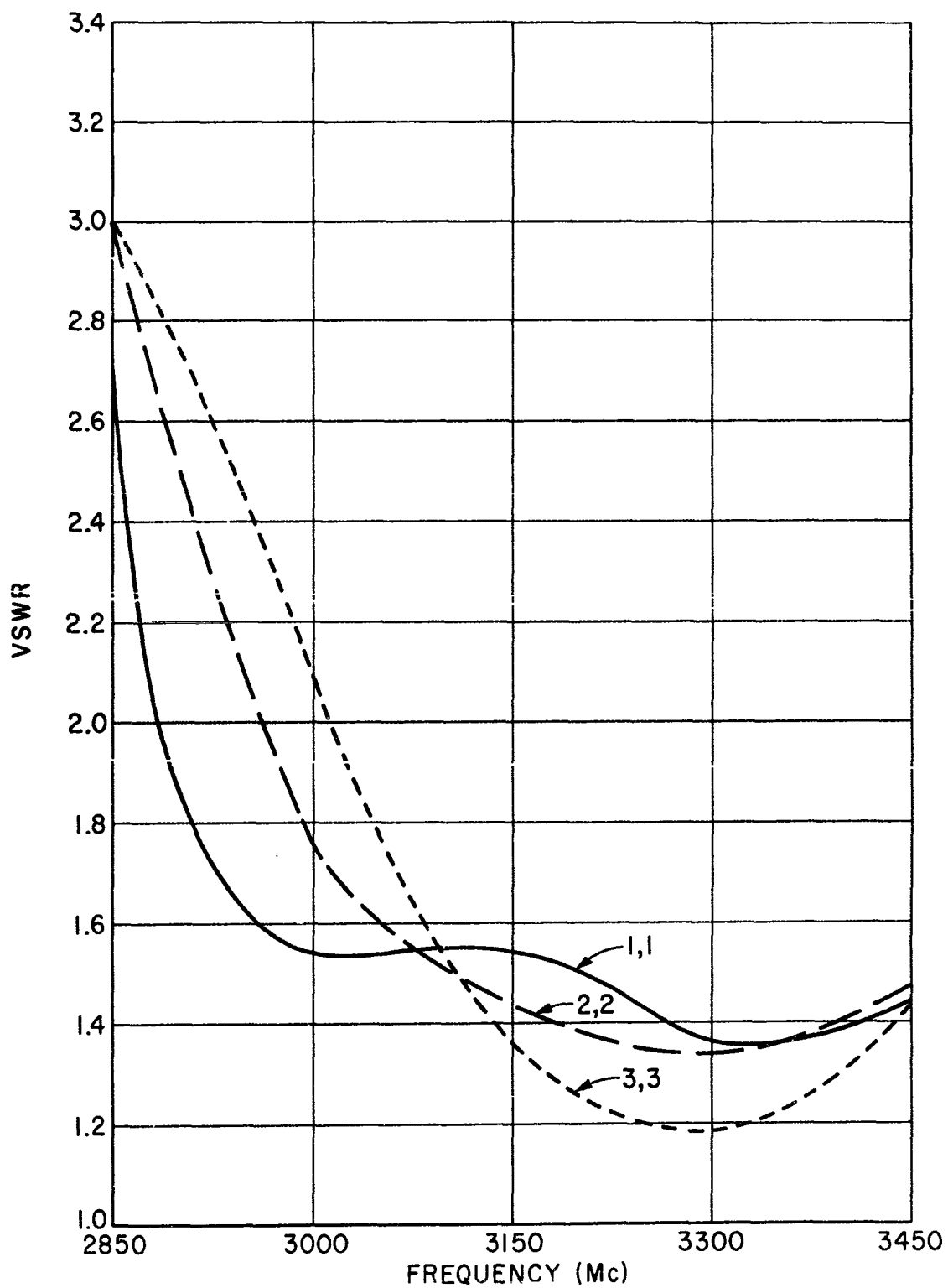


FIG. 7c

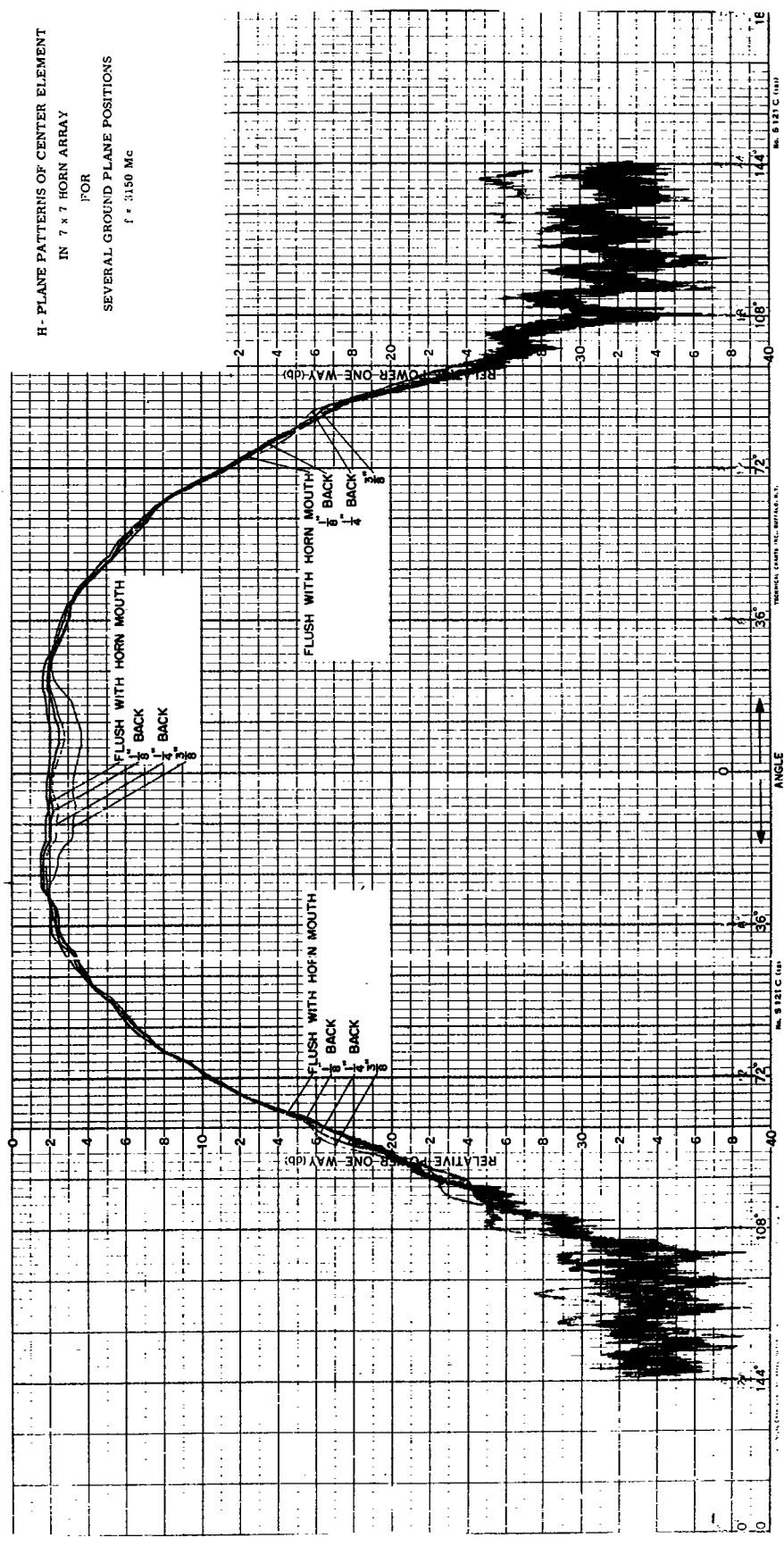
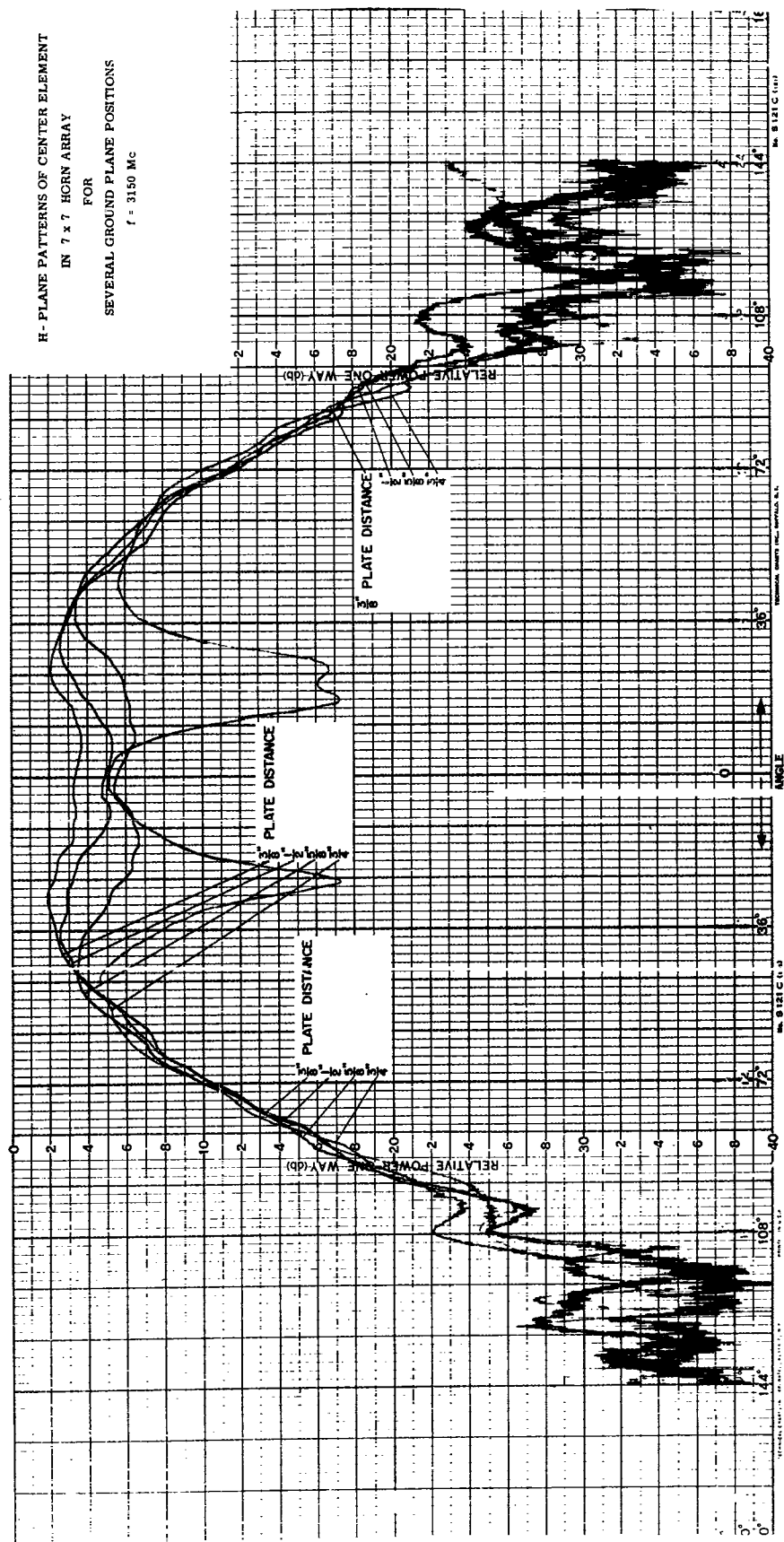


Figure 8a

H- PLANE PATTERNS OF CENTER ELEMENT
IN 7 x 7 HORN ARRAY
FOR
SEVERAL GROUND PLANE POSITIONS
 $f = 3150 \text{ Mc}$



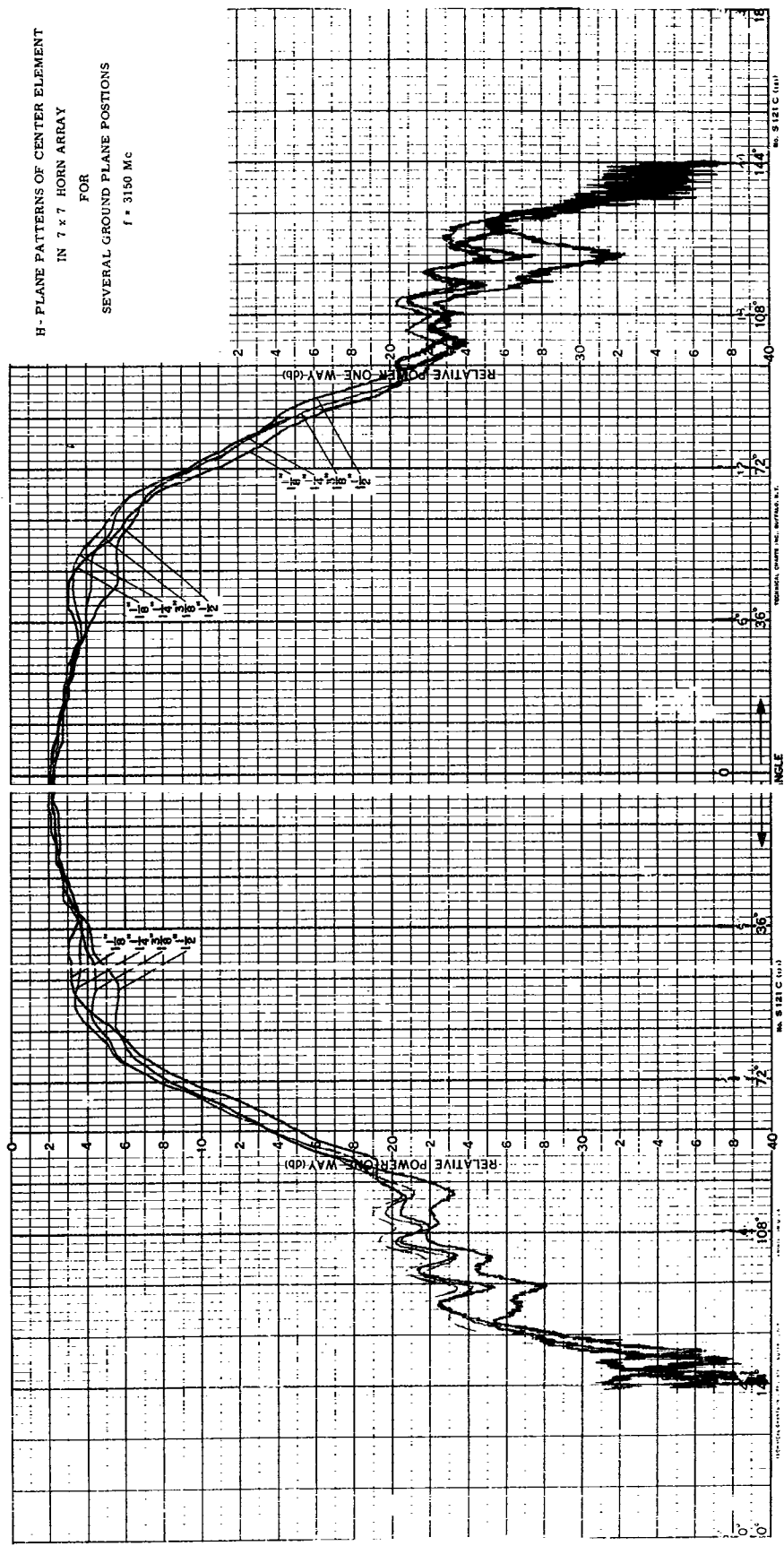


Figure 8d

E-PLANE PATTERNS OF CENTER ELEMENT
IN 7 x 7 HORN ARRAY
FOR
SEVERAL GROUND PLANE POSITIONS
 $f = 3150$ Mc

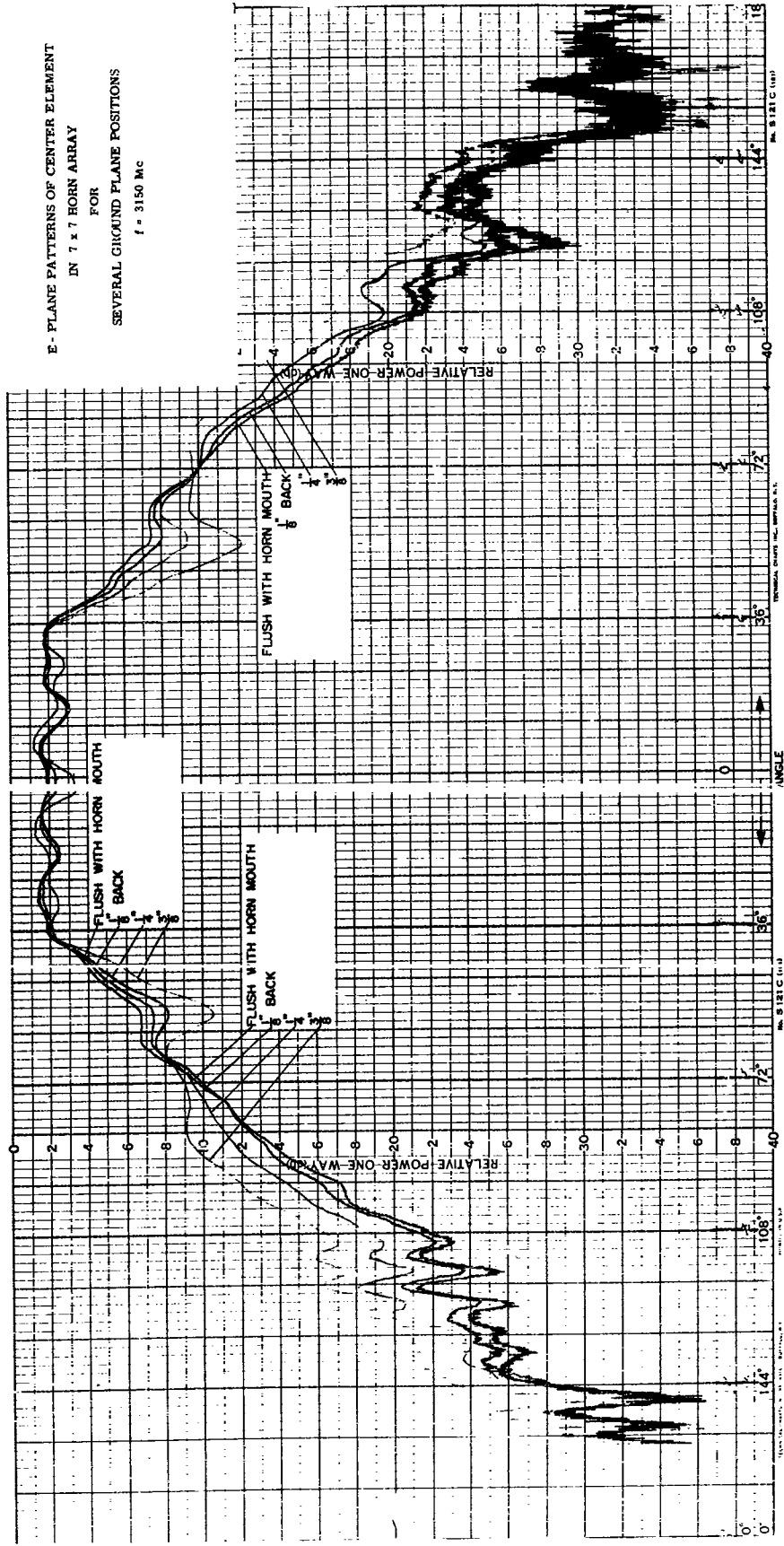


Figure 9a

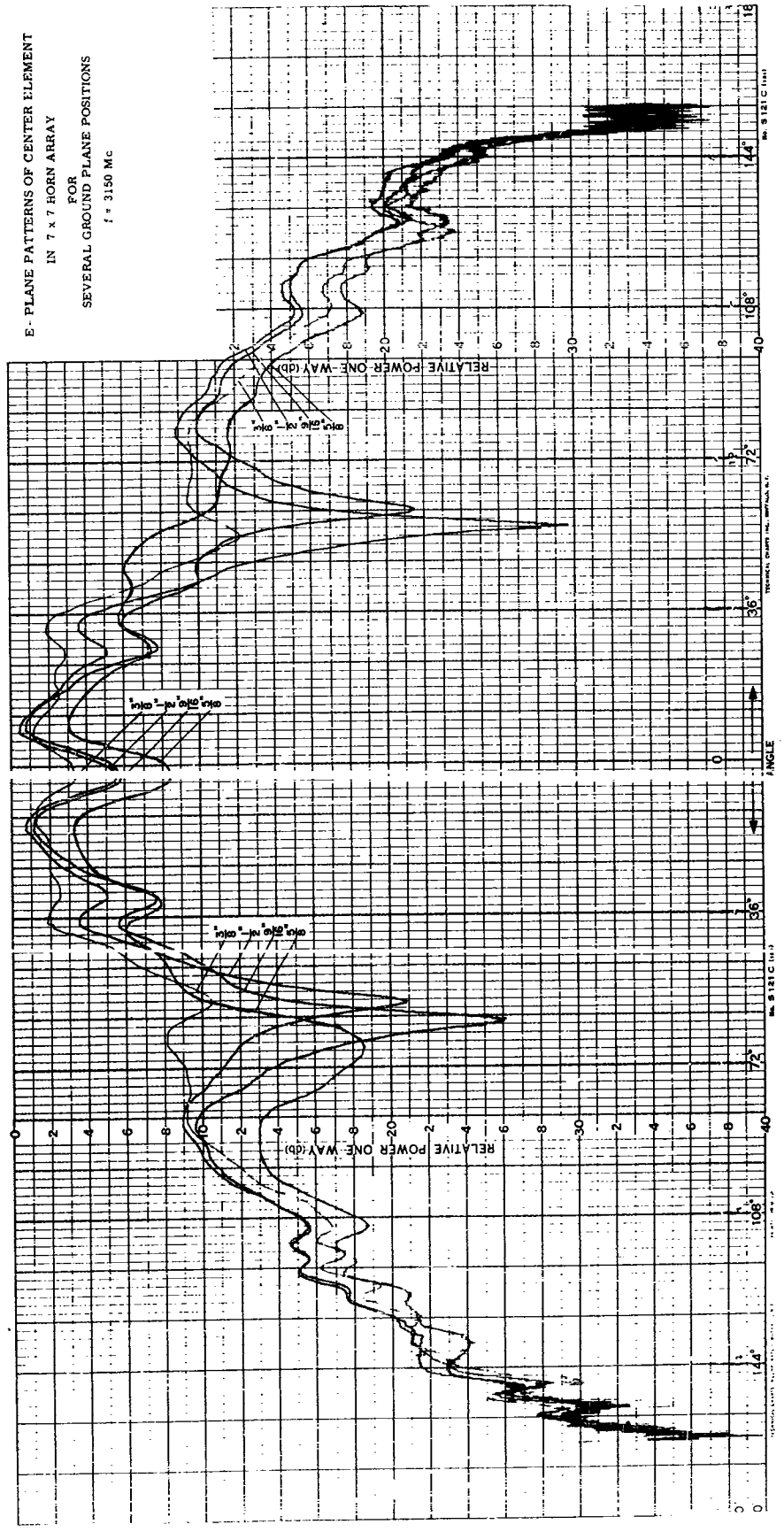


Figure 9b

E-PLANE PATTERNS OF CENTRE ELEMENT
IN 7 x 7 HORN ARRAY
FOR
SEVERAL GROUND PLANE POSITIONS
f = 3150 Mc

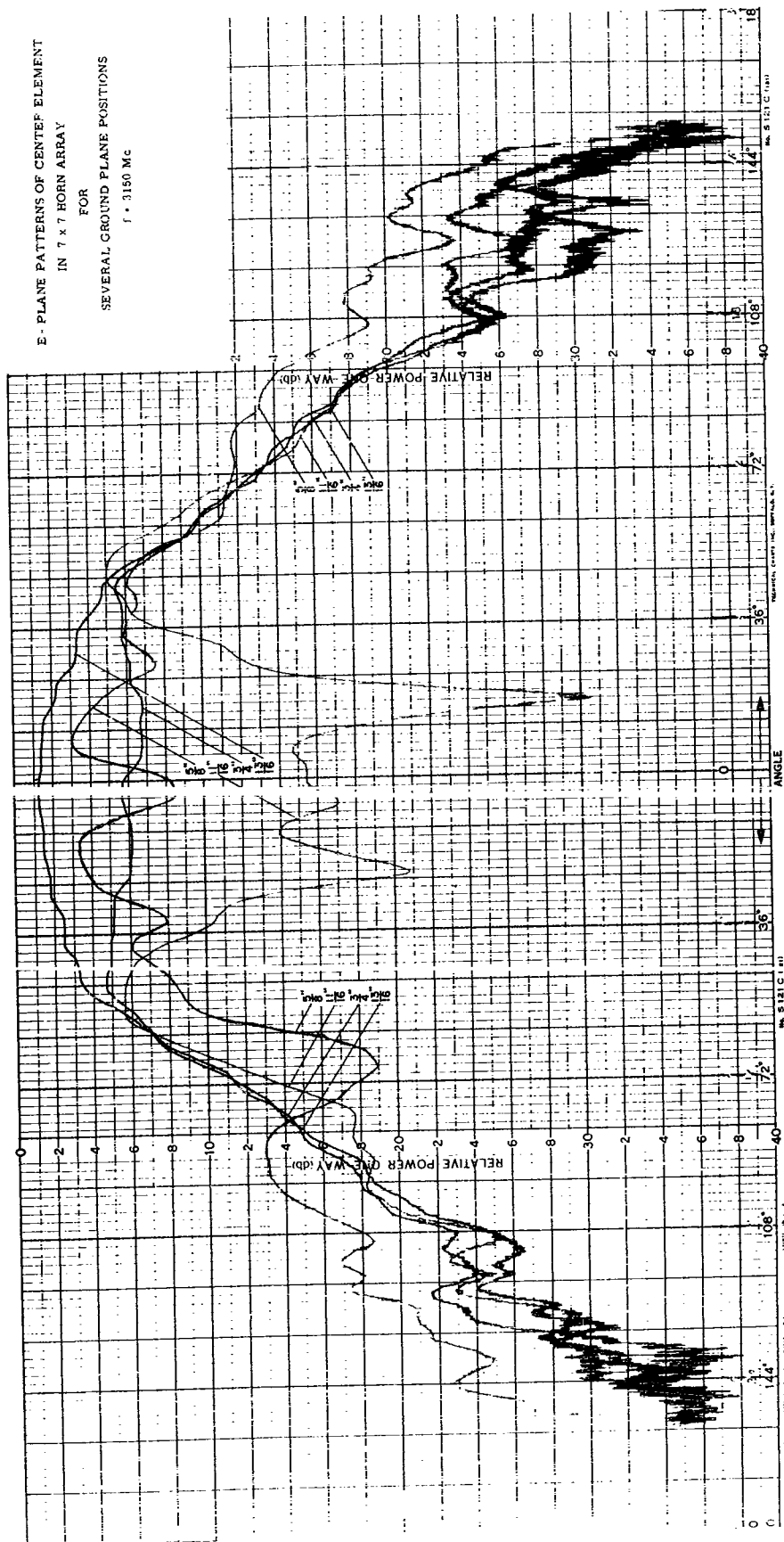


Figure 9c

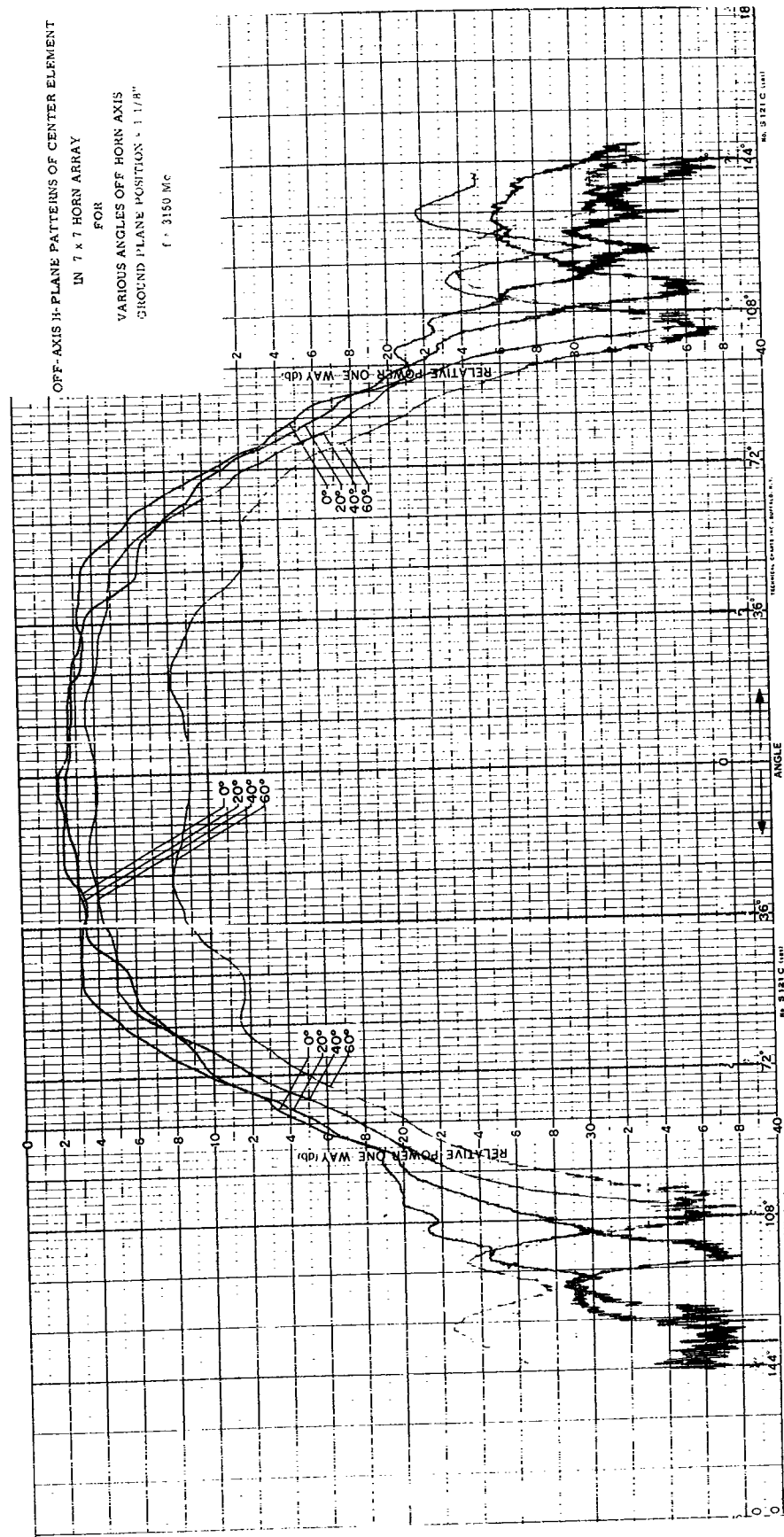


Figure 10

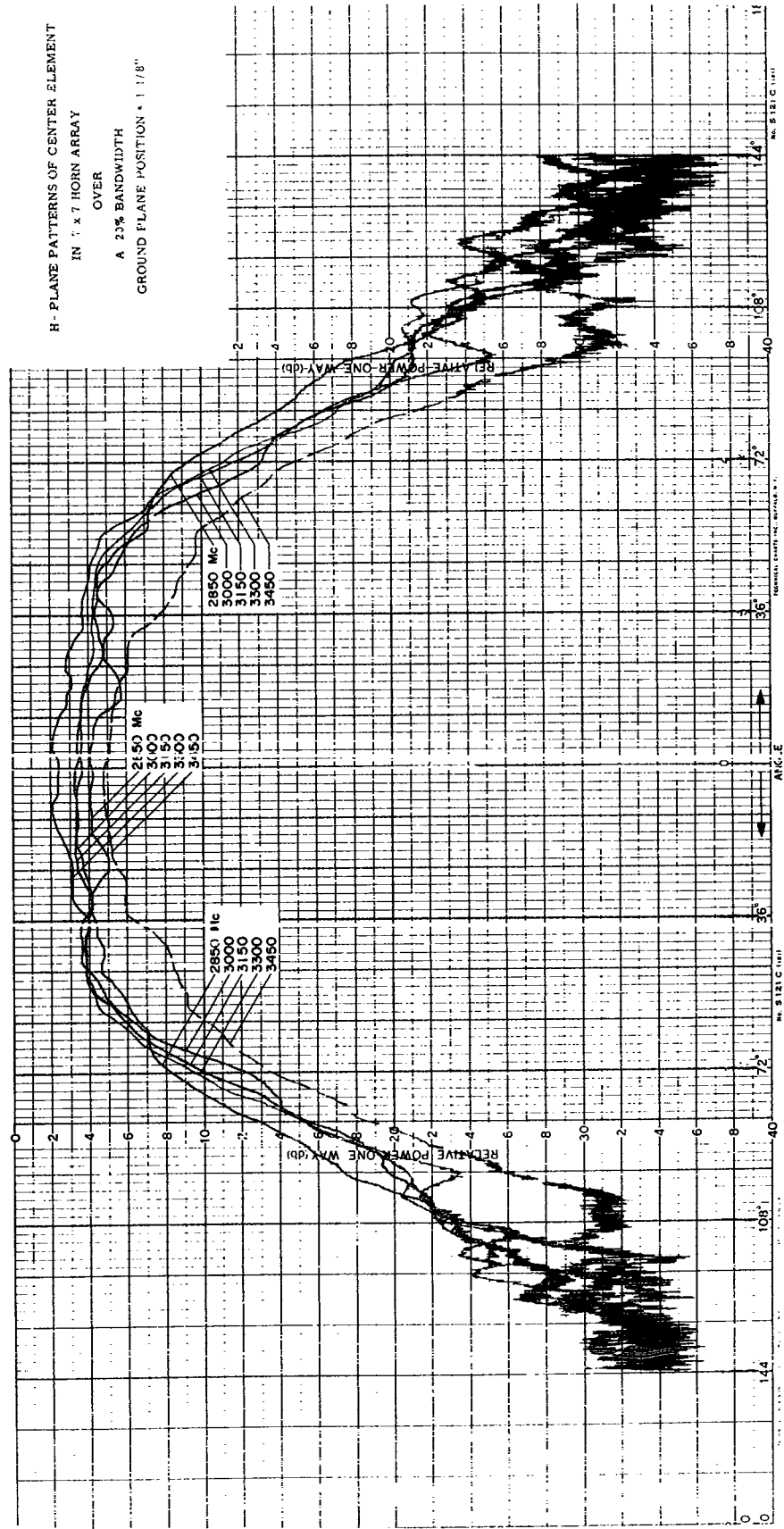


Figure 11a

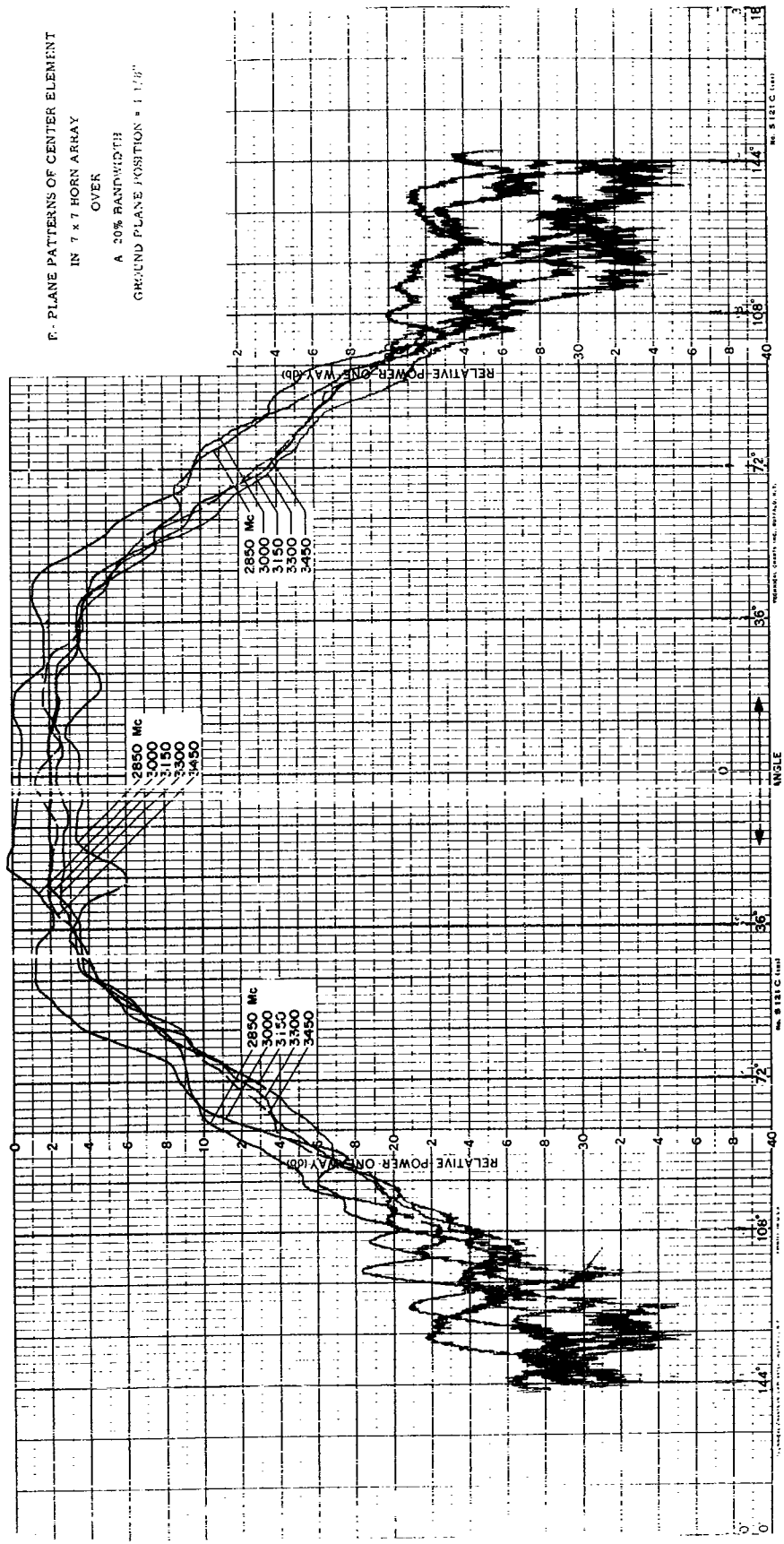


Figure 11b

COUPLING EFFECTS WITH SLOT AND SPIRAL ANTENNAS

R. M. Kalafus, R. B. Harris, Y. K. Kwon
and J. A. M. Lyon

Cooley Electronics Laboratory
The University of Michigan
Ann Arbor, Michigan

INTRODUCTION

The purpose of the work to be described has been to devise the means of predicting the coupling between two arbitrary antennas in close proximity (i. e. , spacings of a few wavelengths or less). Emphasis is on rapid and reliable evaluations of coupling for use in radio frequency interference problems. While the final presentation of data from this research may be somewhat different, it has been expedient up to now to express coupling between two antennas on a power basis, rather than by mutual impedance. The power coupling described here assumes a matched load in the receiving antenna.

The first type of antenna chosen for these studies was the rectangular slot fed by waveguide. This antenna can be made to correspond to an idealized simple slot in a conducting plane. It is one of the most accurately reproducible of all antenna types and is one of the commonly used flush mounted types. In addition to these practical considerations, the slot antenna is relatively easily studied by analytical procedures. It has a single main lobe with no side lobes and a gain of 5.15 db in a ground plate.

A second type of antenna, the Archimedean spiral, which is best described as a traveling wave antenna, has also been studied for coupling properties. The pattern defects present in any practical Archimedean spiral contribute noticeably to the observed coupling between spirals. The spirals have a desired circular polarization of the on-axis main lobe, degenerating to linear polarization at the ground plane. The presently available analyses of the Archimedean spiral are not as accurate as those for the slot. The main reason for the limitation on theoretical analysis is the uncertainty regarding current distribution. The latter depends upon the mode of feeding, the mutual coupling between adjacent turns of the spiral, and reflections. It is believed that the analysis of the coupling results presented here will ultimately permit a more complete theoretical analysis of the Archimedean spiral. It is expected that coupling information will be useful to those concerned with the design of arrays of Archimedean spirals, as well as to those occupied with the radio frequency interference problems in systems.

From a brief look at power interference between systems, it is possible to find that the isolation of one antenna from another must often account for a large part of the total isolation between the two systems. In considering the isolation between a receiving system and a transmitting system when each uses adjacent antennas on the metal skin of an aerospace vehicle, the isolation required between the two antennas might be 50 db. The latter is comparable to the isolation provided by the filter system of the receiver against unwanted transmitter signals.

It is interesting to observe that the actual orientation of two antennas in a common ground surface is of great importance. While this might have been anticipated in the case of slot antennas, it is less obvious that two spirals which are presumably axially symmetric can have an orientation for least coupling. In the ultimate application of coupling data to interference problems, the orientation of antennas must be clearly specified.

COUPLING BETWEEN RECTANGULAR SLOTS

The discussion presented here on the coupling between rectangular slots in a common ground plane is an extension of work presented a year ago (Ref. 1). It was shown that the far-field coupling formula, which has a particularly simple form, satisfactorily predicts coupling even for moderately close spacings. In the present paper a formulation is given which considers near-field terms and yields useful improvement at close spacings. The far-field expression is entirely inadequate, however, for predicting the coupling between slots where one or both lies on the axis of the other. Some interesting results are presented here for this case.

The coupling, C , is defined by:

$$C = \sqrt{\frac{W_r}{W_t}} e^{j\psi}$$

where W_t is the total transmitted power, W_r the receiver power, and ψ is the phase difference between the principal mode components in each aperture. This measure differs from that of mutual impedance, because

the receiver is matched, not open-circuited. Mutual impedance, Z_{12} , is more easily measured at low frequencies, while coupling is the more fundamental measurement at microwave frequencies. However, there is no conceptual problem between these parameters, since coupling is related to the mutual impedance by

$$|C|^2 = \frac{|Z_{12}|^2}{4R_t R_r}$$

where R_t and R_r are radiation resistances of the matched transmitter and receiver, respectively. It should be pointed out that R_t and R_r change from their far-field values at very close spacings.

The transmitting slot sets up a field in space which gives rise to a tangential magnetic field H_o on the ground plane. When a second slot is cut, the displacement current thus induced will produce a tangential field \bar{E} in the receiving aperture. However, the field \bar{E} must be consistent with the receiving waveguide boundary conditions as well as with \bar{H}_o . It has been shown that the coupling is stationary with respect to estimates of the tangential fields in either aperture. Therefore, it is reasonable to assume a principle mode distribution in the aperture. The received power is then proportional to the Fourier coefficient of \bar{H}_o (Ref. 1).

$$W_R \sim \left| \int \int H_o \cos \frac{\pi y}{b} dy dx \right|^2$$

By also assuming a dominant mode configuration in the transmitting guide, \bar{H}_o can be calculated. Upon substituting this \bar{H}_o in the above expression

for W_R , the coupling can be found without making far-field approximations. The result is a quadruple integral, which can be reduced to a double integral for computer evaluation. The mathematics are too lengthy to present here, and only the final formulation is given. The calculations may be found in an interim report (Ref. 2). The coupling magnitude for the broadside-to-broadside case is given by:

$$C \sim \int_{\frac{\pi(d-b)}{a}}^{\frac{\pi(d+b)}{a}} dx \left[\frac{\pi b}{a} - \left| x - \frac{\pi d}{a} \right| \right] \int_0^{\pi} \left\{ \left[1 - \left(\frac{\lambda}{2a} \right)^2 \right] (\pi - y) \cos y \right. \\ \left. + \left[1 - \left(\frac{\lambda}{2a'} \right)^2 \right] \sin y \right\} \frac{\exp \left[-j \frac{ka}{\pi} \sqrt{x^2 + y^2} \right]}{\sqrt{x^2 + y^2}} dy$$

and a , b , and d are defined in Fig. 1. The coupling falls away from the simple $1/d$ behavior in the manner shown in this figure. Agreement between theory and experiment is excellent. The coupling is changed merely by the gains of the slots as one or both is rotated, at least until a null is reached on one of the two patterns.

When one antenna lies along the axis of the other, the far-field terms vanish, and the coupling falls off as $1/d^2$ instead of $1/d$. Figure 2 shows this trend even up to close spacings, for slots end-to-end. An interesting behavior occurs when one slot is rotated away from the end-to-end

configuration. Instead of increasing the coupling, it is decreased. That this is reasonable can be seen as follows: The far-field has an H-field in the ϕ -direction, so a slot oriented with its length parallel to the transmitted H-field has the strongest TE_{10} excitation. When it is perpendicular, the slot has no H-field along its length. The transmitting field attempts to set up a mode with its E-field across the length of the slot. On the other hand, in the end-to-end configuration the H-field, while weak, is still in the proper direction to excite the TE_{10} mode. This behavior is shown in Fig. 3. The coupling at the end-to-broadside configuration is below the range of the apparatus, or more than -90 db.

COUPLING EFFECTS WITH SPIRAL ANTENNAS

The widespread use of flush broadband antennas on aircraft and missiles, both singly and in arrays, has motivated a detailed study of the ground plane fields. The Archimedean spiral is representative of this class, and was thus chosen for further study (see Fig. 4). Interest to date has centered largely around the near-axis, far-field properties, which can be obtained with rather crude approximations to current distribution. However, the interference effects between antennas in a common ground plane depend upon ground plane patterns, which require a more detailed knowledge of current distribution.

An interesting factor of spiral ground plane patterns (see Fig. 5) is their lack of omnidirectionality. However, ϕ -variations are not due to imperfections in spiral construction. Even with a perfectly balanced feed

(necessary for the axial mode), and with perfect mechanical symmetry, several db of coupling variation will occur as the spiral is rotated in the ground plane. With the commercial spirals tested, other effects add to the basic ϕ -variations. These variations stem from the following secondary causes and apply to all antennas in this class:

1. In-phase feed currents and the subsequent redistribution of current on the spiral.
2. Reflections from the ends of the spiral elements.
3. Reflections from the cavity.
4. Distributed, induced reflections by neighboring elements.
5. Direct radiation from the feed and balun.

The effects noted above are more critical in coupling properties than in near-axis properties. While it is difficult to isolate the effects of the several secondary causes, such attempts can help in future design of flush antennas. The study presented here is largely an experimental one, with emphasis on physical causes.

Variations in the ground plane coupling pattern are not completely undesirable for they make possible appreciable decoupling by proper orientation. However, the observed ϕ -variations are a strong function of frequency, so decoupling can occur only over a narrow band. For array purposes, it would often be better to have frequency independent ϕ -variations over the band, even at the expense of higher coupling levels.

Two similar circular Archimedean spirals obtained from Aero-Geo-Astro Corporation were tested singly and together. Pertinent data are listed below:

Frequency range:	2 - 4 gc
Number of turns:	13
Width of conductor:	.62 inches
Width of spacing:	.62 inches
Balun type:	Roberts, strip-line
Diameter of cavity:	4 inches

In order to test each antenna singly, a quarter wave monopole probe was used as a transmitter. The ground plane was 4' by 4' using absorbent material all around. The results in this chamber were within .5 db at large couplings (-35 db or more) and within 2 db at lower levels (-50 db) compared to the values using a 12' by 12' plane in an anechoic chamber.

Figure 6 shows typical coupling patterns at 2.5, 3.0, and 3.5 gc between the spiral antenna and a tuned monopole probe. The patterns are fairly consistent as the spiral-to-monopole distance is varied, even at the extremely close spacings, where the probe is 1.5" from the periphery. Even more consistent is the coupling level, which at the pattern maxima follows within .5 db of the ordinary 6 db per (distance) octave variation at distances of 1 wavelength or more. At closer spacings, the level tends to rise somewhat above the 6 db line by up to 1.5 db at 1/2 wavelength. To translate the data obtained by the spiral-to-monopole measurements to a spiral-to-spiral

or mixed configuration, it is necessary only to consider the relative gains of the antennas. A clarifying example is given in Table I. All values are normalized to a spacing of one wavelength center to center.

Frequency	3.5 gc	3.75 gc
Monopole-to-monopole coupling	-19.9 db	-19.9 db
Spiral A at $\phi_A = 0^0$ to monopole	-25.8 db	-25.5 db
Spiral B at $\phi_B = 0^0$ to monopole	-25.7 db	-26.3 db
Predicted spiral-to-spiral coupling at $\phi_A = \phi_B = 0^0$	-31.6 db	-31.9 db
Measured spiral-to-spiral coupling	-32.2 db	-31.6 db
Error	0.6 db	0.3 db

Table I

The predicted coupling is merely the sum:

$$-25.8 \text{ db} + (-25.7 \text{ db} + 19.9 \text{ db}) = -31.6 \text{ db}$$

This calculation assumes that the spiral current distribution is independent of neighboring antennas, which it is in most practical cases.

The general problem of coupling between flush antennas in a ground plane is greatly simplified by the fact that the incident field is linearly polarized, since the tangential E-field must be zero at the conductor. This, plus the fact that in the far field the field looks like an ordinary plane wave, means the great majority of problems can be solved by merely knowing the coupling patterns. This implies the winding sense of the spiral is irrelevant. This viewpoint breaks down in the near-field because the receiving spiral

in a spiral-to-spiral configuration subtends a large enough angle of the other that the phase distribution of the transmitting field over the receiving area is no longer that of a constant phase plane wave. However, this effect can be noted experimentally by comparing the coupling at large and small spacings.

Extensive tests were taken on the coupling patterns, from 1.7 gc to 4.2 gc in 50 Mc increments. Rather than present the numerous curves involved, the reduced data are shown in Figs. 7 and 8. Figure 7 shows the total variation of coupling as a function of frequency. The actual spacing was held constant so that the electrical spacing, in wavelengths, changes with frequency. For comparison, a uniform coupling line is shown in addition. The variations are small at the lower frequencies and increase to extreme levels at the higher frequencies, where sharp nulls occur. Just above the rated frequency band, the coupling increases sharply with small variations. The reason for this appears to be that the second mode, which has a null on the axis of the spiral, becomes predominant. This mode occurs when the feed currents are in-phase. There will be a large in-phase component when the balun is operated outside its designed band. Furthermore, the second mode has more energy concentrated along the ground plane, which would account for the rise in the coupling level.

Figure 8 shows the angular position of the maxima as a function of frequency. An expanded angular scale is used for clarity; one should remember that $\phi = \phi + 2n\pi$ in the figures. At the lower end of the band, the maxima and minima shift quite rapidly. This is due to standing waves

arising from reflections at the ends of the spiral elements. These standing waves are more predominant at lower frequencies because the current traveling wave is not sufficiently attenuated by radiation damping.

It can be shown that if the feed currents are in-phase, the angle at which adjacent currents have the same phase is given by

$$\phi \approx 1/ka \quad \text{or} \quad kr \approx 1$$

where $k = 2\pi/\lambda$. Using the value of k for air, curves varying as $1/ka$ are plotted as well. These show that the progression of the maxima follows the usual interpretation of current belts or active regions.

In order to control the phase of the feed currents, a laboratory spiral was constructed having the balun outside the cavity. For matching purposes, a dielectric-filled cavity was utilized, the spiral being fed by a tapered two-wire line. The cavity depth is .663 inches, a quarter wave-length at the geometric mean frequency in the medium whose dielectric constant is 2.48. The spiral is circular, Archimedean, and has eight turns. Further details are given in Fig. 9.

When the feed currents are balanced, the coupling pattern has 180° symmetry; that is, $C(\phi) = C(\phi + \pi)$. The same is true when the feed currents are in-phase. In both cases, the antenna has mechanical and electrical 180° symmetry. Small amounts of in-phase currents have a large effect on the current distribution, and cause an electrical asymmetry. Experiments showed that when the current phases are within 10° of perfect

balance, the direct radiation from the two-wire line is not significant, although it increases as frequency increases. Even better balance stability is found with the printed circuit balun in the AGA spirals, since the fields are tightly concentrated between the strip-line conductors. If the phases vary by 90° or more from balance, the direct radiation becomes significant, and the feed structure approaches a monopole. When this happens, the radiation from the feed structure becomes comparable to that of the spiral itself, and the coupling level will increase somewhat. The coupling levels and variations observed in the commercial spiral are of the same nature and magnitude as those for the fabricated spiral but differ in detail, since the feed structure and the number and size of turns differ.

CONCLUSIONS

For most situations encountered in practice, coupling and interference effects with flush antennas can be evaluated in terms of the far-field patterns along the ground plane. The coupling between slots is highly predictable and uniform due to its simplicity. The spiral coupling has several secondary causes affecting it, which is characteristic of antennas of its class. In spite of its seeming near circular symmetry, wide variations in the coupling pattern occur. These variations are associated primarily with the current distribution, and are sensitive to changes in the feed current phase. Standing wave effects affect the coupling pattern as well, and direct radiation from the cavity and balun plays a significant role at some frequencies. However, the

coupling level is largely determined by the distribution of energy associated with the idealized axial mode.

ACKNOWLEDGEMENTS

The authors wish to thank Dr. D. K. Adams for many fruitful discussions. The work was performed under Contract AF 33(657)-8178 under the particular guidance of Mr. E. M. Turner and Mr. O. E. Horton of the Aeronautical Systems Division, Wright-Patterson Air Force Base.

REFERENCES

1. D. K. Adams et al., "Power Interference Levels of Rectangular Slot Antennas in a Common Ground Plane by Simplified Analysis and Tests," 12th Annual Symposium on USAF Antenna Research and Development, Monticello, Ill., 1962.
2. D. K. Adams et al., "Derivation of Aerospace Antenna Coupling Factor Interference Prediction Techniques," Interim Technical Report No. 2, Contract AF 33(657)-8178, September 1962.

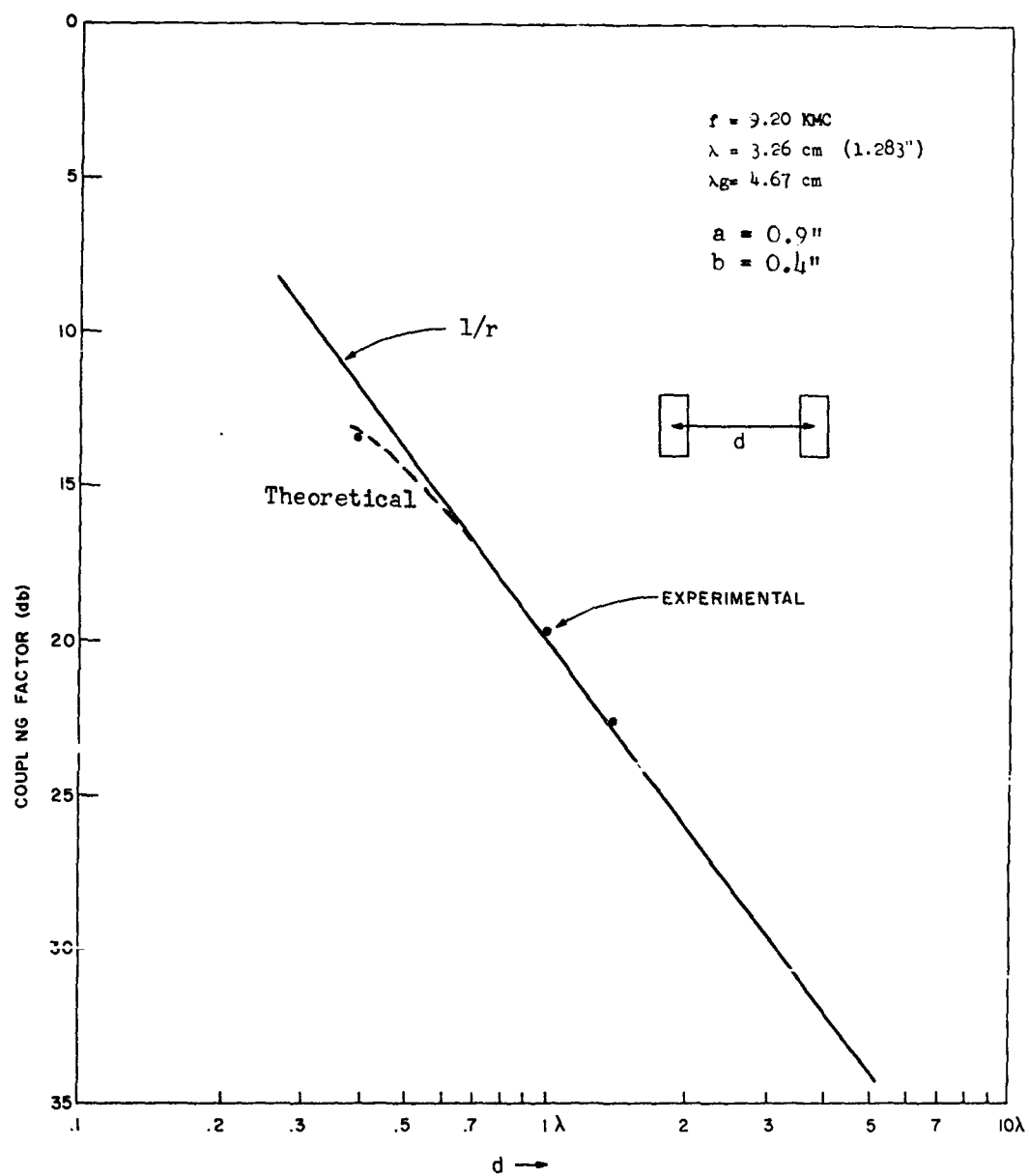


Fig. 1. Broadside-to-broadside slot coupling, showing $1/r$ trend.

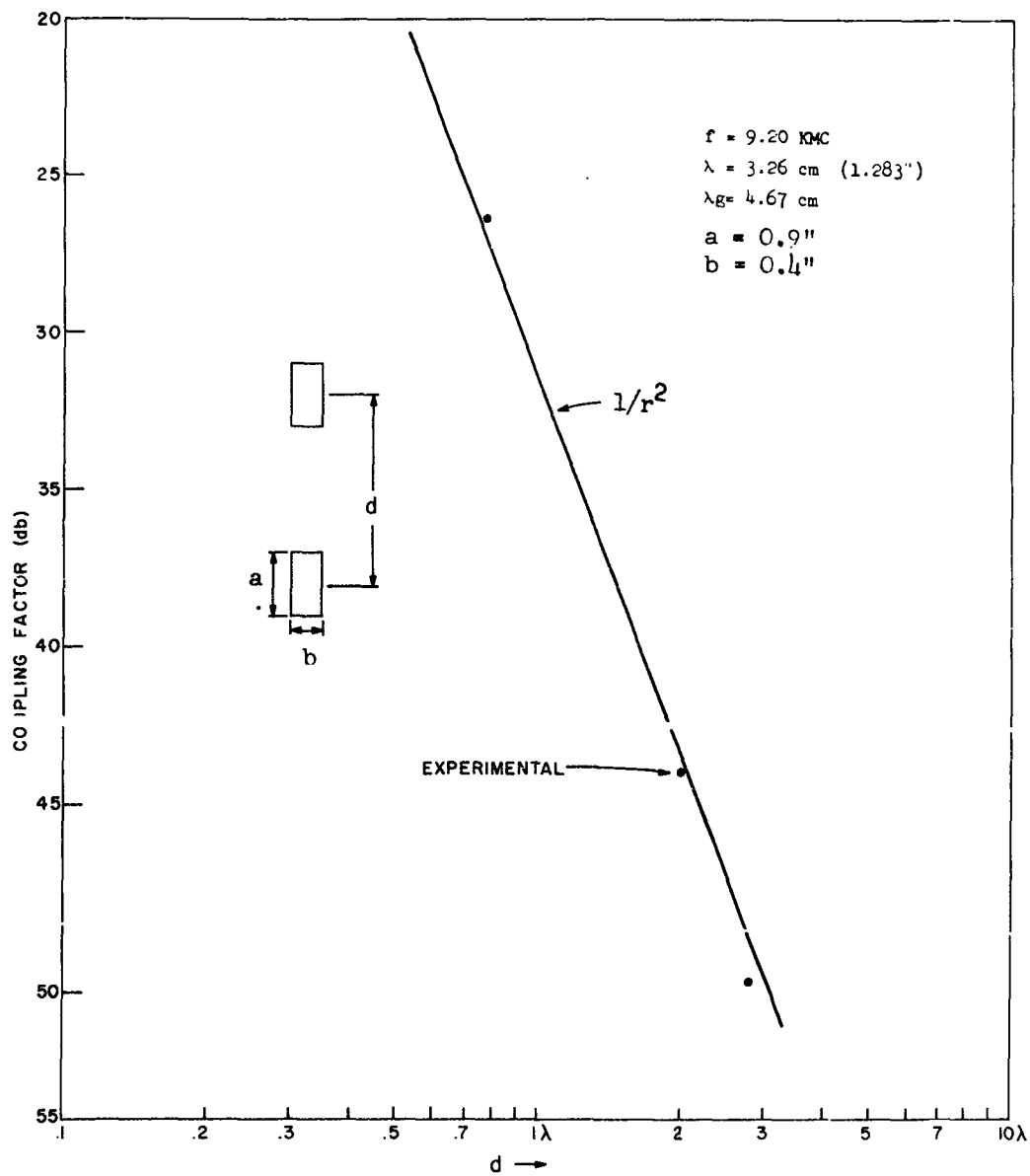


Fig. 2. End-to-end slot coupling, showing $1/r^2$ trend.

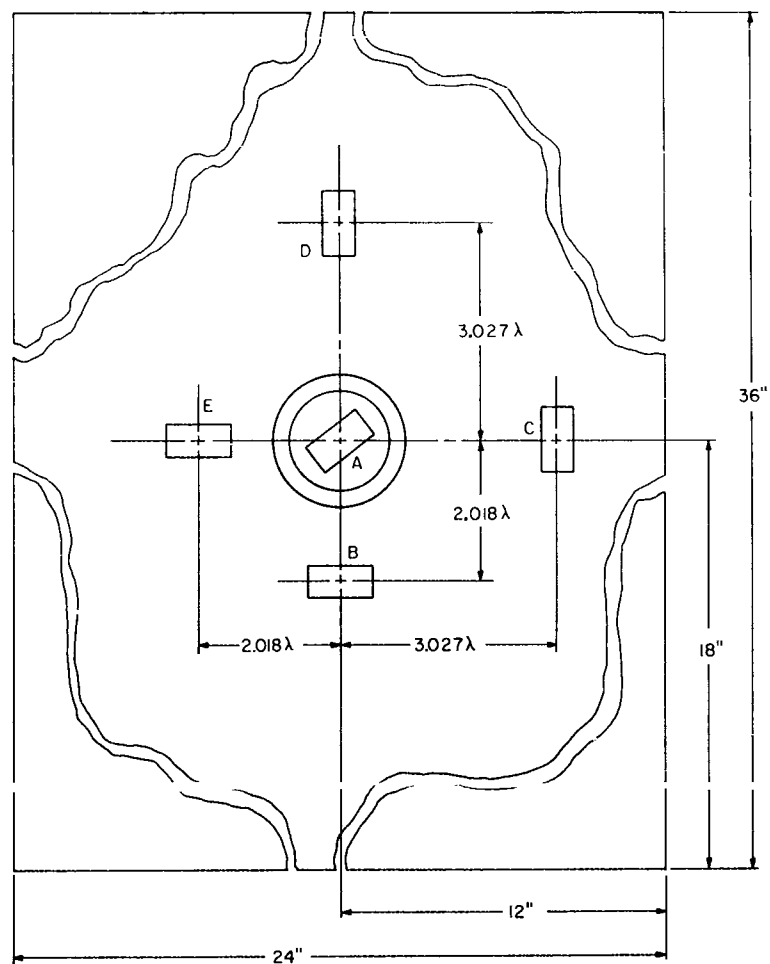


Fig. 3(a) Ground plane arrangement for measuring slot-to-slot coupling. Slot A can be rotated.

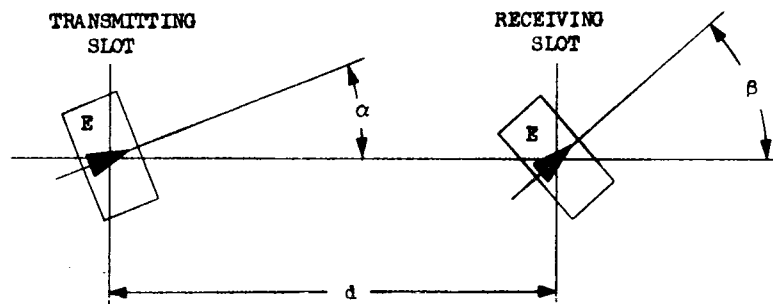


Fig. 3(b) Notation used for recording slot-to-slot coupling data.

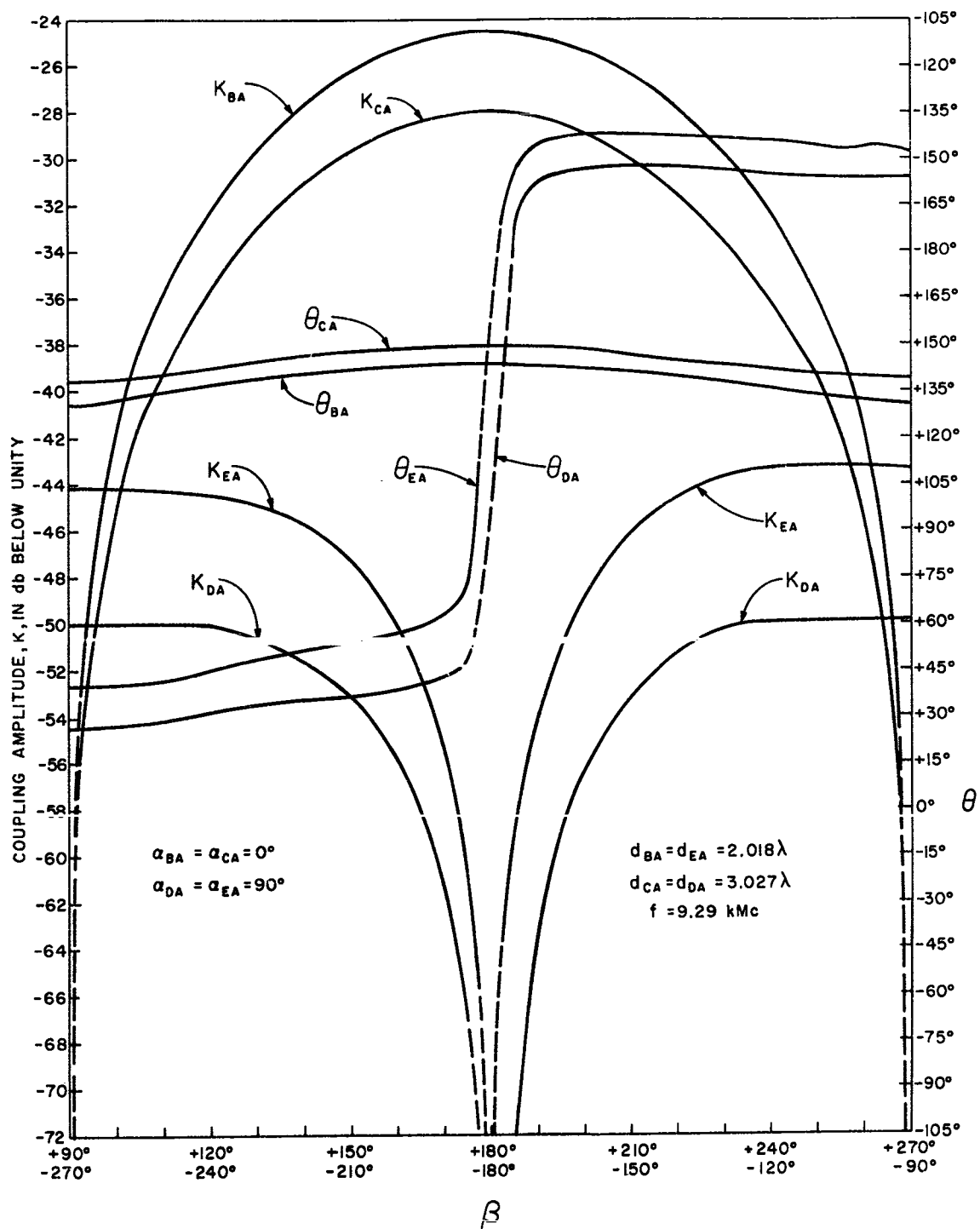
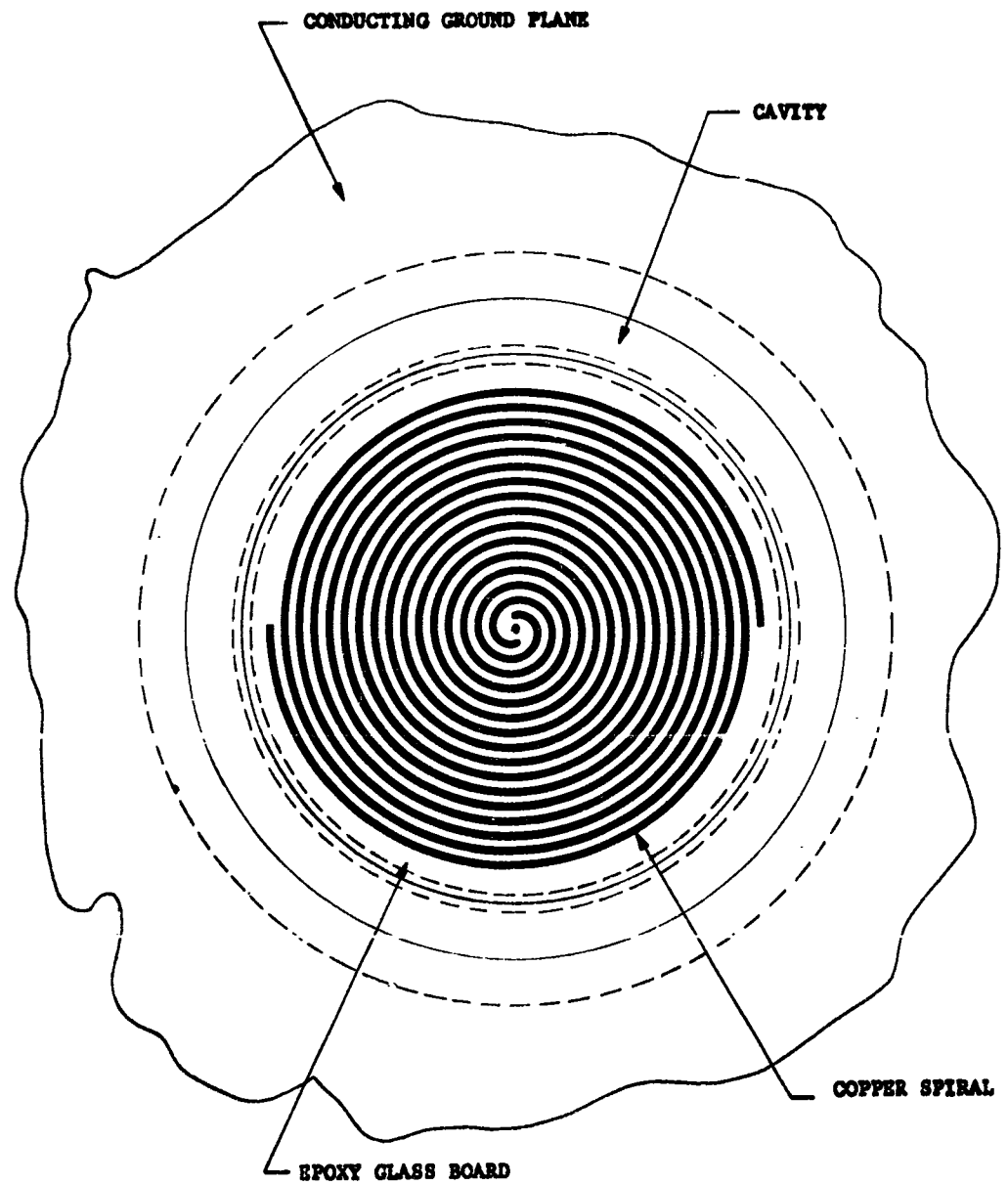


Fig. 3(c) Coupling magnitude and phase information while rotating one slot.



CIRCULAR ARCHIMEDEAN SPIRAL

Fig. 4. Spiral face configuration.

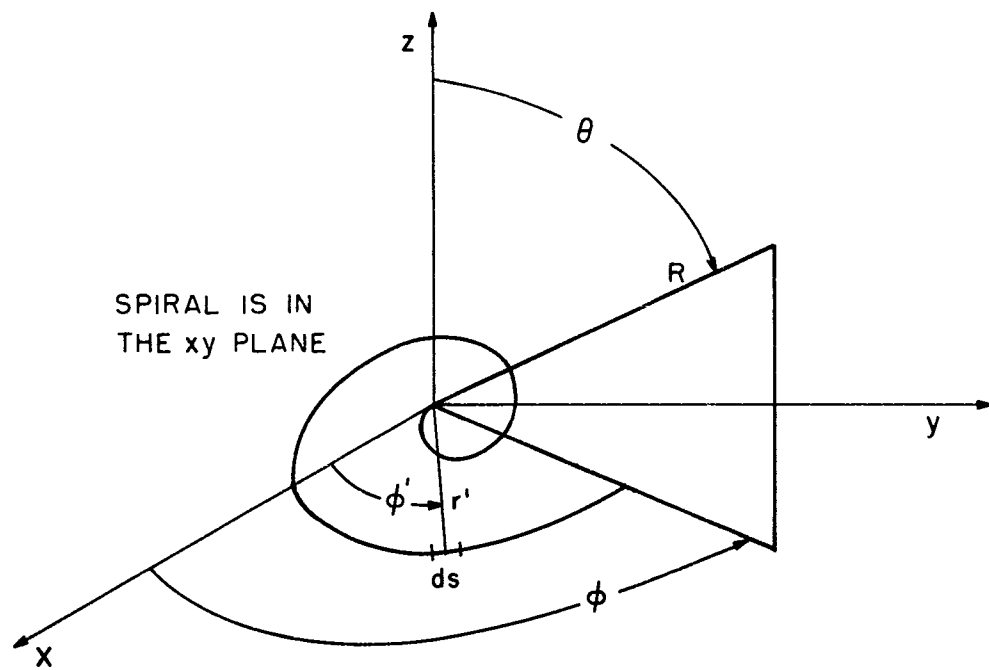


Fig. 5. Spiral geometry.

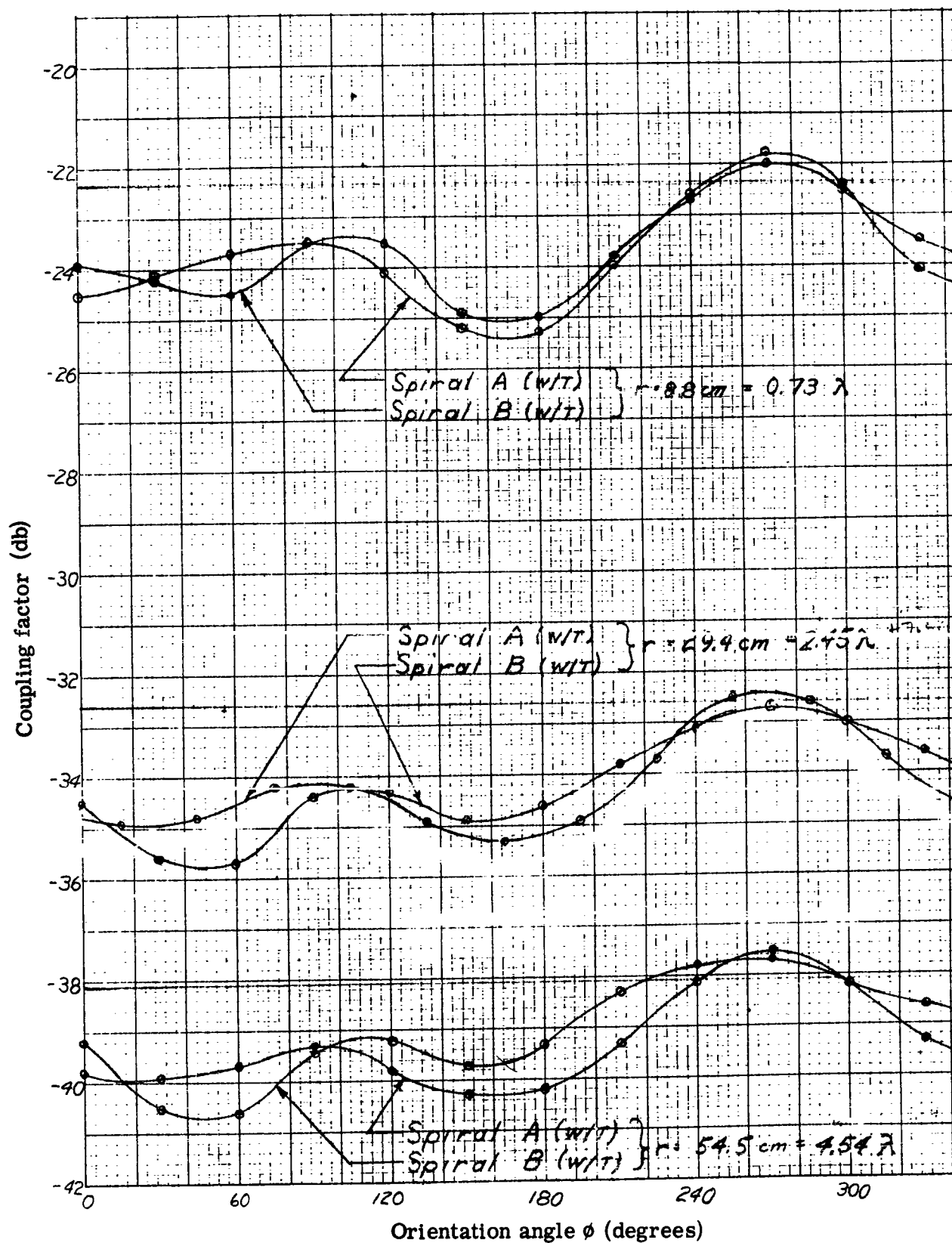


Fig. 6(a). Spiral-to-monopole coupling, 2.5 gc.

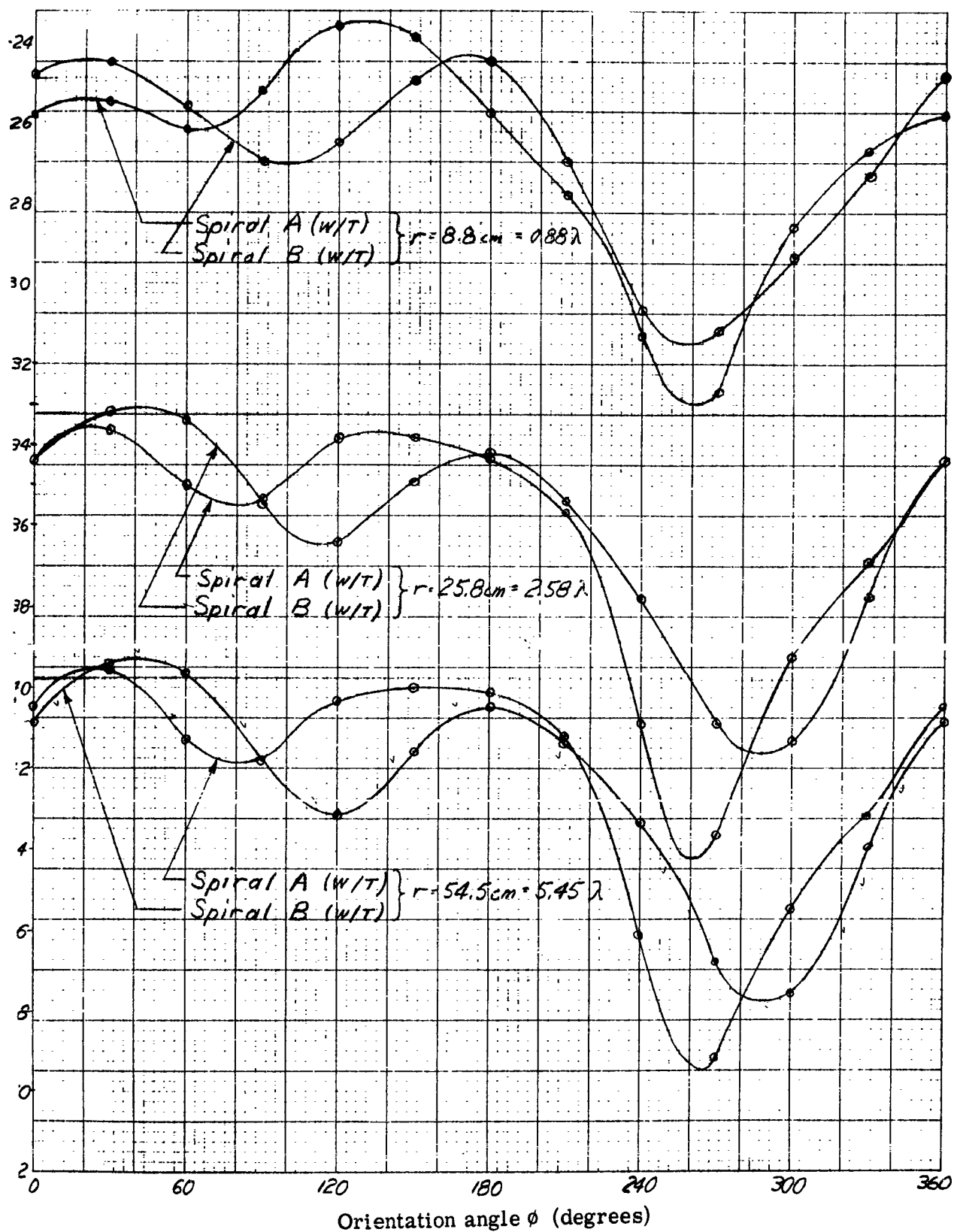


Fig. 6(b). Spiral-to-monopole coupling, 3.0 gc.

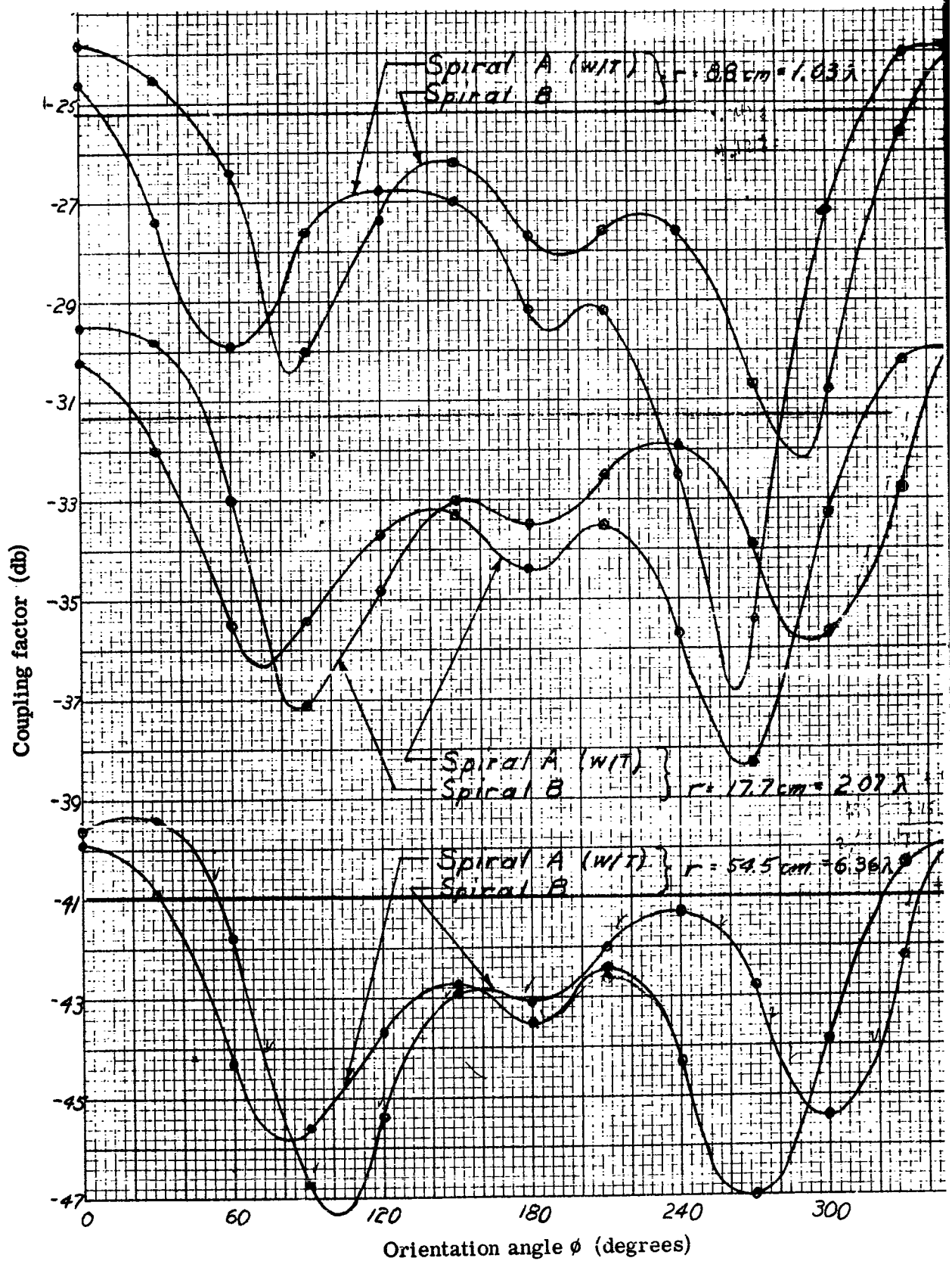


Fig. 6(c). Spiral-to-monopole coupling, 4.0 gc.

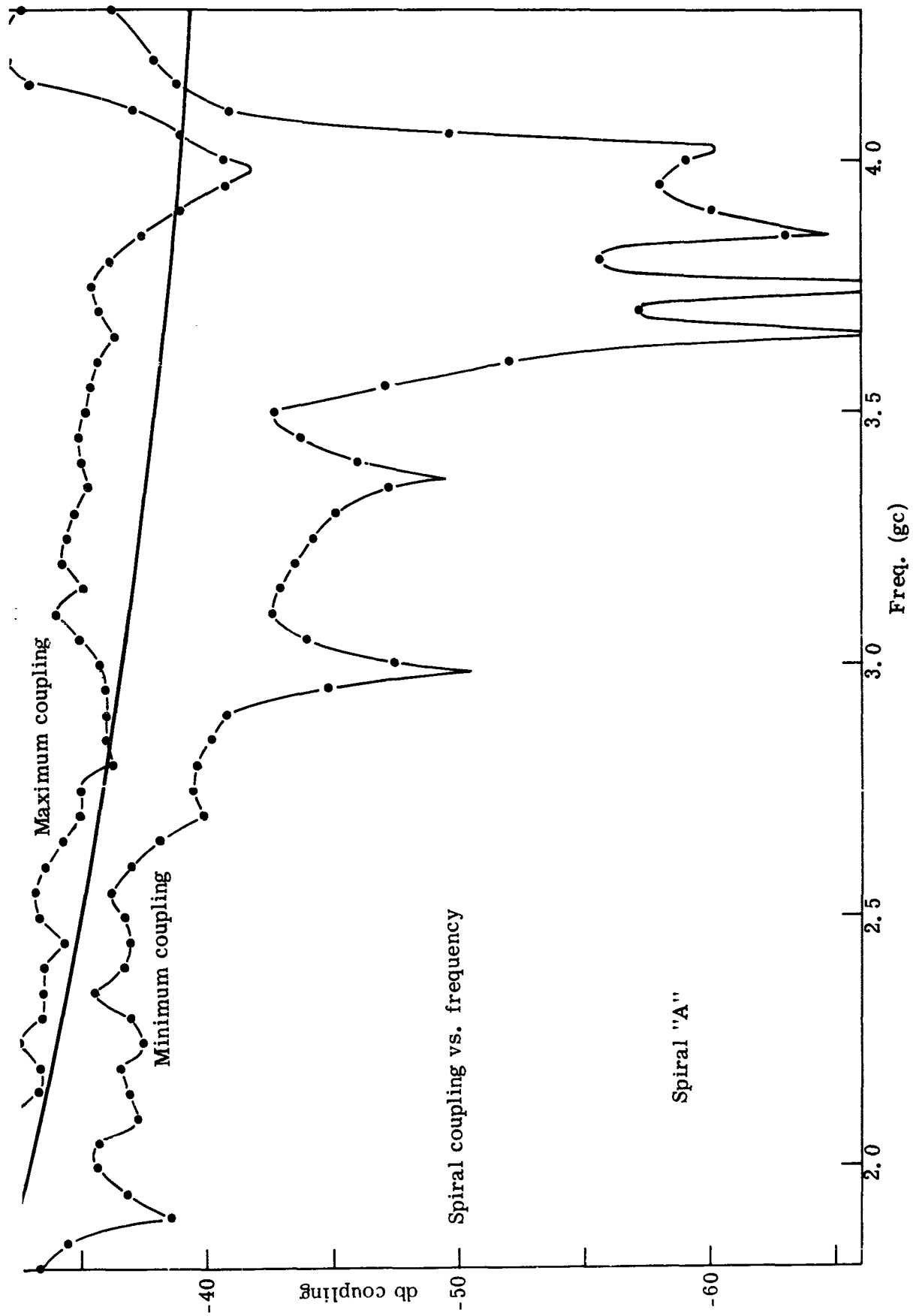
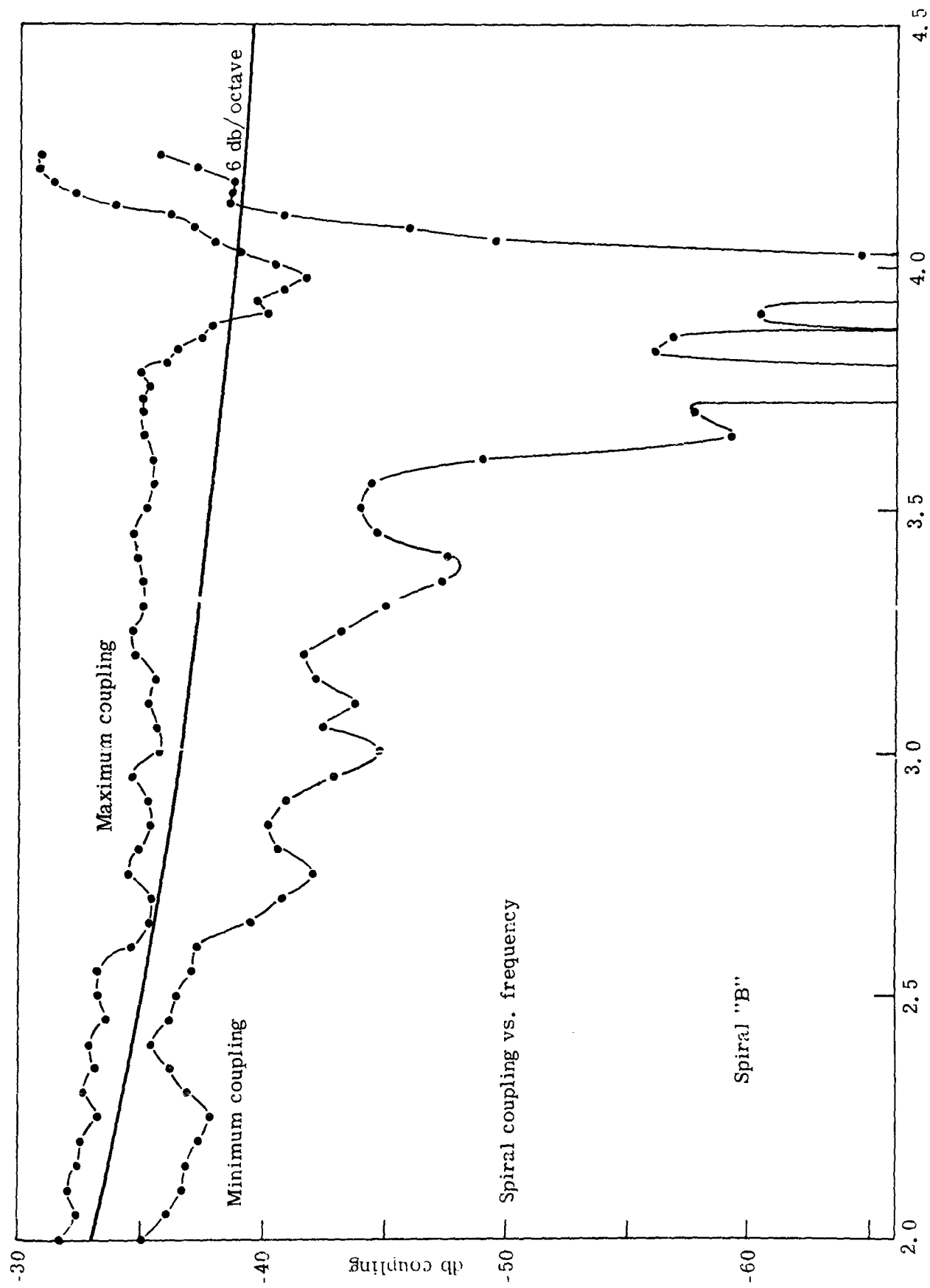


Fig. 7(a). Coupling variation, spiral A.



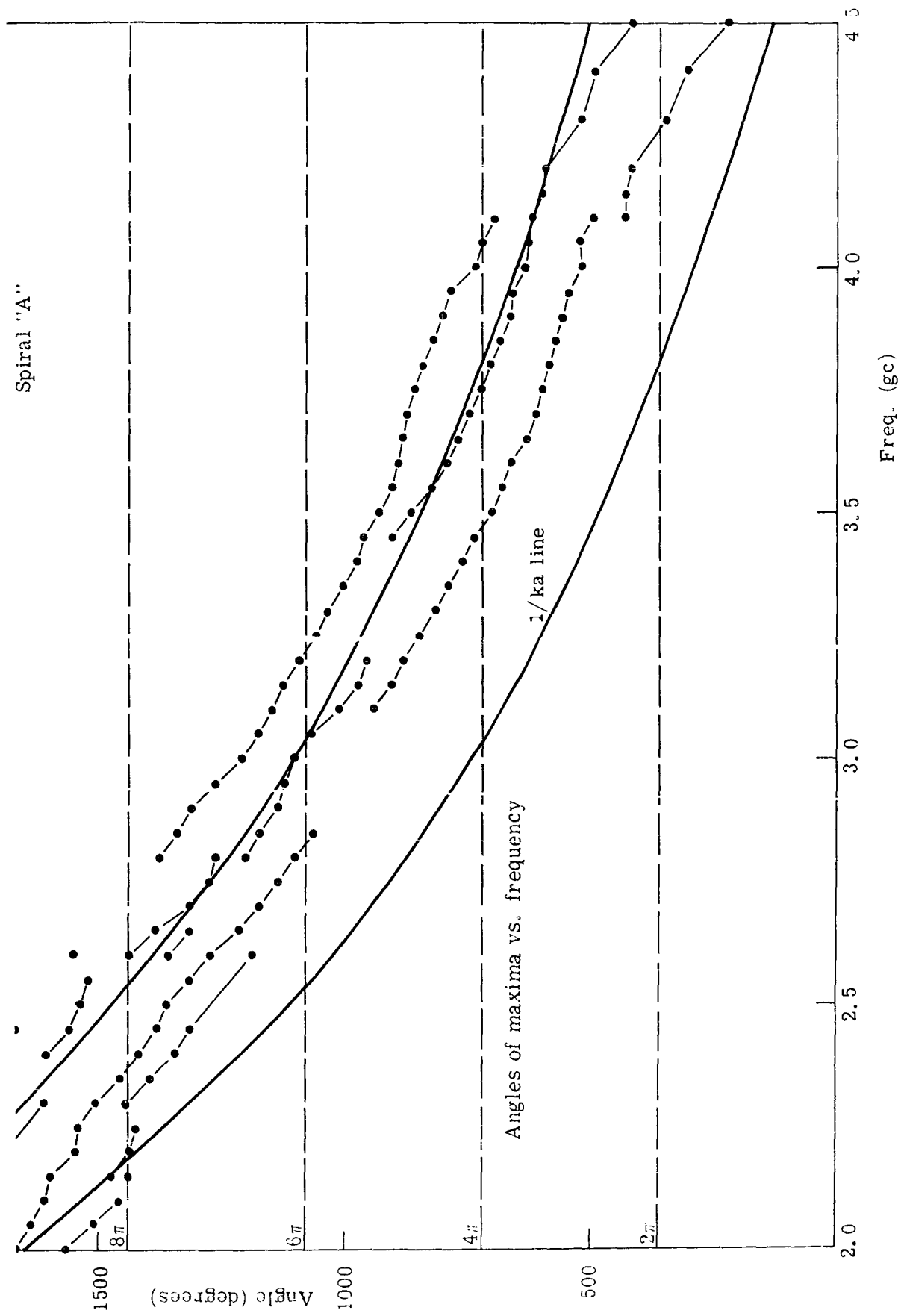
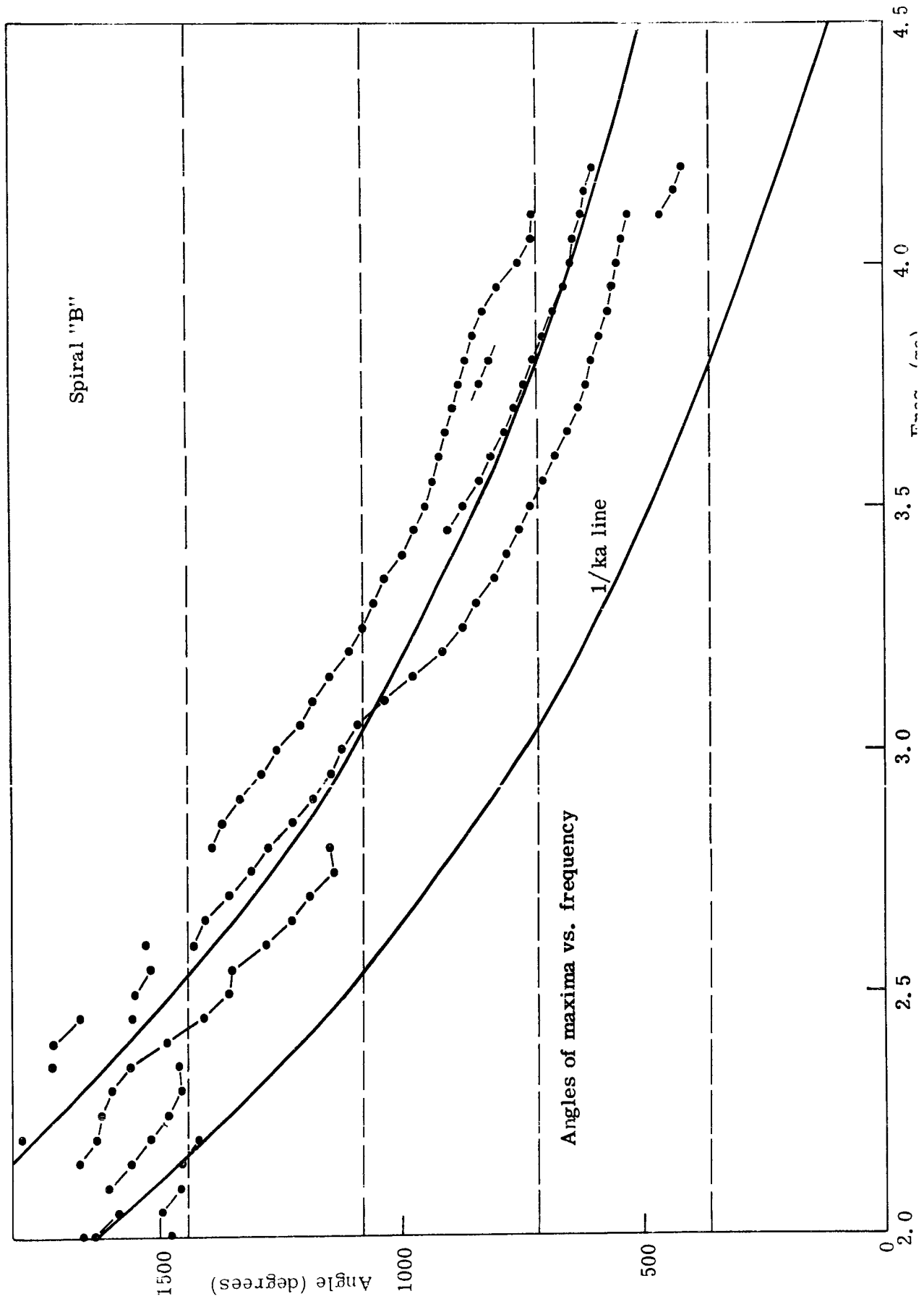
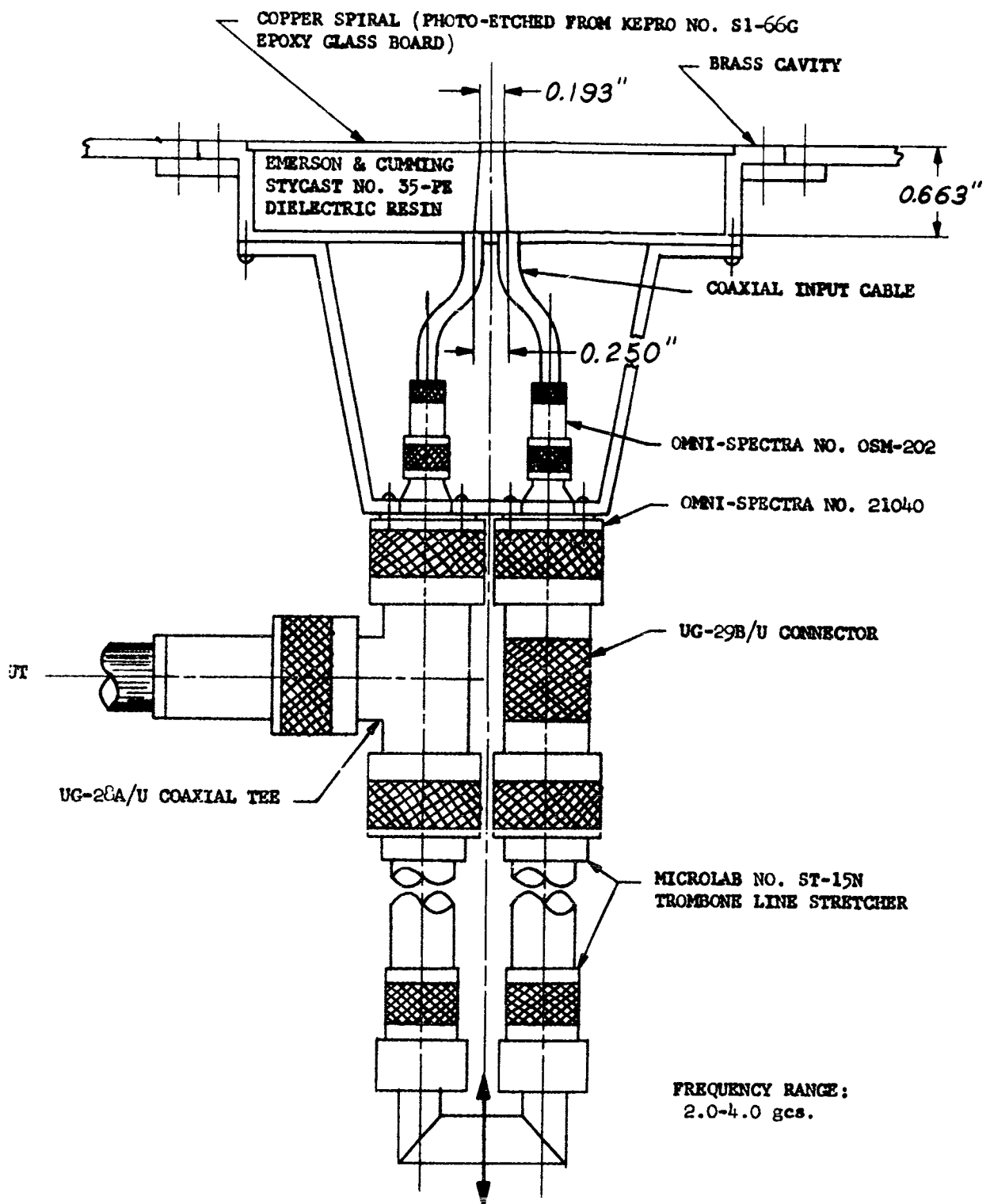


Fig. 8(a). Progression of coupling lobes, spiral A.





CAVITY-BACKED CIRCULAR ARCHIMEDEAN SPIRAL
 WITH EXTERNAL ADJUSTABLE BALUN

Fig. 9. Fabricated spiral detail.

MINIMUM ENERGY ANTENNA PATTERNS

by

Harold C. Hiscox
Senior Engineer
Electronics Division
Westinghouse Electric Corporation
Baltimore, Maryland

I. INTRODUCTION

The use of extremely low noise microwave receivers has caused the antenna of a system to introduce a significant portion of the total noise accepted by the receiver. Therefore a method to reduce to a minimum the noise introduced by the antenna is desired.

With the assumption of random noise sources distributed uniformly in a domain containing the antenna, a criterion which minimizes the antenna contributed noise is derived. Using this criterion, the aperture illumination pattern is derived and the resulting antenna patterns are plotted. In order to depress the near-in sidelobes of the antenna patterns, a slightly modified derivation of the illumination pattern is used. Antenna patterns resulting from this modified derivation are plotted. Finally, an analysis of the antenna pattern variations caused by random phase and amplitude errors in the illumination pattern is made.

Tables of illumination amplitudes corresponding to various antenna pattern peak to worst sidelobe ratios are given. These tables may be used for an array containing 31 or more radiating elements.

II. CRITERION FOR OPTIMUM PATTERN

The recent use of extremely low noise microwave receivers has caused the antenna to be a significant noise source in calculations concerning the noise temperature of a system. Through the use of a maser, receiver noise temperatures of approximately 10° K have been developed. However, if the antenna beam is directed at a hot body such as the sun or earth, the system noise temperature will be much higher than 10° K. When the use of the system requires the antenna beam to be directed at the hot body, nothing can be done to improve the noise figure. However, in the majority of antenna uses, the beam is not primarily directed at hot bodies; it is only the beam sidelobes which are directed at these points.

There are many examples which might be stated in which the interfering objects are distributed randomly about a direction of interest. The criterion to be developed is for the situation where the interfering bodies are uniformly distributed. The probability of the magnitude of each body's interference is not specified as the form of the antenna pattern criterion is not dependent on it.

Let the magnitude of the i^{th} body's interference be A_i which has a probability distribution $p(A_i)$.

Let $p(\theta_i)$ be the probability distribution of the i^{th} object's being at an angle θ relative to the antenna.

Let the i^{th} object be at a distance x_i from the antenna which has a probability distribution $p(x_i)$.

$\epsilon(\theta)$ is the antenna beam pattern and β is the phase shift constant.

The array's response to all I objects is then

$$R = \sum_{i=1}^I A_i \epsilon(\theta_i) e^{j\beta x_i} \quad (1)$$

The mean square average response to the complete ensemble is

$$\begin{aligned} \overline{R^2} = & \iint \cdots \int_{A_i} \int_{\Pi}^I p(A_i) dA_i \iint \cdots \int_{\theta_i} \int_{\Pi}^I p(\theta_i) d\theta_i \\ & \cdot \iint \cdots \int_{x_i} \int_{\Pi}^I p(x_i) dx_i \left[\sum_{i=1}^I A_i \epsilon(\theta_i) e^{j\beta x_i} \right]^2 \end{aligned} \quad (2)$$

Carrying out the indicated operations and, noting that the distribution of the noise sources is uniform over all angles, gives for the array response.

$$\overline{R^2} = I \overline{A^2} \int \epsilon^2(\theta) d\theta \quad (3)$$

That is, for a uniform distribution of interfering objects, the minimum antenna response occurs when the integrated squared value of the pattern is a minimum. Thus the optimum pattern may be referred to as a **Minimum Energy Pattern**.

III. MINIMUM ENERGY PATTERN

A. Derivation

The Utopian antenna pattern would be one which has a finite response at a direction normal to the array and no response at any other direction. This pattern is unrealizable, but at least square approximation to it can be found. Let the unrealizable pattern be represented by $\epsilon'(\theta)$ and the approximate pattern be represented by $\epsilon(\theta)$. Then,

$$\epsilon'(\theta) = \begin{cases} 1 & \text{when } \theta = 0 \\ 0 & \text{when } \theta \neq 0 \end{cases} \quad (4)$$

and

$$\epsilon(\theta) = \sum_{-N}^N (n) A_n \cos(n \beta d \sin \theta) \quad (5)$$

The integrated squared difference, or error, between the two patterns is then given by

$$\epsilon = \int_{-\pi}^{\pi} [\epsilon'(\theta) - \epsilon(\theta)]^2 d\theta \quad (6)$$

Expanding

$$\epsilon = \int_{-\pi}^{\pi} [\epsilon'(\theta)]^2 d\theta - 2 \int_{-\pi}^{\pi} \epsilon'(\theta) \epsilon(\theta) d\theta + \int_{-\pi}^{\pi} [\epsilon(\theta)]^2 d\theta \quad (7)$$

Since $\epsilon'(\theta)$ is equal to zero everywhere except at $\theta=0$, the first two integrals equal zero.

Thus

$$\epsilon = \int_{-\pi}^{\pi} [\epsilon(\theta)]^2 d\theta \quad (8)$$

Therefore the least square approximation to the ideal pattern will produce a minimum energy pattern in accordance with the results of Section II.

It may be desired to reduce the sidelobe level of the approximate pattern at a slight expense of main lobe width. This can be accomplished by a appropriate weighting being placed on $\epsilon(\theta)$ around $\theta=0$. One possibility is not to minimize in the region $\theta=0$. The resulting pattern will then be a minimum energy outside this region. Therefore equation 8 may be rewritten as

$$\epsilon = \int_{-\pi}^{-a} [\epsilon(\theta)]^2 d\theta + \int_a^{\pi} [\epsilon(\theta)]^2 d\theta \quad (9)$$

By varying the value of a in equation (9) various patterns, all minimum energy over the regions $a \leq \theta \leq \pi$, can be produced.

Now substituting equation (5) into equation (9) gives

$$\epsilon = \int_{-\pi}^{-a} \left[\sum_{-N}^N A_n \cos(n \beta d \sin \theta) \right]^2 d\theta + \int_a^{\pi} \left[\sum_{-N}^N A_n \cos(n \beta d \sin \theta) \right]^2 d\theta \quad (10)$$

Expanding gives

$$\begin{aligned} \epsilon = \int_a^{\pi} \sum_{-N}^N (i) \sum_{-N}^N (j) A_i A_j \cos \left[(i+j) \beta d \sin \theta \right] d\theta \\ + \int_a^{\pi} \sum_{-N}^N (i) \sum_{-N}^N (j) A_i A_j \cos \left[(i-j) \beta d \sin \theta \right] d\theta \end{aligned} \quad (11)$$

Now using the identity:

$$\int_0^{\pi} \cos(k \sin \theta) d\theta = \int_0^{\pi} \left[J_0(k) + 2 \sum_{m=1}^{\infty} J_{2m}(k) \cos 2m\theta \right] d\theta \quad (12)$$

But $\int_0^{\pi} (\cos 2m\theta) d\theta = 0$ for all non zero integer values of m .

Thus,

$$\int_0^{\pi} \cos(k \sin \theta) d\theta = J_0(k) \int_0^{\pi} d\theta = \pi J_0(k) \quad (13)$$

Using the result of equation (13), equation (11) may be written as

$$\begin{aligned} \epsilon = \pi \sum_{-N}^N (i) \sum_{-N}^N (j) A_i A_j J_0 \left[(i+j) \beta d \right] - \int_0^a \sum_{-N}^N (i) \sum_{-N}^N (j) A_i A_j \cos \left[(i+j) \beta d \sin \theta \right] d\theta \\ + \pi \sum_{-N}^N (i) \sum_{-N}^N (j) A_i A_j J_0 \left[(i-j) \beta d \right] - \int_0^a \sum_{-N}^N (i) \sum_{-N}^N (j) A_i A_j \cos \left[(i-j) \beta d \sin \theta \right] d\theta \end{aligned} \quad (14)$$

The problem to be solved is to reduce equation (14) to a minimum by a selection of the A_n 's with the condition that

$$\sum_{-N}^N (n) A_n = 1 \quad (15)$$

This side condition results from the fact that the antenna pattern should have a magnitude of 1 at $\theta = 0$. Then

$$\epsilon(\theta) = 1 = \sum_{-N}^N (n) A_n \cos(n\beta d \sin \theta) = \sum_{-N}^N (n) A_n$$

The method of Lagrangian Multipliers will be used to minimize equation (14). Mathematically the technique may be stated as

$$\frac{d\epsilon}{dA_n} + \rho \frac{d\epsilon(0)}{dA_n} = 0 \quad (16)$$

where ρ is Lagrange's multiplier.

Carrying out the operations of equation (16) on equation (14) will give a set of $(2n+1)$ equations with $2(n+1)$ unknowns. The remaining equation is the side condition of equation (15).

The set of equations may be written in matrix form as

$$\begin{bmatrix} C_{ij} \end{bmatrix} \begin{bmatrix} A_n \end{bmatrix} = -\frac{\rho}{4} \begin{bmatrix} 1 \end{bmatrix} \quad (17)$$

where

$$C_{ij} = \pi J_0 \left[(i+j)\beta d \right] - \int_0^a \cos \left[(i+j)\beta d \sin \theta \right] d\theta$$

The region over which the antenna sidelobe energy is minimized was varied by varying the parameter (a) in equation (9). The value of (a) was varied between zero and 0.25 radians in steps of 0.025 radians. For each value of (a) , the coefficients C_{ij} of equation (28) were evaluated and the resulting set of equations were solved for the values of A_n . Using the calculated values of A_n , equation (11) was computed for various values of the angle θ so that the antenna patterns could be plotted. All of the preceeding operations were performed on a digital computer using a value of (d) equal to $\pi/2$. This is equivalent to spacing the radiating elements one-half wavelength apart.

B. Pattern Evaluation

In Figures 1 through 4, a portion of the antenna patterns are plotted. The antenna response for angles from 0° to 90° is shown because the pattern is symmetrical about 0° . Only four of the ten patterns calculated have been plotted as they show the effect of the variation of the minimization interval. These antenna patterns develop when the antenna array contains 31 radiating elements spaced one-half wavelength apart. This number of elements was chosen to be plotted as a compromise. The number of sidelobes is sufficient to show trends and all important details.

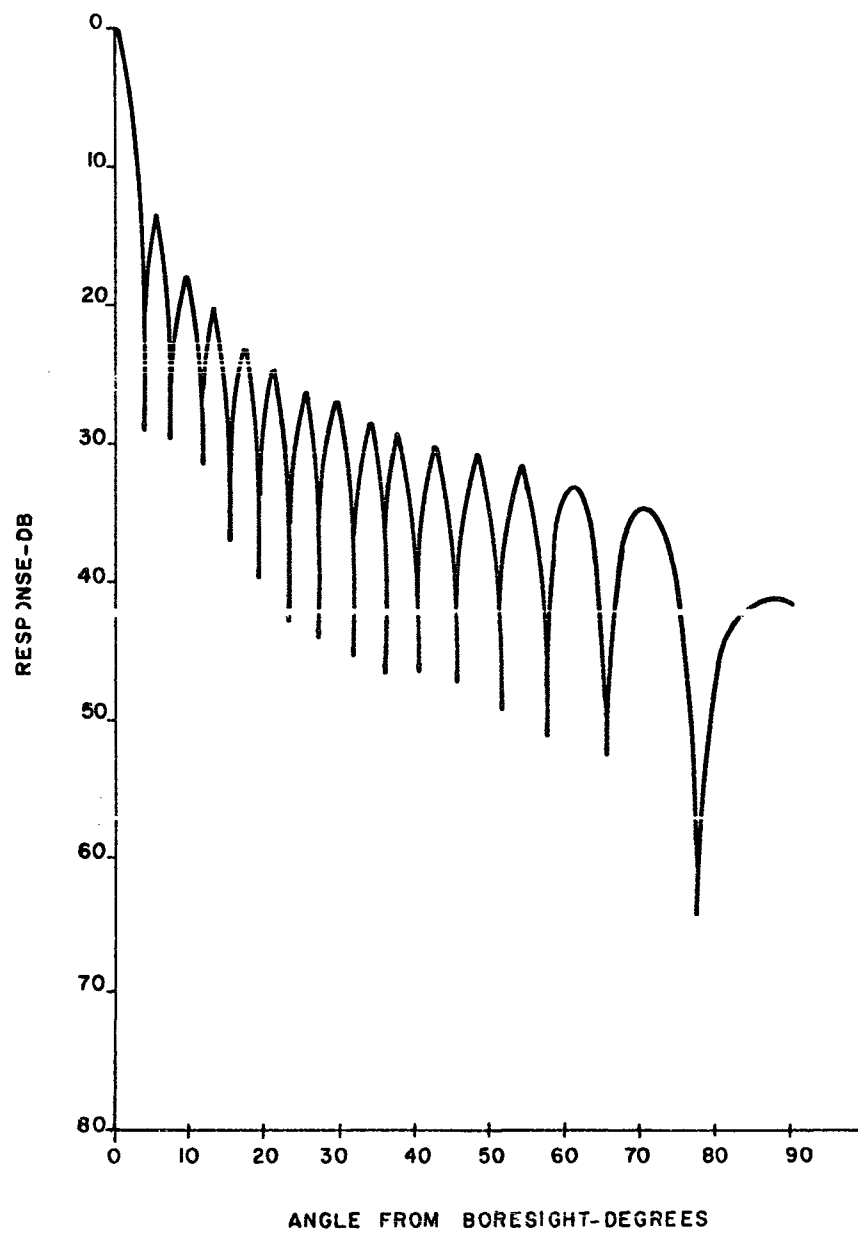


Figure 1. Minimum Energy Pattern, $a = 0$

Figure 1 is the antenna pattern when (a) is equal to zero. This pattern is the approximation to an impulse type of pattern. The sidelobe peaks fall-off all the way out to 90° . In fact, the large lobe in the vicinity of 90 degrees is noticeably depressed. This pattern is very similar to that produced by a uniformly illuminated aperture except for this last lobe which is much lower in the minimum energy pattern.

Figure 2 is the pattern which approximates a rectangular pattern which is 0.1 radians wide. From the figure it may be noted that all the sidelobe peaks are approximately 2 db lower than the corresponding sidelobes of Figure 1.

Figure 3 is the pattern which approximates a rectangular pattern which is 0.15 radians wide. The lower sidelobe trend continues but it is more pronounced in the far sidelobes.

Figure 4 is the pattern which approximates a rectangular pattern which is 0.25 radians wide. The first sidelobe has now increased so that it is equal to the first sidelobe of Figure 1, but the next few are lower than those of Figure 3. The far sidelobes are approximately equal to those of Figure 3.

A curve showing the relationship between the first (worst) sidelobe and the minimization interval is given in Figure 5. It is noted that the first sidelobe is depressed until a value of $a = 0.075$ radians is reached. Then the sidelobe increases in value until it reaches a value 13.3 db down from the peak of the pattern. It holds this value for all $a > 0.14$ radians.

At the commencement of this work, it was anticipated that the first sidelobe would continue to decrease in magnitude as the minimization interval was increased. This has not developed. The reason is that the energy from the reduced far sidelobe has been placed in the first sidelobe and not the main lobe as anticipated. Although the sidelobes have not been suppressed as greatly as desired, the patterns do have minimum energy sidelobes. Therefore under the stated conditions of a uniform distribution of interfering sources, these patterns are the optimum.

Tables I through X list the radiating element amplitudes for the various patterns.

Table I
Illumination Pattern (100 X)
 $a = 0$

<u>Element No.</u>	<u>Magnitude</u>	<u>Element No.</u>	<u>Magnitude</u>
0	3.272	1	3.225
2	3.272	3	3.224
4	3.274	5	3.222
6	3.277	7	3.218
8	3.283	9	3.210
10	3.291	11	3.193
12	3.321	13	3.145
14	3.427	15	3.772

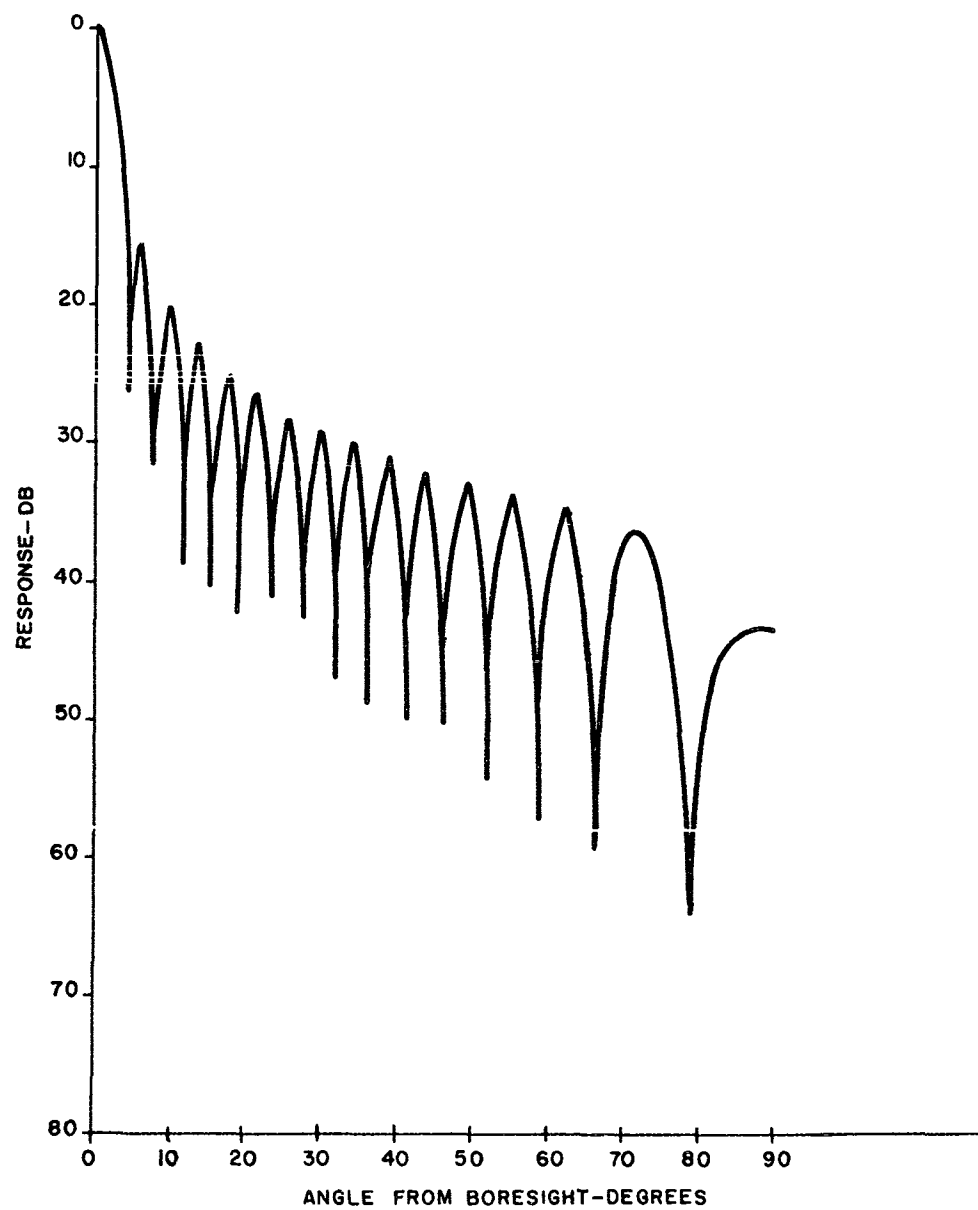


Figure 2. Minimum Energy Pattern, $\alpha = .05$ rad.

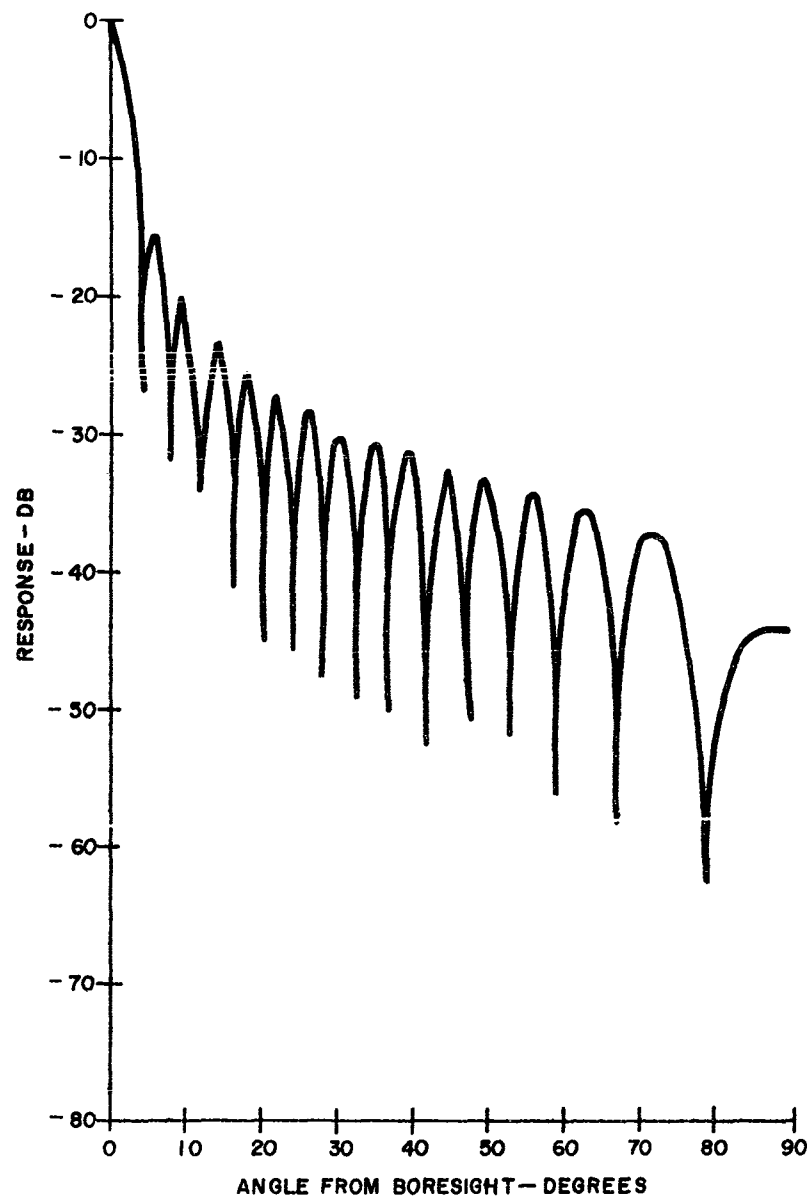


Figure 3. Minimum Energy Pattern, $\alpha = .075$ rad.

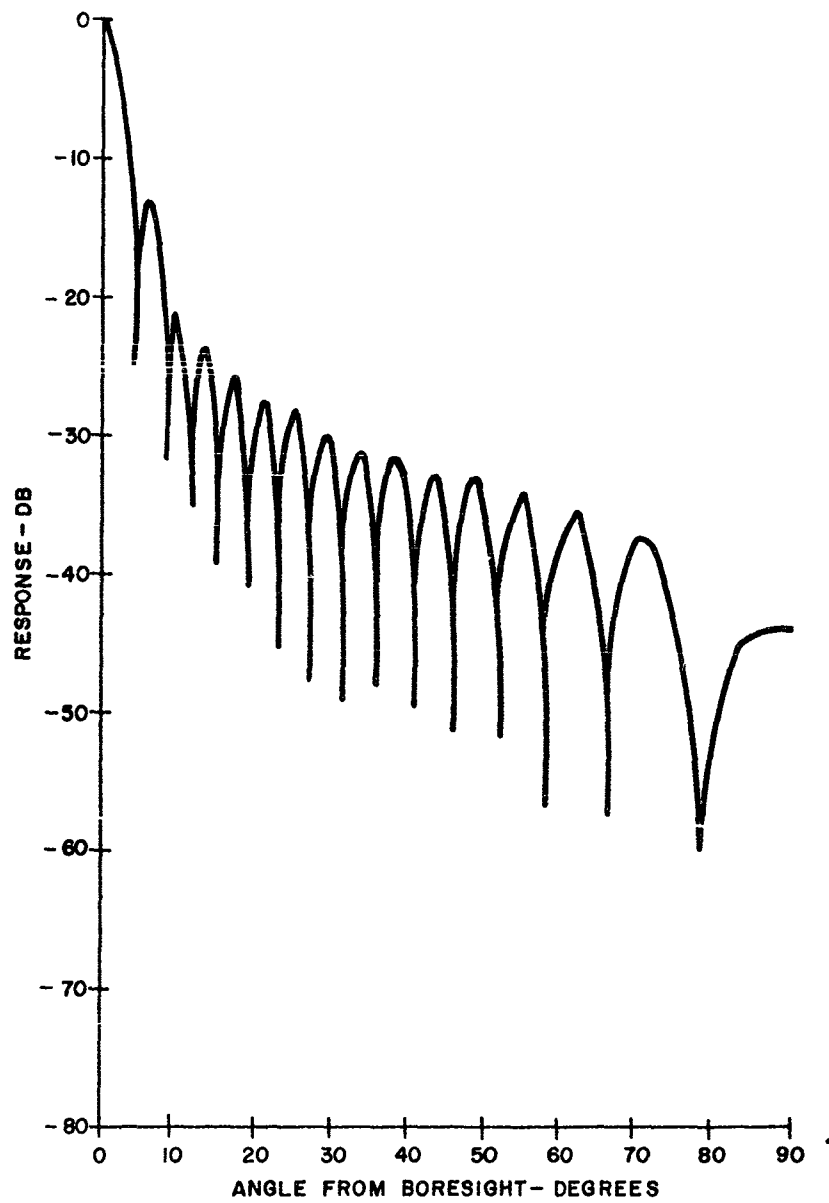


Figure 4. Minimum Energy Pattern, $a = .125$ rad.

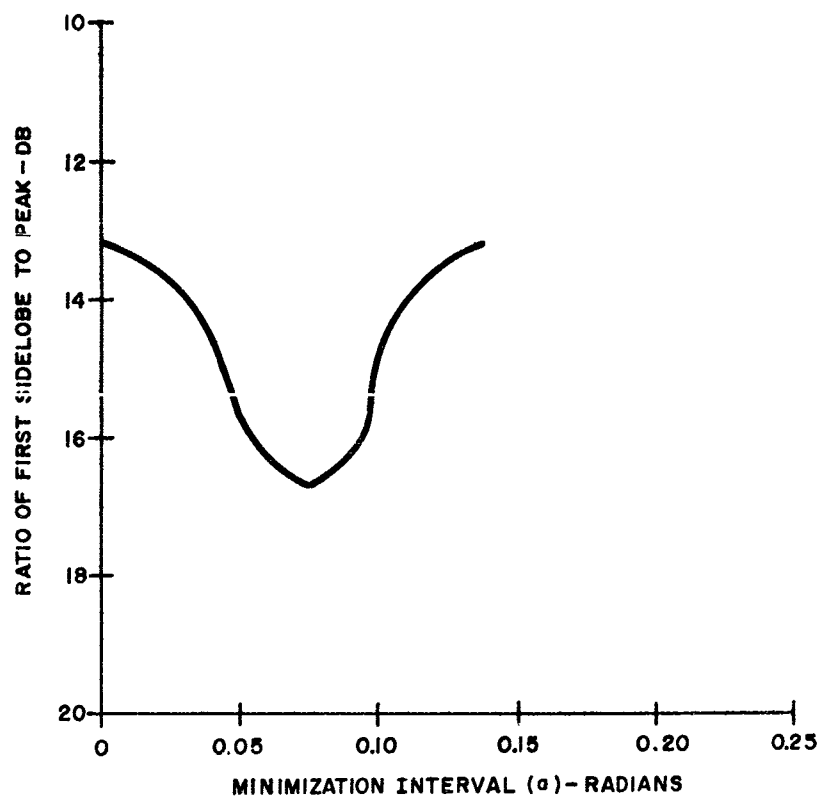


Figure 5. First Sidelobe as a Function of the Minimization Interval

Table II
Illumination Pattern (100 X)
 $\alpha = 0.025$ rad.

<u>Element No.</u>	<u>Magnitude</u>	<u>Element No.</u>	<u>Magnitude</u>
0	3.354	1	3.309
2	3.350	3	3.299
4	3.339	5	3.280
6	3.320	7	3.250
8	3.295	9	3.208
10	3.268	11	3.150
12	3.248	13	3.056
14	3.297	15	2.647

Table III
Illumination Pattern (100 X)
 $\alpha = 0.05$ rad.

<u>Element No.</u>	<u>Magnitude</u>	<u>Element No.</u>	<u>Magnitude</u>
0	3.660	1	3.618
2	3.638	3	3.571
4	3.571	5	3.480
6	3.464	7	3.348
8	3.323	9	3.181
10	3.157	11	2.982
12	2.983	13	2.742
14	2.861	15	2.242

Table IV
Illumination Pattern (100 X)
 $\alpha = 0.075$ rad.

<u>Element No.</u>	<u>Magnitude</u>	<u>Element No.</u>	<u>Magnitude</u>
0	3.823	1	3.780
2	3.788	3	3.710
4	3.686	5	3.574
6	3.526	7	3.383
8	3.321	9	3.150
10	3.087	11	2.886
12	2.850	13	2.593
14	2.671	15	2.076

Table V
Illumination Pattern (100 X)
 $a = 0.1$ rad.

<u>Element No.</u>	<u>Magnitude</u>	<u>Element No.</u>	<u>Magnitude</u>
0	3.554	1	3.519
2	3.551	3	3.509
4	3.536	5	3.478
6	3.491	7	3.405
8	3.397	9	3.269
10	3.241	11	3.055
12	3.026	13	2.754
14	2.815	15	2.169

Table VI
Illumination Pattern (100 X)
 $a = 0.125$ rad.

<u>Element No.</u>	<u>Magnitude</u>	<u>Element No.</u>	<u>Magnitude</u>
0	3.235	1	3.215
2	3.288	3	3.312
4	3.416	5	3.446
6	3.541	7	3.528
8	3.570	9	3.471
10	3.442	11	3.235
12	3.155	13	2.827
14	2.811	15	2.118

Table VII
Illumination Pattern (100 X)
 $a = 0.15$ rad.

<u>Element No.</u>	<u>Magnitude</u>	<u>Element No.</u>	<u>Magnitude</u>
0	3.209	1	3.191
2	3.267	3	3.295
4	3.406	5	3.444
6	3.545	7	3.539
8	3.587	9	3.491
10	3.462	11	3.253
12	3.167	13	2.831
14	2.804	15	2.106

Table VIII
Illumination Pattern (109X)
 $a = 0.175$ rad.

<u>Element No.</u>	<u>Magnitude</u>	<u>Element No.</u>	<u>Magnitude</u>
0	3.351	1	3.312
2	3.334	3	3.286
4	3.318	5	3.293
6	3.363	7	3.364
8	3.456	9	3.429
10	3.478	11	3.337
12	3.296	13	2.968
14	2.919	15	2.165

Table IX
Illumination Pattern (100X)
 $a = 0.2$ rad.

<u>Element No.</u>	<u>Magnitude</u>	<u>Element No.</u>	<u>Magnitude</u>
0	3.458	1	3.402
2	3.372	3	3.259
4	3.229	5	3.166
6	3.232	7	3.266
8	3.415	9	3.454
10	3.556	11	3.442
12	3.391	13	3.030
14	2.921	15	2.130

Table X
Illumination Pattern (100X)
 $a = 0.25$ rad.

<u>Element No.</u>	<u>Magnitude</u>	<u>Element No.</u>	<u>Magnitude</u>
0	3.280	1	3.262
2	3.333	3	3.330
4	3.369	5	3.298
6	3.286	7	3.208
8	3.267	9	3.281
10	3.431	11	3.417
12	3.468	13	3.165
14	3.048	15	2.190

IV. MODIFIED MINIMUM ENERGY PATTERN

A. Derivation

Although the true minimum energy patterns may be useful under certain conditions, a first sidelobe 17.4 db down from the peak is undesirable in other situations. A possible condition could occur when a very large antenna is used and a fair amount of main lobe broadening can be tolerated. In the minimum energy patterns previously calculated, the main lobe width did not increase noticeably. Thus the first sidelobe failed to be depressed. One possible technique which forces the main lobe to broaden is to replace $\sin \theta$ by γ in the minimization process. The antenna patterns derived in this section will follow the same development as that used in the previous section with the exception that $\sin \theta$ is replaced by γ . The antenna pattern derived from the calculated radiating element magnitudes is plotted using values computed from the true antenna pattern equation.

Again as in Section III, the pattern to be approximated is

$$\epsilon'(\gamma) = \begin{cases} 1 & \text{when } \gamma = 0 \\ 0 & \text{when } \gamma \neq 0 \end{cases} \quad (18)$$

Now the antenna pattern will be represented by

$$\epsilon(\gamma) = \sum_{-N}^N (n) A_n \cos(n\beta d\gamma) \quad (19)$$

If $\epsilon(\gamma)$ is to represent an antenna pattern, it must have the characteristics of one. A true antenna representation is periodic with period $\frac{\pi}{m}$, where m is the number of half-wavelengths between adjacent radiating elements. If the radiating elements have the usual $\lambda/2$ spacing, the pattern as given by equation (19) does not have a period of π . Instead it has a period of unity. Therefore, the argument of the cosines should be divided by π if an equation of the form of (30) is to be the model of an antenna pattern. The pattern will then be represented as,

$$\epsilon(\gamma) = \sum_{-N}^N (n) A_n \cos\left(\frac{n\beta d\gamma}{\pi}\right) \quad (20)$$

As in Section III, the error between the desired pattern and the approximate pattern is given by

$$\epsilon = \int_{-\pi}^{-a} [\epsilon(\gamma)]^2 d\gamma + \int_a^{\pi} [\epsilon(\gamma)]^2 d\gamma \quad (21)$$

Substituting equation (20) into equation (21) gives

$$\epsilon = \int_{-\pi}^{-a} \left[\sum_{-N}^N (n) A_n \cos\left(\frac{n\beta d\gamma}{\pi}\right) \right]^2 d\gamma + \int_a^{\pi} \left[\sum_{-N}^N (n) A_n \cos\left(\frac{n\beta d\gamma}{\pi}\right) \right]^2 d\gamma \quad (22)$$

Expanding equation (22) gives

$$\begin{aligned} \epsilon = & 2 \int_a^{\pi} \sum_{-N}^N (n) A_n^2 \cos^2\left(\frac{n\beta d\gamma}{\pi}\right) d\gamma \\ & + 2 \int_a^{\pi} \sum_{-N}^N (i) \sum_{-N}^N (j) A_i A_j \cos\left(\frac{i\beta d\gamma}{\pi}\right) \cos\left(\frac{j\beta d\gamma}{\pi}\right) d\gamma \quad i \neq j \end{aligned} \quad (23)$$

Carrying out the integration gives

$$\begin{aligned} \epsilon = & \sum_{-N}^N (n) A_n^2 \left[\pi - a - \frac{\pi}{2n\beta d} \sin\left(\frac{2n\beta da}{\pi}\right) \right] \\ & + \sum_{-N}^N (i) \sum_{-N}^N (j) A_i A_j \frac{\pi}{(i+j)\beta d} \left\{ \sin\left[(i+j)\beta d\right] - \sin\left[\frac{(i+j)\beta da}{\pi}\right] \right\} \\ & + \sum_{-N}^N (i) \sum_{-N}^N (j) A_i A_j \frac{\pi}{(i-j)\beta d} \left\{ \sin\left[(i-j)\beta d\right] - \sin\left[\frac{(i-j)\beta da}{\pi}\right] \right\} \end{aligned} \quad (24)$$

Again the method of Lagrangian Multipliers will be used to determine the various values of A_n which minimize equation (24). The side condition

$$\sum_{-N}^N (n) A_n = 1 \quad (25)$$

is used again.

The set of equations to be solved may be written in matrix form as

$$\begin{bmatrix} C_{ij} \end{bmatrix} \begin{bmatrix} A_n \end{bmatrix} = - \frac{\rho}{4} \begin{bmatrix} 1 \end{bmatrix} \quad (26)$$

where ρ is the Lagrange multiplier and

$$\begin{bmatrix} C_{ij} \end{bmatrix} = \begin{cases} \pi - a - \frac{\pi}{2n\beta d} \sin \left(\frac{2n\beta da}{\pi} \right) & , i = j \\ \frac{\pi}{(i+j)\beta d} \left\{ \sin \left[(i+j)\beta d \right] - \sin \left[\frac{(i+j)\beta da}{\pi} \right] \right\} & \\ + \frac{\pi}{(i-j)\beta d} \beta \left\{ \sin \left[(i-j)\beta d \right] - \sin \left[\frac{(i-j)\beta da}{\pi} \right] \right\} & i \neq j \end{cases} \quad (27)$$

As was done in Section III, the parameter (a) was varied, the coefficients C_{ij} were evaluated, the A 's computed and the resulting antenna patterns were determined. The one-half wavelength element spacing was used again.

B, Pattern Evaluation

In figures 5 through 9, the antenna patterns were plotted for the modified approximations. Only four of the computed patterns are plotted as they show the effects of the variation of the minimization interval. The array which produces these patterns has the same number of elements as those which produce figures 1 through 4.

A comparison of the two sets of patterns shows that the sidelobe in the region of 90° is suppressed further in the true minimum energy patterns than in the modified patterns for the same value (a). This indicates the weight which is placed on the energy in the vicinity of 90 degrees in the true minimum patterns. It is also noted that the first sidelobes of the modified patterns continue to decrease as the value of (a) increases. This is contrary to the trend exhibited by the true minimum patterns.

Figure 6 is the antenna pattern when (a) is equal to zero. This pattern is the approximation to an impulse type pattern. The individual radiating elements have equal currents on them. Thus figure 6 is very similar to a $\frac{\sin x}{x}$ pattern. In fact, if $\sin 0$ were to have been replaced by γ when the pattern was computed, the pattern would have been of the form $\frac{\sin x}{x}$.

Figure 7 is the pattern which approximates a rectangular pattern which is 0.125 radians wide. The sidelobes are generally 3 db below the corresponding lobes of Figure 2.

Figures 8 and 9 are the patterns which approximate rectangular patterns 0.175 and 0.25 radians wide, respectively. Continued lowering of the sidelobe level is evident. In particular, the first sidelobe has been depressed to 27 db below the peak when (a) equals 0.25 radians.

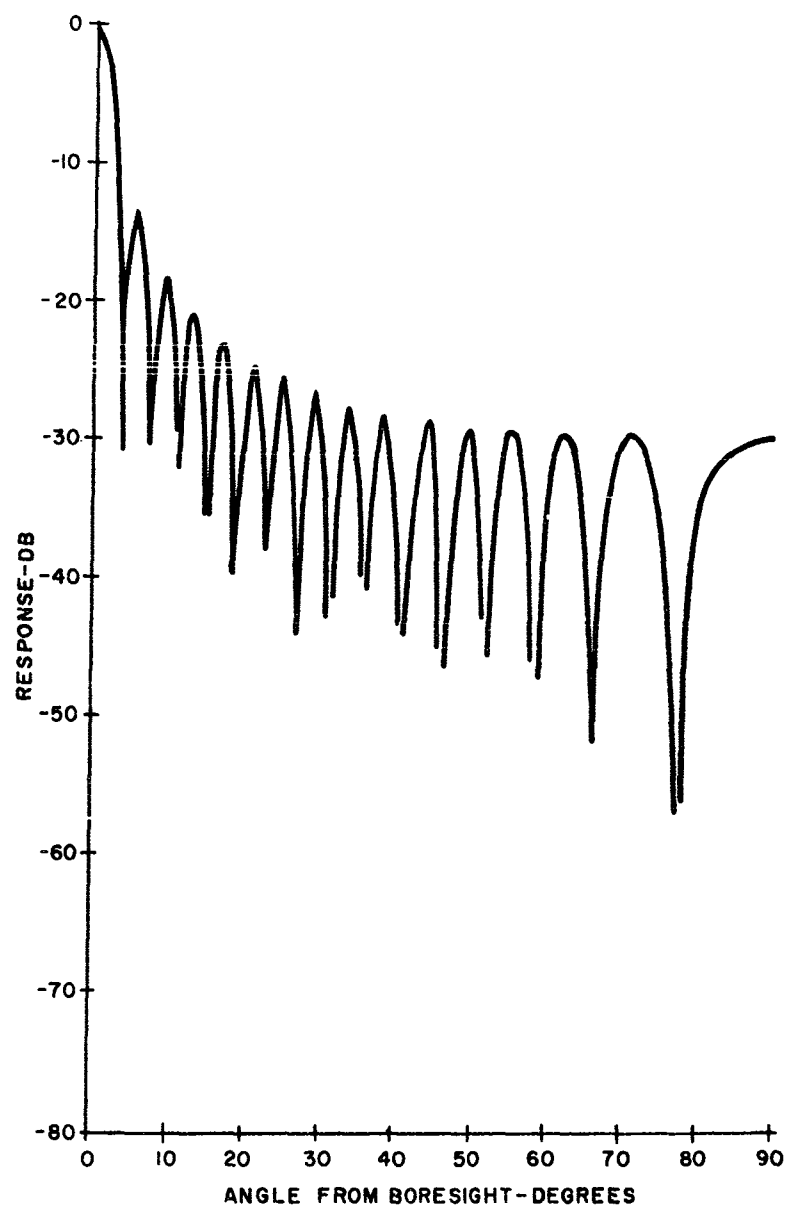


Figure 6. Modified Minimum Energy Pattern, $a = 0$

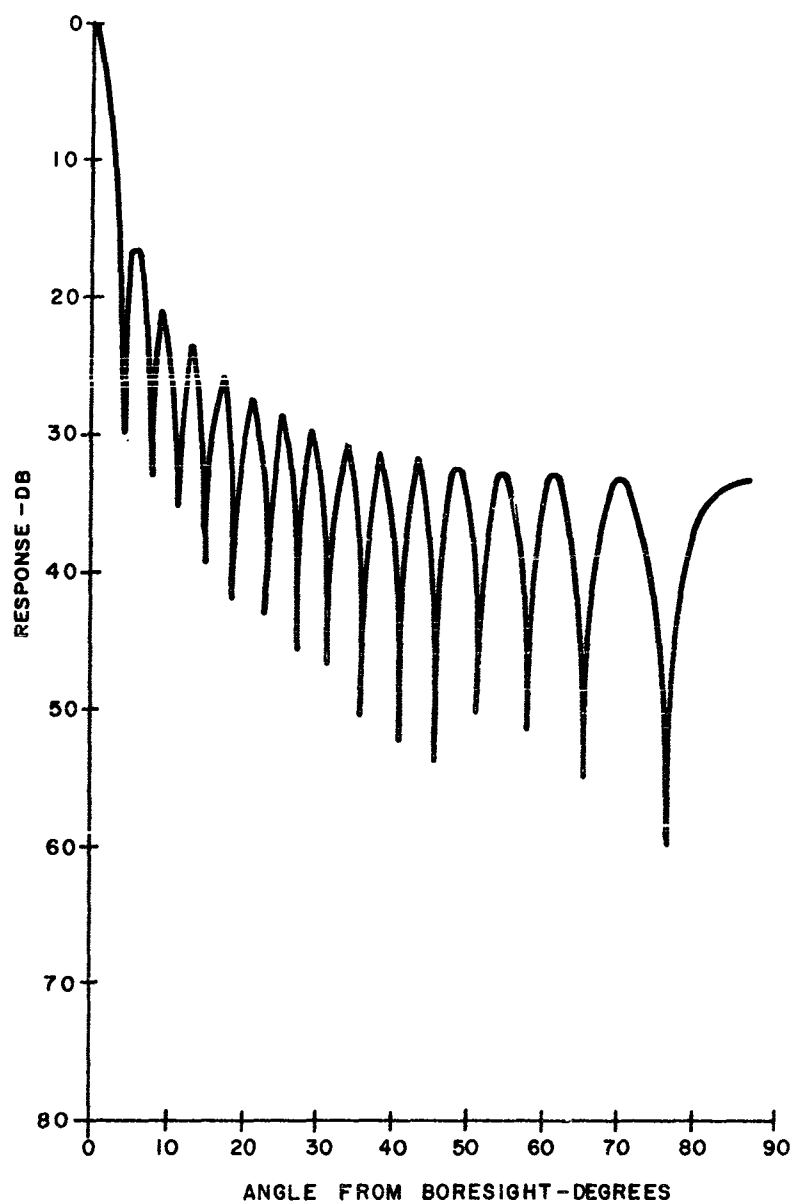


Figure 7. Modified Minimum Energy Pattern, $\alpha = .125$ rad.

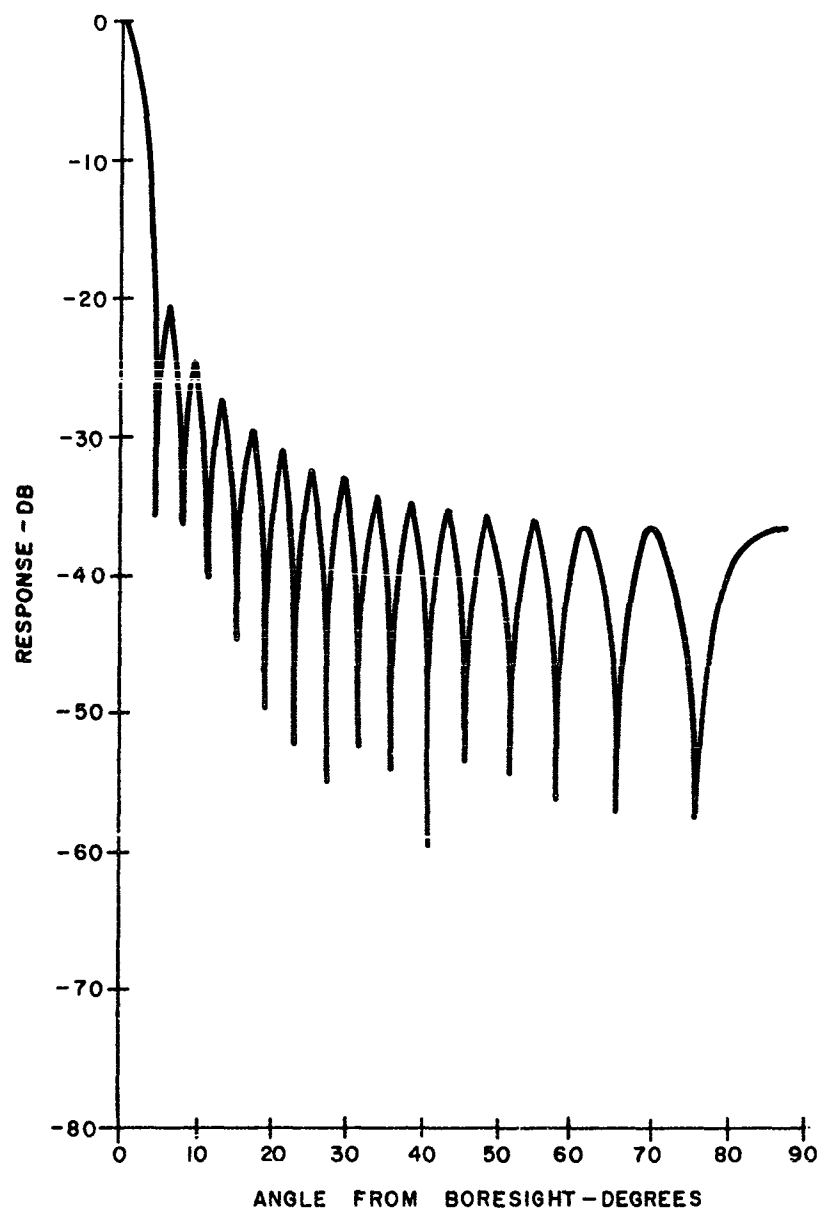


Figure 8. Modified Minimum Energy Pattern, $\alpha = .175$ rad.

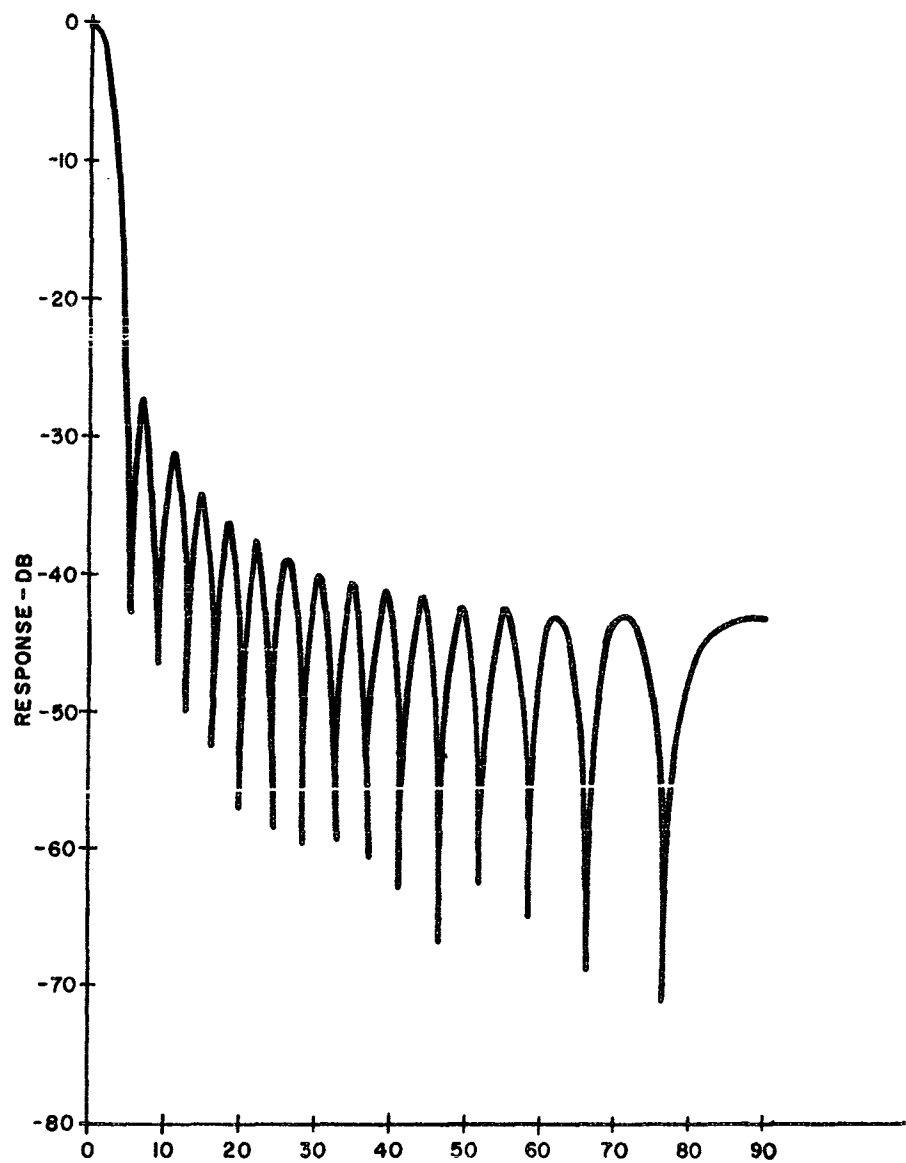


Figure 9. Modified Minimum Energy Pattern, $\alpha = .25$ rad.

A curve showing the relationship between the first sidelobe and the minimization interval is given in Figure 10. It is noted that the sidelobe level continues to decrease as (a) is increased. From the curve it would appear that the sidelobe may be depressed indefinitely as (a) is increased. This is not a fact. As the minimization interval is decreased, a value is reached which causes the first sidelobe to increase. An extension of Figure 10 would show an inflection point the same as Figure 5.

The sidelobes are depressed at the expense of the mainlobe. The minimization process removes energy from the sidelobes and places it in the main lobe region. In the true minimum energy patterns, the mainlobe and first sidelobe shared this energy. Thus there was no noticeable mainlobe broadening. In the modified minimum energy patterns, the mainlobe received almost all of this sidelobe energy. Therefore, a noticeable mainlobe broadening occurred. Figure 11 is a curve of the 6 db pattern width as a function of the minimization interval.

Tables XI through XX list the radiating element amplitudes for the various patterns.

Table XI
Illumination Pattern (100 X)
 $a = 0$

<u>Element No.</u>	<u>Magnitude</u>	<u>Element No.</u>	<u>Magnitude</u>
0	3.225	1	3.225
2	3.225	3	3.225
4	3.225	5	3.225
6	3.225	7	3.225
8	3.225	9	3.225
10	3.225	11	3.225
12	3.225	13	3.225
14	3.225	15	3.225

Table XII
Illumination Pattern (100 X)
 $a = 0.025 \text{ rad.}$

<u>Element No.</u>	<u>Magnitude</u>	<u>Element No.</u>	<u>Magnitude</u>
0	3.232	1	3.232
2	3.231	3	3.231
4	3.231	5	3.230
6	3.229	7	3.228
8	3.227	9	3.225
10	3.224	11	3.222
12	3.220	13	3.218
14	3.216	15	3.214

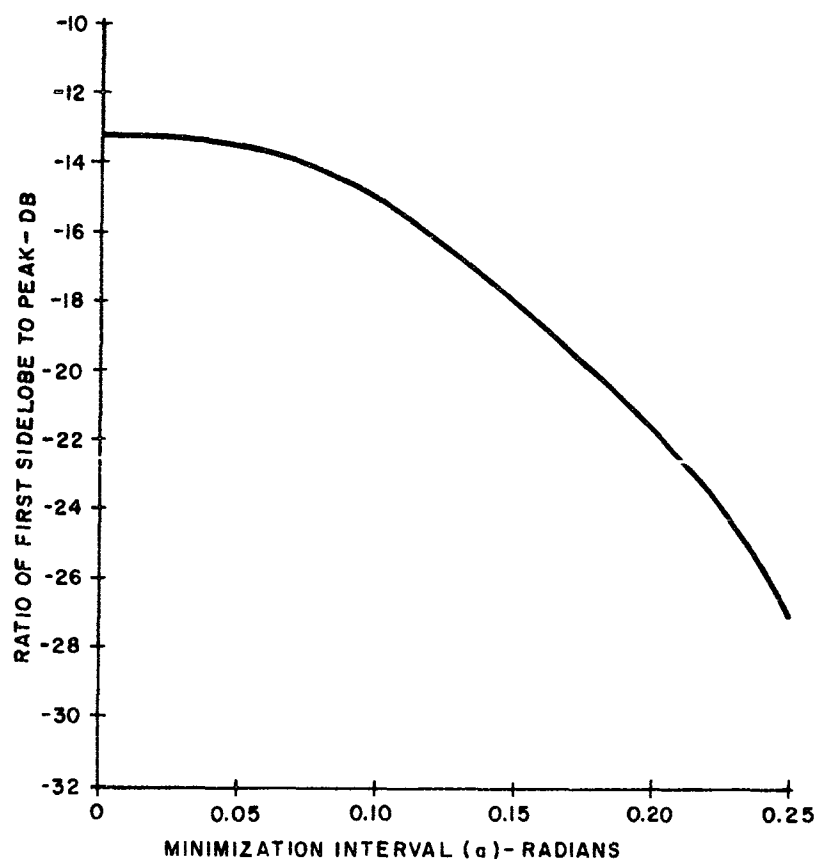


Figure 10. First Sidelobe as a Function of the Minimization Interval

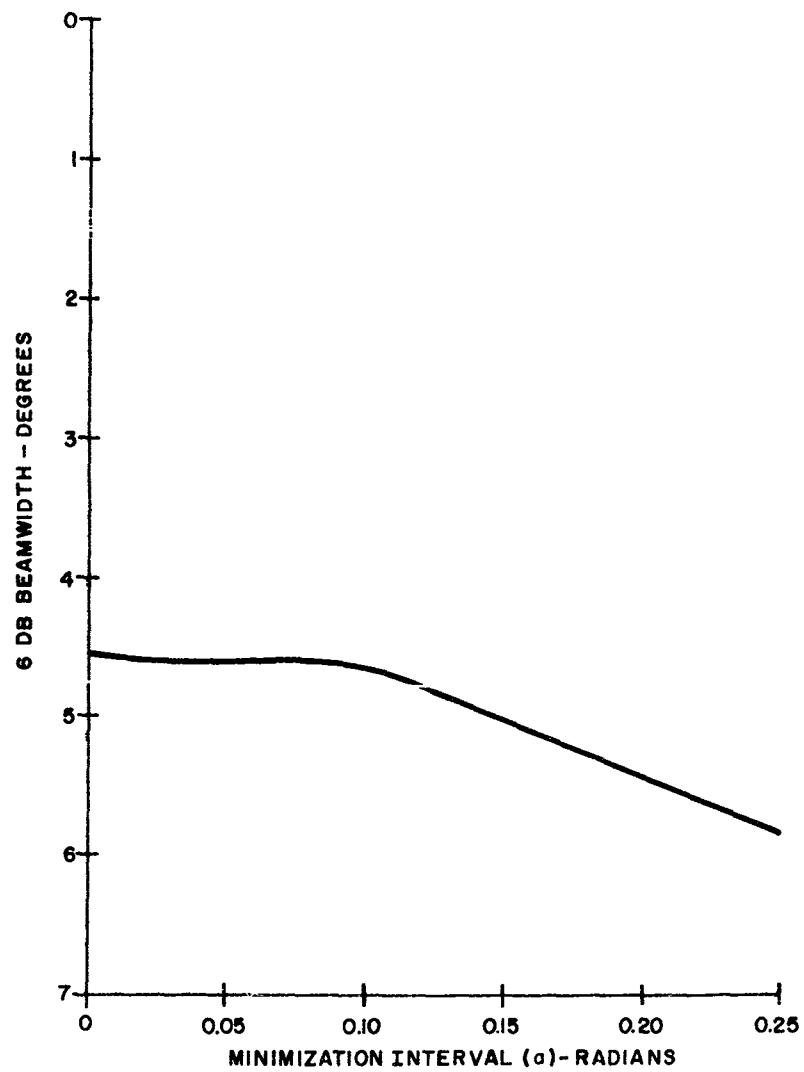


Figure 11. Pattern Width as a Function of the Minimization Interval

Table XIII
Illumination Pattern (100 X)
 $a = 0.05$ rad.

<u>Element No.</u>	<u>Magnitude</u>	<u>Element No.</u>	<u>Magnitude</u>
0	3.274	1	3.274
2	3.272	3	3.269
4	3.264	5	3.259
6	3.252	7	3.244
8	3.235	9	3.224
10	3.213	11	3.200
12	3.186	13	3.171
14	3.155	15	3.138

Table XIV
Illumination Pattern (100 X)
 $a = 0.075$ rad.

<u>Element No.</u>	<u>Magnitude</u>	<u>Element No.</u>	<u>Magnitude</u>
0	3.376	1	3.374
2	3.368	3	3.359
4	3.345	5	3.327
6	3.306	7	3.281
8	3.253	9	3.221
10	3.185	11	3.147
12	3.105	13	3.060
14	3.012	15	2.961

Table XV
Illumination Pattern (100 X)
 $a = 0.1$ rad.

<u>Element No.</u>	<u>Magnitude</u>	<u>Element No.</u>	<u>Magnitude</u>
0	3.541	1	3.537
2	3.524	3	3.503
4	3.474	5	3.436
6	3.391	7	3.339
8	3.279	9	3.212
10	3.138	11	3.059
12	2.973	13	2.883
14	2.787	15	2.688

Table XVI
Illumination Pattern (100 X)
 $a = 0.125$ rad.

<u>Element No.</u>	<u>Magnitude</u>	<u>Element No.</u>	<u>Magnitude</u>
0	3.757	1	3.749
2	3.727	3	3.691
4	3.640	5	3.576
6	3.498	7	3.408
8	3.307	9	3.194
10	3.072	11	2.940
12	2.801	13	2.656
14	2.505	15	2.349

Table XVII
Illumination Pattern (100 X)
 $a = 0.15$ rad.

<u>Element No.</u>	<u>Magnitude</u>	<u>Element No.</u>	<u>Magnitude</u>
0	4.005	1	3.994
2	3.960	3	3.905
4	3.828	5	3.731
6	3.615	7	3.481
8	3.330	9	3.166
10	2.988	11	2.801
12	2.605	13	2.402
14	2.196	15	1.988

Table XVIII
Illumination Pattern (100 X)
 $a = 0.175$ rad.

<u>Element No.</u>	<u>Magnitude</u>	<u>Element No.</u>	<u>Magnitude</u>
0	4.289	1	4.254
2	4.207	3	4.129
4	4.023	5	3.889
6	3.729	7	3.547
8	3.344	9	3.125
10	2.891	11	2.648
12	2.397	13	2.144
14	1.890	15	1.640

Table XIX
Illumination Pattern (100 X)
 $a = 0.2 \text{ rad.}$

<u>Element No.</u>	<u>Magnitude</u>	<u>Element No.</u>	<u>Magnitude</u>
0	4.537	1	4.516
2	4.454	3	4.353
4	4.214	5	4.040
6	3.835	7	3.602
8	3.346	9	3.072
10	2.784	11	2.489
12	2.190	13	1.894
14	1.605	15	1.327

Table XX
Illumination Pattern (100 X)
 $a = 0.25 \text{ rad.}$

<u>Element No.</u>	<u>Magnitude</u>	<u>Element No.</u>	<u>Magnitude</u>
0	5.054	1	5.022
2	4.928	3	4.775
4	4.566	5	4.307
6	4.006	7	3.671
8	3.311	9	2.935
10	2.552	11	2.172
12	1.803	13	1.453
14	1.128	15	0.835

C. Array Size Considerations

Thirty-one radiating elements were used to calculate the patterns shown in Figures 1 through 10. Thus, the array is 15.5 wavelengths long. This number was chosen as a convenience to keep computational work to a minimum and still show trends in the patterns. Slightly different effects occur when the number of elements is increased. The effect of a change of minimization interval is more pronounced on the patterns with a larger number of elements. The general level of the patterns is reduced for a given value of (a). In the minimum energy pattern, the least first sidelobe occurs when (a) equals 0.05 radians when the array is 20.5 wavelengths long and at 0.075 radians when the array is 15.5 wavelengths long. In the modified minimum energy pattern, the first sidelobe is approximately 38 db down from the peak at a value of (a) equal to 0.25 radians when the array is 20.5 wavelengths long and is only 28 db when the array is 15.5 wavelengths. Thus caution must be exercised in drawing conclusions where the parameter (a) is involved.

The fact that the effect of the minimization interval is different for different size arrays is reasonable. An extremely large antenna might have many sidelobes within a few degrees of the boresight. It would seem that some form of normalization in the parameter (a) would make the affect of the minimization interval independent of the array size. The most obvious choice of a normalizing factor is the array size, or, equivalently, the number (N) of elements in the array. Listed in the following table is the first sidelobe level at various values of a normalized parameter (a.N) for antennas containing 21, 31, 41, and 61 elements.

TABLE XXI
First Sidelobe Level

(a.N)	21 elements	31 elements	41 elements	61 elements
3.1		.178	.177	
3.9		.155	.155	
6.2		.0775	.0774	.0693
6.8		.0609	.0610	
7.2	.0498	.0503	.0499	
8.3		.0345	.0351	

A more detailed comparison was made on several of the patterns with various numbers of elements. For example, an array of 31 elements was compared with one containing 61 elements. For $NA = 6.8$, every other illumination magnitude of the 61 element array equaled the corresponding magnitude of the 31 element array. Next, taking into account the different array sizes, a point by point comparison was made between the two antenna patterns. Again the difference between the two patterns was found to be negligible, i.e. less than one percent difference.

Therefore, taking into account the comparisons made from Table XXI, it is a safe assumption that the illumination amplitudes for a particular antenna pattern is not dependent on the number of elements in the array. This assumption is valid for arrays containing more than some minimum number of elements. A comparison using an array of 21 elements shows close agreement with an array of 41. Thus the array illumination patterns may be specified by curves drawn from Tables XI through XX for arrays containing 31 or more elements.

The true minimum energy illumination pattern depends on the number of elements used in the array. A glance at Tables I through X shows that there is a ripple on the amplitudes. This ripple causes the antenna pattern to be depressed in the region of $\theta = 90$ degrees. In order to do this, the ripple period must have a period of two radiating elements. Therefore, drawing a curve from a table in the first set, cannot be used to determine an illumination pattern for a different number of array elements.

The use of tables or curves is an unfortunate requirement to the use of a minimum energy pattern. This requirement arises because a tractable functional form for the array illumination cannot be obtained. Considerable effort was expended in an attempt to determine a functional form. There is still a value in this report to builders of arrays as Tables XI through XX may be used in place of a functional form. Also, if a minimum energy pattern is desired, a great amount of computational effort is saved by using equation (28), Section III for the desired number and spacing of elements.

V. EFFECT OF RANDOM PHASE AND AMPLITUDE ERRORS

The nominal antenna pattern of an array is degraded by phase and amplitude errors on the individual radiating elements. This section derives the variance of the pattern produced by random errors on a linear array of isotropic radiators.

A simple equation specifying the variance of the pattern in terms of the random phase and amplitude errors is given.

The antenna pattern at a specified distance from the array is given by

$$E(t, \theta) = \sum_{n=-N}^N A_n \cos \left[\omega t + n \beta d \sin \theta \right] \quad (28)$$

The important region of the pattern is in the vicinity of $\theta = 0$ degrees because this is the region of the highest sidelobes. Thus it is possible to make the substitution $\frac{\gamma}{\pi} = \sin \theta$ as was done in Section IV. Then the pattern may be represented by

$$E(t, \gamma) = \sum_{n=-N}^N A_n \cos \left[\omega t + \frac{n \beta d \gamma}{\pi} \right] \quad (29)$$

It was tacitly assumed in the derivation that all the radiators were in phase. This is very difficult to accomplish in practice. In addition it is very difficult to achieve the exact illumination desired. Thus two sources of error are inherent in an actual array which cause the pattern to deviate from the ideal pattern:

Let δ = the random per unit amplitude error on each radiating element.

and ϕ = the random phase error on each radiating element. The actual antenna pattern is then,

$$E(t, \gamma) = \sum_{n=-N}^N A_n (1 + \delta) \cos \left(\omega t + \frac{n \beta d \gamma}{\pi} + \phi \right) \quad (30)$$

Expanding equation (30) gives

$$\begin{aligned} E(t, \gamma) = & \sum_{n=-N}^N A_n (1 + \delta) \cos \left(\omega t + \frac{n \beta d \gamma}{\pi} \right) \cos \phi \\ & - \sum_{n=-N}^N A_n (1 + \delta) \sin \left(\omega t + \frac{n \beta d \gamma}{\pi} \right) \sin \phi \end{aligned} \quad (31)$$

If it is assumed that $\delta \ll 1$ and $\theta \ll 1$, then $\cos \theta \approx 1$

$$\sin \theta \approx \theta \quad (32)$$

and second order terms (e.g. $\delta \theta$) are negligible.

Expanding equation (31) and noting that $\delta \theta \ll \theta$ gives

$$\begin{aligned} \epsilon(t, \gamma) \approx & \sum_{-N}^N (n) A_n (1 + \delta) \cos \omega t \cos \frac{n\beta d\gamma}{\pi} - \sum_{-N}^N (n) A_n (1 + \delta) \sin \omega t \sin \frac{n\beta d\gamma}{\pi} \\ & - \sum_{-N}^N (n) A_n \theta \sin \omega t \cos \frac{n\beta d\gamma}{\pi} - \sum_{-N}^N (n) A_n \theta \cos \omega t \sin \frac{n\beta d\gamma}{\pi} \end{aligned} \quad (33)$$

Rewriting equation (33) in complex form gives

$$\begin{aligned} \epsilon(t, \gamma) \approx & \cos \omega t \sum_{-N}^N (n) A_n (1 + \delta - j\theta) \cos \frac{n\beta d\gamma}{\pi} \\ & - \sin \omega t \sum_{-N}^N (n) A_n (j + j\delta + \theta) \sin \frac{n\beta d\gamma}{\pi} \end{aligned} \quad (34)$$

The A_n 's are symmetrical about A_0 and the error terms are small, therefore the second term of equation (34) is negligible compared to the first term. Dropping the time dependent portion of equation (34), the antenna pattern may be represented by

$$\epsilon(\gamma) \approx \sum_{-N}^N (n) A_n (1 + \delta - j\theta) \cos \frac{n\beta d\gamma}{\pi} \quad (35)$$

It will be assumed that the error magnitudes have normal probability density with mean zero; then

$$\begin{aligned} p(\gamma) = & \frac{1}{\sqrt{2\pi} \sigma_\delta} e^{-\frac{\delta^2}{2\sigma_\delta^2}} \\ p(\theta) = & \frac{1}{\sqrt{2\pi} \sigma_\theta} e^{-\frac{\theta^2}{2\sigma_\theta^2}} \end{aligned} \quad (36)$$

The expected value of the pattern is

$$\overline{\epsilon(\gamma)} \approx \iint_{-\infty}^{\infty} \iint_{-\infty}^{\infty} \sum_{n=-N}^N A_n (1 + \delta - j\theta) \cos \frac{n\beta d\gamma}{\pi} \frac{1}{2\pi\sigma\delta\sigma\theta} e^{-\frac{\delta^2}{2\sigma\delta^2} - \frac{\theta^2}{2\sigma\theta^2}} d\delta_n d\theta_n \quad (37)$$

Noting that

$$\int_{-\infty}^{\infty} \frac{1}{\sqrt{2\pi\sigma}} e^{-\frac{x^2}{2\sigma^2}} dx = 1 \quad (38)$$

$$\int_{-\infty}^{\infty} \frac{x}{\sqrt{2\pi\sigma}} e^{-\frac{x^2}{2\sigma^2}} dx = 0 \quad (39)$$

$$\int_{-\infty}^{\infty} \frac{x^2}{\sqrt{2\pi\sigma}} e^{-\frac{x^2}{2\sigma^2}} dx = \sigma^2 \quad (40)$$

Using equations (38) and (39), equation (37) becomes

$$\overline{\epsilon(\gamma)} = \sum_{n=-N}^N A_n \cos \frac{n\beta d\gamma}{\pi} \quad (41)$$

The second moment of the pattern is

$$\overline{\epsilon(\gamma)^2} = \iint_{-\infty}^{\infty} \iint_{-\infty}^{\infty} \left| \sum_{n=-N}^N (1 + \delta - j\theta) A_n \cos \frac{n\beta d\gamma}{\pi} \right|^2 \frac{1}{2\pi\sigma\delta\sigma\theta} e^{-\frac{\delta^2}{2\sigma\delta^2} - \frac{\theta^2}{2\sigma\theta^2}} d\delta_n d\theta_n \quad (42)$$

Expanding equation (42) and carrying out the integrations gives

$$\begin{aligned} \overline{\epsilon(\gamma)^2} = & \sum_{-N}^N (n) A_n^2 \cos^2 \frac{n\beta d \gamma}{\pi} + \sum_{-N}^N (k) \sum_{-N}^N (\ell) A_k A_\ell \cos \frac{k\beta d \gamma}{\pi} \cos \frac{\ell\beta d \gamma}{\pi} \\ & + \sigma_\delta^2 \sum_{-N}^N (n) A_n^2 \cos^2 \frac{n\beta d \gamma}{\pi} + \sigma_\phi^2 \sum_{-N}^N (n) A_n^2 \cos \frac{n\beta d \gamma}{\pi} \end{aligned} \quad (43)$$

$\ell \neq k$

Recognizing the first two terms of equation (43) as the antenna pattern squared and combining terms gives

$$\overline{\epsilon(\gamma)^2} = \left[\sum_{-N}^N (n) A_n \cos \frac{n\beta d \gamma}{\pi} \right]^2 + (\sigma_\delta^2 + \sigma_\phi^2) \sum_{-N}^N (n) A_n^2 \cos^2 \frac{n\beta d \gamma}{\pi} \quad (44)$$

The variance of the pattern is

$$\sigma^2 = \frac{2}{\overline{\epsilon(\gamma)^2} - \overline{\epsilon(\gamma)}^2} = (\sigma_\delta^2 + \sigma_\phi^2) \sum_{-N}^N (n) A_n^2 \cos^2 \frac{n\beta d \gamma}{\pi} \quad (45)$$

Equation (45) was derived for an array whose illumination was symmetrical about its center and whose phase and amplitude errors were small. Since the only other imposed restriction was that $\frac{\gamma}{\pi} \approx \sin \theta$, equation (45) is generally valid for any array.

A useful result of equation (45) is a calculation of the decrease in the peak of the antenna pattern which develops for an error in the amplitudes and phases of the radiating elements. Using Tables XI through XX to specify the A_n 's, the standard deviation of the patterns at $\theta = 0$ was calculated for $(\sigma_\delta^2 + \sigma_\phi^2) = 0.1$. For other values of $(\sigma_\delta^2 + \sigma_\phi^2)$, the ordinate may be linearly scaled. Since the pattern error is the sum of random errors with a Gaussian probability density, the pattern error has a Gaussian probability density. Thus the 10% value of the error is related to the standard deviation by the factor 1.3. A curve showing the results of these calculations is given in figure 12.

In figure 12 it is noted that the reduction of the peak response is increased as the nominal first sidelobe value is decreased. This is a result of the array illumination pattern being more tapered for the low sidelobe cases. This taper results in the center radiating elements having a greater weighting than the average. Thus the center elements have a greater effect on the pattern than do the end elements.

A more pronounced variation occurs when the variance is calculated at a value of γ equal to the location of the first sidelobe. Again using Tables XI through XX, the standard deviation of the patterns were calculated for $(\sigma_\delta^2 + \sigma_\phi^2) = 0.1$. The 90%

probability factor was also used. Figure 13 was plotted from these calculations. The extreme variation in this case is not so much caused by the taper directly, as it is caused by the lowering of the sidelobe itself. In absolute magnitude, the standard deviation varied over an 8% range. But considering the nominal level of the first sidelobe, a large percentage change took place.

Figure 13 shows that the nominal 13.3 sidelobe pattern's first sidelobe has been raised 0.9 db. The nominal 27 db sidelobe pattern's first sidelobe has been raised 6.5 db for the same error in phase and amplitude.

Figures 12 and 13 summarize the effects of random errors on the response of an antenna pattern. Random errors cause a comparatively small variation in the peak response of an antenna. These same errors cause a significant variation in sidelobe levels when the pattern has depressed sidelobe levels. Therefore, antennas designed to produce low sidelobes must have very close tolerances.

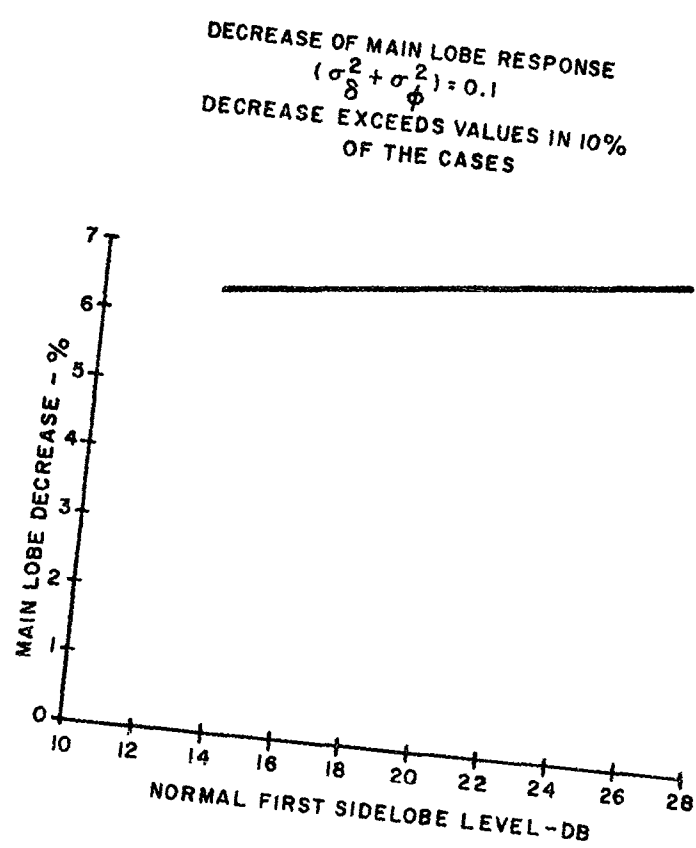


Figure 12. Nominal First Sidelobe Level - db

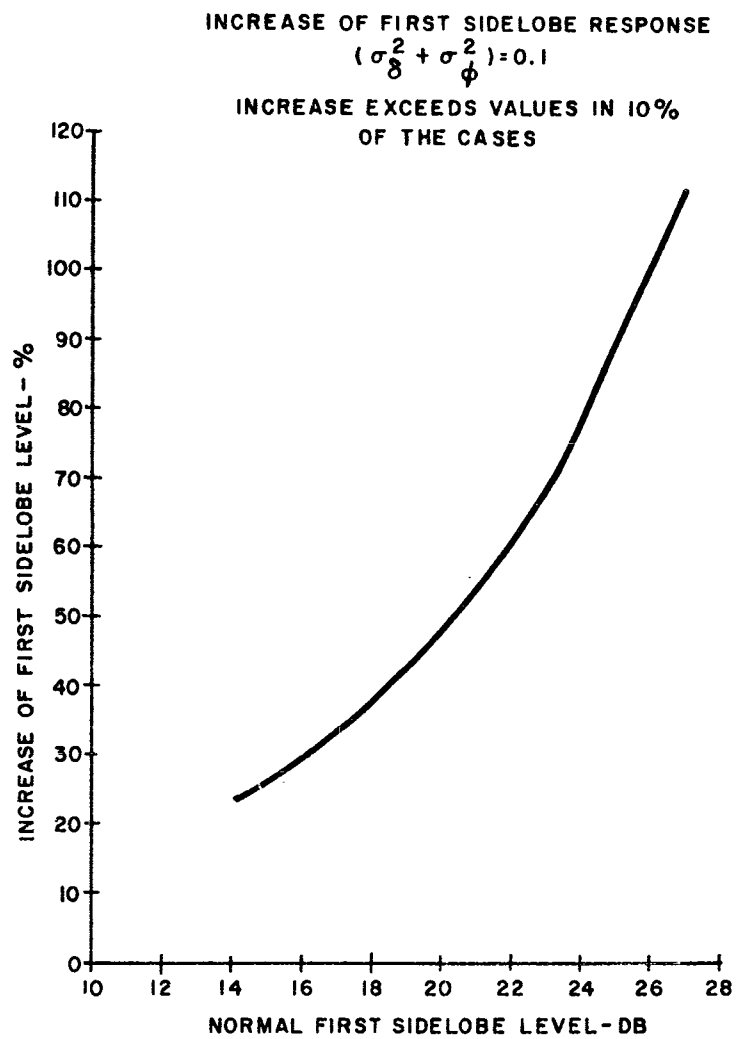


Figure 13. Nominal First Sidelobe Level - db

VI. SUMMARY

The antenna patterns derived in Section IV are the optimum when the noise contributing sources are randomly distributed in space. This condition is fulfilled in a large number of antenna applications. Thus an antenna using a minimum energy pattern accepts the least possible noise. The modified minimum energy derivation produces a pattern which is similar in shape to the true minimum energy but the near sidelobes are depressed. These modified patterns possess both low sidelobe levels and low noise acceptance.

Tables XI through XX may be used to generate the array illumination patterns for the modified minimum energy for an array longer than 15 wavelengths. The array illumination for the true minimum energy patterns must be computed for each array size.

The analysis of the pattern variations caused by random phase and amplitude errors on the radiating elements show that for a given magnitude of error, the sidelobes have a much larger percentage variation than the main lobe. Thus if an antenna is to have low sidelobe levels, the tolerances required are very tight. If the tolerances are allowed to become large, little or no advantage may be procured by using an illumination pattern designed to produce low sidelobes.

BRIEF BIBLIOGRAPHY

1. Apostol, Tom M., Mathematical Analysis; Addison-Wesly Publishing Co.; 1957.
2. Freeman, J.J., Principals of Noise; J. Wiley, New York, N.Y.; 1959.
3. Goldman, Frequency Analysis Modulation and Noise; Mc Graw-Hill, New York, N.Y.; 1948.
4. Kraus, J. D., Antennas; McGraw-Hill; New York, N.Y.; 1950.
5. Reed, H. R. and H. M. Russell, Ultra High Frequency Propagation; J. Wiley, New York, N.Y.; 1953.
6. Wagner, T.C.G., Analytical Transients; J. Wiley, New York, N.Y.; 1959.
7. Watson, G.N., A Treatise On The Theory of Bessel Functions; Cambridge University Press.

ANTENNA POLARIZATION ANALYSIS BY AMPLITUDE MEASUREMENT OF MULTIPLE COMPONENTS

by

L. Clayton[†] and J. S. Hollis^{*}

Introduction

The purpose of this paper is to describe a method of determining completely, including sense of rotation, the polarization characteristics of an antenna by relative gain measurements only. The method permits rapid recording of polarization data without the requirement for phase measuring or continuous polarization scanning equipment. It is ideally suited to use with RDP (radiation distribution printer) instrumentation and associated punched-tape instrumentation for computer analysis of polarization data describing space-vehicle and airborne antenna characteristics over the sphere. It involves simply recording the relative power received by the antenna when illuminated with waves of either four (minimum) or six (recommended) different polarization characteristics, or alternatively, analyzing the wave radiated by the antenna by recording the relative power received by a pickup antenna which can be connected to have four or six different polarization characteristics. Four or six RDP plots are thus required to completely characterize an antenna, compared with a minimum of three required for characterization in terms of the customary two polarization components and phase angle or ellipse tilt angle. However, the relative gain plots can be recorded quite rapidly, and there is considerable merit to having the additional data; one can estimate the polarization performance of an antenna fairly well simply by inspection of its response to waves of four linear and two circular polarizations.

Polarization analysis and characterization have been treated in detail in the literature. See, for example, references 1 and 2. However, the simple and attractive multiple-component method appears to have received little notice, possibly because the requirement for rapid recording of great volumes of data has become critical only recently with the need for detailed analysis of spherical coverage.

[†]V. P. -Research, Scientific-Atlanta, Inc.

^{*}Principal Engineer, Scientific-Atlanta, Inc.

An example of a radiation distribution table is shown in Figure 1. In this presentation, signal level versus angular orientation data are presented by recording signal levels numerically in decibels at preselected intervals of the spherical coordinates θ and ϕ . In the table shown here, the angular increments are 0.5 degree in θ and ϕ , the dynamic range is 40 decibels, and the signal-level resolution is 1 decibel.

The contour effect seen on the graph, which aids in interpreting the table, is obtained by printing the even values of signal level and omitting the odd values. Little information is lost by this procedure since the values of the omitted numbers almost always can be determined by inspection. When the primary purpose is numerical analysis, rather than visual interpretation, one prints both odd and even numbers. If the data are stored on punched tape, both odd and even values are recorded in any event. Greater resolution can be provided by printing all integral decibel values and omitting the numbers which differ from an integral number by more than $1/4$ decibel. In this case the data stored on tape would be recorded with a resolution of $1/4$ decibel.

Each recorded table is for a single polarization component. In the method which will be described, a minimum of four and preferably six recordings are made to describe the complete polarization characteristics of an antenna. Although this at first appears to be an involved procedure, its adaptability to computer processing and the simplicity of the required measuring equipment give it merit in comparison with alternative methods.

Conventional Representations of Polarization Characteristics

The polarization character of the wave radiated by an antenna is customarily specified completely by giving one of the following sets of measured quantities for each direction of interest.

- (a) Magnitudes of two orthogonal linearly polarized components of the total field and the angle δ of their electrical phase difference.
- (b) Magnitudes of two orthogonal linear components, the tilt angle τ of the major axis of the polarization ellipse with respect to the direction of a specified field component, and the sense of rotation of the total field vector.
- (c) Magnitudes of two orthogonal circularly polarized components of the field and the angle δ' of their electrical phase difference.

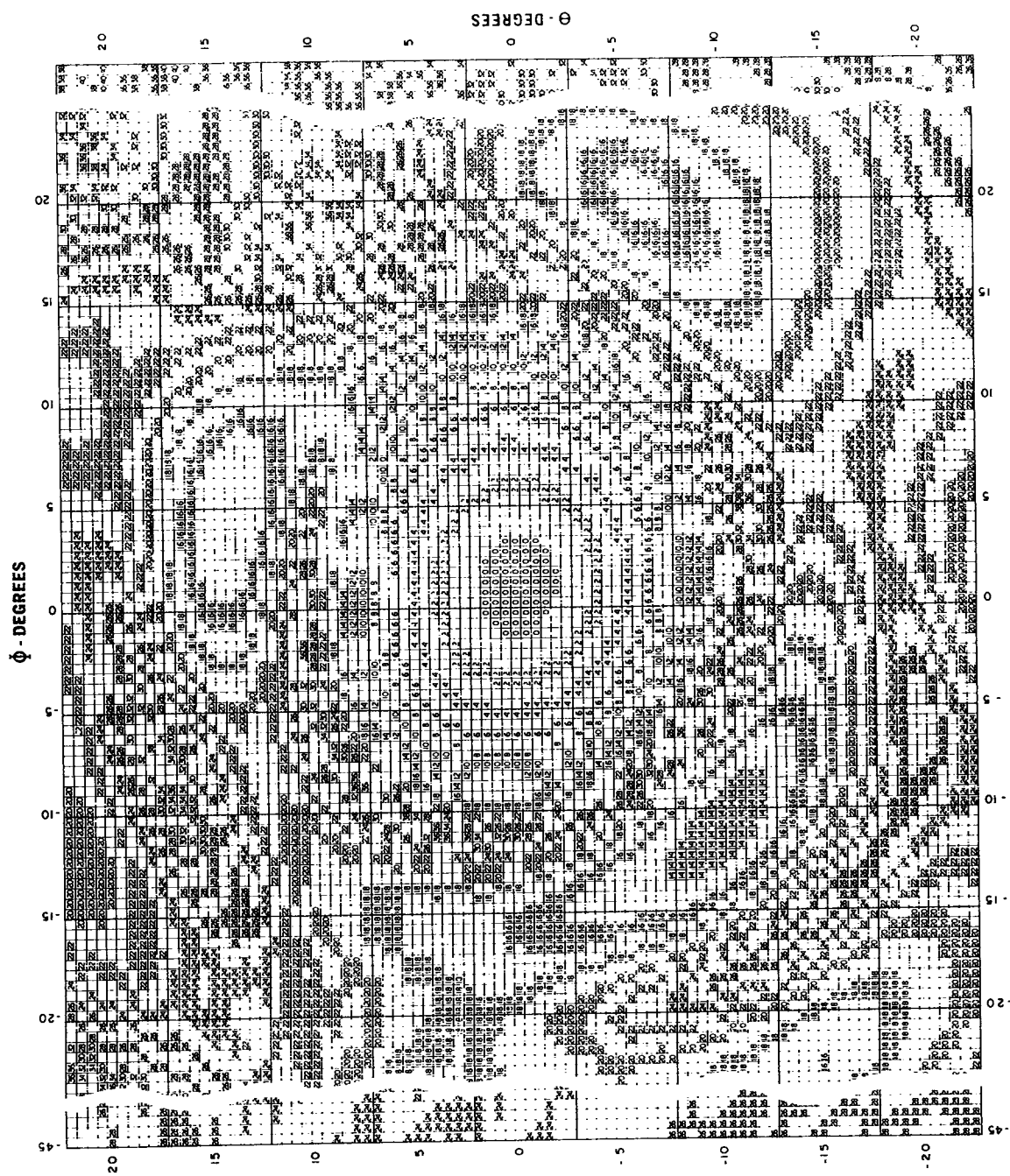


Figure 1. Radiation Distribution Table

- (d) Magnitudes of two orthogonal circular components and the tilt angle τ of the major axis of the polarization ellipse with respect to a specified reference.

Any of these methods of presentation is admitted in the IRIG Standard Coordinate System and Data Format for Antenna Patterns.³ The IRIG standard does not explicitly require specification of sense in method (b), but it would be necessary if the method were used with antennas of other than purely linear polarization characteristic. Method (d) is recommended by Pike⁴ as the most generally useful.

The data gathered in the multiple-component method proposed here are readily reduced to any of these formats in the course of a communications-link analysis. If, as is recommended, one records four linear-component responses and two circular-component responses, one might, for example, choose to regard the right-circular and the left-circular as the principal components. To complete the specification in method (d), one would then regard the four linear-component recordings as a measure of the tilt angle, which is specified by an equation of the simple form:

$$\tau = \frac{1}{2} \tan^{-1} \frac{E_3^2 - E_4^2}{E_1^2 - E_2^2} ,$$

where the quadrant is identified by inspection of the algebraic signs of the numerator and the denominator. This kind of calculation will generally need to be made only for those points that lie along a specific aspect-angle trajectory or near it. It should be possible to deduce the general behavior of the antenna in regions of less crucial interest by inspection of the multiple component plots.

Properties of an Arbitrarily Polarized Wave

It will be convenient for the present purpose to resolve the electric vector $\vec{E}(t)$ of a plane electromagnetic wave of arbitrary polarization characteristic into two orthogonal vector components,

$$\vec{E}(t) = E_1(t) \vec{u}_1 + E_2(t) \vec{u}_2 , \quad (1)$$

where \vec{u}_1 and \vec{u}_2 are orthogonal unit vectors in the plane perpendicular to the direction of propagation.

If $\vec{E}(t)$ is of a single frequency ω , the component scalar coefficients $E_1(t)$ and $E_2(t)$ can be written, with appropriate choice of the time reference $t=0$,

$$\begin{aligned} E_1(t) &= E_1 \sin \omega t \\ E_2(t) &= E_2 \sin (\omega t + \delta) \end{aligned} \quad (2)$$

$E_1(t)\vec{u}_1$ and $E_2(t)\vec{u}_2$ are the electric vectors of two plane electromagnetic waves of orthogonal linear polarizations, differing in time phase by the angle δ .

In the general case both the magnitude of $\vec{E}(t)$ and its direction in the u_1u_2 plane are time-varying functions such that the tip of the vector $\vec{E}(t)$ describes an elliptical locus which is the familiar polarization ellipse of Figure 2. In accordance with IRE standards, as one watches the incoming wave, if the rotation of $\vec{E}(t)$ is counterclockwise the sense of rotation is right-handed; if one prefers to think of the outgoing wave, the rotation is clockwise for right-hand sense of rotation. The tilt angle τ is the angle between the major axis of the polarization ellipse with respect to a specified field component; the axial ratio is the ratio of the lengths of the major and minor axes of the ellipse.

Consider the instantaneous component (or projection) of $\vec{E}(t)$ in an arbitrary direction in the u_1u_2 plane, defined by the angle χ in Figure 3.

$$E_\chi(t) = E_1(t) \cos \chi + E_2(t) \sin \chi,$$

or

$$E_\chi(t) = E_1 \cos \chi \sin \omega t + E_2 \sin \chi \sin (\omega t + \delta).$$

Expanding $\sin (\omega t + \delta)$,

$$E_\chi(t) = (E_1 \cos \chi + E_2 \sin \chi \cos \delta) \sin \omega t + E_2 \sin \chi \sin \delta \cos \omega t,$$

or

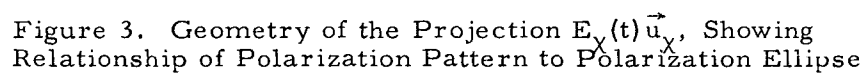
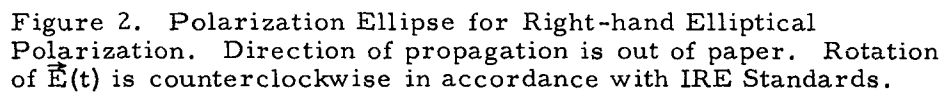
$$E_\chi(t) = E_\chi \sin (\omega t + \gamma)$$

where

$$E_\chi^2 = (E_1 \cos \chi + E_2 \sin \chi \cos \delta)^2 + (E_2 \sin \chi \sin \delta)^2$$

and

$$\gamma = \tan^{-1} \frac{E_2 \sin \chi \sin \delta}{E_1 \cos \chi + E_2 \sin \chi \cos \delta}$$



Expanding the square of E_χ and employing double-angle identities, one obtains:

$$E_\chi^2 = \frac{1}{2} \left[E_1^2 + E_2^2 + (E_1^2 - E_2^2) \cos 2\chi + 2E_1 E_2 \cos \delta \sin 2\chi \right], \quad (3)$$

or

$$E_\chi^2 = \frac{1}{2} \left[E_1^2 + E_2^2 + [(E_1^2 - E_2^2)^2 + (2E_1 E_2 \cos \delta)^2]^{\frac{1}{2}} \cos(2\chi - \psi) \right] \quad (4)$$

where

$$\psi = \tan^{-1} \frac{2E_1 E_2 \cos \delta}{E_1^2 - E_2^2}$$

The sign of the square root is to be taken as positive.

A polar plot of E_χ versus χ is called the polarization pattern of the wave. It gives the maximum projection of $\vec{E}(t)$ in the χ direction, as indicated in Figure 3. E_χ therefore corresponds to the response to the wave of a linear antenna as it is rotated in the $u_1 u_2$ plane. However, as can be seen, the maxima and minima of the polarization pattern coincide with those of the polarization ellipse, and consequently define its eccentricity and orientation with respect to the \vec{u}_1 axis.

From (4) it is seen that $\vec{E}(t)$ has its greatest maximum projection at the angle

$$\tau \equiv \chi \text{ of maximum } E_\chi = \frac{1}{2} \psi$$

or

$$\tau = \frac{1}{2} \tan^{-1} \frac{2E_1 E_2 \cos \delta}{E_1^2 - E_2^2} \quad (5)$$

The tilt angle τ is the angle between the major axis of the polarization ellipse and the \vec{u}_1 direction.

Note that an ambiguity of 180 degrees results when an angle is defined by its tangent alone, and this ambiguity in the inverse tangent of (5) as it stands produces a 90-degree ambiguity in τ . Kraus⁵ states that the angle τ as given by (5), which he derives by a different method, is the angle between the \vec{u}_1 direction and either the major or the minor axis of the ellipse. However, this uncertainty is removed if one identifies the quadrant of ψ , as must be done to maintain consistency between (3) and (4) with the choice of the positive square root in (4). The quadrant of 2τ is identified by the algebraic signs of the

numerator and the denominator of its tangent as expressed in (5), according to Table I.

Table I. Sign Conventions for Identification of Quadrant of 2τ or δ		
2τ or δ	Numerator of (5), (10), or (17)	Denominator of (5), (10), or (17)
1st Quad.	+	+
2nd Quad.	+	-
3rd Quad.	-	-
4th Quad.	-	+
0°	0	+
90°	+	0
180°	0	-
270°	-	0
Undefined	0	0

If 2τ is taken to be a positive angle, the tilt angle is given as a positive angle between 0 and 180 degrees. Since the polarization ellipse is symmetrical with respect to 180-degree rotation, τ angles in the second quadrant may be replaced by their negative supplements if it is desired to express τ as an angle between ± 90 degrees. Included in Table I are cases where 2τ falls precisely on a quadrant boundary, and the case of circular polarization for which τ is undefined. The table applies also to identification of the quadrant of δ described later.

From (4), the ratio of the maximum of the polarization pattern to its minimum is

$$r = \left[\frac{E_1^2 + E_2^2 + [(E_1^2 - E_2^2)^2 + (2E_1 E_2 \cos \delta)^2]^{\frac{1}{2}}}{E_1^2 + E_2^2 - [(E_1^2 - E_2^2)^2 + (2E_1 E_2 \cos \delta)^2]^{\frac{1}{2}}} \right]^{\frac{1}{2}},$$

or, upon multiplication of both numerator and denominator of the quantity within the outside radical by the numerator,

$$r = \frac{E_1^2 + E_2^2 + [(E_1^2 - E_2^2)^2 + (2E_1 E_2 \cos \delta)^2]^{\frac{1}{2}}}{[(E_1^2 + E_2^2)^2 - (E_1^2 - E_2^2)^2 - (2E_1 E_2 \cos \delta)^2]^{\frac{1}{2}}}, \quad (6)$$

or

$$|r| = \frac{E_1^2 + E_2^2 + [(E_1^2 - E_2^2)^2 + (2E_1 E_2 \cos \delta)^2]^{\frac{1}{2}}}{2E_1 E_2 |\sin \delta|} \quad (6')$$

This axial ratio takes a particularly simple form in terms of the circular components to be discussed presently.

Linear-Component Measurements

Suppose that the arbitrarily polarized wave is examined with a linear antenna rotatable in the polarization-axis coordinate χ . When $\chi = 0$ the antenna is aligned with the \vec{u}_1 direction and the magnitude of its terminal voltage is proportional to E_1 ; when $\chi = 90^\circ$ its terminal voltage is a relative measure of E_2 . The received power is proportional to E_1^2 or to E_2^2 for $\chi = 0^\circ$ or 90° , respectively.

When the antenna is positioned diagonally at $\chi = 45^\circ$, equation (3) shows that the received power is proportional to

$$E_{\chi=45^\circ}^2 = \frac{1}{2} (E_1^2 + E_2^2 + 2E_1 E_2 \cos \delta) \quad (7)$$

When the antenna is positioned diagonally at $\chi = 135^\circ$, equation (3) gives

$$E_{\chi=135^\circ}^2 = \frac{1}{2} (E_1^2 + E_2^2 - 2E_1 E_2 \cos \delta) \quad (8)$$

Let

$$E_{\chi=45^\circ}^2 = E_3^2 \quad ;$$

$$E_{\chi=135^\circ}^2 = E_4^2 \quad .$$

Examination of equations (5), (6), (7), and (8) shows that relative measurement of E_1^2 , E_2^2 , and either E_3^2 or E_4^2 is sufficient to determine the tilt angle and the magnitude of the axial ratio. However, if both E_3^2 and E_4^2 are measured the calculations take a particularly simple form, because

$$E_3^2 - E_4^2 = 2E_1 E_2 \cos \delta \quad , \quad (9)$$

so that

$$\tau = \frac{1}{2} \tan^{-1} \frac{E_3^2 - E_4^2}{E_1^2 - E_2^2} \quad (10)$$

(which is to be used with the rules for quadrant identification given previously in Table I), and

$$|r| = \frac{E_1^2 + E_2^2 + [(E_1^2 - E_2^2)^2 + (E_3^2 - E_4^2)^2]^{\frac{1}{2}}}{[(E_1^2 + E_2^2)^2 - (E_1^2 - E_2^2)^2 - (E_3^2 - E_4^2)^2]^{\frac{1}{2}}} \quad (11)$$

Equation (9) gives

$$|\delta| = \cos^{-1} \frac{E_3^2 - E_4^2}{2E_1E_2}$$

but does not show whether the phase angle is positive or negative. Consequently, measurements of linear components alone do not identify the direction of rotation of $\vec{E}(t)$. Similarly, since one does not know whether to use the positive or the negative square root in the denominator of (11), the sign of r is undetermined; otherwise, as will be shown in the circular component case, the sign of r would identify the sense of rotation. (In the numerator the positive square root must be used for consistency with previous assumptions.)

The squared field intensities which appear in these relations may be determined either by relative power measurements with a single antenna successively oriented to $\chi = 0^\circ, 45^\circ, 90^\circ$, and 135° , or by switching connections to two identical stationary coplanar probes oriented orthogonally in the \vec{u}_1 and \vec{u}_2 directions. In the latter case the diagonal intensities are obtained by adding terminal voltages either in-phase or out-of-phase in such manner as to obtain sum voltages proportional to

$$(1/\sqrt{2})[E_1(t) + E_2(t)] = (1/\sqrt{2})[E_1 \sin \omega t + E_2 \sin(\omega t + \delta)] = E_3 \sin(\omega t + \gamma_1)$$

and

$$(1/\sqrt{2})[E_1(t) - E_2(t)] = (1/\sqrt{2})[E_1 \sin \omega t - E_2 \sin(\omega t + \delta)] = E_4 \sin(\omega t + \gamma_2)$$

Expansion of $\sin(\omega t + \delta)$ gives

$$E_3 \sin(\omega t + \gamma_1) = (1/\sqrt{2}) [(E_1 + E_2 \cos \delta) \sin \omega t + E_2 \sin \delta \cos \omega t]$$

and

$$E_4 \sin(\omega t + \gamma_2) = (1/\sqrt{2}) [(E_1 - E_2 \cos \delta) \sin \omega t - E_2 \sin \delta \cos \omega t] ,$$

from which

$$E_3^2 = \frac{1}{2} (E_1^2 + E_2^2 + 2E_1 E_2 \cos \delta) \quad ;$$

$$E_4^2 = \frac{1}{2} (E_1^2 + E_2^2 - 2E_1 E_2 \cos \delta) \quad ,$$

in agreement with (7) and (8).

Circular-Component Measurements

Suppose that the terminal voltages of the orthogonal coplanar linear antennas introduced in the preceding paragraph are now combined in phase quadrature in such manner as to obtain sum and difference voltages proportional to

$$(1/\sqrt{2}) [E_1 \sin \omega t + E_2 \cos(\omega t + \delta)] = E_R \sin(\omega t + \gamma_3) \quad (12)$$

and

$$(1/\sqrt{2}) [E_1 \sin \omega t - E_2 \cos(\omega t + \delta)] = E_L \sin(\omega t + \gamma_4) \quad (13)$$

Expansion of $\cos(\omega t + \delta)$ gives

$$E_R \sin(\omega t + \gamma_3) = (1/\sqrt{2}) [(E_1 - E_2 \sin \delta) \sin \omega t + E_2 \cos \delta \cos \omega t] \quad ;$$

$$E_L \sin(\omega t + \gamma_4) = (1/\sqrt{2}) [(E_1 + E_2 \sin \delta) \sin \omega t - E_2 \cos \delta \cos \omega t] \quad ,$$

from which

$$E_R^2 = \frac{1}{2} (E_1^2 + E_2^2 - 2E_1 E_2 \sin \delta) \quad ; \quad (14)$$

$$E_L^2 = \frac{1}{2} (E_1^2 + E_2^2 + 2E_1 E_2 \sin \delta) \quad . \quad (15)$$

When $E_1 = E_2$, the antenna phasing arrangement corresponding to (12) and (14) produces a maximum response to a wave for which $\delta = -90^\circ$ and null response to a wave for which $\delta = +90^\circ$. In either case, equation (4) shows that the projection of $\vec{E}(t)$ is independent of direction (χ) in the $u_1 u_2$ plane; both waves are circularly polarized. When $\delta = -90^\circ$, $E_2(t)$ lags $E_1(t)$ and inspection of Figure 2 shows the $\vec{E}(t)$ appears to rotate in a counterclockwise direction when viewed from the direction of propagation with the wave approaching. In the IRE convention followed in the antenna field this condition is identified as "right-circular polarization." When $\delta = +90^\circ$, the rotation of $\vec{E}(t)$ is clockwise, wave approaching, and the polarization of the wave is "left-circular." Thus the antenna phasing arrangement corresponding to (12) and (14) produces a composite right-circularly polarized antenna. Similarly, the phasing arrangement corresponding to (13) and (15) has maximum response to the wave for which $\delta = +90^\circ$ and null response to the wave for which $\delta = -90^\circ$. It constitutes a left-circularly polarized antenna.

At the outset of this discussion a wave of arbitrary polarization characteristic was defined in terms of two orthogonal linearly polarized components and their phase difference. As is well known, the wave can be defined equally well by the amplitudes E_R and E_L of two circularly polarized components and their phase difference $\delta' = \gamma_3 - \gamma_4$. This representation is treated in detail in the referenced literature and is examined further in the Appendix. Here the equivalence of the representations will not be elaborated because the present intent is not to change to an alternate representation, but rather to show how the commonly used measures of wave polarization characteristics can be determined by measurement of both linear and circular polarization component amplitudes. For this purpose it is immaterial whether the linear-component or the circular-component representation is chosen as the basic viewpoint; we will continue to use the former.

It will be recalled that measurements of linear components alone gave only the magnitude of the phase angle δ (in terms of its cosine), and hence left the sense of polarization undetermined. This ambiguity is resolved by measurement of either E_R^2 or E_L^2 , because (14) or (15) gives in addition the sine of δ . However, if both E_R^2 and E_L^2 are measured the calculations are simplified. Since

$$E_L^2 - E_R^2 = 2E_1 E_2 \sin \delta , \quad (16)$$

one obtains with the use of (9):

$$\delta = \tan^{-1} \frac{E_L^2 - E_R^2}{E_3^2 - E_4^2} \quad , \quad (17)$$

the quadrant of δ being determined by the signs of $E_L^2 - E_R^2$ and $E_3^2 - E_4^2$ in accord with Table I. Table I includes cases for which δ falls precisely on the quadrant boundaries, and the special cases of linear polarization directed along the u_1 or u_2 axis for which δ is undefined.

Equation (4) for E_χ^2 is also simplified by substitution of circular-component quantities. The product of (14) and (15) gives

$$\begin{aligned} E_R^2 E_L^2 &= \frac{1}{4} [(E_1^2 + E_2^2)^2 - (2E_1 E_2 \sin \delta)^2] \\ &= \frac{1}{4} [(E_1^2 - E_2^2)^2 + (2E_1 E_2 \cos \delta)^2] \quad , \end{aligned}$$

or

$$2E_R E_L = [(E_1^2 - E_2^2)^2 + (2E_1 E_2 \cos \delta)^2]^{\frac{1}{2}} \quad . \quad (18)$$

The sum of (14) and (15) gives

$$E_R^2 + E_L^2 = E_1^2 + E_2^2 \quad . \quad (19)$$

Substitution of (18), (19), and (5) in equation (4) gives

$$E_\chi^2 = \frac{1}{2} [E_R^2 + E_L^2 + 2E_R E_L \cos 2(\chi - \tau)] \quad . \quad (20)$$

From (20), the ratio of the maximum of the polarization pattern to its minimum is just

$$r = \left[\frac{(E_R + E_L)^2}{(E_R - E_L)^2} \right]^{\frac{1}{2}} \quad .$$

The sign of the square root is chosen by convention such that

$$r = \frac{E_R + E_L}{E_R - E_L} \quad , \quad (21)$$

which gives a positive axial ratio for right-handed polarization and a negative axial ratio for left-handed polarization. This relationship is evident (except for the sign convention) from inspection in the circular-component representation where one considers $\vec{E}(t)$ to be the resultant of two contra-rotating vectors of amplitudes E_R and E_L .

Practical Considerations

Measurement Techniques - In setting up an antenna range to make polarization measurements by the multiple-component method, the following requirements must be met:

- (1) the correct polarizations must be established for each of the six polarization components,
- (2) the measuring system gain must be maintained fixed during the measurement interval,
- (3) conditions such as suppression of extraneous reflections, etc., associated with measurements of a single polarized component must be satisfied.

One can of course invoke reciprocity and interchange the roles of the transmitting and receiving antennas. It has been convenient to consider the case in which the wave radiated by the antenna under test is examined with receiving probes, but it is commonly preferred to operate antenna ranges in the opposite manner. One then measures the receiving response of the antenna under test when it is illuminated by waves of various polarization characteristics.*

* A note of caution is warranted. The polarization properties of an antenna are defined here, as is customary, by polarization parameters of the wave the antenna radiates, and must be so interpreted even though the relative component magnitudes actually may be determined from measurement of the receiving response of the antenna under test. E_R and E_L can be measured by the receiving responses of the antenna under test when it is illuminated respectively with right-circular and left-circular incident waves, as would be expected. The linear components must be measured, however, with illuminating waves whose \vec{E} vectors are parallel in space with the \vec{E} vectors of the corresponding components of the wave which would be radiated by the antenna under test. Since in the multiple-component method one measures amplitudes only (and not phase polarities, which are deduced from relative amplitudes), this condition is of consequence only in setting up the "diagonal" linearly polarized illuminations. E_3 and E_4 must be measured with illuminating waves whose \vec{E} vectors are directed respectively at $\chi = 45^\circ$ and $\chi = 135^\circ$ in the coordinate system defined with respect to the antenna under test. (Not at the corresponding angles of the coordinate system which would be used to define the polarization properties of

The linearly and the circularly polarized sampling or illuminating antennas can be of any convenient type. While only relative amplitude measurements are required for polarization analysis, it is necessary to insure that all components are measured with respect to the same reference. Good practice requires that this condition be verified experimentally in any case, through techniques familiar to the antenna engineer.

The principal considerations in application of the multiple-component method can be illustrated by discussion of several suggested means of implementation.

(a) Three-Antenna and Polarization-Positioner Method

Probably the simplest method of establishing the required aperture fields is that shown in Figure 4. A linearly polarized source antenna, mounted on a polarization positioner, is employed to establish the four linear polarizations at the test

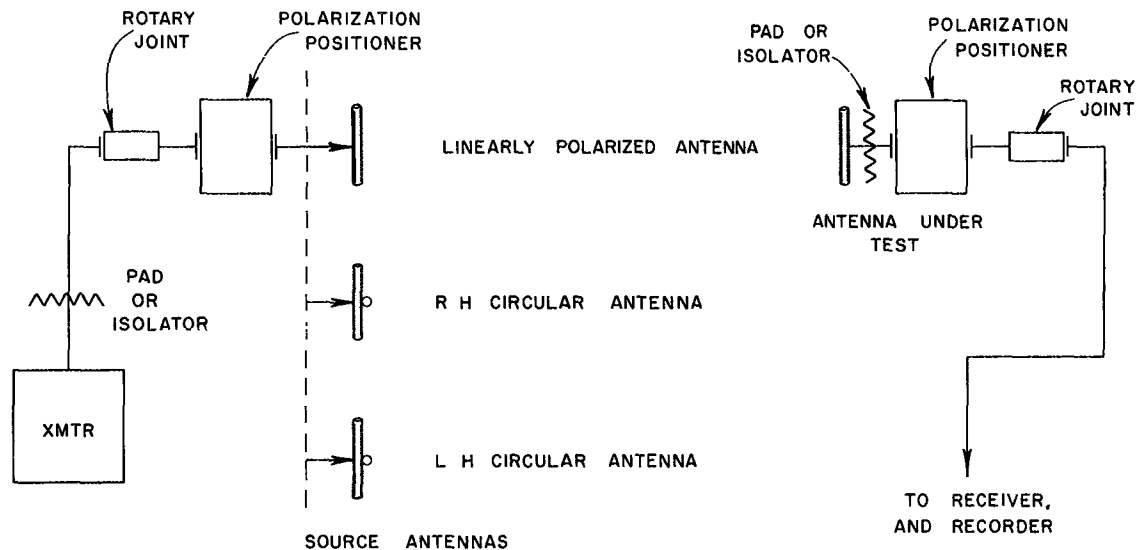


Figure 4. Schematic Showing Three-Antenna Method of Providing Six Polarizations Over Test Aperture

aperture. Two additional antennas are employed to establish the right-hand and left-hand circular polarizations. In the absence of reflections, the same signal

the illuminating wave itself. The polarization parameters of an illuminating wave to which a receiving antenna is polarization-matched are not, in general, identical to those of the wave the antenna radiates! No subtle non-reciprocity is involved here; it is simply a matter of the way coordinate systems are established by convention for defining polarization properties of waves.)

levels are automatically provided for the four linear polarizations if the axis of the polarization positioner is aligned with the center of the test aperture and if the axis of the transmitted beam is aligned with the axis of the polarization positioner. The gains of the two circularly polarized antennas do not have to be identical to each other or the same as that of the linearly polarized antenna; a reference antenna can be employed at the test aperture to permit adjustment of the system gain to compensate for relative gain differences of the three antennas.*

If an absolute gain reference level is to be determined by the comparison method, a standard gain antenna is required and can be employed for the reference antenna. In both applications it is necessary to provide a means for displacing the antenna under test from the test position and inserting the reference antenna in its place. If the absolute gain reference level is determined by pattern integration and calculation of antenna loss, the standard gain antenna is, of course, not required. In this case, an uncalibrated linearly polarized reference antenna can be employed to check the circularity of the circular fields and the purity and orientation of the linear fields.

(b) One-Antenna and Polarization-Positioner Method

The arrangements shown schematically in Figures 5a and 5b provide the required polarizations with a single antenna and a polarization positioner. The circuit

* In the discussions under the section headings, Linear Component Measurements and Circular Component Measurements, the signal amplitudes E_3 , E_4 , E_R , and E_L were produced by adding signals equal to $(1/\sqrt{2}) E_1(t) \hat{u}_1$ and $(1/\sqrt{2}) E_2(t) \hat{u}_2$ in the proper phase relationships. This requires that the total gain of the sampling antenna be constant for the six polarizations. In the practical measurements problem, based on receiving or transmitting with the antenna under test, it is sufficient that the total measuring system gain from the transmitter to the recorder be constant, with a linearly polarized reference antenna of constant gain substituted for the antenna under test. The reference antenna is aligned with two orthogonal linear polarization components of the source antenna in use to measure two partial system gains, which are added to give the total gain. Thus relative gain differences of the transmitting antennas can be compensated by altering the gain of the receiver or recorder or the power output of the transmitter.

For the circularly polarized case, one-half of the system gain is in each of two orthogonal linear polarization components. Therefore, in setting the total system gain equal for the linear and circular polarization cases, the partial system gain for one polarization component is set three decibels lower than the system gain for the linear case, where the total gain is in a single component. As a check, it is desirable to rotate the polarization of the linearly polarized probe through 360 degrees to see that the partial system gain is constant for all linear polarization components, insuring circularity of the aperture field.

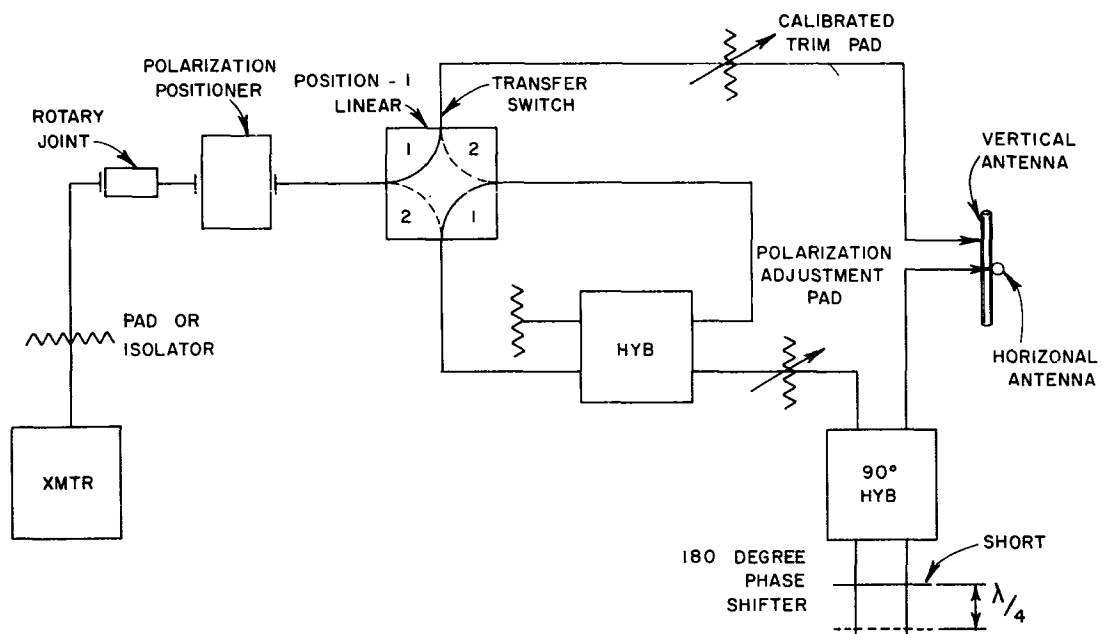


Figure 5a

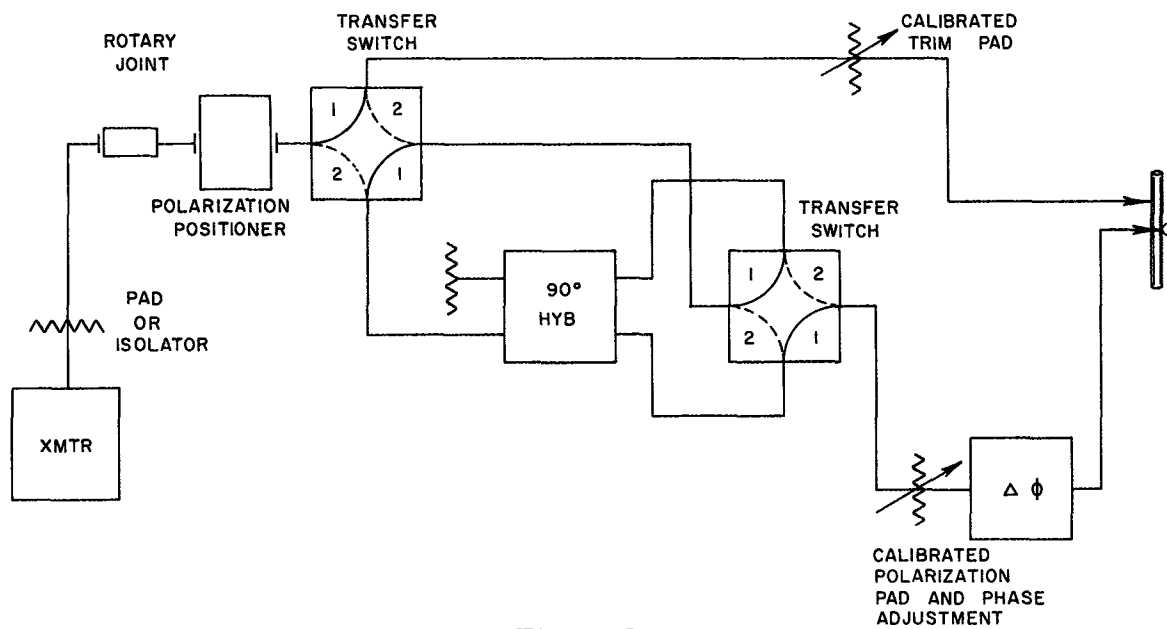


Figure 5b

Figure 5. Schematics Showing One-Antenna and Polarization-Positioner Method of Providing Six Polarizations Over Test Aperture

provides for switching the polarization of the source antenna from linear to right-hand circular or to left-hand circular. The four required linear polarizations are achieved by rotation of the polarization positioner to 0° , 45° , 90° , and 135° orientations. The orientation can be measured manually or indicated by a synchro data takeoff of the type in common use. Several switching arrangements are possible; the method of Figure 5a uses a hybrid and a movable short as a 180-degree phase changer to reverse the sense of rotation. At the higher frequencies rotary-vane phase shifters and attenuators are of a convenient size and can be employed. The method of Figure 5b switches the outputs of a hybrid between the two orthogonal antenna elements to reverse the sense of rotation. Trim adjustments are necessary to compensate for unequal power divisions by the hybrids, to compensate for differences of transmission line attenuation, and to effect precise ± 90 -degree phase relationships between the two components for the circular polarization cases. Attenuator and phase shifter settings can be recorded and manually set as required, or the attenuators and phase shifter can be arranged for programming to the predetermined setting, the method employed depending on the desired degree of automation.

Use of a polarization positioner to obtain the four linear component orientations has the advantage that the polarization purity of the linear components is not dependent on electrical adjustments. However, a reference antenna is required as in the previous method, to provide a check on system gain and polarization purity.

(c) One-Antenna Method

The circuit shown in Figure 6 provides the six specified polarizations without use of a polarization positioner.

If switches A and B are in position 1, the polarization is vertical linear; if switch B is rotated to position 2 the polarization is horizontal linear. With switch A in position 2 and switch B in position 1, the polarization is determined by (1) the relative total phase shift $\phi_2 - \phi_1$ (from reference plane aa to the terminals of the two antennas) and (2) the partial gains for the two polarization components referred to plane aa. Right- and left-circular polarizations are provided by ± 90 -degree relative phase delays and equal gains. Linear polarizations at 45-degree and 135-degree orientations are provided by adjusting (1) $\phi_2 - \phi_1$ equal to zero and 180-degrees and (2) the two gains equal.*

*See footnote, page 14.

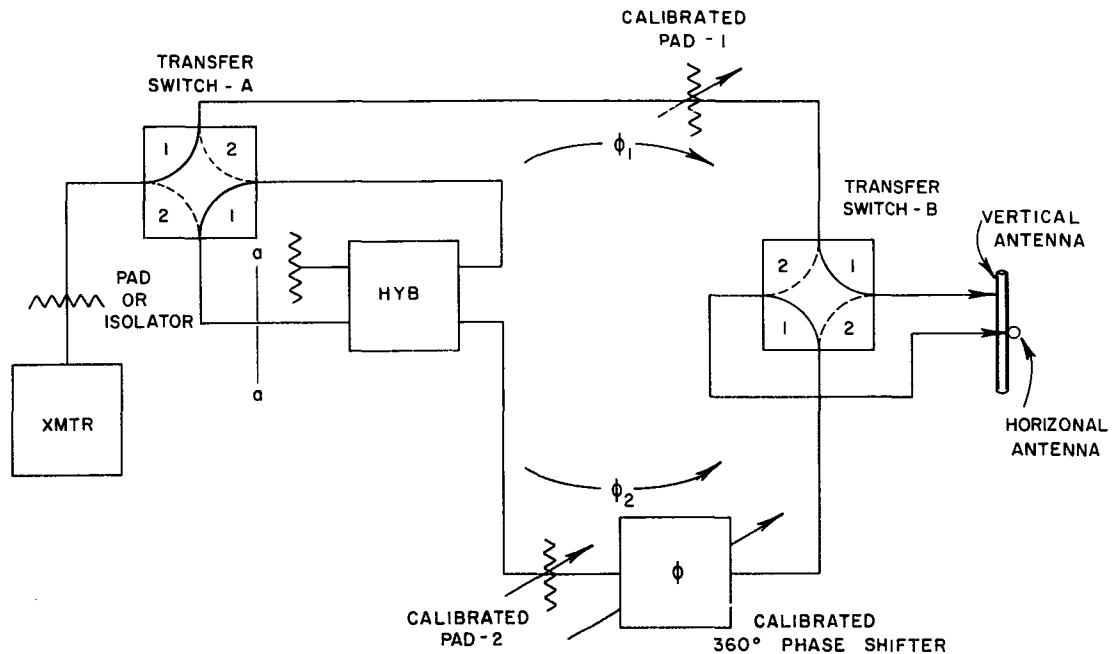


Figure 6. Schematic Showing One-Antenna Method of Providing Six Polarizations over Test Aperture

Provision of two calibrated trim pads permits the total gain to be set equal for the six polarizations. The attenuator and phase shifter settings can be recorded and manually set as required, or the attenuators and the phase shifter can be arranged for programming to predetermined settings. A rotatable linearly polarized reference antenna is required at the receiving test site to permit initial calibration of the system and to provide gain and polarization checks.

Sensitivity to Error--The multiple-component method, like the conventional methods, is subject to errors introduced by cross-polarization components in the probe or illuminating antennas, amplitude readout errors, and gain-reference setting or drift errors. These matters have been discussed by Bohnert⁶. Readout errors due to digital recording roundoff must be considered in what is expected to be the major application of the multiple-component method: where amplitudes are measured at discrete sample points over a large solid-angular sector (or entire sphere) and are recorded to the nearest decibel on punched tape or angular grid plate for subsequent computer analysis of communications link adequacy. One can illustrate by the following example the kind of point-to-point scatter one would expect to result from a maximum ± 0.5 db roundoff error if the computer program did not provide for data smoothing. Suppose that at a

particular sample point the actual relative magnitudes of the components were as given in the first column below (in decibels relative to an arbitrary common reference), and that the levels were recorded with roundoff as in the second column.

Component	Actual Level db _{ref}	Recorded Level db _{ref}
E ₁	- 8.739	- 9
E ₂	-13.510	-14
E ₃	- 7.791	- 8
E ₄	-19.230	-19
E _R	-10.500	-11
E _L	-10.500	-10

The actually equal E_R and E_L have been oppositely rounded so as to have maximum effect upon the calculated axial ratio. Use of the recorded data in (21) gives $r = -17.39$ (24.8 db, left-elliptical), and (10) gives $\tau = 29.7$ degrees. Actually, the wave is linearly polarized, $\tau = 30$ degrees. Equation (17) gives $\delta = 8$ degrees; actually it is zero. Equation (20) gives E_T (the maximum of the polarization pattern) as -7.47 db_{ref}; Equations (4) and (9) give it as -7.76 db_{ref}; actually it is -7.49 db_{ref}.

This kind of accuracy from raw data is quite acceptable for most applications, but it could lead to erroneous results in a data-link analysis if over a particular region the transmitting and receiving antennas were exactly cross-polarized; the difference between a 25 db loss and no signal at all is substantial. It is our understanding that the IRIG link analysis computer program provides for multi-point data sample interpolation prior to computation to reduce errors from this source.

Similar errors result from plot-to-plot jitter in precise point of sampling. These errors are most pronounced in regions where the antenna pattern has steep slope with respect to the angular coordinates. Multi-point interpolation prior to computation is also effective in reducing these errors.

Still more effective data refinement can be based upon the redundancy that exists if six components are measured. The simplest constraint is, of course, that the actual values of $E_1^2 + E_2^2 = E_3^2 + E_4^2 = E_R^2 + E_L^2$. This condition can be invoked

in a fitting process, and it can be used as the basis of data validity testing to reject data showing evidence of reference-setting blunders or excessive drift. More elaborate constraints, e.g.,

$$(E_1^2 - E_2^2)^2 + (E_3^2 - E_4^2)^2 + (E_R^2 - E_L^2)^2 = \frac{1}{3} [(E_1^2 + E_2^2)^2 + (E_3^2 + E_4^2)^2 + (E_R^2 + E_L^2)^2],$$

require more sophisticated programming to introduce in an optimum manner. One could, of course, simply compute polarization parameters from several alternate expressions involving different measured quantities and average the results, but one would not expect to arrive at an optimum fit through such a procedure.

Summary of Results

Definition of Measured Quantities -- Subscripted E's are relative measures of component amplitudes taken with respect to a common reference. They are defined here as terminal voltages of receiving probes used to examine an arbitrarily polarized wave radiated by an antenna under test. Their common reference is such that the various probes develop the same terminal voltages when illuminated separately by waves of the corresponding pure polarization characteristics having equal power densities. (Proper reference can be established with actual antennas by receiver or recorder gain setting.) Specifically,

E_1 is the measure of the component that is linearly polarized in a direction \vec{u}_1 in a plane of measurement normal to the direction of propagation.

E_2 measures a linear component in a direction \vec{u}_2 , orthogonal to \vec{u}_1 , in the plane normal to the direction of propagation. The positive direction of \vec{u}_2 is the direction $\chi = 90$ degrees, where

χ is an angle defining a direction \vec{u}_χ in the $u_1 u_2$ plane, measured from the \vec{u}_1 direction counterclockwise as seen by an observer who faces the $u_1 u_2$ plane such that he sees the antenna under test behind the plane with its radiated wave approaching him.

E_3 measures a "diagonal" component linearly polarized at $\chi = 45^\circ$.

E_4 measures a diagonal component linearly polarized at $\chi = 135^\circ$.

E_R measures a right-circularly polarized component.

E_L measures a left-circularly polarized component.

Notes:

(a) E_1 and E_2 correspond to E_θ and E_ϕ , respectively, in the IRIG format.

(b) The common reference of the E_i 's is such that $E_1^2 + E_2^2 = E_3^2 + E_4^2 = E_R^2 + E_L^2$, a measure of the total power density of the wave at the sampling point. They provide measures of relative electric field strengths in the following manner: If the number-subscripted E_i 's are taken to represent relative peak field strengths of the corresponding linearly polarized components, e.g.,

$$\vec{E}_1(t) = E_1 \sin \omega t \vec{u}_1,$$

then in the same units the constant magnitudes of the field strengths of, the circular components are given by

$$\xi_R = 1/\sqrt{2} E_R \quad ; \quad \xi_L = 1/\sqrt{2} E_L.$$

(c) The component magnitudes and other polarization parameters discussed here characterize the polarization properties of an antenna in terms of the nature of the wave it radiates and must be so interpreted. The components may be more conveniently measured, however, by invoking reciprocity and testing the receiving response of the antenna when it is illuminated by waves of various polarizations. In setting up the incident fields one then must observe precautions discussed in the footnote, p. 14.

Polarization Characterization--The measured quantities E_i give directly the relative magnitudes of the corresponding components in terms of which an arbitrary wave can be characterized; their common reference is such that the square of any E_i gives the relative power contained in that component. A set of four E_i 's consisting of one "principal" linear component (E_1 or E_2), one "diagonal" linear component (E_3 or E_4), one circular component (E_R or E_L), and any fourth component is sufficient for complete characterization. Such a set can be used without further reduction for communications link analysis if the equations for power transfer between antennas are written in compatible form. However, it may be preferred to regard one pair of

orthogonal components as "principal" components (E_1 and E_2 or E_R and E_L) and use the other amplitudes in calculating, as a third parameter to complete the description, one of the customarily used quantities

τ = ellipse tilt angle*, the angle between the major axis of the polarization ellipse and the \vec{u}_1 direction, measured in the sense defined in the previous subsection for the angle χ ;

δ = phase angle by which $E_2(t)$ leads $E_1(t)$; or

δ' = phase angle by which $E_R(t)$ leads $E_L(t)$, when circular component phases are defined so that $\delta' = 0$ for linear polarization in the \vec{u}_1 direction.

Measurement of all six component magnitudes instead of the minimum of four is recommended because doing so provides greater insight into antenna behavior through direct inspection, redundancy for verification and refinement of data, and simple expressions for the parameters

$$\delta = \tan^{-1} \frac{E_L^2 - E_R^2}{E_3^2 - E_4^2}, \quad (17)$$

$$\tau = \frac{\delta'}{2} = \frac{1}{2} \tan^{-1} \frac{E_3^2 - E_4^2}{E_1^2 - E_2^2} \quad (10); (A6)$$

Quadrants can be identified through the numerator-denominator sign rules given in Table I.

Other useful expressions are the following:

$$r = \frac{E_R + E_L}{E_R - E_L}, \quad (21)$$

where the axial ratio r is the ratio of the major axis of the polarization ellipse to its minor axis; by convention, r is positive for right-handed polarization and negative for left-handed polarization.

* Completes description only when used with E_R and E_L ; does not give sense of ellipticity when used with E_1 and E_2 .

$$E_{\chi}^2 = \frac{1}{2} [E_R^2 + E_L^2 + 2E_R E_L \cos 2(\chi - \tau)] \quad , \quad (20)$$

where E_{χ} is the magnitude of the polarization pattern (the projection of the polarization ellipse) in the direction specified by the arbitrary angle χ , defined in the previous subsection.

REFERENCES

1. V. H. Rumsey, G. A. Deschamps, M. L. Kales, and J. I. Bohnert, "Techniques for Handling Elliptically Polarized Waves with Special Reference to Antennas," Proceedings of the I. R. E. 39, pp. 533 - 552 (1951); also the immediately following paper by M. G. Morgan and W. R. Evans, "Synthesis and Analysis of Elliptic Polarization Loci in Terms of Space-Quadrature Sinusoidal Components."
2. J. D. Kraus, Antennas. New York: McGraw-Hill, 1950, pp. 464 - 484.
3. Inter-Range Instrumentation Group, IRIG Standard Coordinate System and Data Format for Antenna Patterns. IRIG Document No. 102-61; Sept. 1961. Available from U. S. Department of Commerce, Office of Technical Services, Washington 25, D. C.
4. B. W. Pike, Power Transfer Between Two Antennas. Pacific Missile Range, Range Development Department Technical Note No. 1-61C, July 1962. To be published as a PMR Technical Memorandum Report. Mr. Pike very kindly provided us a draft copy prior to publication.
5. Kraus, op. cit., p. 476.
6. Rumsey et al., op. cit., p. 551.

APPENDIX
FURTHER EXAMINATION OF CIRCULAR COMPONENTS

In the text the terminal voltage of a probe antenna responsive to the right-circular component of an arbitrary wave is represented as proportional to the quantity

$$E_R \sin(\omega t + \gamma_3) = (1/\sqrt{2}) [(E_1 - E_2 \sin \delta) \sin \omega t + E_2 \cos \delta \cos \omega t], \quad (A1)$$

and that of a left-circular probe is represented as proportional to

$$E_L \sin(\omega t + \gamma_4) = (1/\sqrt{2}) [(E_1 + E_2 \sin \delta) \sin \omega t - E_2 \cos \delta \cos \omega t]. \quad (A2)$$

E_R^2 and E_L^2 are related to E_1^2 , E_2^2 , and δ by (14) and (15). In continuation of this development it is first necessary to evaluate the phase difference

$$\delta' = \gamma_3 - \gamma_4. \quad (A3)$$

It will be convenient to represent γ_3 and γ_4 by their sines and cosines, which from (A1) and (A2) are:

$$\begin{aligned} \sin \gamma_3 &= \frac{E_2 \cos \delta}{\sqrt{2} E_R} & \cos \gamma_3 &= \frac{E_1 - E_2 \sin \delta}{\sqrt{2} E_R} \\ \sin \gamma_4 &= \frac{-E_2 \cos \delta}{\sqrt{2} E_L} & \cos \gamma_4 &= \frac{E_1 + E_2 \sin \delta}{\sqrt{2} E_L} \end{aligned}$$

From trigonometric identity,

$$\sin \delta' = \sin \gamma_3 \cos \gamma_4 - \cos \gamma_3 \sin \gamma_4 ;$$

$$\cos \delta' = \cos \gamma_3 \cos \gamma_4 + \sin \gamma_3 \sin \gamma_4 ,$$

so that

$$\sin \delta' = \frac{E_1 E_2 \cos \delta}{E_R E_L} ; \quad (A4)$$

$$\cos \delta' = \frac{E_1^2 - E_2^2}{2E_R E_L} . \quad (A5)$$

Therefore

$$\tan \delta' = \frac{2E_1 E_2 \cos \delta}{E_1^2 - E_2^2} .$$

Comparison with (5) in the text shows that

$$\delta' = 2\tau . \quad (A6)$$

If circularly polarized probe antennas are to be used to determine τ by measurement of δ' , it is essential to note that δ' is defined, as in (A3), as the angle by which the right-hand component leads the left-hand component, and that the antennas must be adjusted so that $\delta' = 0$ for an incident wave that is linearly polarized in the \vec{u}_1 direction. The opportunity for confusion is substantial because the literature is rather casual in specifying the sense of δ' . *

One might find it helpful to sketch out two contra-rotating \vec{E} vectors (right- and left-circular components) whose resultant is a linearly polarized wave and note how (A6) can be arrived at geometrically. It is then clear that an advance of the phase of the right-hand component in its cycle relative to that of the left-hand component in its cycle increases τ in its positive direction.

Transformation from a wave representation in terms of E_R , E_L , and δ' to one in terms of E_1 , E_2 , and δ can be accomplished in the following manner:

* For example, Kraus' equation (15-65) of Reference 2 gives δ' the opposite sense from that defined by his null measurement technique described in his Figure 15-32 and associated discussion. The latter agrees with our (A3) and (A6).

From (A4),

$$\cos \delta = \frac{E_R E_L}{E_1 E_2} \sin \delta' .$$

From (16),

$$\sin \delta = \frac{E_L^2 - E_R^2}{2E_1 E_2} .$$

Therefore

$$\delta = \tan^{-1} \frac{E_L^2 - E_R^2}{2E_R E_L \sin \delta'} , \quad (A7)$$

where the quadrant can be identified by numerator-denominator sign conventions as in Table II.

From (A5),

$$E_1^2 - E_2^2 = 2E_R E_L \cos \delta' .$$

Adding or subtracting (19) gives

$$E_1^2 = \frac{1}{2}(E_R^2 + E_L^2) + E_R E_L \cos \delta' ; \quad (A8)$$

$$E_2^2 = \frac{1}{2}(E_R^2 + E_L^2) - E_R E_L \cos \delta' , \quad (A9)$$

which agrees with the result of substituting $\chi = 0$ or $\pi/2$, $2\tau = \delta'$ in (20).

LOG-PERIODIC HELICAL DIPOLE ARRAYS

D. T. Stephenson and P. E. Mayes
University of Illinois
Urbana, Illinois

SUMMARY

The low-frequency cutoff of the logarithmically-periodic dipole array occurs when the length of the longest dipole is approximately one-half wavelength. For applications in and below the high frequency (3-30 Mc) band the antenna becomes quite large. By replacing the linear dipoles with normal-mode helical elements, the dipole length can be reduced. Near-field measurements show the similarity in propagation constants in arrays of linear and helical elements. Data are shown for LP helical dipole arrays with elements of length $\lambda/4$ at the lowest frequency. Frequency-independent backfire patterns are maintained and maximum VSWR less than 2:1 has been achieved.

1. INTRODUCTION

Since its introduction by Isbell¹ in 1959, the log-periodic dipole has become a very popular broadband antenna. Its structural simplicity makes it a practical design for applications where portability or rotatability are desired.

As is true with most antennas, the LPD must be fairly large if it is to work well at low frequencies. The longest dipole in the LPD array must be about one-half wavelength long at the lowest frequency of operation. There is also a requirement on the boom length of an LPD: directivity suffers if the parameters are chosen so as to make the antenna too short for a given operating bandwidth². Thus if one wishes to reduce the overall size of an

LPD antenna in terms of wavelengths, one must contend with both the dipole lengths and the boom length. The latter seems most likely to have a basic limitation on directivity, i.e., a minimum boom length is required to achieve a unidirectional pattern.

No such severe limitation with respect to directivity should exist in the case of dipole lengths, however, since the pattern of short dipoles is almost the same as for half-wavelength dipoles. This paper describes a method of reducing the lengths of the dipoles in an LPD array. The results of this reduction are discussed, with emphasis on the comparison between the performances of the resulting antenna and the original LPD design. The effect on boom length is discussed.

Dipole Length Reduction

The method chosen for shortening the dipoles in the LPD array is to replace them with normal-mode helical dipoles. By proper choice of pitch angle, a helical dipole may be made to resonate at a frequency much lower than the frequency for which the dipole is a half-wavelength long.

This method was chosen in preference to inductive base-loading because of its higher efficiency, and in preference to capacitive end-loading because of structural considerations. Dielectric-loading of the entire array is impractical at low frequencies. The helical dipole also features a uniform geometry which simplifies construction in some respects.

There are, however, several reasons why the use of helical dipoles in place of linear ones would be expected to change the performance of the array. For any considerable degree of length reduction, the radiation resistance of a helical dipole is rather low³. Since in a log-periodic array the relationship between dipole impedance and feeder characteristic impedance has a major effect on active region efficiency, and therefore on directivity, end effect, etc., it would be expected that the substitution of helical dipoles would change these properties considerably. These properties are also functions of the mutual impedances between the dipoles in the array. The mutual impedances of a helical array would be expected to differ from those of a linear array.

Unlike a linear dipole, the helical dipole produces elliptically-polarized radiation⁴, but in the range of dipole parameters used in this investigation this effect is quite small and the polarization is nearly linear.

These considerations lead one to expect a certain degree of deterioration in the performance of the log-periodic helical dipole array as dipole lengths are reduced. A major purpose of this investigation has been to determine to what degree one must compromise in return for obtaining a narrower array.

2. EXPERIMENTAL RESULTS

Much of the experimental work on the helical dipole array was based on previous work of a similar nature that had been done in the Antenna Laboratory on linear dipole arrays. Such measurements include input impedance and far-field radiation pattern as a function of the design parameters, and the $k\text{-}\beta$ (Brillouin) diagram obtained by probing the near field of a uniformly-periodic array of dipoles.

Whenever directivity is mentioned in this report it was calculated from the approximate formula⁵

$$\text{Directivity in db} = 10 \log \frac{41,253}{(BW)_E (BW)_H}$$

where $(BW)_E$ and $(BW)_H$ are the half-power beamwidths, in degrees, in the E-plane and the H-plane, respectively.

Figure 1a shows the geometry of a log-periodic helical dipole array (LPHDA) and the design parameters used in its construction. The design of the individual helical dipoles is not discussed here, except to point out that the relationship between the dipole half-length h and the free-space quarter-wavelength is given by $h = s \frac{\lambda}{4}$, where s will be called the shortening factor. Thus, for a linear dipole, $s = 1$. Figure 1b illustrates the method of feeding the dipoles, and shows the effective 180 degree twist in the feeder between dipoles. The helices were wound on cylindrical polystyrene forms, and all helix dimensions in the log-periodic models were scaled by the factor τ as closely as was permitted by available standard wire sizes.

2.1 Active Region Efficiency vs. s

As an initial investigation, it was necessary to determine the degree to which the dipole shortening affected the efficiency of the active region, i.e., the number of dipoles which must be excited in order to radiate completely the signal propagating along the feeder. Two uniformly periodic ($\tau = 1$) pattern

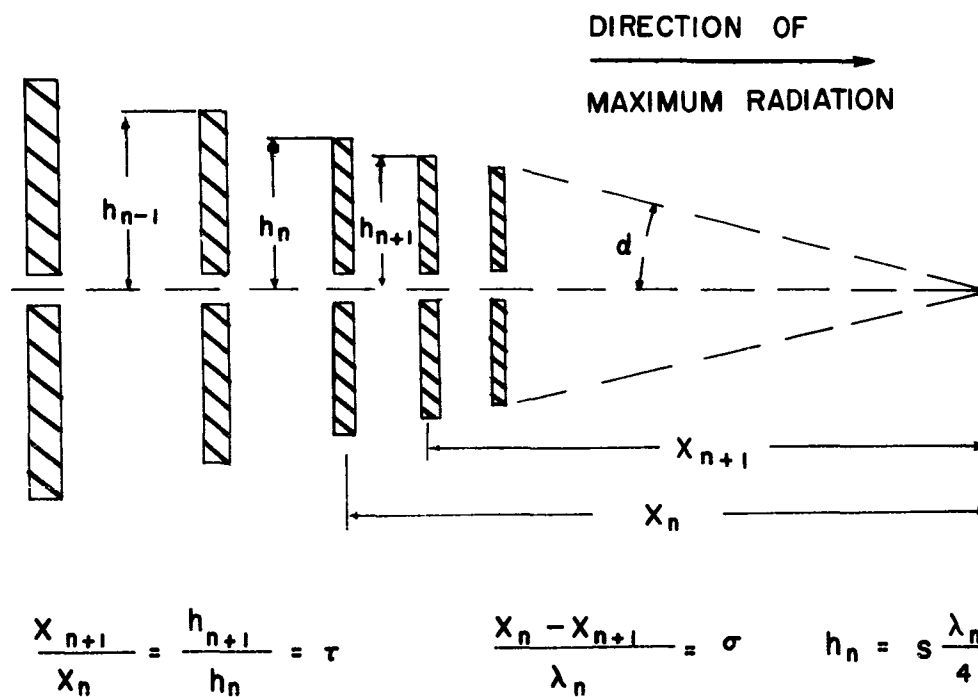


Figure 1a. Parameters of an LPHDA.

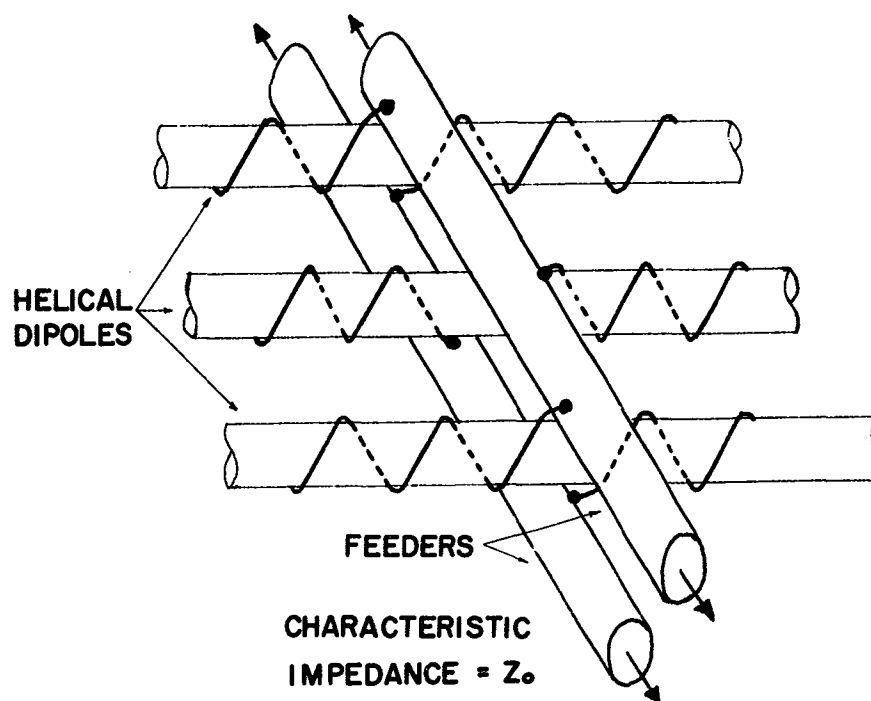


Figure 1b. Feeder and dipole detail of an LPHDA.

models were built, each containing five dipoles. The shortening factor s was 0.26 on the first model, 0.57 on the second. The second model exhibited unidirectional backfire radiation at the dipole resonant frequency, while the first showed a bidirectional pattern. Only when five more dipoles were added to the first model, giving it a total of ten dipoles, did it exhibit backfire radiation.

These results indicate that in the $s = 0.26$ model each of the original five dipoles radiated relatively little of the energy that was propagated towards them along the feeder. The remainder of the energy continued to the rear end of the feeder, and was reflected back towards the feed point. This reflected signal excited the dipoles once again, producing strong radiation in a direction opposite to that produced by the incident feeder signal; hence the bidirectional pattern. A log-periodic array built with such a low value of s would therefore suffer from strong end-effect and poor patterns, unless the scale factor τ were very close to unity. Such a τ would lead to an extremely long antenna for any appreciable operating bandwidth.

For these reasons, all subsequent LPHDA models were built with s in the range 0.5 to 0.6.

2.2 Direct Comparison of Arrays of Linear and Helical Dipoles

To gain further insight into the effect of dipole shortening, a direct comparison was made of two log-periodic arrays. These arrays were identical in all respects except for the use of linear dipoles in one and helical dipoles, with $s = 0.54$, in the other. The design was taken from Carrel², and based on minimum boom length for 9 db directivity.

Figure 2 shows the far-field H-plane radiation patterns of the two arrays at four different frequencies. The patterns of the array of linear dipoles, represented by dashed lines, are quite consistent over the entire range of frequencies for which the antenna was built. By contrast, the patterns of the helical dipole array (solid lines) deteriorate quite noticeably at the extreme ends of the frequency range (400 and 1033 Mc). These results suggest that the active region on the LPHDA includes a larger number of dipoles than does the active region on an LPD.

The 610 Mc pattern is typical of the mid-range performance of this array. It is seen that both directivity and front-to-back ratio suffer somewhat by comparison with the LPD.

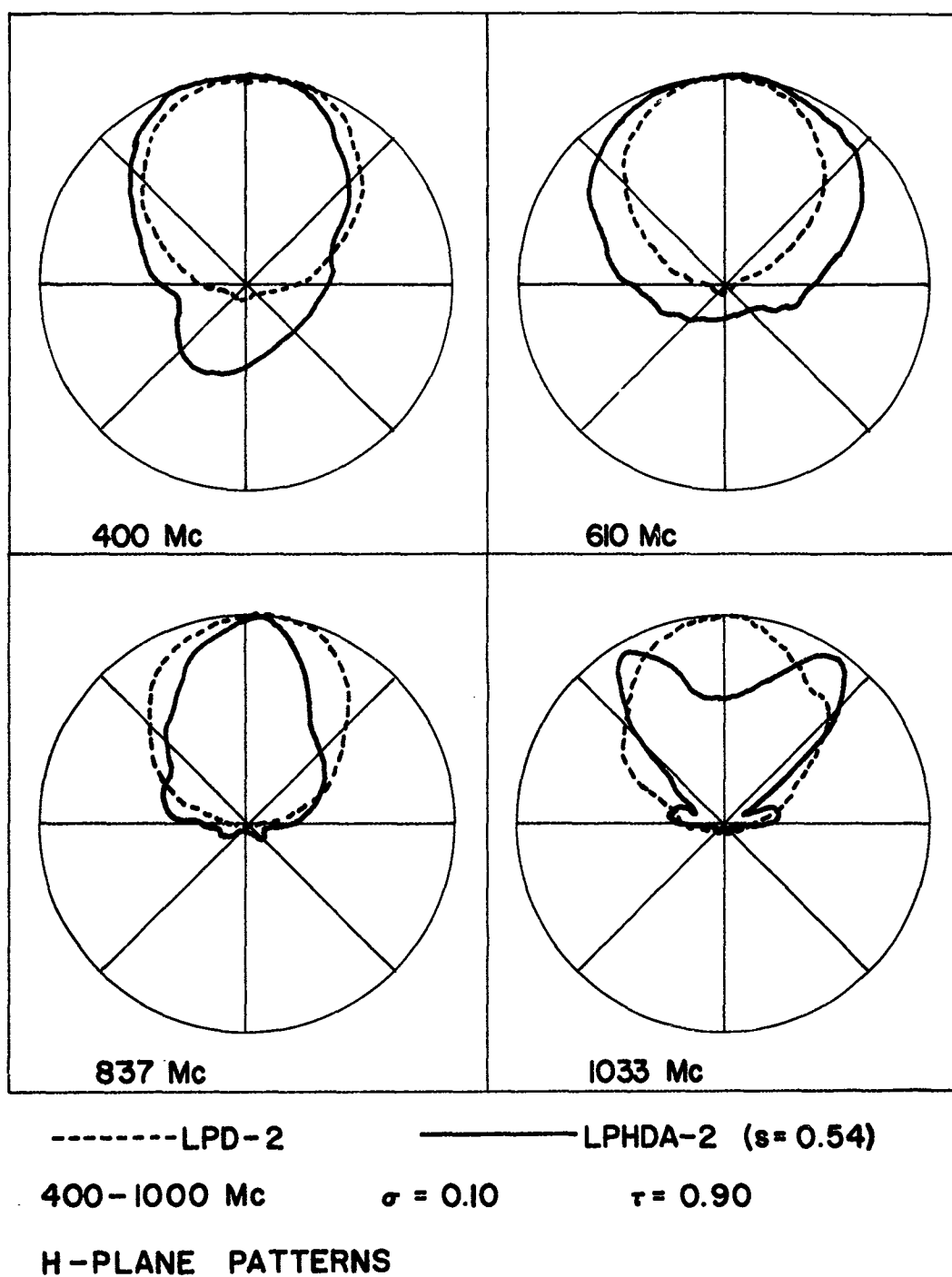


Figure 2. Radiation patterns of an LPD and an LPHDA.

Figure 3 illustrates the variation with frequency of the input impedances at the feed-points of the antennas. For both antennas, readings were taken at three frequencies per log-period; that is, if f_n is the resonant frequency of the n -th dipole, the frequencies chosen were f_n , $\tau^{-1/3}f_n$, $\tau^{-2/3}f_n$, $\tau^{-1}f_n = f_{n+1}$, etc. The individual points shown are the impedances for the helical dipole array, from 400 to 1000 Mc. The circle encloses all of the impedances measured on the linear dipole array, over the same frequency range. The VSWR with respect to the mean input impedance varies as follows:

Linear dipole array: VSWR = 1.5, 400-1000 Mc

Helical dipole array: VSWR = 4.85, 400-1000 Mc

VSWR = 3.2, 400-753 Mc.

The point-by-point progression of impedance vs. frequency is not shown in Figure 3, but it should be remarked that the orderly, clockwise movement of impedance as frequency is increased, a feature of log-periodic dipoles, was present in the helical model.

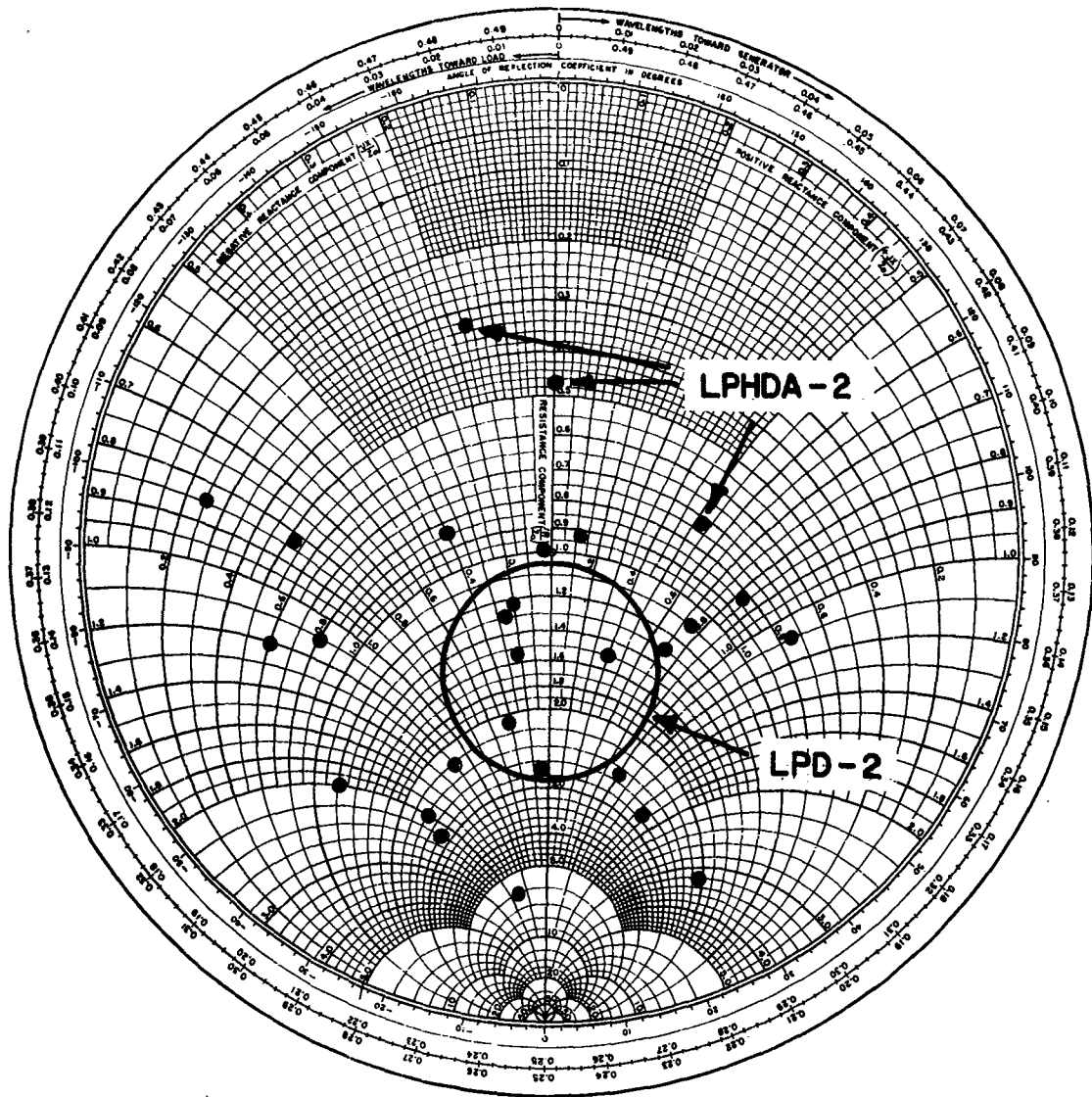
The measured data may be summarized as follows: the LPHDA, built with the same design parameters as the linear dipole array but with the dipole shortening factor of 0.54, featured an operating bandwidth about 65% as wide as that of the LPD, an average directivity of 6.37 db compared to 9 db for the LPD, an average front-to-back ratio of 15.4 db compared to a minimum of 20 db for the LPD, and the input VSWR comparison given in the table above.

This degradation in performance was anticipated, as mentioned earlier. The usefulness of the LPHDA will depend on the degree to which performance may be improved by adjusting the various design parameters. The effects of varying these parameters were investigated next, and the results are described below.

2.3 LPHDA Performance vs. τ , σ , and Z_0

The goal in this investigation was to determine which values of τ , σ , and Z_0 lead to optimum performance of an LPHDA with $s \approx 0.5$, in terms of far-field pattern directivity, input VSWR, and overall boom length.

Three LPHDA models were built to cover a 400-800 Mc frequency range. These models featured a feeder impedance, Z_0 , equal to 100 ohms, and a scale factor τ of 0.90, 0.92, and 0.95, respectively. Figure 4 is a photograph of the $\tau \approx 0.92$ model. The spacing of the dipoles along the feeder, and hence the spacing factor σ , could be varied over a wide range. In all three models, $s = 0.54$.



LPD-2 and LPHDA-2 ($s = 0.54$)

$\sigma = 0.10$

$\tau = 0.90$

400 - 1000 Mc

Figure 3. Input impedance of an LPD and an LPHDA.

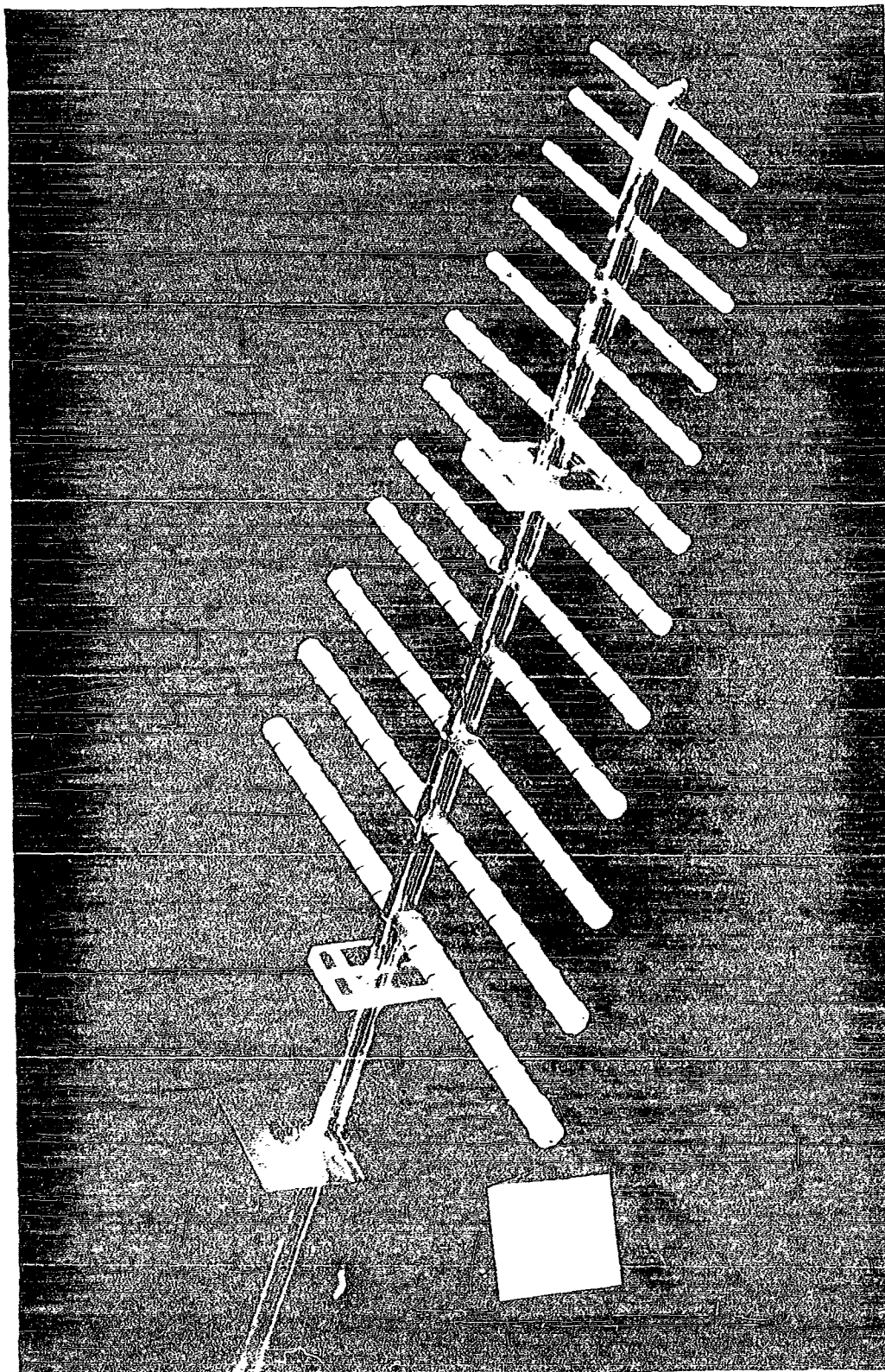


Figure 4. LPHDA laboratory model.

Measurements of input impedance (at the feed-point) and far-field radiation patterns, as a function of frequency, were made for several different values of σ on each model.

Figure 5 shows the variation of VSWR (with respect to mean input impedance) as a function of σ . The $\tau = 0.90$ model with $\sigma = 0.16$ (design "A") gave the lowest VSWR, just under 2, but the boom length of the antenna at this σ setting was quite long. The $\tau = 0.92$ model performed almost as well in terms of VSWR, and with $\sigma = 0.07$ (design "B") it was a shorter, more compact array. The $\tau = 0.95$ model with $\sigma = 0.05$ (design "C") appears to be shorter yet, but the increase in τ offsets the decrease in σ and actually produces a longer antenna. Thus from the standpoint of VSWR and boom length, the best design of those three appears to be design "B". In Figure 6 are plotted the input impedances for this model at frequencies throughout the range of 414 to 800 Mc.

The far-field radiation patterns showed rather small changes from one value of σ to the next, but in all three models the optimum patterns (in terms of directivity and front-to-back ratio) and the optimum VSWR were found at the same value of σ . Figure 7 shows the H-plane patterns at six frequencies for design "B". The directivity of this model is about 6.5 db, and the front-to-back ratio averages 19 db from 514 to 800 Mc and 15 db from 400 to 800 Mc.

It is difficult to compare the boom length of this model with the boom length of an array of linear dipoles which has the same directivity, because existing LPD design charts do not give complete figures for directivities lower than about 7.5 db. It is clear that the linear dipole array would be somewhat shorter. It is also worthwhile to note that the insertion of $\tau = 0.92$, $\sigma = 0.07$ into the LPD design charts gives a directivity of about 8.8 db.

In order to investigate the effect of Z_o on the performance of the LPHDA, a new model was built in which Z_o could be varied over the range 100 to 300 ohms. Design "B" was chosen for τ and σ . At a feeder impedance, Z_o , of 250 ohms, the VSWR was found to be 1.95; it increased to 2.33 and 2.31 at $Z_o = 230$ and 275 ohms, respectively. Figure 8 shows the impedance of this model. Pattern measurements showed results that were essentially the same as those measured with Z_o equal to 100 ohms.

Measurements are currently underway on another variable Z_o model on which Z_o may be set at values much higher than 300 ohms.

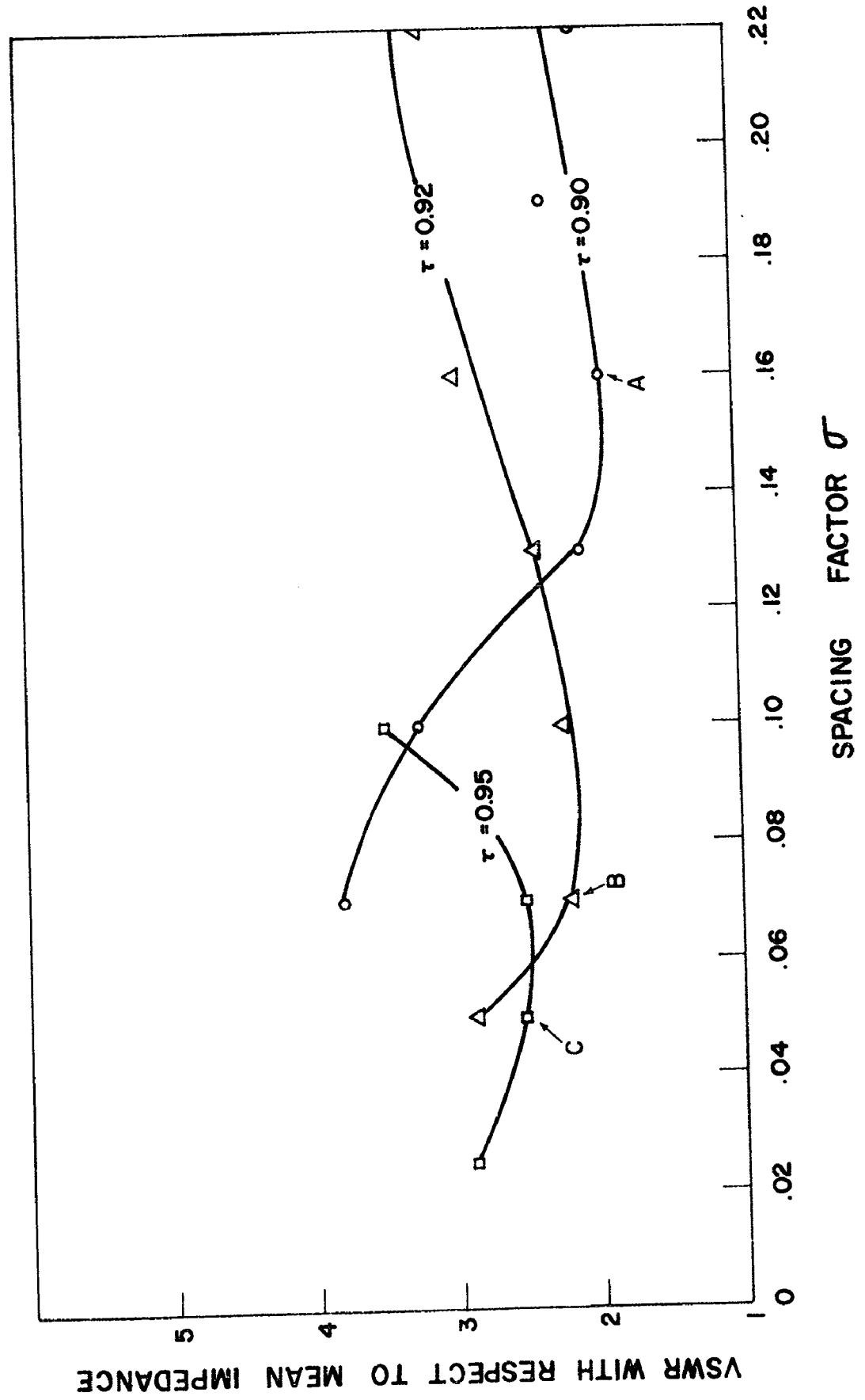
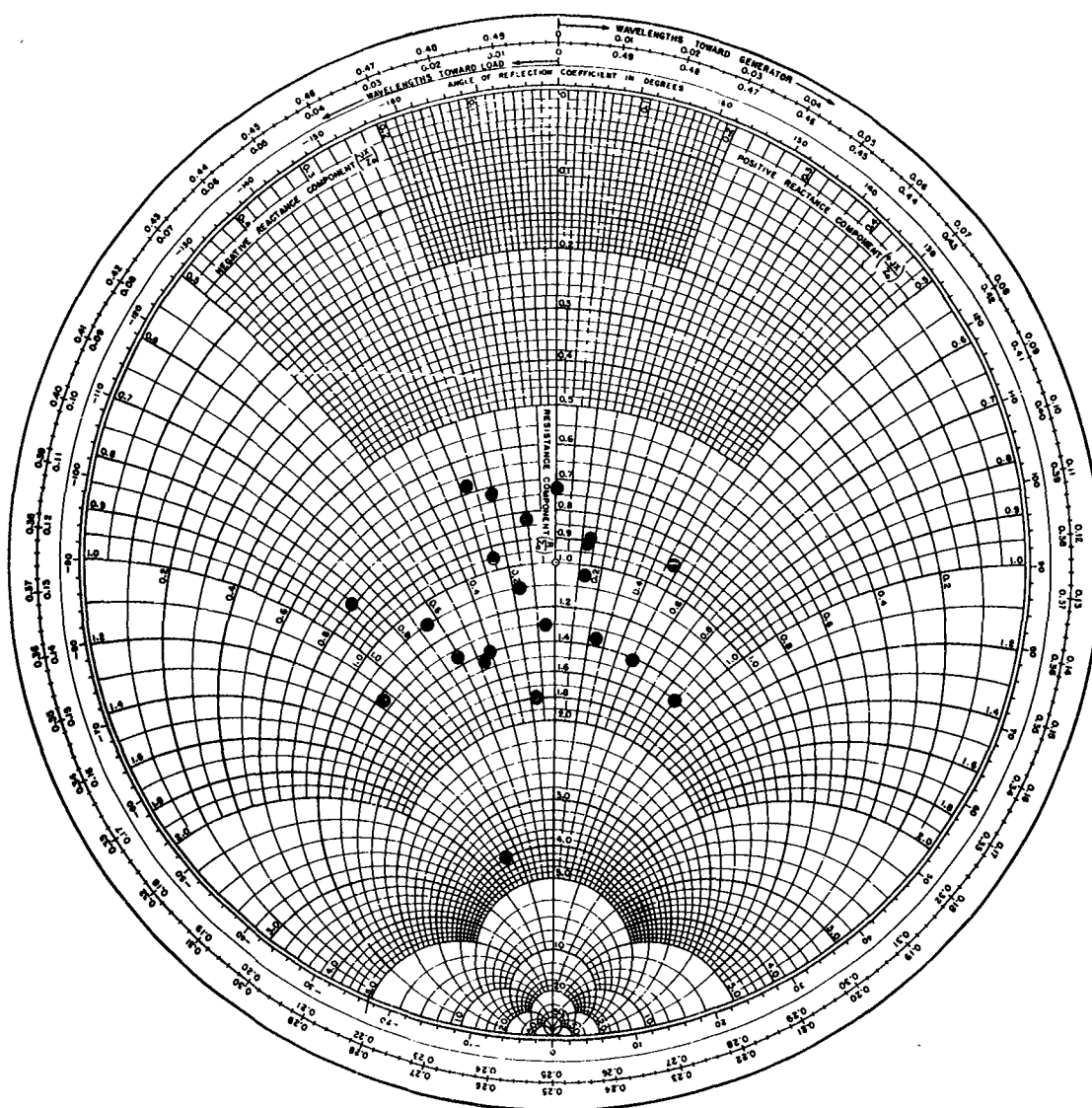


Figure 5. Input VSWR vs. σ for three LPHDA models.



LPHDA - 4 a

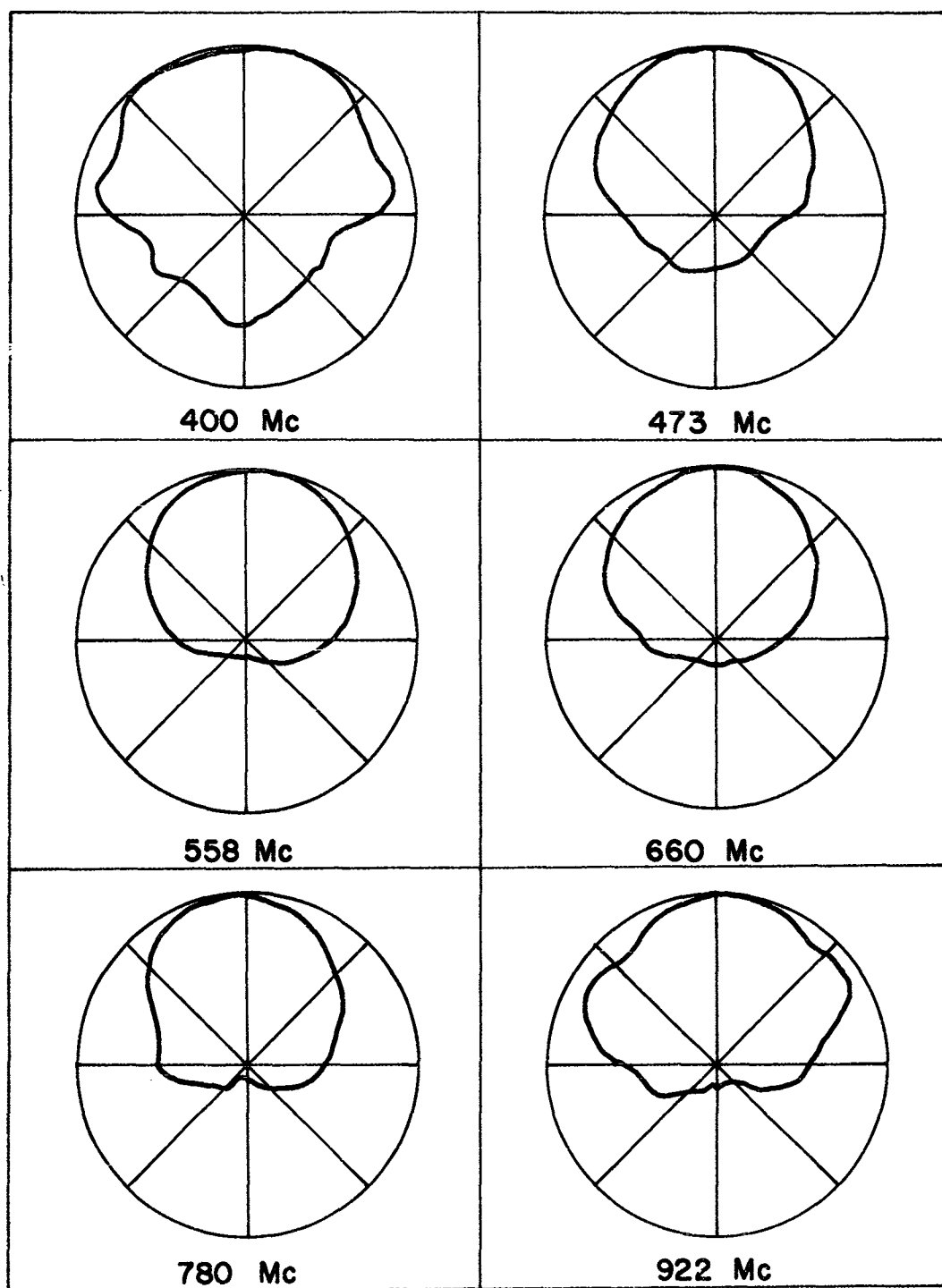
($s = 0.54$)

$\sigma = 0.07$

$\tau = 0.92$

414 - 800 Mc

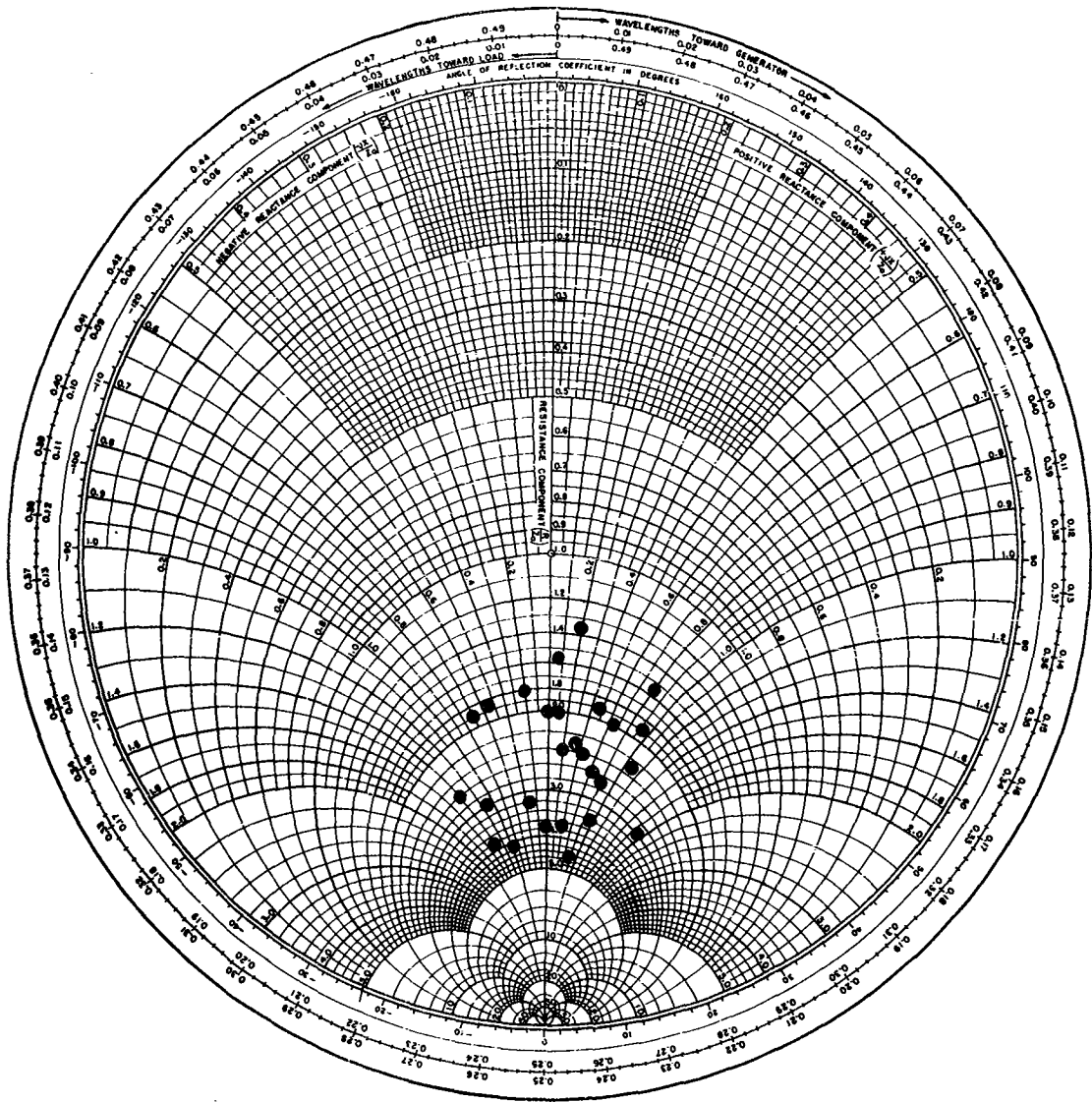
Figure 6. Input impedance of LPHDA design "B".



LPHDA - 4 $\sigma = .07$ $\tau = .92$ $S = .54$

H - PLANE PATTERNS

Figure 7. Radiation patterns of LPHDA design "B".



LPHDA-6a ($s=0.54$)

$\sigma=0.07$ $\tau=0.92$

$Z_o=250 \Omega$ 400-800 Mc

Figure 8. Input impedance of LPHDA design "B" with optimum z_o .

2.4 k- β Diagram of a Uniform Array

The far-field pattern of a radiating periodic structure is closely related to the k- β characteristic of its near field. The k- β diagram of a uniformly periodic array of linear dipoles has been obtained and studied, both experimentally and theoretically^{5,6}. Although the full meaning of this k- β diagram is not yet completely understood, it was felt that it would be of interest to obtain experimentally the k- β diagram for a uniformly periodic helical dipole array (UPHDA) for purposes of comparison.

The UPHDA that was constructed for this measurement contained 14 identical dipoles, equally spaced with a spacing factor σ equal to 0.087. The shortening factor s was 0.53. Its near field was probed, in a direction parallel to the feeder, by a small shielded loop that was oriented to respond to the magnetic field produced by the axial component of the dipole currents and reject the field produced by the feeder currents. Relative amplitude and phase of the probe signal were measured at many frequencies as a function of distance along the feeder. This distance was defined in terms of a "cell" of length a , the distance from one dipole to the next. The resulting data appear in the form of a k- β diagram and a curve of attenuation per cell; these are shown in Figure 9.

The k- β curve, showing points in the vicinity of the first two stop bands, is similar in appearance to k- β diagrams obtained from linear dipole arrays. Measurements of the far-field radiation patterns of this array were made at the frequencies shown, and the agreement of these patterns with corresponding points on the k- β diagram is excellent. Points are shown only for those frequencies at which reliable phase data were obtained; at some frequencies the presence of more than one mode on the structure leads to ambiguous phase plots.

The curves of attenuation per cell are also similar in form to those obtained from linear dipole arrays. The big difference lies in the maximum values of attenuation obtained. Linear dipole arrays have produced in the neighborhood of 20 db attenuation per cell, while the maximum value obtained on the helical dipole array is about 6 db. This result agrees with the concept of a wider active region on the LPHDA.

2.5 The Log-Periodic Mixed Dipole Array

This investigation was motivated by the observation that in an application where size reduction in a broadband array is desired, the need for size

reduction is present only in the longest dipoles; half-wave linear dipoles are still satisfactory for use at the high-frequency end of the array. An antenna in which only the few longest dipoles are made helical would combine the well-behaved characteristics of a conventional LPD array at the higher frequencies with dipole length reduction (and a change in performance) only where it is needed most.

Two log-periodic mixed dipole array (LPMDA) models were built and tested. The models differed in τ and σ , but were similar in that on each model the first four dipoles were helical and the rest were linear. The helical dipoles were scaled differently than those on previous models had been: all four were the same length. The first dipole was built with $s = 0.5$, and the pitch of the following dipoles (and consequently the value of s) was increased progressively so that (on one model) the fourth dipole had a value of $s = 0.9$. Consequently the resonant frequencies of these first four dipoles were increased log-periodically, while their lengths remained the same. The result of this was a gradual transition from helical to linear dipoles. Figure 10 is a photograph of these two antennas.

Pattern and impedance measurements displayed uniform characteristics over the frequency range in which the linear dipoles were active. As the frequency was reduced to bring the helical dipoles into operation, the performance changed gradually to broader patterns and higher VSWR. The following table illustrates this change for the first of these models, in which $\tau = 0.825$, $\sigma = 0.06$, and $Z_0 = 135\Omega$ (f_n denotes the resonant frequency of the n -th dipole).

<u>Freq. Range</u>	<u>VSWR</u>	<u>Front-to-Back Ratio</u>
f_5 and above	1.91	21.5 db minimum
$f_4 - f_5$	1.91	20.28 db
$f_3 - f_4$	2.11	11.69 db
$f_2 - f_3$	2.27	8.22 db
$f_1 - f_2$	3.58	3.36 db

The VSWR performance for this model is illustrated in Figure 11. The sixteen points shown are spaced evenly through the first four log-periods. The point labelled " f_1 " is at the resonant frequency of the first helical

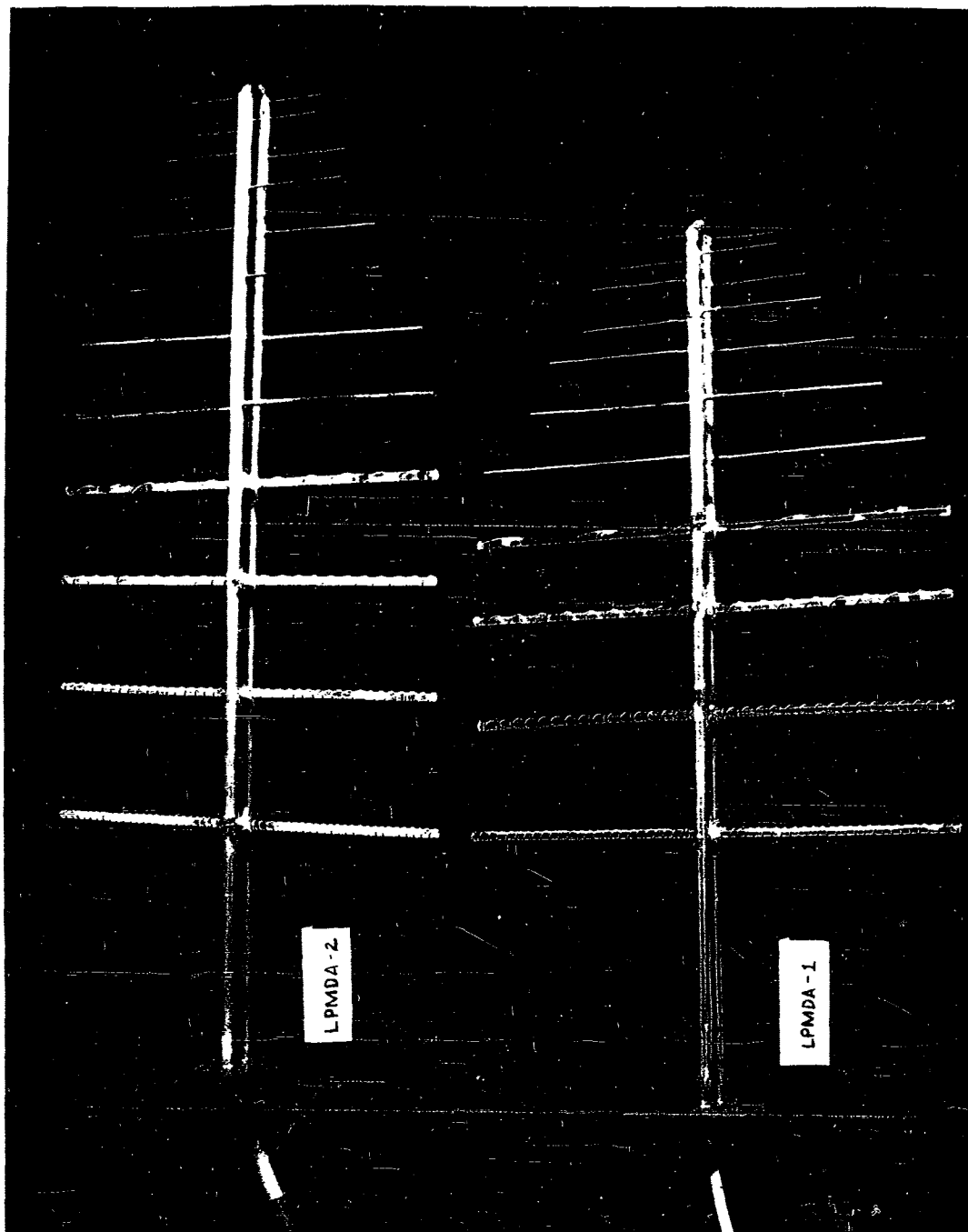
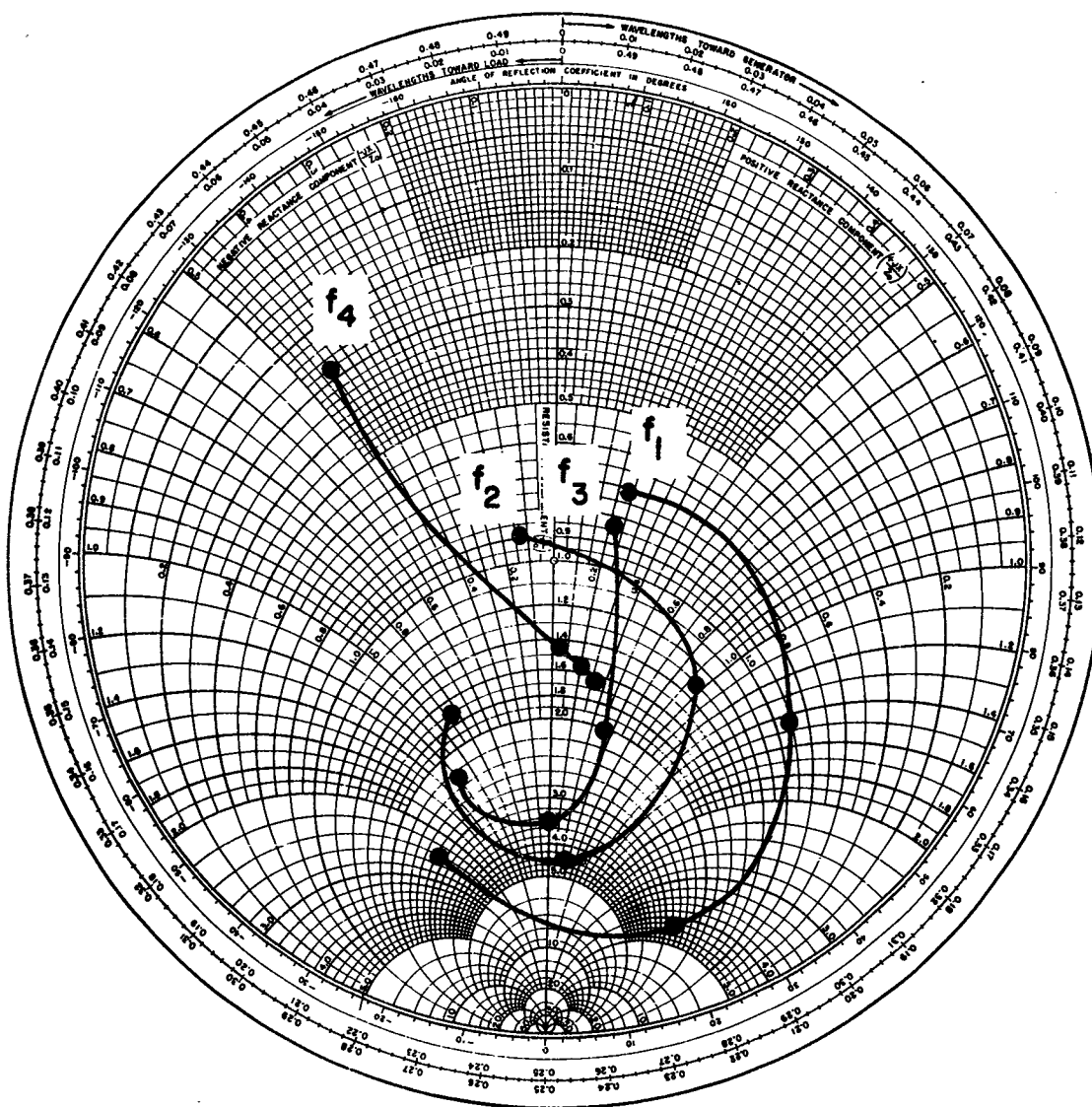


Figure 10. LPMDA laboratory models.



LPMDA-1: FIRST FOUR LOG-PERIODS

$\sigma=0.06$ $\tau=0.825$ $\alpha=36^\circ$

Figure 11. Input impedance of LPMDA-1.

dipole; the next three points connected to it by the line correspond to frequencies of $\tau^{-1/4}f_1$, $\tau^{-1/2}f_1$, and $\tau^{-3/4}f_1$. The next point is the point labelled " f_2 ", etc. As frequency is increased, the impedance pattern (with the exception of the point labelled " f_4 ") spirals inward towards a progressively lower VSWR. Above frequency f_5 the impedance points are clustered around $1.5 + j0$ with a VSWR of less than 2.

These and other data obtained from the LPMDA models suggest that a practical way to design such an antenna might be to add one log-period to the intended frequency bandwidth, i.e., to build the array one dipole longer on the low frequency end. Also, τ and σ could be changed to more suitable values in the helical portion of the antenna.

3. CONCLUSIONS

With the aid of the above experimental results, the drawbacks and advantages of the LPHDA may be summarized. It has been shown that the array must be made longer as the dipoles are shortened in order to maintain good directivity and VSWR over the same bandwidth. Thus the antenna designer who is faced with space limitations may find the LPHDA to suit his needs where low-frequency coverage is desired if he is willing to give up bandwidth in exchange for reduced dipole length. An installation in which the antenna is fixed with respect to surrounding objects could possibly make good use of a longer but narrower array.

An LPHDA may be well suited for low-frequency applications where mechanical support is a problem. A long boom on which are mounted long dipoles requires support in several directions in order to stiffen the whole array. By using shorter helical dipoles wound on tubular fiberglass poles, for example, the support problem could be reduced to that of supporting the boom alone.

In such applications, the LPHDA (or LPMDA) could be useful even if it is found necessary to increase the design bandwidth of the array by one or two log-periods on the low-frequency end in order to maintain good performance at the original low-frequency limit.

The results described in this paper suggest a number of other investigations which should be made. For example, the effect of Z_0 , as mentioned earlier, continues to be studied. Research on the conventional LPD antenna showed that Z_0 had a major effect on mean input impedance level and a secondary effect on input

VSWR and active region efficiency. Much work is yet to be done on changing the parameters of the LPMDA in that portion of the antenna which contains the helical dipoles. Using the $k-\beta$ diagram as a guide, extra phase shift might be inserted in the feeder between dipoles in order to improve directivity. A mathematical analysis, similar, for example, to Carrel's analysis of the LPD, might prove useful in verifying experimental results and in providing data for LPHDA design charts.

The authors anticipate that further work on these and other factors will make the LPHDA and related antennas useful members of the family of log-periodic dipole arrays.

BIBLIOGRAPHY

1. D. E. Isbell, "Log-Periodic Dipole Arrays", Technical Report No. 39, Contract No. AF33(616)-6079, Antenna Laboratory, University of Illinois, June, 1959.
2. R. L. Carrel, "Analysis and Design of the Log-Periodic Dipole Antenna," Technical Report No. 52, Contract No. AF33(616)-6079, Antenna Laboratory, University of Illinois, October, 1961.
3. T. Li, "The Small-Diameter Helical Antenna and Its Input-Impedance Characteristics," Ph. D. Thesis, Electrical Engineering Department, Northwestern University, June, 1958.
4. H. A. Wheeler, "A Helical Antenna for Circular Polarization," Proc. IRE, Vol. 35, pp. 1484-1488, December, 1947.
5. J. D. Kraus, "Antennas," McGraw-Hill, New York, p. 25, 1950.
6. P. E. Mayes, G. A. Deschamps, W. T. Patton, "Backward Wave Radiation from Periodic Structures and Application to the Design of Frequency-Independent Antennas," Tech. Report No. 60, Contract No. AF33(657)-8460, Antenna Laboratory, University of Illinois, December, 1962.
7. R. Mittra and K. E. Jones, "Theoretical Brillouin (k - β) Diagram for Monopole and Dipole Arrays and Their Application to Log-Periodic Antennas," Tech. Report No. 70, Contract No. AF33(657)-10474, Antenna Laboratory, University of Illinois, April, 1963.

ACKNOWLEDGEMENT

This work was supported by the Naval Electronics Laboratory, San Diego, California, under Contract No. N123(953)-30508A. The authors acknowledge with thanks the work of student technicians Henry H. Hegener and Werner Y. Lain.

OCTAVE BANDWIDTH MULTIPLE BEAM ARRAY

by

Martin E. Mehron
Advanced Development Laboratories, Inc.
Nashua, New Hampshire

Presented at the Thirteenth Annual Symposium
on USAF Antenna Research and Development

University of Illinois
15-18 October 1963

The work reported in this document was sponsored by
the Aeronautical Systems Division, AFSC, under
Contract Number AF 33(657)-8896

OCTAVE BANDWIDTH MULTIPLE BEAM ARRAY

Program Objective

In 1960 a unique corporate feed network capable of deriving multiple beams from a single array of antenna elements was developed.^{1,2} The most significant feature of these networks, commonly referred to as Butler Matrices, is that the beam forming has an efficiency of 100%, that is, the only loss is due to attenuation. A number of relatively narrow band phased arrays have been developed using the multiple beam matrix with the major effort centered in L and S Bands. The prime purpose of this paper is to present the results of a program to develop an 8 element/8 beam phased array capable of operating over the octave band of 2 to 4 Gc. Since this array was developed for potential use on aircraft and satellites the matrix was to be fabricated in strip line in order to minimize weight and volume. Also, the antenna elements and beam forming matrix were to be designed as a single integrated unit to obviate the necessity for connectors and cables.

Operating Principles of Multiple Beam Forming Matrix

The basic components contained in a multiple beam forming matrix are a 3 db quadrature coupler and fixed phase shifters. The 3 db coupler is a 4 port device such that if a signal is applied to one of the ports, equal outputs will appear at two other ports with a relative phase of 90° , while the fourth port will be isolated. A simple 2 beam array can be achieved by connecting 2 elements by means of a single 3 db coupler as shown in fig. 1. This can be expanded to a

4 beam array by connecting 4 elements by means of 4 couplers and a pair of 45° fixed phase shifters as shown in fig. 2. If a signal is applied to the beam port marked 1 Left it will excite all the elements with a relative phase shift of 45° between elements. Assuming $\lambda/2$ spacing between elements this would result in a beam peak at 14.5° to the left of boresight. The beam port marked 2 Left would produce a phase gradient of 135° between elements which would produce a beam peak at 48.5° , again assuming $\lambda/2$ spacing of elements. From symmetry it can be seen that the 1 Right and 2 Right beam ports would produce the reverse phase gradients and thus produce similar beams to the right of boresight.

Certain properties of the beams are of interest. At the space angle corresponding to the peak of any beam, all other beams have zero amplitude, that is, the beams are orthogonal. This is a fundamental requirement for lossless beam forming. As the operating frequency is increased all beams will tend to move toward boresight with a beam squint given by

$$d\theta = \tan\theta \frac{df}{f}$$

where $d\theta$ is in radians, θ is the beam pointing angle measured from boresight and $\frac{df}{f}$ is the fractional change in frequency. Since the beamwidth also decreases as the frequency is increased the overlap between beams remains constant at roughly -3.9 db.

Since each beam makes use of all the antenna elements the gain of all the beams is determined by the total antenna aperture. The fact that the beam forming is passive insures reciprocity so that the array is equally useful for transmitting or receiving.

If the beam ports are excited singularly the elements will be excited with equal amplitude and the familiar $\sin x/x$ pattern will result with -13 db maximum sidelobes. If a pair of adjacent beam ports are excited, in phase and with equal amplitudes, a cosine amplitude distribution can be achieved which will produce a pattern with -23 db theoretical side lobes. Likewise, 3 ports can be excited to give cosine² taper etc.

Development Effort

A schematic diagram of the 8 element array developed on this program, is shown in fig. 3. A photograph of this array is shown in fig. 4. The major items requiring development during this program were connectors, directional couplers, fixed phase shifters, and radiating elements

The first item to be investigated was a coax-to-strip connector since these are required on all the tests of the other components. Available type N connectors have a mismatch as high as 1.4:1 over the 2-4 Gc band. This amount of mismatch would make it impossible to measure to the precision required. It was possible to reduce the mismatch to 1.15:1 by modifying the connector design.

A variety of 3 db couplers can be fabricated in strip circuitry, including branch line couplers and traveling wave or Shimizu³ couplers. The Shimizu coupler was selected because it has better broadband characteristics. The major development effort needed on these couplers was to increase the isolation. The resulting performance over the 2-4 Gc band was isolation greater than 24 db, VSWR less than 1.2:1 and power split within $\pm .5$ db.

By far the greatest difficulty was experienced in developing the fixed phase shifters. The design utilized was based on broadband fixed phase shifters developed by Shiffman⁴. In these units a constant phase shift between two lines is achieved by including a coupled region in one of the lines. The primary difficulty was due to the very large mismatches in the line with the coupled section. By modifying the coupled section it was possible to reduce the mismatch to less than 1.3:1. The phase variations over the octave band are about $\pm 3^\circ$.

The antenna array consists of 8 square Archimedes spirals in the form of a linear array with a spacing of 0.5λ at center frequency. The spirals and balun are printed on epoxy fibreglass material, NEMA G-10. The sides of the spiral are 1.810 inches long (about $.5\lambda$ at center frequency) and the depth of the cavity is 1".

Typical measured data for the antenna elements are VSWR < 1.8, gain +3 db WRT isotropic circular, and axial ratio less than 3 db over the band.

Test Results

The major significance of this program was the design of the octave bandwidth matrix in strip line. The performance achieved was quite comparable to results of the much simpler narrow band units previously designed.

Amplitude Distribution

Whenever a beam port is excited the signal should divide equally among all eight antenna elements resulting in a 9 db attenuation.

The measured variation in amplitude on any beam is about $\pm .5$ db while typical insertion loss is 0.6 db.

Phase Distribution

The ideal phase gradients of an 8 element matrix are $\pm 22 \frac{1}{2}^\circ$, $\pm 67.5^\circ$, $\pm 112.5^\circ$ and $\pm 157.5^\circ$, for beams 1 thru 4 respectively. The measured values of phase gradient are shown in Table I and indicate very close agreement with the theoretical values. Likewise, Table II indicates the extent of phase error, or ripple, at the antenna elements. Typical RMS phase errors are less than 5° with a maximum error of 7.1° .

Computed Beam Patterns

In an attempt to isolate the effects of phase and amplitude errors contributed by the beam forming matrix a series of computed beam patterns was derived. These patterns were obtained by means of a computer program developed by M.I. T. Lincoln Laboratory. Measured phase and amplitude data for each beam and at 5 spot frequencies across the 2-4 Gc band were supplied to Lincoln Laboratory. Samples of the computed beam patterns are shown in fig. 5. The beam patterns have maximum side lobes of -12 db compared to -13.2 db theoretical. (It should be noted that the computed beam patterns assume ideal isotropic elements).

Because of the large variation in element spacing (in terms of wavelength) across the band, the peaks of the beams will move toward boresight as the frequency is raised and away from boresight as the frequency is lowered. Also, at 4 Gc grating lobes appear when

the outside beams are excited, as is to be expected. At 2 Gc the outside beams actually disappear since they have moved beyond the plane of the array.

In order to confirm the computed patterns and to determine the effects of the spiral elements a set of measured beam patterns is presently being derived.

This work was performed under Contract AF 33(657)-8896 for the Antenna and Radome Section of the Aeronautical Systems Division, Mr. O. E. Horton, Project Engineer. As a continuation to this program a strip line phased array covering the frequency range of 7-11 Gc is presently being developed.

Bibliography

1. Butler, J and Lowe, R., "Beam Forming Matrix Simplifies Design of Electronically Scanned Antennas", Electronic Design, Apr. 1961.
2. Shelton, J and Kelleher, K., "Multiple Beams from Linear Arrays", IRE Transactions on Antennas and Propagation, VO AP-9 No. 2, March 1961.
3. Shimizu, J. K., "A Strip Line 3 DB Coupler", SRI Project 1592, Scientific Report No. 1, June 1957.
4. Schiffman, E. M., "A New Class of Broadband Microwave 90 Degree Phase Shifters", IRE Transactions on Microwave Theory and Techniques, Apr. 1958.

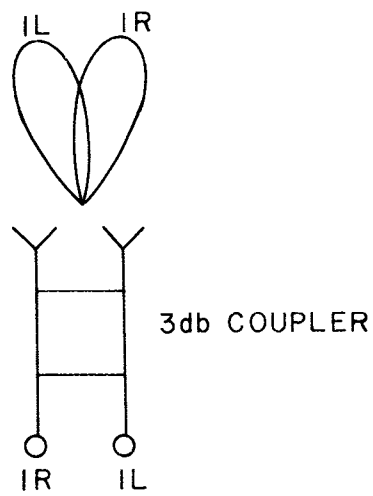


FIGURE 1 2-BEAM ARRAY

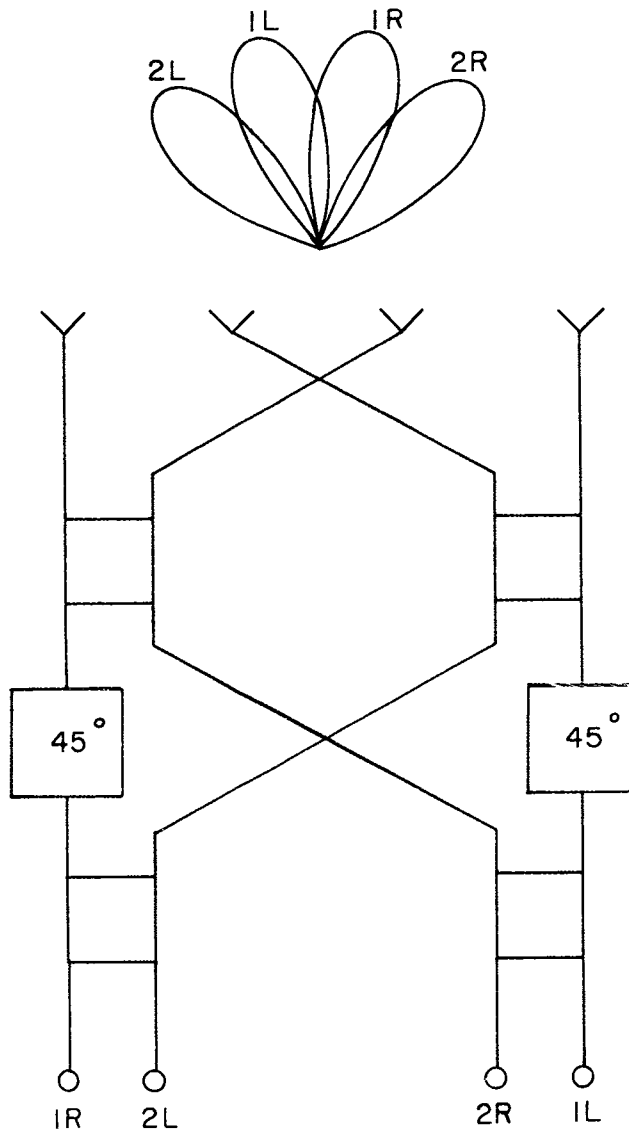


FIGURE 2. 4-BEAM ARRAY

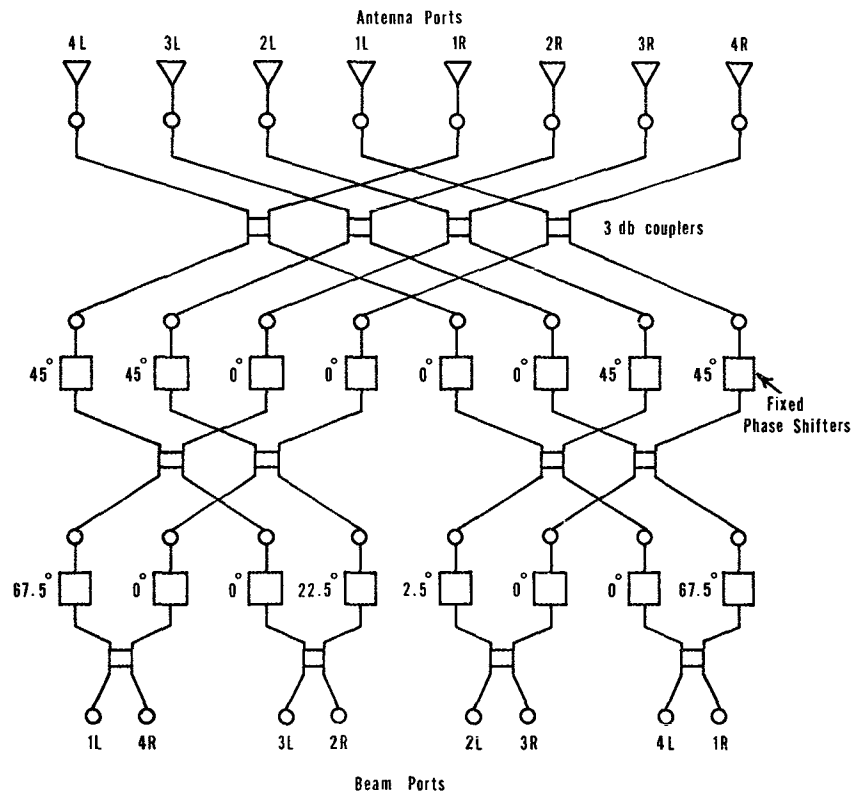


FIGURE 3 8 BEAM ARRAY

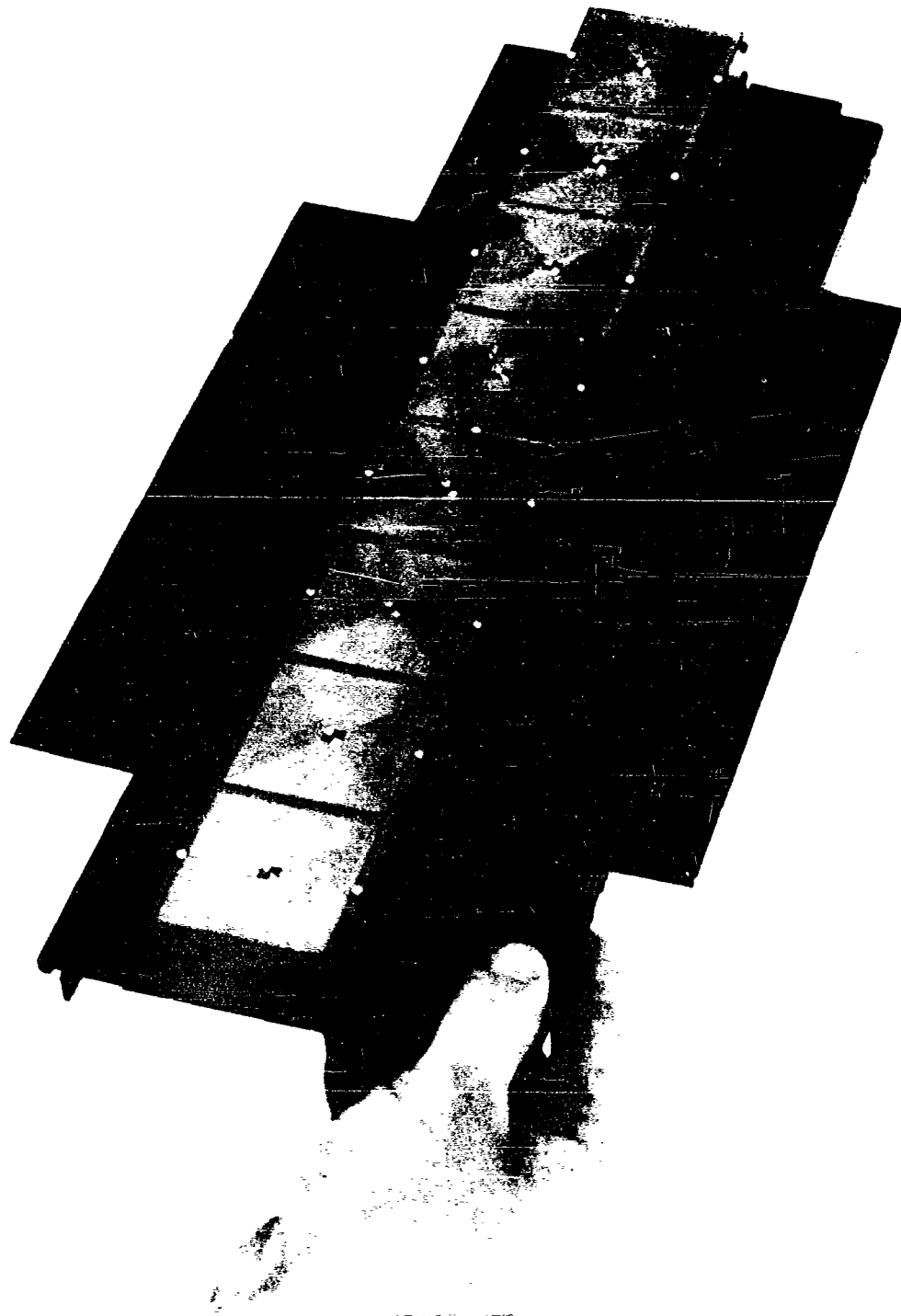


FIGURE 4 EIGHT ELEMENT MULTIPLE BEAM ARRAY

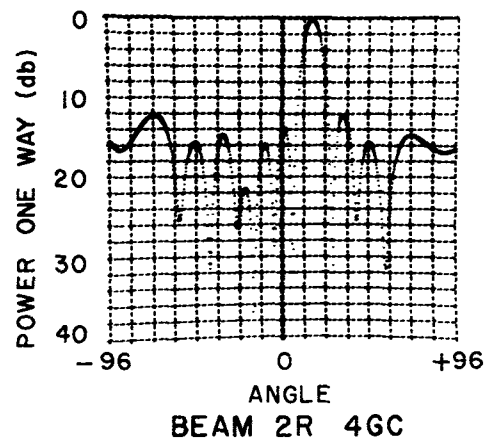
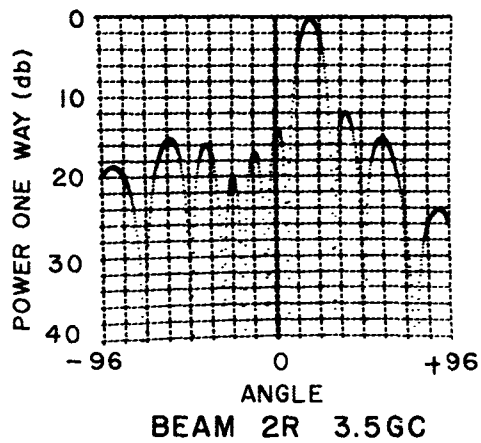
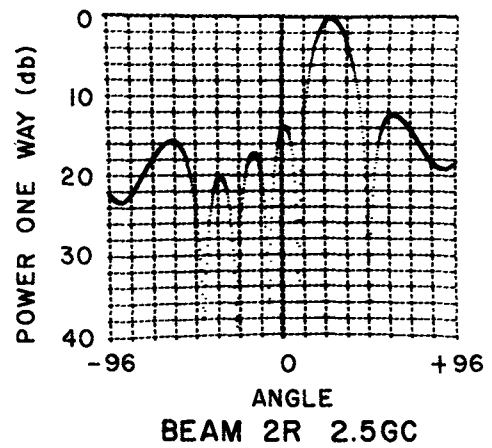
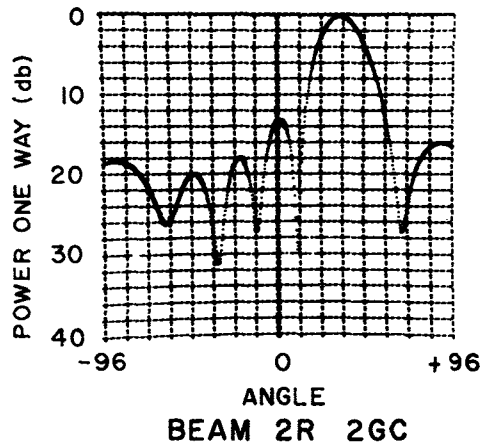


FIGURE 5 COMPUTED BEAM PATTERNS

TABLE I

FREQ. (Gc)	BEAM PORT							
	B4L	B3L	B2L	B1L	B1R	B2R	B3R	B4R
2.00	158	112	68	22	23	67	113	158
2.25								
2.50	157	112	68	23	23	68	113	157
2.75								
3.00	157	112	68	22	22	68	112	158
3.25								
3.50	157	113	67	22	23	68	112	157
3.75								
4.00	158	112	68	22	23	68	112	157
DESIGN	157.5	112.5	67.5	22.5	22.5	67.5	112.5	157.5

BEAM PHASE GRADIENT (DEGREES)

TABLE II

FREQ. (Gc)	ANTENNA PORT							
	A4L	A3L	A2L	A1L	A1R	A2R	A3R	A4R
2.00	2.1	3.3	4.3	1.8	1.6	3.8	6.2	3.6
2.25								
2.50	5.2	3.7	3.6	5.2	4.2	4.3	4.7	5.2
2.75								
3.00	5.4	4.0	5.8	6.0	6.0	3.5	4.9	5.1
3.25								
3.50	6.0	4.6	6.1	5.0	4.9	4.2	6.3	4.8
3.75								
4.00	7.1	4.5	4.5	3.9	4.3	4.7	2.3	6.4

BEAM RMS PHASE ERROR (DEGREES)

ARRAY FACTORS WITH ZONE-PLATE SPACINGS

BY A. J. MONY AND R. M. HOGE

(North American Aviation, Inc., Columbus, Ohio)

A B S T R A C T

INTRODUCTION

It is generally known that phased arrays with a non-uniform spacing factor have several advantages over uniformly spaced arrays. These include a reduced number of elements to obtain given beamwidth, bandwidth, steerability and suppression of grating lobes in the scanned volume.

Attendant disadvantages include increased complexity in the generation of element excitations and variation of element source impedances over the aperture.

In recent years non-uniform spacing techniques have been based upon empirical spacing selection and verification of results by high speed computation. In spite of the absence of a satisfactory theory, some limited applications have been achieved. The number of elements involved were on the order of hundreds.

More recently, the probabilistic approach⁽¹⁾ to arrays with a large number of elements, on the order of tens of thousands, appears more satisfying on a theoretical basis. In this approach, synthesis of arrays is based upon a class of probability density functions from which the random element locations are obtained. This method provides an analytical evaluation of side-lobe structure, beamwidth and gain.

There are two general design techniques which may be distinguished. The first is concerned with strictly non-uniform spacings based upon a probability density function or other criteria, while the second is based upon the random removal of elements from a uniformly spaced array.⁽²⁾ It is expected that the latter method will favor implementation of actual arrays due to the integral phase relationship of the element excitations.

Finally we observe that most investigators of phased arrays with a non-uniform spacing factor have limited their attention to linear arrays. Study of planar arrays with non-uniform spacing factor has been primarily concerned with circular apertures and thinning or space taper, based upon a reference amplitude taper which is known to produce satisfactory side-lobe structure.

OBJECTIVES

The work reported in this paper concerns the evaluation of a particular method for random removal of elements from arrays of uniformly spaced elements. The method evaluated results in array factors with low close-in side-lobes and slowly decreasing remote side-lobe level. Thus, it is similar to other known criteria which produce desired space factors and good resolution. In addition it is possibly easier to apply high speed digital computation than some method

The technique which has been designated the zone-plate method was suggested by the Huygens-Fresnel construction but has no theoretical connection therewith⁽³⁾

The zone-plate consists of a central disk and concentric annular rings whose inner and outer radii are proportional to the square roots of successive

integers. In the arrays evaluated a reference zone-plate pattern of rings designate those elements which are retained from an array of uniformly spaced elements. Inter-element spacings of one-half wavelength were found convenient to use.

Space factors were obtained for symmetrical linear arrays and planar arrays with circular apertures using this method. Computer programs were prepared for the IBM 7090 of the North American Aviation, Inc. facility. The general program for planar arrays employs an unusual sparse-data subroutine which makes efficient use of the available fast memory. A rectangular lattice of 22,801 element positions allows the synthesis of planar arrays of any configuration, not necessarily circular.

RESULTS

Linear Arrays - Symmetric linear arrays with apertures of 50 and 75 wavelengths were evaluated. These were constructed from elements uniformly spaced by one-half wavelength only within the zone-plate intervals:

$$\Delta X_{1j} = \pm \left(D \sqrt{\frac{1}{4n}}, \quad D \sqrt{\frac{j}{4n}} \right),$$

where D is the aperture in wavelengths

$n = 2 N_r - 1$, N_r = number of rings used in the reference zone-plate pattern.

$(i = 0, 2, 4, \dots, 2N_r - 2)$

$(j = 1, 2, 3, \dots, 2N_r - 1)$

Linear Arrays - (Continued)

Space factors were computed by means of a simple program capable of handling arrays with 23,000 element pairs.

For $D_\lambda = 50$ and $N_r = (3, 10)$, the number of elements averaged 63 and the maximum side-lobe level averaged -12.05 db from the main-lobe. For $D_\lambda = 75$ and $N_r = (5, 15)$, the number of elements averaged 91 and maximum side-lobe level averaged -12.13 db.

Planar Arrays - It is expected that most antenna applications of interest will require pencil beams. Planar arrays with circular symmetry are therefore indicated.

The zone-plate criterion was used for design of arrays with overall circular apertures of 50 and 75 wavelengths and varying number of rings in the reference zone-plate pattern as a parameter. The filled array on this basis used the $\triangle X_{1j}$'s previously defined as the radii of annular rings which designate the elements to be retained from those in a regular lattice. All others are considered to be removed. Choice of elements to be retained or removed in some cases where the ring intersects an element cell is arbitrary. However, the randomness which results is not an adverse factor since the number involved is small compared to the total number of elements in the array. A filled zone-plate array results in an array thin to about 57% of a filled circular aperture of the same overall size.

Planar Arrays - (Continued)

In the first case evaluated, the space factor was computed by means of the general computer program. In order to reduce computer time, a modified program was prepared which takes advantage of the circular symmetry of the array simplification of the mathematical expression for the space factor. The results of the modified program were compared with those of the general program and found to be in very close agreement.

For 50 wavelength aperture, the average number of elements is 4619 and the average maximum side-lobe level was -19 db down from the main-lobe. The half-power beamwidth was 1.15 degrees.

The 50 wavelength aperture array of 4521 elements was selected for further thinning on a uniform basis. This was done by inspection over an octant of the array by thinning each of the 9 rings equally and duplicating the thinning in the remaining octants. The number of elements ranged from 4521 down to 1048 and resulted in an average maximum side-lobe of -17.8 db down with no change in the beamwidth.

NON-UNIFORM THINNING

It is possible to further reduce the maximum side-lobe level by selective apodization. In selected cases where the maximum side-lobes are close to the main beam, by inspection of the side-lobe pattern one can delete elements contributing to those maxima. In one case of an 80% thinned zone-plate array of 1610 elements, a side-lobe maximum of -23.4 db was obtained by apodization.

SUMMARY

The zone-plate method of designating sources to be removed from a uniform lattice has been found to provide space factors of symmetric linear and planar arrays with substantial reduction in number of elements required with no significant deterioration of side-lobe structure. The small variation in side-lobe pattern show that the number of rings in the reference zone-plate is not critical. Finally, the method is well adapted to high speed digital computation.

REFERENCES

- (1) Y. T. Lo, "High Resolution Antenna Arrays with Randomly Spaced Elements". IRE Trans., Vol. AP-11, January 1963, pp. 95-96 (also 1963 PTGAP Digest of International Symposium on Space Communications, Boulder, Colorado, 9 - 11 July 1963, hereafter called Reference "A"); A. Ishimaru and Y. Chen, "Broadband Antenna Arrays by Unequal Spacings", Reference "A"; A. L. Maffett, "Array Factors with Non-Uniform Spacing Parameter", IRE Trans., Vol. AP-10, March 1962, pp. 131-136.
- (2) T. M. Maher and D. K. Cheng, "Random Removal of Radiators from Large Linear Arrays", IRE Trans., Vol. AP-11, March 1963, pp. 106-112; M. G. Andreassen, "Linear Arrays with Variable Inter-Element Spacings". IRE Trans. Vol. AP-10, March 1962, pp. 137-143; M. I. Skolnik, G. Nemhauser, L. C. Kefauver and J. W. Sherman, "Thinned Unequally Spaced Arrays Designed by Dynamic Programming" - Reference "A"; D. D. King, R. F. Packard and R. K. Thomas, "Unequally Spaced, Broadband Antenna Arrays", IRE Trans., Vol. AP-8, July 1960, pp. 380-384.
- (3) Born and Wolf, "Principles of Optics", pp. 369-373. Jenkins and White, "Fundamentals of Optics", pp. 355-356.

A 500:1 SCALE MODEL OF WARLA - A WIDE APERTURE RADIO LOCATION ARRAY

J. W. Greiser & G. S. Brown^{*}

ABSTRACT

This paper describes the design, construction, and testing of a microwave scale model of a circular array of broadband antennas. The ultimate goal of this work is the construction of a high gain direction finding array using frequency independent antennas which would permit efficient operation over the 2-32 Mc range. The scale model is an attempt to experimentally verify certain theoretical results which were obtained from calculations performed on a computer.

Restrictions imposed on the array by the necessity of keeping inter-element phase center spacings less than approximately .75 wavelengths have forced the use of three sets of log-periodic elements - one set being added for each higher frequency band. The model discussed here represents only the lowest frequency band of the full array. A scaled frequency range of 1000 to 2500 Mc (array diameter of 29 in.) which corresponded to the 2-5 Mc range (array diameter of 1210 ft.) was employed as the model frequency limits. Typical radiation patterns of the model are presented and their relation to computed patterns are discussed.

^{*} University of Illinois Antenna Laboratory, University of Illinois, Urbana, Illinois.

1. INTRODUCTION

The ultimate goal of this work is the construction of a circular, high-gain direction finding array using frequency-independent antenna elements which would permit efficient operation over the 2-32 Mc range. Design of the array is being done by the University of Illinois Antenna Laboratory and the Radiolocation Laboratory for the Navy Bureau of Ships. The array will produce a fan-shaped beam, narrow in azimuth, which can be rapidly rotated so as to scan the entire horizon many times each minute. Essentially WARLA is a high efficiency, wide frequency band version of the present Wullenweber Antenna located southwest of Champaign, Illinois, and operated by the Radiolocation Laboratory. The efficiency of the new array should permit transmitting as well as receiving modes of operation.

The initial phases of the work were limited to investigation of individual vertically-polarized antennas which might be suitable for use in the proposed array. Since several log-periodic antennas are presently available, which are satisfactory for this application, attention is now being given to the problems associated with operating the circular array over the desired 16:1 bandwidth. This paper describes the initial feasibility study which was performed at a greatly reduced scale for economy and convenience. The measurements were made to corroborate calculated results obtained on a digital computer and to provide preliminary data on some anticipated design problems. However, since the scale factor of 500:1 is so great, an intermediate scaled design is contemplated before full scale construction is attempted. Testing of the 500:1 scale model was made possible by the recent acquisition of a 20 foot square ground-plane pattern range which has a sufficiently large aperture plate and by the application of printed circuit techniques to the construction of log-periodic antennas for frequencies above 1000 Mc.

Before discussing the scale model, it would seem appropriate to mention some of the physical and electrical specifications for the full-sized array. The overall diameter of the circular array will be between 1000 to 2000 feet. This figure will ultimately be fixed by both economic and electrical considerations. Frequency coverage of 2 Mc to 32 Mc is desired, with an efficiency adequate for transmitting purposes. Thanks to recent developments in vertically-polarized frequency-independent antennas, this bandwidth and efficiency can be

readily achieved in a single antenna. The present study, therefore, is limited to the problems associated with a broadband circular array utilizing log-periodic elements. In regard to the radiation pattern which is produced by about a 120° sector of elements, the goal is to achieve the narrowest possible beamwidth along with -10 db or better sidelobes. Studies on groups of 2 or 3 log-periodic elements firing at one another have shown that an array in which the active sector of elements fired inward and therefore through the inactive elements on the opposite side of the circular array would have serious pattern distortion - especially in the vertical plane. Thus, attention has been focused on outward firing arrays composed of 120 to 180 log-periodic elements of varying size.

The sidelobe level constraint places a restriction on the maximum phase center spacing between active elements. By banding the frequency range into three segments and switching in more elements for each band, the phase center spacing can be kept, for the most part, below .75 wavelengths - a value which both theoretical calculation and experimental work suggests is a maximum. Two factors control the phase center spacing: the diameter of the array and the number of elements therein. With the value of $.75 \lambda$ in mind, a diameter of 1210 feet was selected. The three frequency bands chosen for the preliminary design were 2-5 Mc, 5-12.5 Mc, and 12.5-32 Mc. There were 40 large elements covering the 2-32 Mc band spaced every 9° ; 40 elements covering the 5-32 Mc band and placed in between the large ones; 80 elements covering the 12.5-32 Mc band placed in between the previous elements. A sketch of this scheme is given in Figure 1c.

Due to the difficulty of modeling the array to fit into a 29 in. diameter circle which is allowable with the Scientific Atlanta ground screen aperture plate, only the lowest frequency band elements were constructed and spaced at 9° increments. A printed circuit version of the Bent Log-Periodic Zigzag^{1,2} was designed for a range of about 1000 Mc to 3000 Mc, and served as the radiating elements. The full array of 40 elements was made - even though 28 were not excited - in order to check on the possibility of a trapped wave traveling around the circle.

2. DESIGN OF MODEL

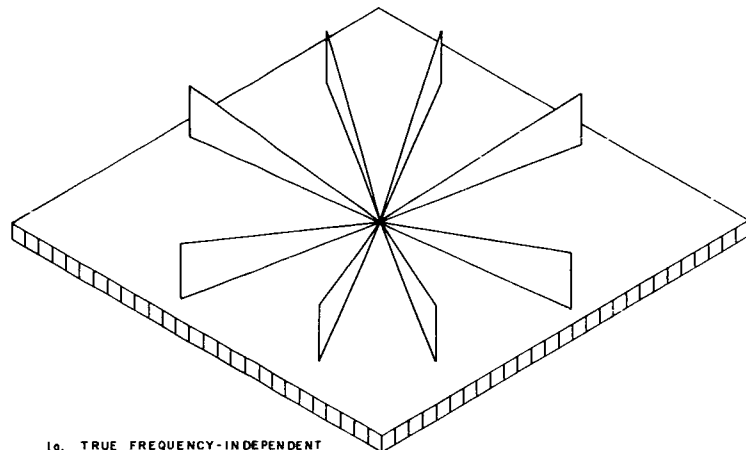
Array Excitation and Configuration

It is known that co-phased, uniform amplitude excitation of the elements produces the minimum beamwidth along with a sidelobe level somewhat higher

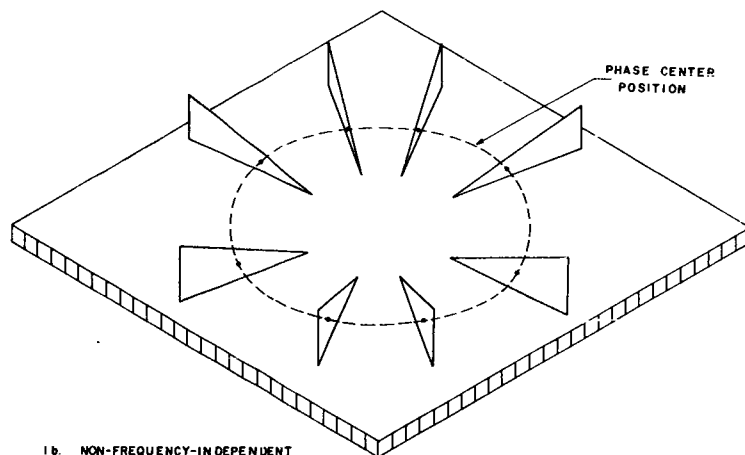
than -13 db.³ The uniform amplitude is desirable from the standpoint of simplicity in the feed network. On the other hand, any type of phase distribution could be achieved with constant time delay networks, such as sections of air dielectric coaxial cable. From an operational standpoint it was felt that sidelobes no higher than -10 db could be tolerated. Also it is important for accuracy in D-F work to have the minimum possible beamwidth. Thus the uniform amplitude co-phased excitation seemed the best choice.

Several array element configurations were considered at the beginning of the project. They are illustrated in Figures 1a, 1b and 1c. The first scheme, Figure 1a, was briefly considered because of several theoretical advantages. It is the only frequency-independent array since it places the virtual apices of the individual elements at a point so that the electrical distance between phase centers is constant with frequency. With the virtual apices at a point, the input terminals of all the elements lie conveniently on a small ring and thus, the length of feed cable is minimized. However, there are also several disadvantages with this scheme. First, the effective aperture of the array would remain constant with frequency, so that even though a large amount of real estate is occupied, no use would be made of it in terms of increased gain and accuracy at the higher frequencies. Next, all frequency-independent antennas suitable for use in the proposed array are backfire devices. Therefore, the active sector of elements would fire through the elements on the opposite side of the array. Experimental tests have shown that severe pattern distortion can be expected from this arrangement⁴. A final disadvantage results from the physical requirements that the array imposes on the elements themselves. In order to achieve high gain with the array of Figure 1a, the elements would have to be very long, i.e., the diameter of the array is increased. Not only does this create substantial mechanical problems, but the radiation pattern of the elements becomes very directive creating the need for more elements to prevent beam coggling effects. These are the main reasons why the frequency-independent array scheme was abandoned.

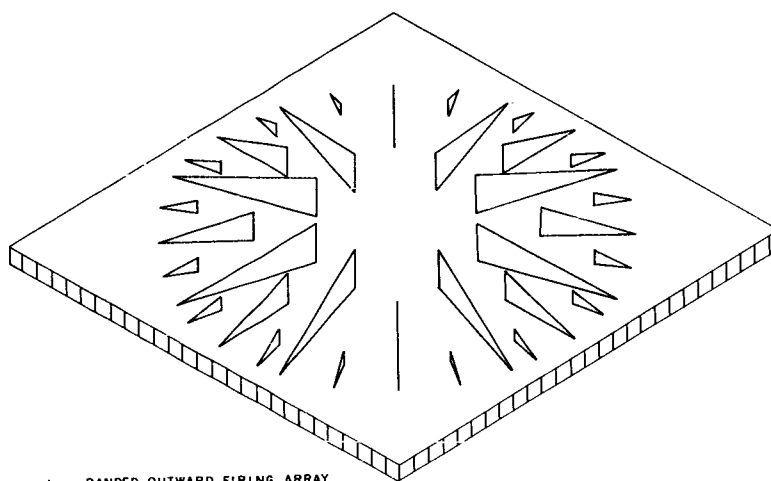
The array shown in Figure 1b is a modification of the frequency-independent design just discussed. It is an attempt to alleviate some of the problems encountered with the inward-firing array while partially preserving the good features. However, tests have shown that pattern distortion in both the horizontal and vertical planes still persists. Thus, the inward-firing



1a. TRUE FREQUENCY-INDEPENDENT
ARRAY



1b. NON-FREQUENCY-INDEPENDENT
ARRAY--INWARD FIRING



1c. BANDED OUTWARD FIRING ARRAY

Figure 1. Array Configurations.

arrays were abandoned in favor of the outward-firing arraying scheme of Figure 1c.

The outward-firing array of Figure 1c does have some advantages over the others. For example, scattering from the unexcited sector of elements is completely eliminated. Also, this array makes the best possible use of the site in terms of achieving high directivity. In fact as the frequency is varied from 2 Mc to 32 Mc, the azimuthal beamwidth will decrease from about 30° to a little over 1° . The accuracy of the array when used for direction finding will correspondingly increase.

A disadvantage of the array of Figure 1c appears when the movement of the element phase centers is considered. As the frequency of operation is raised the phase centers move outward toward the vertices of their respective elements. Thus the criterion of .75 wavelengths mentioned earlier could be quickly exceeded unless corrective measures are undertaken. These measures consist of dividing the range of 2-32 Mc into 3 bands: 2-5 Mc, 5-12.5 Mc, and 12.5-32 Mc. Assume that frequency-independent elements are available which cover the full range of 2-32 Mc. These are spaced every 9° around the array circle. The active sector in the 2-5 Mc band is then composed of 12 of these 40 large elements. When the banding frequency of 5 Mc is reached another set of 40 smaller frequency-independent elements is switched in. These elements lie in between the large elements and cover a frequency range of 5-32 Mc. When 12.5 Mc is reached a final set of 80 elements covering 12.5 - 32 Mc is added to the array. Figure 1c shows how this system might look. The active sector of elements (somewhat less than 120°) increases from 12 to 24 to 48 elements for the three bands so that when the proper array diameter is chosen, the .75 wavelength criterion is never exceeded.

Banding Considerations

The banding scheme just described was born out of a union of electrical necessity and economic practicality. It may have already occurred to the reader that the .75 wavelength criterion could be simply met without using three sets of frequency-independent elements by placing the full range elements at smaller angular increments. In this way the phase center spacing would be set at $.75 \lambda$ for 32 Mc and decrease from that value at lower frequencies. However, this is objectionable from both the electrical and economic standpoint.

If the phase center of an element lies at .59 wavelengths from the virtual apex for all frequencies and assuming a total array diameter of 1210 ft. the required angular spacing is found to be 2.25° . Therefore, $\frac{360}{2.25} = 160$ elements would be needed for the array. But each of these elements must cover the full frequency range of 2-32 Mc. So that there would be 160 elements 220 ft. long and about 130 ft. high at the large end in the array and this is economically undesirable.

Even more objectionable than the economics involved is the serious electrical problem this arraying scheme creates. Impedance studies on groups of log-periodic elements suggest that phase center spacings of less than .15 wavelengths cause a considerable increase in the VSWR of the individual elements⁵. Mutual coupling, undoubtedly, is the reason. With large elements spaced every 2.25° the phase center spacing at 2 Mc would be $.025 \lambda$ - much less than the minimum figure. The banded arraying scheme described previously has a value of $.10 \lambda$ at 2 Mc.; still below the $.15 \lambda$ figure. More impedance investigations will be needed to determine exactly the minimum spacing for the particular type of frequency-independent element used in the ultimate array.

Summarizing these considerations, it is noted that the three band system keeps the interelement phase center spacings in the range of $.10$ to $.75 \lambda$. It also uses the minimum number of large expensive elements by replacing many of these with smaller, less expensive ones. Two band and four band systems have also been considered previously and rejected for one or both of the reasons given above.

Design of Log-Periodic Array Elements

It was clear that if any sort of meaningful results were to be obtained from a microwave antenna model with a scale factor of 500:1 a high degree of constructional accuracy would have to be maintained. An error of 1/16 in. in the model represented over 31 in. in the full-sized array. Perhaps the most critical parts of the whole model were the 40 log-periodic elements. Construction techniques such as hand soldering pieces of wire or tubing or the use of miniature coaxial cable were too inaccurate to produce 40 identical antennas operable from 1000 Mc to 3000 Mc. In addition, it would have been a long and tedious job to build the elements by any hand method. Printed circuit techniques applied to the bent log-periodic zigzag antenna have resulted in a generally satisfactory model element.

All of the successful bent log-periodic zigzags built previously were three dimensional structures. So the first problem was to reduce the antenna to two dimensions; the second problem was to achieve satisfactory pattern and impedance performance. The printed element finally developed is shown full-sized in Figure 2. A small meander delay line takes the place of the phasing stubs of the original bent zigzag antenna. Low frequency pattern performance is improved by a parasitic reflector seen as a broad conducting strip behind the zigzag element. Only three connections on the antenna have to be made:

1. Connection of the feed point at the small end to the feed cable or to ground in the case of unexcited elements;
2. Connection of the last tooth of the zigzag to ground;
3. Connection of the parasitic reflector to ground.

All of the critical construction work was eliminated -- even the drafting work for the printed circuit negative was simplified by drawing it seven times life size and then photographically reducing the drawing.

The antennas were printed on an .025 in. thick epoxy-fibreglass circuit board with 2 oz. copper on one side. Numerous samples of circuit board were secured before this particular one was chosen. Even though teflon-fibreglass board had a lower dissipation factor, the epoxy fibreglass board was used because of its superior rigidity. A thickness of .025 in. was the thinnest practical in line with securing reasonably strong and stable elements.

Very little is known about the slowing properties of small meander lines set on edge such as used to phase this antenna. Therefore their design tended to be a cut-and-try process. Inspection of the radiation patterns of some early designs indicated that as the frequency was increased the epoxy-fibreglass dielectric of the circuit board exerted a greater effect on the phase delay of the meander line sections. Reducing the length of these phasing sections at the small end of the antenna more rapidly than at the low frequency end counteracted the dielectric slowing effect to some extent.

The pattern performance attained with these printed circuit elements was not as good as that found for conventional bent log-periodic zigzags at lower frequencies. Representative H-plane patterns of a single element are shown in Figure 3. No E-plane patterns are given because they were reasonably uniform, having a half-power beamwidth that decreased from about 40° at 1000 Mc to around 30° at 2500 Mc. The patterns were taken for an element whose feedpoint was 14.5 in. off the center of rotation, so some of the scallops may be due to the

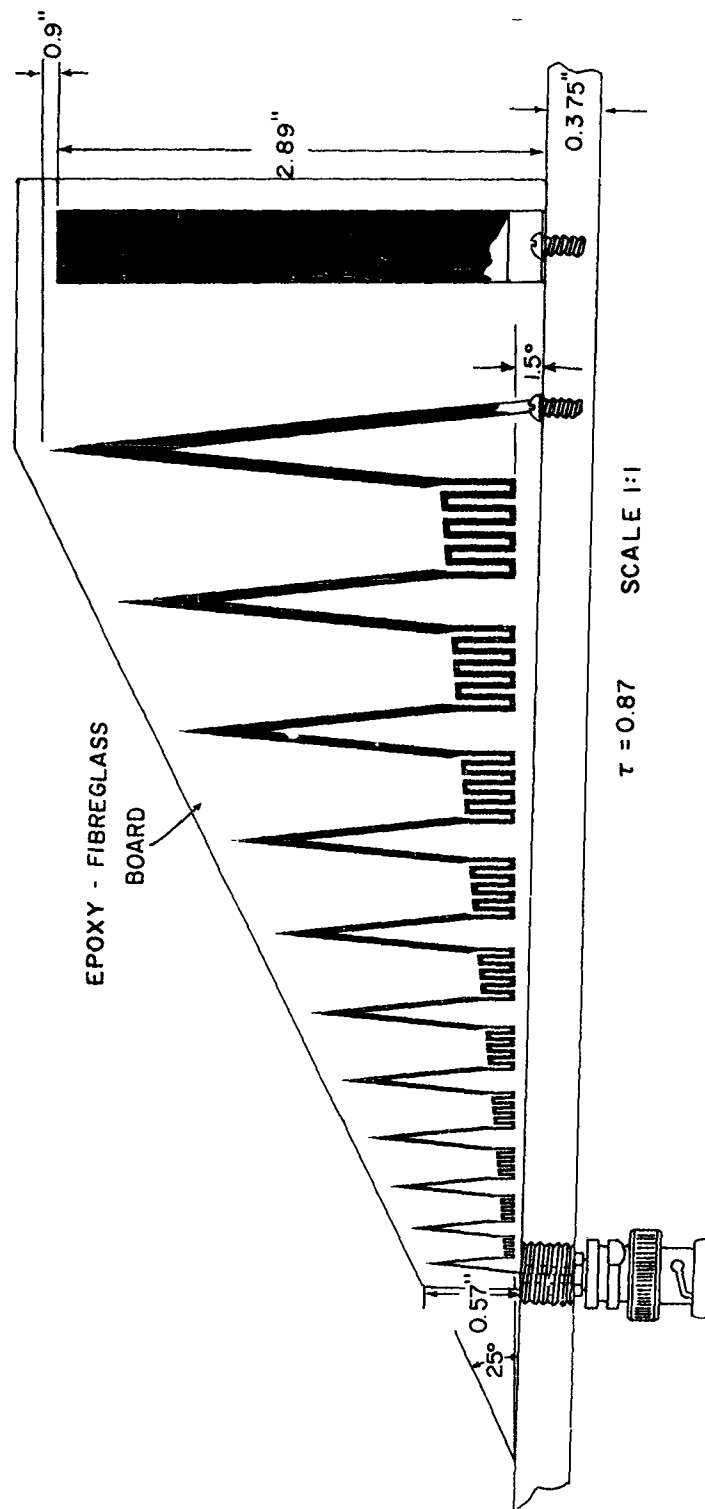


Figure 2. Printed Circuit Element used in the Array.

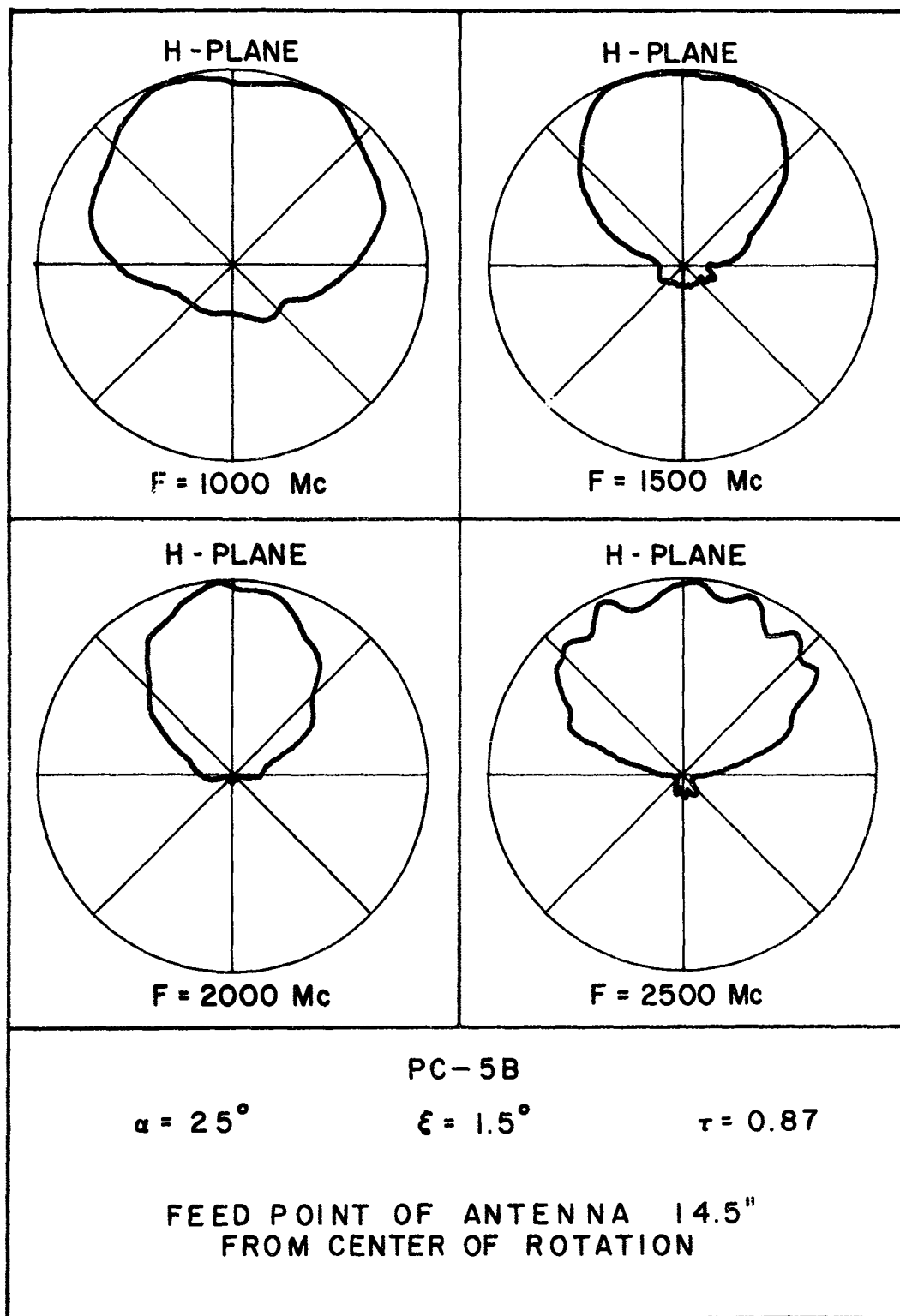


Figure 3. Patterns of a Single Printed Circuit Element.

motion of the element (used for transmitting) and the presence of edge effect on the finite ground screen. Also, because the dielectric constant of the sheet was about 5 and its thickness was .025 in. pattern scallops could have resulted from the circuit board itself, modifying the radiation pattern⁶. Finally, element pattern distortion could stem from radiation by the meander phasing line.

It will be seen in a later part of this report that element patterns even more distorted, less directive, and with a lower front-to-back ratio than the ones shown here had little effect on the total array pattern when twelve elements were operated in unison. The H-plane patterns of a single element were considerably degraded when tested in the presence of the other 39 elements. Still, as will be shown, good array patterns were measured.

Past experience with new log-periodic designs usually found impedance control rather more difficult than pattern control. This was particularly expected in a microwave design. Therefore, since a signal source with an output in excess of 25 watts would be available, each element of the active sector was padded with a 10 db. resistive pad. The pad also provided an impedance transformation from $150\ \Omega$ to $50\ \Omega$ which was thought to be necessary on the basis of impedance data of other bent zigzag antennas. As expected, the VSWR of the printed antenna was quite poor: ranging from 2:1 to 8:1 generally, with values of 11:1 and higher for frequencies above 2600 Mc. The impedance locus very approximately circled the $75\ \Omega$ point on the Smith chart. However, with the resistive pad in place the VSWR was under 2:1 with respect to $50\ \Omega$ for the entire band of 1000-2500 Mc. The importance of a good impedance match for the array elements is discussed in a later section.

Another characteristic of the printed antenna which is most important in array work is the phase center position. Studies on other types of log-periodic antennas have established that the main beam phase center lies at a constant electrical distance from the virtual apex of the structure^{7,8}. It was found that the phase center fell in the active region of the antenna, somewhat ahead of the half-wavelength element. Work with bent log-periodic zigzags, however, had suggested that the phase center position for these devices was probably at or very near to the quarter-wavelength element (this corresponds to the half-wavelength element on a free space antenna). Facilities for measuring the phase center position were not available at the time construction was

started on the phasing network for the 500:1 model, so the assumption was made that the phase center position resided directly at the quarter-wavelength element for all frequencies. This gave a distance of .54 wavelengths from the virtual apex -- which of course is strictly a geometrical result, dependent only on the α angle (see Figure 5a) of the structure.

Later, when measurements could be taken, it was found that this was a good assumption to have made. A graph of the measured phase center distances is shown in Figure 4. These were taken at an elevation of 15° and a $\pm 60^\circ$ swing about the main beam in azimuth. It can be seen that the distance in wavelengths is not a constant, as expected. The frequency dependency apparently results from the active region impinging on the truncations of the structure. These measured values of phase center position were used in the computer program to calculate the array patterns.

The Magnavox Company in Urbana, Illinois did the printing and etching job to produce the 500:1 scale antennas from the negative and circuit board supplied to them.

Feed System

The feed system for the circular array had to meet two fundamental requirements: the first was the equal distribution of power to all active elements; the second was the cophasal excitation of all active elements. As mentioned previously, cophasal and uniform amplitude excitation ensure the arrival of maximum signal at the receiver input when receiving with the array and in the case of transmitting with the array, uniform signal at the active antennas.

The first step in designing the feed system was the calculation of the phase delay necessary for cophasal excitation of the array. Defining P_n (see Figure 5b) as the phase difference between element 1A and the n th element, it is easily shown that

$$P_n = \left(\frac{D_A}{2\lambda} - \frac{d}{\lambda} + \frac{b}{\lambda} \right) \left(\cos \frac{\phi_E}{2} - \cos \frac{(2n-1)}{2} \phi_E \right) \left(360^\circ \right) \quad n = 2, 3, 4, 5$$

where D_A is the diameter of the array, d is the distance from the virtual apex of the element to the phase center of the element, and b is the distance from the virtual apex to the feed point of the element. To elevate the main beam to some angle θ (cophasal angle) above the horizon, multiply P_n by $\cos \theta$.

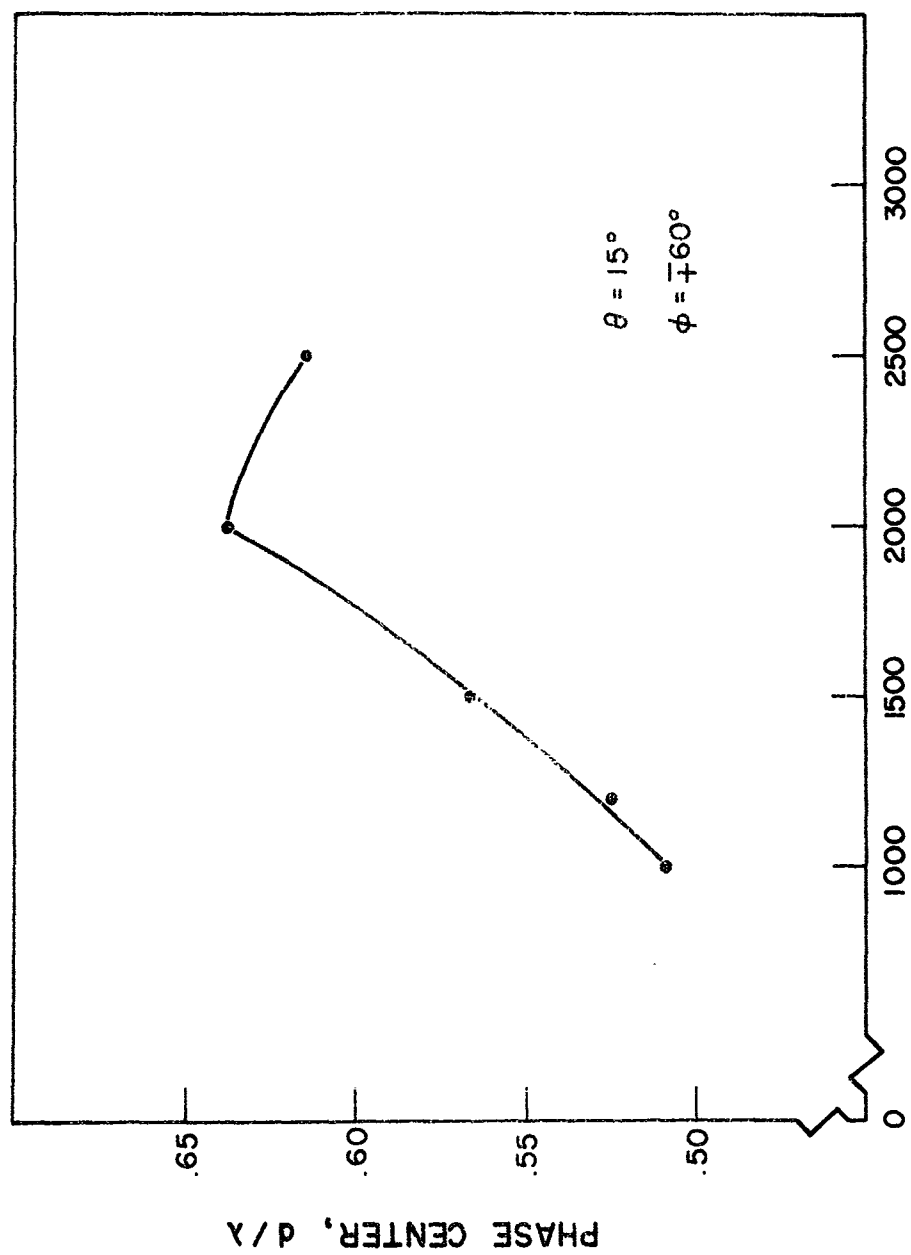


Figure 4. Phase Center Position in Wavelengths from the Virtual Apex of the Printed Circuit Elements.

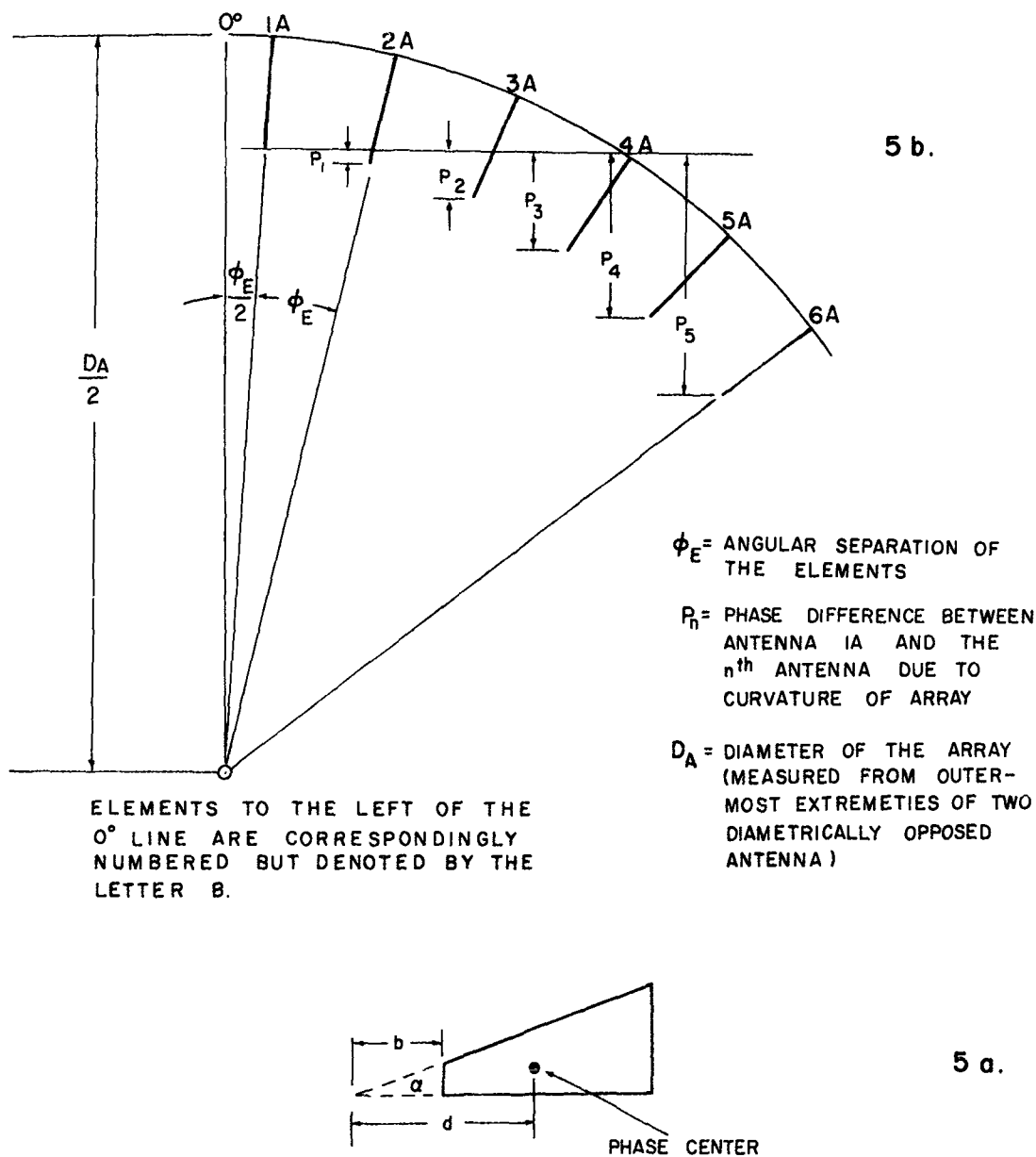


Figure 5. Geometry of the Individual Elements in the Array.

For the particular version of the bent log-periodic zigzag antenna used in the array,

$$\frac{d}{\lambda} = 0.54 \quad D_A = 29 \text{ in.}$$

$$\phi_E = 9^\circ \quad \theta = 0^\circ$$

$$b = 1.07 \text{ in.}$$

First the phase difference between antenna 1A and the other antennas over the 1000-2500 Mc frequency band was calculated; then these figures were converted to the phase delay necessary for cophasal excitation. With respect to phasing of the array it was decided to use fixed lengths of coaxial cable which would be cut so as to provide the proper phase delay at 2000 Mc. Although this approach was employed mainly because of its economic merit, it was also used to give an indication as to how much phase deviation in the feed system could be tolerated. As was mentioned previously in this report, the ratio d/λ was found not to be a constant but varied as a function of frequency as shown in Figure 4. Since the cables were cut for $d/\lambda = 0.54$, the variation in d/λ caused the phase delay to vary more radically than expected. Figure 6 gives an indication as to how the actual measured phase delay compared to the required delay. In the expression for P_n , d/λ becomes an important factor at the lower frequencies and because the actual measured d/λ was smaller than the calculated value of 0.54, the net effect was to increase phase deviation at the lower frequencies and shift the zero deviation mark to some frequency greater than 2000 Mc. The phase deviation between the corresponding A and B feed systems is due to slightly different lengths of coaxial cable and/or different paths of travel through the power divider-pad combination. To check on how this phase deviation between corresponding A and B elements affected the patterns, the phasing cables to corresponding A and B elements were interchanged. Upon comparison of the patterns of the array operating in its normal phasing and patterns of the array operating in interchanged phasing (A to B, B to A), no noticeable deviation was detected. This indicated that mutual coupling between elements in the array might be a very dominant factor (that is, more of a factor than nominal deviation in the phasing of the individual antennas).

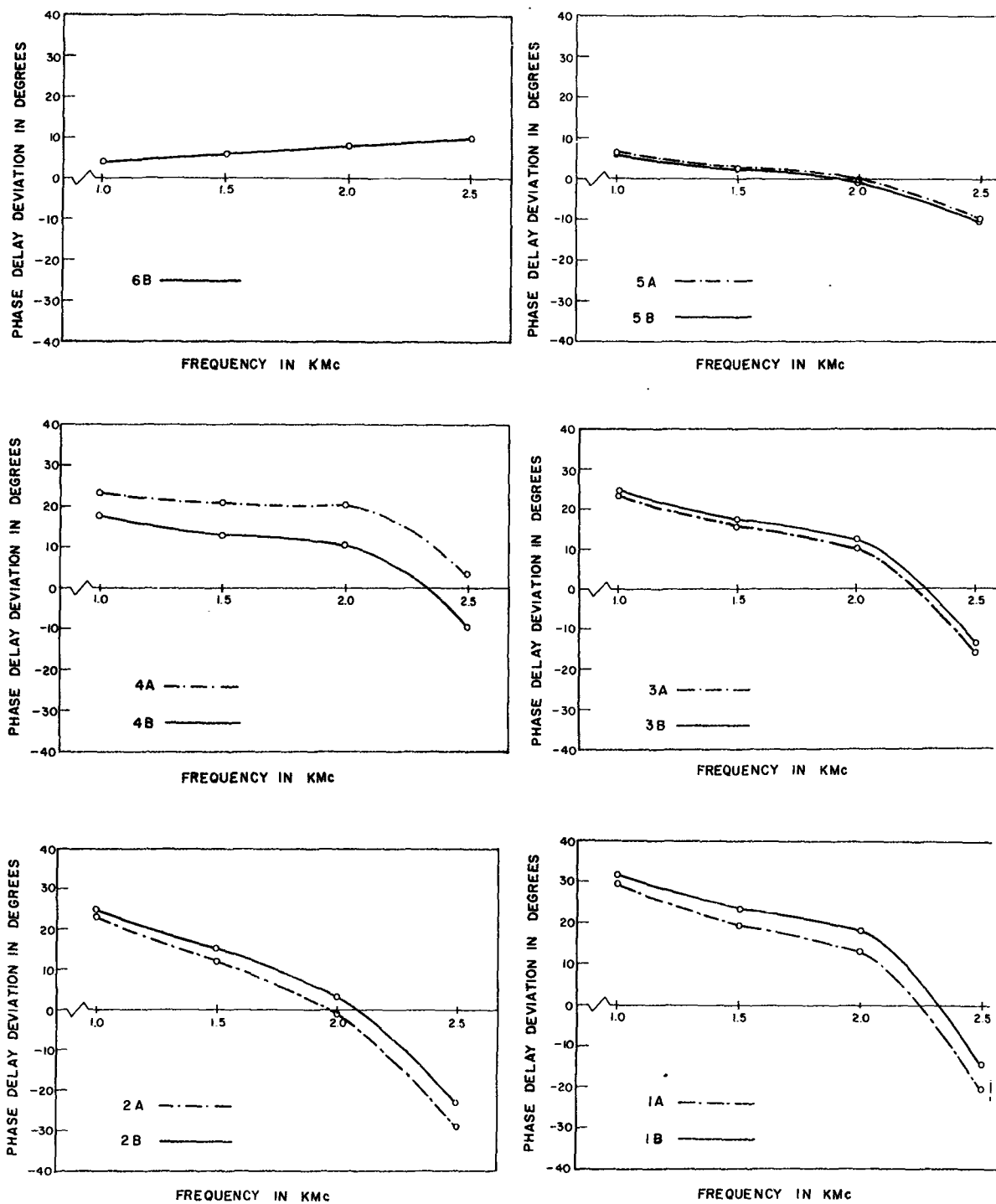


Figure 6. Deviation in Phase Delay from that Necessary for Cophasal Excitation of the Array.

The construction of the phasing cables was made comparatively simple by the fact that all lengths of cable could be made relative to a single reference length of cable. Therefore, since element 6A(6B) required 0° of phase delay over the entire band of frequencies, its feed cable was selected as a convenient reference. Cable 6A was cut long enough to reach from the power divider, which was some distance under the aperture plate, to element 6A. From previous calculations and using the velocity factor of the teflon insulated coaxial cable it was possible to calculate approximately how long to make the other cables. Then to exactly determine these lengths, the following measurement procedure was employed (see Figure 7): the null position (X_R) with the shorted reference cable attached to the slotted line was recorded, then the shorted cable under test was connected to the slotted line and the next null position toward the load (X_x) was recorded.

If the required additional length is less than 180° , the measured additional length is $\left[\frac{X_x - X_R}{\lambda} \right] 360^\circ$. If the required additional length is greater than 180° , the measured additional length is $n180^\circ + \left[\frac{X_x - X_R}{\lambda} \right] 360^\circ$, where n is the largest integer ratio of the required phase delay to 180° . The cables were initially cut to a length given by

$$l = l_o + \left[\frac{\phi_n}{360} (0.69\lambda) \right] + 1/2 \text{ in.}$$

where l_o = reference cable length, ϕ_n is the required phase delay for the n th element, 0.69 is due to teflon insulation, and the $1/2$ in. ensures that the cable will never be too short and yet will not be greater in length than $\lambda/4$ or 90° .

As stated previously in this report, 150Ω to 50Ω resistive (10 db loss) impedance transforming pads were employed on the individual elements which limited the VSWR to a maximum value of 2:1 with respect to 50Ω . Since the lines feeding the individual elements are terminated by the elements when the array is operated in the transmitting mode, the VSWR on the feed lines is determined by the impedance of the elements. Thus, it was decided to transmit with the array and use a power divider which was uncompensated with respect to impedance, i.e., no impedance transforming devices.

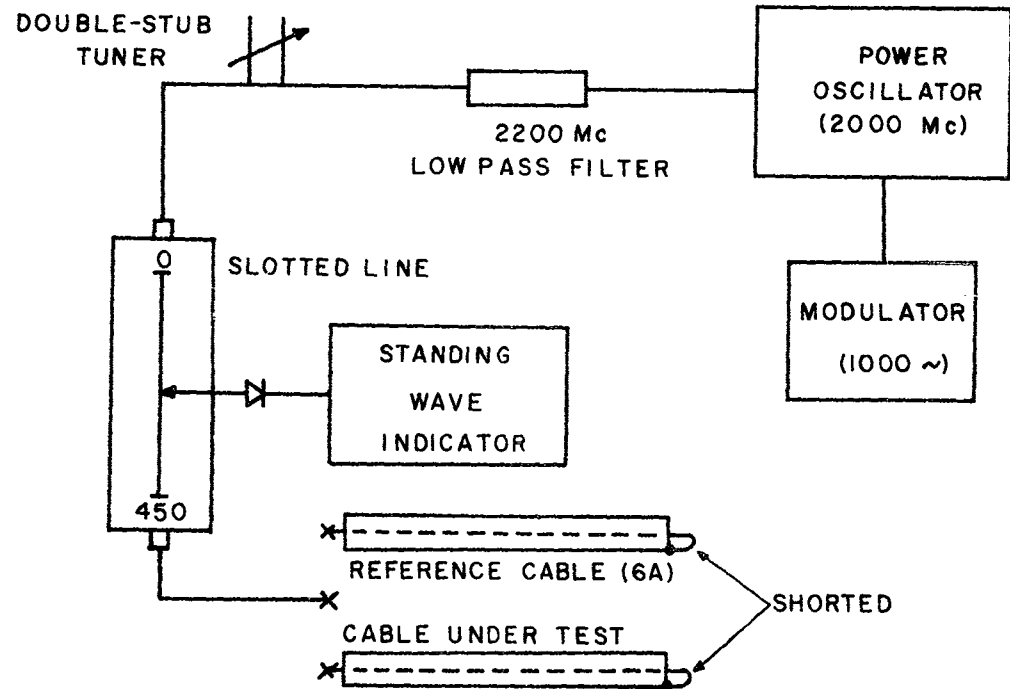


Figure 7. Block Diagram of Equipment Setup for Measurements Performed on Phasing Cables.

The main consideration in designing the uncompensated power divider was keeping all output arms of equal length. Also, as the number of outputs increases the transition from the outputs to one input becomes more difficult to construct. It was found that two six-output power dividers were easier to make than one twelve-output. The end result is shown in Figure 8. The BNC connectors are Amphenol 31-356 "Quick Crimp" and the type N connectors are UG-58A/U.

3. CONSTRUCTION OF MODEL

Mounting Plate and Radiating Structure

Although the rotating aperture of the Scientific-Atlanta ground screen is 36 in. in diameter, only 31 1/4 in. is accessible from the underside due to the presence of a supporting lip. The array diameter of 29 in. was chosen to provide clearance for the BNC connectors, resistive pads, and phasing cables which were attached to the active elements from below. The element placement on the aperture plate is illustrated in the drawing of Figure 9. A photograph of the completed array is shown in Figure 10.

The active sector of driven elements was composed of 12 of the 40 printed antennas giving an angular sector of 108° . Slightly more directivity might have been obtained by extending this to 117° with 13 driven elements but, that would have made the power distribution and phasing more difficult. An odd number of elements would have destroyed the symmetry of the power splitters -- symmetry which critically affected the power division in the mismatched system.

Elements immediately adjacent to the last active elements (6A and 6B) were terminated with $50\ \Omega$ commercial loads through $50\ \Omega$ to $150\ \Omega$ pads. The next two elements on either side were terminated with $150\ \Omega$ loads made in the laboratory with BNC connectors and miniature carbon film resistors. These four matched elements served to simulate the actual array situation wherein all unused antenna elements would be connected to matched cables. Both in the interest of holding down costs and for simplicity in construction all of the rest of the elements were connected to ground at their feed points.

Sufficient strength for the support of the elements was secured from the three connections; although some difficulty was experienced with open circuits

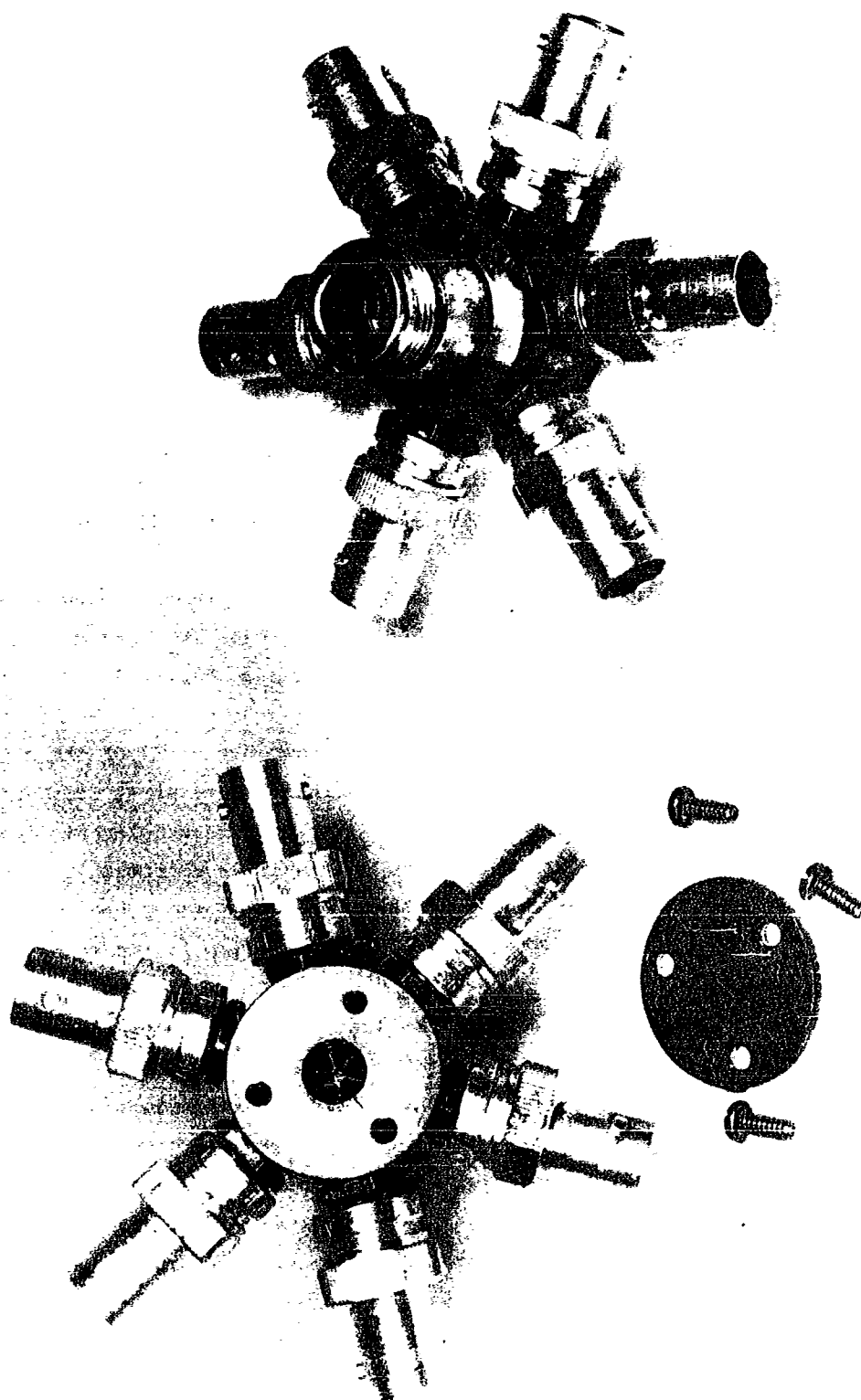


Figure 8. Power Dividers used in the Feed System for the WARLA Model.

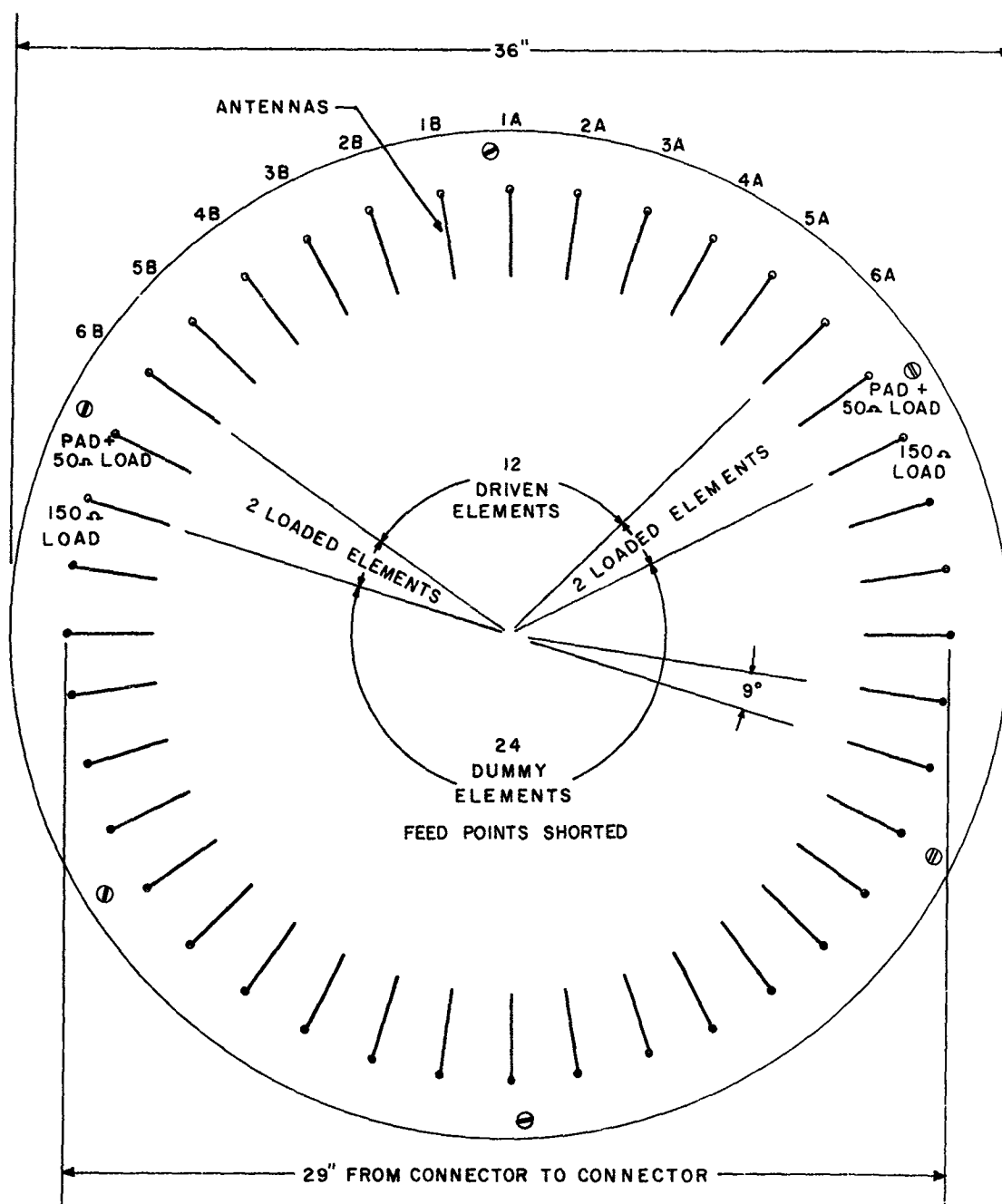


Figure 9. Element Location on Aperture Plate.

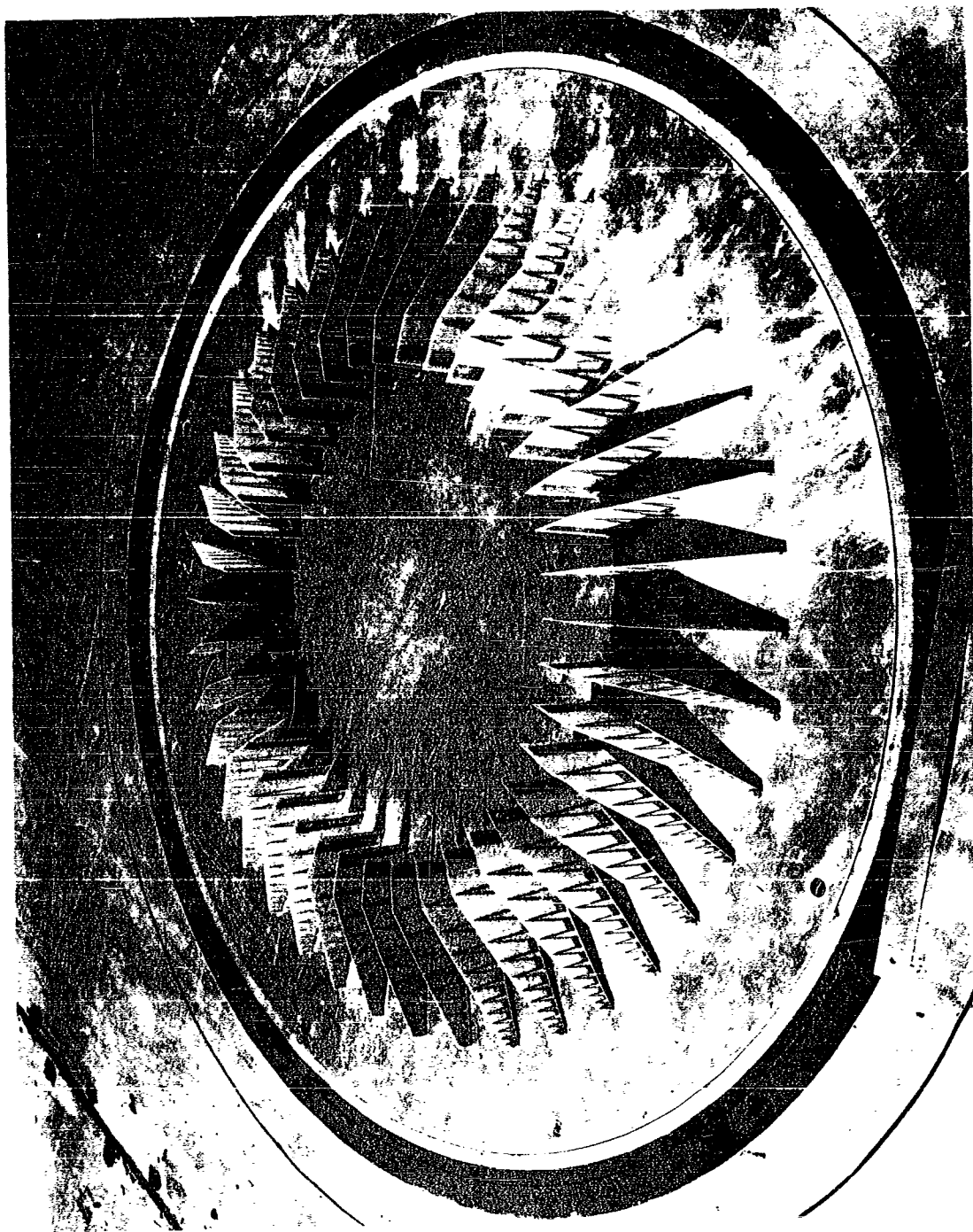


Figure 10. Finished WARLA Scale Model.

at the feed points. The copper elements at the tip of the antenna were so narrow that the metal would pull away from the circuit board with any slight strain. To remedy this a small piece of copper wire was soldered along the first vertical conductor and thence to the center conductor of the BNC connector. Plastic cement was then run between the copper wire and the printed circuit board to provide a strong joint.

A final detail should also be mentioned. It was desired to have a small, neat transition from the coaxial system to the feed points of the elements; but ordinary BNC panel feed-throughs not only seemed too large and abrupt, but also were difficult to mount properly on the 3/8 in. aluminum aperture plate. A satisfactory solution was found with the use of Ampheol 31-351 "Quick Crimp" BNC connectors. These connectors have a tube .380 in. long and .168 in. in diameter through which the coaxial cable enters. This tube was sweat soldered into a brass plug which was then threaded and screwed into the aluminum plate. The assembly is visible in Figure 2.

The Computer Program

A Bendix G-20 computer was employed in the analysis of the radiation pattern for various element configurations and excitations. The synthesis of an optimum array pattern (in the sense of Dolph) for a circular array of discrete elements has not yet been satisfactorily solved³. Imposing the cophasal excitation requirement further complicates the problem. On the other hand, pattern analysis with the aid of computers is both simple and rapid. And it is an approach which has been widely used in practical design work in the past and found to give satisfactory results.

Basically, the computer performed a vector addition of the contributions from the active elements at given azimuth and elevation angles. Every characteristic of the circular array could be changed at will; array diameter, size, length, orientation, and spacing of the elements; element radiation pattern and phase center position; array phase and amplitude excitation. Two major assumptions had to be made: mutual coupling and scattering effects were taken as zero; the ground was a perfect conductor. The effect of these assumptions will be considered in the next section.

As a check on the program and computer several data points were hand calculated. Agreement to three significant figures was obtained.

4. EXPERIMENTAL AND COMPUTED RADIATION PATTERNS

Test Facilities and Measurement Procedure

As stated in the introduction, one of the reasons for going ahead with the 500:1 model was the availability of the new Scientific-Atlanta ground-plane pattern range. A few words about this facility and its associated equipment are necessary before proceeding to consideration of the patterns measured.

The basic ground-plane is 20 feet square with a fibre-glass boom carrying the probe antenna that swings parallel to two sides of the screen in the vertical plane. A photograph showing part of the ground-plane and boom is given in Figure 11. The separation between the probe antenna and the model under test is 15 feet. Visible in the photograph is a wire mesh extension to the ground-plane which was found to be necessary in tests after the facility was erected. Scientific-Atlanta's design had the probe antennas swinging in an arc that was outside the perimeter of the ground-plane. Thus, when vertical plane patterns were attempted serious pattern distortions resulted from edge diffraction as the probe antenna illuminated the side of the plane which lay between. Several things were tried with absorbers and rolled edges, but only the ground screen extension seen in Figure 11 had much effect. The extension carries the ground-plane out past the probe antennas so that its edge is not illuminated very strongly. Edge diffraction, although reduced in severity, still remained -- becoming more serious at higher frequencies. Further extension of the ground-plane, with special shaping of the side, it is hoped, will eliminate this problem altogether.

The plane itself serves as a roof of a 20 ft. by 20 ft. equipment room, which in turn is mounted on a metal tower. There are a few buildings which could have caused scattered fields as the energized array was rotated. Some scattering could also have been produced by the fibre-glass boom and the metal structure to which it was fastened. However, the latter was protected with absorbing material set along either side of the ground-plane when azimuthal patterns were being taken.

With the longer boom of the Scientific-Atlanta range, the $\frac{2D^2}{\lambda}$ criterion was satisfied at all frequencies in the model frequency limits. The projected aperture of the array was 1.06λ across at 1000 Mc, giving a value of 2.43 ft.

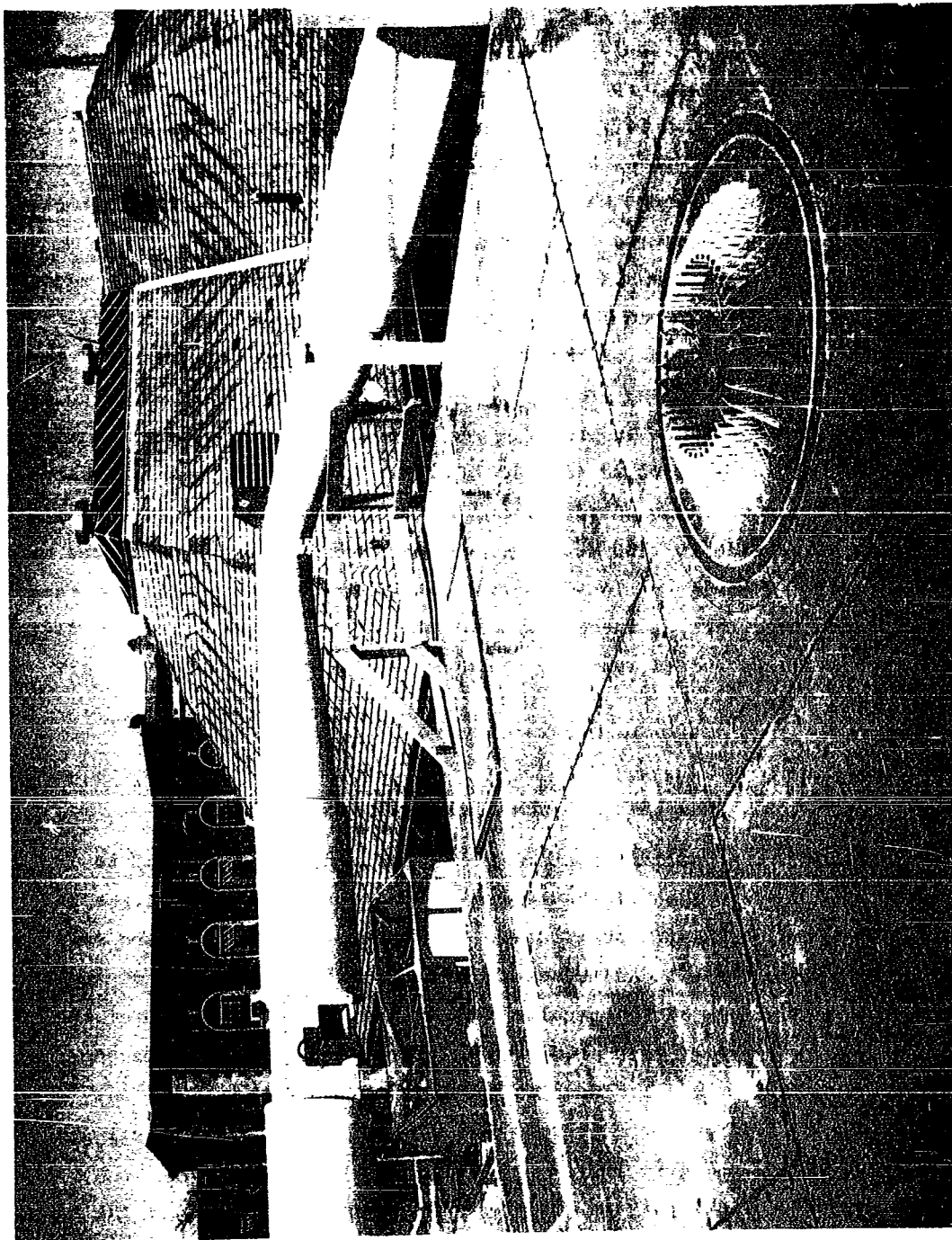


Figure 11. View of WARLA Model on Ground Plane Pattern Range.

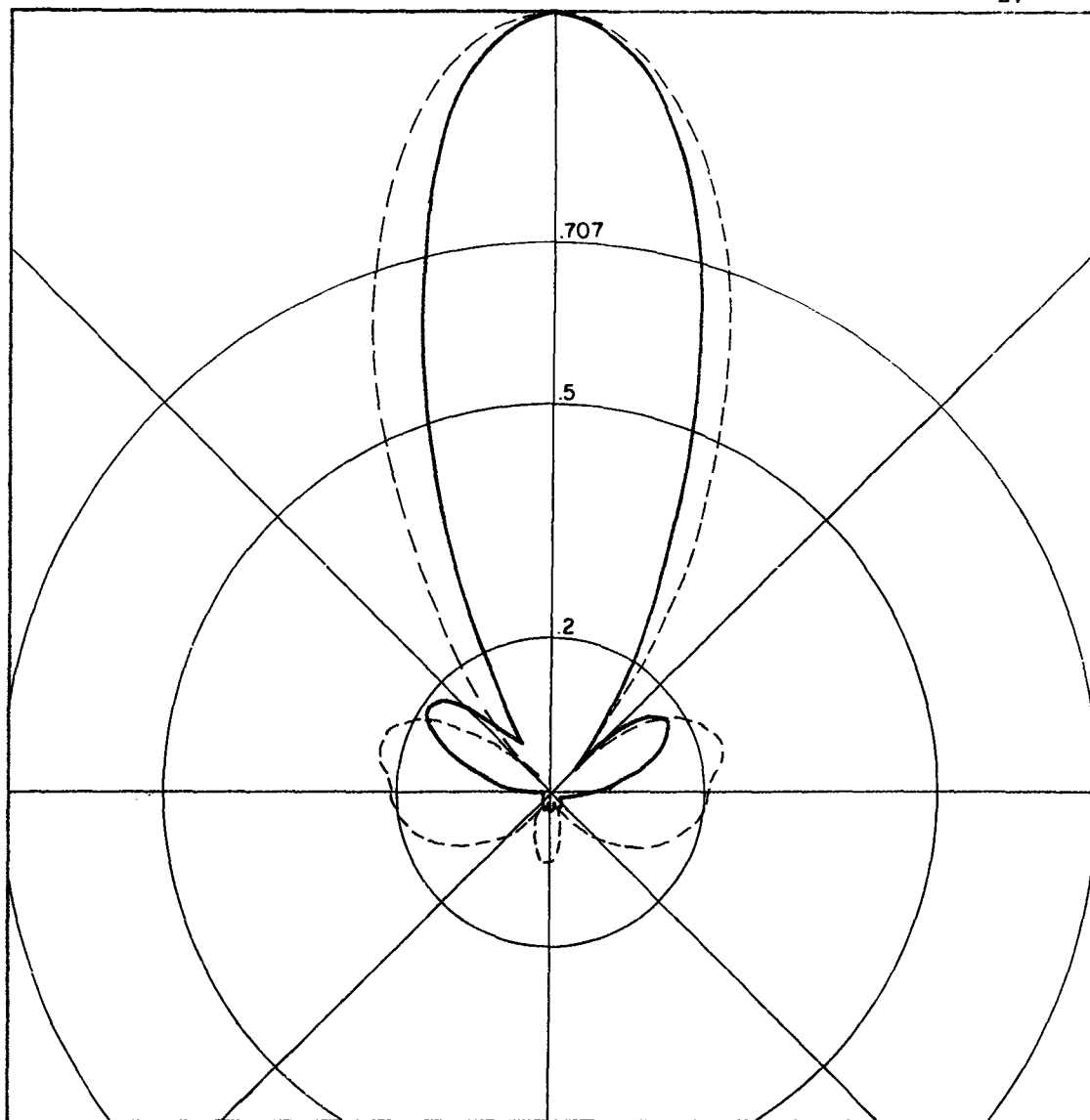
for $\frac{2D^2}{\lambda}$. At 2500 Mc the projected aperture was 4.05λ and $\frac{2D^2}{\lambda}$ was 12.96 ft. - inside the probe to model spacing. It is interesting to note that the ITE Antenna Handbook gives the following relation for uniformly illuminated rectangular apertures: half-power beamwidth = $\frac{51}{D/\lambda}^\circ$. In the present case this turns out to be 48.2° at 1000 Mc and 12.6° at 2500 Mc. Considerably narrower beams than those were measured on the actual model.

The pattern recorder was a new Scientific-Atlanta polar recorder, model APR30 with a model PFA-25 pen function amplifier. A crystal detector was used on the square-root mode of the pen amplifier. It had been intended to use a bolometer for detection, but the power oscillator which was supposed to supply over 25 watts did not function properly and so most patterns were taken with a GR Unit Oscillator. At 1500 Mc and 1800 Mc there was enough signal to use a bolometer, and a comparison between the crystal patterns and bolometer patterns showed some difference at 1500 Mc. However, at 1800 Mc the patterns were essentially identical. A corner reflector served as the probe antenna for the range 1000-2000 Mc; above that, a waveguide horn was used. Care was taken to filter the rf signal source and to avoid overloading the crystal detector for all measurements.

5. MEASURED AND COMPUTED RADIATION PATTERNS

Probably the most salient feature in the patterns of Figures 12 to 15 is the fact that the beamwidth of the measured radiation patterns averages about 25% less than the calculated beamwidths. The number and level of the sidelobes generally match up; but, in all cases the measured sidelobes occur at angles closer to beam maximum. In particular the measured sidelobes are lower than predicted at 2 Mc and higher than predicted at 5 Mc. An excellent front-to-back ratio is maintained at all frequencies in spite of the rather low front-to-back ratios of the element patterns at some frequencies. Measured vertical plane patterns are shown in Figure 16.

A large part of the pattern differences undoubtedly stems from the basic assumptions which must be made in programming pattern calculations on the computer. First and foremost of these is the assumption that no mutual coupling exists between elements in the array. Of course, this is not true; but a program which attempted to evaluate such a factor (if such a factor



1000 MC
(2 MC)

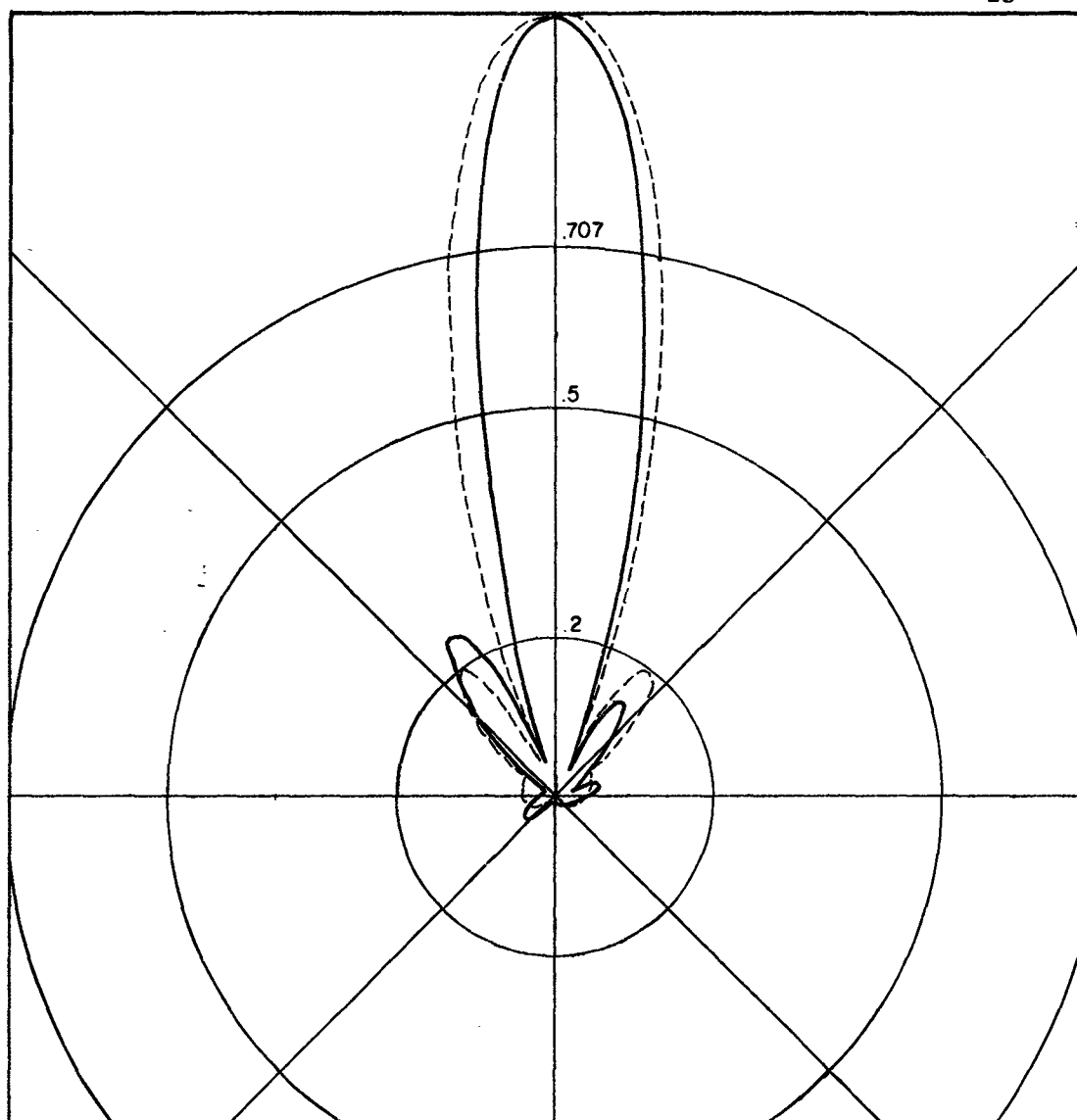
MEASURED —————
 TOTAL ELEMENTS 40
 COPHASAL ANGLE 0°
 OUTWARD FIRING ARRAY
 BEAMWIDTH CALC. 37.4°
 MEAS. 28.7°
 FRONT TO BACK RATIO CALC. 21.3 DB
 MEAS. 40 DB
 ELEMENT PATTERN FUNCTION
 $(\cos .5 \phi_0)^{1.08}$

COMPUTED - - - - -
 ACTIVE ELEMENTS 12
 ELEVATION ANGLE 5°
 ARRAY DIAMETER 29" (1210')
 SIDE LOBE LEVEL

ϕ	57°	75°
CALC.		-13.0 DB
MEAS.	-15.4 DB	

 PHASE CENTER POSITION (d/λ)
 0.509

Figure 12. Computed and Measured Array Patterns (Horizontal Plane).



1500 MC
(3 MC)

MEASURED _____

TOTAL ELEMENTS 40

COPHASAL ANGLE 0°

OUTWARD FIRING ARRAY

BEAMWIDTH CALC. 22°
MEAS. 17.1°

FRONT TO BACK RATIO CALC. OVER 40DB
MEAS. 40 DB

ELEMENT PATTERN FUNCTION

$(\cos .75 \phi_e)^{1.345}$

COMPUTED - - - - -

ACTIVE ELEMENTS 12

ELEVATION ANGLE 5°

ARRAY DIAMETER 29" (1210')

SIDE LOBE LEVEL

ϕ	-32°	37°
CALC.		-14.1 DB
MEAS.	-12.1 DB	-16.4 DB

PHASE CENTER POSITION (d/λ)
0.567

Figure 13. Computed and Measured Array Patterns (Horizontal Plane).

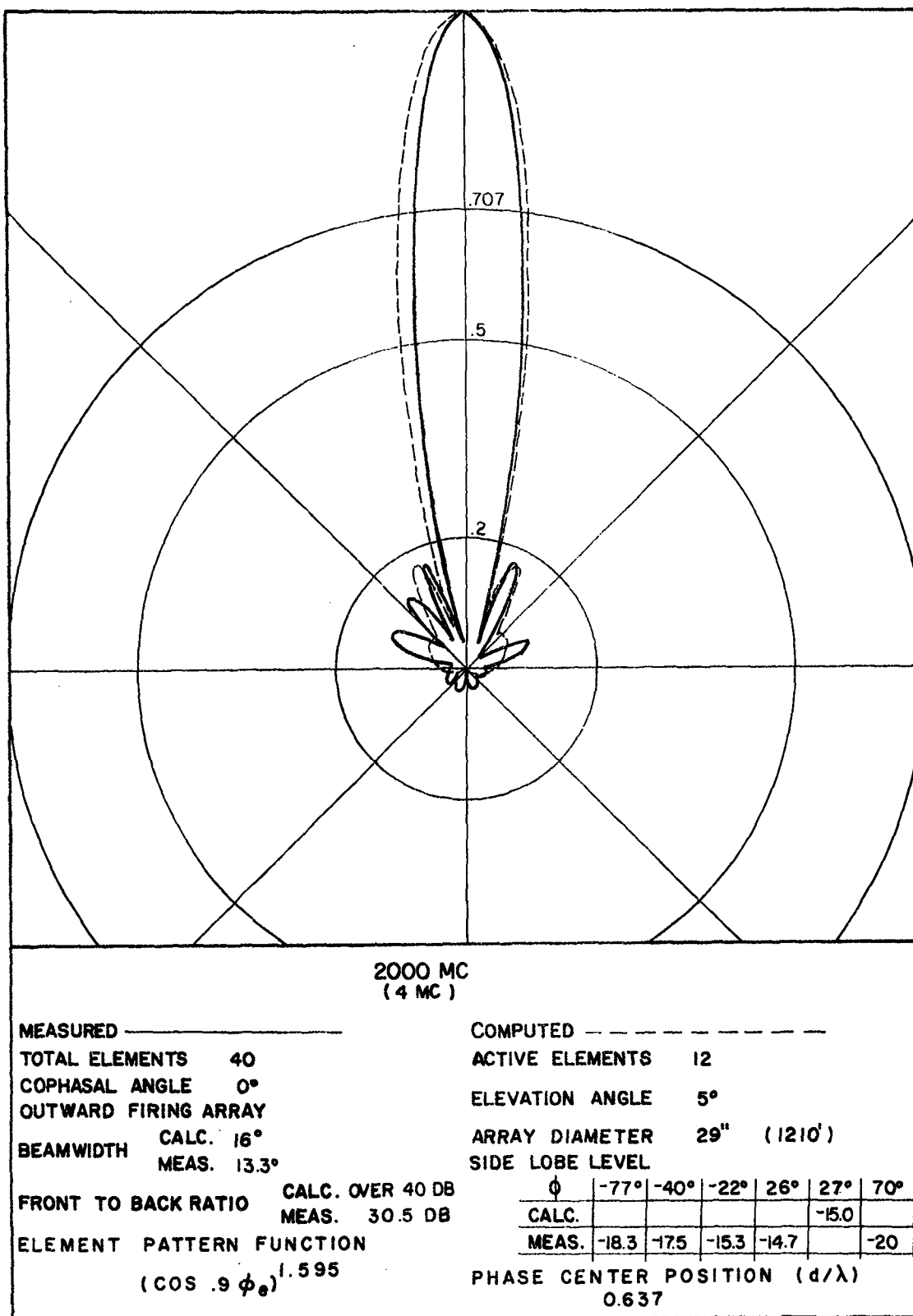


Figure 14. Computed and Measured Array Patterns (Horizontal Plane).

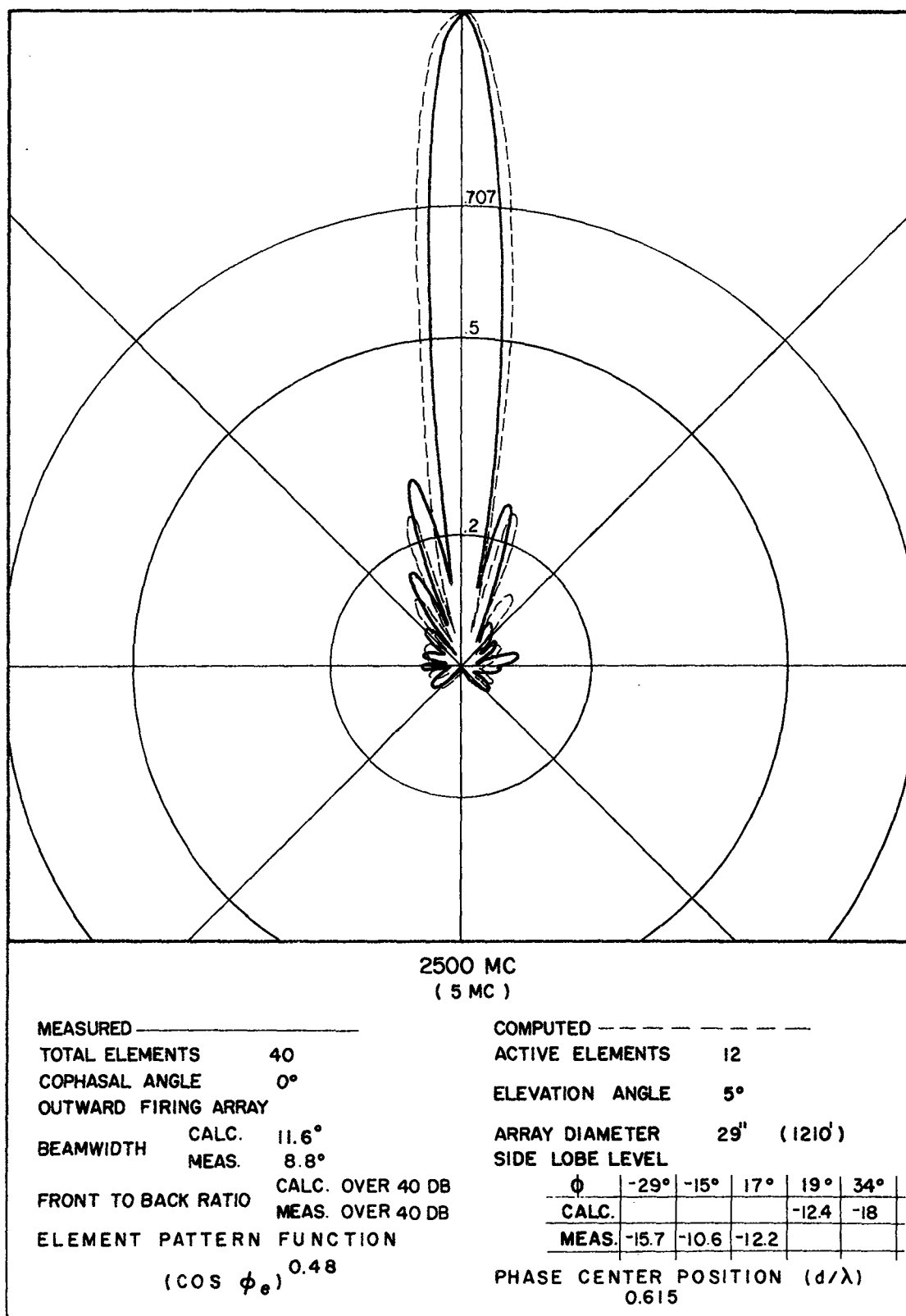


Figure 15. Computed and Measured Array Patterns (Horizontal Plane).

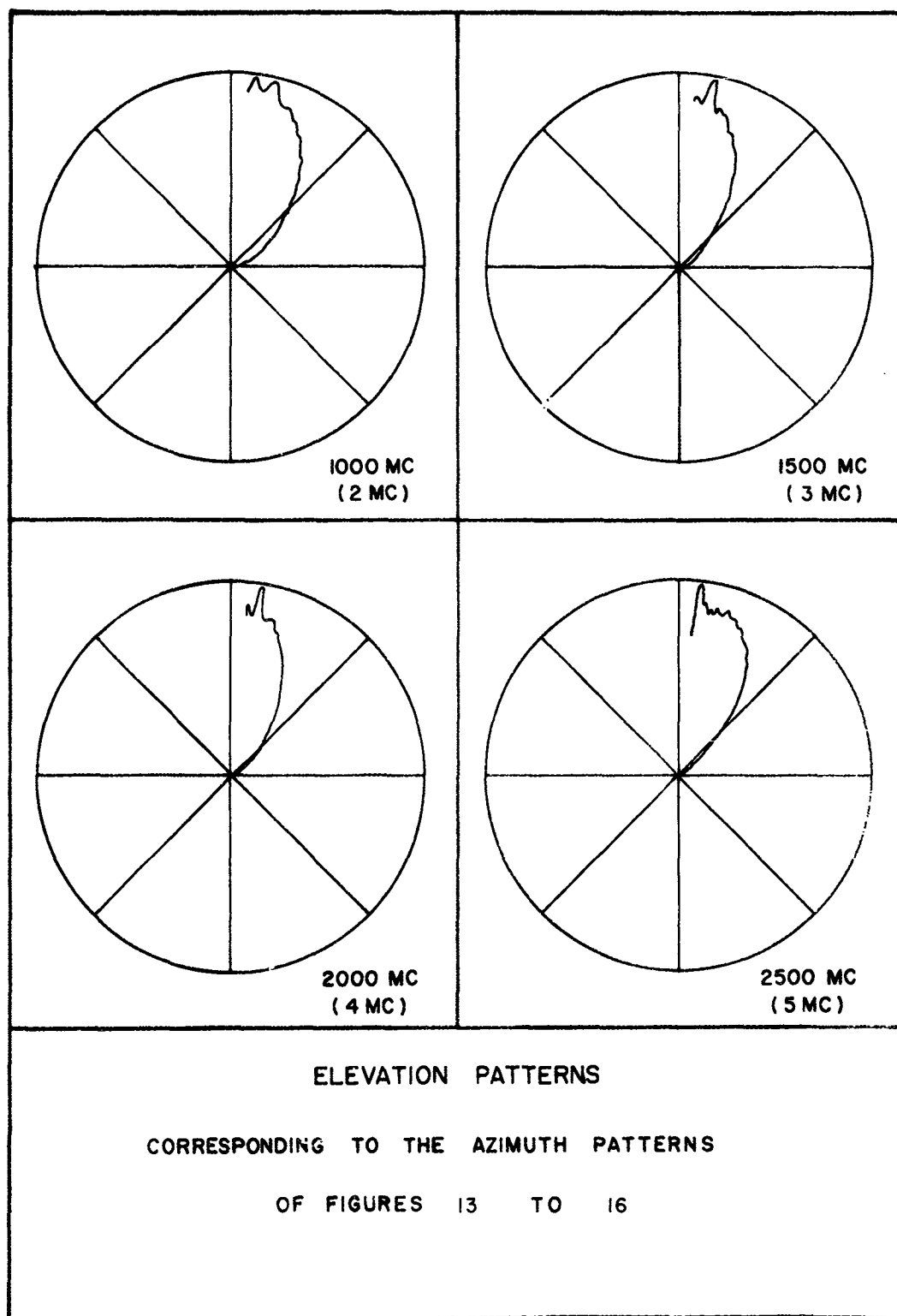


Figure 16. Measured Array Patterns (Vertical Plane).

could be calculated) would be difficult, indeed, to write. When the patterns of a single printed circuit element are taken in the presence of the other 39 elements of the array, considerable distortion results. Some representative patterns are shown in Figure 17. It is interesting to note, however, that while on one hand the mutual coupling and scattering causes the element patterns to broaden out considerably, it produces on the other hand a narrowing in the array pattern.

Another assumption -- or in this case, idealization -- is that the phase and magnitude of the element currents are close to the ones desired. Several factors influence the power distribution and phasing of the active elements. First the environment of each element plays a part. For instance, the elements at the extremes of the active sector have an excited element on one side and an unexcited element on the other; while elements near the center have excited elements on both sides. The difference in environment causes differences in impedance and mutual coupling, and thus, differences in power distribution and phasing.

A second assumption is that co-phasal excitation has been achieved, or at least approximated in the feed system of the scale model. It was known in advance that co-phasal excitation theoretically could be obtained at only one frequency in the band if lengths of coaxial line were employed as the delay mechanism. However, for a 2.5:1 band, the maximum deviation (including errors in construction and movement of phase center position) for any element of the array from the desired phase distribution was about 30° . This maximum error occurred at the band limit frequencies of 1000 Mc and 2500 Mc. The patterns show that the measured sidelobes, at least, are best predicted at the midband frequencies.

The H-plane half-power beamwidths and the directivity plotted against frequency are shown in Figures 18 and 19 respectively. Kraus's formula¹⁰:

$$D = 10 \log_{10} \frac{41,253}{E_H E_V}$$

was used to calculate the directivity. Both elevation and azimuth patterns were taken from a frequency of 800 Mc to 3,200 at intervals of 100 Mc. Already

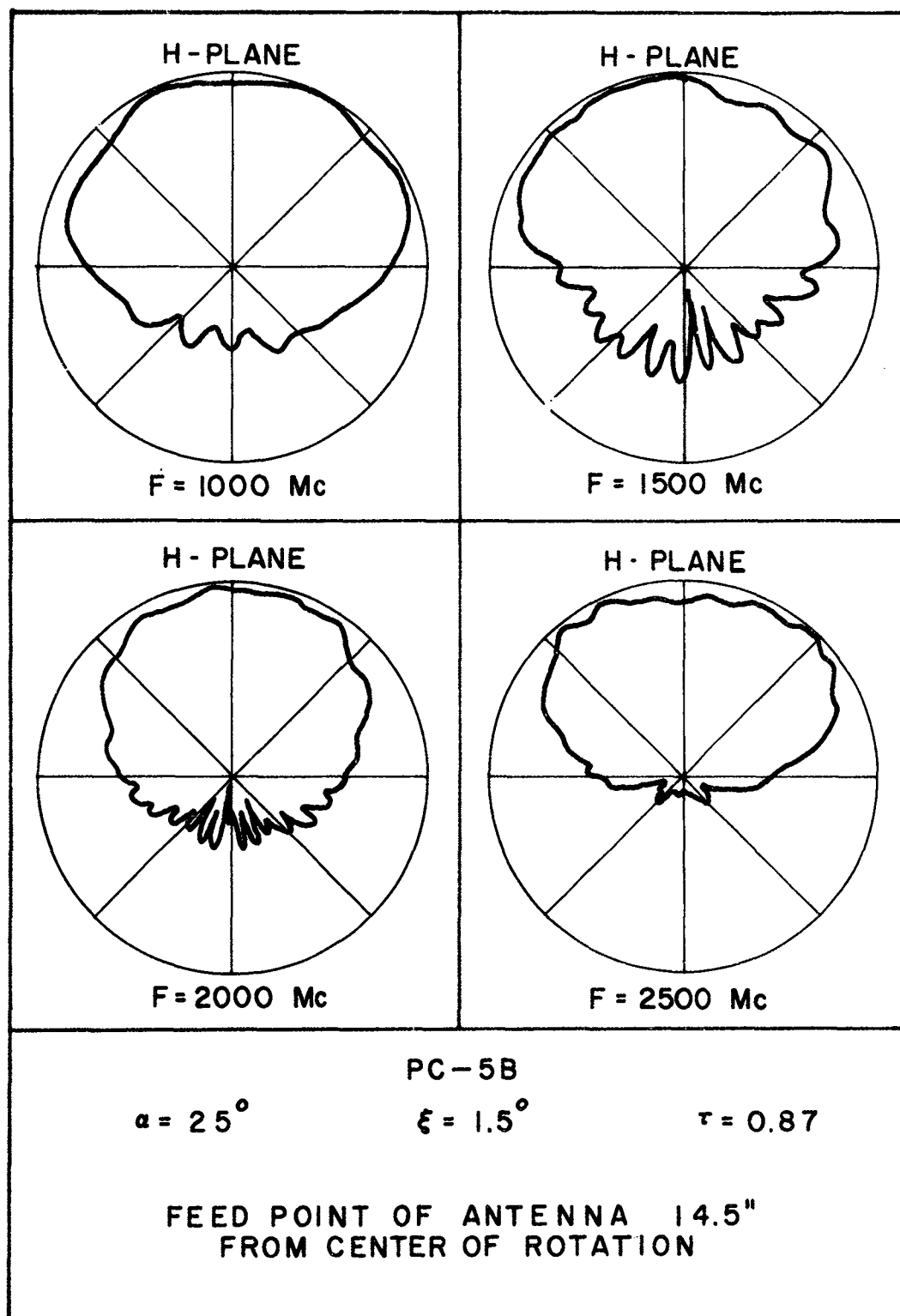


Figure 17. Patterns of a Single Printed Circuit Element in the Presence of 39 Other Elements.

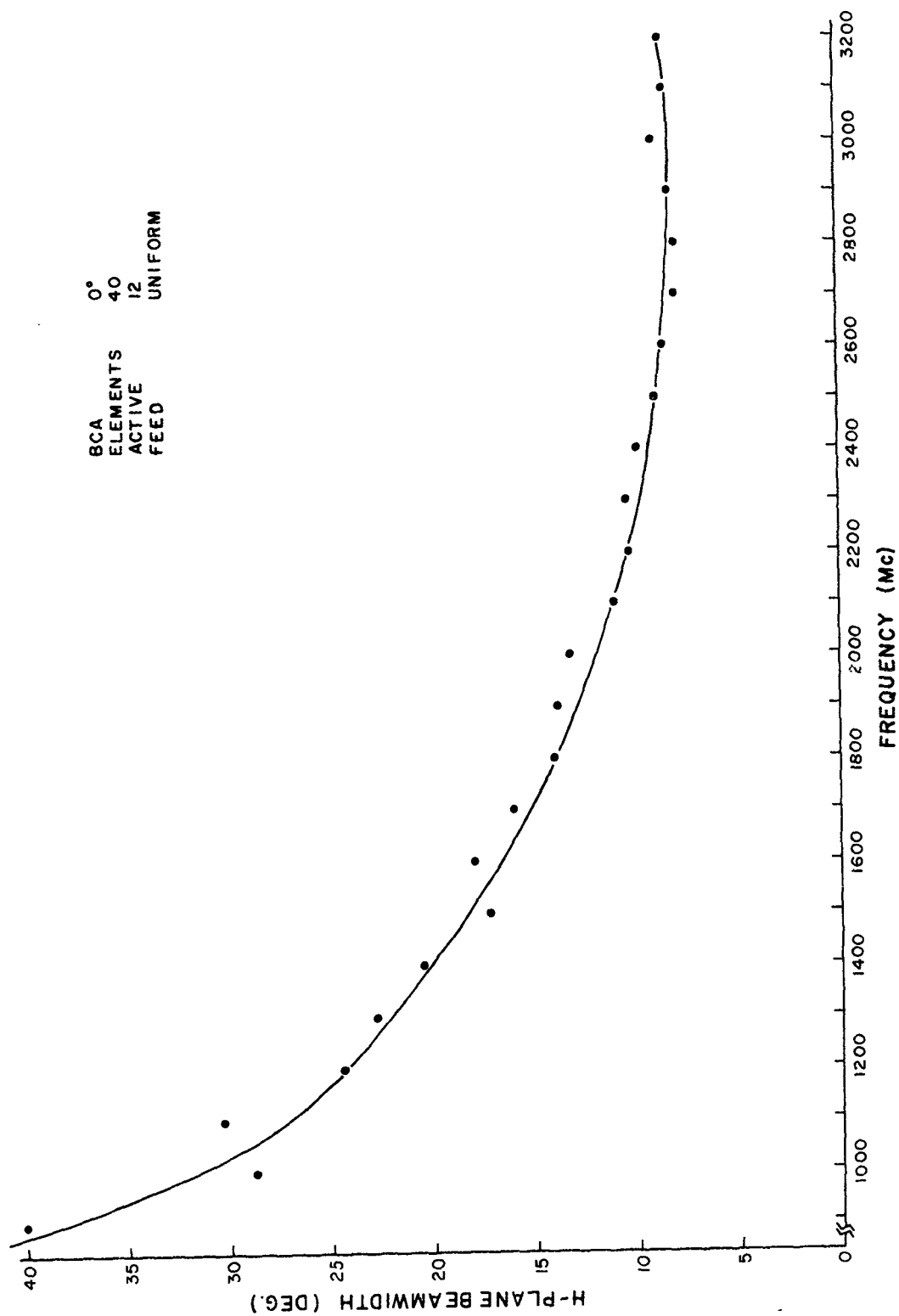


Figure 18. Beamwidth of the Array as a Function of Frequency.

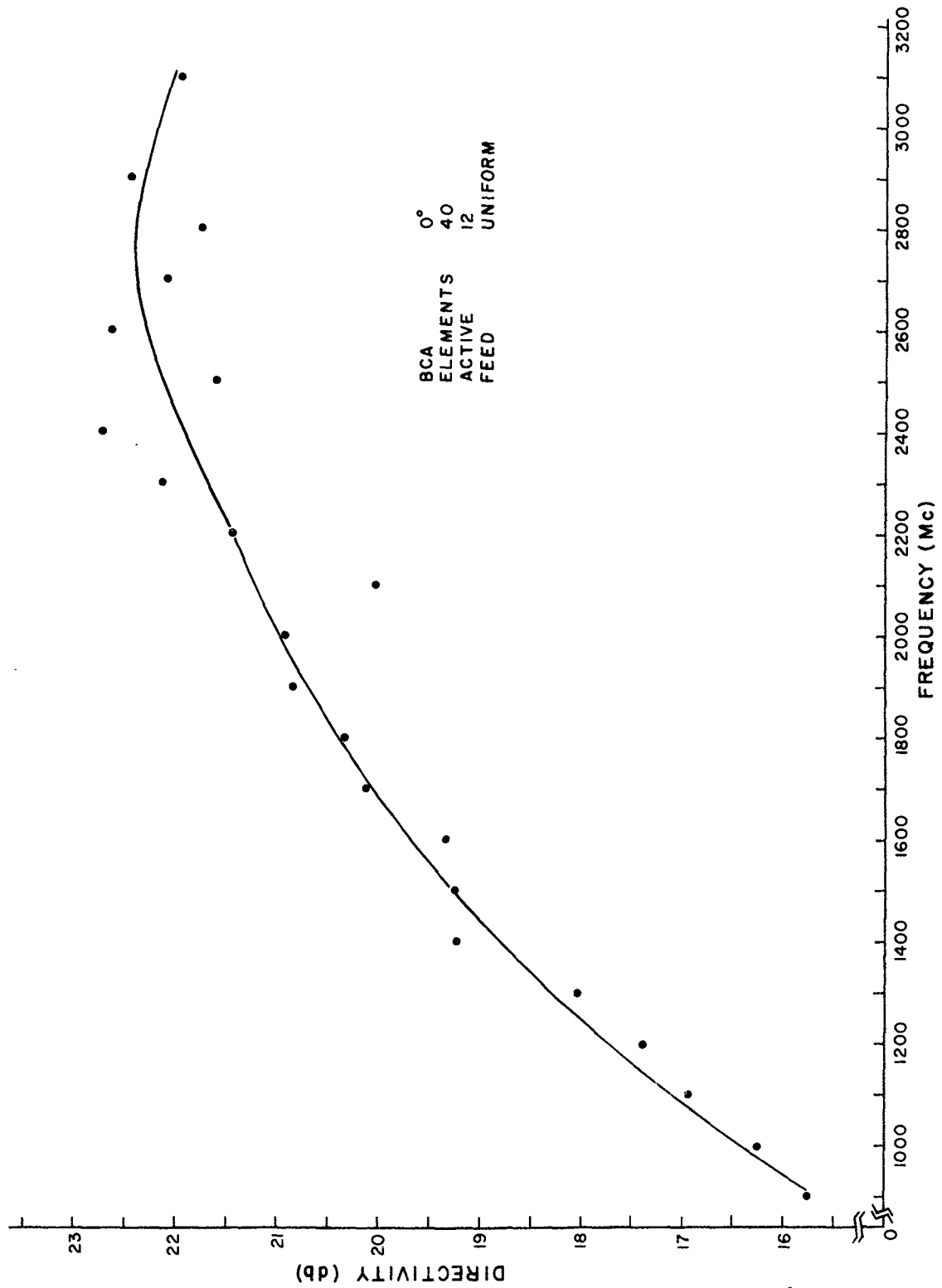


Figure 19. Directivity of the Array as a Function of Frequency.

at 900 Mc the front-to-back ratio was 19.6 db with sidelobes well below that. However, the azimuthal beamwidth was 40° . At 3000 Mc sidelobes were still down 10.9 db or more and the front-to-back ratio was over 25 db. A 21.5° beamwidth was found in the vertical plane.

Study of the whole series from 800-3200 Mc indicates that good pattern control is certainly possible over the low frequency 2.5:1 band. Conical cuts were also made in order to check the azimuth patterns at elevations of 15° and 30° . In general, both the beamwidths and sidelobe levels increased. For example, at 1500 Mc the following values were found:

Elevation Angle	0°	15°	30°
Beamwidth	17.1°	17.2°	19.3°
1st Sidelobe Level	-14.25 db	-13.39 db	-13.27 db ave.

However, at 2500 Mc, the sidelobe decreased with elevation angle:

Elevation Angle	0°	15°	30°
Beamwidth	8.8°	9°	10.6°
1st Sidelobe Level	-11.42 db	-12.97 db	-14.54 db.ave.

The strong influence of the vertical plane pattern of the individual elements on the array pattern tends to prevent any unexpectedly large sidelobes or beam irregularities at high elevation angles. Vertical plane patterns will be run on the computer in the future as a further safeguard against anomalous behavior.

To see what effect the outermost elements (6A and 6B) had on the H-plane patterns, tests were repeated with these elements unexcited. With an active sector of 10 elements the following data was obtained:

Freq.	H-plane Beamwidth		1st Sidelobe Level	
	12 elements	10 elements	12 elements	10 elements
1000 Mc	28.7°	34.0°	-14.93 db	-15.7 db
1500 Mc	17.1°	20.6°	-14.25 db	-12.90 db
2000 Mc	13.3°	14.5°	-15.02 db	-17.77 db
2500 Mc	8.8°	10.1°	-11.42 db	-12.60 db

On the average the beamwidths increased by 17% and the sidelobes went down by an additional .84 db. This seems to be a rather high price to pay for sidelobe reduction -- which, fortunately, is unnecessary because of the -10 db criterion originally stipulated. In fact, it would be nice to find an excitation that would produce a narrower beamwidth than the uniform-cophasal excitation -- even if higher sidelobes came with it. Such an excitation is unknown if super-gain arrays are excluded.

6. CONCLUSIONS

Perhaps the most important conclusion to be drawn from this work is that in spite of certain idealizations necessary for the computer program, reasonable correspondence to the measured data has been obtained. While this report is being written, additional pattern calculations are being carried out for which phase and amplitude corrections have been made in order to more closely simulate the experimental situation.

The experimental patterns show that good results are possible over the 2.5:1 frequency band even though appreciable (30° - 40°) phasing deviations are introduced by the fixed length phasing cables and the motion of the element phase centers. It appears that there will be no difficulty in meeting the -10 db sidelobe criterion or in maintaining a high front-to-back ratio over the operating band. In fact, a satisfactory array pattern should still be available some 10% below the lowest planned frequency of 2 Mc according to the measurements made on the present array. However, impedance considerations may, in the end, be the determining factor in the case of low frequency operation.

If the full 3 band array were built according to the present scheme a total of 160 antenna elements would be necessary. This report establishes that good pattern characteristics can be expected over the low frequency band. However, it has not been established that 160 is the minimum number of elements necessary. In other words, angular separations greater than 9° may still be satisfactory -- or even necessary when impedance is considered. Another unknown yet to be closely studied is the scattering effects of the high-band elements when only the low band elements are energized.

Future plans include a better simulation of the WARLA model on the computer for pattern calculation purposes; the construction of another 500:1 scale WARLA model with 12° between large elements; and the insertion of high band elements to study scattering effects especially near the band change-over frequency.

BIBLIOGRAPHY

1. J. W. Greiser & P. E. Mayes, "Vertically Polarized Log-Periodic Zigzag Antennas", Proc. Nat. Elect. Conf., Vol. 17, pp. 193-204, 1961.
2. J. W. Greiser, "The Bent Log-Periodic Zigzag Antenna", Supplement of Interim Engineering Report No. 4, NOBSR 85243, University of Illinois Antenna Laboratory, Urbana, Illinois, May 31, 1962.
3. R. H. DuHamel, "Pattern Synthesis for Antenna Arrays on Circular, Elliptical, and Spherical Surfaces", Technical Report No. 16, N6-ORI-71, Task XV, ONR Project No. 076-161, Engineering Experiment Station, University of Illinois, Urbana, Illinois, May 1952.
4. Interim Engineering Report No. 2, NOBSR 85243, University of Illinois Antenna Laboratory, Urbana, Illinois, September 30, 1961.
5. F. R. Ore, Technical Note (soon to be published), NOBSR 85243, University of Illinois Antenna Laboratory, Urbana, Illinois.
6. K. G. Balmain, "The Radiation Pattern of a Dipole on a Finite Dielectric Sheet", Technical Report No. 41, AF33(616)-6079, University of Illinois Antenna Laboratory, Urbana, Illinois, August 1, 1959.
7. R. L. Carrel, "Analysis and Design of the Log-Periodic Dipole Antenna", Technical Report No. 52, AF33(616)-6079, University of Illinois Antenna Laboratory, Urbana, Illinois, 1 October 1961.
8. R. H. DuHamel and D. G. Berry, "Logarithmically Periodic Antenna Arrays", CTR-206, Collins Radio Co., Cedar Rapids, Iowa, September 22, 1958, also WESCON Conference, August 1958.
9. I.T.E. Antenna Handbook, I-T-E Circuit Breaker Co., Philadelphia, Pennsylvania, Second Edition.
10. J. D. Kraus, Antennas, McGraw-Hill, New York, 1950, p. 26.

ACKNOWLEDGEMENT

The authors are happy to acknowledge the advice and assistance of the project directors, Professor P. E. Mayes of the Antenna Laboratory and Professor E. C. Hayden of the Radio Location Laboratory. Mr. F. R. Ore of the Antenna Laboratory staff was also helpful. A number of the ideas given in this paper resulted from discussions among these people and the authors. Pattern calculations performed on the Bendix G-20 computer were carried out by Mr. K. G. Tan. Also deserving credit is a long line of student technicians who executed the construction and testing phases of this program.

It is a pleasure to acknowledge the support of the Navy Bureau of Ships under Contract NOBSR 85243.

A TRANSISTORIZED BEAM-CONTROL ARRAY*

John R. Copeland, William J. Robertson
and Robert G. Verstraete

Antenna Laboratory
Department of Electrical Engineering
The Ohio State University
Columbus, Ohio

ABSTRACT

A four-element array of transistorized dipole antennafiers has been used for electronic beam shaping. An equal-amplitude corporate feed was used, but the effective amplitude taper was controlled by circuit gain adjustments on the individual antenna-circuit integrated elements. Patterns have been taken with various amplitude distributions, such as uniform, edge, binomial, and Dolph-Chebyshev.

The antennafier element used was a gamma-matched half-wave dipole integrated with a 2N1742 VHF transistor amplifier. Adjustable base bias was used for gain control. Up to 12 db circuit gain was obtainable in each element with an effective overall noise temperature under 400°K at 148 Mc.

* The work reported here was sponsored in part by Aeronautical Systems Division, Wright-Patterson Air Force Base, Ohio under Contract AF 33(657)-10386 with The Ohio State University Research Foundation.

A TRANSISTORIZED BEAM-CONTROL ARRAY*

John R. Copeland, William J. Robertson,
and Robert G. Verstraete

Antenna Laboratory
Department of Electrical Engineering
The Ohio State University
Columbus, Ohio

I. INTRODUCTION

Antenna arrays are usually designed so that amplitude distributions and phase relationships are fixed by the feed arrangement. For example, the corporate feed structure is a method of exciting all elements of a planar array in the same phase to produce a broadside main beam. If equal power division is made at each tee, a uniform amplitude taper is obtained which gives the characteristic 13 db reduction of first side lobes. Other amplitude distributions give different pattern shapes, but always with the main beam aligned broadside to the plane of the array if the distribution is symmetrical.

The amplitude taper need not be fixed by the power division ratios in the feed structure, however. The techniques of integrated antenna-circuit design can be used to provide electronically controllable gain in each array element, allowing adjustment to any effective amplitude taper without changing the equal-amplitude corporate feed.

II. FOUR-ELEMENT BROADSIDE ARRAY

Such an array described above has been built and tested using four controllable-gain dipole antenna elements spaced $\lambda/2$ apart at 148 Mc, as sketched in Fig. 1. Figures 2 through 5 show representative array patterns which can be obtained by adjusting only the

* The work reported here was sponsored in part by Aeronautical Systems Division, Wright-Patterson Air Force Base, Ohio under Contract AF 33(657)-10386 with The Ohio State University Research Foundation.

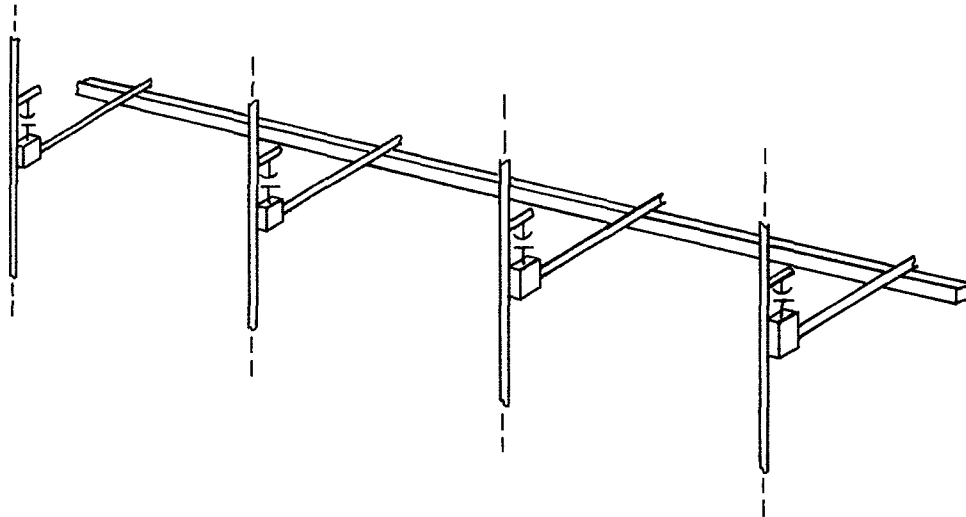


Fig. 1. Four-element antennafier array.

individual bias control voltages on the integrated transistor amplifiers. Also shown are the computed array patterns for the appropriate amplitude distributions, which are uniform, binomial, edge, and 15 db Dolph-Chebyshev, respectively.

The bandwidth over which good patterns could be obtained with reasonable gain was about 25 per cent in all cases. For example, Fig. 6 shows the Dolph-Chebyshev pattern taken at 130 Mc, and Fig. 7 is the same distribution taken at 170 Mc. This represents approximately the useful bandwidth of the elements themselves, beyond which the array patterns begin to deteriorate sharply.

The power gain of the array was measured with respect to a half-wave passive dipole constructed similar to the antennafier elements. Since both directivity and circuit gain contribute to the over-all power gain, the convention of specifying patterns, gains, and noise temperatures as separate parameters has been adopted.

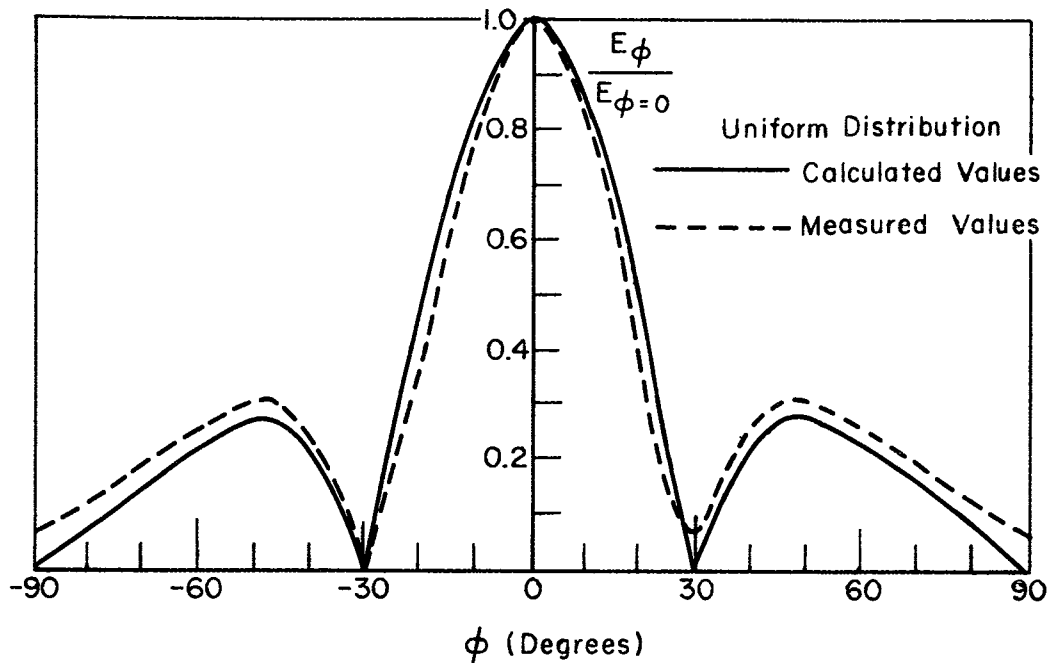


Fig. 2. Uniform distribution (1:1:1:1).

These measurements are summarized in Table I.

TABLE I
Performance of 4-element broadside antenna array
with $\lambda/2$ spacing, measured at 148 Mc

Distribution	Half-power beamwidth	Gain over $\lambda/2$ dipole, db	Noise temperature
Uniform	29°	9.0	850° K
Binomial	37°	9.0	1020° K
Edge	18°	7.0	455° K
15 db Dolph-Chebyshev	29°	9.5	1090° K
Maximum gain	29°	17.0	515° K

Note: The noise temperatures are effective values equivalent to the input noise temperature of a single amplifier following a conventional array.

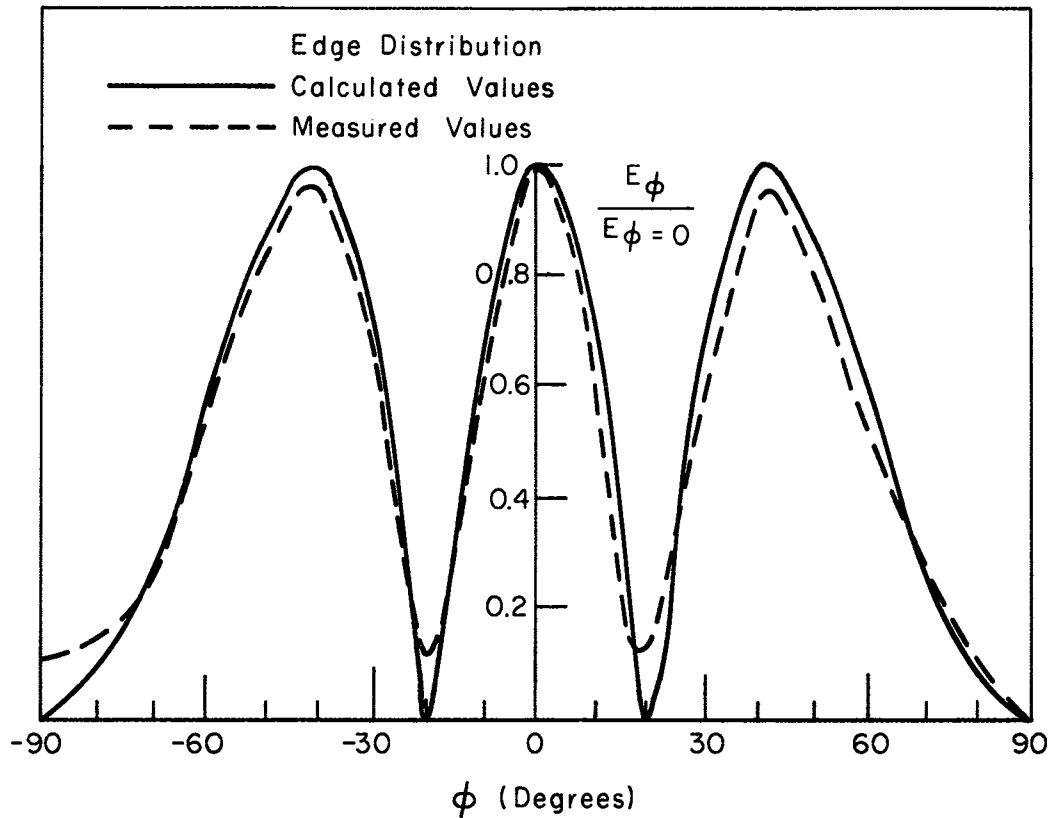


Fig. 3. Edge distribution (1:0:0:1).

Two distinct methods of gain adjustment in the individual antenna-fier elements were investigated: reverse and forward bias techniques. Reverse gain control reduces gain of the transistor amplifier by reducing the amount of forward bias normally applied between emitter and base, thus operating the transistor close to cutoff bias. Forward gain control, on the other hand increases the forward bias, driving the transistor toward saturation. However, a bypassed resistor is used in series with the collector circuit, and the resulting DC drop across it at high currents forces the transistor to operate at very low collector potential, greatly reducing its gain.

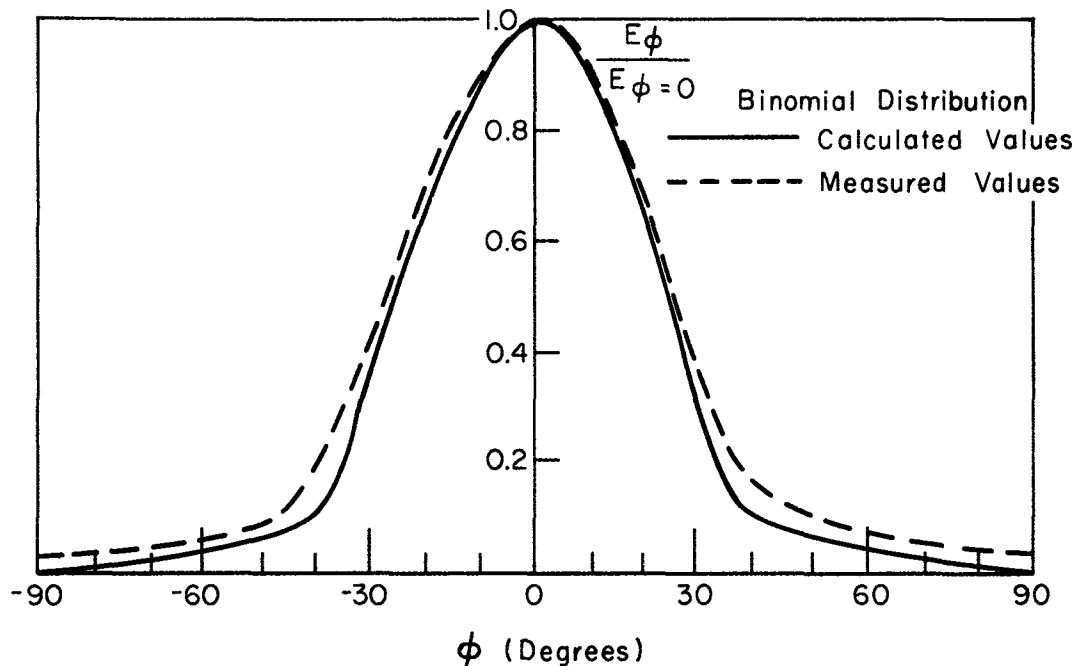


Fig. 4. Binomial distribution (1:3:3:1).

Forward gain control has the advantage of being inherently much more resistant to overload than reverse control, but phase shift through the amplifier was found to change enough as a function of gain to alter the array patterns somewhat. This effect was almost entirely absent for reverse control, so the latter was used for all measurements shown here. The pattern distortion was of such minor nature, however, that forward gain control would be recommended for any application requiring the additional resistance to high-signal overload.

Noise performance of antennafiers is the most difficult property to measure accurately. In the past, good results have been obtained by comparing the noise performance of a given antennafier to an identically constructed passive antenna. This method has the advantage of not requiring a measurement of effective antenna aperture.

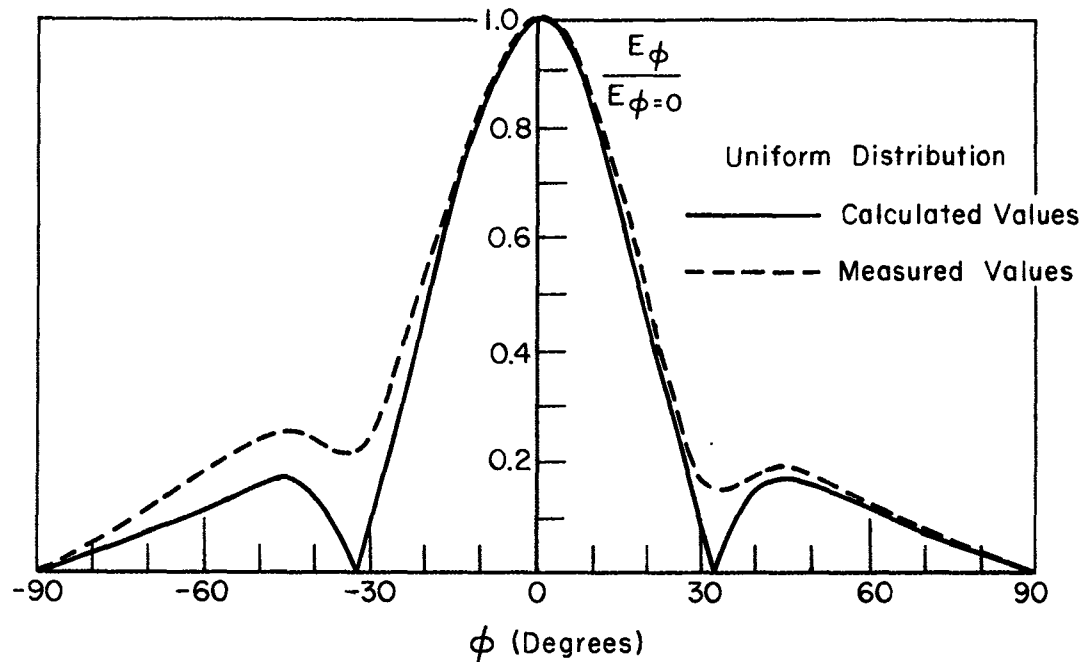


Fig. 5. 15-db Dolph-Chebyshev distribution (1:1.72:1.72:1).

For the array measurements, however, it was inconvenient to construct the identical passive antenna array, so comparisons were made to a single half-wave dipole antenna, and the array directivity was computed from the patterns. It was necessary to know the directivity because the total output noise is the amplified input noise plus the excess noise. The input noise is amplified only by the circuit gain, however, so the total gain of the array must be reduced by the array factor in order to evaluate the excess noise of the amplifiers.

It should be noted that the noise temperatures shown in Table I are derived from the excess noise divided by circuit gain, and represent the input temperature of an equivalent lumped amplifier.

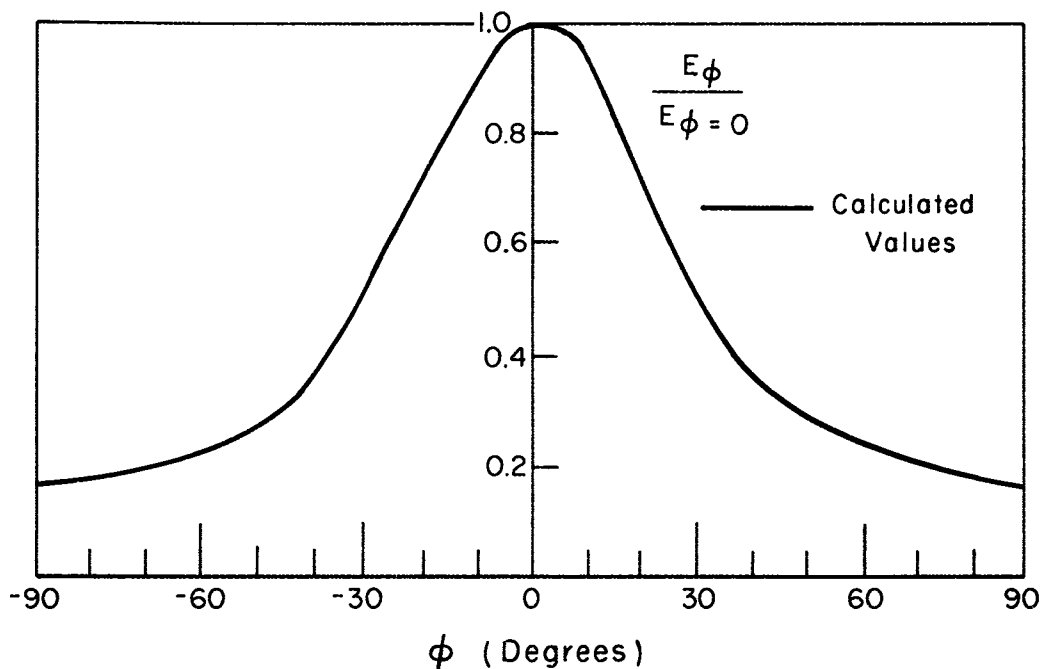


Fig. 6. 15-db Dolph-Chebyshev at 130 Mc.

III. THE TRANSISTORIZED DIPOLE ANTENNAFIER ELEMENT

The array is comprised of four transistorized half-wave dipoles. Figure 8 shows a schematic diagram and Fig. 9 is a photograph of one such antennafer element constructed for 148 Mc. The antenna was connected with a gamma-match directly into the base of the 2N1742 VHF transistor. The length of the gamma rod and resonating capacitance were made adjustable for proper matching between the antenna and the transistor.

The output circuit was a parallel resonant tank, using the parasitic output capacitance of the transistor alone in order to achieve maximum bandwidth. The 50-ohm coaxial output was tapped part-way up from the cold end of this tank circuit for an impedance match. Other tap points

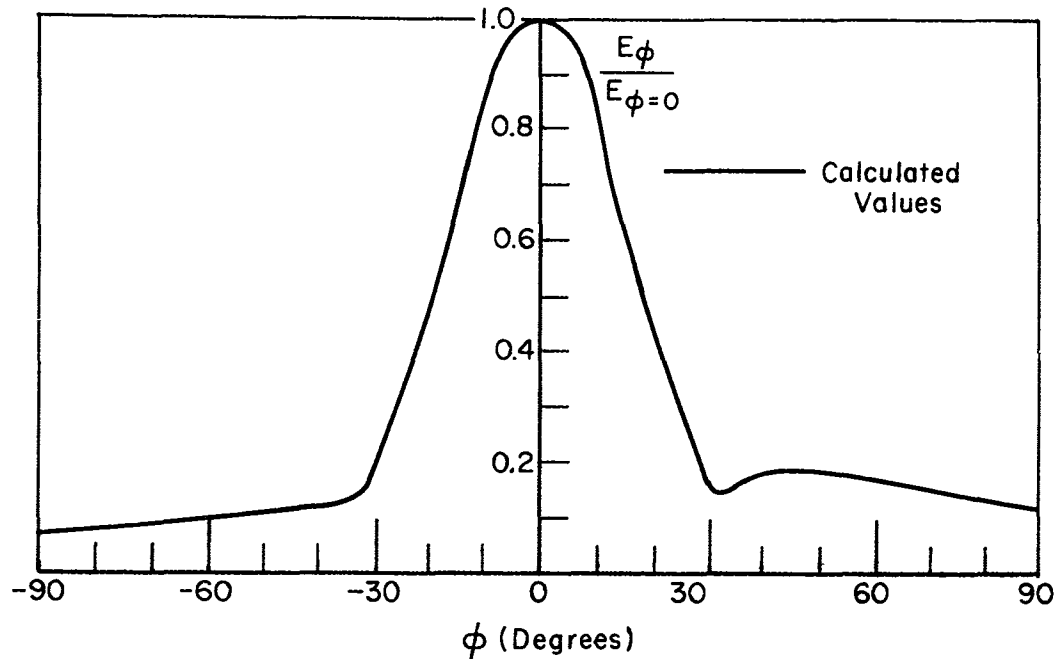


Fig. 7. 15-db Dolph-Chebyshev at 170 Mc.

could be used in the output circuit at the expense of power gain, but the condition of matched impedance was chosen here. This choice resulted in a half-power bandwidth of about 20 Mc which corresponds to an operating Q of about 7.5.

It will be shown later that at these bandwidth limits the antenna VSWR is so low that the total bandwidth is determined by the operating Q of the collector circuit.

The $\lambda/4$ sleeve balun in Figs. 8 and 9 was required only to prevent antenna currents from flowing on the supporting structure of the dipole. This is a common fault of the gamma-match type of unbalanced feed arrangement, and if uncorrected can lead to asymmetrical radiation patterns of the dipole.

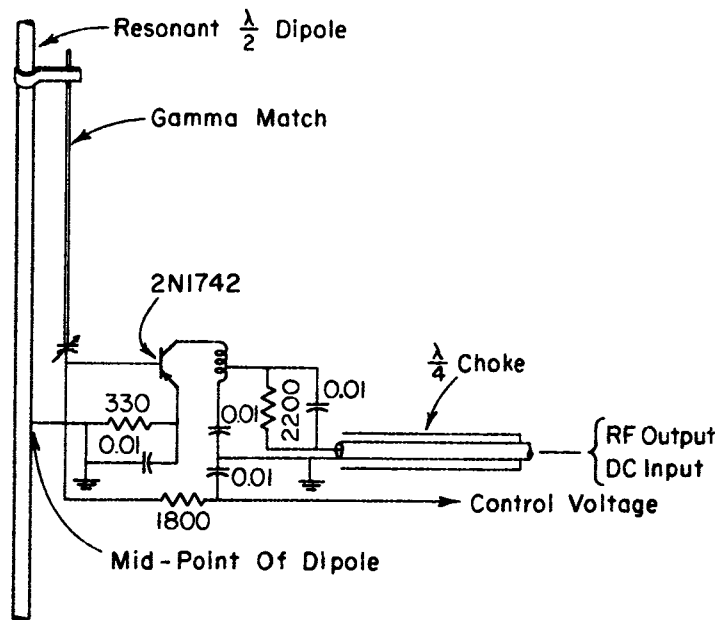


Fig. 8. The transistorized dipole antenna amplifier.

The power supply used for the 2N1742 transistor amplifier was 12v DC connected to the RF output line with an RF choke and DC block arrangement for isolation. A Microlab HW-02N monitor tee was well suited to this purpose.

The gain of the transistor was measured as 12.5 db relative to the reference dipole. The pattern was identical to the reference dipole pattern as shown in Fig. 10. The 12.5 db gain difference was removed for better comparison of the two patterns. It was found that the controllable-gain antenna amplifier of Fig. 8 could be adjusted over the range from 20 db loss to 12.5 db gain by variation of the control voltage.

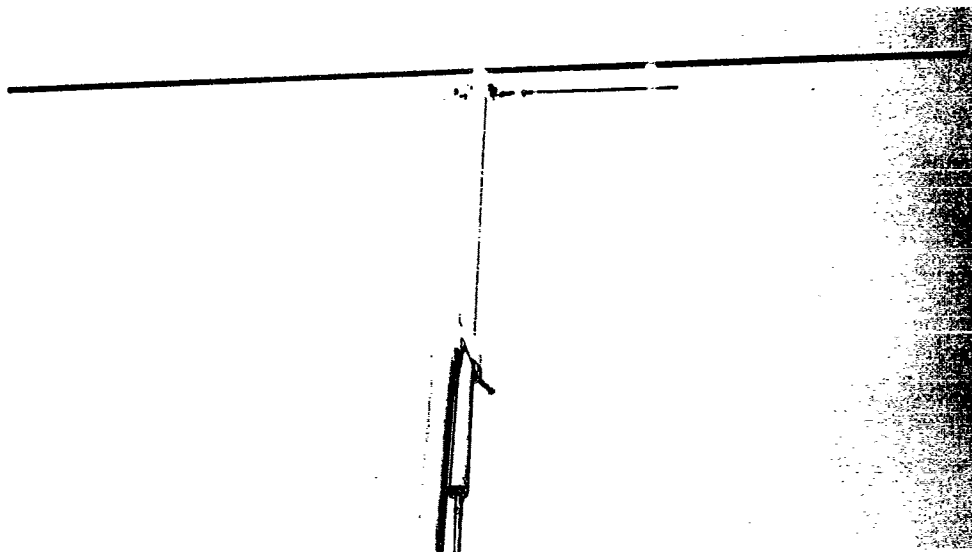


Fig. 9. The transistorized dipole antennafier.

Figure 11 shows the frequency response of the antennafier. This curve was obtained from comparison with the response of a reference dipole constructed to the same dimensions as the antennafier, with an identical reference dipole used as a transmitting antenna. Figure 12 shows a VSWR curve of the two identical reference dipoles. In this way the frequency behavior of the transmitting antenna was known and accounted for in the frequency-response measurements.

As mentioned earlier, since the half-power bandwidth of the antennafier corresponds to VSWR limits of less than 2 on the antenna (a VSWR of 5.8 would correspond to a half-power mismatch), the bandwidth of the antennafier is determined by the choice of loaded Q in the collector circuit.

The spot noise temperature, measured at 146 Mc, was about 350° for the complete antennafier. This turns out to be slightly better than the approximately 425° K measured for the same transistor in an amplifier test circuit. This difference is believed to arise from the losses which inevitably occur in the input circuit of the amplifier, and which have been eliminated in the integrated design.

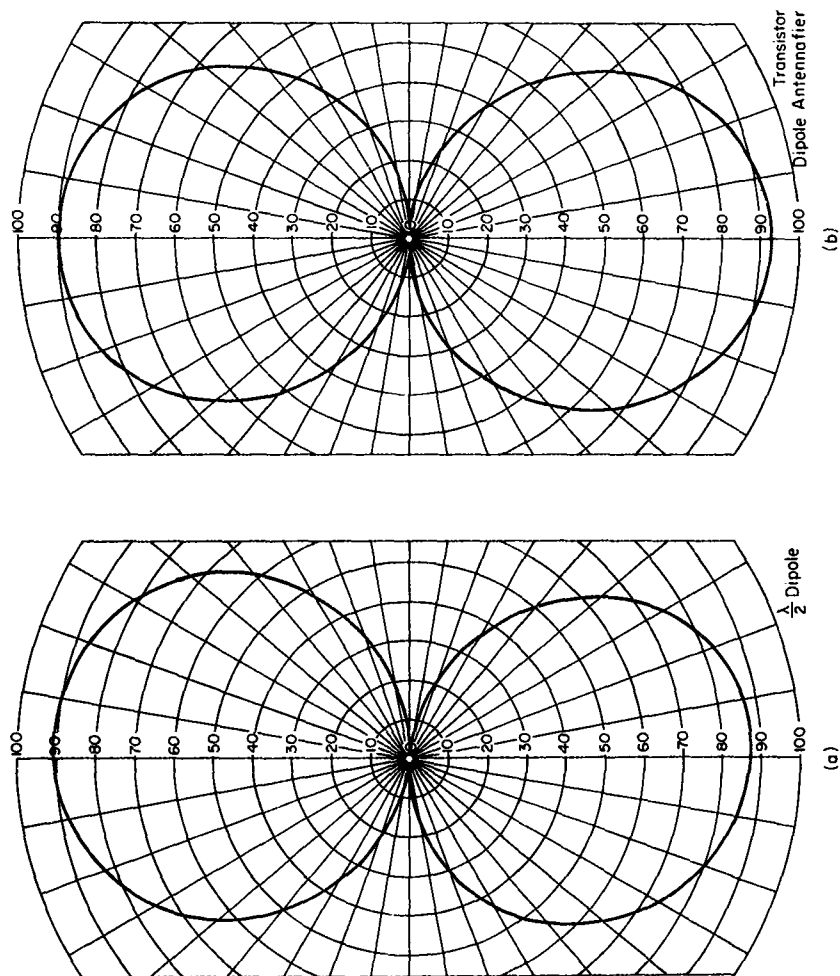


Fig. 10. Field patterns of transistorized dipole antennafier and reference dipole antenna.

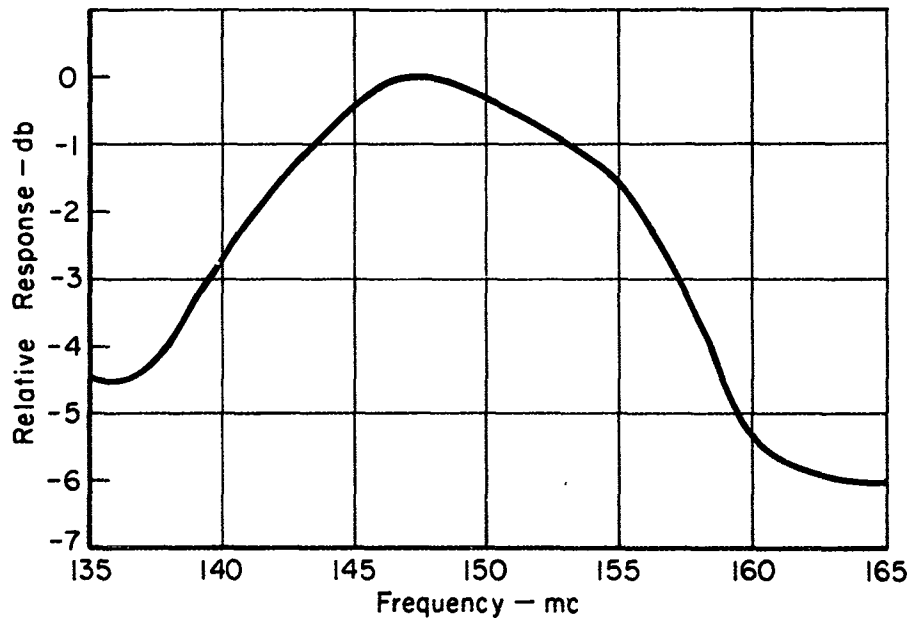


Fig. 11. Frequency response of the transistorized dipole antenna.

It is interesting to note that even at this frequency of 146 Mc, the noise temperature of the antenna approximates the lowest level of cosmic noise temperature to be found in the coldest regions of the sky, and this element is therefore well-suited to VHF communication applications.

IV. CONCLUSIONS

The described active array, comprised of four controllable-gain transistorized dipole antennafiers spaced one-half wavelength apart, illustrates rapid main-beam and sidelobe control in a broadside receiving array in the VHF range. The techniques of integrated design of antenna and receiving systems accomplish this beam control inexpensively, with very few parts, and maintain high signal-to-noise ratios throughout the receiving process. Furthermore, the transistor amplifiers are suited to "forward" gain control to minimize overload or cross-modulation products from strong signals.

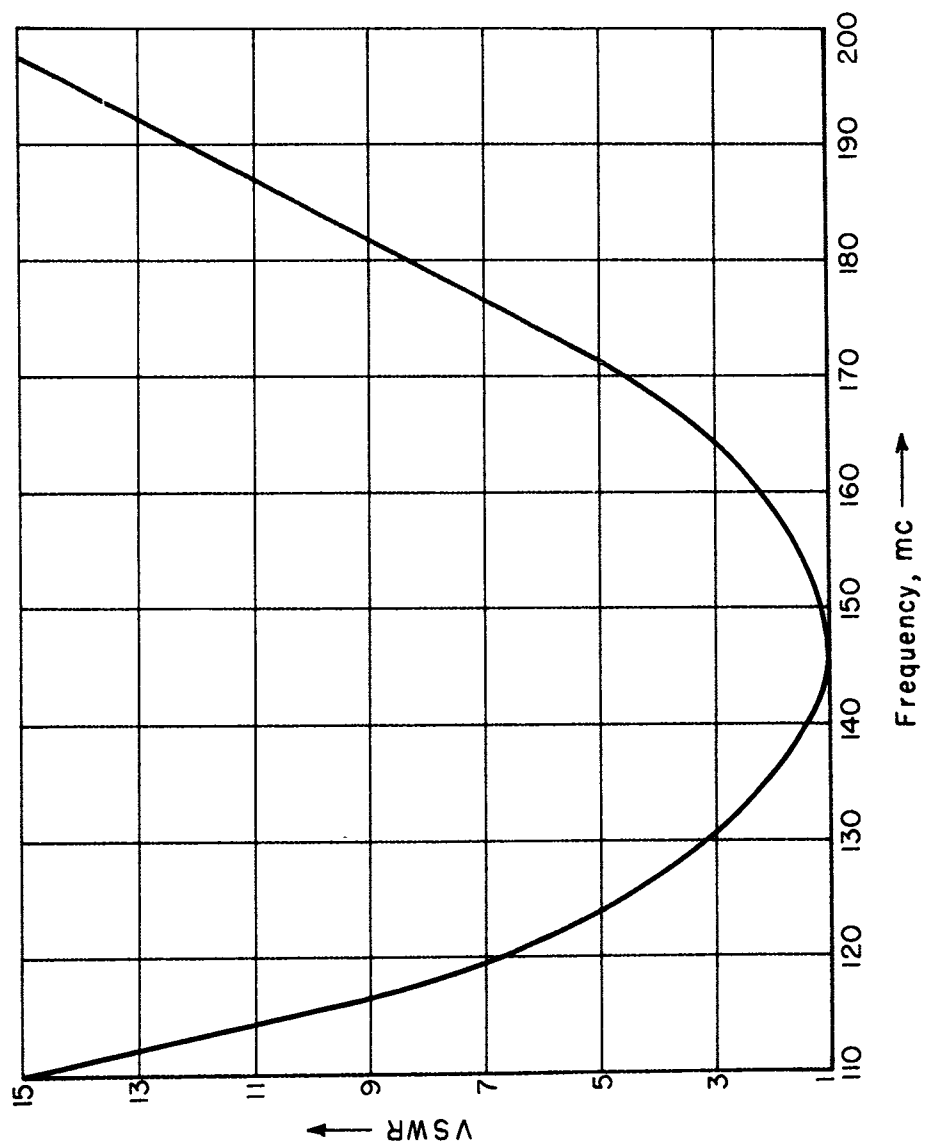


Fig. 12. VSWR of reference dipole antenna.

This four-element array was intended only to demonstrate an application of antennafier elements in larger systems. It seems clear that the economies in weight, size, complexity, and cost shown here, along with the improved performance, would be of very considerable value when multiplied by the dozens or hundreds of elements now being used and proposed for new receiving arrays.

Future work in this direction will include electronic phase control, as well as amplitude control, for complete beam control, including steering as well as shaping.

V. ACKNOWLEDGEMENT

Mr. Robert L. Riegler performed many of the measurements reported.

LOADED ANTENNAS

CURRENT DISCONTINUITY DEVICES

Burt J. Bittner
Sr. Staff Scientist
Kaman Nuclear
Colorado Springs, Colorado

INTRODUCTION

The concept of flux linkage coupling between transmission elements is very mature and well understood. Therefore the extrapolation process to the new class of components discussed in this summary report should have been accomplished 25 years ago! As a result, the "inventive-process" which produced the filters, wave traps and new antenna configurations is probably more startling in its basic simplicity.

This simplicity has proven to extend to the prototype and final products and generally has produced design objectives with a minimum of research and development effort. Discussion of some current discontinuity aspects will be limited due to licensing restrictions.

Fundamental Configuration

The current discontinuity device in its simplest form consists of small, series connected, formed coupling loops which lie parallel to a transmission line element and the coupled loops are resonated by a capacitor. The device acts to impede the current flow at resonance by the magnetostatic force on a moving charge due to the closely coupled electrons

in the associated loops - the law of Biot-Savart - and thus provide a rejection "trap." Basic uses of this configuration are as a wave trap on an antenna structure and as a band-reject filter in a coaxial configuration. In both of the preceding applications it can be seen that the approach allows the center conductor to remain structurally undisurbed and experimental tests have shown that the physical arrangement illustrated in Figure 1 is sufficient to effectively "couple" or enclose the magnetic field. Prior to the experimental investigation at Kaman Nuclear, it was rather arbitrarily and erroneously assumed that a loosely wound torroidal configuration would not be effective. The assumption was that the configuration could not properly contain the flux and, for some isolated cases this may still be true. However, for most applications, sufficient coupling is obtained with the configuration of Figure 1, as opposed to that of Figure 2.

Figure 1 also illustrates the type of configuration used to achieve directional coupling, in which case the arrangement (without the condenser) becomes a re-entrant coupled transmission line element with the advantages that it is physically shortened, has a much higher coupling-per-unit-length capability and considerable bandwidth.

Under circumstances where the center conductor is of such a size that the total length of coupling elements required to surround the conductor might begin to approach self-resonance, the paralleled inductance counter-wound configuration of Figure 2 may be utilized. This arrangement also allows the

two terminals to be physically separated which is a requirement for high power applications. This method also permits the length of each coupling element to be increased, which linearly increases the mutual coupling in the classical equation for mutual coupling in R.F. Transformer design.

Some Additional Applications

Figure 2 illustrates that the current discontinuity device is capable of being used around a structure of significant size, but not greater than a portion of a wavelength; however, models have been constructed, as illustrated in Figures 3 and 4, where by paralleling many elements, a structure with a circumference greater than a wavelength can be properly excited. In this case, as well as for the small structures, the device becomes a means for feeding the structure as well as its distinctively different application as a parasitically excited system. A most important application is shown in Figure 3, wherein it has been found that a figure of revolution is not essential and thus a linear section, $\lambda/2$, of a missile or aircraft can be excited by a small flat coil arrangement current discontinuity device without structurally or electrically isolating a section of the airframe. Broadbanding techniques for this application have been discovered.

Another application of considerable merit is in the use of the current discontinuity device around each leg of a radio tower to effectively provide isolation which would otherwise be achieved with bulky insulators or shunt feeding.

Results

The research to date has shown that the wave trap concept yields results as is shown in Figure 5 for a one-element current discontinuity parasitically excited and the addition of a colinear array of these elements yields results which will be discussed in the presentation. It must be emphasized that the device functions properly as a wave-trap when placed at a desired current maximum as opposed to parallel resonant wave traps which must be placed at voltage maxima. The device is also different than the parallel resonant wave trap in that at frequencies "off-resonance" it does not perturb the transmission line appreciably and it may be physically "slid-along" the antenna element.

Figure 6 illustrates the plot of admittance of a specific tunable current discontinuity band-reject, band pass filter design tested in an NBS tracking station. As a simple band reject filter it was matched ($VSWR < 1.1$) from DC through to 115 mc and from 131 mc through to over 300 mc. The reject "notch" was tunable from 5 mc to 256 mc.

The theoretical analysis of the device indicates that there are no transcendental, or harmonically related spurious response characteristics of significance.

Additional Applications

Current discontinuity devices have direct application as:

- (a) Rotary joint couplers (multi-port).
- (b) Parametric amplifiers.
- (c) Coaxial to waveguide feeds.
- (d) Plasma modulators
- (e) Miniature flush antennas on large structures.
- (f) Baluns and other Z transformers.
- (g) Multiband long wire array antennas plus other applications such as switching, modulating and phase-shifting.

Limitations

The concept inherently is a current or flux linkage device most applicable to low impedance transmission lines.

CURRENT DISCONTINUITY DEVICES

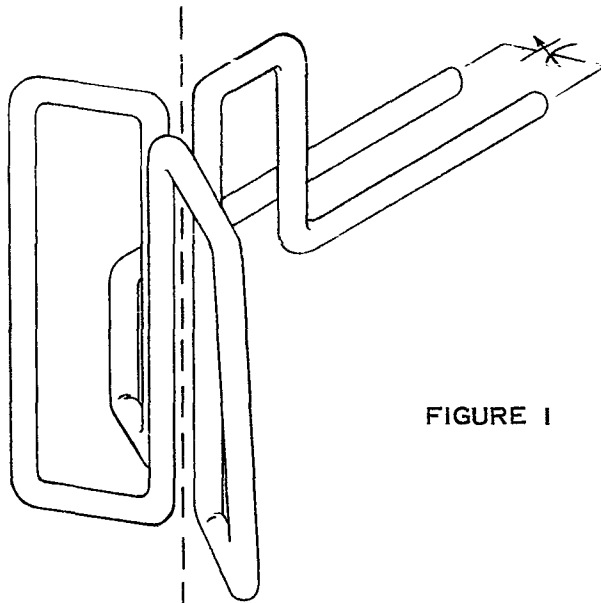


FIGURE 1

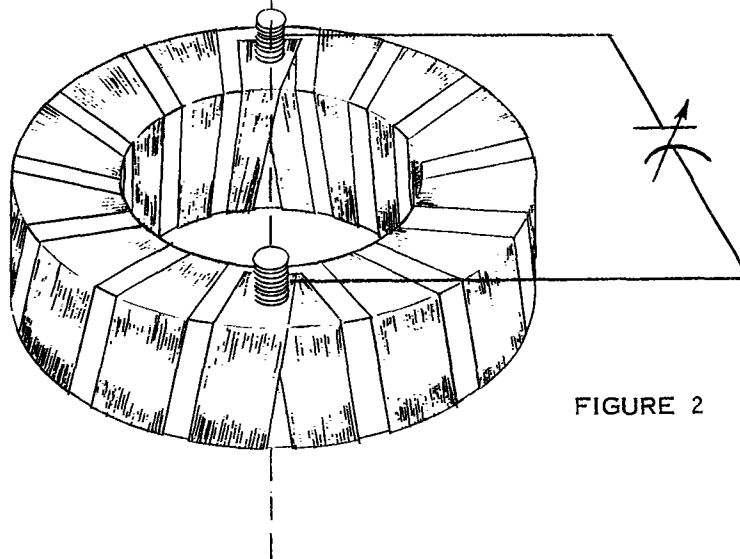


FIGURE 2

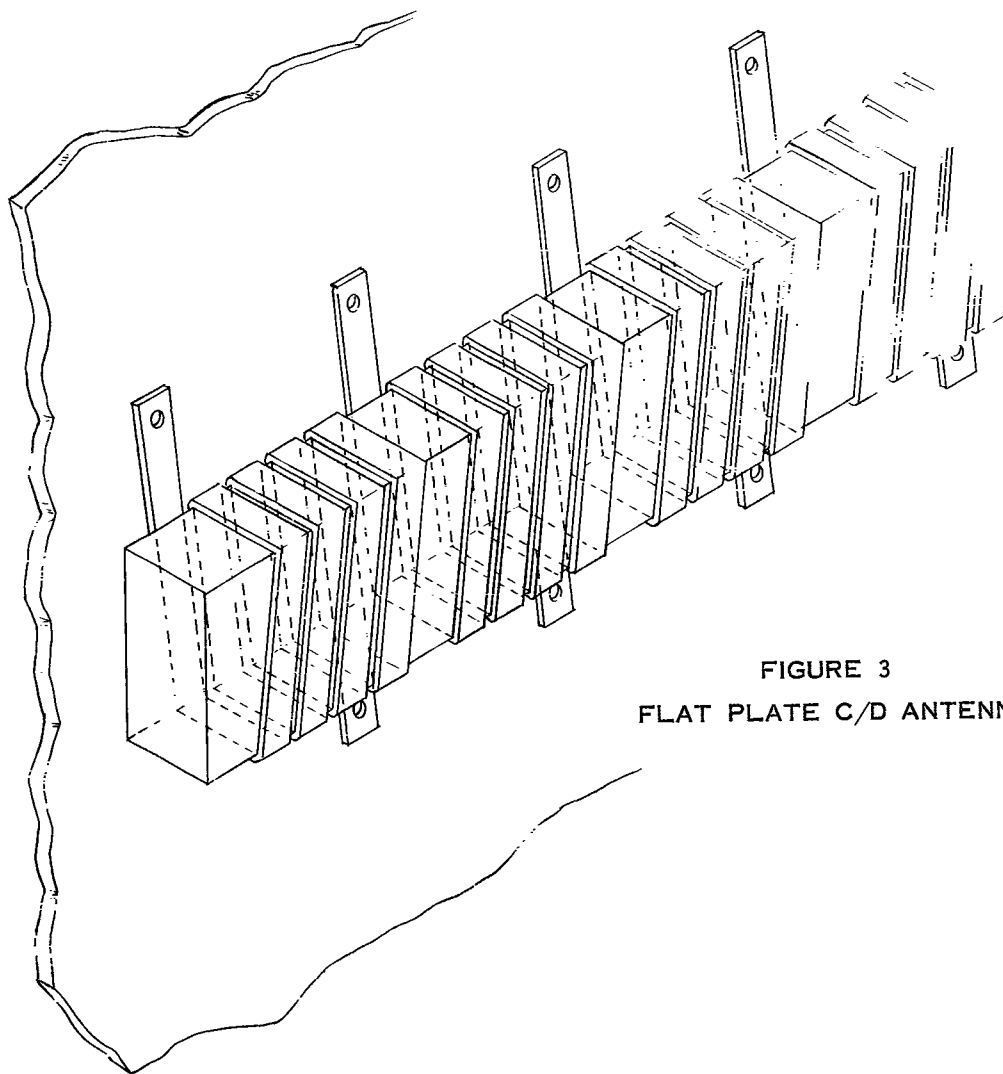


FIGURE 3
FLAT PLATE C/D ANTENNA

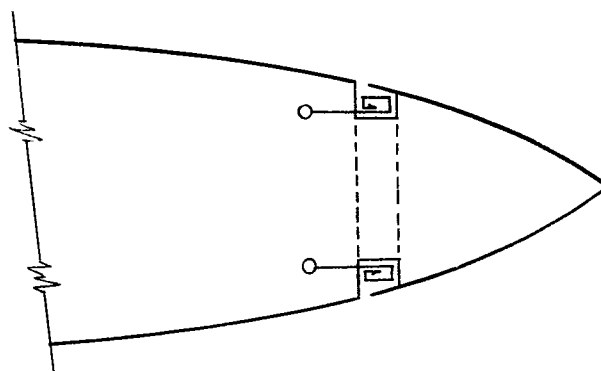
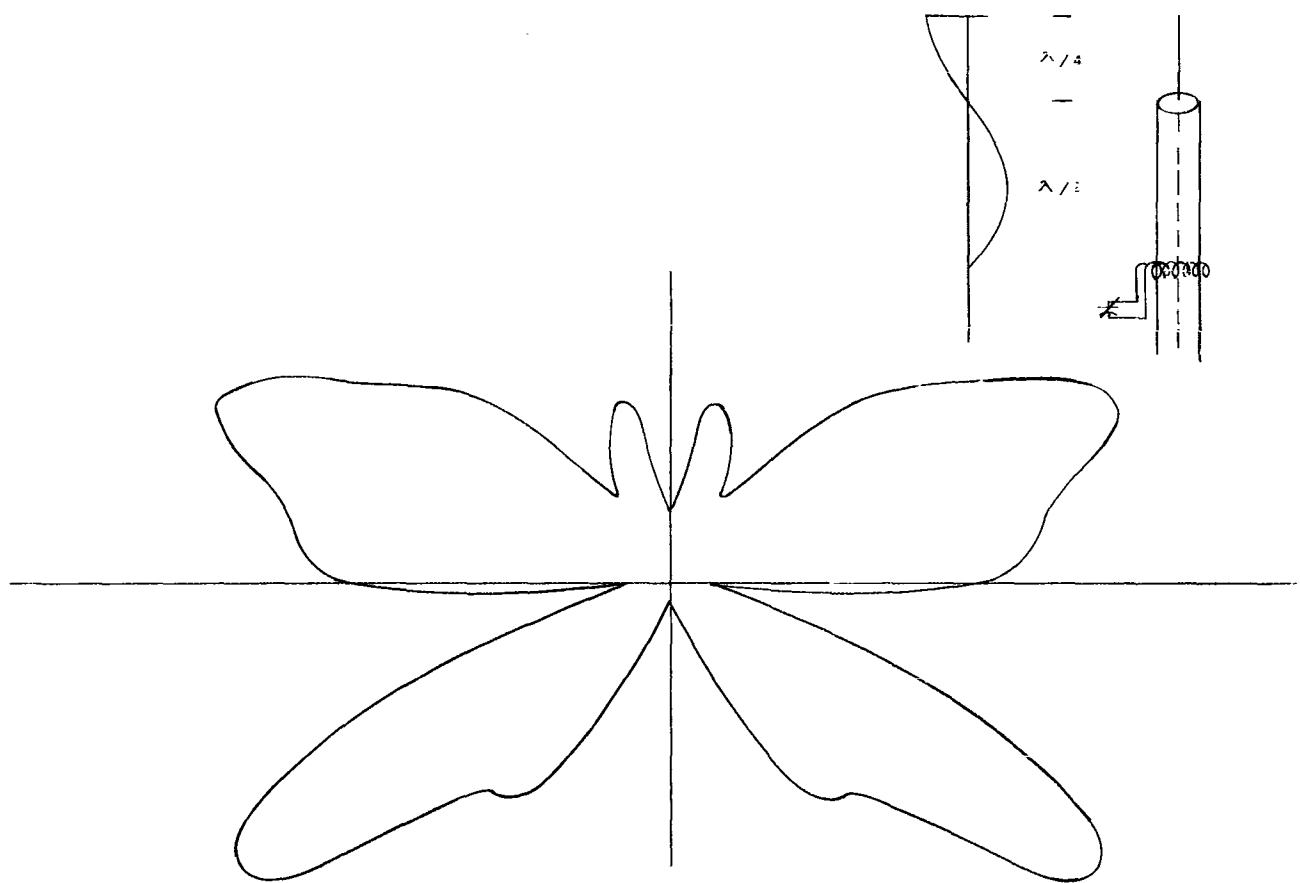
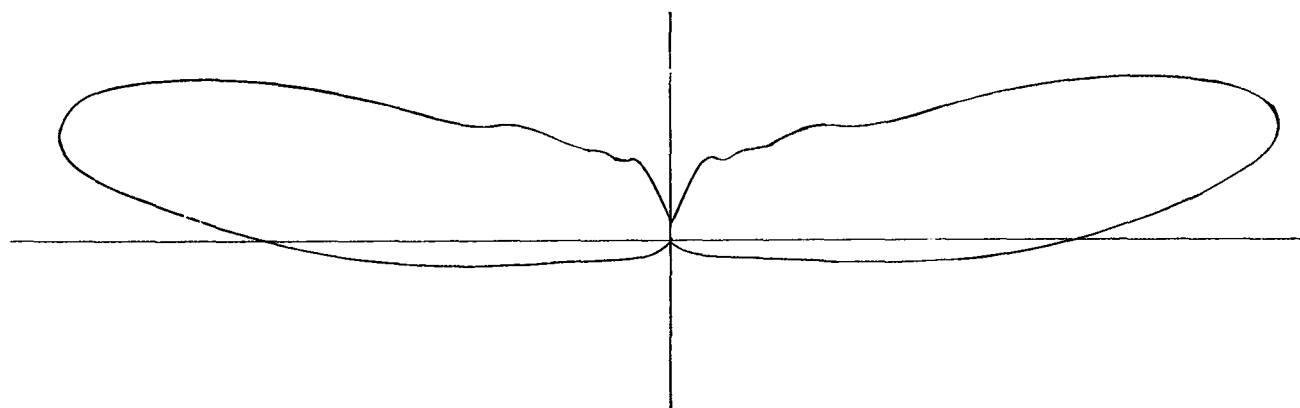


FIGURE 4
LARGE DIAMETER ANTENNA
 $ka > 1$



PATTERN WITHOUT C/D (DETUNED)



PATTERN WITH C/D

FIGURE 5
CURRENT DISCONTINUITY PASSIVE ARRAY METHOD

FILTER

TYPICAL Y PLOT TUNED TO 123 MC

FERRITE LOADED-SLOT AND TRAVELING-WAVE ANTENNAS

By

A. T. Adams, J. A. M. Lyon
and J. E. Herman

The University of Michigan
Ann Arbor, Michigan

ABSTRACT

This presentation summarizes some of the results of a theoretical and experimental investigation of the use of ferrite materials in various types of antennas. Promising results have been obtained with a rectangular-slot antenna backed by a ferrite-loaded cavity. Preliminary results have been obtained with equiangular spirals using ferrite materials. The work with slots has been analytical with substantial experimental confirmation. So far, the work with spirals has been almost entirely experimental.

It is interesting to note that others are currently attempting to obtain useful modifications of antennas through the use of materials. Recent Russian work, as described in Ref. 1, covers the use of materials with Helices. Although the title of this reference indicates dielectric materials are used, the mathematical analysis could be extended without undue difficulty to situations where the material has a relative permeability greater than 1. It is interesting to note that this reference claims a more

directional radiation of energy is possible. Of course, the retardation of waves in the Helix has made possible axial modes at a lower frequency than if the dielectric core material were not present.

In the work to be described on slots, the observed changes in radiation pattern were slight. Comparatively large reductions in dimensions were possible but only at the sacrifice of efficiency and bandwidth. However, it is believed that a slot antenna modified through the use of ferrite will be very useful in some types of established communications. The reduction in efficiency is not great if carefully selected ferrite is used. The reduction in bandwidth is substantial, and all such ferrite-filled slots produced to date are necessarily limited to narrowband usage.

The introduction of the use of ferrite material for equiangular-spiral antennas has resulted in a given equiangular-spiral antenna being operable at considerable lower frequency than otherwise would be possible. This situation can also be interpreted as a reduction in the lineal dimensions. Unfortunately, at the present time the known available ferrite materials do not maintain high permeability, high permittivity and high effective Q over a sufficiently wide frequency band. Improvements in ferrite materials, with respect to maintenance of characteristics over a wider frequency band, may very possibly make feasible the reduction in the lineal dimensions of the face of an equiangular spiral and yet retain the wideband characteristics of such a spiral.

Very preliminary results on the utilization of ferrite materials with a scimitar antenna are presented. These results appear interesting, but so far no time has been spent on the mathematical analysis of this type of antenna utilizing ferrite materials.

COMPARISON OF SLOTS

The inherent limitations on electrically small antennas have been known for some time.²⁻⁴ It appears that it is possible within these limitations to effect significant size reduction at what is believed to be a tolerable reduction in both bandwidth and efficiency. Figure 1 shows three antennas loaded respectively from left to right with air, powdered-ferrite material, and solid-ferrite material. The performance characteristics of these three antennas are tabulated in Table I. Please note that the operation of all three antennas is in the vicinity of 300 Mc tests. The choice of this operating range of frequency has been based upon the characteristics of the ferrite material. These characteristics are described in Table II. The antenna on the extreme left consists of a rectangular air-filled waveguide fed by a T bar. The middle antenna in the figure consists of a rectangular waveguide filled with powdered-ferrite material and also utilizing a T bar feed. The third antenna on the extreme right consists of a rectangular waveguide filled with solid bars of ferrite material and utilizing a simple cylindrical probe as a feed. All of these antennas

have the obvious advantage of suitability for flush mounting and possession of a single-lobe radiation pattern.

THEORETICAL ANALYSIS OF SLOTS

Using the results of a variational analysis, it has been possible to predict the characteristics of flush-mounted slot antennas of the type shown in Fig. 1. The resonant frequency or frequency at which the VSWR (voltage standing wave ratio) is a minimum, can be predicted within a few percent. Bandwidth and efficiency can be predicted within about 25 percent. The beam pattern when mounted in a ground plane can be accurately predicted.

The method of analysis is as follows: Fig. 2(a) shows a semi-infinite waveguide loaded with isotropic homogenous medium characterized by ν_r and ϵ_r . This waveguide opens into a conducting ground plane of infinite extent. A variational expression for the normalized aperture admittance was obtained using an analysis similar to that of Lewin⁵ for the unloaded waveguide.

$$\begin{aligned} \frac{Y}{Y_0} &= \frac{G}{Y_0} + j \frac{B}{Y_0} = \frac{1 - R}{1 + R} \\ &= - \frac{ab\mu_r}{\Gamma_{10}} \frac{\int_0^a \int_0^b \int_0^a \int_0^b E_x(x, y) E_x(\xi, \eta) G(x, y; \xi, \eta) dx dy d\xi d\eta}{\left[\int_0^a \int_0^b E_x(x, y) \sin \frac{\pi y}{a} dx dy \right]^2} \end{aligned}$$

where $E_x(x, y)$ = electric field in the aperture

R = complex dominant mode aperture reflection coefficient

$$\Gamma_{10} = \sqrt{\frac{\pi^2}{a^2} - k^2}$$

$$k^2 = \mu_r \epsilon_r k_0^2$$

$$k_0 = \omega \sqrt{\mu_0 \epsilon_0}$$

$$G_1(x, y; \xi, \eta) = \left(\frac{\partial^2}{\partial y^2} + k_0^2 \right) \frac{e^{-jk_0 r}}{2\pi r} +$$

$$\left(\frac{\partial^2}{\partial y^2} + k^2 \right) \sum_{m=1}^{\infty} \sum_{n=0}^{\infty} \frac{4 \epsilon_{mn}}{ab \mu_r \Gamma_{mn}} \sin \frac{m\pi\eta}{a} \cos \frac{n\pi\xi}{b} \sin \frac{m\pi y}{a} \cos \frac{n\pi x}{b}$$

The equivalent circuit which has been useful in further calculations, as well as in visualization, is shown in Fig. 2(b). Using the dominant mode assumption for $E_x(x, y)$, a quadruple integral reduces to a double-integral suitable for machine computation. The numerical results of such a computational effort have given the normalized values of B and G as functions of μ_r , ϵ_r , b/a , and frequency. Detailed numerical values are available in Ref. 7. All this data have been checked experimentally for a few cases and shows an agreement within about two percent.

Using these basic data for B/Y_0 and G/Y_0 , resonant frequency and bandwidth of the antenna shown in Fig. 3 can be calculated by simple equivalent circuit calculations based upon the representation shown in Fig. 4.

For instance, resonant frequency may be calculated by neglecting the shunt reactance B'_p introduced by the probe and by calculating the frequency at which the short reactance (looking toward the left) cancels the aperture reactance. Predictions of resonant frequency based upon this method are accurate to within a few percent. Perturbation calculations may be made to take the feed configuration into account. Typical calculations yield corrections of less than one percent to the resonant frequency due to consideration of the probe feed. Similarly, bandwidth can be calculated by taking into account the variation with frequency of aperture admittance and the admittance of the shorted section to the left. For simplicity, G'_p may be assumed constant over the frequency range under consideration. The effect of losses on bandwidth may be assayed by multiplying the bandwidth in the lossless case by $(1/\text{efficiency})$. The effect of these assumptions are more serious for bandwidth prediction. Accuracy of bandwidth prediction in the cases which have been tested was 25 percent or better.

The variational data may be used to calculate efficiency. The theoretical formulation is given in Ref. 6. For the case of high Q material with magnetic losses much greater than dielectric or wall losses, the following approximate formula may be used:

$$\text{Efficiency} = \frac{1}{P_L/P_R + 1}$$

$$\frac{P_L}{P_R} = \frac{\mu''}{\mu'} \frac{\left[k^2 a^2 \left(\frac{2d}{a} \right) + \frac{(k^2 a^2 - 2\pi^2) \sin 2\beta 10^d}{\sqrt{k^2 a^2 - \pi^2}} \right]}{(1 - R^2) \sqrt{k^2 a^2 - \pi^2}}$$

where:

$$\begin{aligned}d &= \text{cavity length} = d_1 + d_2 \\ \beta_{10} d &= \text{electrical length of cavity} \\ &= k^2 a^2 - \pi^2 (d/a) \\ \mu &= \mu' - j\mu''\end{aligned}$$

Table III shows a comparison of theoretical and experimental data for several ferrite and dielectric loaded models. Figure 5 shows a comparison of the theoretical and experimental beam patterns for the solid-ferrite loaded antenna shown on the extreme right in Fig. 1.

The analytical results indicated on slots, when compared with the experimental data, show that reasonably accurate results have been obtained in spite of the necessity of assumptions dealing with the following:

- (a) The aperture field;
- (b) The effect of the probe; and
- (c) The finite length of the cavity.

PRACTICAL CONSIDERATIONS ON FERRITE SLOTS

Experiments were made on a number of loaded rectangular cavity slot antennas, using ferrite-powder materials, solid-ferrite material, and dielectric material. In all cases it was possible to match the antenna by a single adjustment, namely, the adjustment of the probe feed depth. The location of the type N fitting for the probe was not critical. In most cases

optimum bandwidth was obtained with a fitting approximately centered in the broad wall of the waveguide.

The effect of the flange on antenna characteristics other than beam pattern is minor. Typical results showed an increase of 0.5 percent in resonant frequency.

The variational data given in Ref. 7 indicates that for a given set of dimensions a and b and also a given $\mu_r \epsilon_r$ product, as well as a given frequency, the admittance is directly proportional to μ_r , and the ratio of G/B is constant. As a result, an optimum choice of material properties may be made. The efficiency and bandwidth depend very critically upon:

$$|T|^2 = 1 - |R|^2$$

or the squared magnitude of the transmission coefficient which has a maximum value for that value of μ_r which makes:

$$B/Y_0 = \sqrt{\frac{1}{1 + k^2}}$$

where $k = G/B$.

Since B is directly proportional to μ_r for a given $\mu_r \epsilon_r$ product, the optimum μ_r can be readily predicted. For instance, Fig. 6 shows a plot of bandwidth and $|T|^2$ as functions of μ_r , for $\mu_r \epsilon_r = 9$, $b/a = 0.3$, $ka/\pi = 1.8$ (80 percent above cutoff). The optimum value of $|T|^2$ occurs at $\mu_r = 6.79$ at which point $B = \sqrt{1/1 + k^2}$.

The optimum bandwidth occurs at about $\mu_r = 5$. The difference in optimum values is explained by the fact that the bandwidth also depends upon the cavity length, which increases with increasing μ_r . The bandwidth for ($\mu_r = 5.0$, $\epsilon_r = 9/5$) is almost double that for purely dielectric loading ($\epsilon_r = 9.0$, $\mu_r = 1$). This is borne out by the bandwidth data in Table II.

EXTENSION TO OTHER ANTENNA TYPES

By the early comments on Ref. 1, it would seem logical to consider helical antennas loaded with ferrite. This reference has stated as a conclusion, "In order to increase frequency bandwidth of the aerial investigated, we can use, instead of a continuous dielectric rod in the helix, a stratified dielectric or a magneto-dielectric medium." This statement does not appear to be based firmly on either the experimental or analytical work of that paper. The helix is fairly readily analyzed and in the near future it is contemplated to study ferrite loaded helices. However, it suited the purposes of the program discussed here to do some preliminary work on the use of ferrites with equiangular-spiral antennas and with the scimitar antenna.

FERRITE-LOADED SPIRAL ANTENNA

The VSWR of the cavity-backed equiangular spiral shown in Fig. 7(a) was measured both with and without ferrite loading. The feed, shown in Fig. 7(b), is of the "infinite balun" type used by Dyson.⁹ Standard 50 ohm coaxial cable was used for the feed construction.

The VSWR for the simplest loading condition is shown in Fig. 8. The cavity was fully loaded with the ferrite powder. A thin layer of ferrite powder was also placed on top of the spiral. The fully loaded case produced a reduction of the lower cutoff frequency by a factor of approximately 2. The introduction of the ferrite powder introduces a narrowbanding effect due to the fact that the magnetic Q becomes small above 700 Mc as shown in Table IV. This is a superficial effect, however, since it is a function of the type of material used. Thus it is expected that with the development of wideband, high Q ferrites, moderate widebanding of the spiral antenna could be achieved. However, with presently available materials, a 2 to 1 size reduction is possible.

Figure 9 shows that approximately the same result can be obtained by loading only one arm of the spiral. This method has the advantage of using less ferrite material.

Figure 10 shows the response of the bidirectional spiral without a cavity in both the loaded and unloaded conditions. The curves have the same general shape as for the cavity backed spiral. Thus the cavity introduces little basic deterioration of the antenna response.

Preliminary efficiency measurements for the loaded spiral indicate an efficiency of about 80%. Efficiencies of unloaded spirals are typically greater than 90%.

FERRITE-LOADED SCIMITAR ANTENNA

Measurements of VSWR and efficiency were made on a ferrite-loaded scimitar shown in Fig. 11(a). The introduction of the ferrite-powder loading lowers the cutoff frequency by a factor of about 2-1/2 as shown in Fig. 11(b). The efficiency of the loaded scimitar is approximately 80% as shown in Fig. 12. Efficiencies of unloaded scimitars are typically greater than 95%. It is interesting to note that the reduction of bandwidth and efficiency with ferrite loading is less serious than it was in the case of the loaded rectangular slot antenna.

CONCLUSIONS

Upon the basis of the results of detailed studies of a number of types of antennas it can be concluded that:

1. Some reduction in the size of an antenna can be made through the use of properly placed ferrite materials.

2. Some reduction in efficiency may be anticipated even with the best ferrite materials now available. This reduction in efficiency may in practice be entirely tolerable.
3. The bandwidth reduction is severe in some of the antennas studied.
4. The bandwidth can be sufficient for some communications.
5. The bandwidth of a slot antenna using ferrite may be extended by optimizing the value of permeability as compared to permittivity.

Additional effort is contemplated on several antenna types. The possibility of increasing the bandwidth by using periodic structures of numerous essentially narrowband elements is being surveyed. The elements may be both smaller and narrowbanded due to the use of ferrite.

ACKNOWLEDGEMENTS

The results presented here were obtained under Contract No. AF 33(657)-10607, issued by the Aeronautical System Division, Wright-Patterson Air Force Base. The numerous contributions and the encouragement of Mr. E. M. Turner, Chief, and Mr. O. E. Horton,

Project Engineer, both of the Antenna-Radome Section, Electromagnetic Environment Branch of the Electromagnetic Warfare and Communications Laboratory of ASD, are gratefully acknowledged. Likewise, Mr. Sang Bin Rhee of the Cooley Electronics Laboratory of The University of Michigan has been very helpful.

REFERENCES

1. V. P. Shestopalov, A. A. Bulgakov and B. M. Bulgakov, "Theoretical and Experimental Investigations of Helix-Dielectric Aerials," *Radiotekhnika i elektronika*, 6, No. 7, pp. 1136-1145, 1961.
2. T. T. Taylor, "A Discussion of the Maximum Directivity of an Antenna," *IRE Proceedings*, May 1948, pp. 1134-1135.
3. L. J. Chu, "Physical Limitations of Omni-Directional Antennas," *Journal of Applied Physics*, Vol. 19, December 1948, pp. 1163-1175.
4. H. A. Wheeler, "Fundamental Limitations of Small Antennas," *IRE Proceedings*, December 1947, pp. 1479-1484.
5. L. Lewin, "Advanced Theory of Waveguides," Iliffe and Sons, Ltd., London, 1951.
6. A. T. Adams and R. M. Kalafus, "Study and Investigation of a UHF-VHF Antenna," Cooley Electronics Laboratory, Bimonthly Report No. 1, 1963.
7. A. T. Adams, J. E. Herman and S. B. Rhee, "Study and Investigation of a UHF-VHF Antenna," Cooley Electronics Laboratory, Bimonthly Report No. 2, 1963.
8. A. T. Adams, J. E. Herman and S. B. Rhee, "Study and Investigation of a UHF-VHF Antenna," Cooley Electronics Laboratory, Bimonthly Report No. 3, 1963.
9. J. D. Dyson, "The Equiangular Spiral Antenna," IRE Transactions on Antennas and Propagation, April 1959, pp. 181-187.
10. W. Rotman, "Metal-Clad Progressive Phase, Dielectric Antennas," *AFCRC*, November 1951.
11. R. E. Franks and C. T. Elfing, "Reflector Type Periodic Broadband Antennas," IRE WESCON Convention Record, 1958, pp. 266-271.
12. F. P. Brownell and D. E. Kendall, "Miniaturized Cavity Fed Slot Antennas," 1960 WESCON Record, Part I, pp. 158-166.

	Size	Volume	Bandwidth With Flange VSWR = 3.0 VSWR = 6.0	Bandwidth - No Flange VSWR = 3.0 VSWR = 6.0	Efficiency	Directivity	Weight	Operating Frequency (Mc)
Air Loaded Antenna	30" x 7½" x 10"	2250 cu. in.			90%	5.8	25-3/4 pounds	300
Ferrite Powder Loaded Antenna	12" x 3" x 9"	144 cu. in.	22 Mc	50 Mc	65%	5.0	16-3/4 pounds	320
Solid Ferrite Loaded Antenna	5" x 2" x 1½"	15 cu. in.	19 Mc	34 Mc	30%	5.0	3.6 pounds	352

Table I. Performance comparison of rectangular cavity-slot antennas.

Ferrite Powder

$$\mu'\epsilon' = 8.3$$

$$\mu' \approx 2.2$$

$$Q = \mu'/\mu'' = 30 \text{ at } 300 \text{ Mc}$$

Solid Ferrite

$$\mu' = 6.63$$

$$\epsilon' = 12.6$$

$$Q = \mu'/\mu'' = 30 \text{ at } 300 \text{ Mc}$$

Table II. Characteristics of ferrite material.

RESONANT FREQUENCY

	<u>Theoretical</u>	<u>Experimental</u>
Solid Dielectric Cavity	313 Mc	316 Mc
Solid Ferrite Cavity	351.7 Mc	347 Mc
Maximum Error = 1.3 %		

HALF-POWER BANDWIDTH

	<u>Frequency (Mc)</u>	<u>Theoretical</u>	<u>Experimental</u>
Solid Dielectric Cavity	316	4.9 %	5.7 %
Solid Ferrite Cavity	352	8.5 %	9.7 %
Powder Ferrite Cavity	352	12.6 %	15.6 %
Maximum Error = 24 %			

EFFICIENCY

	<u>Frequency (Mc)</u>	<u>Theoretical</u>	<u>Experimental</u>
Powder Ferrite Cavity	315	62 %	66.5 %
	227	40 %	47 %*
Solid Ferrite Cavity	352	21 %	30 %*

Table III. Comparison of theoretical
experimental data.

* Only an approximate efficiency measurement was obtainable.

<u>Frequency (Mc)</u>	<u>Q</u>
100	8.8
200	37.4
300	34.5
400	27.8
500	27.5
600	21.8
700	16.1
800	13.5
900	8.1

Table IV. Q of ferrite powder. *

* A. T. Adams and R. M. Kalafus, Study and Investigation of a UHF-VHF Antenna, Quarterly Progress Report No. 10, Cooley Electronics Laboratory, The University of Michigan, January 1963.

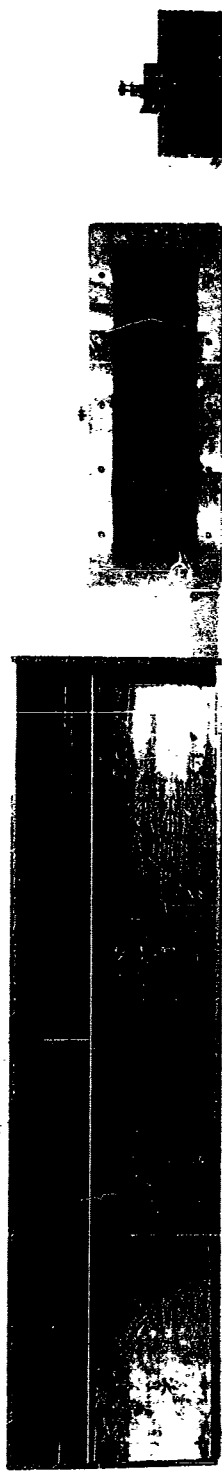


Fig. 1. Physical comparison of loaded-slot antennas.

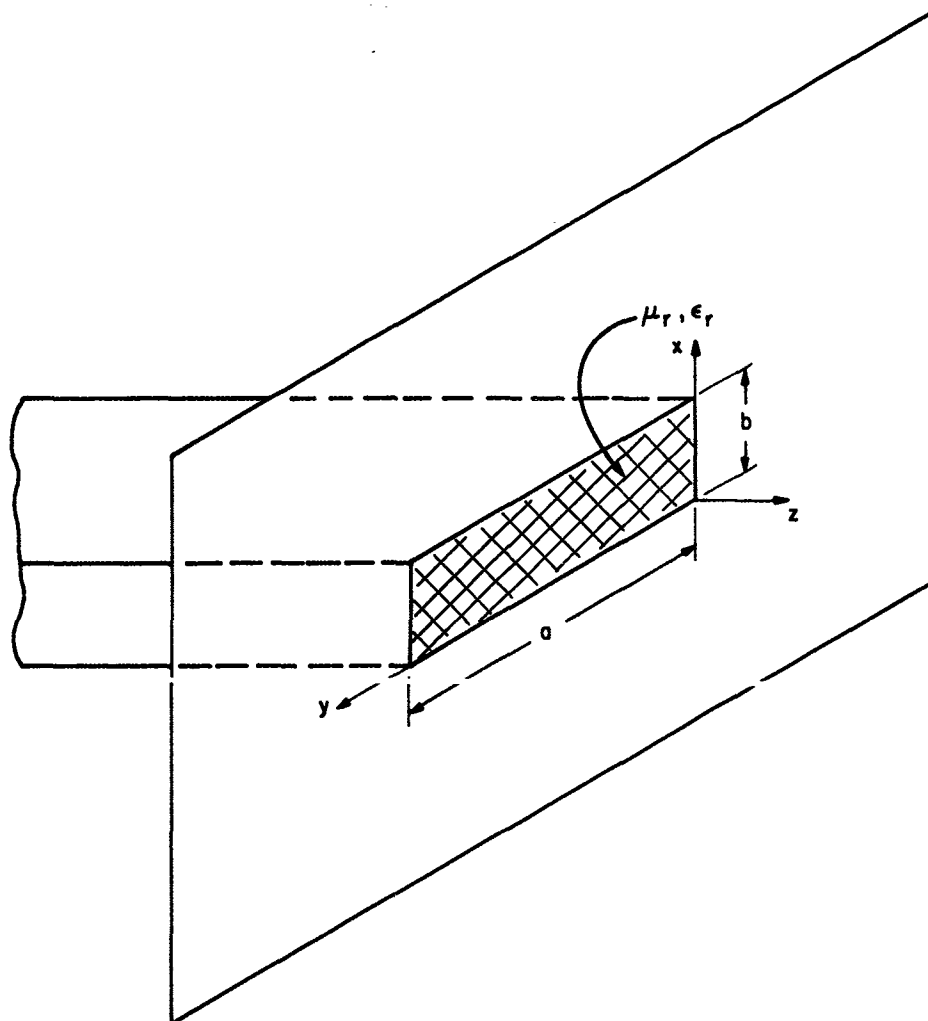


Fig. 2. (a) A loaded waveguide radiator.

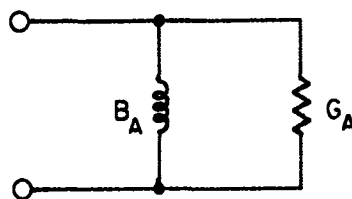


Fig. 2. (b) Equivalent circuit.

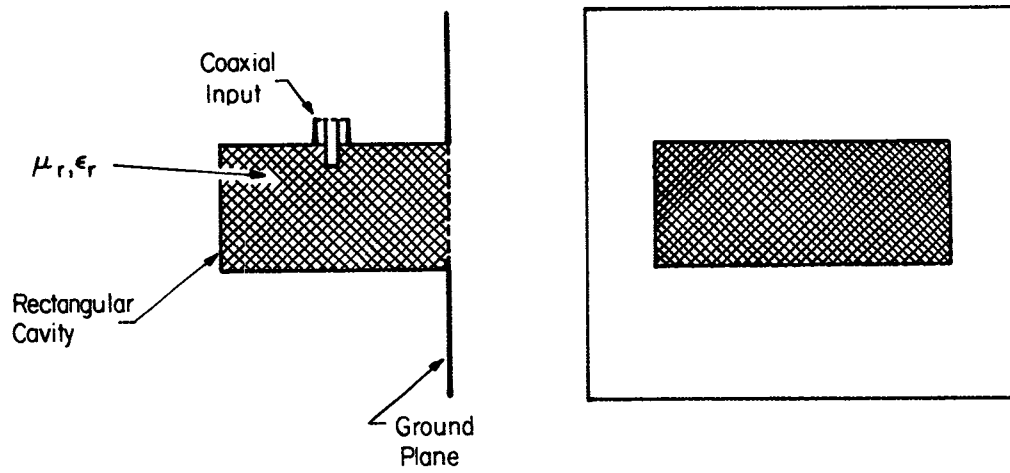
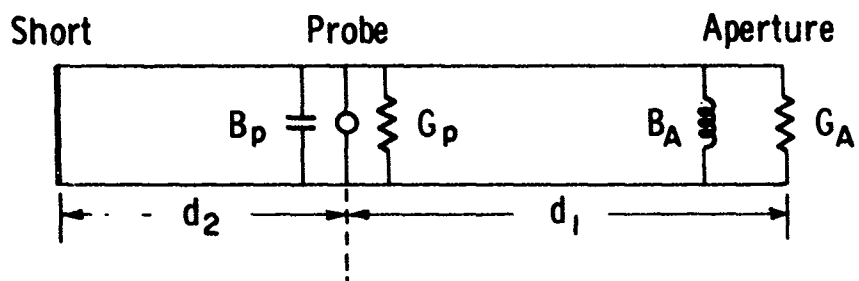
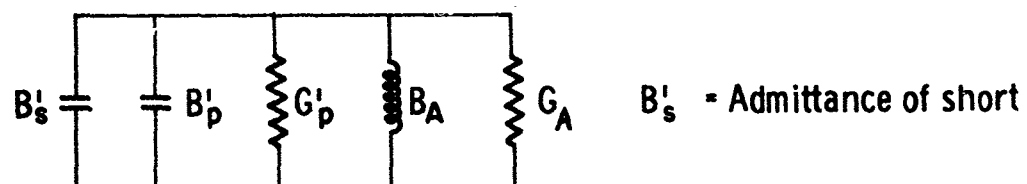


Fig. 3. A loaded rectangular cavity-slot antenna.



Transforming to the aperture:



At resonance:

$$G'_p = G_A$$

$$B'_s + B'_p + B_A = 0$$

Fig. 4. Simplified equivalent circuit.

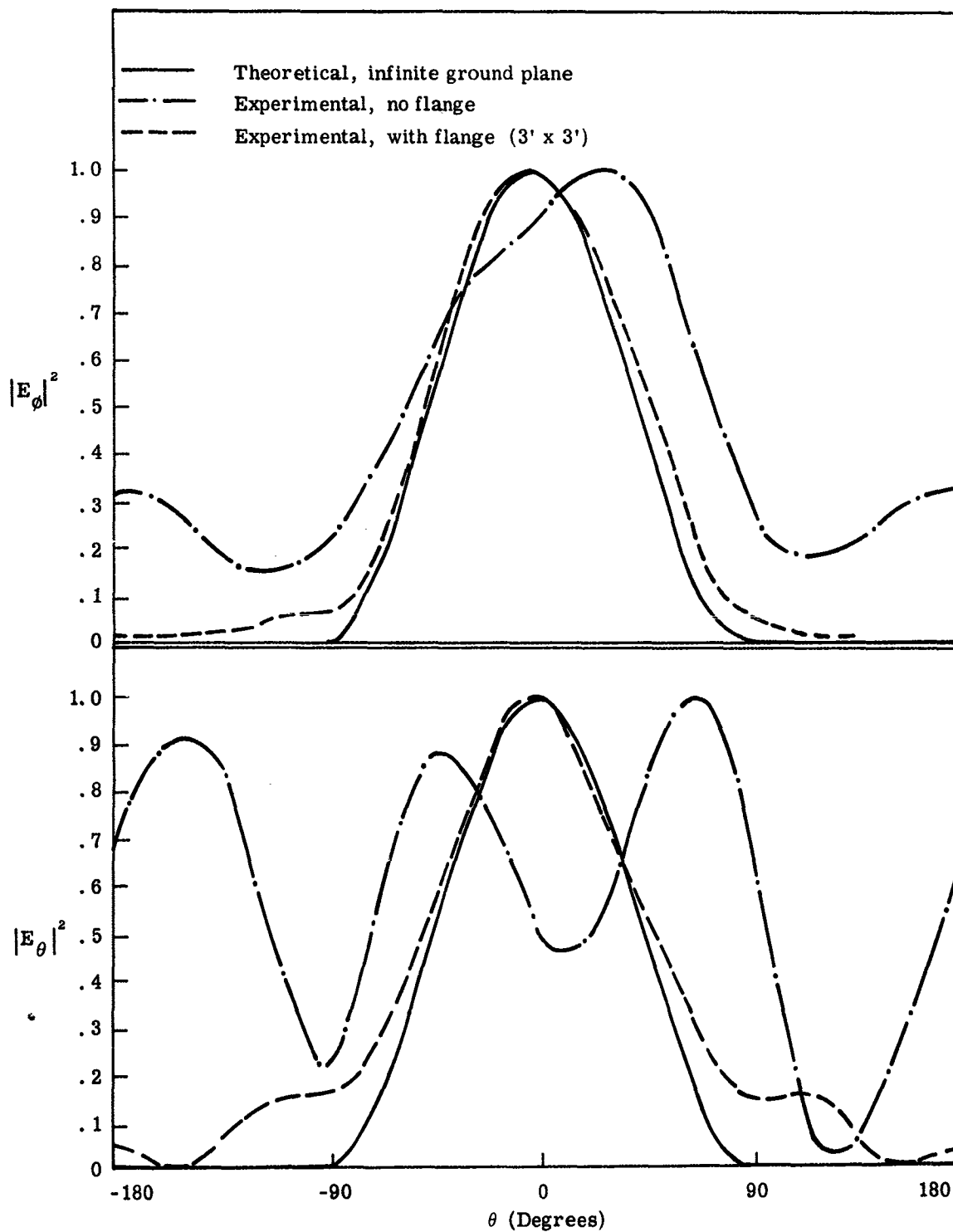
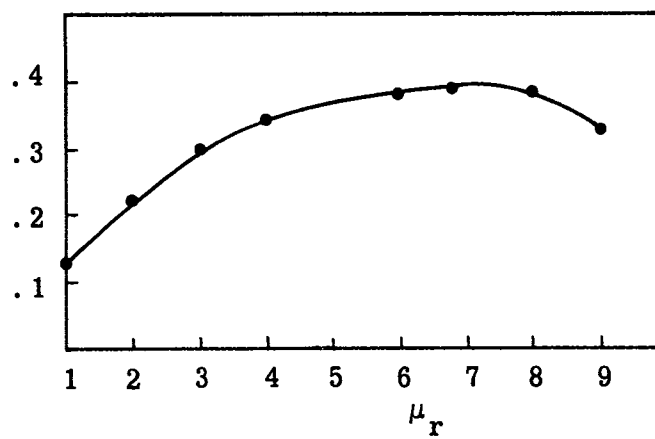


Fig. 5. Comparison of theoretical and experimental beam patterns of a solid-ferrite loaded antenna.

Square of
Aperture
Transmission
Coefficient



Half-Power
Bandwidth
%

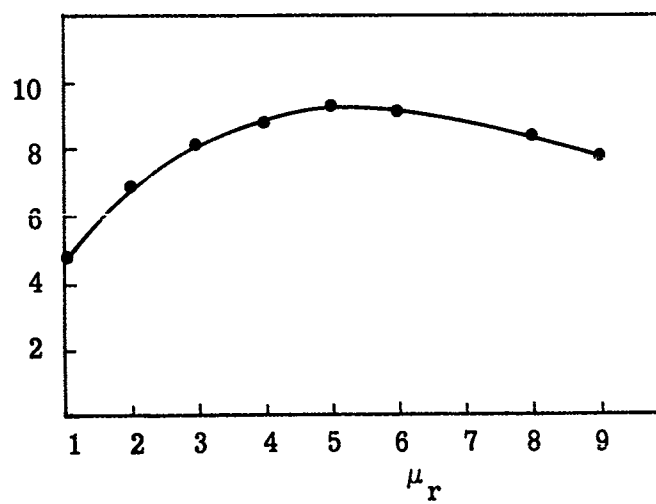


Fig. 6. Optimum choice of materials.

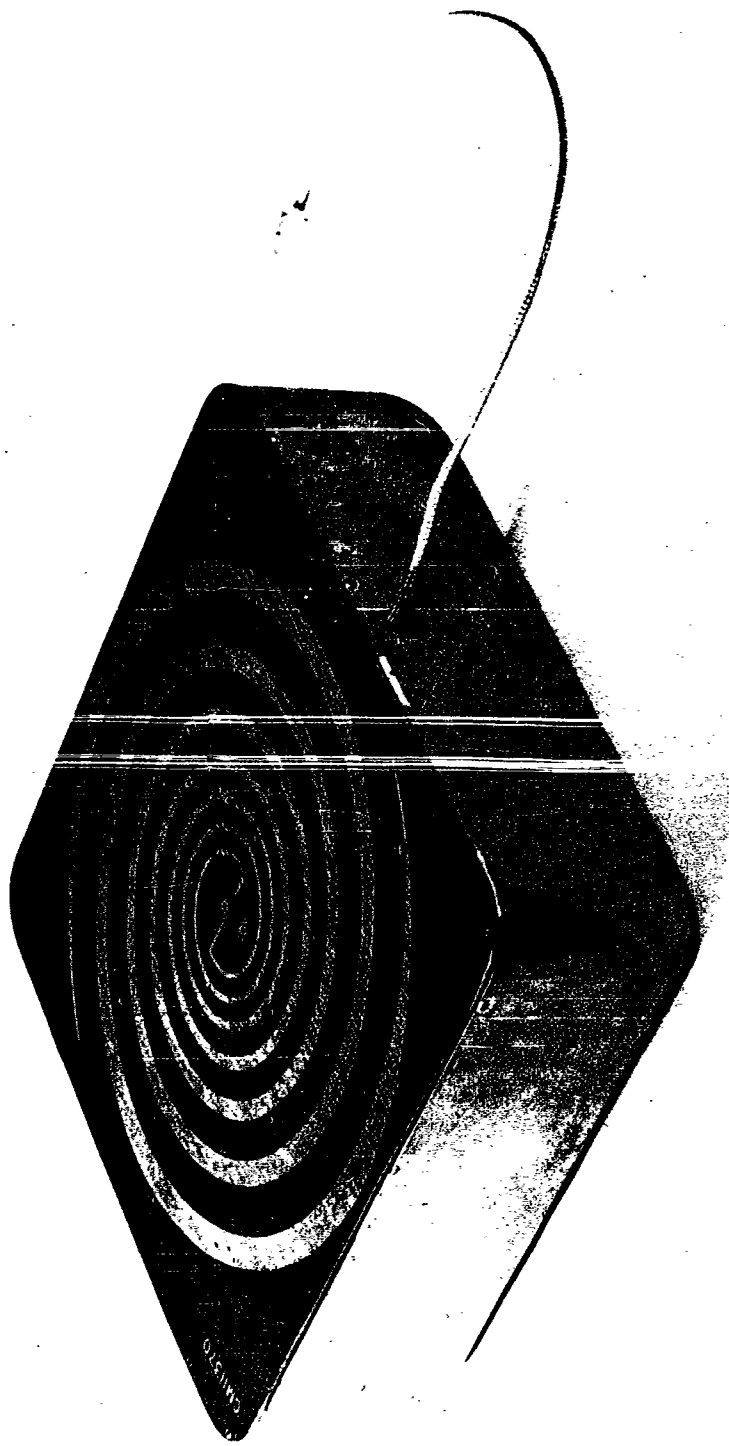


Fig. 7(a). Equiangular spiral.

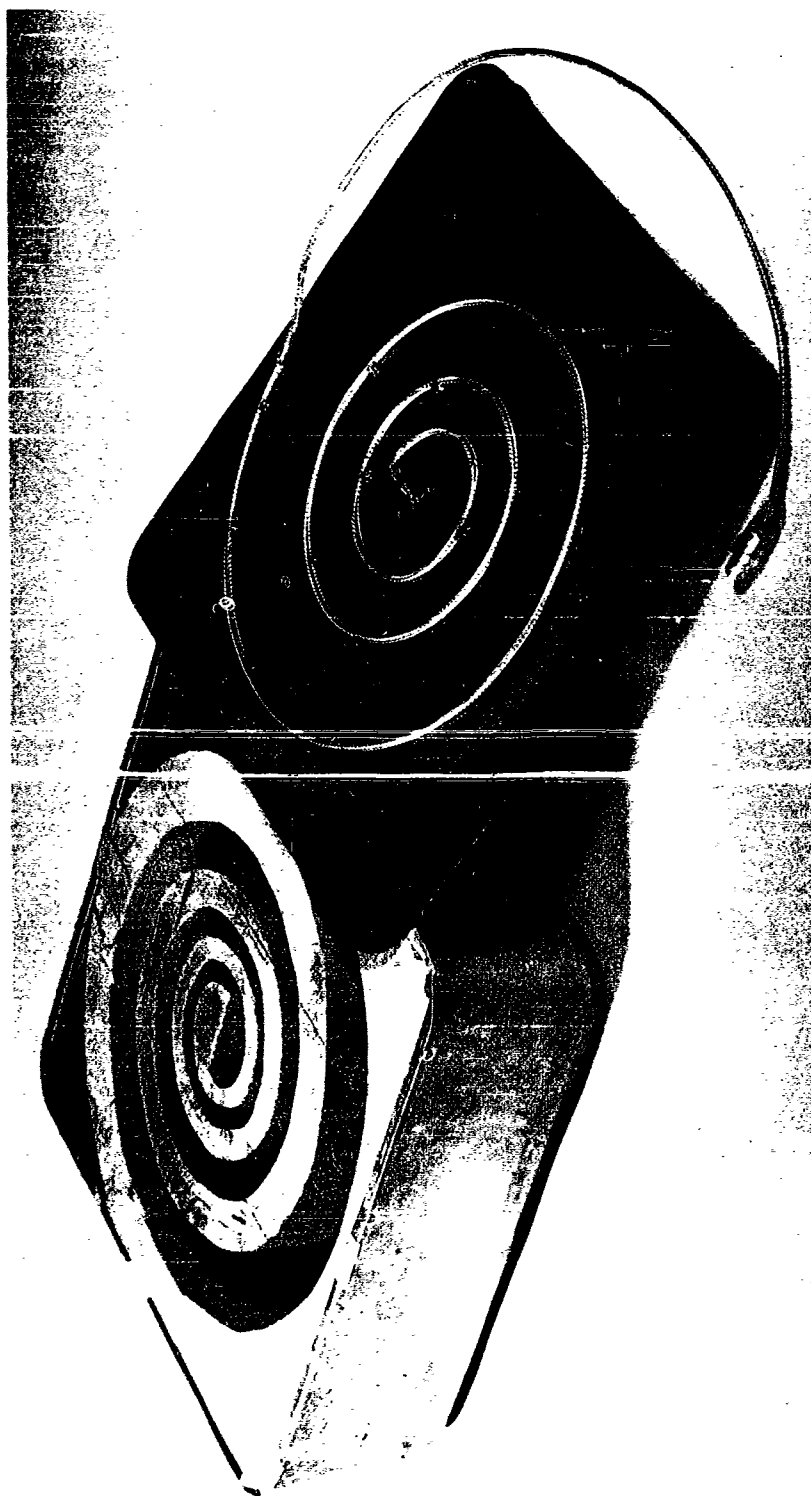


Fig. 7(b). Constructor showing feed and loading.

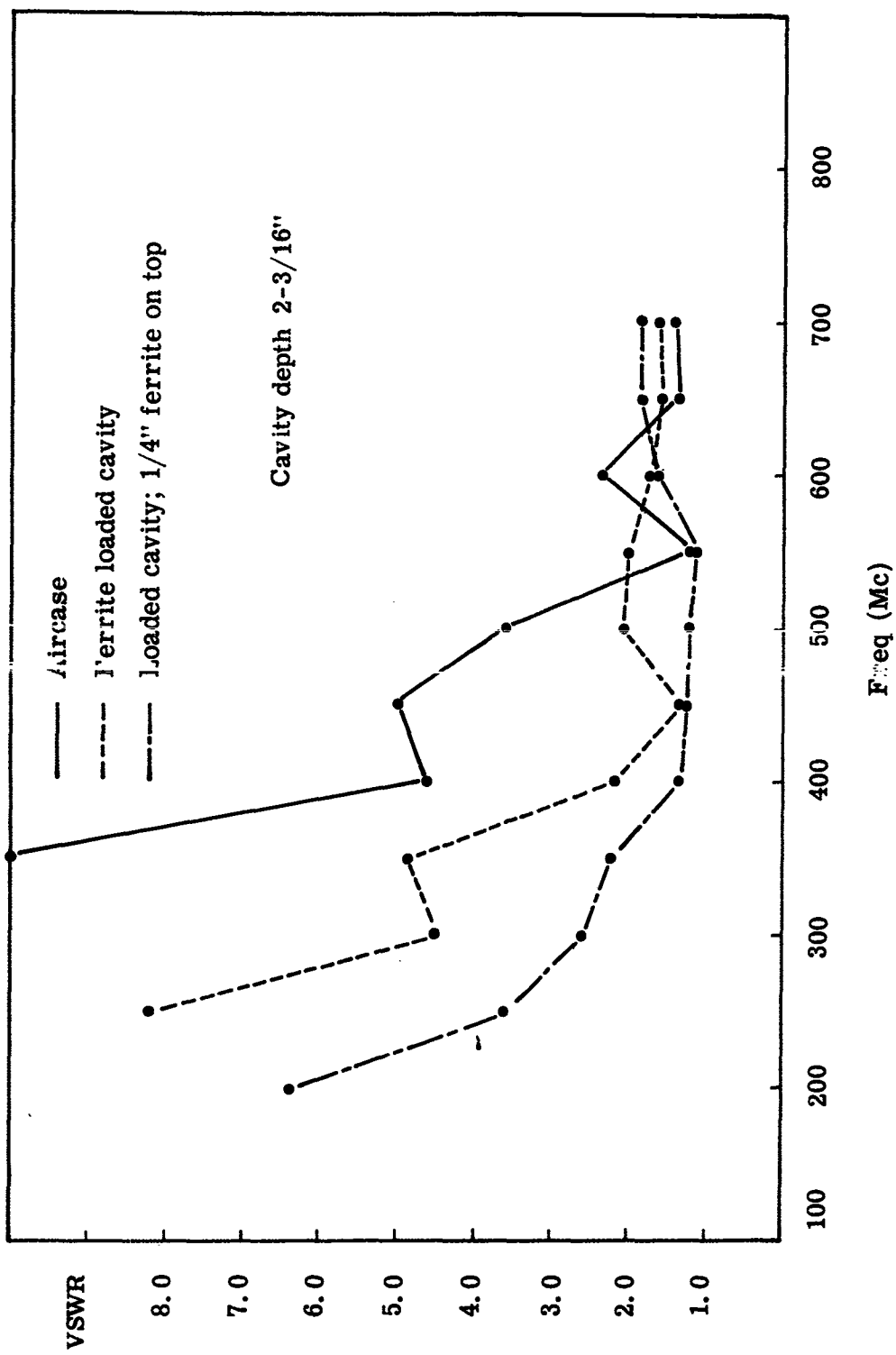


Fig. 8. VSWR for fully-loaded spiral.

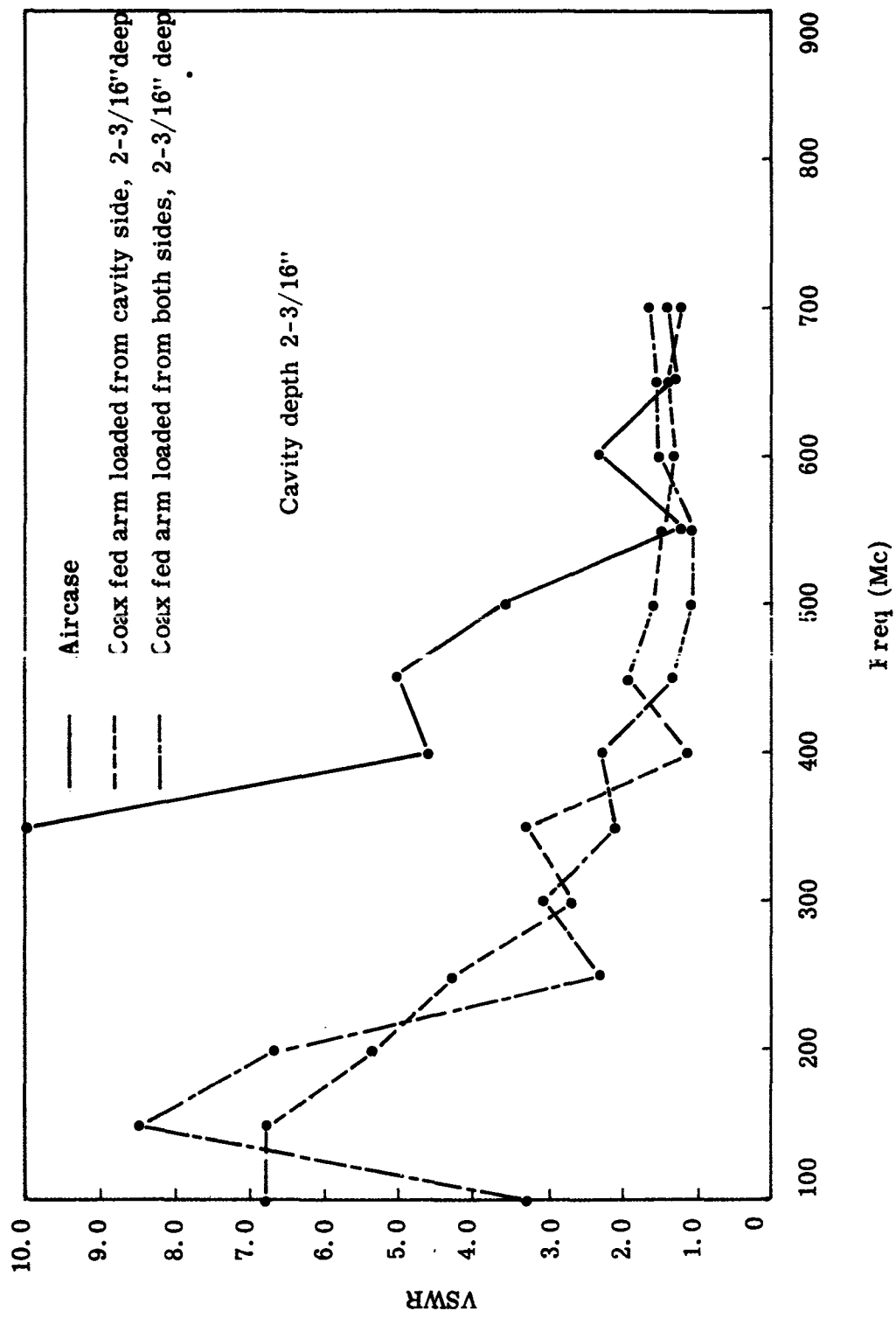


Fig. 9. VSWR for single-filar loading.

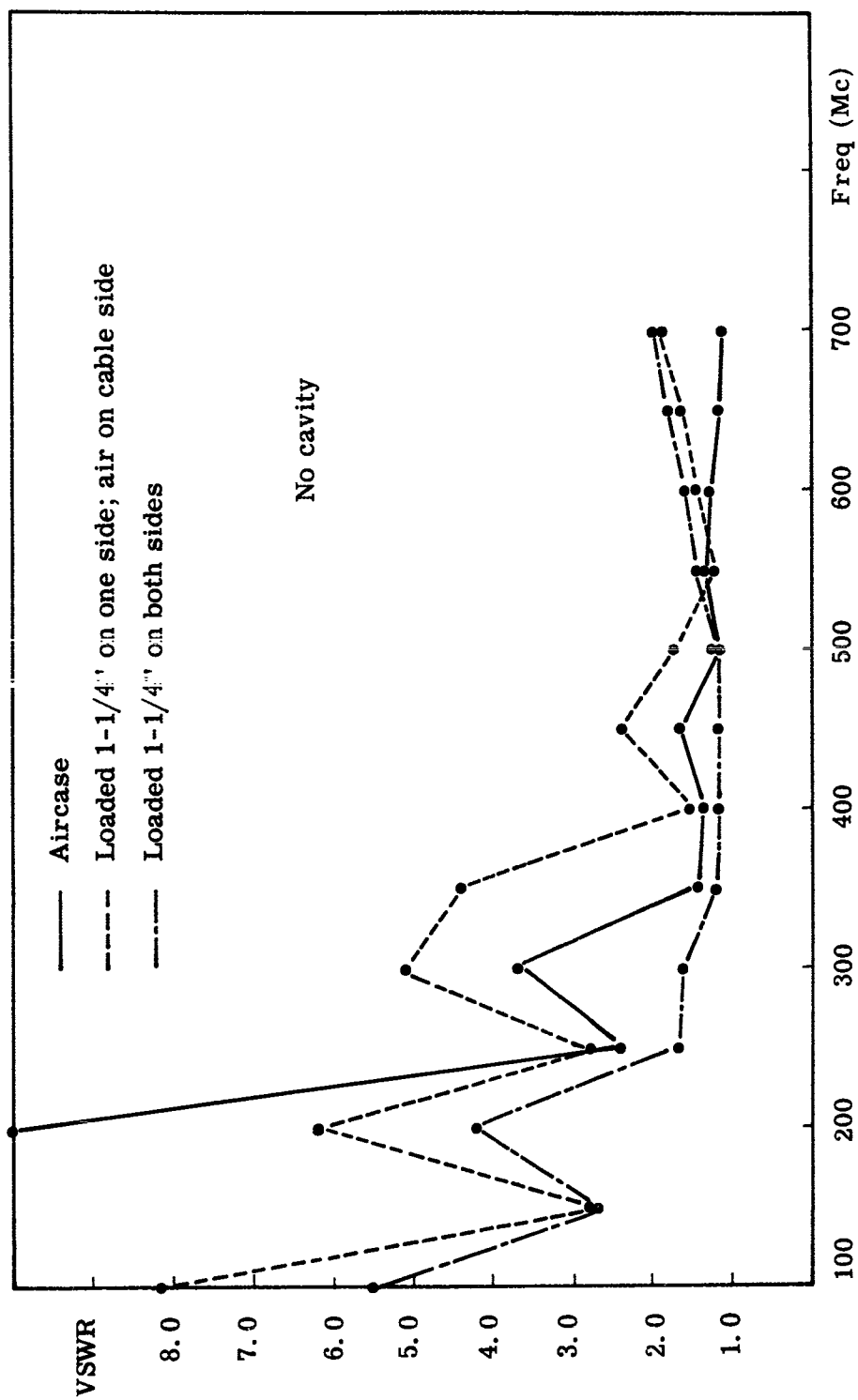


Fig. 10. VSWR for loaded spiral with no cavity.

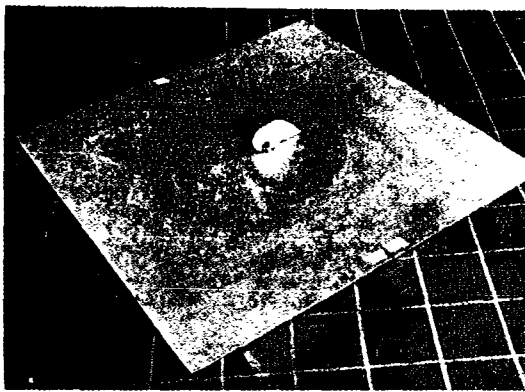


Fig. 11(a). Scimitar antenna.

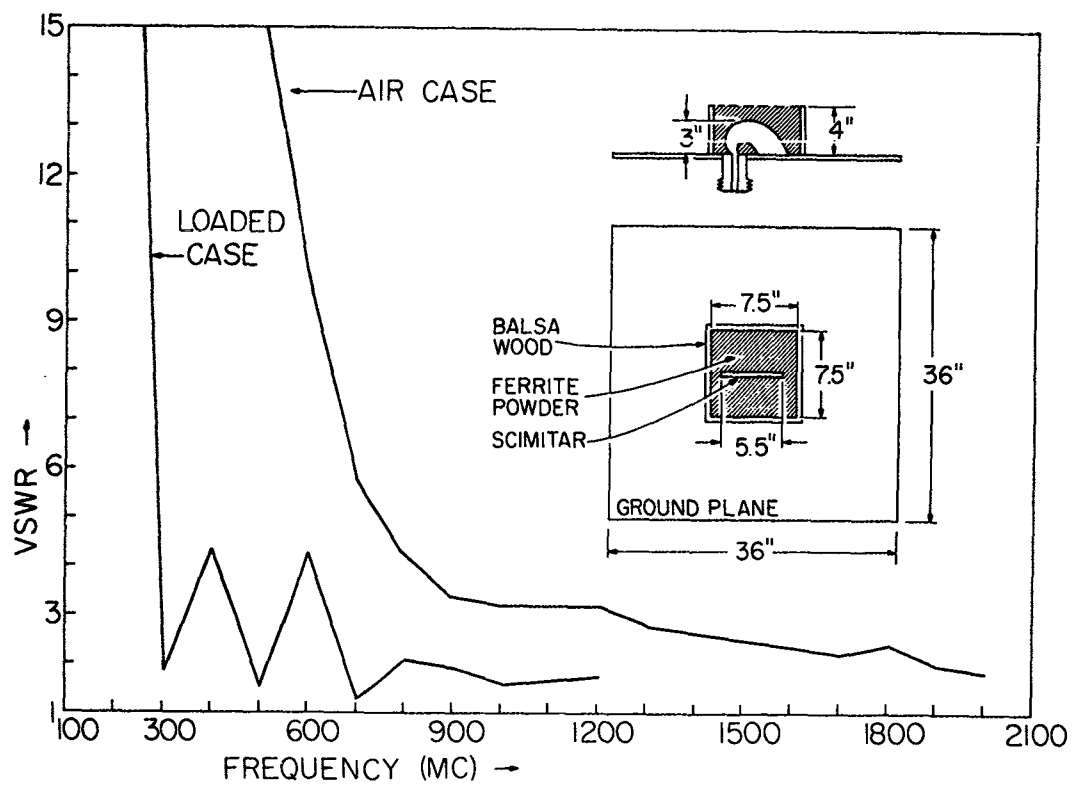
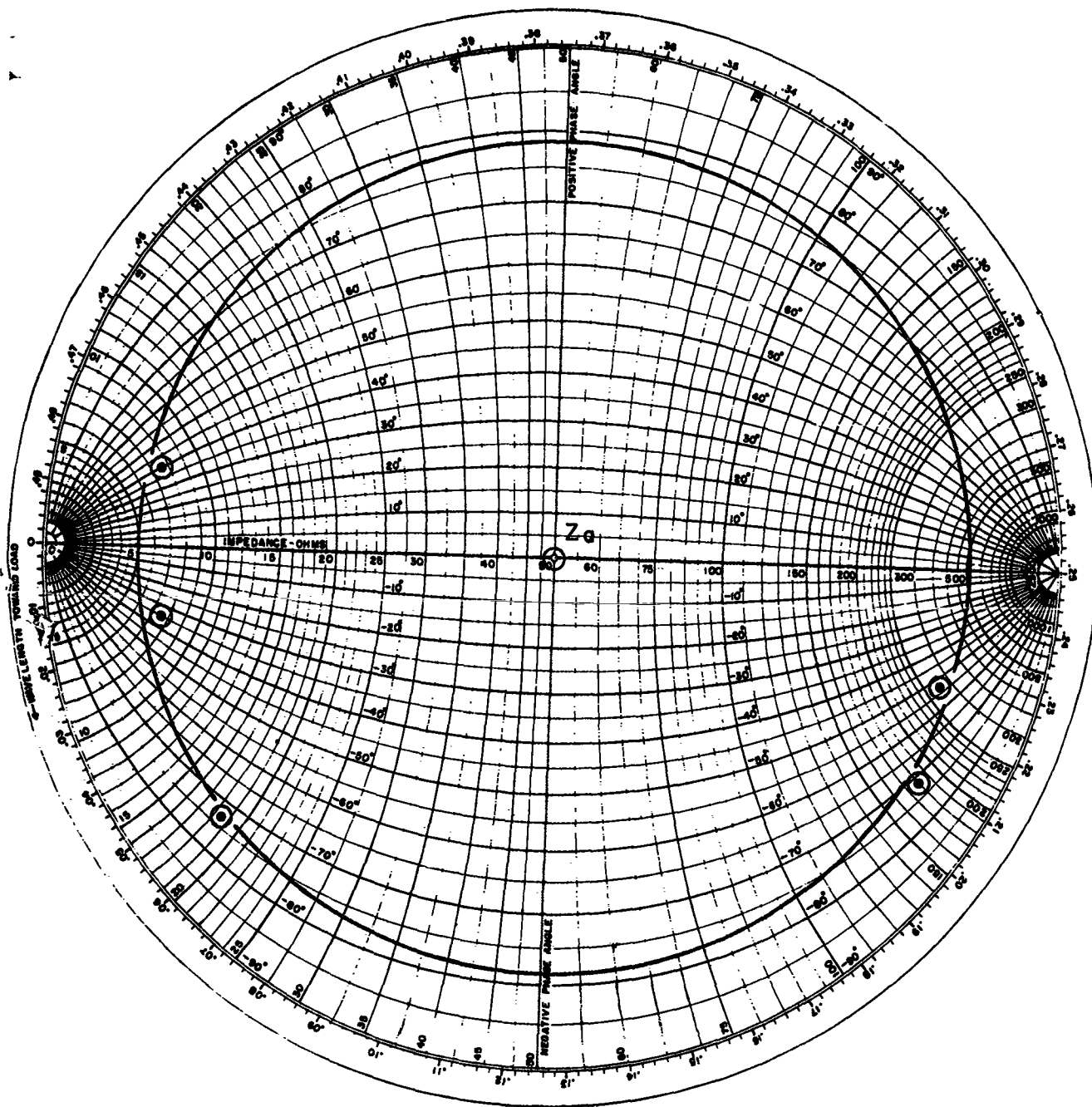


Fig. 11(b). VSWR of Scimitar antenna with and without ferrite loading.



Frequency = 400 Mc
 Efficiency = 79%

Fig. 12. Efficiency of loaded scimitar antenna.

ANALYSIS AND DESIGN OF TUNNEL-DIODE-LOADED DIPOLE ANTENNAS*

Kyohei Fujimoto

Antenna Laboratory
Department of Electrical Engineering
The Ohio State University
Columbus, Ohio

ABSTRACT

Tunnel-diode-loaded dipole antennas have been studied. Various configurations have been used to facilitate matching and to optimize the placement of a tunnel diode amplifier in the dipole. The combined antenna and amplifier is called an antennafier.

The analysis is based on an equivalent circuit of the loaded dipole that can be obtained by decomposing the loaded dipole antenna into a radiating component and a non-radiating component. Using the equivalent network, antennafier properties such as gain, noise performance, etc., can be obtained. Four types of antennafiers, differing in the location of the tunnel diode loading, are analyzed and design considerations are discussed.

The stability condition of an antennafier is discussed and is found to depend not only on the static situation but also on field effects, including reflection and coupling.

It is shown that the reradiation in the antenna mode of an antennafier may be found from the reflection factor at the output of the equivalent source of the antennafier. This is illustrated with some examples.

Measurements for selected models were made. Typical values are 10 db gain and 6 db noise figure at 420 mc.

* The work reported here was sponsored in part by Aeronautical Systems Division, Wright-Patterson Air Force Base, Ohio under Contract AF 33(657)-10386 with The Ohio State University Research Foundation.

ANALYSIS AND DESIGN OF TUNNEL- DIODE-LOADED DIPOLE ANTENNAS*

Kyohei Fujimoto

Antenna Laboratory
Department of Electrical Engineering
The Ohio State University
Columbus, Ohio

I. INTRODUCTION

This paper deals with the integration of amplifier circuitry into an antenna structure, the resulting device is called an antennafier. Specifically, tunnel diode circuitry is integrated into modified dipoles. This is but one phase of the growing field of integrated circuits and antennas. This is a challenging field for antenna engineers because it requires not only a good knowledge of antennas but also of circuits and leads to a more sophisticated concept of an antenna system. The antenna may no longer be a passive, linear, and reciprocal device but in general may be active, nonlinear and nonreciprocal.

The π -match or double-H antenna structure¹ (Fig. 1) is used to facilitate matching and to optimize the placement of a tunnel diode amplifier in the dipole. In principle the loaded π -match antenna can be decomposed into two parts, e. g., radiating and non-radiating components. This facilitates the determination of the equivalent network of the antennafier, from which the antennafier properties such as impedance, gain, and noise performance can be found by applying ordinary network theory.

Four types of antennafiers depending on the place of tunnel diode loading, as shown in Fig. 2, have been considered. In addition a coaxial type has also been studied.

* The research reported here was supported in part by Aeronautical Systems Division, Wright-Patterson Air Force Base, Ohio under Contract AF 33(657)-10386 with The Ohio State University Research Foundation.

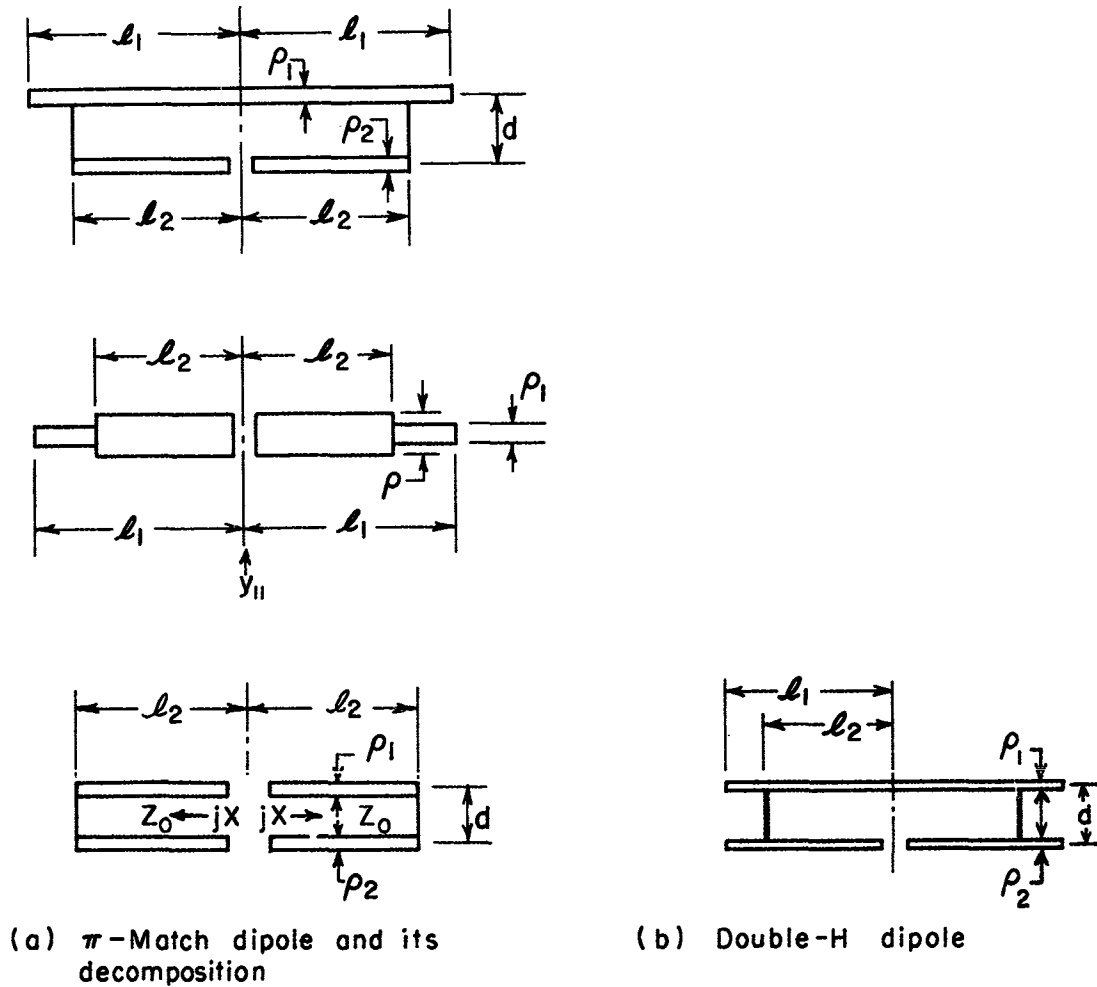


Fig. 1. π -match and double-H dipole antenna

The stability of an antennafier is considered not only from the standpoint of the static situation (no field present) but also under the effect of an incident electromagnetic field, which may cause a shift in the antennafier parameters.

Re-radiation or backscattering is also an important factor in the design of an antennafier. The magnitude of backscattering in the antenna mode may be uniquely determined by knowing the reflection factor at the input terminals of the equivalent network of the antennafier.

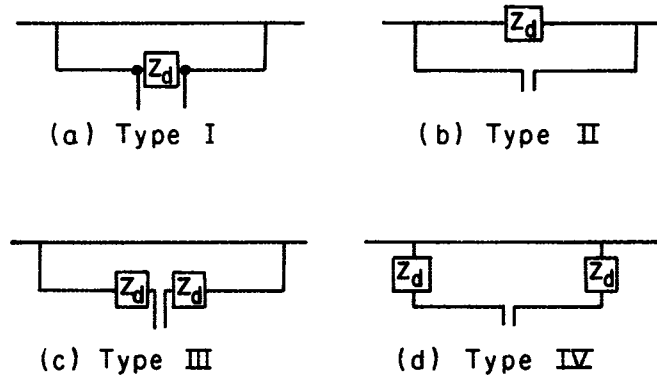


Fig. 2. Four types of loaded π -match dipole antenna.

In general antenna impedance is not given in analytical form, therefore theoretical calculation of antenna performance is limited. If measurements can be carried out with sufficient accuracy, graphical methods using the experimental results seem to be most useful. A modified Smith chart may be used for studying the stability and re-radiation problems.

II. ANALYSIS

1. Input Impedance and the Equivalent Circuit

By means of a decomposition of induced currents and voltages on the antenna element, one can obtain an equivalent circuit for the π -match antenna.^{1,2} By the same principle, one may obtain the input impedance of a loaded π -match antenna. The input admittances of the four types of loaded π -match antennas shown in Fig. 2 are given as follows,²

$$\text{Type I} \quad : \quad Y_{AI} = v_i^2 Y_{11} + \frac{1}{j2X} + Y_d, \quad (1)$$

$$\text{Type II} \quad : \quad Y_{AII} = \frac{v_i^2 Y_{11} + \frac{1}{j2X} (1 + Y_{11} Z_d)}{1 + Z_d \left\{ \frac{1}{j2X} + (1 - v_i)^2 Y_{11} \right\}}, \quad (2)$$

$$\text{Type III : } Y_{AIII} = \left[\left(\nu_i^2 Y_{11} + \frac{1}{j2X} \right)^{-1} + 2 Z_d \right]^{-1}, \quad (3)$$

$$\text{Type IV : } Y_{AIV} = \nu_i^2 Y_{11} + \frac{1}{2Z_0} \cdot \frac{Z_0 + j Z_{d2} \tan \beta \ell_2}{Z_{d2} + j Z_0 \tan \beta \ell_2}$$

$$- \frac{2 \nu_i^2 Y_{12} Z_{d2} \frac{1}{\cos \beta \ell_2}}{Z_{d2} + j Z_0 \tan \beta \ell_2} - j \frac{\nu_i^4 Y_{12}^2 \tan \beta \ell_2}{Y_0 + j Y_{d2} \tan \beta \ell_2} \quad (4)$$

The quantities are (see Fig. 1)

Y_{11} : admittance of the equivalent dipole

ν_i : the current division factor¹

Y_d : tunnel diode admittance ($= 1/Z_d$)

jX : impedance of the equivalent transmission line ($= jZ_0 \tan \beta \ell_2$)

Y_{d2} : $1/Z_{d2} = 1/Z_d + Y_{22}$

Y_{12} : the admittance mutually existing between the point where Z_d is located and input terminal,

Y_{22} : the admittance seen at the equivalent terminal where loading Z_d 's are placed.

Equivalent networks can be obtained from the impedance equations. For example, an equivalent network of the Type I antenna-fier is shown in Fig. 3.

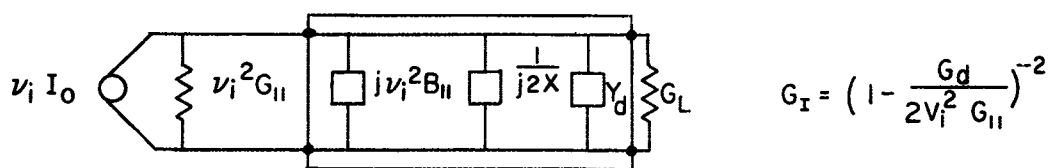


Fig. 3. Equivalent circuits of loaded dipole antenna and antenafier Type I.

2. Gain

The gain of an antenafier is considered to be a measure of increase of load power due to the addition of the tunnel diode to the antenna. Using the Fig. 4 network parameters A, B, C, and D,

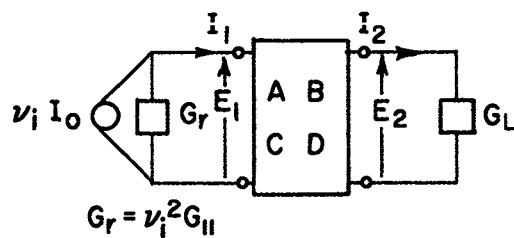


Fig. 4. Equivalent network of π -match antenna.

gain is given by

$$g = \frac{4 G_r G_L}{|G_r (A + B G_L) + C + D G_L|^2} \quad (5)$$

Using values of A, B, C, and D obtained from the input impedance equations, we can find the gain of an antenafier.

3. Noise Performance

In an integrated system, the determination of the noise contribution of the network components would appear to be quite difficult because of the inaccessibility of terminals. A practical technique for integrated systems based on field-strength sensitivity measurements has been previously reported.³ The system with amplifier is compared to the system with the amplifier either actually or effectively removed. Referring to Fig. 5, we can find a noise figure F_T of the total system as

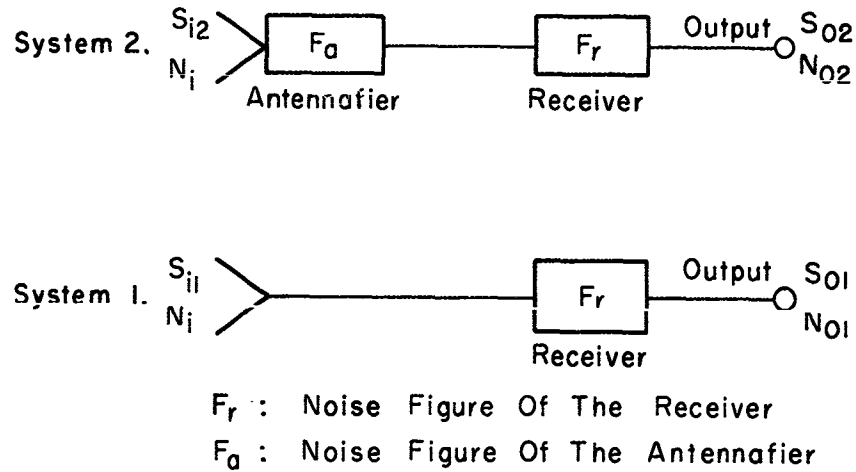


Fig. 5. Block diagram of representation used in determining noise figure of antennafier.

$$F_T = \frac{R}{\xi} \cdot F_r,$$

and the noise figure F_a of the antennafier

$$F_a = F_T \left\{ \frac{F_r(1 - \eta) + \eta}{F_r} \right\}, \quad (7)$$

where

$$R = \frac{S_{02} / N_{02}}{S_{01} / N_{01}}, \quad \xi = \frac{S_{i2}}{S_{i1}} \quad \text{and} \quad \eta = \frac{N_{02}}{N_{01}}. \quad (8)$$

The ratio R is important because it tells immediately the effect of adding the amplifier circuitry to the antenna. The quantities ξ and R (including η) can be obtained by measurements. Also, R can be found theoretically by using the equivalent circuit for noise contribution of the network components.

4. Stability

Stability of an antennafier may be treated for two cases. First, the antennafier should not show any unstable behavior in the static situation (no field present). In general, if the transfer function of antennafier network is given by

$$g(p) = \frac{1}{|f(p)|} \quad (9)$$

where $p = \sigma + j\omega$, the complex frequency function, stability requires

$$f(p) \neq 0 \quad \text{for } \sigma > 0. \quad (10)$$

As an alternate form a network as shown in Fig. 6(a), for example, may be said to be stable if

$$\operatorname{Re} \{G_r + Y_{i1}\} > 0,^* \quad \text{for } G_L \geq 0, \quad (11a)$$

or

$$\operatorname{Re} \{G_L + Y_{i2} + Y_d\} > 0, \quad \text{for } G_r \geq 0. \quad (11b)$$

* Y_{i1} includes Y_d .

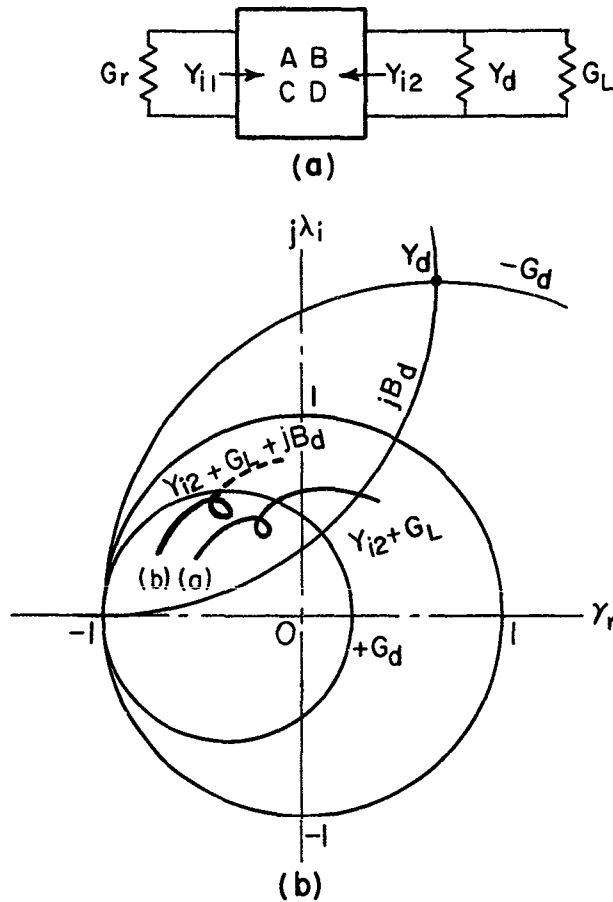


Fig. 6. Example of stability testing.

Graphical determination of Eq. (11b) is shown in Fig. 6(b) where the heavy line portion of the curve (b) shows the stable region.

Second, the case of an antennafier placed in an electromagnetic field is considered. It is possible that the signal might cause a shift in the bias point of the tunnel diode even when the signal strength is within the dynamic range. The variation of bias and thus the negative resistance will affect the stability. Besides the effect of signal strength, the effect of reflection from obstacles or the effect of coupling with other antenna elements will also affect the stability because these effects may change the antenna impedance. Therefore, the stability of the antennafier must be secured for a shift in the network parameters such as negative resistance and antenna impedance due to an incident field. In this case, one may write for the stability condition

$$f(p) + \frac{\partial f(p)}{\partial G_d} dG_d + \frac{\partial f(p)}{\partial Y_r} dY_r \neq 0 \quad \text{for } \sigma > 0, \quad (12a)$$

or using Eq. (11b),

$$\operatorname{Re} \left(G_L + Y_{i2} + Y_d + \frac{\partial Y_{i2}}{\partial Y_r} d Y_r + d G_d \right) > 0. \quad (12b)$$

It is clear that the same procedure used in Fig. 6 can be applied for this case with slight modification.

One must also notice that the shift in the network parameters affects the gain considerably. The sensitivity of gain to the variation of the network parameters increases as the gain becomes high. Hence, the sensitivity of gain must not be ignored in the design procedure.

IV. RE-RADIATION

The field scattered by an antenna as a function of load impedance Z_ℓ may be expressed by⁴

$$\bar{E}(Z_\ell) = \bar{E}(Z_r^*) + \Gamma \bar{E}^{AM}, \quad (13a)$$

where

$$\bar{E}^{AM} = \frac{Z_r^2}{2 R_r} I(0) \bar{E}^T, \quad (13b)$$

$$\Gamma = \frac{Z_r^* - Z_\ell}{Z_r + Z_\ell} \quad (* = \text{conjugate}) \quad (13c)$$

$\bar{E}(Z_r^*)$ is called the structural scattering which is the scattered field resulting when the antenna is matched ($Z_r^* = Z_\ell$), \bar{E}^{AM} is called the antenna mode scattered field and has the same field distribution as the transmitting pattern of the antenna, and Γ is a modified current reflection factor which is observed at the output of the antenna (or the input of the equivalent network). The impedances Z_r and Z_ℓ are, respectively, antenna and load (equivalent network input) impedance. $I(0)$ is the current through the load $Z_\ell = 0$ and \bar{E}^T is the electric field transmitted by the antenna when excited by a unit voltage source. Since the input impedance of the equivalent network may have negative real value, Γ may have a number larger than unity.

Modifying Eq. (13) we have

$$\frac{\bar{E}(Z_\ell)}{\bar{E}^{AM}} = \frac{\bar{E}(Z_r^*)}{\bar{E}^{AM}} + \Gamma \quad (14)$$

Since $\bar{E}(Z_r^*)$ and \bar{E}^{AM} are constant quantities for an individual antenna, it may be said that Γ determines the portion of the scattered field which depends on the network parameters. Vector representation of Eq. (14) on the chart (Fig. 7) gives an easy way to visualize and to obtain the magnitude of the backscattering of an antennafier. Since Γ may be larger than unity, the backscattered field can be widely controlled by adjusting Γ by means of the network parameters.

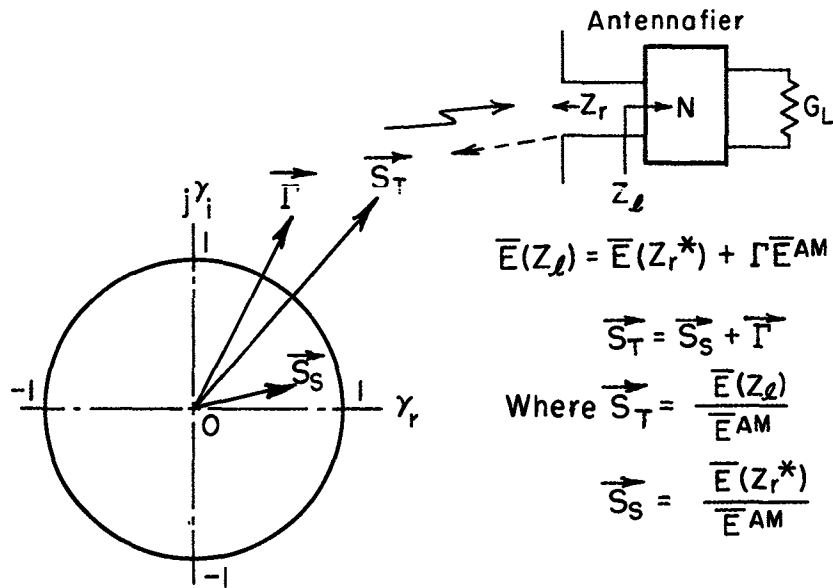


Fig. 7. Graphical determination of backscattering.

V. MODIFIED COAXIAL DIPOLE ANTENNAFIERS

When $v_i = 1$, the antenna structure becomes coaxial rather than two parallel wires (Fig. 8). The radiation current flows only on the outer conductor and the non-radiation current only on the inner conductor. The treatment is simpler than for the ordinary π -match antenna.

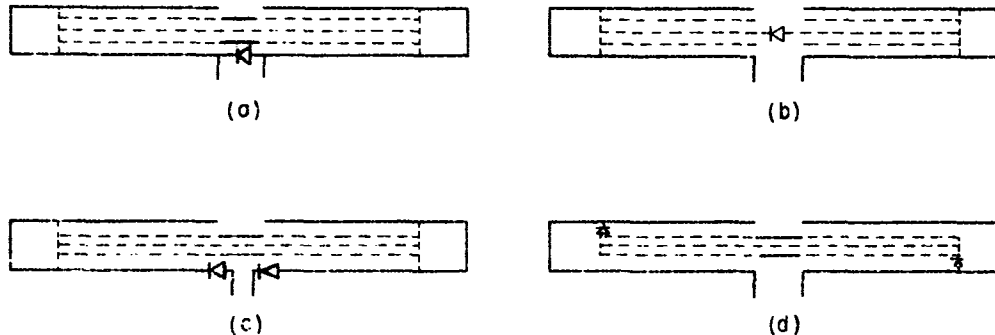


Fig. 8. Models of coaxial type antennafier.

VI. EXPERIMENTAL RESULTS

The tunnel diodes used were TD-1 and TD-1A. Measurements were made in the UHF region, centered at 420 mc.

Using a Type I antennafier (double-H), maximum gain obtained was approximately 12 db at a bias voltage -120 mV with shunt resistance 470 ohms and $l_2 = 1.2$ inches. Measured patterns of a Type II antennafier (coaxial) are shown in Fig. 9. Bandwidth of this type of antennafier was found to be approximately a few percent of the center frequency and noise figure was 5.8 db.

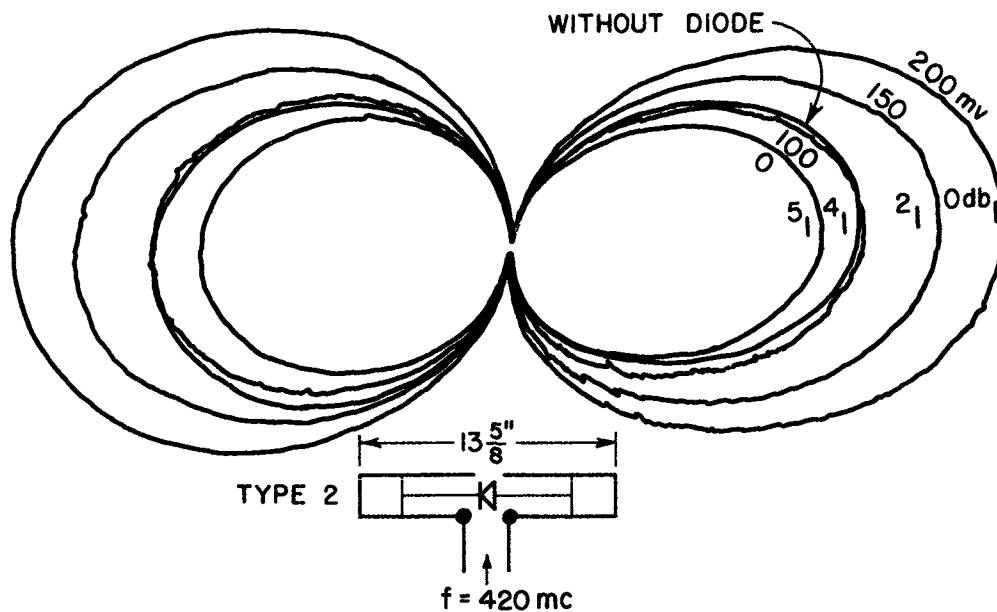


Fig. 9. Measured pattern of a loaded-dipole (coaxial type) antenna Type II.

VII. CONCLUSIONS

An antennafier incorporates both circuit principles and antenna principles. A practical structure in the form of a tunnel diode loaded dipole can be represented by an equivalent circuit and readily analyzed. The tunnel diode loaded dipole is a relatively simple device giving a gain of about 10 db and a noise figure of 5-6 db at 420 mc.

Antennafiers should prove to be useful devices. They can reduce the size and weight of a system while increasing reliability. Applications include not only amplification of a received signal but backscattering (echo) control and array applications (pattern control).

VIII. ACKNOWLEDGEMENT

The author wishes to thank Dr. C. H. Walter for many helpful comments and suggestions.

IX. REFERENCES

1. Uda, S. and Mushiake, Y., Yagi-Uda Antenna, Maruzen Co., Tokyo, Japan, 1954.
2. Fujimoto, K., "Analysis and Design of Tunnel Diode Dipole Antennafiers," Report 1566-1, May 1963, Antenna Laboratory, The Ohio State University Research Foundation; prepared under Contract AF 33(657)-10386, Aeronautical Systems Division, Wright-Patterson Air Force Base, Ohio.
3. "Electronic Reconnaissance Antenna," (Final Engineering Report, Vol. II, Part I), Report 903-16, 1 December 1960, Antenna Laboratory, The Ohio State University Research Foundation; prepared under Contract AF 33(616)- 6211, Aeronautical Systems Division, Wright-Patterson Air Force Base, Ohio. AD 253 642.
4. Green, R. B., "The Effect of Antenna Installation Upon the Echo Area of an Object," Report 1109-3, September 1961, Antenna Laboratory, The Ohio State University Research Foundation; prepared under Contract AF 33(616)-7386, Aeronautical Systems Division, Wright-Patterson Air Force Base, Ohio. AD 274 041

HIGH SPEED FERRITE PHASE SHIFTERS

RAYMOND F. MIX

Electronics Engineer

GENERAL DYNAMICS/POMONA

Pomona, California

August 1963

High Speed Ferrite Phase Shifters

I. INTRODUCTION

With the advent of high speed conical scanning antennas, it is necessary to provide methods for beam nutation. Scan rates as high as 20 kilocycles per second are now becoming obtainable. This paper deals with a particular type of ferrite phase shifting device for use in high speed conical scanning antennas.

Applying magnetic flux to ferrites through the waveguide housing has always been a problem at high frequency scan rates. This is due mainly to the shorted turn effect caused by the waveguide wall. The wall acts as a shorted secondary of a transformer. A discussion on the elimination of this shorted turn effect is also discussed herein.

II. FERRITE SELECTION

The selection of ferrites for this purpose was accomplished through manufacturers data and empirical data. High loss tangents eliminated many ferrites due to the low allowable loss in this phase shifter application. Other limiting factors were saturation moment, line width and Curie temperature. Data research narrowed down the selection to four ferrite materials, any one of which is suitable for the application.

1. Trans Tech, Inc., Type TT 390
2. General Ceramics, Type R1
3. Solid State Research, Type MM14
4. Raytheon, Type R151

Their characteristics are as follows:

- 1.

Type	Saturation Moment $4\pi M_s$	Line Width ΔH	Dielectric Constant ϵ'	Loss Tangent $\tan \delta$	Curie Temp. $^{\circ}\text{C}$
TT 390	2150	540	13	5×10^{-4}	320
R1	1760	490	13	5×10^{-4}	290
MM 14	2100	> 300	13	5×10^{-4}	280
R 151	2300	400	12	5×10^{-4}	300

Each of these ferrites was tested under simulated conditions and curves of the DC hysteresis loop and AC sensitivity were made.

The DC hysteresis loop is a plot of phase shift versus DC current. The result is shown in Figure 1. The area between the curves is representative of the hysteresis loss of the ferrite material. The AC sensitivity is a plot of the phase shift caused by a constant AC drive voltage for different values of DC current. A typical curve of AC sensitivity is shown in Figure 2.

Comparative curves were made on each of the four ferrites, and a selection made based on the curves and the loss at microwave frequencies.

III. THE SHORTED TURN EFFECT

There are a few methods available to reduce the shorted turn effect. Some of these are:

- a) Longitudinal slots (non-radiating) in the waveguide wall
- b) Windows
- c) Plastic waveguide walls with a thin metallic plated interior

d) Solid dielectrics with a thin metallic plated exterior

Longitudinal slots in the waveguide wall must be placed in the center of the narrow wall of the waveguide for minimum attenuation. Experiments prove that slots in the broad wall cause a great deal more attenuation. The slots for minimum attenuation are located as shown in Figure 3. The coil in this figure is shown split in order to illustrate the location of the slot.

With this arrangement, microwave attenuation is approximately proportional to the length of the slot. As an example, the loss of this device with no slot is approximately 0.3 db, and is increased at a rate of 0.5 db per inch of slot in Ku band waveguide. The frequency at which this, and all ensuing tests were performed was at approximately 10.5 GC.

The phase shift obtained by this method at high scan frequencies is greatly improved over a phase shifter with no slots. The phase shift requirement for testing purposes was 100° peak to peak phase shift for two inches of ferrite. In order to drive a phase shifter at 15 kilocycles without slots, it would take more than the 8 watts provided by the modulator. With a slot in the waveguide, the AC power dropped to only 2.3 watts per phase shifter. Little gain was obtained in power reduction when the slot was made longer than 110% of the length of the coil.

A method to eliminate part of the loss incurred by the waveguide longitudinal slot has been devised. It is the waveguide window.

Essentially it is an extremely thin film of metal placed over the slot to reduce the RF leakage. This method causes a slight increase in drive power, and does reduce the RF loss. The thin metallic plating is superior to this method, both in electrical characteristics and manufacturing ease.

The third method for reducing the shorted turn effect is a plastic waveguide wall with a thin metallic plating. A metal waveguide wall thin enough to reduce the shorted turn is not self supporting, therefore, it becomes necessary to support the waveguide wall by other means. For this reason, the plastic waveguide is used.

In determining theoretically just how thin a waveguide wall could become with negligible attenuation, consider the skin depth, δ , of copper waveguide at 10.5 GC.

$$\delta = \frac{1}{2\pi} \sqrt{\frac{\lambda \rho}{30\mu}}$$

For copper, the conductivity ρ is 1.72×10^{-6} ohm-cm, and the permeability μ is unity therefore

$$\delta = 6.45 \times 10^{-5} \text{ cm.}$$

From this fact, it can be seen that the waveguide wall need be only 25 microinches thick to support conduction of the microwave energy at 10.5 GC. Waveguide walls this thin are not feasible because the surface would have to be absolutely smooth and without roughness. In plating plastics with metals, the plastic should have some degree of roughness in order to provide reasonable adhesion. For these reasons, plating thicknesses less

than 48 or 100 microinches were not considered. The lower limit of these tests was set at .0001 inches.

When the inside of a plastic waveguide is plated, the type of plastic used is relatively immaterial. Any plastic of sufficient rigidity meeting environmental requirements can be chosen. This method lends itself to modification of existing designs to high frequency scanning applications. The waveguide housing the ferrite is molded from plastic. The piece is then plated with copper to a thickness of about .0002 inches. The exterior surfaces are then etched away leaving the copper on the inside only.

This method has several advantages. The power requirement for operation at approximately 15 Kilocycles was 1.2 watt for the phase shifter test requirement. The loss of this unit is only 0.3 db. This result can be extended far beyond 15 kilocycles by selection of a nickle ferrite such as Motorola's M052 with an increase in loss to about 0.8 db. The power requirements to operate this phase shifter reduce appreciably with lower frequency scan rates. For example, at 2 kilocycles the requirement is only about 0.45 watt.

Another method utilizing the thin waveguide wall is to plate the outside of a dielectric medium. The dielectric constant of this medium must be carefully chosen. First of all, the dielectric constant should be much smaller than that of the ferrite material since the microwave energy will propagate mainly in the higher dielectric. Secondly, low dielectrics do

not have sufficient mechanical rigidity under environmental conditions. Considering both these factors dielectric constants between 2 and 4 were considered.

The second consideration was the loss tangent, which eliminated all but a few dielectrics. These were Polytetrafluoroethylene (Teflon), Polystyrene, Polyethylene and Emerson Cumming's LoK. Teflon has excellent characteristics both in loss tangent and dielectric constant, the only disadvantages being weight and the tendency to cold flow. Emerson Cumming's LoK characteristics seemed to vary too much from sample to sample and was eliminated. Polystyrene and Polyethylene exhibited like characteristics and both proved excellent for the application.

An irradiated cross-linked polystyrene was used for most of the experiments. In order to plate this material it must first be assembled with the ferrite embedded in the plastic. Then it was cleaned and slightly roughened with a mild abrasive. It was slightly etched and then washed with deionized water. The first layer of copper is put on by chemical reduction of copper compounds, and this is then built up by electrolytic copper to the thickness desired. A protective flash plating of gold is used to prevent oxidation of the electrolytic copper.

The big advantage of this method is the reduction of physical size. A slight reduction in drive power is also noted. The loss of this device is 0.4 db, and the drive power is 1 watt at 15 kilocycles.

IV. CONCLUSIONS

The best results obtainable for high speed ferrite phase shifters are obtained by using an extremely thin metal wall on a dielectric body. Dependent on the AC drive frequency the walls should be as thin as possible without exceeding the microwave skin depth.

The power required to drive a phase shifter at these high scan rates is dependent on wall thickness. For example, at 15 kilocycles, the AC drive power for a wall thickness of .0002 inches is approximately 1 watt, but for a thickness of .0007 the requirement is 1.35 watts. The increase in power throughout the interim range is fairly linear.

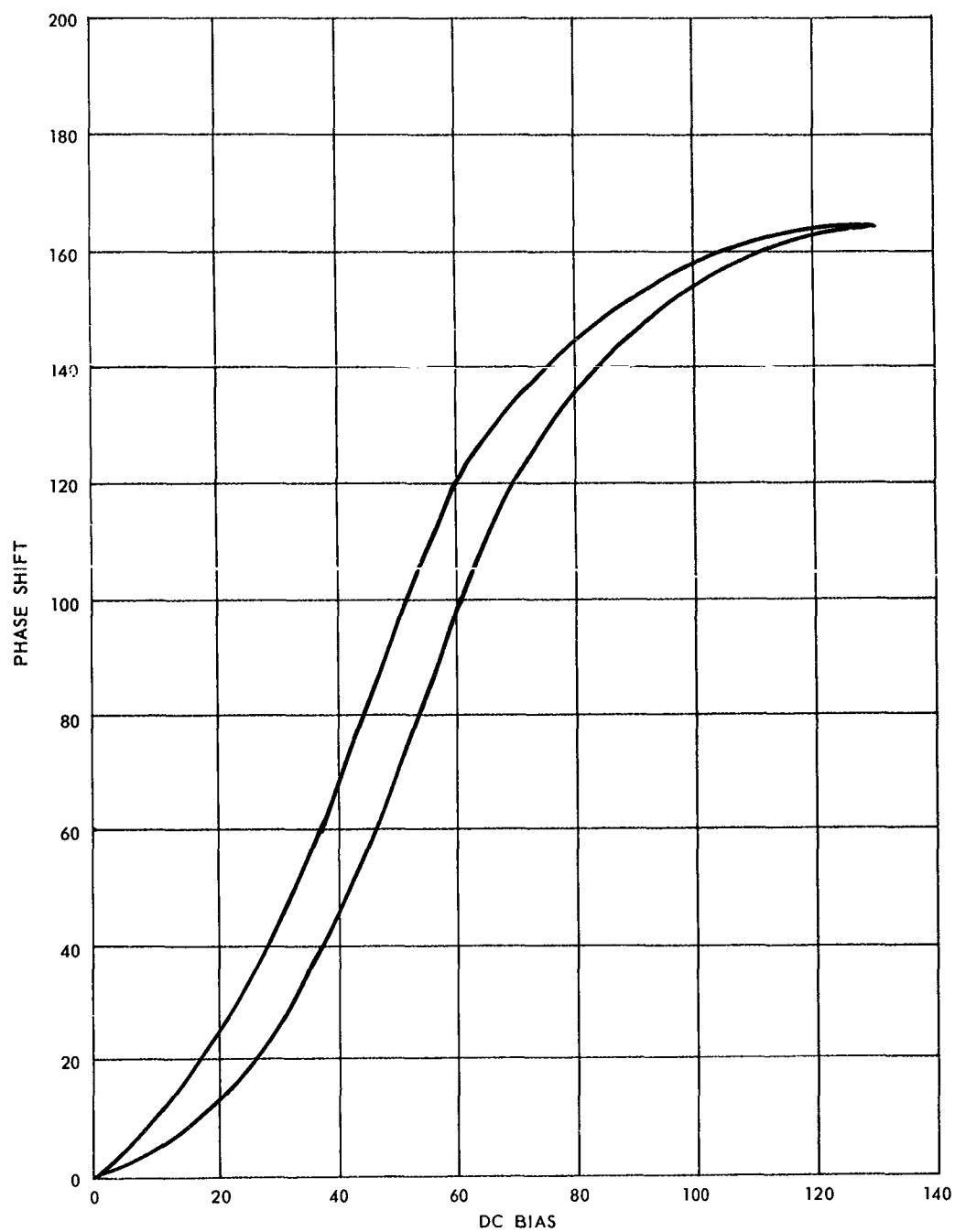


FIGURE 1 DC HYSTERESIS, AC VOLTAGE 0

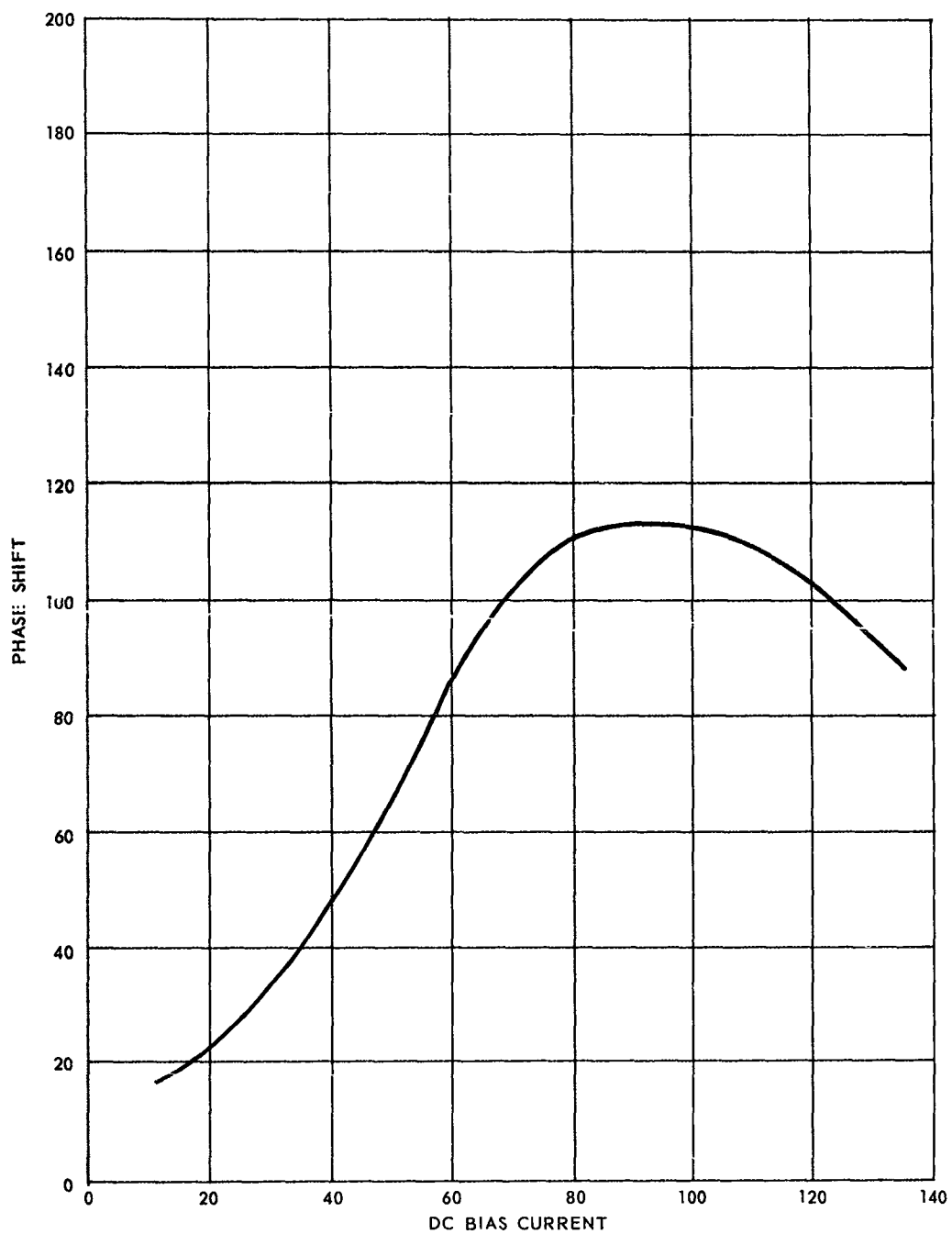
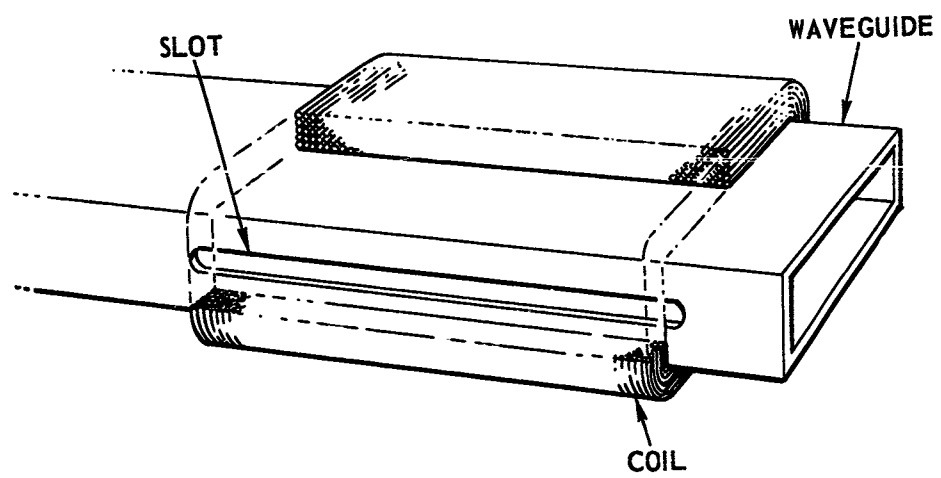


FIGURE 2, AC SENSITIVITY, AC VOLTAGE 10



BIBLIOGRAPHY

1. F. Reggia and E. G. Spencer, "A New Technique in Ferrite Phase Shifting for Beam Scanning of Microwave Antennas", Proc. IRE, 45, p.1,510 - 1,517, Nov. 1957.
2. A. Clavin, "Reciprocal Ferrite Phase Shifters in Rectangular Waveguide", Trans. IRE, MTT-6, p. 334, July 1958.
3. P. A. Rizzi and B. Gatlin, "Rectangular Guide Ferrite Phase Shifters Employing Longitudinal Magnetic Fields", Proc. IRE, 47, P. 446 - 447, March 1959.

Preparation and Submission of Procurement Proposals

Edwin M. Turner
Research and Technology Division
Wright-Patterson Air Force Base, Ohio

The U. S. Government is spending 13.2 billion dollars annually on research, which is said to represent approximately 87% of the total in the country. To give this figure some meaning in terms easily understood; the entire cost of the public educational system runs something over 10 billion dollars annually.

This money is spent to procure many thousands of items including basic research, development, testing, prototypes, design, standardization, pilot runs, research facilities, and test equipment; plus the salaries of many thousands of scientists, engineers, technicians, and support personnel. It is estimated that 3 percent of the entire cost of R&D contracts are spent on the preparation and submission of proposals. It is obvious that if we are to keep a democratic competitive process in our economy some of these costs are inevitable. The process must be continued in a manner somewhat as it exists today with rules prescribed by congress. This does not mean however, that our procedures cannot be improved, and that the cost cannot be lowered. It does mean that the door must be kept open to those who are capable and desire to bid on any particular procurement even though this process within itself is costly. Discussions with large numbers of contractors indicate that the average cost of preparing proposals on electronic (R.F.P.'s) average around \$2000 each; meaning an average of 2% cost on a \$100,000 item. With an average of 10 contractors per proposal the cost may well be 20 to 25 percent of the cost of the PR. This seems to be an unreasonable expenditure of public funds just to get the contractor selected.

Streamlining administrative procedures will go a long way toward reducing these costs. The problem is as pressing for the government as it is for industry. In order that the evaluation process for proposals be better understood, a copy of the AFSC Form 51A is included herein for your examination. You will note that three major categories of evaluation are listed, namely: (1) Scientific/Engineering Approach, (2) Qualifications based on past experiences, (3) Management. A predetermined weighing factor is put on each element of the evaluation; and each proposal is evaluated where possible by at least three persons to minimize the human factor. The Scientific/Engineering approach is made by the engineering laboratories, while the past performance and management capabilities are made by the procurement agency.

These evaluations are perfunctory and are at best only a judgment limiting device. The final judgment must be an act of faith and confidence between the government representatives and the company. The request for proposals are made with several procedure and constraints prescribed by congressional action based on such factors as low-employment areas, small business equalization, price, procurement policies, plus a large number of administrative procedures established by the Department of Defense and its subordinate agencies, plus the normal constraints inherent in budget discipline. The procurement agency is interested in obtaining a reasonable number of well prepared proposals, but not enough to overload the engineering and procurement personnel to a point where the time factor becomes excessive. As an example, if 100 or more proposals were submitted on one PR it would bog down the engineering staff for an unreasonable time; likewise, many such responses would bog down the entire procurement system. Fortunately, most procurements range from 5 to 10 proposals which is considered reasonable. My purpose here is to give the engineers who prepare the proposals some criteria which will be helpful to them in preparing proposals, and will hopefully avoid the expenditure of preparing proposals that are unproductive. The proper consideration of the following factors will certainly increase the fruits of your labor.

- a. Be sure that your approach is feasible for the application stated.
- b. Make your proposals positive. Don't discuss several alternatives, and then not state which one you are choosing.
- c. The objective of most R&D investigations is to advance the state-of-the-art. Be progressive and suggest approaches that has a reasonable risk, but one that may be reduced to practice when feasibility has been established. We generally are buying brains and not hardware.
- d. Remember that you will be graded by what you say, and not by what you may think. Be sure to give adequate time to semantics. Poor communications are likely to cost you the contract. A critical reading by someone well grounded in English as well as Engineering will be helpful.
- e. Do not turn the task of editing your proposal over to your subordinates, however talented; particularly your junior engineers as they will not ordinarily appreciate the value of good communications or will they have the experience to reflect the perspective or maturity needed to impress the evaluator.
- f. Don't dilute your talent by bidding on everything that comes across your desk. Without some prior experience in a field your proposal will appear amateurish and immature and is likely to be unproductive. Even a small scale in-the-house effort will fortify you with enough knowledge to make your proposal have a ring of authority.

g. Your proposal will be judged primarily by its contents and not by its size; be concise and to the point. Avoid the use of extraneous and unusual words that take special effort on the part of the evaluator. Stick to either the English or Metric system of measurements; but by all means don't mix them up, especially in the same sentence or paragraph. Avoid the use of complex formulas and derivations unless absolutely essential to your theme. Use as many pictures and easily interpreted graphs as are needed to tell your story. Provide ample margins and bind neatly, but not lavishly. Minimize biographical data except for outstanding individuals. Emphasize past accomplishment in related areas. Pictures of hardware in related fields may be helpful.

Finally, remember that you are writing to please someone else and not yourself. Always be alert to false assumptions, avoid extreme views, unproved statements, communication voids, and individual biases.

1

AFSC TECHNICAL EVALUATION WORKSHEET - "NON-HARDWARE" PROCUREMENTS
(INCLUDING R&D, STUDIES, AND SERVICES)

ITEM DESCRIPTION

BIDDERS/OFFERORS	SCIENTIFIC/ENGINEERING APPROACH (4)																											
	UNDERSTANDING OF PROBLEM						SOUNDNESS OF APPROACH						COMPLIANCE WITH REQUIREMENTS						SPECIAL TECHNICAL FACTORS									
	NO DATA	UNSAT	POOR	AVERAGE	V GOOD	EXC	SCORE	NO DATA	UNSAT	POOR	AVERAGE	V GOOD	EXC	SCORE	NO DATA	UNSAT	POOR	AVERAGE	V GOOD	EXC	SCORE	NO DATA	UNSAT	POOR	AVERAGE	V GOOD	EXC	SCORE
1.																												
2.																												
3.																												
4.																												
5.																												
6.																												
7.																												
8.																												

BIDDERS/OFFERORS	QUALIFICATIONS BASED ON OUR EXPERIENCE (5)																											
	TECHNICAL						QUALITY OF PRODUCT OR SERVICE						OVERRUN HISTORY						ABILITY TO MEET SCHEDULE									
	NO DATA	UNSAT	POOR	AVERAGE	V GOOD	EXC	SCORE	NO DATA	UNSAT	POOR	AVERAGE	V GOOD	EXC	SCORE	NO DATA	UNSAT	POOR	AVERAGE	V GOOD	EXC	SCORE	NO DATA	UNSAT	POOR	AVERAGE	V GOOD	EXC	SCORE
1.																												
2.																												
3.																												
4.																												
5.																												
6.																												
7.																												
8.																												

BIDDERS/OFFERORS	QUALIFICATIONS BASED ON BIDDERS/OFFERORS DATA (50)																											
	SPECIFIC EXPERIENCE							TECHNICAL ORGANIZATION							SPECIAL TECHNICAL EQUIP & FACILITIES							ANALYTICAL CAPACITY						
	NO DATA	UNSAT	POOR	AVERAGE	V GOOD	EXC	SCORE	NO DATA	UNSAT	POOR	AVERAGE	V GOOD	EXC	SCORE	NO DATA	UNSAT	POOR	AVERAGE	V GOOD	EXC	SCORE	NO DATA	UNSAT	POOR	AVERAGE	V GOOD	EXC	SCORE
1.																												
2.																												
3.																												
4.																												
5.																												
6.																												
7.																												
8.																												

DATE OF EVALUATION	EVALUATORS	
	PROJECT ENGINEER	PARTICIPATING EVALUATOR

HARDENED ANTENNAS FOR ATLAS AND TITAN

MISSILE SITE COMMUNICATIONS *

The possibility of nuclear warfare has created a need for reliable post-blast communications to assist implementation of our retaliatory capabilities. Antennas designed to withstand environments resulting from nuclear blasts must resist severe nuclear and thermal radiation as well as extreme dynamic effects. Radiating structures capable of withstanding this environment have required the application of unique electro-mechanical techniques and materials technology.

Atlas and Titan Missile Bases require both H.F. and U.H.F. communications capabilities. Collins Radio Company has developed and is producing hardened antennas for this requirement.

The H.F. Antenna is a $1/4$ wave vertical monopole stored within an underground protective silo during a nuclear attack. After the attack the structure can be erected automatically by a remote command to a maximum height of 117 feet above the ground. It can also be retracted to the hardened condition after the command signal is given.

A frequency range of 2 - 30 Mc is covered with an associated VSWR of less than 2:1 over 99% of the band. No matching device is required.

Structurally the fully erected antenna can withstand winds of over 150 mph and can be raised in winds of 40 mph with gusts to 60 mph.

- * By D. L. Holzschuh Collins Radio Company Dallas, Texas
- * Developed for Air Force Ballistic Systems Division on Contract AF04(694)-132

Two versions of the H.F. antenna are being provided and differ only in the time of erection and level of shock protection. The Collins Radio 237Q-2 erects fully in 1 minute and can withstand a greater overpressure environment than the 237Q-2A that erects in 2 minutes. Weight of the 237Q-2 is 3300 pounds and 2800 pounds for the 237Q-2A.

Constructed primarily of high strength structural aluminum, the antenna consists of a telescoping tubular mast, a rectangular shaped supporting crib, a drive assembly, a height-sensing assembly, control box, 28 volt D.C. power supply, 480/115 volt transformer, and two shock isolation assemblies. A control module, the Collins Radio 637G-1 (or G-2 for two antenna operations) is supplied as an accessory and is located in the Launch Control Center.

Ten movable mast sections can be elevated from the supporting crib by eight rubber-faced, chain-driven, articulated drive wheels. An automatic ball-latch mounted at the top of each mast tube locks the adjacent sections together. Interior keys assure alignment of the latches as they erect. Spring-loaded soft-aluminum contact brushes mounted in the latch castings assure electrical continuity between sections. Computer techniques simplified design of the mast. Maximum combined stress, unit horizontal wind loading, an initial tube size, fixed clearance between tubes, the overlap between them, as well as fixed lengths for 10 tubes were programmed into an IBM 7070. The computer solved the differential deflection equation of the loaded mast as derived from the radius of curvature formula. The program divided the mast into 100 increments of length (10 on each of the 10 tubes) and solved for their outside diameters and wall thickness as

well as total weight. The tubes vary in size from 2" O.D. to 12-7/8" O.D. Average wall thickness is 1/4". A non-movable tube is 14-1/4 O.D. and houses the movable sections; it is electrically insulated from the supporting crib and functions as the center conductor of a 50 ohm coaxial transmission line. The structural support crib in addition to supporting all other systems also functions as the outer conductor of the 50 ohm line.

Natural rubber of 55-60 durometer was chosen after exhaustive tests for facing the drive wheels. This material was chosen due to its high coefficient of friction under wet conditions, low hysteresis loss, good electrical properties as well as excellent resistance to nuclear radiation. The 8 drive wheels are held in compression against the mast by a unique wire-rope tensioning system. The wire rope is laced over pulleys mounted at the extremities of the drive wheel shafts in such a way that a mechanical advantage is provided similar to a block and tackle. Two extension springs mounted on the sides of the support crib provide variable tension to the wire rope and to opposing sets of wheels. A force of 2000 pounds is exerted by each pair of wheels with the antenna fully erected. The drive wheels are powered by two 3.1 or 2.2 H.P. gear motor assemblies. The motors are 480 volt 3~60 cps and mount 90 volt D.C. brakes for rapid stopping.

A height sensing device located at the base of the antenna, provides position information for the Control Module. A glass-reinforced Teflon tape is attached to the inside of the 2" mast section. The tape passes over a metering wheel attached to a synchro transmitter. Holes in the tape match projections on the wheel and

prevent slippage. The tape is held in tension by a constant force 'Negator' spring attached to the tape storage reel.

A control box containing automatic re-setting circuit breakers, aircraft type contactors, terminal strips and the brake rectifier is mounted on the structural crib. A 28 VDC power supply as well as a 480/115 volt transformer for silo lighting are also mounted on the crib.

Limit switches are provided that serve as interlocks for the silo door pneumatic actuating system as well as limiting antenna travel.

Two shock isolation systems were designed to suit two maximum overpressure shock criteria. Both designs limit the induced shock to less than 5.5 g under combined horizontal and vertical displacements. Aircraft quality extension and compression springs are used throughout. The shock isolation systems differ in that a lock-out system is required for the 237Q-2 due to the greater displacements of the springs. The springs are locked out prior to raising the antenna. Calculated natural frequencies of both shock isolations were in the vicinity of 1 cps and were verified by full scale tests. Coupling between the horizontal and vertical motions did not present a problem due to the inherent damping of the system. R.F. electrical continuity between the antenna and the silo door is assured by 8 flexible cables between the antenna and silo.

The 237Q-1 or Q-2 control module allows selection of the exposed "soft" or protected "hard" H.F. antennas by rotating the antenna selection knob on the front panel from "S" to "H" position. Antenna resonant frequency is selected by rotating a knob and observing

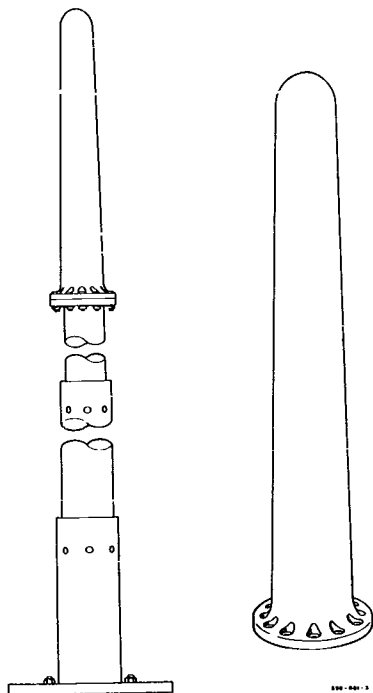
frequency indications shown on a moving non-linear tape located in the control module. The knob also rotates a 10 turn pot in a bridge circuit. Pressing the "Actuate" button on the panel causes the antenna silo door to open and the antenna to extend. A synchro receiver located in the module drives a follow-up pot in the bridge circuit. The synchro receives position signals from the height-sensor synchro on the antenna. A "null" condition is detected by a sensitive meter-movement relay and causes the antenna drive motors to stop. A green "ready" light then comes on. The antenna is quickly stowed by rotating the antenna selection knob to the "S" position.

Two U.H.F. antennas are being produced for the Atlas-Titan program. The Collins Radio 437B-3 is a stacked collinear dipole array hardened for a moderate overpressure environment. For a very high overpressure environment a stub monopole designated the 437B-4 is utilized.

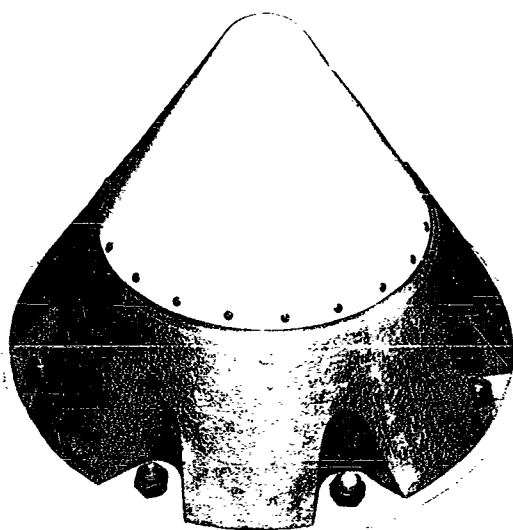
The 437B-3 stacked array is mounted on a hardened mast 12 ft. above the ground and is protected by a glass reinforced phenolic radome coated with a proprietary ceramic. The radiated pattern is omnidirectional with primary lobes on the horizon. Gain is 5 db over isotropic.

The 437B-4 stub monopole antenna is mounted on a reinforced concrete foundation. The 5-1/2" diameter cast steel radiating 1/4 wave monopole is approximately 18" above the foundation and is supported by two heavy glass-reinforced phenolic insulators. The insulators mount in a galvanized cast iron base weighing 2500 pounds. The upper insulator is protected from the high thermal environment by a coating of proprietary ceramic material. The exposed portion of the probe as

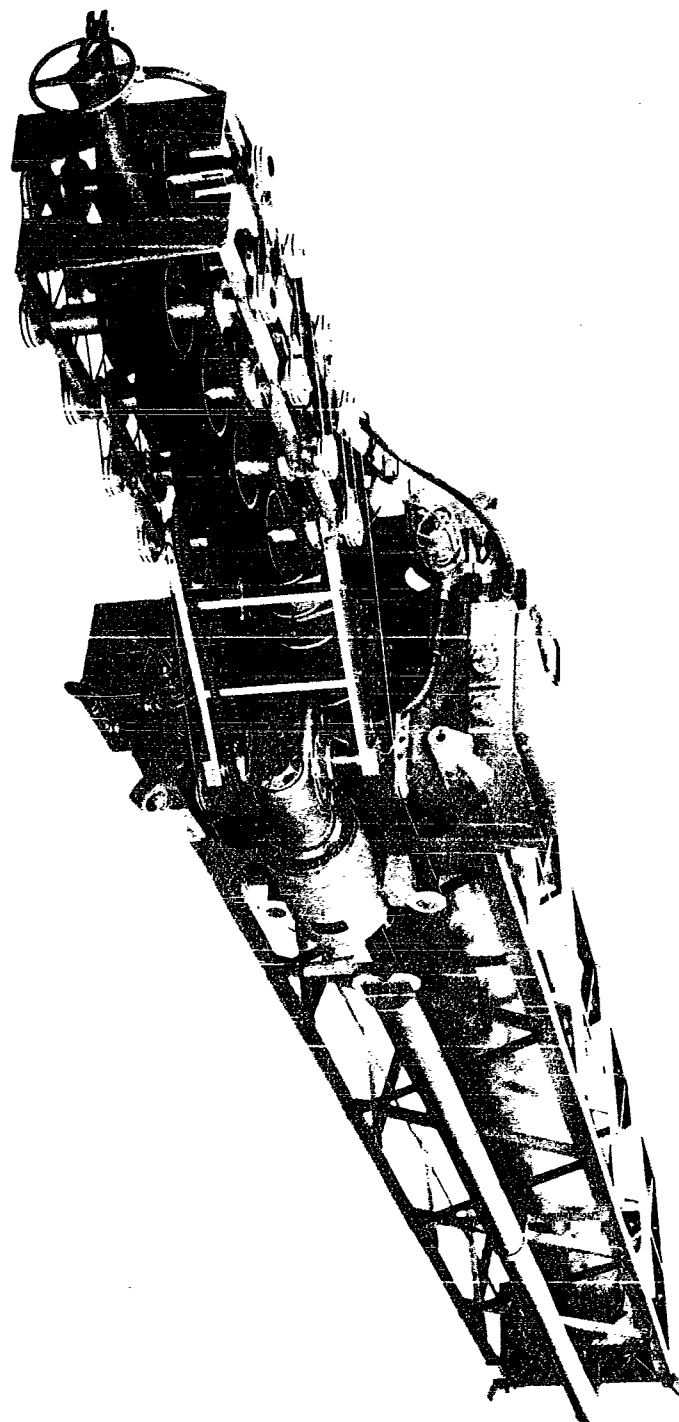
well as the upper insulator can ablate appreciably and be operable. Heat stored in the probe during the blast is reduced to a safe working level at the antenna terminals by a heat-radiating line located in the foundation of the antenna. A frangible glass-reinforced polyester weather dome protects the antenna from rain exposure. Radiation pattern of the 437B-4 is omnidirectional with the major lobe on the horizon. The VSWR over the band is 2:1 or better.



Collins Radio Company
437B-3 UHF Antenna



Collins Radio Company
437B-4 UHF Antenna



Collins Radio Company
237Q-2A HF Antenna

A PROGRESS REPORT ON 2000°F ANTENNA ELEMENTS

Summary of a Paper to be Presented at
U. S. Air Force Antenna Research Symposium
University of Illinois
15-18 October 1963

by

J. J. Earshen and R. J. Blum

Cornell Aeronautical Laboratory, Inc.
Buffalo 21, New York

I. INTRODUCTION

A research program aimed at developing antenna elements suitable for countermeasure and communication use on supersonic vehicles is currently being conducted at the Cornell Aeronautical Laboratory under the sponsorship of the Electromagnetic Warfare and Communication Laboratory, AFSC Aeronautical Systems Division under Contract No. AF33(657)-11100. This paper reports progress to date in the development of antennas, development of special testing instrumentation, and investigation of related materials problems.

The objective of the current program is to perform exploratory research on antenna elements having:

1. Ability to operate at surface temperatures ranging up to 2000°F for a period of at least several hours.
2. Ability to handle high-peak and average power levels approaching 1 kw at pressure altitudes corresponding to 80,000 feet; break-down thresholds should be those of the ambient airstream, not the antenna structure.

3. Ability to handle broadband signals (2.5 - 4.5 Gc), while exhibiting a VSWR of less than 1.5:1.
4. Suitability for flush mounting to minimize aerodynamic drag.
5. Ability to withstand mechanical and thermal shock environment encountered on supersonic vehicles.

II. ANTENNA DEVELOPMENT

After a preliminary analytic evaluation of slot, scimitar, helix, spiral, dipole, and stub antennas, it was concluded that flush mounted types which do not possess high field concentrations are most likely to meet the previously listed objectives. Of these types, the slot and sunken stub (annular slot) have been chosen for detailed experimental study. Of the less desirable protruding types, the scimitar has been chosen for experimental evaluation. It has a low drag profile, can be rugged and its grounded far end provides a good heat shunt for conducting heat from the antenna.

The slot antennas require dielectric windows to assure a smooth aerodynamic surface and to provide a means for pressurized sealing. Pressurization maximizes the breakdown power threshold. Unfortunately, the most promising refractory materials (fused quartz, beryllium oxide, and aluminum oxide) currently under consideration, have dielectric constants at least several times that of free space. The discontinuities introduced in the antenna structures have a serious affect on driving point characteristics. Models of S-band slot and annular slot antennas have been constructed to develop matching devices necessary to compensate for window discontinuities.

On the basis of dimensions determined by model testing and the results of materials investigation, an S-band, waveguide fed slot antenna capable of pressurization (shown in Figure 1) is currently being fabricated. The waveguide has dimensions of WR-284 and is constructed of columbium. The window is 1/16" thick beryllium oxide. These two high temperature materials were chosen because they have similar thermal expansion coefficients. Experimental pressure-tight seals between the materials have been made at CAL using a nickel brazing alloy with the window material being initially metalized at the joint with molybdenum.

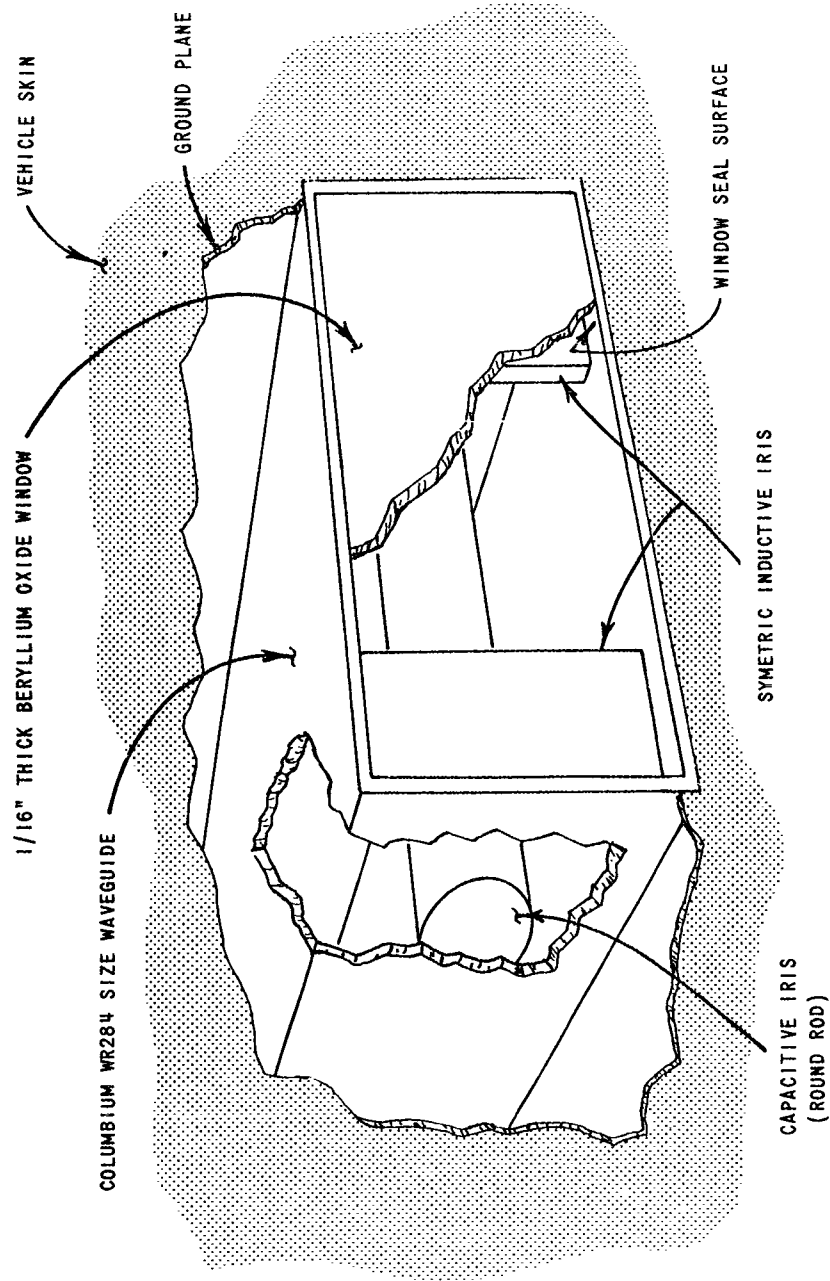


Figure 1 WAVEGUIDE FED SLOT ANTENNA

The matching elements consist of a thick symmetrical inductive iris which matches the capacitive susceptance of the slot over a narrow frequency band. Broadband matching is obtained by the addition of a round bar acting as a capacitive iris. A VSWR of less than 1.6:1 has been obtained over a frequency range of 2.3 to 4.0 Gc for the model slot antenna. Both the inductive and capacitive irises should handle high power since they have no sharp corners and thus no high local field intensities.

To cool the inboard end, a simple water jacket will surround the waveguide. Experiment has shown that a jacket located 1 foot from the 2000°F window requires 0.25 gallon/min. of 150°F cooling water. The water will experience a 1°F rise.

Another version of the WR-284 slot antenna, consisting of a quartz waveguide internally metal coated and sealed directly to a quartz window, is also being fabricated. Metal-coated quartz matching elements are used. In this version the difficult, high temperature, dielectric to metal seal problem is avoided but a problem of connection to the ground plane arises. A non-contacting choke system between ground plane and waveguide is being investigated for this version.

III. TESTING INSTRUMENTATION

The experimental antenna assemblies will be tested under simulated thermal conditions similar to those encountered in actual vehicular installations. This requires that the outer surface of the ground plane, the dielectric window (if present) and any antenna structure projecting beyond the ground plane, be at the high temperature. Heat would then flow from these hot surfaces through the supporting structure to the interior of the vehicle which acts as a heat sink.

A reasonably low temperature, say 100° C to 150°C, must be maintained at the point where the antenna feed line is connected to the r-f source and test instruments. The latter are standard laboratory devices capable of operating only at the temperatures stated. The temperatures of other parts of the experimental assembly are not of critical importance but, in general, should be kept low to reduce heat losses.

To provide a means for simulating the vehicular thermal environment, an 18-inch diameter, electrically heated ground plane assembly has been developed. The basic unit is shown in Figure 2. It contains a specially constructed heating element composed of refractory material inlaid with spiral high-temperature heating coils of Kanthal resistance wire. The assembly is covered with a stainless steel ground plane. Antennas under test are mounted in the center well of the assembly. Temperature of the ground plane is monitored with thermocouples whose outputs are used to control a saturable reactor in series with the heating coils. Stabilized temperature control is thus obtained.

At the high temperatures involved, the major heat dissipation takes place by radiation. It is possible to reduce the required heat input to the ground plane from an estimated 35 kilowatts to approximately 10 kilowatts by covering the plane with an 1/8" thick fiberfrax insulation. The effective dielectric constant of fiberfrax is very low and thus no noticeable effect on the antenna patterns has been observed due to the presence of insulation at room temperatures. Any substantial increase in dielectric constant at elevated temperatures can cause distortion of patterns.

Preliminary investigation of thin aluminum-oxide windows instrumented with monitoring thermocouples, has revealed that it is not possible to establish a uniform 2000°F temperature across the window by heating the edges through contact with the ground plane. It has therefore been necessary to develop a removable, electrically powered face heater which is used to bring the window up to temperature and then removed immediately prior to conduct of r-f measurements. The temperature at the center of the window was measured with a thermocouple. Starting at 2000°F, the temperature decays asymptotically to 1000°F with the plane exposed, and to 1250°F with the fiberfrax insulation covering. In the first minute, the drops are respectively 540° and 315° F.

To enlarge the effective electrical size of the ground plane a thermally isolated ground plane is superimposed over the heated ground plane at a distance of approximately one quarter wavelength. The over-all dimensions are approximately 42 x 48 inches.

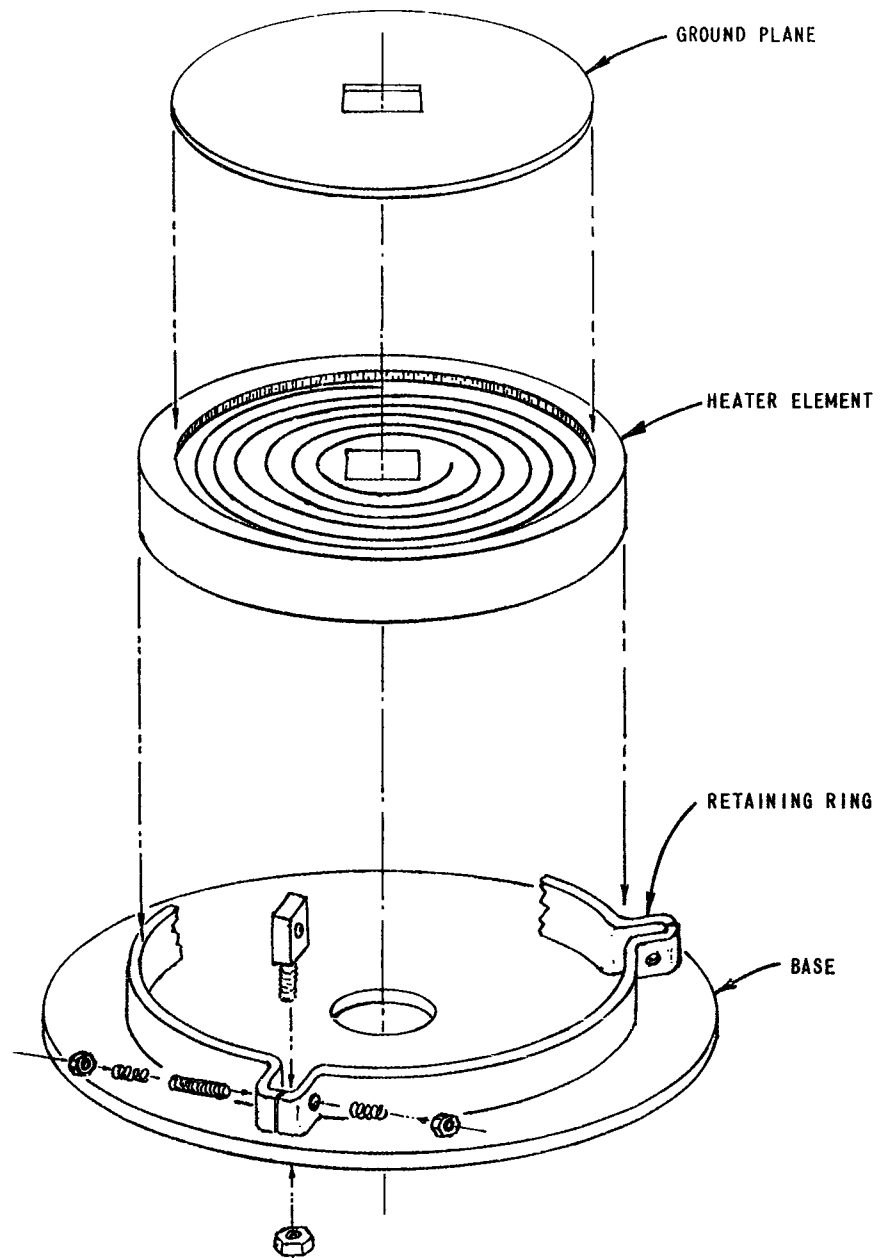


Figure 2 HEATED GROUND PLANE

Testing of experimental antennas is aimed at:

1. Determining their ability to survive in the thermal environment. Since corrosion effects are materially affected by the ambient atmospheric pressure, survivability tests are conducted at 80,000' pressure altitude in a vacuum test chamber.
2. Determining the thermal effect on driving-point electrical characteristics, radiated patterns, and efficiency. These tests are made at low r-f power. It has been noted that radiation patterns of slot antennas are not significantly affected by change in window dielectric constant. Thus driving point impedance and VSWR measurements provide a more sensitive indication of change in dielectric properties. Gross efficiency measurements are made by comparing the absolute magnitudes of the radiation pattern produced for the same input power under hot and cold conditions.
3. Determining the maximum power handling capabilities. The same types of measurements described in (2) are made in this instance. The driving power is increased in gradual steps till incipient failure is observed. Presently a CW power source having a maximum output of 200 watts is available. It can be pulsed to produce peak power output in excess of 1 kw at high duty cycles.

IV. MATERIALS INVESTIGATIONS

Materials-oriented activities on this program result in materials selection and recommendations for fabrication. Investigations of high temperature coatings, sealing techniques and materials properties have been conducted in support of the stated objectives.

Several approaches to the fabrication of antennas have been examined.

1. Structural Metal Waveguides with Sealed Dielectric Windows

One form of such an antenna, now being fabricated, combines columbium and beryllium oxide. Only rarely has use been made of sealed structures operating at temperatures approaching 2000°F.

Thus an investigation of stresses in seals as a function of operating temperature, brazing temperature, material combination and material dimension has been undertaken. Stresses are determined by X-ray diffraction measurements of lattice dimension or from curvature of sealed samples.

At high temperatures columbium is subject to oxidation and thus a protective coating of chromium-titanium-silicon will be employed.

2. Refractory Dielectric Structure with Conducting Coatings

A form of this antenna is now being fabricated from fused quartz. This approach minimizes or eliminates the problem of achieving high-temperature pressure seals since the component parts to be joined are of the same material. Investigations to date of suitable metal conductive coatings have shown platinum to be satisfactory at temperatures up to 900°C.

3. Unsealed Covered Slots and Waveguides

In the current program such configurations have proved useful for preliminary investigations of properties of dielectric windows and associated metallic parts. Such antenna structures may be simplest of all to fabricate but have the significant disadvantage of low breakdown power thresholds.

V. CONCLUSIONS

Progress to date in the program described includes: the development of several high temperature antenna configurations to be tested, development of high temperature testing instrumentation, and the formulation and compilation of materials data necessary for high temperature antenna design. During the concluding portion of the program, the antennas under construction will be evaluated and the results of all investigations will be reported in form suitable for providing preliminary guidelines for design of high temperature antennas.

The authors acknowledge the constructive technical guidance of Messrs. L. L. Brown and E. M. Turner of the Electromagnetic Warfare and Communications Laboratory of ASD. Principal investigators contributing to development of test instrumentation are Messrs. J. B. Coleman and W. H. Leipold. Dr. H. P. Kirchner has been the principal investigator of materials problems.

DIELECTRICS FOR ANTENNAS

By

Eino J. Luoma* and David J. Epstein†

The materials used in antennas are electrical conductors, dielectrics, and sometimes semi-conductors or lossy dielectrics. Electrical conductors, i. e. metals, such as steel, brass, copper, aluminum, or silver are the most common antenna material, but many antenna designs could not be achieved without the use of dielectric material. It is the purpose of this paper to briefly survey these uses of dielectrics in antennas; to examine the properties of presently available dielectrics as related to antenna applications; and to suggest new special dielectrics for use in antenna design.

A. DIELECTRIC APPLICATIONS IN ANTENNAS

Table I is a typical list of applications of dielectrics in antennas demonstrating very wide variety. The "Antenna Engineering Handbook" by Jasik (Reference 1) was used in preparing this table.

B. DIELECTRIC PROPERTIES AND OPERATING TEMPERATURES

Against this preceding background of applications it is instructive to consider what is available in dielectric materials. Figure 1 is a graph of the relationship between dielectric constant and operating temperature capability of the more common dielectric materials. It is interesting to note that for the pure compounds or one component systems there is a general correlation between the dielectric constant and operating temperature capability. This is to say that if the designer needs a higher operating temperature in a dielectric he may generally expect to have to go to higher dielectric constants and higher densities. On the other hand, any of the single component dielectric materials may be diluted with air e. g. foams and powders or other low dielectric constant material to achieve the lower dielectric constants and lower densities at a possible sacrifice of strength and changes in the other mechanical properties. The designer is fortunate if, as in the case of Fiberglas-plastic laminates, for example, the dilution results in improved mechanical properties.

*Emerson & Cuming, Inc.

†Consultant to Emerson & Cuming, Inc.

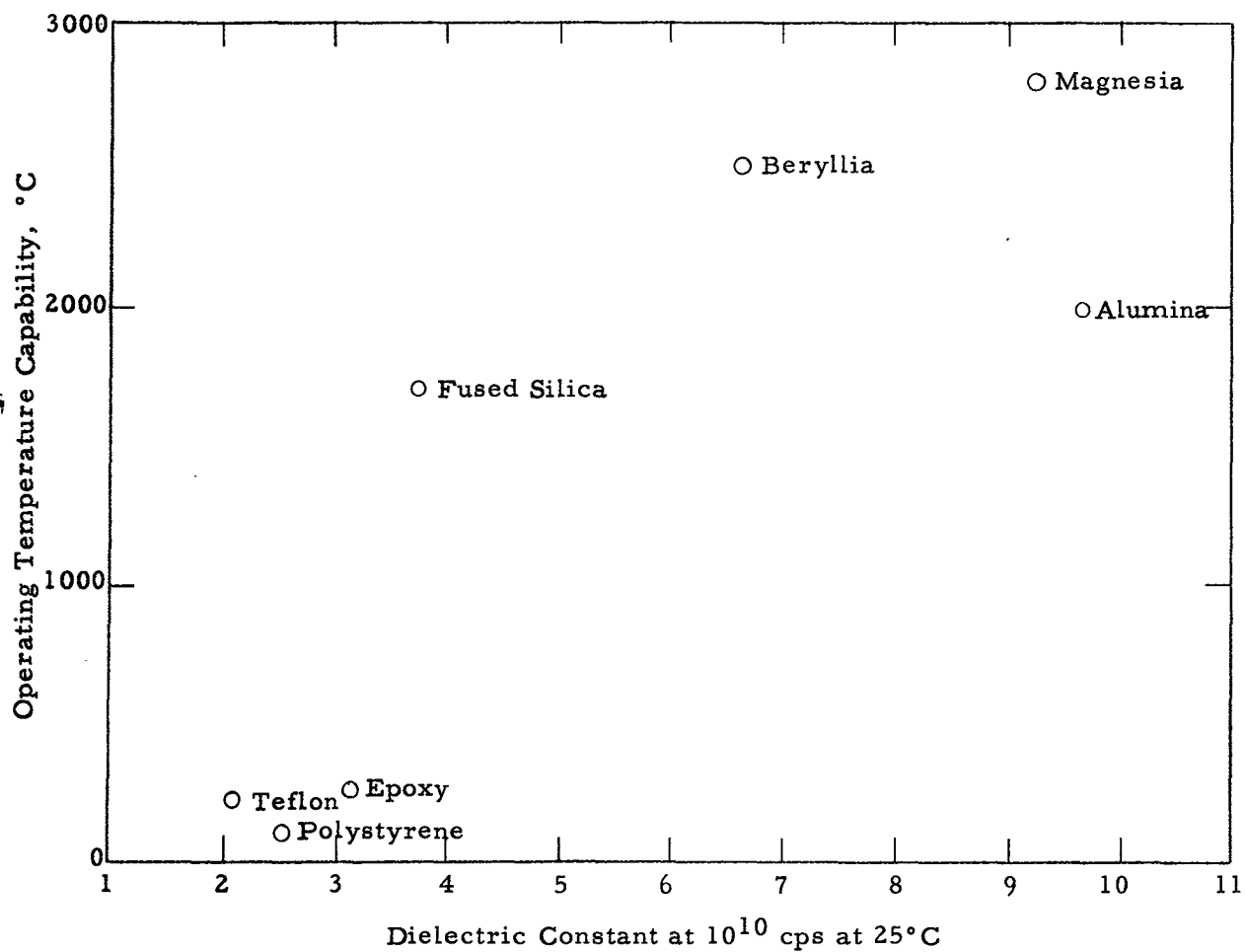
TABLE I

TYPICAL APPLICATIONS OF DIELECTRICS IN ANTENNAS

Type of Antenna	Antenna Application	Dielectric Material
Luneberg Lens spherical or cylindrical	1. Omnidirectional focussing device for feed. 2. Reflector	1. Natural dielectric - plastic foam 2. Artificial dielectric - for light weight.
Non-Spherical Lenses concave, convex, plane, etc.	Focussing device for horn.	Natural or artificial dielectric.
Dielectric Rod or Spike	Surface wave antenna often a member of a linear array.	Mostly polystyrene; sometimes plastics or ceramics with higher dielectric constants are used.
Trough-Guide Antennas	Surface wave antenna for flush mounting on aircraft.	Plastic or ceramic.
Dielectric Sheets on Ground Plane	Flush mounted beacon antennas.	Plastic or ceramic.
Tunnel Horn	Low side lobe, broad beam antenna.	Absorber used to line inside of horn.
Circularly Polarized Feed	Feed	Low loss plastic used as septum.
Tail Cap Antenna for Aircraft	H-F communication antenna.	Fiberglas-plastic used as insulation.
Radome	Wide variety of antennas for protection.	Plastics or ceramics; Fiberglas- plastic laminate.
Phased Array	Electronic scan antennas.	Ferrite ceramics used for phase control. (ferrites are considered beyond scope of this paper)

FIGURE 1

DIELECTRIC CONSTANT VS OPERATING TEMPERATURE CAPABILITY



Note 1 - Temperatures indicated for the oxides are melting temperatures.

Note 2 - Temperatures indicated for the plastics are softening temperatures.

The operating temperature ranges shown for typical materials in Figure 1 are the temperatures above which substantial degradation in dielectric or structural properties take place. This is not to say there has been no change in dielectric constant or reduction of strength at the indicated operating temperature limit. Without exception all of the materials lose strength substantially as the limiting temperature is approached. With the exception of silica all of the materials change in dielectric constant and loss tangent as the limiting temperature is approached. Thus if the antenna application is at all critical as to the exact value of dielectric constant, great care must be used in choosing the right dielectric.

Figure 2 shows the variation in dielectric constant with temperature of typical dielectric materials. Figure 3 shows the variation in loss tangent with temperature of the same materials.

C. DISPERSIVE DIELECTRICS

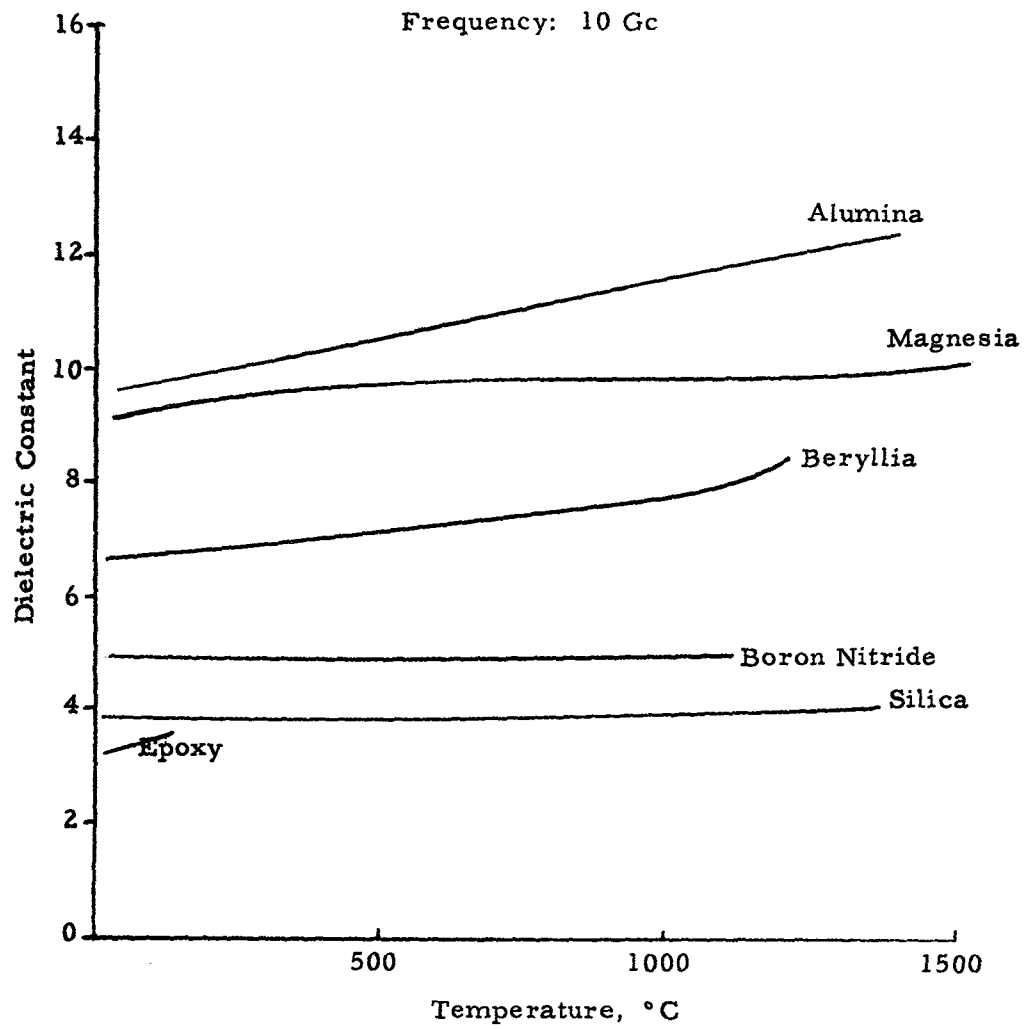
Dispersion is the change in dielectric constant of a dielectric material with frequency. The well known low loss dielectrics such as polystyrene, teflon, silica and alumina exhibit very little dispersion. On the other hand, if best performance is achieved with a section of dielectric which is, say, a quarter wave or half wave thick, and, if this performance is desired over a substantial frequency band, the right kind of dispersion can be a useful property. Unfortunately, dispersive dielectric constants are always accompanied by high loss tangents. Also substantial dispersion occurs more commonly in liquid dielectrics, which are difficult to apply in antenna design. Figure 4 shows the dielectric constant and loss tangent as a function of frequency for one of the more dispersive solid dielectrics, barium titanate.

D. ARTIFICIAL DIELECTRICS

An artificial dielectric, as contrasted with a natural dielectric, is a multi-component material in which two or more materials at least one of which is a metal are mixed to produce desired dielectric properties. For example, a small quantity of aluminum flake or aluminum slivers can be distributed throughout a plastic foam to produce a marked increase in dielectric constant with practically no increase in weight and very little increase in loss tangent. There are two approaches to the achievement of uniform dielectric properties in an artificial dielectric: one is to distribute the loading particles as randomly as possible; the other is to organize the distribution of the loading particles both as to their orientation and spatial distribution. In the former approach, the limitation to achieving perfect homogeneity is due to departure from perfect randomness; in the latter approach the limitation is in the ability to achieve mechanical perfection in the intended distribution. The former approach is commonly used today; the organized approach should be considered. These problems are discussed in more detail in Reference 2. Figure 5 is a graph showing the relationship between dielectric constant and aluminum loading for an artificial dielectric foam.

FIGURE 2

DIELECTRIC CONSTANT VS TEMPERATURE



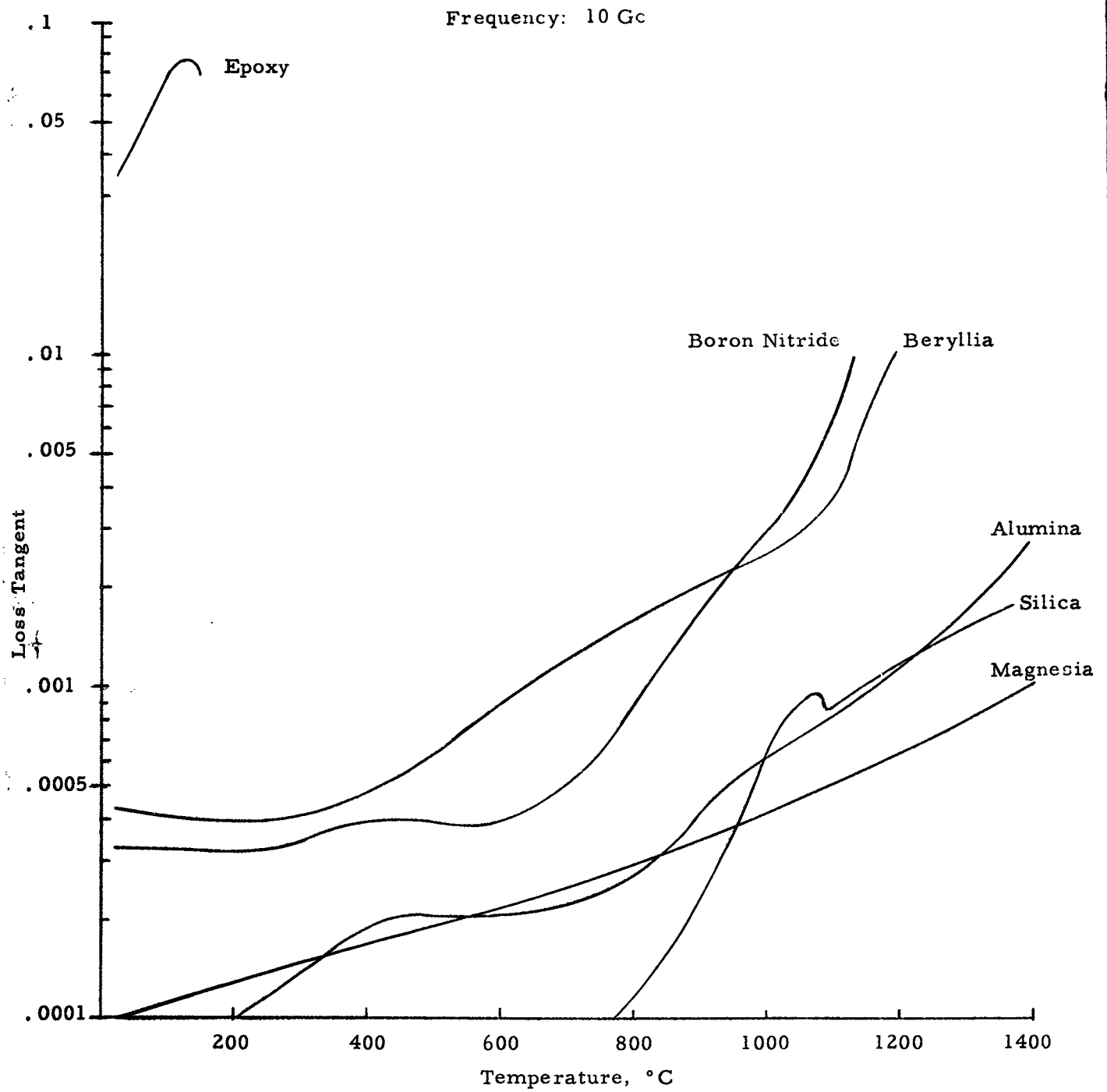


FIGURE 3

LOSS TANGENT VS TEMPERATURE

FIGURE 4

DISPERSION CURVES FOR BARIUM TITANATE

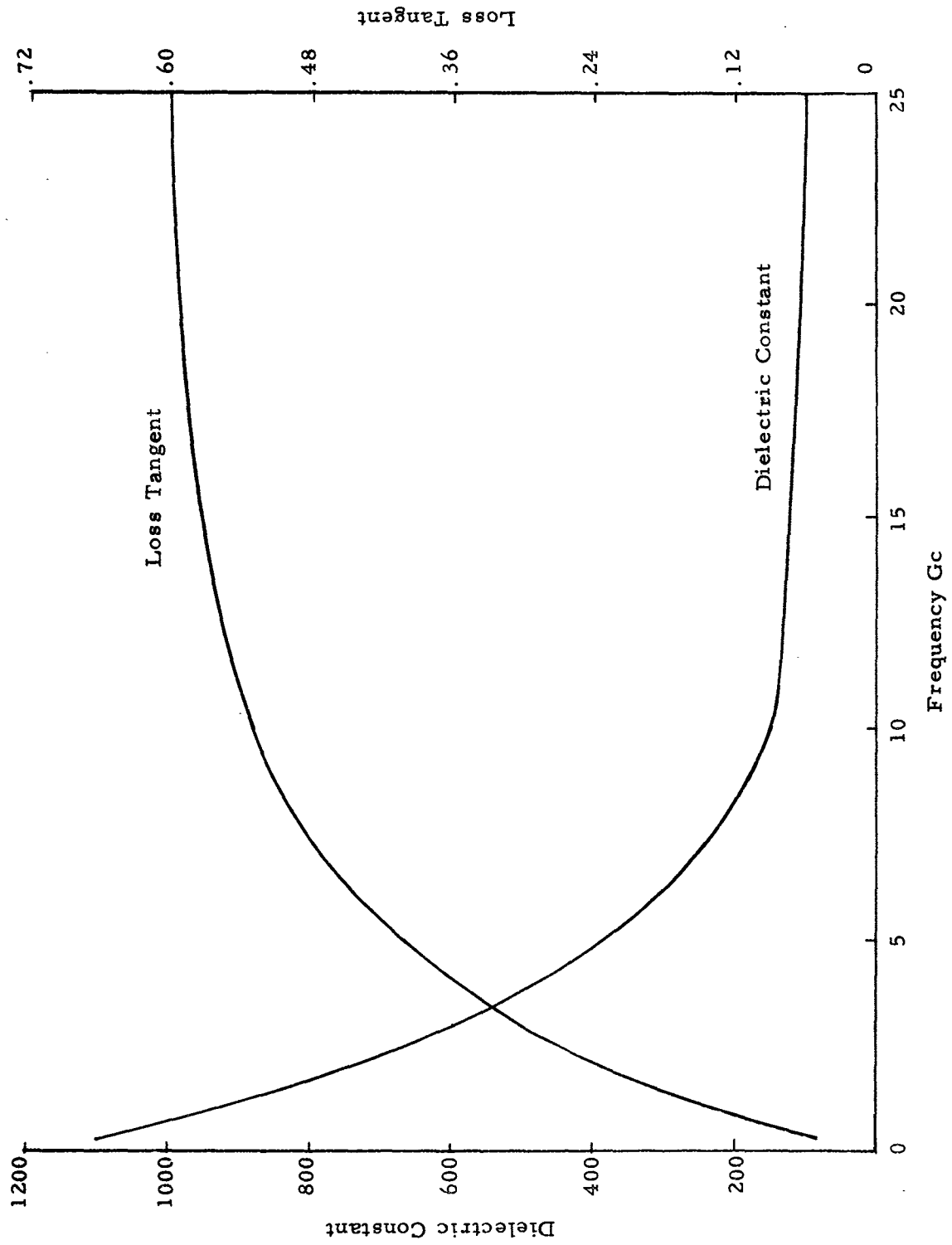
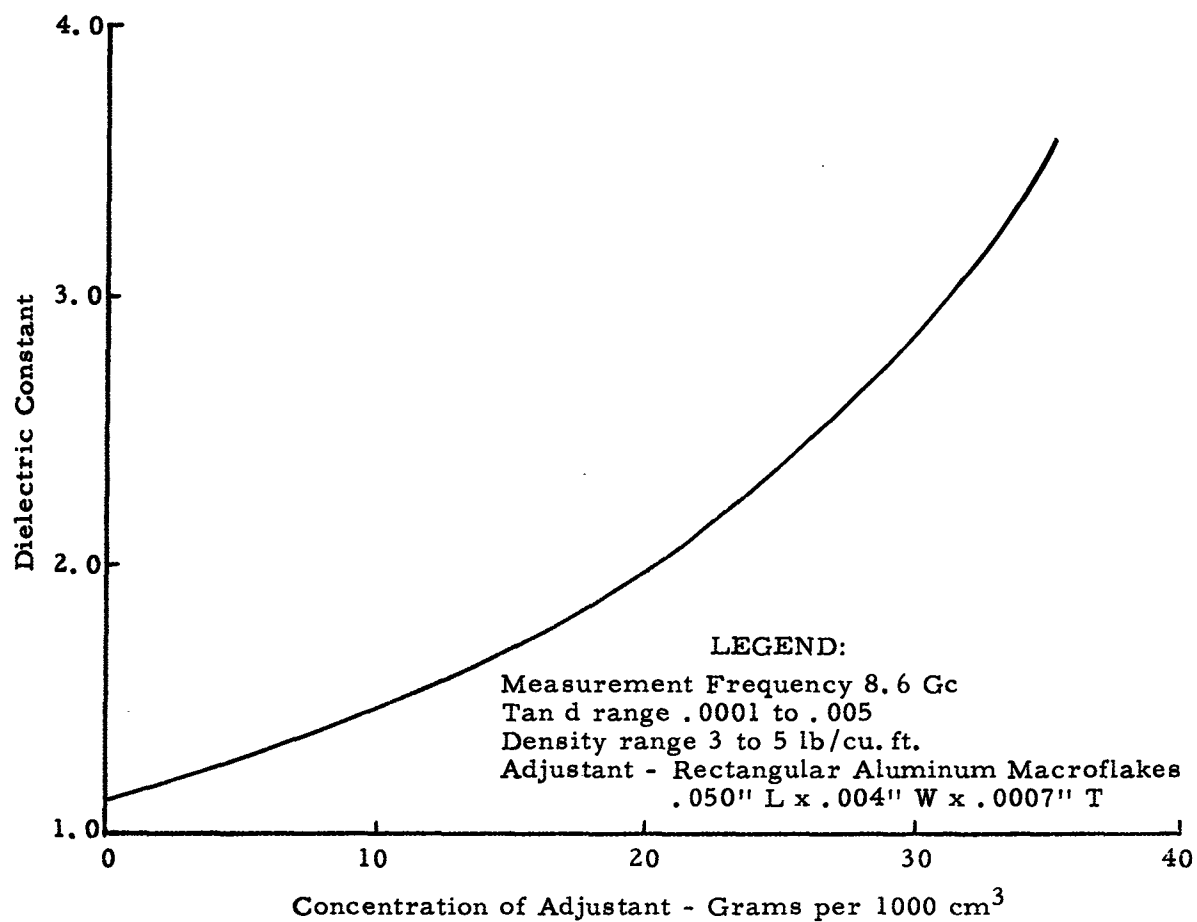


FIGURE 5

DIELECTRIC CONSTANT OF LIGHT WEIGHT
ALUMINUM ADJUSTED ARTIFICIAL DIELECTRIC
FOAMS AS A FUNCTION OF ALUMINUM LOADING



E. ANISOTROPIC DIELECTRICS

Usually, the antenna designer is interested in a dielectric with the same dielectric constant in all directions. Anisotropic dielectrics, in which this is not the case, are introduced here to call attention to the fact that they are practical although little if any use has been made of them. Reference 3 (H-Waves in Anisotropic Slabs) considers the problem of how anisotropic dielectrics might be used to increase the frequency bandwidth of surface-wave antennas. In practice, anisotropic dielectrics would be constructed of thin layers of alternately low and high dielectric constant. Conceivably, anisotropy ratios of 100 to 1 could be achieved.

F. HOMOGENEITY

Wherever a dielectric plays a part in shaping the beam of the antenna, inhomogeneity in the dielectric can be troublesome. This is particularly true in lens applications. Therefore, the antenna designer should be aware of the degrees of homogeneity that can be achieved with dielectric materials as they are manufactured today. A variation in dielectric constant no greater than ± 0.01 is probably sufficient for even the most critical applications. This homogeneity is achievable with only the one-component dielectric materials. With multi-component dielectric materials and artificial dielectrics the antenna designer should expect to get a homogeneity no better than ± 0.15 . In applying these ground rules, a word of caution is in order. The ceramics generally are not pure one-component systems although they may approach 100% purity. They are subject to porosity and impurities. Therefore, a homogeneity of ± 0.05 is typical of the better ceramic materials today.

G. MEASUREMENT TECHNIQUES

One of the biggest problems associated with obtaining homogeneity in dielectric materials has been its measurement. Most measurement techniques have required the cutting of a small mechanically precise sample of the dielectric for insertion into a cavity or shorted waveguide. Although the measurement made on this sample was very precise it yielded little information on homogeneity. A non-destructive sampling and measurement technique was needed. Within the last year, this has been established at Emerson & Cuming, Inc. (Reference 4). The technique developed uses a microwave interferometer capable of making a measurement on a highly localized segment of a large sample. This differs from previous interferometer techniques in that both dielectric constant and loss tangent can be measured. The principle of measurement is as follows: Insertion loss and insertion phase are measured at 45° incidence on the flat sheet. Dielectric constant and loss tangent are then determined from these measured values by use of conversion tables.

Special interferometer horns were developed which permit the inspection area for a given measurement to be reduced to one square wavelength of the flat sheet of the dielectric material.

H. DIELECTRIC POWDERS

One dielectric product which has recently been introduced by Emerson & Cuming, Inc. deserves special mention. This is a line of free flowing dielectric powders known as Eccoflo HiK. They are available in dielectric constants up to 10, have loss tangents below 0.001, and are of interest to antenna designers because they can be used in plasma simulation experiments.

REFERENCES

1. Jasik, Henry, "Antenna Engineering Handbook", McGraw-Hill Book Company, Inc., 1961
2. Rowe, P. E., Luoma, E. J., Volk, M. C., "Invariant Microwave Lenses from Artificial Dielectrics", August 1963, Final Report by Emerson & Cuming, Inc. on Subcontract 129331 for the Applied Physics Laboratory, The Johns Hopkins University
3. Luoma, E. J. and Mason, S. J., "H-Waves on an Anisotropic Slab", Final Report on Contract AF19(628)-463 by Emerson & Cuming, Inc. for Air Force Cambridge Research Laboratories
4. Luoma, E. J. and Volk, M. C., "Measurement of Dielectric Homogeneity with a Microwave Interferometer", Final Report on Subcontract 285 under Prime Contract AF19(628)-500 by Emerson & Cuming, Inc. for M. I. T. Lincoln Laboratory
5. "Tables of Dielectric Materials", Volume V, April 1957, Contract Nonr-1841(10), Technical Report 119, Laboratory for Insulation Research, Massachusetts Institute of Technology
6. Westphal, W. B., Letter Report, "High-Temperature Microwave Dielectric Measurements", July 1962, Laboratory for Insulation Research, Massachusetts Institute of Technology
7. Zellner, G. C., Pentecost, J. L., Eliason, L. K. of Melpar, Inc., "Accurate Microwave Measurements of Dielectric Properties to Temperature of 1600°C", Proceedings of the ASD-OSU Symposium on Electromagnetic Windows, July 1962
8. Von Hippel, A. R., "Dielectric Materials and Applications", 1954, The Technology Press of M. I. T., and John Wiley & Sons, Inc.

DIELECTRICS FOR ANTENNAS

By

Eino J. Luoma* and David J. Epstein[†]

The materials used in antennas are electrical conductors, dielectrics, and sometimes semi-conductors or lossy dielectrics. Electrical conductors, i.e. metals, such as steel, brass, copper, aluminum, or silver are the most common antenna material, but many antenna designs could not be achieved without the use of dielectric material. It is the purpose of this paper to briefly survey these uses of dielectrics in antennas; to examine the properties of presently available dielectrics as related to antenna applications; and to suggest new special dielectrics for use in antenna design.

A. DIELECTRIC APPLICATIONS IN ANTENNAS

Table I is a typical list of applications of dielectrics in antennas demonstrating very wide variety. The "Antenna Engineering Handbook" by Jasik (Reference 1) was used in preparing this table.

B. DIELECTRIC PROPERTIES AND OPERATING TEMPERATURES

Against this preceding background of applications it is instructive to consider what is available in dielectric materials. Figure 1 is a graph of the relationship between dielectric constant and operating temperature capability of the more common dielectric materials. It is interesting to note that for the pure compounds or one component systems there is a general correlation between the dielectric constant and operating temperature capability. This is to say that if the designer needs a higher operating temperature in a dielectric he may generally expect to have to go to higher dielectric constants and higher densities. On the other hand, any of the single component dielectric materials may be diluted with air e.g. foams and powders or other low dielectric constant material to achieve the lower dielectric constants and lower densities at a possible sacrifice of strength and changes in the other mechanical properties. The designer is fortunate if, as in the case of Fiberglas-plastic laminates, for example, the dilution results in improved mechanical properties.

*Emerson & Cuming, Inc.

[†]Consultant to Emerson & Cuming, Inc.

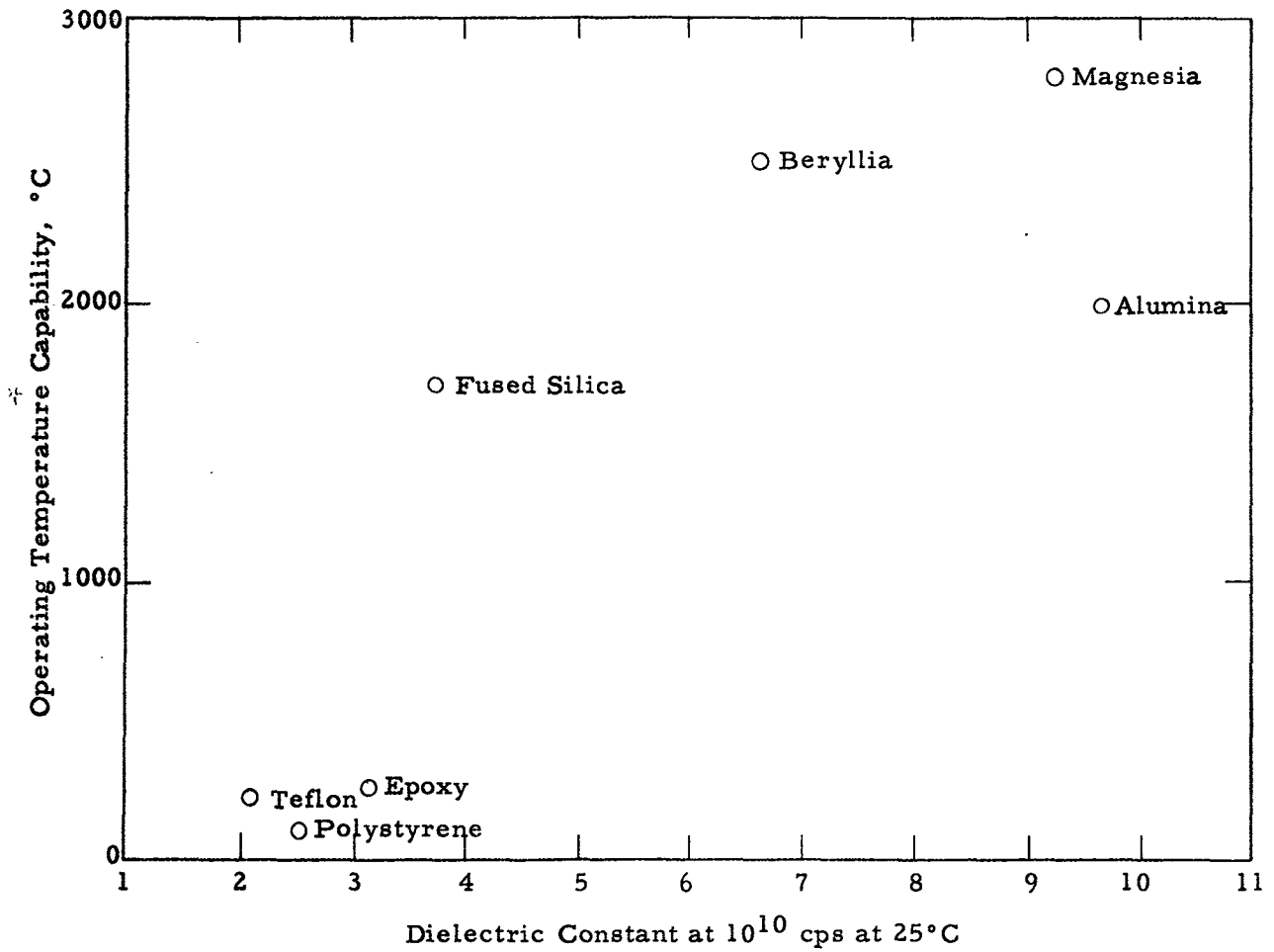
TABLE I

TYPICAL APPLICATIONS OF DIELECTRICS IN ANTENNAS

Type of Antenna	Antenna Application	Dielectric Material
Luneberg Lens spherical or cylindrical	1. Omnidirectional focussing device for feed. 2. Reflector	1. Natural dielectric - plastic foam 2. Artificial dielectric - for light weight.
Non-Spherical Lenses concave, convex, plane, etc.	Focussing device for horn.	Natural or artificial dielectric.
Dielectric Rod or Spike	Surface wave antenna often a member of a linear array.	Mostly polystyrene; sometimes plastics or ceramics with higher dielectric constants are used.
Trough-Guide Antennas	Surface wave antenna for flush mounting on aircraft.	Plastic or ceramic.
Dielectric Sheets on Ground Plane	Flush mounted beacon antennas.	Plastic or ceramic.
Tunnel Horn	Low side lobe, broad beam antenna.	Absorber used to line inside of horn.
Circularly Polarized Feed	Feed	Low loss plastic used as septum.
Tail Cap Antenna for Aircraft	H-F communication antenna.	Fiberglas-plastic used as insulation.
Radome	Wide variety of antennas for protection.	Plastics or ceramics; Fiberglas- plastic laminate.
Phased Array	Electronic scan antennas.	Ferrite ceramics used for phase control. (ferrites are considered beyond scope of this paper)

FIGURE 1

DIELECTRIC CONSTANT VS OPERATING TEMPERATURE CAPABILITY



Note 1 - Temperatures indicated for the oxides are melting temperatures.

Note 2 - Temperatures indicated for the plastics are softening temperatures.

The operating temperature ranges shown for typical materials in Figure 1 are the temperatures above which substantial degradation in dielectric or structural properties take place. This is not to say there has been no change in dielectric constant or reduction of strength at the indicated operating temperature limit. Without exception all of the materials lose strength substantially as the limiting temperature is approached. With the exception of silica all of the materials change in dielectric constant and loss tangent as the limiting temperature is approached. Thus if the antenna application is at all critical as to the exact value of dielectric constant, great care must be used in choosing the right dielectric.

Figure 2 shows the variation in dielectric constant with temperature of typical dielectric materials. Figure 3 shows the variation in loss tangent with temperature of the same materials.

C. DISPERSIVE DIELECTRICS

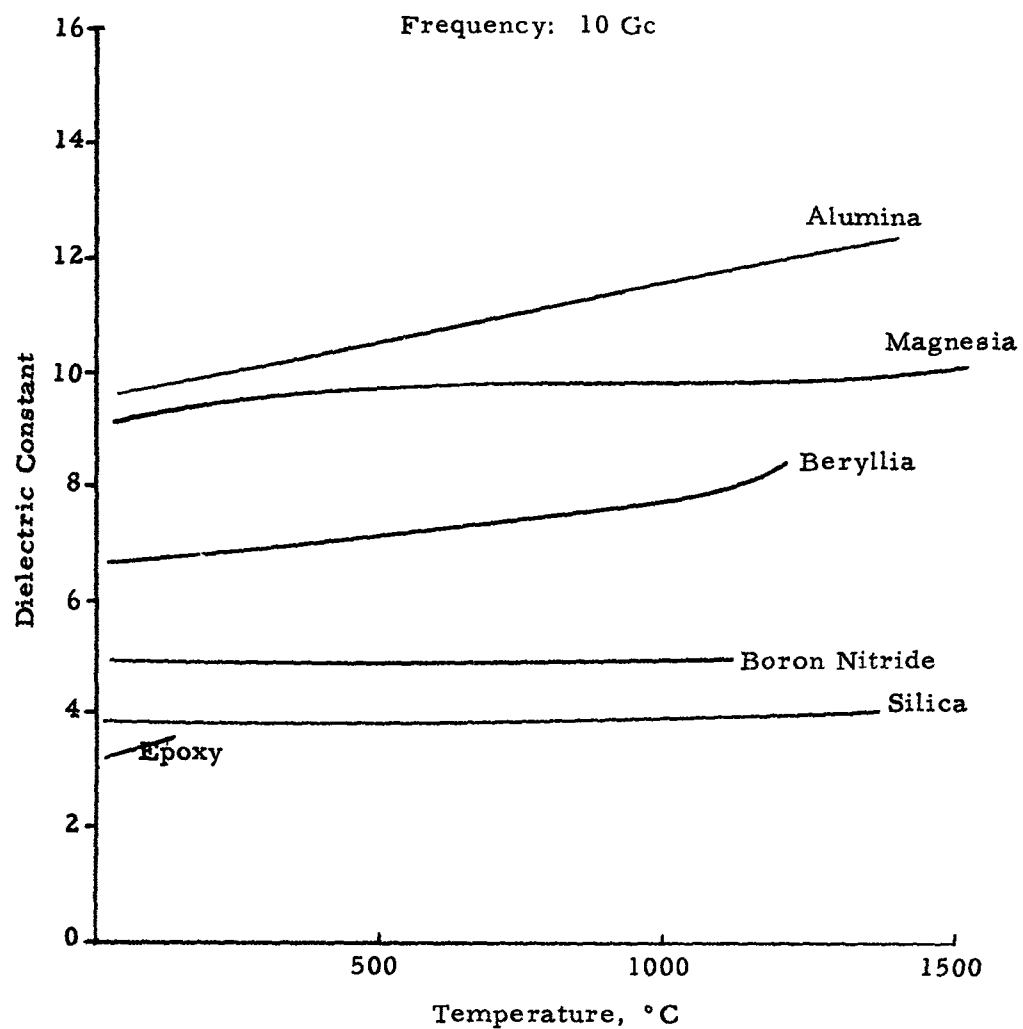
Dispersion is the change in dielectric constant of a dielectric material with frequency. The well known low loss dielectrics such as polystyrene, teflon, silica and alumina exhibit very little dispersion. On the other hand, if best performance is achieved with a section of dielectric which is, say, a quarter wave or half wave thick, and, if this performance is desired over a substantial frequency band, the right kind of dispersion can be a useful property. Unfortunately, dispersive dielectric constants are always accompanied by high loss tangents. Also substantial dispersion occurs more commonly in liquid dielectrics, which are difficult to apply in antenna design. Figure 4 shows the dielectric constant and loss tangent as a function of frequency for one of the more dispersive solid dielectrics, barium titanate.

D. ARTIFICIAL DIELECTRICS

An artificial dielectric, as contrasted with a natural dielectric, is a multi-component material in which two or more materials at least one of which is a metal are mixed to produce desired dielectric properties. For example, a small quantity of aluminum flake or aluminum slivers can be distributed throughout a plastic foam to produce a marked increase in dielectric constant with practically no increase in weight and very little increase in loss tangent. There are two approaches to the achievement of uniform dielectric properties in an artificial dielectric: one is to distribute the loading particles as randomly as possible; the other is to organize the distribution of the loading particles both as to their orientation and spatial distribution. In the former approach, the limitation to achieving perfect homogeneity is due to departure from perfect randomness; in the latter approach the limitation is in the ability to achieve mechanical perfection in the intended distribution. The former approach is commonly used today; the organized approach should be considered. These problems are discussed in more detail in Reference 2. Figure 5 is a graph showing the relationship between dielectric constant and aluminum loading for an artificial dielectric foam.

FIGURE 2

DIELECTRIC CONSTANT VS TEMPERATURE



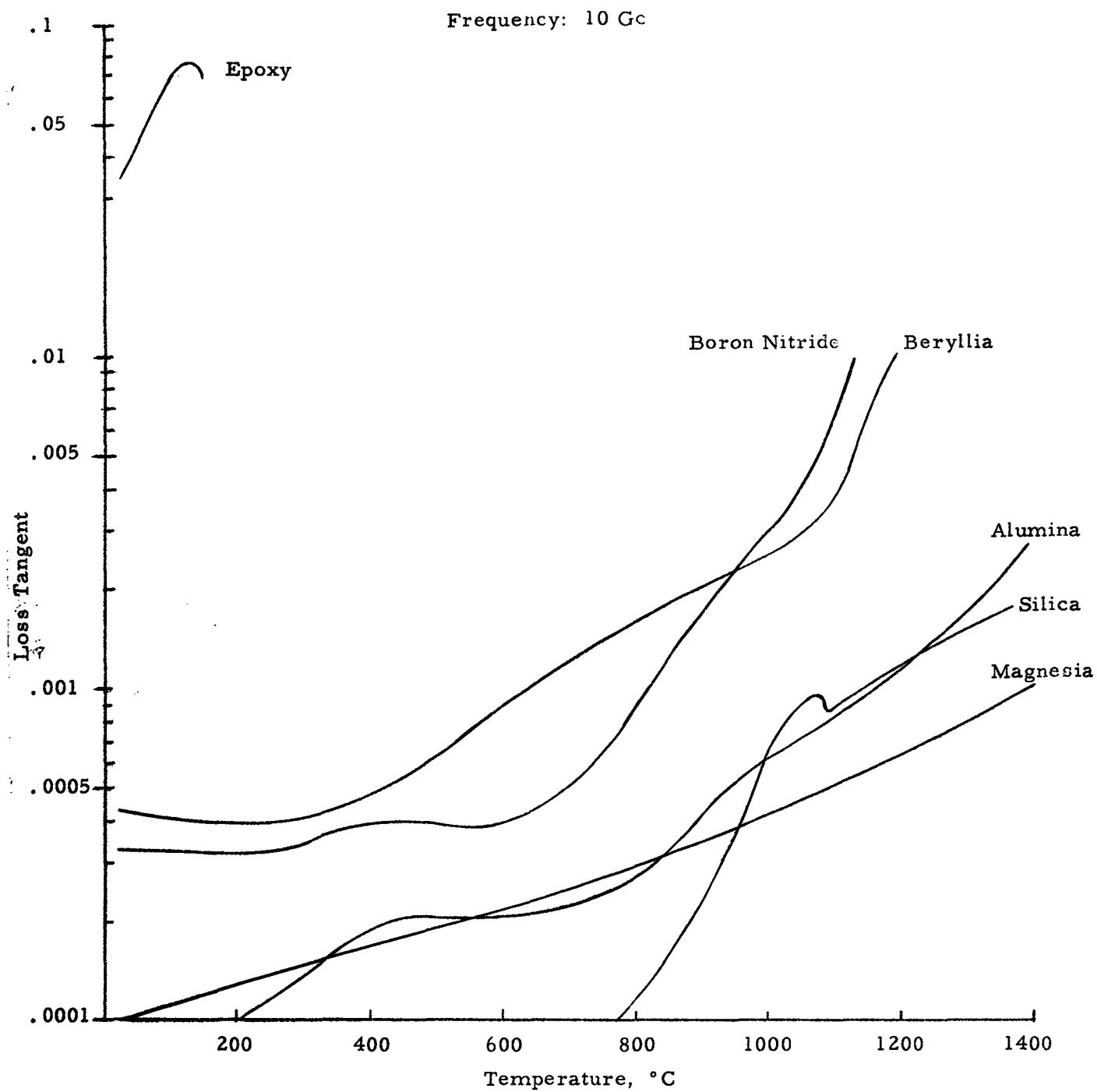


FIGURE 3

LOSS TANGENT VS TEMPERATURE

FIGURE 4

DISPERSION CURVES FOR BARIUM TITANATE

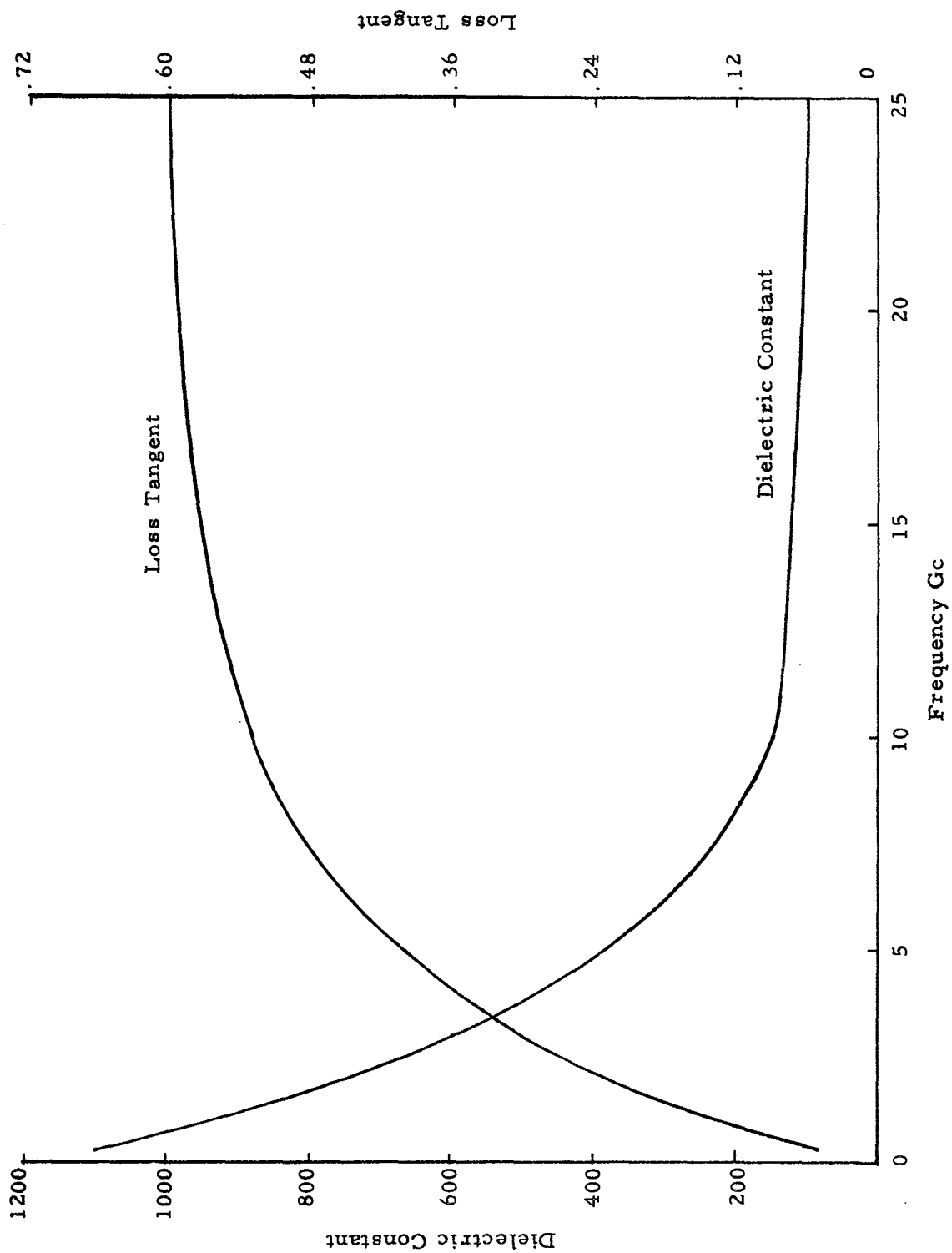
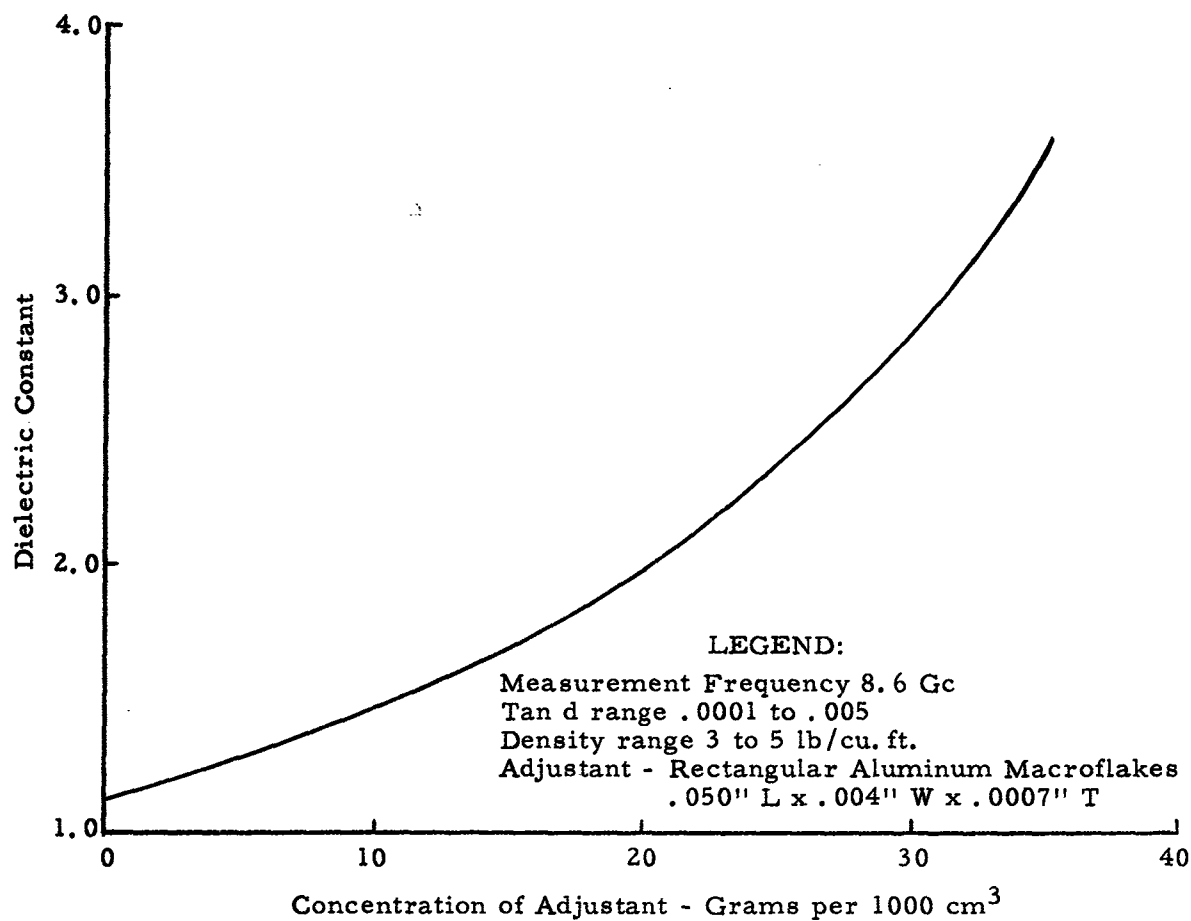


FIGURE 5

DIELECTRIC CONSTANT OF LIGHT WEIGHT
ALUMINUM ADJUSTED ARTIFICIAL DIELECTRIC
FOAMS AS A FUNCTION OF ALUMINUM LOADING



E. ANISOTROPIC DIELECTRICS

Usually, the antenna designer is interested in a dielectric with the same dielectric constant in all directions. Anisotropic dielectrics, in which this is not the case, are introduced here to call attention to the fact that they are practical although little if any use has been made of them. Reference 3 (H-Waves in Anisotropic Slabs) considers the problem of how anisotropic dielectrics might be used to increase the frequency bandwidth of surface-wave antennas. In practice, anisotropic dielectrics would be constructed of thin layers of alternately low and high dielectric constant. Conceivably, anisotropy ratios of 100 to 1 could be achieved.

F. HOMOGENEITY

Wherever a dielectric plays a part in shaping the beam of the antenna, inhomogeneity in the dielectric can be troublesome. This is particularly true in lens applications. Therefore, the antenna designer should be aware of the degrees of homogeneity that can be achieved with dielectric materials as they are manufactured today. A variation in dielectric constant no greater than ± 0.01 is probably sufficient for even the most critical applications. This homogeneity is achievable with only the one-component dielectric materials. With multi-component dielectric materials and artificial dielectrics the antenna designer should expect to get a homogeneity no better than ± 0.15 . In applying these ground rules, a word of caution is in order. The ceramics generally are not pure one-component systems although they may approach 100% purity. They are subject to porosity and impurities. Therefore, a homogeneity of ± 0.05 is typical of the better ceramic materials today.

G. MEASUREMENT TECHNIQUES

One of the biggest problems associated with obtaining homogeneity in dielectric materials has been its measurement. Most measurement techniques have required the cutting of a small mechanically precise sample of the dielectric for insertion into a cavity or shorted waveguide. Although the measurement made on this sample was very precise it yielded little information on homogeneity. A non-destructive sampling and measurement technique was needed. Within the last year, this has been established at Emerson & Cuming, Inc. (Reference 4). The technique developed uses a microwave interferometer capable of making a measurement on a highly localized segment of a large sample. This differs from previous interferometer techniques in that both dielectric constant and loss tangent can be measured. The principle of measurement is as follows: Insertion loss and insertion phase are measured at 45° incidence on the flat sheet. Dielectric constant and loss tangent are then determined from these measured values by use of conversion tables.

Special interferometer horns were developed which permit the inspection area for a given measurement to be reduced to one square wavelength of the flat sheet of the dielectric material.

H. DIELECTRIC POWDERS

One dielectric product which has recently been introduced by Emerson & Cuming, Inc. deserves special mention. This is a line of free flowing dielectric powders known as Eccoflo HiK. They are available in dielectric constants up to 10, have loss tangents below 0.001, and are of interest to antenna designers because they can be used in plasma simulation experiments.

REFERENCES

1. Jasik, Henry, "Antenna Engineering Handbook", McGraw-Hill Book Company, Inc., 1961
2. Rowe, P. E., Luoma, E. J., Volk, M. C., "Invariant Microwave Lenses from Artificial Dielectrics", August 1963, Final Report by Emerson & Cuming, Inc. on Subcontract 129331 for the Applied Physics Laboratory, The Johns Hopkins University
3. Luoma, E. J. and Mason, S. J., "H-Waves on an Anisotropic Slab", Final Report on Contract AF19(628)-463 by Emerson & Cuming, Inc. for Air Force Cambridge Research Laboratories
4. Luoma, E. J. and Volk, M. C., "Measurement of Dielectric Homogeneity with a Microwave Interferometer", Final Report on Subcontract 285 under Prime Contract AF19(628-500 by Emerson & Cuming, Inc. for M. I. T. Lincoln Laboratory
5. "Tables of Dielectric Materials", Volume V, April 1957, Contract Nonr-1841(10), Technical Report 119, Laboratory for Insulation Research, Massachusetts Institute of Technology
6. Westphal, W. B., Letter Report, "High-Temperature Microwave Dielectric Measurements", July 1962, Laboratory for Insulation Research, Massachusetts Institute of Technology
7. Zellner, G. C., Pentecost, J. L., Eliason, L. K. of Melpar, Inc., "Accurate Microwave Measurements of Dielectric Properties to Temperature of 1600°C", Proceedings of the ASD-OSU Symposium on Electromagnetic Windows, July 1962
8. Von Hippel, A. R., "Dielectric Materials and Applications", 1954, The Technology Press of M. I. T., and John Wiley & Sons, Inc.

CORONA AND BREAKDOWN AS A FUNCTION OF
HUMIDITY AT LOW AIR-PRESSURE

by Paul F. Stang

Presented at the Thirteenth Annual Symposium
 on USAF Antenna Research
 and Development
 University of Illinois
 15-18 October 1963

 Lockheed-California Company
A Division of Lockheed Aircraft Corporation
 Burbank, California

Summary:

Insufficient information in published literature concerning the effect of relative humidity at low air-pressure on corona and breakdown prompted an investigation by the Lockheed-California Company. The studies were conducted in view of increasing penetration into the upper atmosphere by aircraft like the U2 or F104. The Supersonic Transport currently under study will cruise at 85,000 feet and will be equipped with HF SSB transceivers of 1 kw power output. Reliable communication is tied to the prevention of corona or voltage breakdown at the antenna. Breakdown measurements were found to be largely affected by the degree of humidity either present or deliberately injected into the rarefied atmosphere. An increase of breakdown potential was observed by other investigators when percentage of humidity was increased at ambient air pressure. This effect was found to depend on gap spacing at D.C. and A.C. (50 cps). At HF the breakdown potential is found to be a function of electrode configuration also.

To obtain more information on breakdown phenomena, measurements in this frequency range were made in a cylindrical pyrex bell jar 12.0" in diameter and 36" high. This chamber was evacuated to air pressures simulating altitudes up to 100,000 feet. Various electrode configurations were studied. A humidity recorder was placed inside the chamber; a method of changing the degree of humidity was devised. Results of tests are shown in graphical presentation; typical corona and glow discharges are shown in color slides.

Introduction:

This paper presents experimental results of voltage breakdown and corona at low air pressure corresponding to altitudes up to 100,000 feet in the H.F. frequency range. Investigations of voltage breakdown and corona were made as a function of water vapor content. These tests were made to investigate particularly the H.F. range as little is known about how the effective electric field changes when water vapor at low air pressure is present. Quantitative experimental results were obtained at room temperature, 76° F, and 15% to 100% humidity for air pressure to altitudes of 80,000 to 100,000 feet. Different spark gap distances and electrode shapes were used. The applied radio frequency was varied from 2 Mc to 8 Mc. The results obtained indicate that a higher voltage must be applied to produce corona discharge or complete breakdown as the percentage of humidity is increased.

No references were found in current literature on this subject in respect to the influence of humidity at low air pressure corresponding to the upper stratosphere.

Experimental Procedure:

The experimental set up used for the test is shown in Figure 1. The HF power source was a surplus Navy TDE-2 transmitter. An autotransformer was designed and built to boost the output voltage to a maximum of 13,000 volts. The pyrex glass discharge chamber is 12.0 inches in diameter and 36.0 inches in length and mounted vertically. Wet blotters of different sizes were inserted to control the degree of humidity in successive steps. A relative humidity recorder was located inside the glass chamber and provided a continuous plot of humidity percentage and temperature. The measurements were conducted for the following electrode configurations:

- 1) needle to needle
- 2) 0.18" sphere to 0.18" sphere
- 3) 0.5" sphere to 0.5" sphere
- 4) 1.0" sphere to 1.0" sphere
- 5) 1.0" sphere to 8.0" diameter circular plate
- 6) 5.0" Teflon covered square to 5.0" aluminum square

The electrodes were mounted on the vertical axis of the cylindrical test chamber with the lower electrode grounded.

The critical breakdown voltage discussed in this paper is defined as the potential between electrodes just prior to the initial appearance of a glow discharge (corona) or breakdown. The initiation of corona or breakdown is evidenced by a slight dip of the voltmeter pointer. The tests were conducted at room temperature (76° F) with spark gaps of 5.0 and 11.0 inches.

Experimental Observation:

The test conditions for glow discharge were established at approximately 10% - 20% humidity and a reduced air pressure to simulate 80,000 feet altitude. The HF power was then increased until glow discharge was initiated. When this

occurs, the glow discharge is a uniform bluish cloud surrounding the upper electrode, the surface of the electrode being covered by a salmon-pink-colored glow.

If the HF power is slowly increased beyond the initial breakdown value, the bluish glow drifts toward the grounded electrode. When the HF power has been increased approximately 10% over the initial breakdown value, the bluish-colored cloud will have filled the spark gap area and a pink glow will suddenly adhere to the grounded electrode. If the HF power is further increased, the salmon pink-colored glow will expand from both electrodes to fill the gap between. When the two expanding columns snap together, complete breakdown has occurred.

For the purposes of establishing standard test conditions, the HF power is limited to that value which causes all glow discharge or breakdown phenomena to exist at only the ungrounded electrode.

At very low relative humidity, the glow is very bright and extends through most of the chamber. As the percentage of humidity is increased at a given altitude, the glow diminishes and eventually disappears completely. Greater HF power must be applied to the electrodes for the glow phenomena to reappear. Beyond 30% humidity, the glow has only a narrow bluish column; eventually it becomes a bluish streamer between each of the electrodes, approaching a complete breakdown in a highly ionized small region. The cross-sectional area of the bluish-colored streamer is found to be directly proportional to the electrode area.

Experimental Results:

Gaseous discharges, such as electric sparks, arcs, or air glows, create ions in the volume of the gas. For arcs or glows in low air pressure, a considerable volume of densely ionized and excited gas is produced when a critical HF potential is reached, (commonly called plasma). It has about an equal number of positive ions and electrons, except near the electrodes and near the chamber bounding surface or walls.

Mobility of the ions is considerably affected by the degree of injected water vapor. The water vapor particles remove electrons from the ionization process by attachment. A higher field potential would speed up the electrons but attachment is improbable. Test results have shown a direct, nearly linear relationship between breakdown potential and percentage of humidity. Electrode configuration has the effect of determining the ratio of breakdown potential versus percentage humidity at a given air pressure. It was found that the humidity effect is less pronounced between sharp points or needle electrodes. Needle points have a highly concentrated field; at low air pressure, the breakdown potential is relatively independent of gap size.

As the relative humidity is slowly increased in a constant field, ionization begins to disappear as a result of the short mean free path length of electrons. The electrons become attached to the H_2O molecules and a

higher field potential must be applied to detach the electrons. It is well known that sharp needle electrodes with their highly concentrated field will detach the electrons at a lower potential than with an electrode of greater radius.

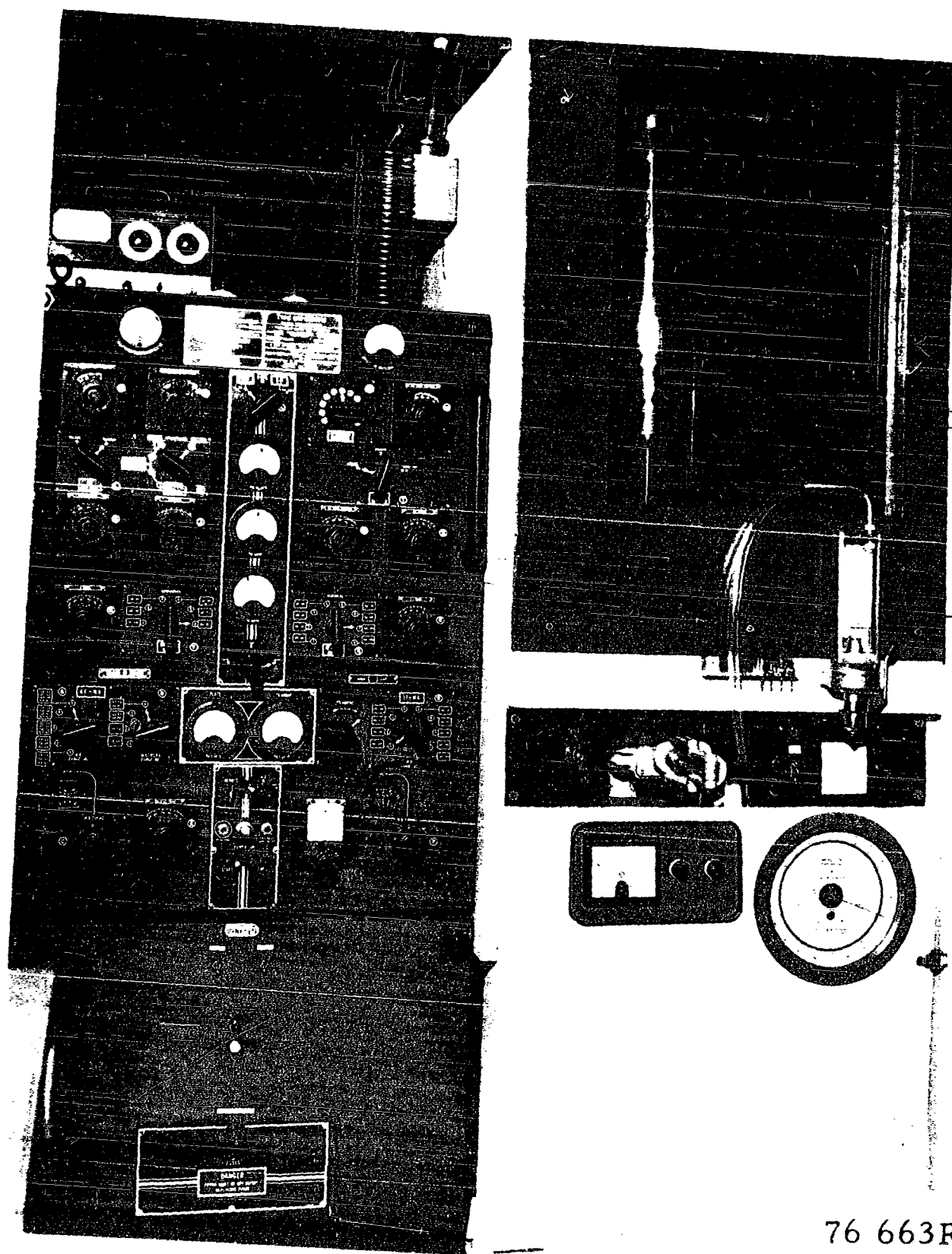
The field distribution is also a deciding factor in the detachment of electrons in the space between electrodes of different configurations when the gap size is held constant. A study of this phenomena has been made by the Lockheed-California Company and reported in the Eleventh Antenna Symposium on USAF Antenna Research and Development.

Test results obtained during the present study program are plotted in the graphs, Figures 2 through 8.

Conclusion:

It has been shown that relative humidity greatly affects the breakdown potential. Electrode configuration with its associated field distribution is also a deciding factor. An increase in humidity at a given altitude is found to require a corresponding increase in gap potential to invoke glow discharge or breakdown. It appears that water vapor has a large re-attachment probability. Glow discharge at high relative humidity disappears and only complete breakdown is observed without the characteristic bright glow column. The observed bluish streamer between electrodes is proportional in cross-sectional area to size of electrode surface with a given air pressure and percentage humidity.

TEST SET UP



76 663R

Fig. No. 2

H.F. Breakdown as a function of humidity and altitudes.

$f = 2 \text{ Mc}$

gap = 5.0 inches

used electrodes: 1.0 sphere - 8.0" circular plate

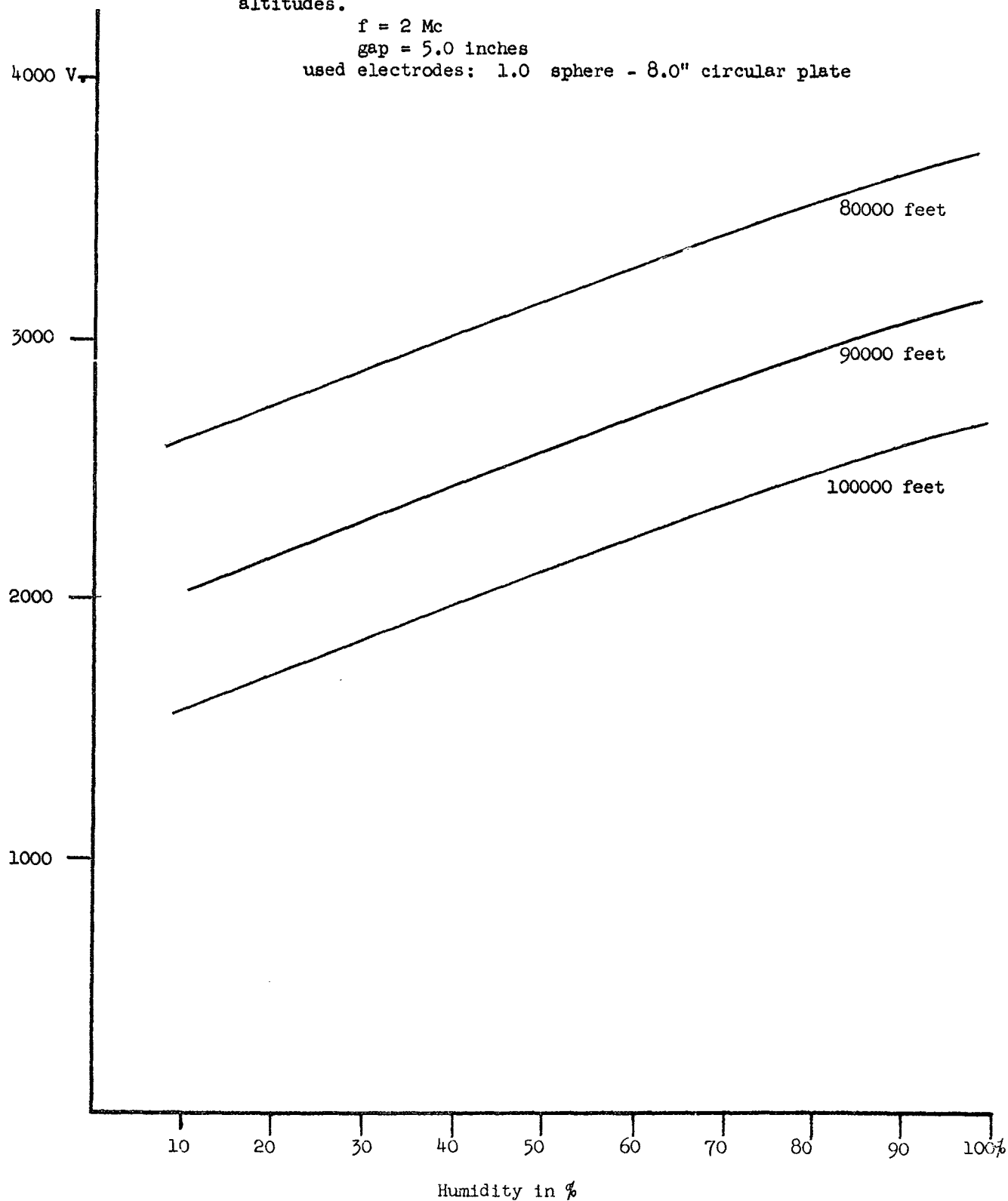


Fig. No. 3

H.F. Breakdown as a function of humidity and
altitude

$f = 4 \text{ Mc}$
gap = 5.0 inches
used electrodes: 1.0" sphere - 8.0" circular plate

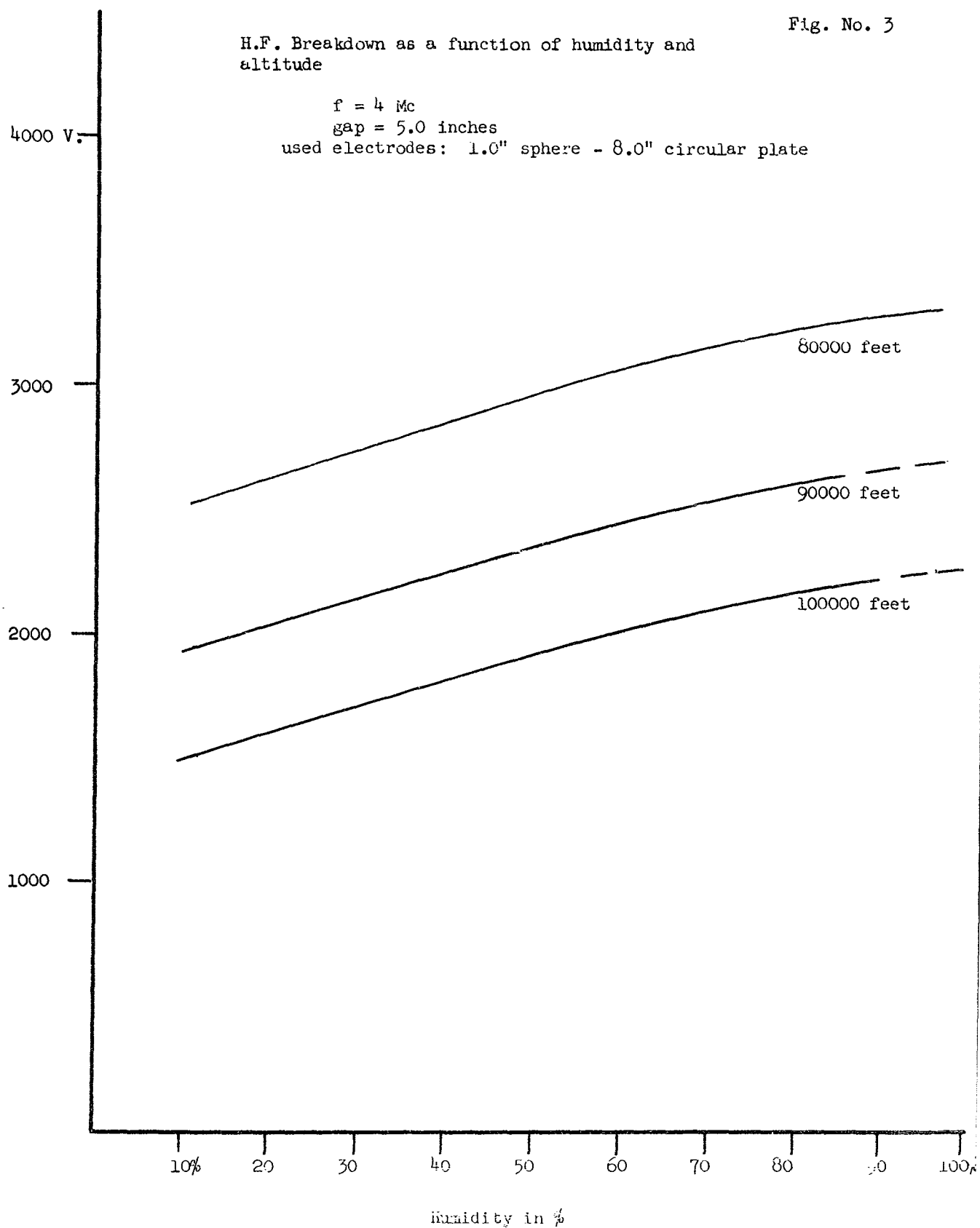


Fig. No. 4

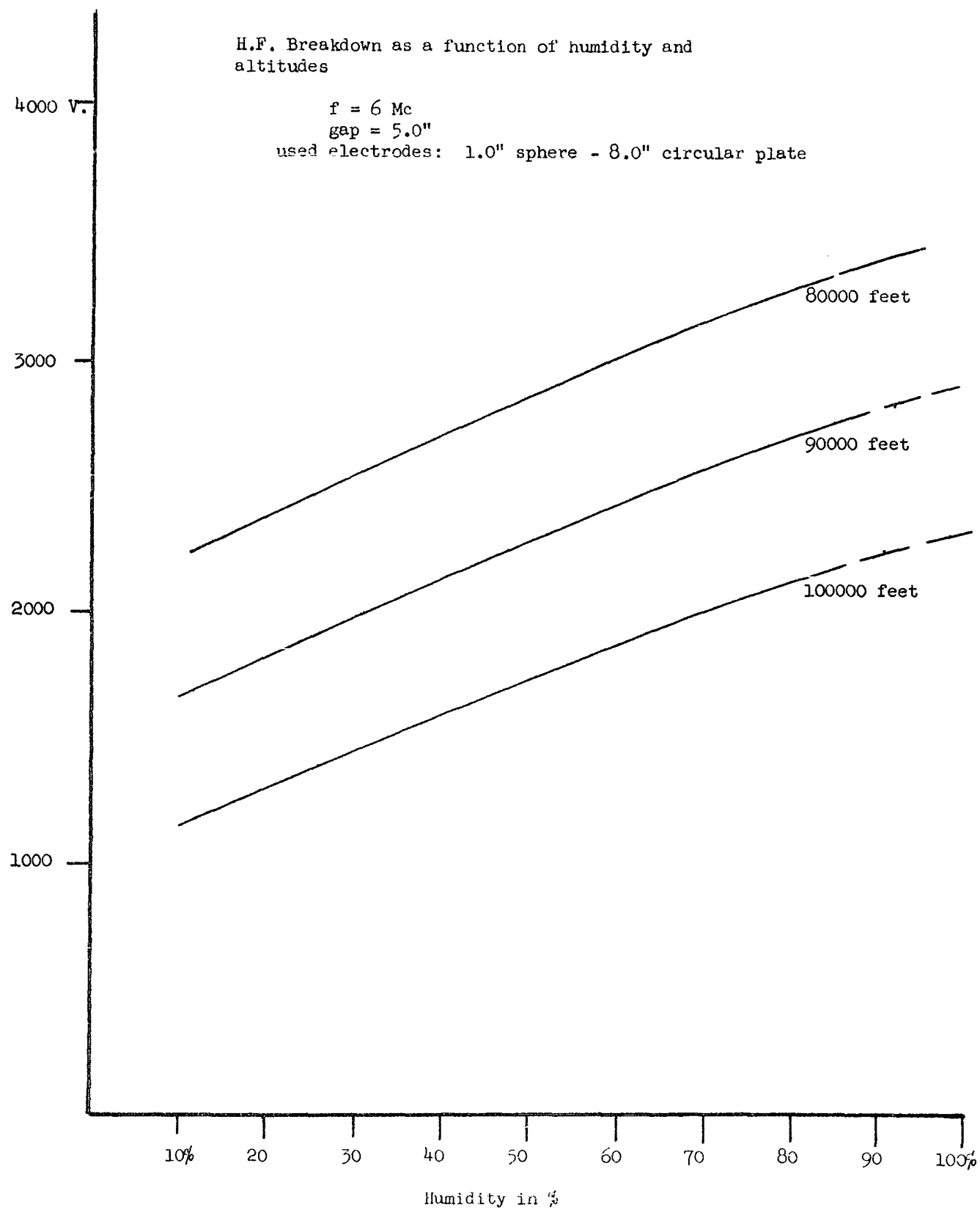


Fig. No. 5

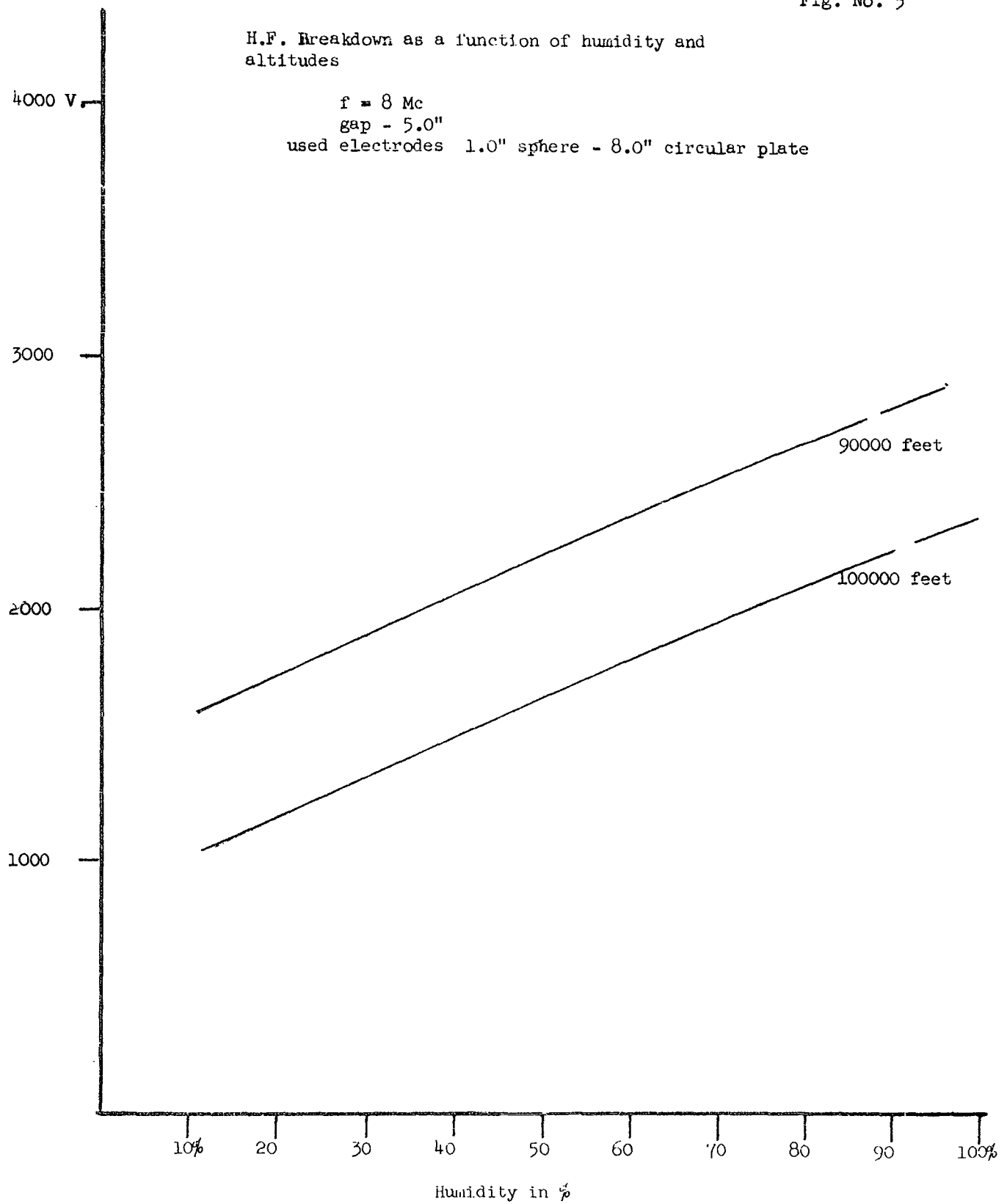


Fig. No. 6

H.F. Breakdown as a function of humidity and altitudes

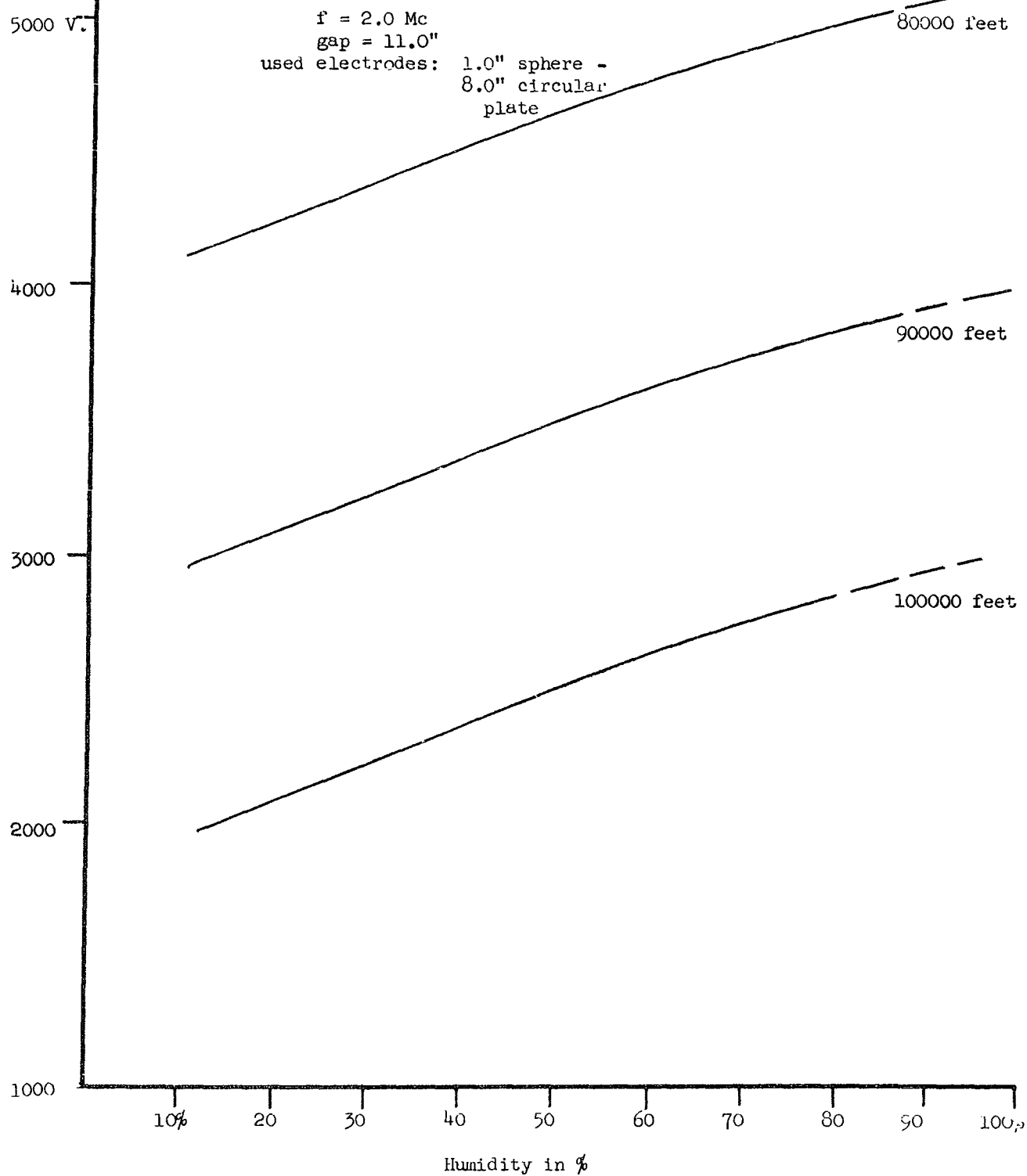


Fig. No. 7

H.F. Breakdown as a function of humidity and altitudes

$f = 6 \text{ Mc}$

gap = 11.0"

used electrodes: 1.0" sphere to 8.0" circular plates

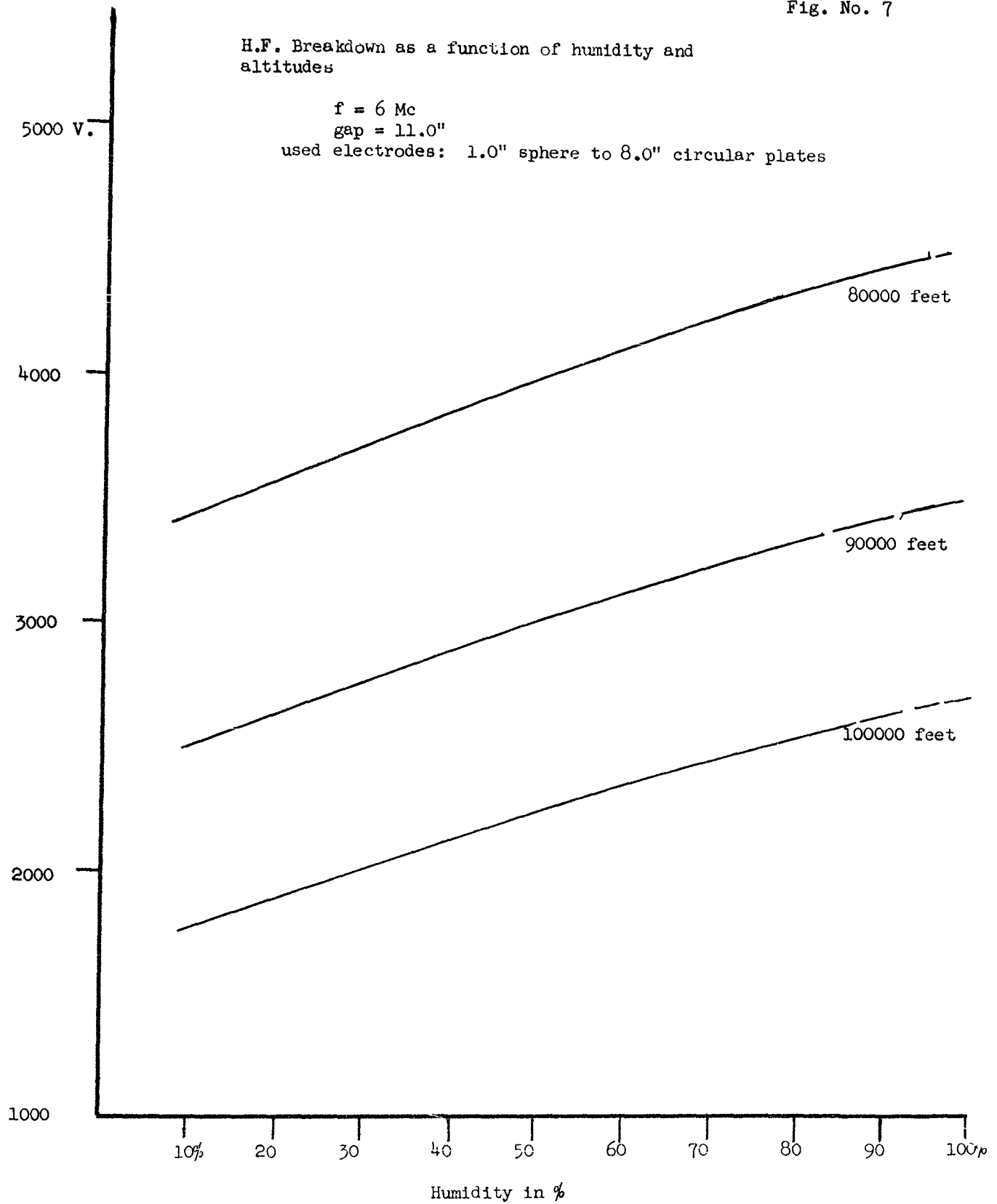
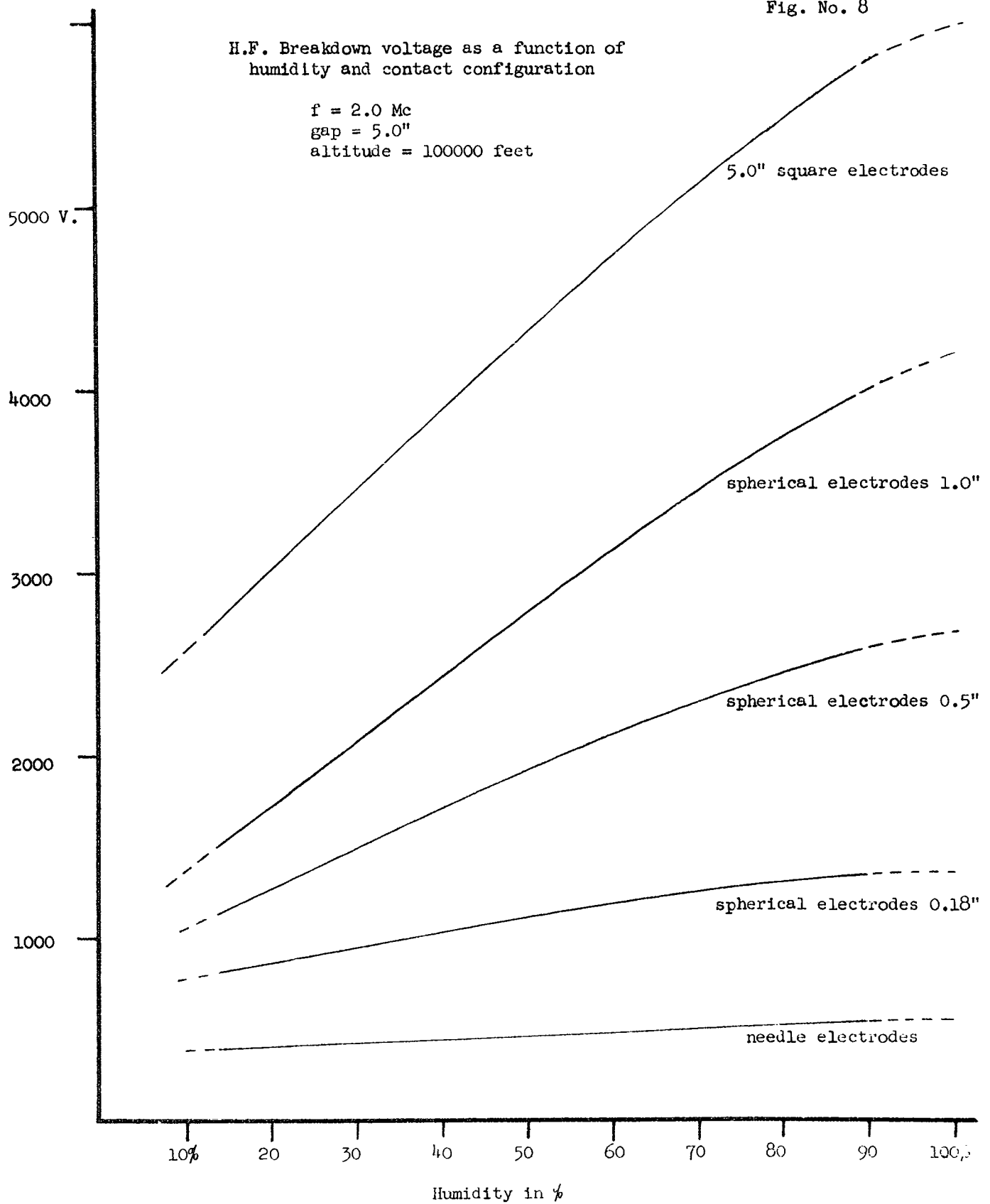


Fig. No. 8

H.F. Breakdown voltage as a function of
humidity and contact configuration

$f = 2.0 \text{ Mc}$
gap = 5.0"
altitude = 100000 feet



IONIZATION ENHANCED ANTENNA
VOLTAGE BREAKDOWN

C. A. Hinrichs
Space and Missile Division
McDonnell Aircraft Corporation

ABSTRACT

The concepts and parameters of voltage controlled breakdown are reviewed and the significance of the collision frequency is shown. The importance of the energy dependence term defining collision frequency is illustrated. A heuristic development relates the gas conditions within and without the breakdown region. It is shown that when the energy dependence of the collision frequency is incorporated into the basic breakdown expression and when the gas conditions are related, the breakdown function is uniformly lowered as the ambient ionization level is increased, thereby yielding first order agreement with experimental data.

1. INTRODUCTION

A common conception of voltage breakdown is an arc or corona, i.e. a bright discharge. The bright discharge is accompanied by a discrete change in the power level. The voltage breakdown applicable to antennas is a process that occurs at a voltage level below that required to initiate an arc or a corona and is called the dark discharge. This condition is not accompanied by an abrupt change in power level.

A propagating electromagnetic wave is seriously attenuated when it must pass through an ionized medium whose plasma frequency, corresponding to electron density, is equal to or greater than, the frequency of the propagating wave. If this ionized medium, viz a plasma, is created by the electric field of the electromagnetic wave, the system is said to be in a state of voltage breakdown.

Classic breakdown theory considers the molecule, which is struck by the electron, to be at a much lower energy level than the electron. Thus the rate of these ionizing collisions is primarily a function of particle spacing.

When the gas is already at a high energy state, a modification to the breakdown expression must be made. One method redefines the collision frequency in terms of particle densities and another method redefines the collision frequency to incorporate a temperature term. Both methods however result in a minimal variation in the breakdown function for various initial ionization levels. When an expression is utilized, which includes the energy effects on collision frequency, a smooth transition of the breakdown function results for varying initial gas energy levels thereby giving closer agreement with experimental data.

Because of the extremely large number of parameters involved in this problem (gas parameters, collision probabilities, collision cross sections, mean free paths, energy states, gas constituents, gas chemistries, and geometry) and the relative inaccuracies in the present knowledge of these parameters, as well as the inherent problems in the application of such theories (complex missile antenna geometries, upper air constituents, hot gas chemistry, prediction of aerothermodynamic flow fields); the approach in this paper will be generally heuristic and aimed primarily towards the engineering solution.

2. THE BREAKDOWN EXPRESSION

The development of the breakdown expression, by ionization,

$$\partial n / \partial t = \nu_i + \nabla^2 D n + n_0, * \quad (1)$$

has been documented by Brown¹ and others. The solution to this equation, for the condition of breakdown, i.e. the production of electrons equal to the depletion of electrons, has been noted by Chown² as,

$$\nu_i = \nu_a + D/\lambda^2 + \frac{1}{\tau} \ln n_r/n_0. \quad (2)$$

The requirement for breakdown to occur in accordance with this expression is that the production of electrons exceed the loss of electrons. Examination of the breakdown equations terms shows the ionization rate, ν_i , must equal the attachment rate, ν_a , plus the diffusion rate, D/λ^2 , plus a term introduced to account for the rate of electron build-up to a particular level. A comparison of the defining relationships for breakdown as described by Brown¹ and those of Cobine³ show a superficial difference. The breakdown relationships of Cobine describe an arc, i.e., a visible column, or a glow relationship. These are definite "break points" of the characteristic voltage-current relationship. When a potential is initially applied across a gap a linear relationship between voltage and current is apparent until saturation occurs, i.e., the usual vacuum tube characteristics. Further application of potential results in the electrons gaining sufficient energy such that electron-neutral particle collisions result in ionization. This process is described by the first Townsend coefficient. Still further application of potential results in the secondary electrons, produced by electron-electron-neutral particle collisions, gaining sufficient energy to create further ionization. This process is described by the second Townsend coefficient. Finally this process proceeds to the point where a conducting path is produced and the potential drops, while the current increases rapidly, and a glow or arc is produced. The glow or arc or a succession of both is a function of electrode geometry.

Antenna breakdown as described by Brown, is defined as that electron density about a radiating element which seriously attenuates the propagating electromagnetic wave, i.e. the condition of

$$\omega_p \geq \omega. \quad (3)$$

This relationship usually occurs in the region defined by the first Townsend coefficient.

* See attached list of symbols.

The plasma frequency, a term that appears with the units of cps in the derivation of the Appleton-Hartree equation, is expressed as

$$\omega_p = 2\pi \cdot 10^3 n^{1/2} \quad (4)$$

Once the loss terms, attachment and diffusion, are suitably defined such that a net ionization rate is known, a conversion to electric field intensity and thus antenna power may be affected. The net ionization to electric field intensity correlation was made by Chown² utilizing the experimental data of Gould and Roberts⁴ and Brown¹. This curve is given in Figure 1. The conversion is made by writing equation (2) for a CW system of parallel plates in air from the data of Gould and Roberts, and expressing attachment and diffusion in the same terms as the data. The results of this analysis define the effective AC electric field intensity, which would produce the same energy transfer to the electrons as a DC electric field. This factor is related to the electric field intensity of the propagating signal, by Brown¹, as

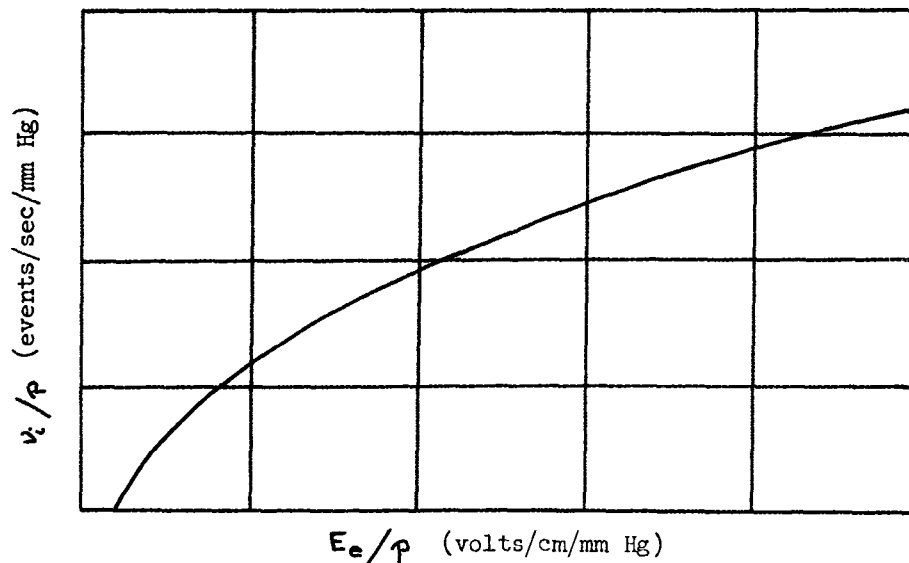
$$E_e = E / [1 + (\omega/\nu_c)^2]^{1/2} \quad (5)$$

The correlation of electric field intensity and antenna power can be made utilizing the Poynting Theorem. MacDonald⁵ has shown the derivation and expressed one such result as

$$(P/A)^{1/2} = 0.82 E, \quad (6)$$

where P is in kilowatts, A is in square centimeters and E is in kilovolts per centimeter. The true electric field intensity contributing to antenna breakdown is of course the near field.

FIGURE 1
THE RELATIONSHIP BETWEEN THE NET IONIZATION
RATE AND THE EFFECTIVE ELECTRIC FIELD



2.1 The Terms of the Breakdown Expression. - The attachment term, ν_a , is that rate at which the free electrons are captured by the ions. MacDonald has expressed the attachment frequency as

$$\nu_a = 4 \cdot 10^{-6} \nu_c = \psi \nu_c . \quad (7)$$

The diffusion term, D/Λ^2 , is that rate at which the ionization diffuses from, i.e. leaves, the area of interest. The diffusion coefficient from Cobine³ is

$$D = l^2 \nu_c / 3 . \quad (8)$$

Equation (8) describes diffusion for low ionization levels and is sometimes called the free diffusion coefficient. When the level of ionization is "appreciable", i.e. when the ions must diffuse between electrons, the diffusion rate is decreased. This process is called ambipolar diffusion. The ambipolar diffusion coefficient is related to the free diffusion coefficient by the expression noted in Whitmer and MacDonald⁶,

$$D_a = D_f / 40 . \quad (9)$$

The level at which ionization becomes large enough to effect a transition from free to ambipolar diffusion is given by Whitmer and MacDonald⁶ as

$$n_o = 10^4 n_c , \quad (10)$$

or by Chown² as

$$n_o \gg 2 \epsilon_o kT / e^2 \Lambda^2 . \quad (11)$$

The diffusion length, Λ , is that distance which the ions must diffuse to leave the domain of interest, e.g. the antenna area. The diffusion length for parallel plates in air is commonly expressed as

$$\Lambda = d / \pi . \quad (12)$$

Chown² has postulated a modification of the diffusion length expression to account for the various breakdown levels experienced with slot antennas employing dielectrics other than air, e.g. see the data of Scharfman and Morita⁷. It is easily seen that when a dielectric more dense than air is in the immediate area where the ionization is produced, the ionized particles may more readily lose their energies to the more dense dielectric, thus the effective

diffusion length is decreased, over that of air. Chown's² modification introduces a constant, q , into the expression, thus

$$\Lambda = d / q \pi \quad (13)$$

where

$$q = 4 \quad (14)$$

for the specific case of

$$\epsilon = 5 \quad (15)$$

Chown² also postulates a variation in the effective diffusion length to account for high velocity air flow across the breakdown gap.

The rate factor, $\frac{1}{\tau} \ln_e n_r / n_o$, of equation (2) relates the time required, τ , for the ionization to build up to the required density, n_r , in the presence of an ambient density, n_o . Since a finite time is required to produce a given density of electrons, it is seen that a pulse system may operate at higher power levels than a continuous wave system. The rate factor is zero in a CW system as the "pulse length" is infinite.

2.2 Collision Frequency. - Collision frequency is of prime importance in determining breakdown since both attachment and diffusion are functions of collision frequency. Although the energy dependence of collision frequency is a widely accepted concept, many authors^{2,5,6} express collision frequency as a function of particle density alone, viz

$$\nu_c = 5.3 \cdot 10^9 p_{oa} \quad (16)$$

where p_{oa} is a mythical pressure which has the units of mm Hg and is defined as 3.5×10^{16} molecules per cubic centimeter for p_{oa} equal to 1 mm Hg. Chown's experimental results indicate that the use of equation (16) does not result in a smooth transition of the breakdown function for various ambient electron densities.

Shkarofsky⁸ has shown the collision frequency for any degree of ionization to be

$$\nu_c = 5.36 \cdot 10^8 \frac{p}{p_o} \tau + 3.63 \frac{N_e}{T^{3/2}} \ln 1.235 \cdot 10^4 \frac{T^{3/2}}{N_e^{1/2}} \quad (17)$$

Where the first term represents the electron-neutral particle collisions and the second term represents the electron-ion particle collisions. The Shkarofsky collision frequency expression is in good agreement with the tabulated data of Shkarofsky, Bachynski and Johnston⁹ and the curves of Langberg, Baldwin and Yos¹⁰.

When the Shkarofsky collision frequency expression is plotted on a modified Mollier diagram, Figure 2, in conjunction with electron densities from Sisco and Fiskin¹¹ a relatively simpler collision frequency expression,

$$\nu_c = 1.2 \cdot 10^{11} P_{ia} / p_0 = 3 P_{ia} / p_0, \quad (18)$$

can be formulated which holds, within a factor, over a wide range of values.

In comparing the collision frequency equations (16) and (18); one must note that equation (16) is expressed in terms of the pressure outside the breakdown region, while equation (18) is expressed in terms of the pressure inside the breakdown region. A problem arises as to which gas parameter, if any, is constant within and without the breakdown region. Assuming that both expressions give valid results through the regions of electron densities where most experiments have taken place, the equations may be compared by assuming either (a) constant pressure, (b) constant particle density or (c) constant air density within and without the breakdown region. The enthalpy, entropy and temperature are obviously not the same within and without the breakdown region.

Assuming constant pressure throughout, i.e.

$$P_{oa} = P_{ia}, \quad (19)$$

then (16) and (18) are different by a factor of 33.6.

Assuming constant particle density throughout, i.e.

$$N_{Mia} = N_{Moa}, \quad (20)$$

together with the defining relationships of

$$N_M = Z (P/p_0) L_0 \quad (21)$$

and

$$P/p_0 = Z (P/p_0) (T/T_0) \quad (22)$$

then (18) reduces to

$$\nu_c = 0.58 \cdot 10^6 P_{oa} T_{ia}, \quad (23)$$

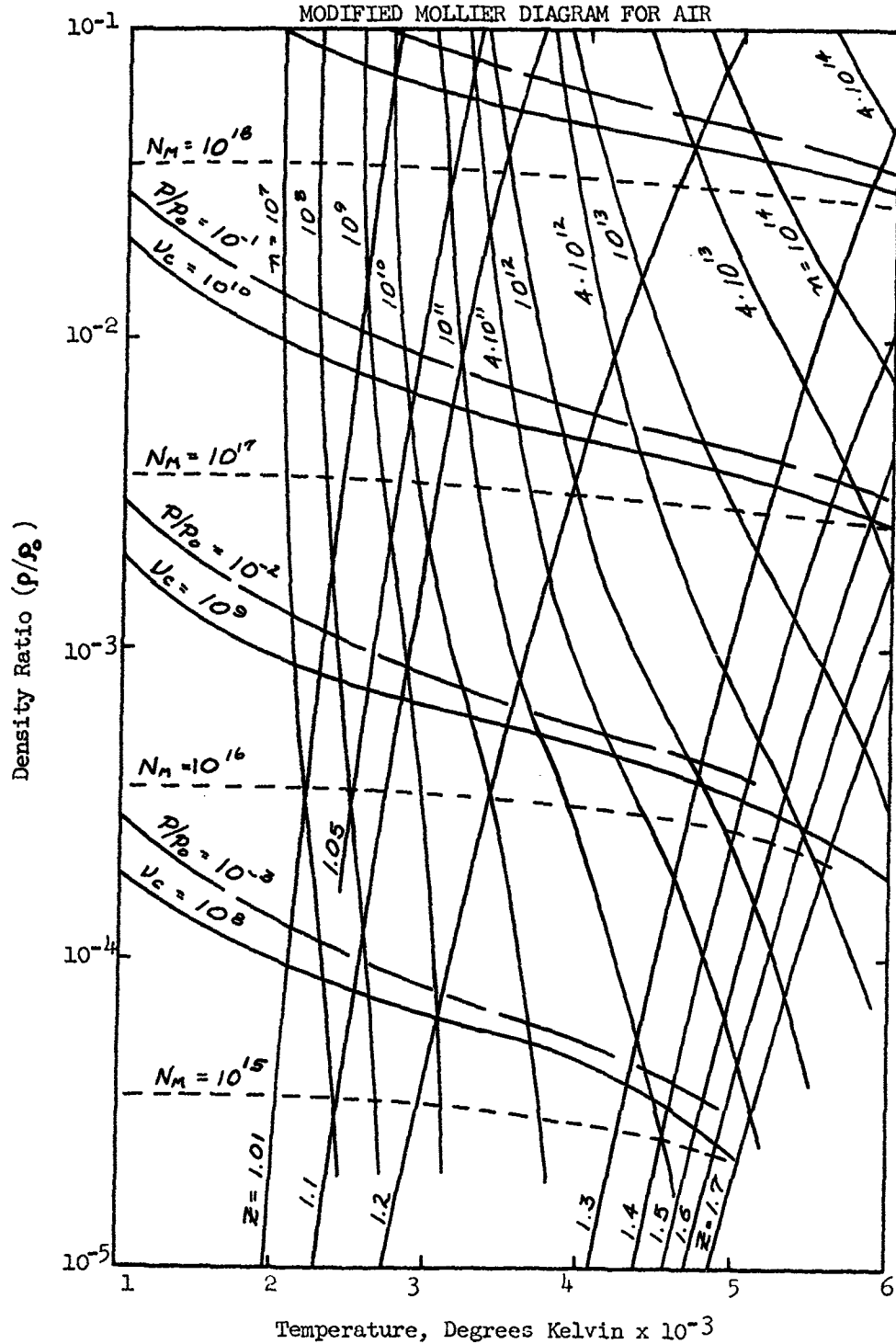
as $T_{oa} = T_0$ and $Z_{oa} = 1$.

For the gas domain about X-band breakdown, i.e. $n = 10^{12}$, from Figure 2

$$T \approx 4 \cdot 10^3, \quad Z_{ia} > 1 \quad (24)$$

FIGURE 2

MODIFIED MOLLIER DIAGRAM FOR AIR



then (23) agrees with (16) to within a factor of 2.29.

Assuming constant density throughout, i.e.

$$\rho_{o2} = \rho_{i2} , \quad (25)$$

then (18) reduces to

$$\nu_c = 0.58 \cdot 10^6 Z_{i2} \rho_{o2} T_{i2} . \quad (26)$$

Equation (26) agrees with (16) to within a factor of $2.29/Z_{i2}$.

Thus expressions (16) and (18) are in the best agreement if the densities within and without the breakdown region are assumed equal.

2.3 The Specific Breakdown Expression. - Combining the basic defining relationships of

$$\nu_c = \omega / L \quad (27)$$

$$L = 1 / N_M \sigma_E \quad (28)$$

and

$$\sigma_E = \mathcal{S} \omega \quad (29)$$

the collision frequency may be expressed as

$$\nu_c = \omega^2 \mathcal{S} N_M . \quad (30)$$

From (21) then

$$\nu_c = \omega^2 \mathcal{S} Z \frac{\rho}{\rho_0} L_0 . \quad (31)$$

Taking the velocity distribution as Maxwellian, i.e.

$$\omega = (8kT/\pi m_e)^{1/2} = \gamma T^{1/2} , \quad (32)$$

equation (31) can be written as

$$\nu_c = \gamma^2 T \mathcal{S} Z \frac{\rho}{\rho_0} L_0 . \quad (33)$$

Combining (33) and (18) and using the defining expression of (22) gives

$$\mathcal{S} = \mathcal{Z} / \gamma^2 L_0 T_0 . \quad (34)$$

The diffusion coefficient from (8) may be written as

$$D = 1/3 N_M \mathcal{S} , \quad (35)$$

using (28) and (30). Substituting from (34) and (21) gives

$$D_f = \gamma^2 T_0 / 3 \zeta (P/P_0) z. \quad (36)$$

The attachment term from (7) together with (18) and (22) is then

$$\nu_a = \psi \zeta z (P/P_0) T/T_0. \quad (37)$$

Substituting from (36) and (37) the breakdown equation (2) may be written as

$$\nu_i = \psi \zeta z (P/P_0) T/T_0 + \gamma^2 T_0 / 3 z \zeta (P/P_0) \Lambda^2 + \frac{1}{z} \ln n_r/n_0 \quad (38)$$

where $\zeta=1$ for free diffusion and $\zeta=40$ for ambipolar diffusion, from (9).

It is convenient at this point to define three domains about the breakdown region by subscripts. The domain removed from the breakdown region will be described by subscript 1. This is the free space region for the given altitude. The domain in the region of breakdown before breakdown takes place will be defined by subscript 2. Region 2 may or may not be separated from region 1 by a shock front. The domain within the region of breakdown will be defined by subscript 3.

For the simple case of no ambient ionization, i.e. for the case of free diffusion, (38) reduces to

$$\nu_i = 1.76 \cdot 10^3 z T_3 (P_1/P_0) + 2.94 \cdot 10^2 / z_3 (P_1/P_0) \Lambda^2 + \frac{1}{z} \ln n_r/n_0. \quad (39)$$

For the case of ambipolar diffusion (38) reduces to

$$\nu_i = 1.76 \cdot 10^3 z_3 T_3 (P_2/P_0) + 7.35 / z_3 (P_2/P_0) \Lambda^2 + \frac{1}{z} \ln n_r/n_0. \quad (40)$$

The net ionization is normalized for the correlation with effective electric field intensity. The normalization is in terms of a "pressure" in that region where the ionization will take place. One restriction in the development of this correlation is that the "pressure" is really a particle density for reference temperature conditions. For the case of no ambient ionization, region 1 is the same as region 2; and within the restrictions of the analysis in Paragraph 2.2, the density in region 3 may be considered the same as that of region 1 thus the "pressure" normalization is that pressure for that density ratio at reference temperature conditions. For the case of ambient ionization with no shock between regions 1 and 2, within the restrictions of

Paragraph 2.2, all the densities may be considered the same, and the "pressure" normalization is that pressure at reference temperature conditions for that gas density in question. For the case of ambient ionization with a shock between regions 1 and 2, the densities of 1 and 2 are different and the "pressure" normalization is that pressure for density ratio of region 2 at reference temperature conditions.

Note that the use of this mythical pressure for the normalization of the net ionization results in a normalization in terms of particle densities.

An alternate breakdown expression may be formulated by considering S constant and the velocities non-Maxwellian. Such a development affects only the diffusion coefficient, and then by a factor of only 1.6. Attachment is the predominant factor at high pressures and the rate term is the predominant factor at intermediate pressures for pulse systems, thus whichever assumption may be considered more correct the area of its importance is generally restricted in "real" systems. The consideration of a Maxwellian velocity distribution results in the most pessimistic analysis from a systems viewpoint.

3. APPLICATION TO TYPICAL MISSILE ANTENNAS

Two examples of typical missile transmission links will be analyzed; a continuous wave system at VHF, and a pulsed system at X-band. The antennas will be assumed to be slots or variations of slots, with a dielectric constant of 5.

The procedure is to (a) determine the density ratios for the pressures or altitudes in question from standard atmospheric tables; (b) determine the electron density required for cut-off for the operating frequency from equation (4); (c) determine for each pressure in question the collision frequency, compressibility factor and temperature for the electron density in question from Figure 2; (d) determine the net ionization rate by equation (39) or (40) and then the effective electric field from Figure 1; (e) convert the effective field to the actual electric field by equation (5); and finally (f) compute the antenna power from equation (6).

Figures 3 through 6 show the terms of the breakdown equation and the resulting breakdown characteristics for the two systems. The antenna configurations were assumed to be a 1.5" x 5.75" slot for the VHF and a 0.4" x 0.9" open ended waveguide for the X-band.

An interesting characteristic of a graph of the terms of the breakdown equation is (1) that each term appears to be a straight line over the area investigated and (2) it is readily apparent which loss terms are of prime importance throughout the various pressure domains.

In the CW case the initiation of breakdown is controlled by free diffusion, and once breakdown has been established the level required to sustain the breakdown is controlled by ambipolar diffusion.

In a pulsed system, for the condition of the ambient electron density equal to that required for breakdown, the breakdown function is the same as for a CW system.

In the figures, the pressure noted by the abscissa is that pressure in region 1 for zero ambient ionization. This pressure in region 1 is the same mythical pressure as that in region 2 when no shock front separates regions 1 and 2. When this shock front is present the pressures noted correspond to the mythical pressures of region 2.

FIGURE 3
THE TERMS OF THE VHF BREAKDOWN EQUATION

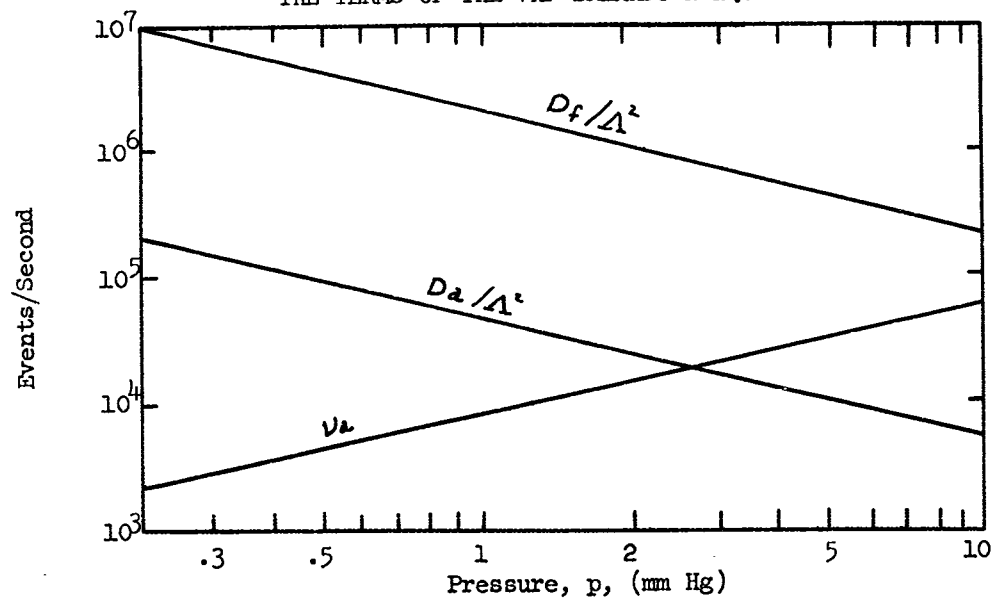


FIGURE 4
THE VHF BREAKDOWN FUNCTION

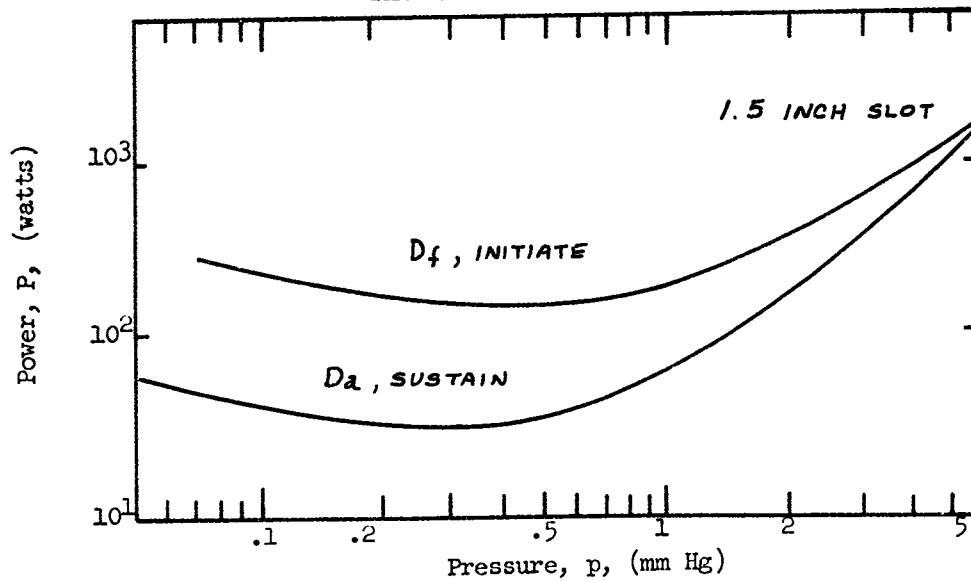


FIGURE 5

THE TERMS OF THE X BAND BREAKDOWN EQUATION

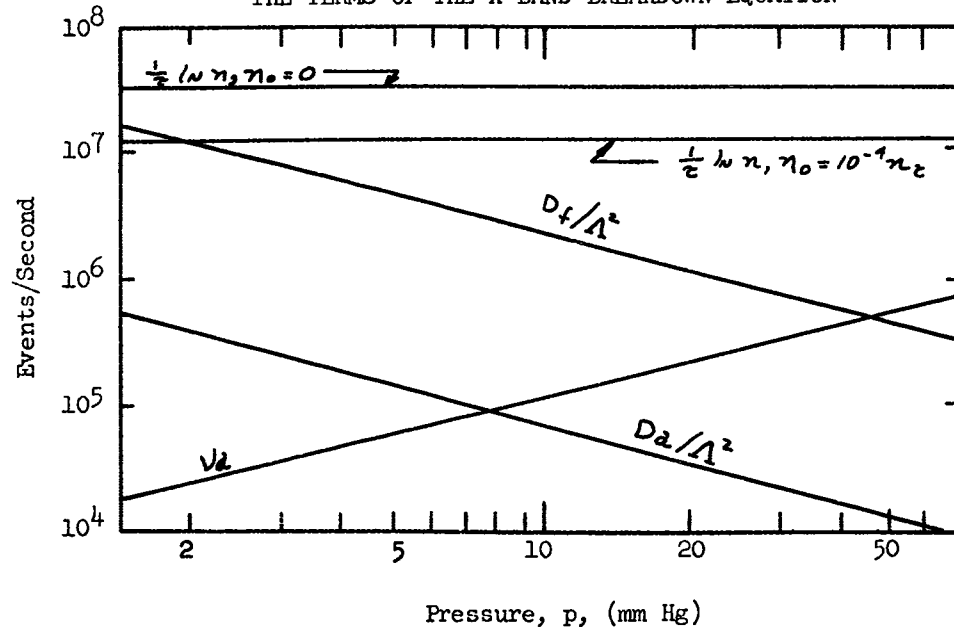
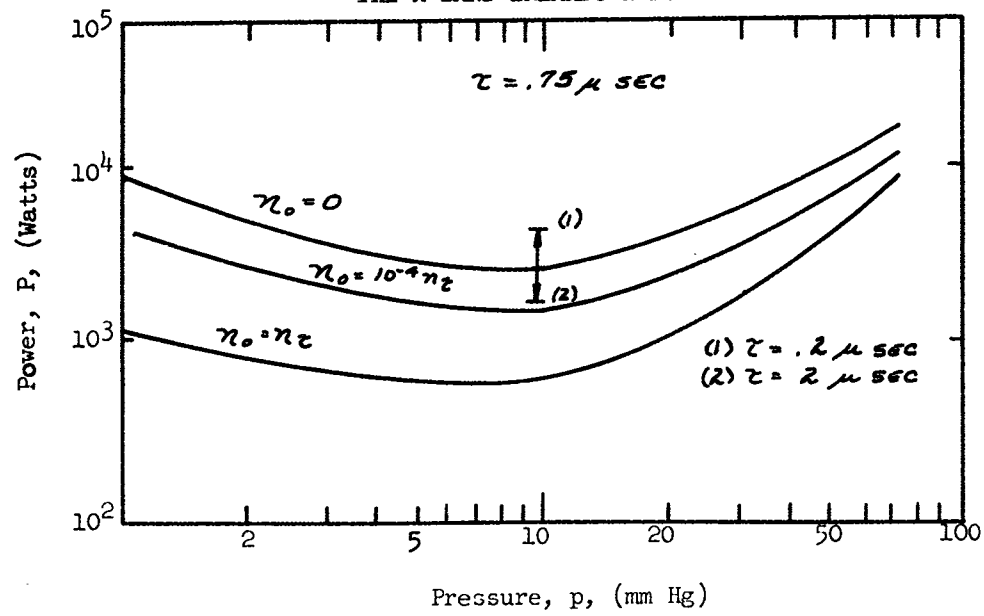


FIGURE 6

THE X BAND BREAKDOWN FUNCTION



4. CONCLUSIONS

The application of the energy dependence of the collision frequency term to the diffusion controlled voltage breakdown expression has been shown. It has been shown that the utilization of such an expression results in the uniform reduction of the power required for breakdown as the ambient ionization level is increased.

Two areas which require further investigation to confirm and expand this theory are the verification of the net ionization - effective electric field intensity correlation, and the degree of variation of the diffusion length with various dielectrics in the vicinity of the ionization. The first of these problems involves a determination of the breakdown power levels for each of the domains of ionization loss, attachment and diffusion, when considering an energy dependent collision frequency expression. The second problem requires the correlation of ionization intensity in the presence of a dielectric. Sufficient data would permit the diffusion length-dielectric constant function to be defined and an adequate theory formulated.

LIST OF SYMBOLS

A	area in cm^2
c	velocity of light in cm per second
D	diffusion coefficient
D_a	ambipolar diffusion coefficient
D_f	free diffusion coefficient
d	separation in cm
E	electric field intensity in volts per cm
E_e	effective electric field intensity
E_p	peak electric field intensity
e	electron charge in e.s.u.
k	Boltzman's constant in ergs per degree Kelvin
L_0	Loschmidt number in molecules per atmosphere cm^3
l	electron mean free path in cm
m_e	electron rest mass in grams
N_M	number of particles per cm^3
n	electron density in electrons per cm^3
n_L	electron density lost
n_0	initial electron density
n_r	electron density corresponding to the operating frequency
P	power in watts
p_c	probability in collision
p	pressure in mm Hg
g	factor relating Λ and d
T	temperature in degrees Kelvin
t	time in seconds

LIST OF SYMBOLS (CONT.)

t_a	time for attachment
v	velocity in cm per second
z	compressibility factor of air
γ	factor relating v and T
ϵ	dielectric constant
ξ	factor relating v_c and ρ
Λ	diffusion length in cm
λ	wavelength in cm
ν	total ionization rate
ν_a	attachment rate
ν_c	collision frequency
ν_i	net ionization rate
ξ	factor relating ξ and v
ρ	density
σ_e	effective collision cross section in cm^2
τ	pulse length in sec
ψ	factor relating ν_a and ν_c
ω	operating frequency in radians per second
ω_p	plasma frequency

Subscripts

o	reference conditions
ia	inside the breakdown region
oa	outside the breakdown region
1	the region removed from the breakdown region
2	in the region of breakdown before breakdown occurs
3	in the breakdown region
f	correction factor

REFERENCES

- (1) Sanborn C. Brown, "High Frequency Gas-Discharge Breakdown", Proc. of I.R.E., Vol. 39, No. 12, p 1493, December 1951.
- (2) J. B. Chown, "Study of Plasma-Induced Voltage-Breakdown at Low Pressure", S.R.I. Project No. 3369, July 1961.
- (3) J. D. Cobine, "Gaseous Conductors", Dover Publications, Inc., N.Y., N.Y., 1941.
- (4) J. Gould and L. W. Robert, "Breakdown of Air at Microwave Frequencies", J. Appl. Phys., Vol. 27, No. 10, October 1956.
- (5) A. D. MacDonald, "High-Frequency Breakdown in Air at High Altitudes", Proc. of I.R.E., Vol. 47, No. 3, March 1959.
- (6) R. F. Whitmer and A. D. MacDonald, "Antenna Breakdown in the Plasma Sheath", Planetary and Space Science, Vol. 6, June 1961.
- (7) W. E. Scharfman and T. Morita, "Power Handling Capability of Antennas", Planetary and Space Science, Vol. 6, June 1961.
- (8) I. P. Shkarofsky, "Generalized Appleton-Hartree Equation for Any Degree of Ionization and Application to the Ionosphere", Proc. of I.R.E., Vol. 49, No. 12, December 1961.
- (9) I. P. Shkarofsky, M. P. Bachynski and T. W. Johnston, "Collision Frequency Associated with High Temperature Air and Scattering Cross-Sections of the Constituents", Planetary and Space Science, Vol. 6, June 1961.
- (10) E. Langberg, K. Baldwin, J. Yos, "Radiation and Propagation of Telemetry Signals During Hypersonic Re-Entry", Proc. of 1958 Sym. on Telemetry, September 1958.
- (11) W. B. Sisco and J. M. Fiskin, "Basic Hypersonic Data of Equilibrium Air for Electromagnetic and Other Requirements", Planetary and Space Science, Vol. 6, June 1961.

RADCOM

A DIVISION OF THE SYSTEMS
GROUP OF LITTON INDUSTRIES



C-BAND BEACON ANTENNAS

FOR

PROJECT APOLLO

By

W. O. Puro

F. X. Linder

Presented at

The Thirteenth Annual Symposium on
USAF Antenna Research and Development
Monticello Facility, University of Illinois
15-18 October 1963

5009 CALVERT ROAD
COLLEGE PARK, MARYLAND

C-BAND BEACON ANTENNAS FOR PROJECT APOLLO

As presently contemplated, the Apollo three-man spacecraft will go through several flight phases in the moon voyage. These are launch, abort (if launch into orbit is not successful), earth orbit, travel to vicinity of the moon, moon orbit, return to vicinity of earth, reentry into earth's atmosphere, and landing. Present plans are to launch the command module in which the astronauts are located, the service module and the lunar excursion module into earth orbit and subsequent travel to the moon and moon orbit. The service module will be discarded during the moon-to-earth phase of the mission, while the command module alone returns to earth.

Antenna requirements for the Apollo manned spacecraft include the C-band beacon antennas for radar tracking. The C-band beacon antennas will be operable during all near earth phases and up to 4,000 nautical miles. Therefore, the C-band beacon antennas must withstand all the environmental conditions that the command module itself is exposed to. Further, not only must the antennas operate electrically in a reliable manner, but, since the antennas pass through the vehicle's outer structure, including the heat shield, they must be designed to withstand the extremely high temperatures that the heat shield, itself, will be subjected to.

A brief statement of the electrical requirements for each of the antennas is as follows:

- (1) VSWR: 1.5 or less
- (2) Power Handling Capability: 3 kw peak and 3 watt average

- (3) Circular Polarization
- (4) Pattern Coverage such that 4 antennas will approximate spherical coverage.
- (5) Frequency: 5600-5800 mcs

The environmental conditions for the pre-launch phase are those normally associated with missiles which must withstand the seaside atmosphere of the launch site for an indefinite period. The normal conditions during launch are not particularly severe, except if an abort is required, under which condition the abort rocket engines will cause rather high heating rates to be incurred by the command module. The earth orbit and the travel to the moon and back impose the requirements of radiation and operation in extreme vacuum environments for long periods of time. The most severe environment that the antennas must perform in is, of course, the reentry into the earth's atmosphere. The temperatures expected during this phase are such that nearly two inches of ablative heat shield material will surround the capsule in the most vulnerable area.

Several design approaches were originally considered for this antenna application. One approach would be to place the antenna aperture beneath the surface of the ablative heat shield so that it would be protected from the reentry heating. This approach must be discarded because the heat shield material chars when heated and becomes very lossy for microwave frequencies. A second approach would be to design an antenna having a window incorporated into the heat shield with the window made of an ablative material which would

not char. Such materials commonly used are mixtures of teflon with other materials, usually quartz fibers or powdered quartz. However, the heat rates expected for the Apollo are such that the ablation of teflon mixtures would be at a very high rate and probably would be high enough so that no material would remain to protect the interior of the antenna after reentry. Furthermore, the heat shield material is designed to retain its physical dimensions even after charring so that, if an ablative window which decreased in thickness due to ablation were incorporated, a discontinuity in the vehicle surface would cause extremely high localized heating by such discontinuity. A second problem arising from use of an ablative window in this application is the difficulty in retaining a satisfactory impedance match with varying thicknesses of window material.

The approach decided upon by RADCOM for this application resolved itself around these requirements.

(1) The C-band energy must be conveyed to the outer surface of the ablative heat shield through a dielectric having low loss tangents over a temperature range of -250°F to $+3,000^{\circ}\text{F}$.

(2) Even under the most severe heating encountered by the capsule, the temperature of the coaxial connector at the inner surface of the antenna must remain below 300°F . Therefore, the dielectric must have a low coefficient of thermal conductivity.

(3) The window material must not ablate when exposed to the reentry environment or if it does ablate slightly must absorb a large amount of heat

in doing so in order to retain the rest of the antenna at a reasonable temperature.

Figure 1 shows the cross section through the antenna which was designed for this application. The only dielectric material known to satisfy all the requirements of this application is fused quartz. Since ordinary fused quartz is transparent to radiant energy in the frequency range created by the plasma during the reentry phase, it is necessary to use an opaque quartz. This is available in a slip cast form from Corning Glass Company. The radiator uses the same basic design as has been proved to be extremely successful in the Gemini Program. This design employs a helix radiator effectively imbedded within the quartz dielectric. The helix is actually wound around a smaller diameter quartz cylinder which is then fitted into a blind hole, ground into the aft face of the main body of the radiator. Since the helix is separated from the high temperature external atmosphere by a considerable thickness of quartz having a low thermal conductivity, the helix material can be ordinary copper or beryllium copper. The helix dimensions are adjusted to provide a 50 ohm impedance to match the input TNC connector.

It is important, of course, to avoid any high conductivity thermal paths from the exterior of the vehicle inward; therefore, the RF cavity surfaces surrounding the quartz are formed with a very thin plating of nickel. This plating extends the full length of the window and also provides the electrical connection between the connector assembly and the window assembly. Since the metal skin is only a few thousandths of an inch thick, it provides no

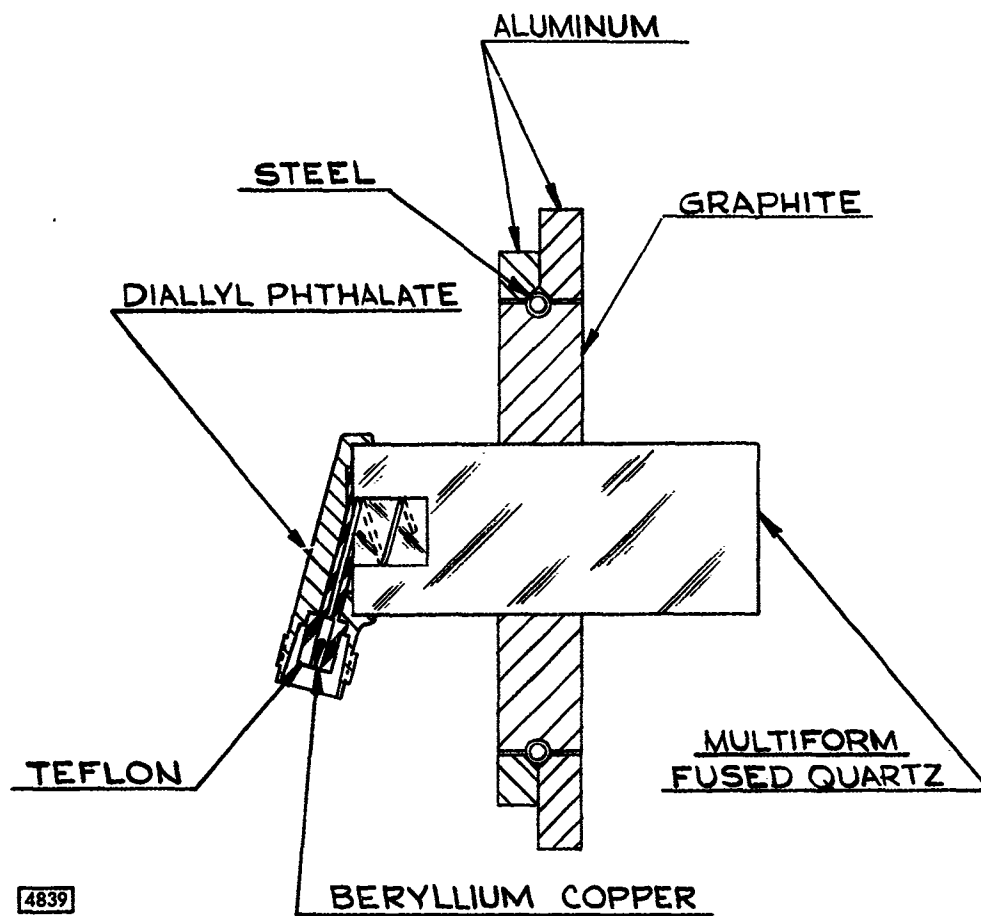


Figure 1. Cross Section of Proposed Apollo Antenna

mechanical support. Therefore, the quartz window is also the antenna structure.

Preliminary thermal calculations indicated that with the heating rates expected to be encountered, sufficient heat would be transferred through the quartz to raise the temperature of the connector far above the 300^oF specified. Therefore, the design includes a heat sink surrounding the quartz window at the interface between the vehicle heat shield and the basic honeycomb structure. The design of this heat sink has posed some of the most difficult problems in the antenna design because of the difference in thermal coefficient of expansion between the quartz and any metallic flange.

Referring again to Figure 1, a design incorporating the split flange of graphite held in place with an outer ring of aluminum has been developed. Spring tension between the mounting ring and the graphite sections is used to hold the graphite in intimate contact with the quartz window. By releasing the spring tension the flange assembly may be positioned on the quartz to any desired location for use on vehicle sections having various thicknesses of ablative heat shield material.

The antenna design described has been tested and satisfies electrical performance requirements. Theoretical calculations indicate that it will meet the thermal conditions specified. A comprehensive environmental test program including tests which simulate the heat input during reentry is currently underway.

This work was performed under subcontract to North American Aviation, Space and Information Systems Division

UHF CROSSED-SLOT ANTENNA AND APPLICATIONS

September 1963

W. L. Snow

Advance RF Systems Group

MARTIN COMPANY
Denver, Colorado
Aerospace Division of Martin-Marietta Corporation

UHF CROSSED-SLOT ANTENNA AND APPLICATIONS

Printed circuit methods are used to develop a circularly polarized, crossed-slot antenna whose radome contains all necessary elements. A hybrid junction of balanced strip-line is built into the radome and connected to two microstrip, dual probe feeds. Each dual probe excites one of the two slots and isolates the slots from each other by the symmetrical probe location. Right- or left-hand circular polarization can be obtained by connecting to the respective hybrid junction input port. Pattern beamwidths with regard to circular and linear polarization is 130 degrees and 160 degrees, respectively. The operating bandwidth for a VSWR maximum of 2:1 is approximately 44 percent. The operating bandwidth, limited by a 50 percent efficiency and 2.5 db axial ratio, is approximately 16.8 percent. The dimensions of a 415 MC antenna are 12-3/8 by 12-7/8 inches by 7 inches deep, including mounting flanges. The crossed-slot antenna was developed to provide a quasi omidirectional antenna system composed of two antennas on opposite sides of a cylindrical vehicle. The directivity for the two antenna system is 2.20db, with respect to circular polarization, and provides a -9.0 db directive gain over 95 percent of the sphere of coverage. It has been shown that, due to the fact that the two antennas have only minor pattern overlap, an increase in vehicle diameter has very little affect on the coverage.

Introduction

The crossed-slot antenna, operating in a circular polarized mode, provides a very broad beamwidth to both circularly and linearly polarized transmitting antennas. Circular polarization is particularly desirable for space vehicle applications to prevent cross-polarization with ground antennas. Very few flush mounted, circularly polarized VHF and UHF antennas are available. A brief comparison of two of these, the cavity backed crossed-slot and Archimedian spiral (printed circuit spiral), shows the crossed-slot is more efficient and provides a broader beamwidth. The spiral, however, has a greater operating bandwidth. These antennas are approximately the same size and weight.

This paper discusses an UHF, crossed-slot antenna design consisting of a printed-circuit, laminated antenna cover mounted on a square cavity. The antenna cover contains a four port hybrid junction of balanced stripline with two output ports each connected to a microstrip, dual-probe feed. Each dual probe excites one of the slots. A summary of the electrical characteristics for a 415 MC antenna shows the operating bandwidth to be approximately 16.8 percent. The 415 MC antenna size is 12-3/8 inches by 12-7/8 inches by 7.0 inches deep including mounting flanges and weighs 6 lbs. A photograph of the 415 MC antenna is shown in Figure 1.

This crossed-slot antenna was developed to provide a nearly omnidirectional pattern with two antennas. Two crossed-slot

antennas on opposite sides of a cylinder permit a minimum of interference between the individual antenna patterns. The system directivity is, therefore, affected very little by a change in vehicle diameter.

Theory

A compact method of construction was incorporated which included stripline and microstrip printed-circuit elements for the feed system and slot radiator. The antenna cover consists of four teflon fiberglass sheets (see Figures 2 and 3). A blank sheet is used as a protective cover on the upper and lower sides of the unit. The two center sheets contain printed-circuit elements and the crossed-slot is printed on the back side of one of these sheets and positioned between them. One port of the hybrid feed circuit is coupled through the two center sheets to the lower printed-circuit elements. All four sheets are bonded into a solid unit which mounts on a cavity which is one-quarter wave length deep at the center frequency. Circular polarization is obtained by individually feeding the two planar, bisecting, quadrature slots, one slot being fed 90 electrical degrees out of phase with respect to the other. The 90 degree phase shift is introduced by a one-quarter wavelength section of strip-line added to one leg of the feed system. A calculation of the bandwidth, limited by a maximum axial ratio degradation of 2.0 db due to phase shift error with frequency, is ± 14.6 percent. This bandwidth is more than adequate to meet the requirements.

Any cross coupling between slot radiators or power division error between slot feeds will result in a deterioration of the axial ratio. A dual-probe feed assembly was designed from microstrip transmission line to excite each slot individually and isolate one slot from the other by a cancellation of fields due to the symmetrical location of the probes. Isolation of the slots is obvious in Figure 3 and a complete discussion is given in the Reference. An unequal power division also results in a corresponding difference in the axial ratio. For equal slot excitation, a hybrid ring junction is used as a power divider and output isolator. The standard hybrid ring provides a division of 3.1 ± 0.3 db and an isolation between output ports of greater than 20 db over at least a ± 10 percent bandwidth.

Design Considerations

A single unit antenna cover to be placed over a cavity was the original design goal. The printed-circuit design simplifies construction and reduces vibration problems to a minimum. The electrical attachment to the antenna cover is made by two coaxial connectors through the cavity flange to the hybrid feed circuit. Figure 2 shows the cover assembly.

For simplicity, a microstrip transmission line was used for the probe feed design. This dual-probe feed must have a junction point before the output of the hybrid ring. Since the hybrid has a 50-ohm output, the probe feed lines were designed for 100 ohms. To determine the proper feed location, a single

microstrip line was built which fed one side of a single slot and incorporated a one-wavelength taper to match 50 ohms to 100 ohms at the slot. The 100-ohm line crossed over one end of the slot and was terminated in a sliding short circuit. By tuning the short and varying the position of the line over the slot, a minimum VSWR was observed. It was then calculated that an open-circuit, an odd multiple of one-quarter wavelengths toward the slot, would result in a location near the probe. The 100-ohm line was open-circuited at the predetermined point near the slot and this open-circuited stub is used as a tuning element (see Figure 3). This test resulted in an operating bandwidth of approximately 8.5 percent for a VSWR less than 2:1. A flat diamond shaped probe was built at the slot to broadband the feed by reducing the reactance. This test improved the operating bandwidth of a single slot to approximately 10 percent. The probe stub length and position over the slot are not extremely critical but the position of the probes with respect to the center of the crossed slot must be equal to give good isolation between the slots.

Single Antenna Test Results

A 415 MC antenna was constructed to test the efficiency of the crossed-slot antenna. An operating bandwidth of 44 percent for a VSWR of less than 2:1 was obtained (see Figure 4). This broad operating band is due to the hybrid and 90 degree phase shift section. The antenna gain, with respect to a circularly polarized isotropic radiator, is 3.92 db. This gain was compared to a directivity

of 4.4. db for the same antenna to show the efficiency to be 89.6 percent at the center of the band. The usable operating band can only be determined from the limits of efficient operation and polarization degradation. Figure 5 shows the relative gain of the antenna versus frequency and Figure 6 shows the axial ratio across the band. From the curves of Figures 5 and 6 and considering a minimum efficiency of 50 percent and a maximum axial ratio of 2.5 db, the operating band is 65 MC centered at 415 MC or 16.8 percent. The antenna patterns for this antenna with a linearly and circularly polarized transmitting antenna are shown in Figures 7 and 8, respectively. A beamwidth of 160 degrees was obtained with a linearly polarized transmitter and 130 degrees with a circularly polarized transmitter. The axial ratio of the crossed-slot antenna increases from a minimum value normal to the antenna to a large value 90 degrees from the normal.

Antenna System Tests

Two 4070 MC antennas were designed for the two-antenna system tests on cylinders to simulate the space vehicle. Antenna patterns were recorded with these antennas fed 90 degrees out of phase and located on opposite sides of the cylinder whose size gave a ka^1 factor of 13.2. The transmitting antenna for these tests is circularly polarized. This system provided a directivity

$1_{ka} = \frac{2\pi a}{\lambda}$, cylinder circumference in wavelengths, where "a" is the cylinder radius and λ is the wavelength.

of 2.20db. These antenna patterns were again recorded under the same conditions on a cylinder with a ka factor of 66 to determine the change in directivity with a larger cylinder equal to 50 feet diameter for 407 MC. The directivity was increased by 0.12db and indicates very little affect on the patterns by a change in frequency or cylinder diameter for ka values greater than 13. Figures 9 and 10 show respectively the pitch and roll patterns of a two-antenna system on a cylinder with a ka factor of 66. A measure of the uniformity of the radiation pattern of the two-antenna system can be shown by the fact that a directive gain of at least -9.0 db is obtained over 95 percent of the sphere of coverage for a ka factor of 13.2.

Conclusions

A crossed-slot antenna with printed-circuit construction is capable of a 16 percent bandwidth in the circularly polarized mode. Though the VSWR is below 2:1 over a broad bandwidth (44 percent), the operating bandwidth is limited by efficiency and axial ratio degradation. The efficiency over the 16 percent band is 50 percent and the axial ratio is better than 2.5 db. The size of the antenna for a 415 MC band center is 12-3/8 inches by 12-7/8 inches by 7 inches deep and the overall weight of the UHF antenna is 6 pounds.

A broad beamwidth is realized and is dependent upon the associated antenna. A beamwidth of 160 degrees to linear antennas and 130 degrees to a similar circularly polarized antenna is achieved. A near omnidirectional antenna system is obtained with two antennas on opposite sides of a cylinder. With one antenna phased 90 electrical degrees with respect to the other a -9.0 db minimum

directive gain is obtained over 95 percent of the coverage sphere for a ka factor 13.2. Tests show that a change in cylinder diameter, above ka = 13, has little effect on the overall coverage. The directivity with ka = 13.2 is 2.20db and with ka = 66 is 2.32 db.

References

R. C. Payne, P. Painter, "A Flush Mounted VHF Telemetry Antenna with Hemispherical Coverage," Dynatronics Inc., Orlando, Fla., 1960.

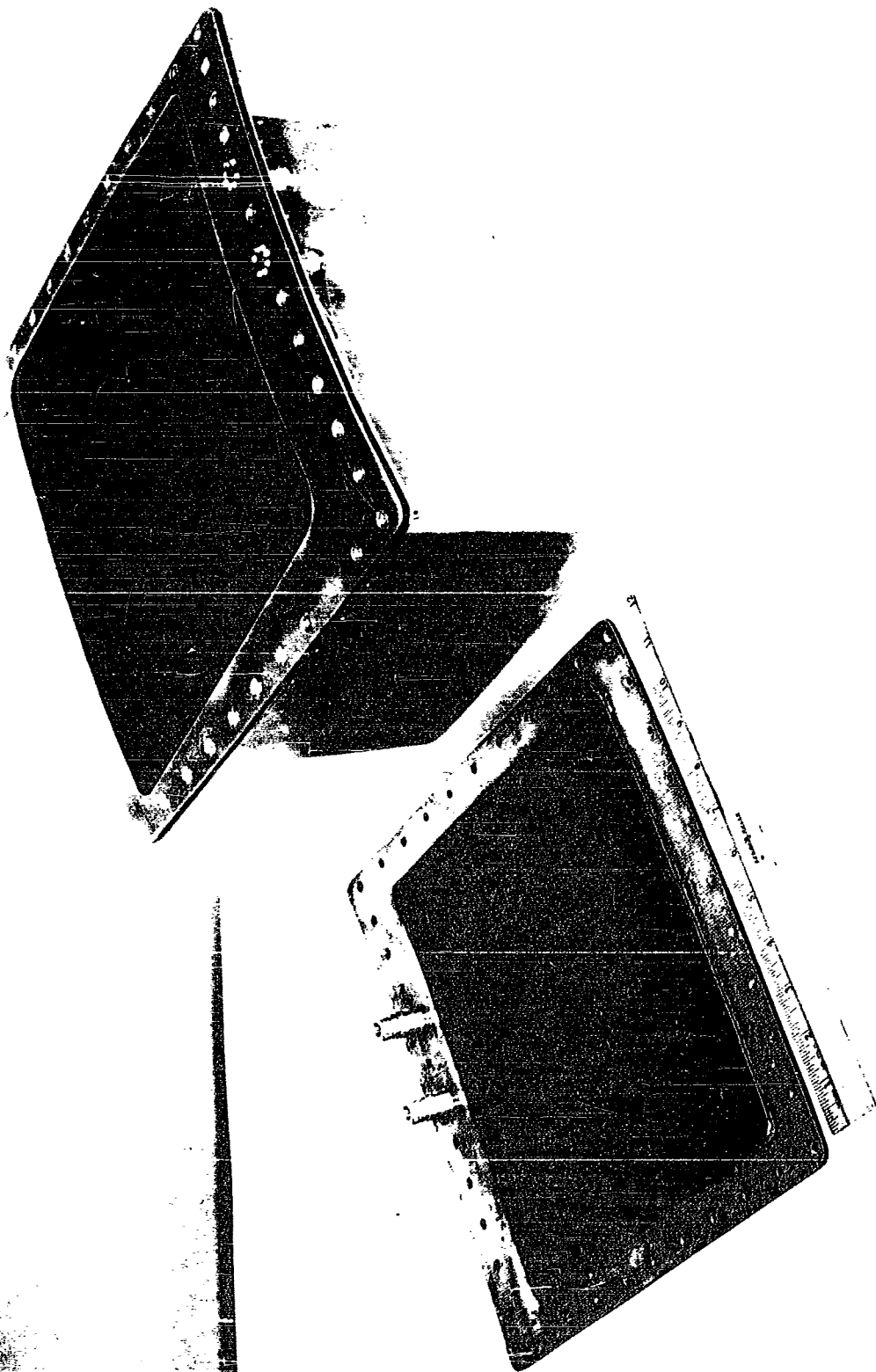
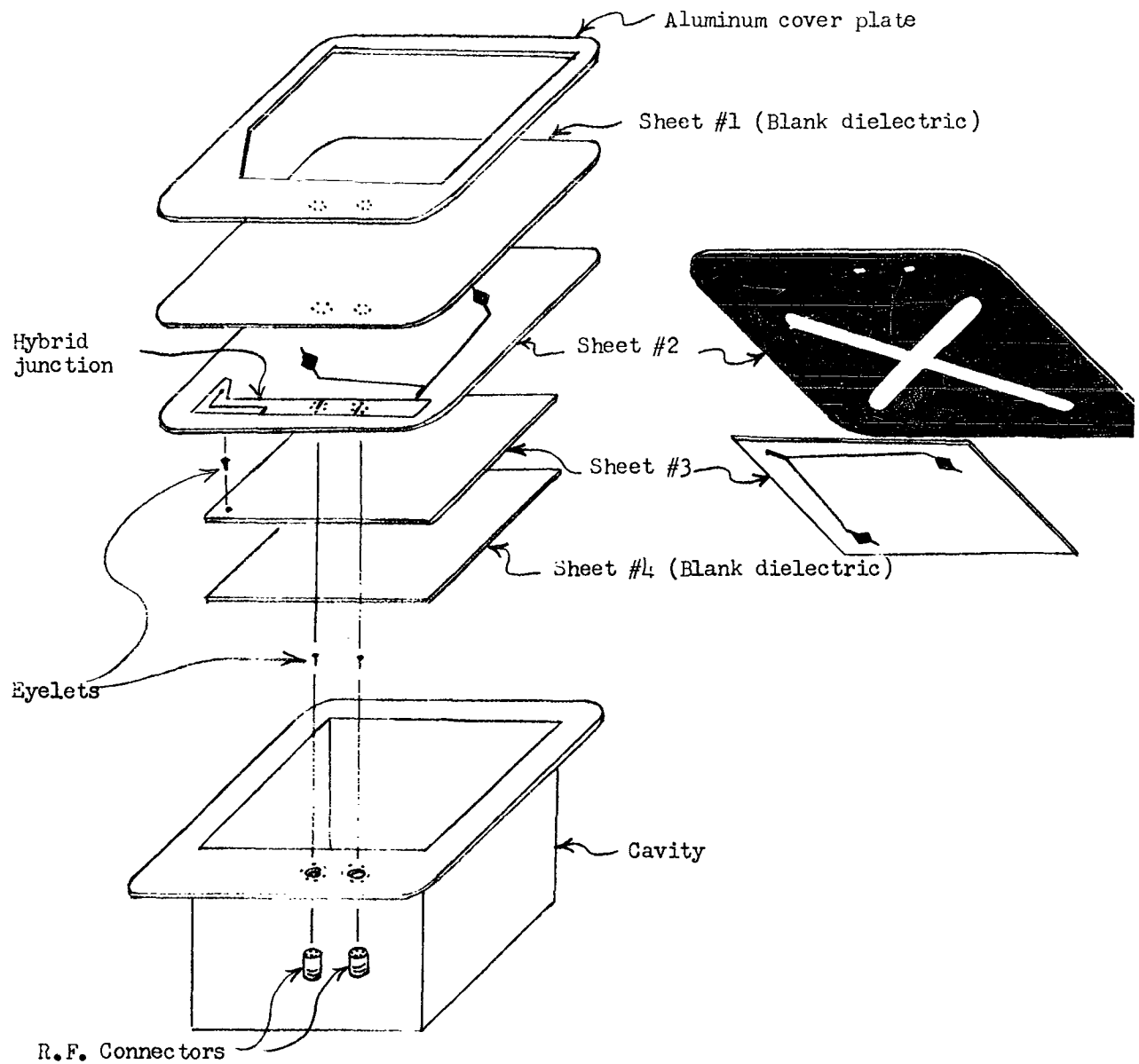


Figure 1 - UHF crossed-slot antenna showing antenna cover and cavity.



Notes : All solid areas are copper material.

The four dielectric sheets and the aluminum cover are bonded together.

Figure 2- Crossed-Slot antenna in exploded view showing antenna cover and cavity

Surface Designation:

- Upper dual probe and hybrid junction (top of upper sheet)
- Crossed-Slot (under side of upper sheet)
- - - - Lower dual probe (under side of lower sheet)

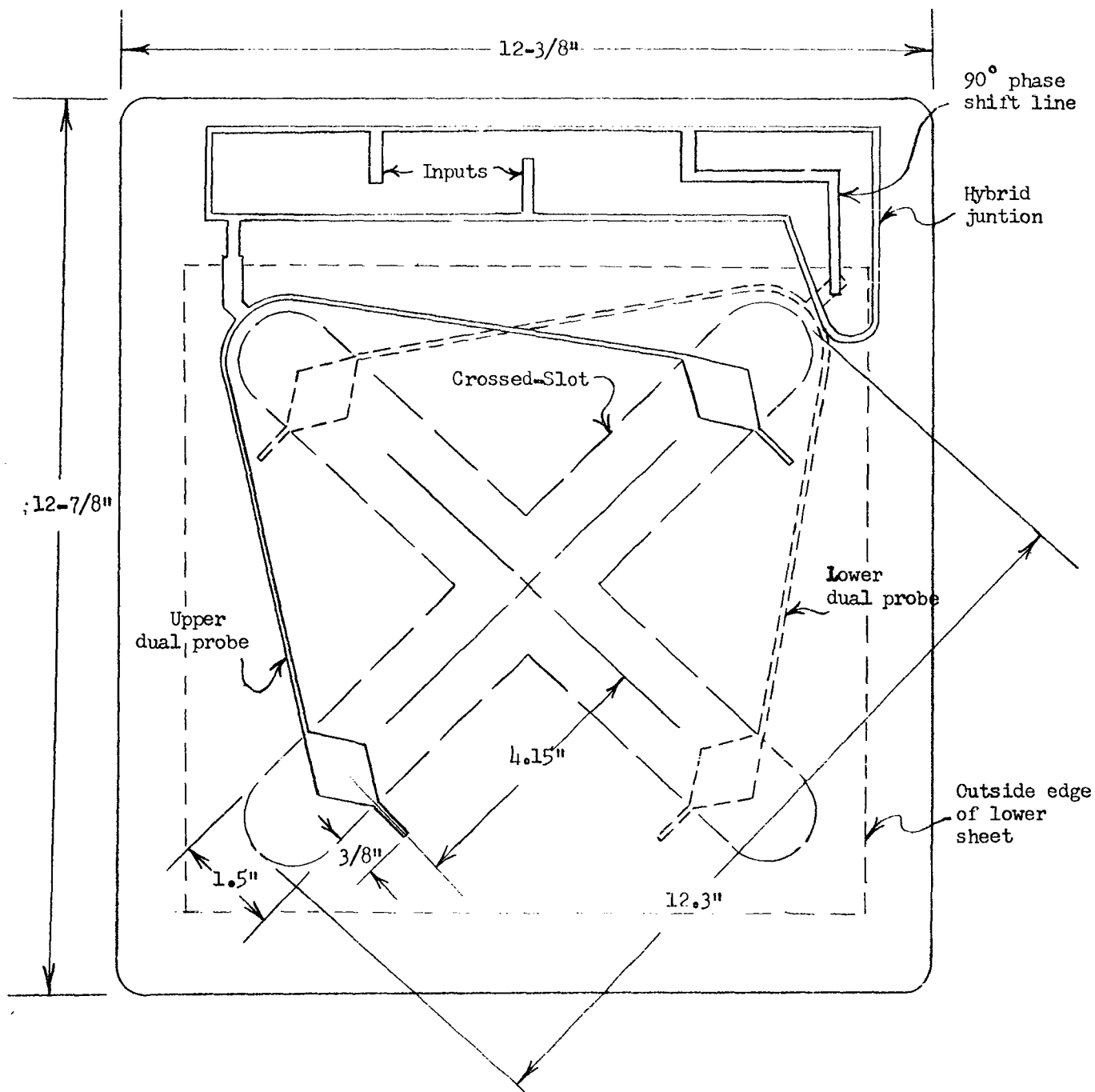


Figure 3- Crossed-Slot antenna cover showing printed-circuit element locations with top and bottom blank dielectric sheets removed.

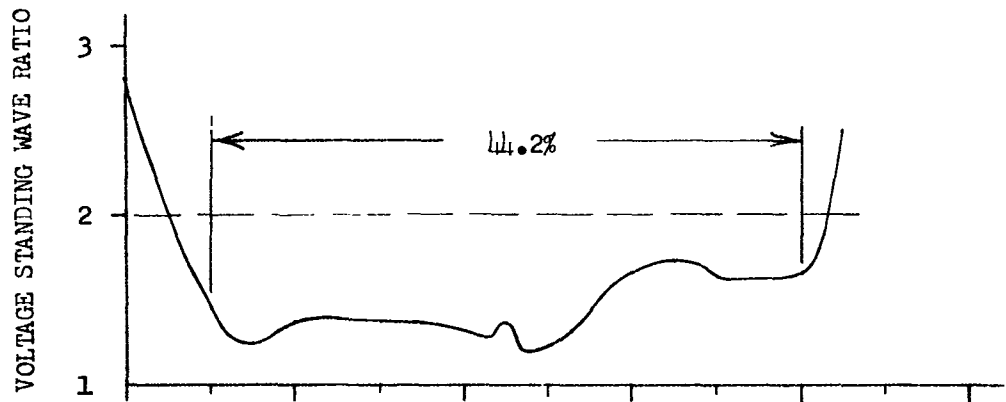


Figure 4 - Crossed-Slot antenna VSWR for left-hand-circular mode (S/N 106)

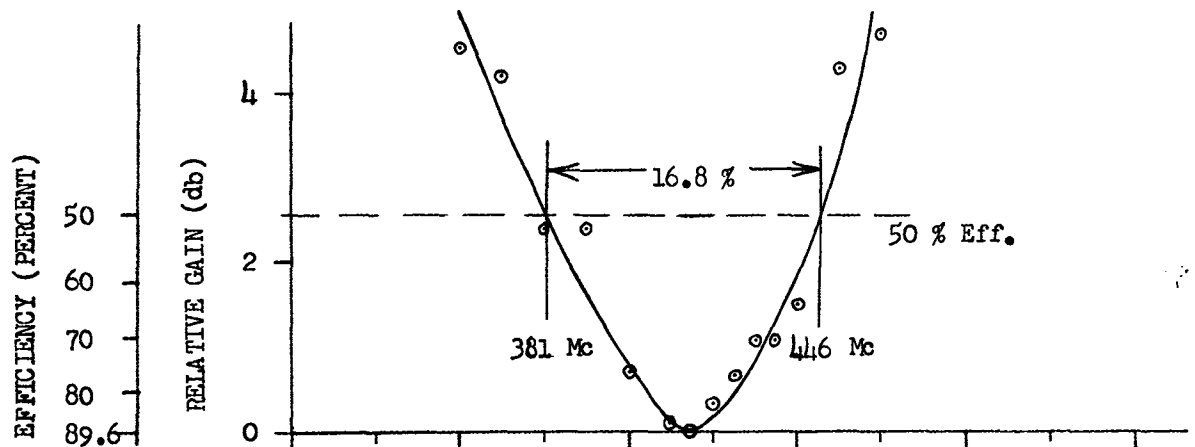


Figure 5 - Crossed-Slot antenna relative gain for left-hand-circular mode (S/N 106)

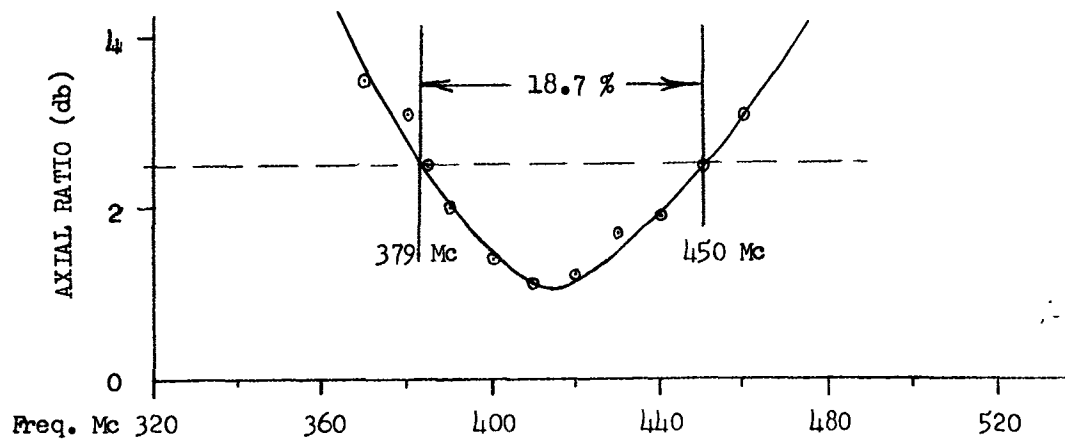
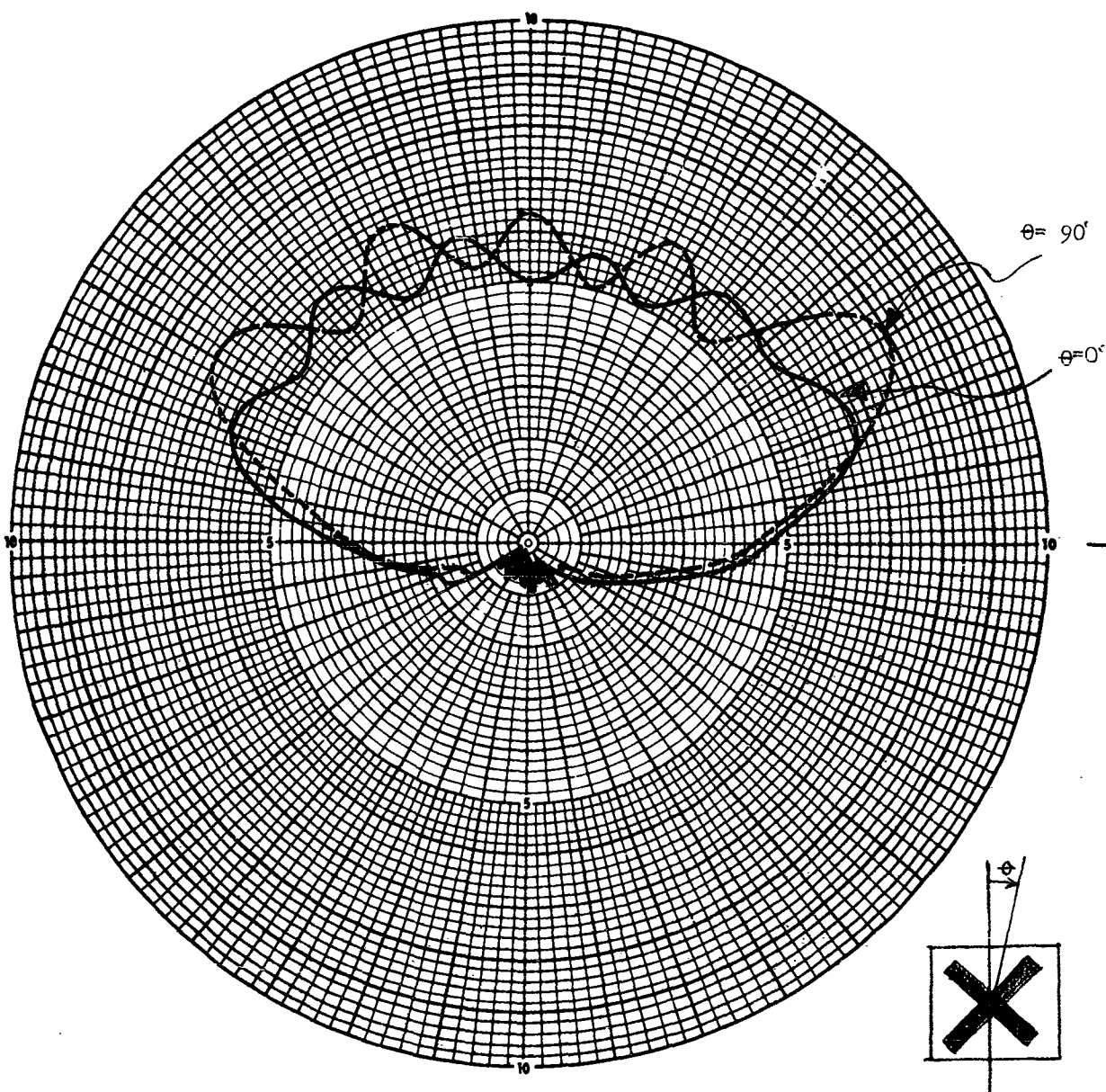


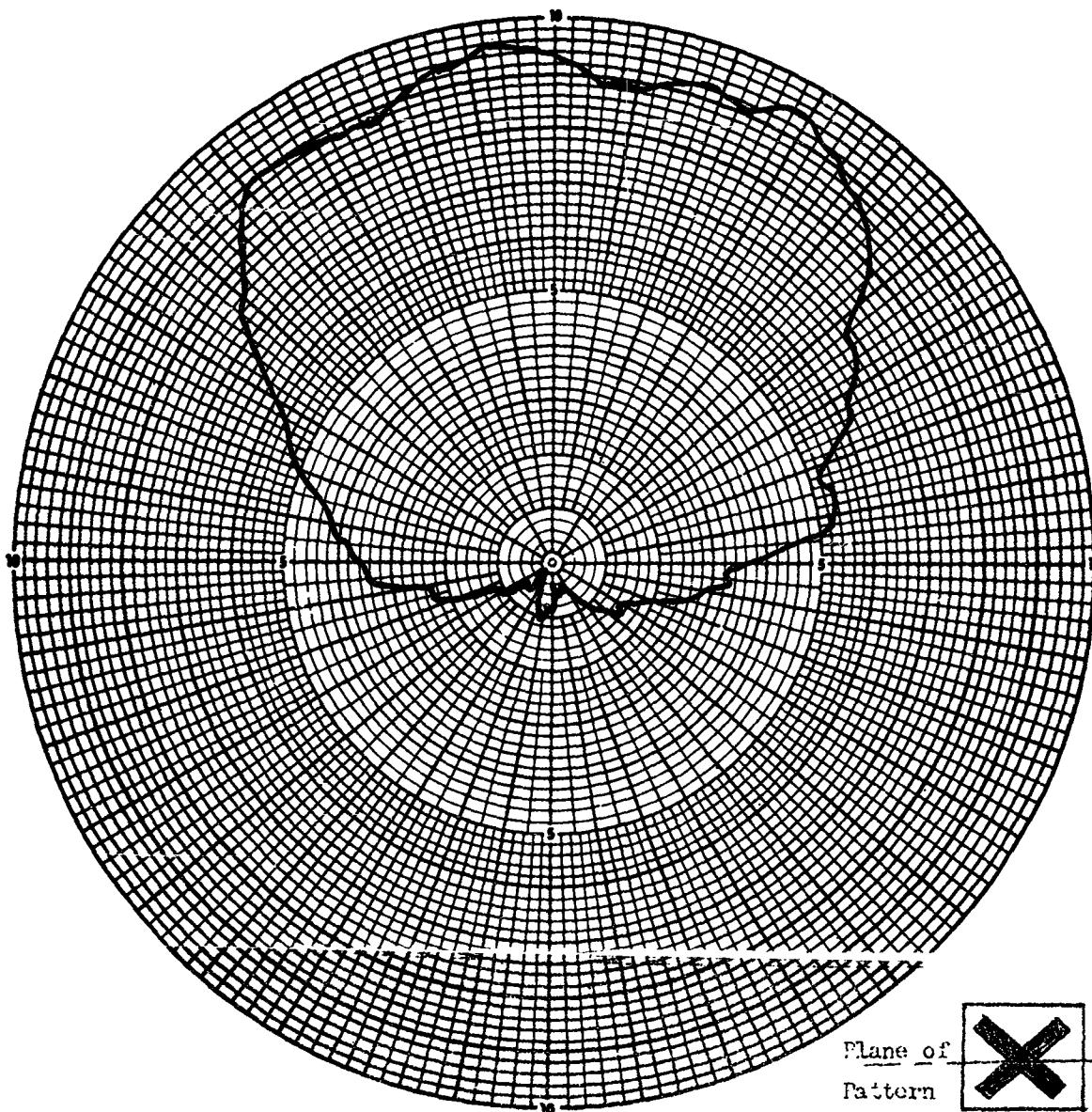
Figure 6 - Crossed-Slot antenna axial ratio for left-hand-circular mode (S/N 106)

Figure 7- Crossed-Slot Antenna Patterns with E_ϕ
Positioned Linear Polarized Transmitting Antenna



ANTENNA TYPE	Crossed Slot	LOCATION	USE
TEST MODEL:	_____	FREQUENCY:	<u>1150</u> MCS
MODEL SCALE:	_____	SCALE FREQUENCY:	_____ MCS
CONDITIONS:	_____	POLARIZATION:	_____
CURVES PLOTTED IN:	_____	E θ :	_____
VOLTAGE <input checked="" type="checkbox"/>	_____	E ϕ :	<input checked="" type="checkbox"/>
POWER _____	_____	PATTERN AREA:	_____
ENGINEER _____	OPERATOR _____	FILE NO. _____	DATE <u>8/2/62</u>

Figure 8 - Crossed-Slot Antenna Patterns with
L- Π Circularly Polarized Transmitting Antenna



ANTENNA TYPE Crossed Slot LOCATION		USE	
TEST MODEL: _____		FREQUENCY: <u>1150</u> MCS	
MODEL SCALE: _____		SCALE FREQUENCY: _____ MCS	
CONDITIONS: _____		POLARIZATION: <u>L-Π CIRCULAR</u>	
CURVES PLOTTED IN: _____		E θ : _____	
VOLTAGE <u>✓</u> _____		E ϕ : _____	
POWER _____		PATTERN AREA: _____	
ENGINEER _____	OPERATOR _____	FILE NO. _____	DATE <u>8/15/62</u>

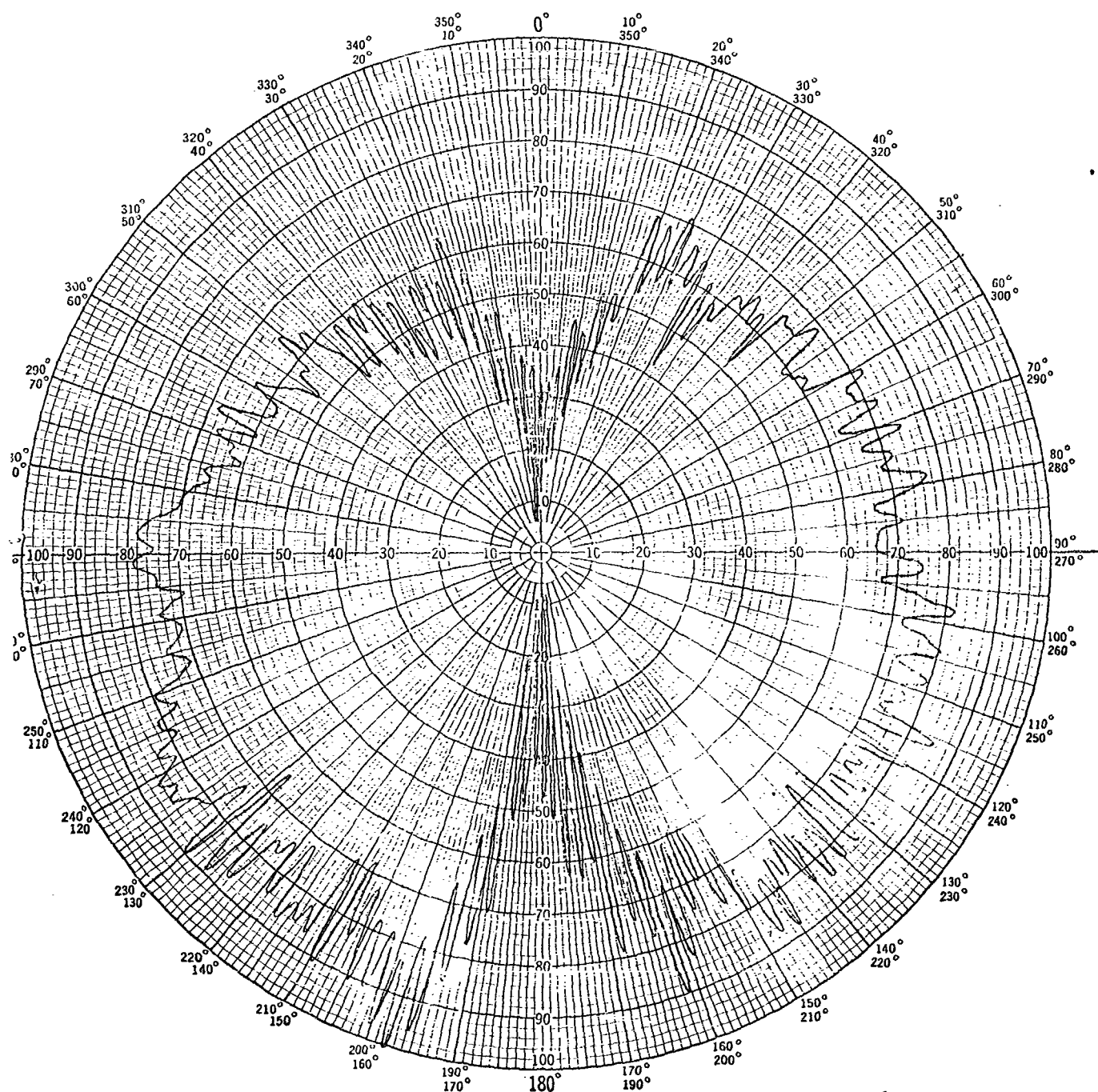


Figure 9- Pitch-plane antenna pattern of two crossed-slot antennas on opposite sides of a cylinder having a ka factor of 66.

Polar Chart No. 127L
SCIENTIFIC ATLANTA, INC.
ATLANTA, GEORGIA

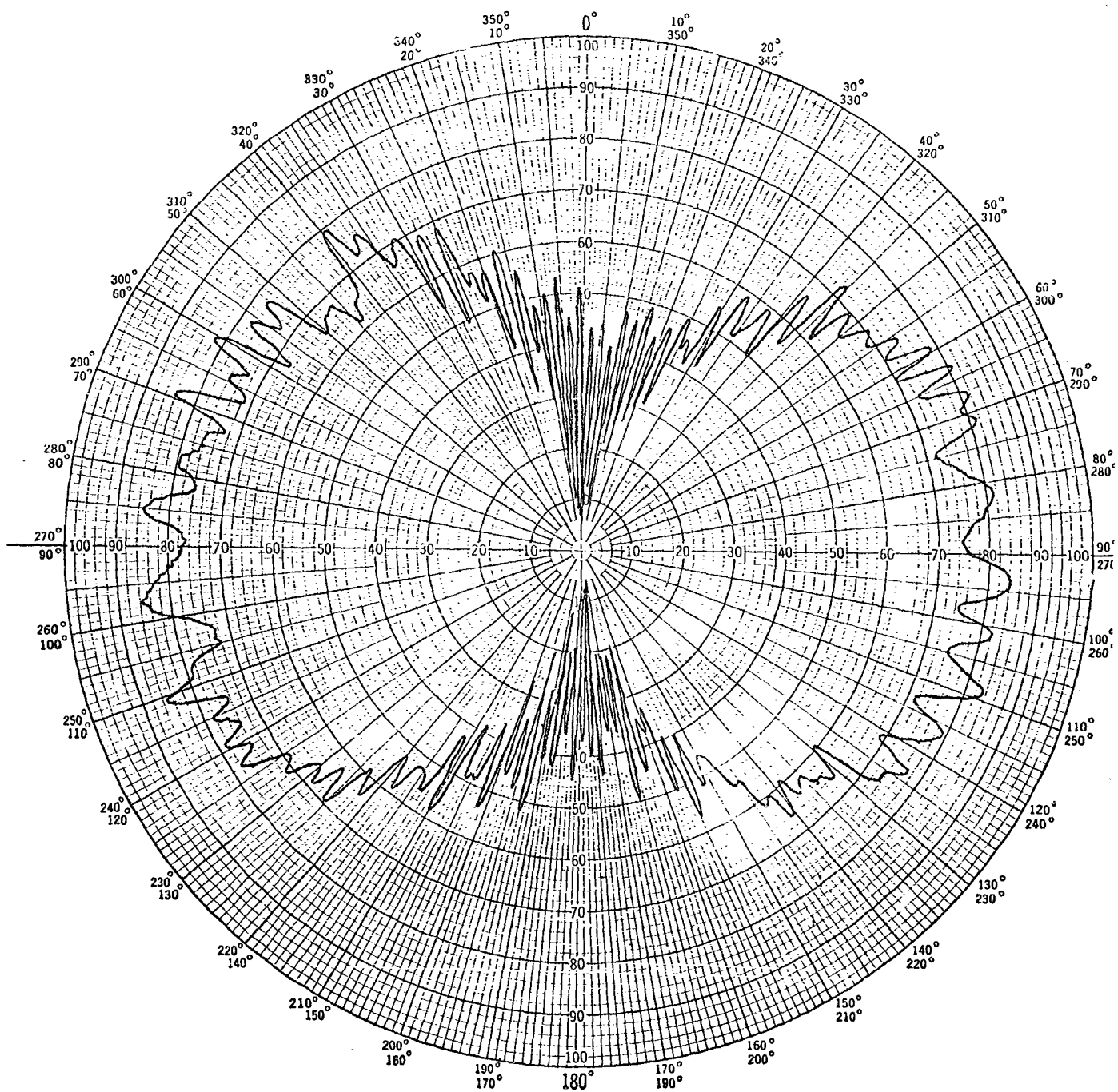


Figure 10— Roll - plane antenna pattern of two crossed-slot antennas on opposite sides of a cylinder having a ka factor of 66.

Polar Chart No. 127L
SCIENTIFIC ATLANTA, INC.
ATLANTA, GEORGIA

A WAVEGUIDE RESONANT RING ANTENNA
YIELDING AN OMNIDIRECTIONAL PATTERN

By

Dr. T. E. Charlton

E. R. Murphy

J. W. Pool



MOTOROLA INC.
Military Electronics Division
WESTERN CENTER
8201 EAST McDOWELL ROAD GAITHERSBURG, MARYLAND

ABSTRACT

A waveguide resonant ring antenna many wavelengths in diameter is described which yields an omnidirectional pattern. The waveguide ring is fed by a T-junction so that equal waves are launched in clockwise and counterclockwise directions around the ring. Radiating elements are coupled to the waveguide at equal intervals around the ring and the combination of element coupling, element spacing, ring diameter, and waveguide phase velocity create a resonant effect. Dipole radiators mounted in the waveguide broadwall and probe coupled to the guide are employed. Polarization and elevation plane pattern are controlled by an extension of the sidewalls of the waveguide, thus forming a 360-degree sectoral horn. This design provides a lightweight antenna that can be flush-mounted upon spherical or cylindrical vehicles such as satellites.

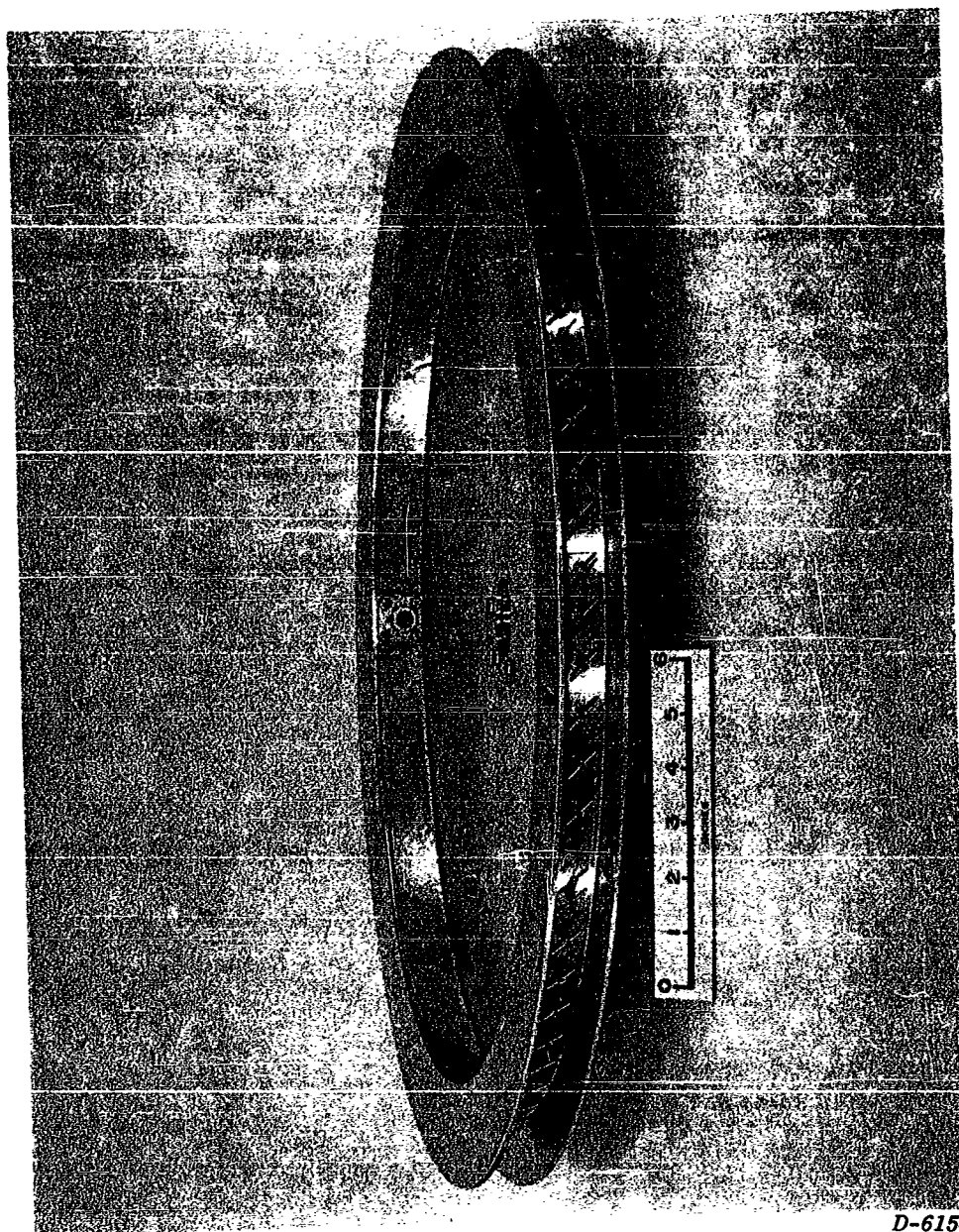
The antenna design and fabrication are discussed and measured performance is presented.

INTRODUCTION

The antenna described in this paper is the result of a study to produce an antenna for space applications. The investigation is still under way at this time, some experimental work yet remaining to be done. However, the available data tend to verify the theory and measured free space patterns will be presented as evidence of the performance of the antenna.

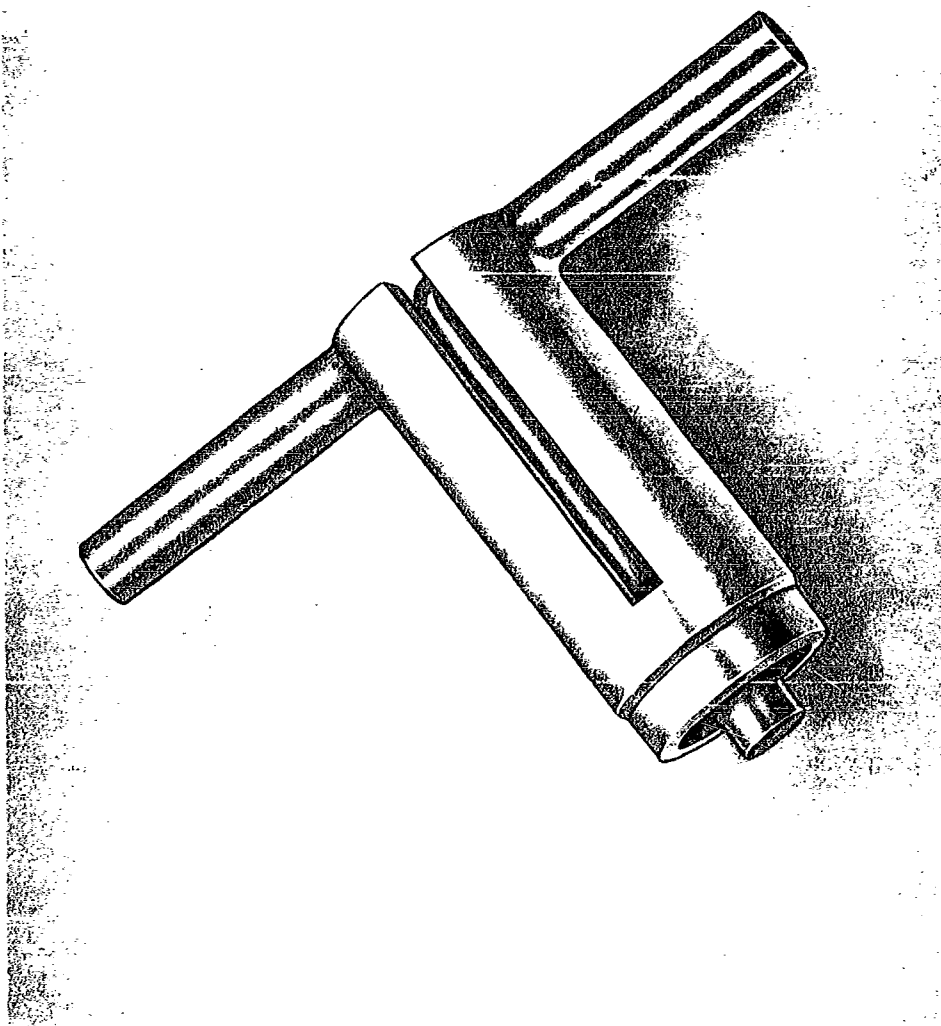
The antenna (shown in Fig. 1) is in the form of a waveguide resonant ring many wavelengths in diameter. The broadwall of the guide is perpendicular to the plane of the ring. The radiating elements, halfwave dipoles, are distributed uniformly around the periphery of the guide and the combination of dipole coupling, dipole spacing, ring diameter and waveguide phase velocity create a resonant effect. By reversing the sense of alternate dipoles, the minimum spacing between adjacent dipoles is reduced to one-half guide wave length. The dipoles (shown in Fig. 2) are probe coupled to the wave guide. The waveguide ring is probe excited from the rear of the waveguide between two dipole probes so that equal waves are launched in clockwise and counter-clockwise directions around the ring. Circular polarization is achieved by inclining the dipoles parallel to the broadwall of the waveguide and extending the narrow walls of the waveguide to form a 360-degree sectoral horn. The difference in phase velocity of the vertical and horizontal components of the field established by the dipoles in the sectoral horn provides the necessary phase shift to produce circular polarization. This sectoral horn is also used to control the elevation plane (θ plane) pattern.

This antenna will provide a relatively smooth azimuth pattern with an independent control over the elevation plane pattern. The polarization can be made to be circular on axis, regardless of the width of the elevation pattern, by proper design of the sectoral horn width and slant length. The location of the feed point, being near the edge rather than at the ring center, allows several antennas to be stacked for operation on several bands with a relatively simple feed arrangement.



D-6154

Figure 1. Ring Array



D-6153

Figure 2. Dipole

TECHNICAL DISCUSSION

Ring Design

Consider the waveguide junction shown in Figure 3 with traveling waves entering and leaving

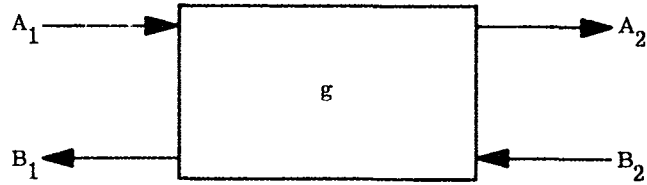


Figure 3. Waveguide Junction

both sides. The traveling waves can be related by

$$B_1 = S_{11}A_1 + S_{12}B_2 \quad (1)$$

$$A_2 = S_{21}A_1 + S_{22}B_2 \quad (2)$$

where in general the S 's are complex coefficients that characterize the network. Equation (2) can be written as

$$A_1 = \frac{1}{S_{21}} A_2 - \frac{S_{22}}{S_{21}} B_2 \quad (3)$$

Combining equations (3) and (1)

$$B_1 = \frac{S_{11}}{S_{21}} A_2 - \left(\frac{S_{11}S_{22} - S_{12}S_{21}}{S_{21}} \right) B_2 \quad (4)$$

In matrix form, equations (3) and (4) become

$$\begin{bmatrix} A_1 \\ B_1 \end{bmatrix} = \frac{1}{S_{21}} \begin{bmatrix} 1 & -S_{22} \\ S_{11} & -\det S \end{bmatrix} \begin{bmatrix} A_2 \\ B_2 \end{bmatrix} \quad (5)$$

where $S_{22}S_{11} - S_{12}S_{21} = \det S$

In order to get A_1 and B_1 in terms of the normalized junction conductance, g , rather than the complex coefficients, S_{ij} , the transformation matrix¹

$$T = \frac{1}{S_{21}} \begin{bmatrix} 1 & -S_{22} \\ S_{11} & -\det S \end{bmatrix} \quad (6)$$

is introduced.

It has been shown² that the transformation matrix can also be expressed as

$$T = \frac{1}{2} \begin{bmatrix} 1 & 1 \\ 1 & -1 \end{bmatrix} U \begin{bmatrix} 1 & 1 \\ 1 & -1 \end{bmatrix} \quad (7)$$

where U has the same properties as T and for a shunt element with normalized conductance g is given by

$$U = \begin{bmatrix} 1 & 0 \\ g & 1 \end{bmatrix} \quad (8)$$

From equations (7) and (8)

$$T = \begin{bmatrix} 1 + \frac{g}{2} & \frac{g}{2} \\ -\frac{g}{2} & 1 - \frac{g}{2} \end{bmatrix} \quad (9)$$

Combining equations (9), (6), and (5) gives:

$$\begin{bmatrix} A_1 \\ B_1 \end{bmatrix} = \begin{bmatrix} 1 + \frac{g}{2} & \frac{g}{2} \\ -\frac{g}{2} & 1 - \frac{g}{2} \end{bmatrix} \begin{bmatrix} A_2 \\ B_2 \end{bmatrix} \quad (10)$$

or

$$A_1 = (1 + \frac{g}{2})A_2 + \frac{g}{2}B_2, \quad (11)$$

and

$$B_1 = -\frac{g}{2}A_2 + (1 - \frac{g}{2})B_2. \quad (12)$$

Now the power input to the junction is given by

$$P_i = \frac{(A_1 + B_1)^2}{Z_0}. \quad (13)$$

Combining equations (11) and (13) yields

$$P_i = \frac{(2 + g)^2}{4} \frac{(A_2 + B_2)^2}{Z_0} \quad (14)$$

The power dissipated in the normalized conductance g of Figure 3 can be obtained since

$$P_i = P_r + P_t + P_d \quad (15)$$

where P_i = incident power,
 P_r = reflected power,
 P_t = power transmitted beyond g along the line, and
 P_d = power dissipated in g .

By definition:

$$P_r = P_i |\rho|^2, \quad (16)$$

where ρ is a reflection coefficient, and

$$\rho = \frac{\frac{Y_0}{Y_0} - \frac{(Y_0 + G)}{Y_0}}{\frac{Y_0}{Y_0} + \frac{(Y_0 + G)}{Y_0}} = \frac{1 - 1 - \frac{G}{Y_0}}{1 + 1 + \frac{G}{Y_0}} \quad (17)$$

where G is the actual shunt conductance and Y_0 is the characteristic line admittance.

Thus

$$\rho = \frac{-G}{2 + g} \quad (18)$$

and

$$P_r = P_i \frac{g^2}{(2 + g)^2} \quad (19)$$

Combination of equations (19) and (15) yields

$$\begin{aligned} P_t + P_d &= P_i - P_r = P_i \left[1 - \frac{g^2}{(2 + g)^2} \right] \\ &= P_i \frac{4(1 + g)}{(2 + g)^2} \end{aligned} \quad (20)$$

Since

$$\frac{P_d}{P_t} = g \quad (21)$$

then

$$P_d \left(1 + \frac{1}{g}\right) = P_d \frac{g+1}{g} = P_i \frac{4(1+g)}{(2+g)^2} \quad (22)$$

and

$$P_d = P_i \frac{4g}{(2+g)^2} \quad (23)$$

Then by equations (14) and (23),

$$P_e = g \frac{(A_2 + B_2)^2}{Z_0} \quad (24)$$

The significance of equation (24) should be emphasized. This equation shows that:

1. At a junction of conductance g with waves entering and departing from both sides, the radiated power can be determined entirely by the waves on one side of the junction. This further implies that:
2. If equal waves are introduced at each end of a waveguide containing N junctions, the radiated power from each junction will be equal, if the junctions have equal conductances. It will be shown later that this is true as long as $g < g_c$ where g_c is a certain critical conductance.

Equation (24) and its interpretations tend to suggest a waveguide ring array containing N junctions and excited in some fashion so as to launch equal waves in opposite directions around the ring from some point on the ring. Such an antenna was constructed and is shown in Figures 1 and 4. Dipoles were selected as the radiating elements,³ first, since by reversing the sense of alternate dipoles the minimum element spacing for in-phase radiators can be reduced to one-half guide wavelength and, secondly, the orientation of the electric field can be changed by simply rotating the dipole. The second feature was desired to permit greater control over polarization. The technique for obtaining circular polarization is discussed in the section on that subject. The dipole elements are coupled to the waveguide ring by a probe extending through the center of the broadwall of the guide.^{4,5}

Control of dipole coupling can be obtained by adjustment of probe length. The waveguide ring is excited by means of another broadwall probe midway between two of the radiating elements and extending through the opposite guide wall.

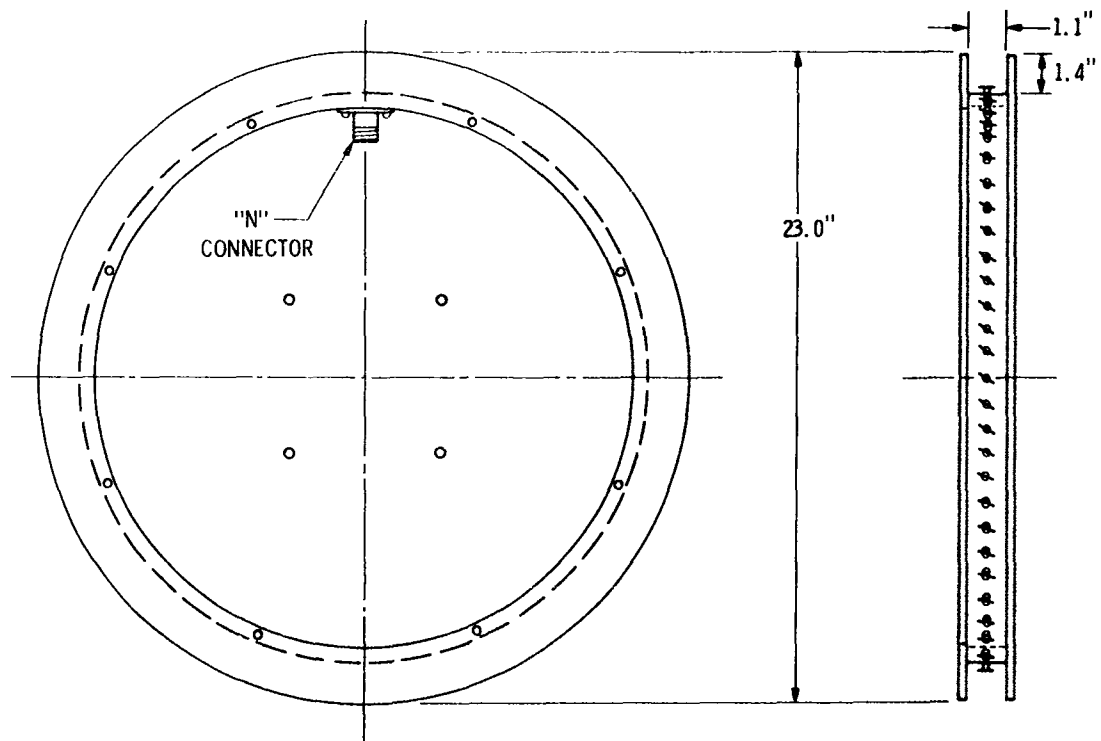


Figure 4. Ring Array

Critical Conductance

The critical conductance mentioned earlier can be determined for any fixed array geometry. Consider, for example, the five-element array of Figure 5, where the element spacing is $\lambda g/2$. The critical conductance is defined as that conductance which reduces the wave traveling from

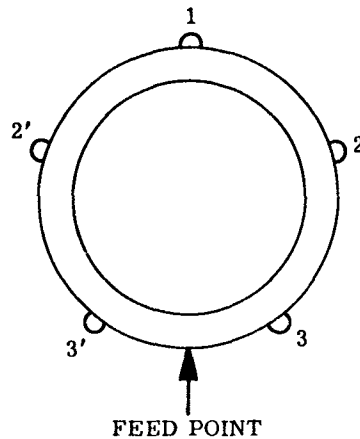


Figure 5. Five Element Array

elements 3 and 3¹ toward the feed point to zero. The value of this critical conductance can be found as follows. In Figure 5, it can be assumed from symmetry that the waves arriving and departing both sides of element 1 are equal, that is, in Figure 3 $A_1 = B_2$ and $A_2 = B_1$. Assume further that $A_1 = B_2 = 1$ and then by equations (11) and (12) A_2 and B_1 can be found for a given g . Now A_1 and B_1 at the left side of element 1 are the same as at the right side of element 2¹ for a half-wave spacing while A_2 and B_2 at the right side of element 1 are the same as at the left side of element 2 for half-wave spacing. Equations (11) and (12) are again employed to find the waves on the opposite side of elements 2¹ and 2. These new waves are the same as are presented to elements 3¹ and 3 and again equations (11) and (12) are used to determine the waves on the opposite side of elements 3¹ and 3¹. The waves traveling from elements 3¹ and 3 toward the feed can be changed by changing g , the element conductance, which is the same for all elements. That value of g which reduces these waves to zero at the feed is the critical conductance. Stated more precisely, in an array of N elements, N being odd, equations (11) and (12) can be written for the n th element as

$$A_1(n) = (-1)^{n+1} \left[\frac{1 + (2n-1)\frac{g}{2}}{1 + \frac{g}{2}} \right], \quad (25)$$

and

$$B_1(n) = (-1)^{n+1} \left[\frac{1 - (2n-1)\frac{g}{2}}{1 + \frac{g}{2}} \right] \quad (26)$$

where $n = \frac{(N+1)}{2}$.

The n th element is adjacent to the feed point and g_c is that value of g found from equation (26) when $B_1(n) = 0$, that is, when no wave travels from the n th element toward the feed. When $g = g_c$, both waves launched in the waveguide from the feed are completely radiated. If $g > g_c$ the waves are attenuated by radiation too quickly and successive elements farther from the feed point do not radiate as much energy as those elements nearer the feed point, resulting in a non-omnidirectional radiation pattern. If $g < g_c$, the elements radiate uniformly; however, some energy returns to the feed point and creates a mismatch. This can be corrected by tuning the antenna input.

Polarization Technique

To obtain circular polarization, the dipoles are inclined in a plane parallel to the broadwall of the waveguide to provide E_θ and E_ϕ field components. The necessary phase shift between these two field components is obtained by extending the narrow-walls of the guide to form a sectoral horn. To determine the angle of dipole inclination and horn dimensions, consider Figure 6. The total field at "a" is the sum of E_θ and E_ϕ , both direct and reflected components.

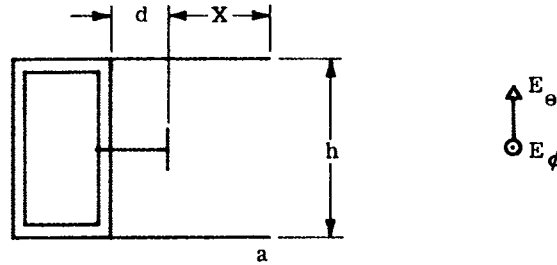


Figure 6. Section of Ring Array

This can be expressed as

$$E_t = E_\theta \left\{ e^{j\Gamma_\theta x} + e^{j[\Gamma_\theta (x + 2d) + \pi]} \right\} + E_\phi \left\{ e^{j\Gamma_\phi x} + e^{j[\Gamma_\phi (x + 2d) + \pi]} \right\} \quad (27)$$

which can be rewritten as

$$E_t = -2 \sin(\Gamma_\theta d) E_\theta e^{j[\Gamma_\theta (x + d) + \frac{\pi}{2}]} - 2 \sin(\Gamma_\phi d) E_\phi e^{j[\Gamma_\phi (x + d) + \frac{\pi}{2}]} \quad (28)$$

For equal amplitudes of E_θ and E_ϕ at "a" it is necessary that the dipoles be inclined to produce the ratio

$$\frac{E_\theta}{E_\phi} = \frac{\sin(\Gamma_\phi d)}{\sin(\Gamma_\theta d)} = 1. \quad (29)$$

A difference in the elevation plane pattern (θ plane) for E_θ and E_ϕ may require a modification of the ratio in equation (28). This is best done experimentally. E_θ and E_ϕ are in quadrature when,

from equation (28),

$$e^{j\Gamma_{\theta}(x+d)} = e^{j\Gamma_{\phi}(x+d) + \frac{\pi}{2}} \quad (30)$$

or, rearranging,

$$\Gamma_{\theta} - \Gamma_{\phi} = \frac{\pi}{2(x+d)} \quad (31)$$

It is seen, then, that

$$\frac{1}{\lambda_0} - \frac{1}{\lambda_g} = \frac{1}{4(x+d)} \quad (32)$$

since

$$\Gamma_{\theta} = \frac{2\pi}{\lambda_0} \quad (33)$$

and

$$\Gamma_{\phi} = \frac{2\pi}{\lambda_g} \quad (34)$$

where λ_0 is the free space wavelength, and λ_g is the waveguide wavelength determined by the sectoral horn height, h . Equation (32) can be solved for λ_0 since

$$\lambda_g = \frac{\lambda_0}{\sqrt{1 - \frac{\lambda_0^2}{4h^2}}} \quad (35)$$

The result of substituting equation (35) into (32) and solving for λ_0 is

$$\lambda_0 = \frac{8h^2(x+d)}{h^2 + 4(x+d)^2} = \frac{8(x+d)}{1 + 4\left(\frac{x+d}{h}\right)^2} \quad (36)$$

Figure 7 is a plot of equation (36) for constant ratios of $\frac{(x+d)}{h}$.

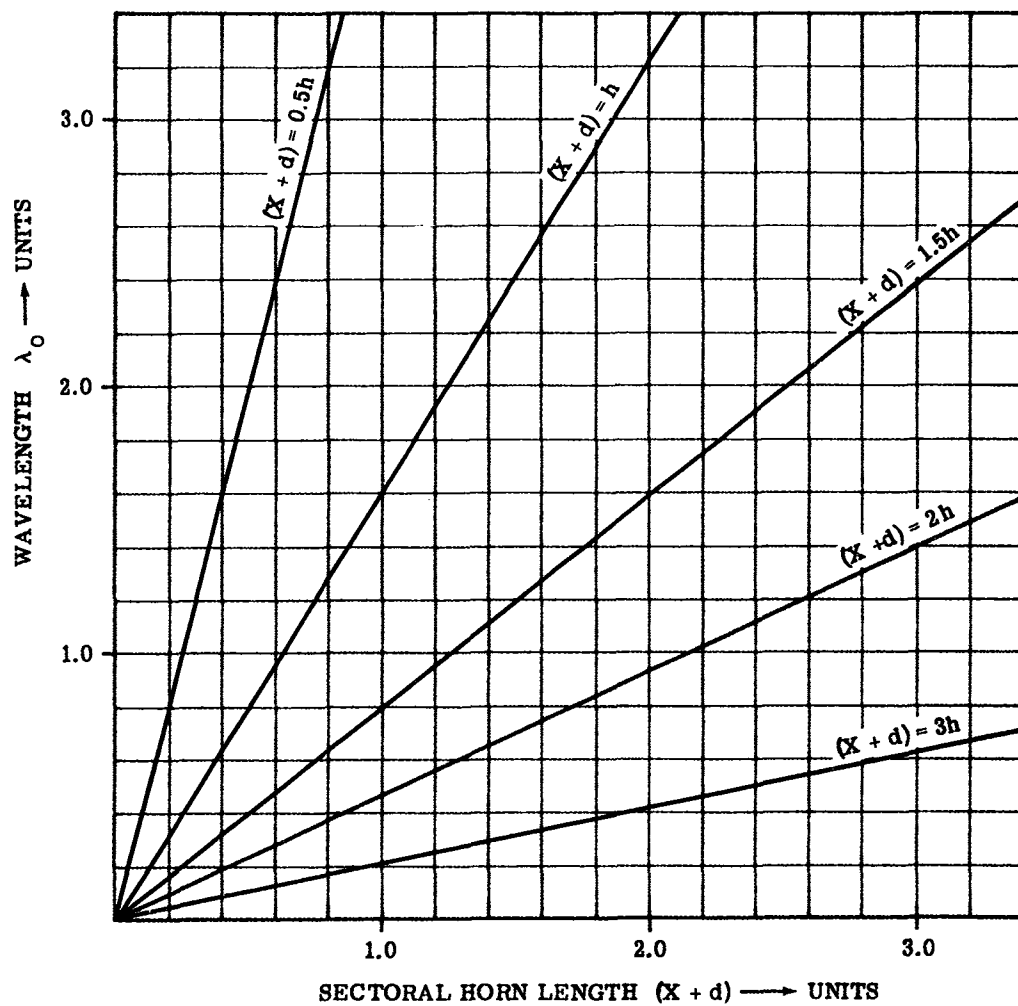


Figure 7. Wavelength vs Horn Length for Circular Polarization

EXPERIMENTAL RESULTS

Preliminary measurements indicate the antenna is performing as predicted. The azimuth pattern, Figure 8, has a ripple with a maximum excursion of about ± 2.5 db. This is explained, in part, by unequal power being radiated from the dipole elements. It was later discovered that manufacturing tolerances on the dipole elements were excessive, allowing an objectional variation in their electrical properties. New dipoles are currently being produced with better control on the mechanical tolerances. The average field strength is approximately equal for all azimuth angles indicating that the conductance of the dipole elements has not exceeded the critical conductance. A broad elevation pattern was desired and that this was achieved is shown in the elevation plane pattern, Figure 9. With such a broad pattern, the lobes directly off the top and bottom of the antenna shown on the pattern were expected, since in these directions all the radiating elements appear in phase. Both the azimuth and elevation patterns were measured with a linearly polarized source and the patterns presented are for E_θ ; however, these are typical also of the E_ϕ patterns, that is, the patterns for the two components track one another.

Circular polarization was obtained in the plane of the ring with a dipole inclination of 60 degrees with respect to the plane of the ring. Some variation of axial ratio has been observed as azimuth angle is changed. However, it is anticipated that this effect will be reduced by using the improved dipoles to obtain a more uniform azimuth pattern.

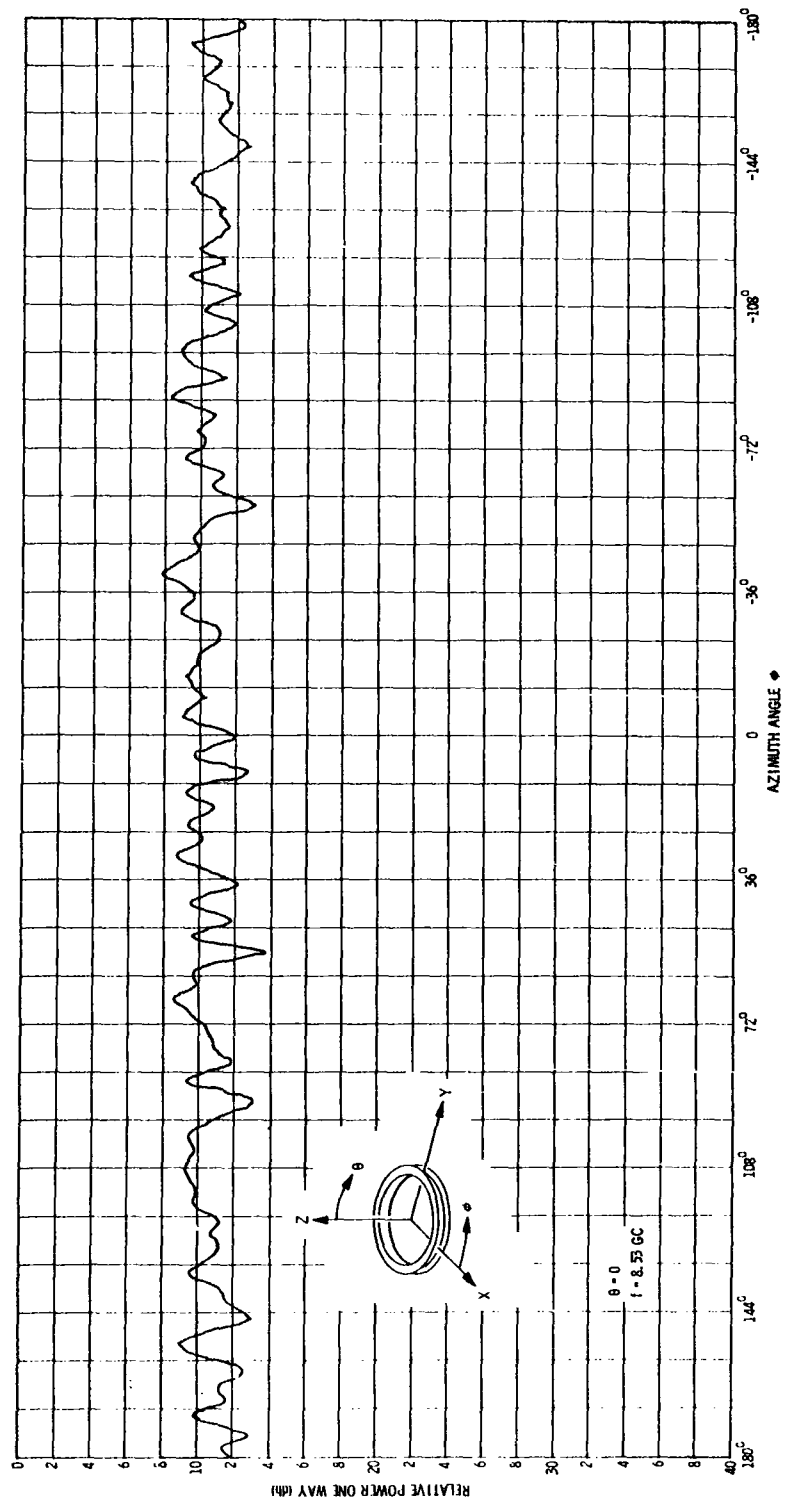
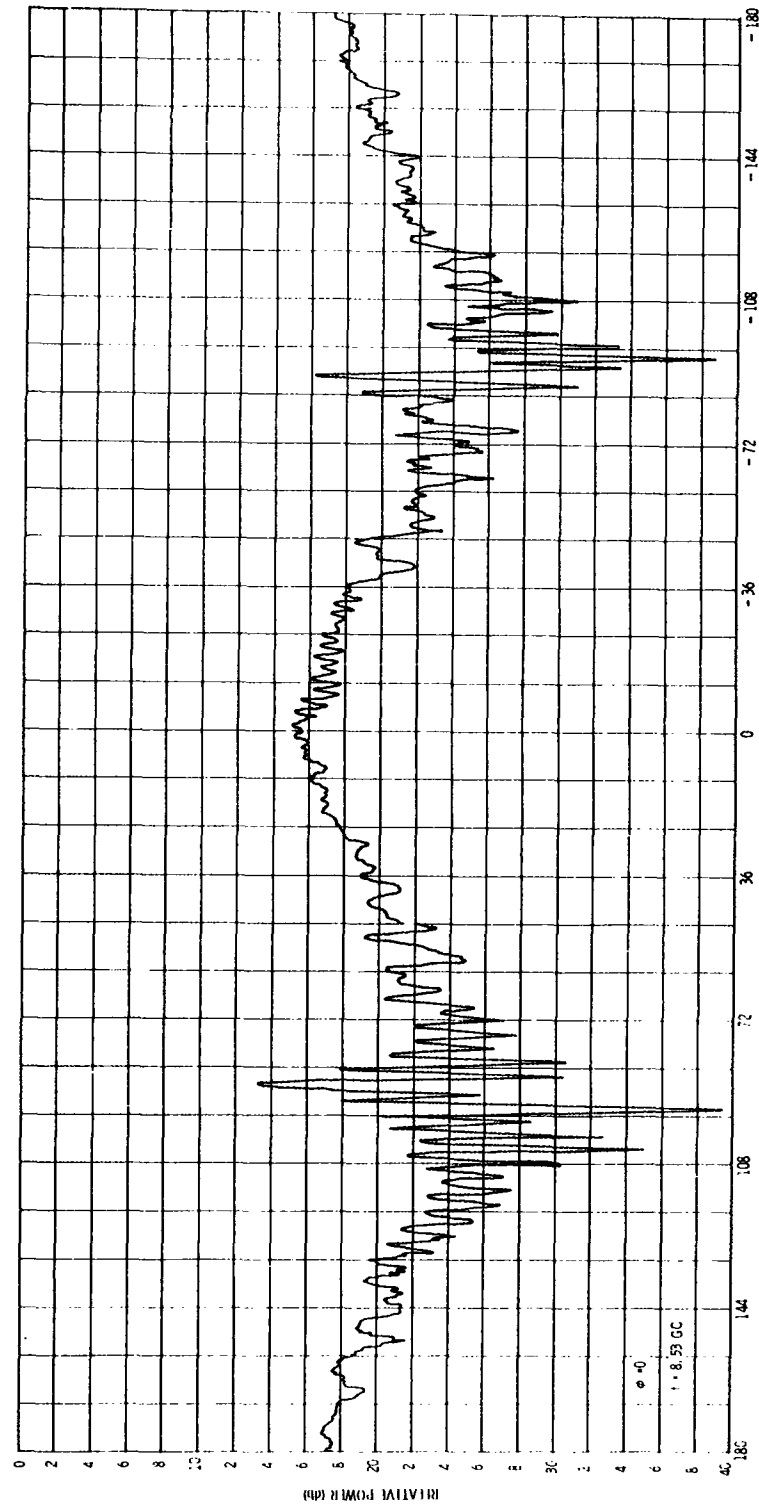


Figure 8. Azimuth Pattern



ELEVATION PATTERN

Figure 9. Elevation Pattern

CONCLUSIONS

Design information has been presented for a circularly polarized omnidirectional waveguide resonant ring array many wavelengths in diameter. Such an array is well suited for space vehicle applications. The resonant ring technique allows a simple single point feed to be used and permits identical radiating elements to be used. These features greatly simplify fabrication requirements. The use of dipole radiating elements permit a minimum element spacing of $\lambda_g/2$ to be used resulting in a more omnidirectional azimuth pattern. Dipoles also allow the electric field to be oriented as desired with a minimum effect on the dipole probe conductance. The vertical plane patterns can be changed while maintaining circular polarization by properly adjusting the sectoral horn dimensions. The antenna patterns presented verify the theory and illustrate the performance of a potential flush-mounted omnidirectional radiator.

ACKNOWLEDGEMENT

The authors would like to express their appreciation for the many helpful comments and suggestions by their colleagues and in particular to Mr. R. J. Eckstein.

REFERENCES

1. C. G. Montgomery, R. H. Dicke, and E. M. Purcell, Principles of Microwave Circuits, Radiation Lab. Series, Vol. 8, McGraw-Hill Book Co. Inc., 1948.
2. Reference Data for Radio Engineers, International Telephone and Telegraph Corp., Fourth Edition, 1956.
3. W. H. Watson, The Physical Principles of Wave Guide Transmission and Antenna Systems, Oxford at the Clarendon Press, 1949.
4. S. Silver, Microwave Antenna Theory and Designs, Radiation Lab. Series, Vol. 12, McGraw-Hill Book Co. Inc., 1949.
5. C. J. Sletten, P. Blacksmith Jr., F. S. Holt, J. E. Holland, "Line Source Antenna Arrays for Control of Pattern Dispersion and Phase", Microwave Physics Lab., Project 4600, June, 1963.

B-70 ANTENNA SYSTEM

by

E. Donald Wegner
Supervisor, Antenna & Radome Engineering
Los Angeles Division, North American Aviation, Inc

**Paper presented at the Thirteenth Annual
Symposium on USAF Antenna Research and
Development.**

INTRODUCTION

The antenna system development for the B-70 was faced with many new and unique problem areas, although electrical performance requirements were somewhat conventional. Military specification requirements formed, for the most part, the basic antenna requirements. The broad thermal spectrum to which B-70 antennas would be exposed was probably the most significant single factor contributing to the need for a state-of-the-art advancement in the antenna area. The high-temperature exposure time of many hours created a high-temperature antenna requirement much different from those based on missile applications which relied on the thermal inertia of the particular part. Although antennas designed for much higher peak temperature conditions were available or at least within the state-of-the-art, the high-temperature soak times of the B-70 could not be tolerated. Crippling loads, in excess of any expected structural or aerodynamic loads, imposed on an antenna assembly of dissimilar materials exposed to this long-duration heat soak, ruled out many of the so-called high-temperature designs. These factors coupled with the low-temperature conditions of letdown and landing necessitated an antenna development program.

The design philosophy of the development program varied during the program based on data refinements in the area of thermal and aerodynamic environments and on a continuing Value Engineering approach which attempted to match performance requirements with the actual mission and air vehicle economic considerations. For example, the original effort was directed toward the development of completely flush-type antennas. This was redirected to the development of external types in some applications based on a value-to-the-mission type of

NA-63-917

analysis. The requirement for an automatic tuning HF coupler was changed to a passive preselected frequency approach on the basis of mission requirement economics. (This coupler design was reported at the Antenna Symposium of 1960 by J. K. Aiton of North American Aviation Inc, Los Angeles Division.) This refinement of requirements and subsequent change in philosophy is discussed below.

REQUIRED FUNCTIONS

The basic electromagnetic radiating functions required on the B-70 are the conventional requirements of a manned system, namely, communications, and navigation and landing aids.

The communications system consisted initially of both UHF and HF requirements. Upon further analyses of the XB-70 mission, the HF requirement resolved into one of making provisions only for HF, and further HF development per se was deferred.

The navigation aids system consists of the TACAN equipment and the air-to-ground beacon transponder (IFF). Both of these equipments operate in the L-band region of the spectrum.

The landing aids system requirement includes the Glide Slope, Localizer, and Marker Beacon functions.

TECHNICAL APPROACH

The development programs for the antenna elements were formulated and refined to their final status by a continuing Value Engineering analysis of each phase of the development program. The results of this analysis showed that the

areas of testing and reporting were the predominant areas in which cost and time savings could be realized without jeopardizing the electrical or mechanical quality of the final part.

Also, during this phase of the program, it was concluded that the antenna should be designed to assume the vehicle structural loads in lieu of having the vehicle structure accommodate for the structural discontinuity caused by the antenna. Thus, the development program was directed toward this objective. Structural analyses of antenna materials were made in parallel with the environment, type, and location analyses. The location of the antennas on the vehicle, as shown in figure 1, was the result of considering the individual and the combined areas of electrical performance and the thermal, aerodynamic, and structural environments. The ultimate location and design was the result of this composite analysis. All of this information was compiled and detailed on individual design control drawings and in specifications for completion of the development by NAA or a subcontractor.

ANTENNA TYPES

UHF ANTENNA SYSTEM

The UHF communications antenna system includes two antennas. One antenna is located on the top fuselage centerline and the other on the lower centerline as shown in figure 1. These antennas are cycled by a C-2193 A/A switch to provide the required antenna pattern coverage.

As previously mentioned, a flush-mounted annular slot type of antenna was considered initially for this application, but upon further refinement of requirements, high-temperature, high-speed blade type antennas were selected. The

NA-63-917

antenna considered was a slot-excited, one-piece blade being developed for the Navy by Transco Products of Venice, California. The Navy antenna was fabricated from a high-temperature aluminum alloy. Although this material would provide adequate strength and stand the thermal environment, the difference in coefficients of expansion between this material and the B-70 skin material would impose failure stresses on the antenna. The material for the B-70 antenna was, therefore, specified to be stainless steel. This material change unveiled problems of sealing the antenna at the mating of the slot dielectric and the stainless steel in order that it would meet the military specification seal-test requirements. This problem will be discussed further. The XB-70 antenna resulting from this program is shown in figure 2.

NAVIGATION AIDS ANTENNA SYSTEM

Both the TACAN and air-to-ground beacon transponder (IFF) systems operate in the L-band region and, therefore, can use identical antennas. As originally planned, the antenna system for these equipments was to be an integrated, two-antenna system incorporating an antenna selector (C-2193), a lobing switch (SA-498 A/A), and two F-339/A filters. NAA/LAD experience on the T-39 Sabreliner flight-test program and Air Force and industry experience subsequently indicated that the attenuation and loss of adjacent channels caused by the filters was not tolerable during service conditions. Therefore, the integrated antenna system concept was deleted and separate antennas were planned for each function. The antennas are located on the upper and lower fuselage centerlines as shown in figure 1.

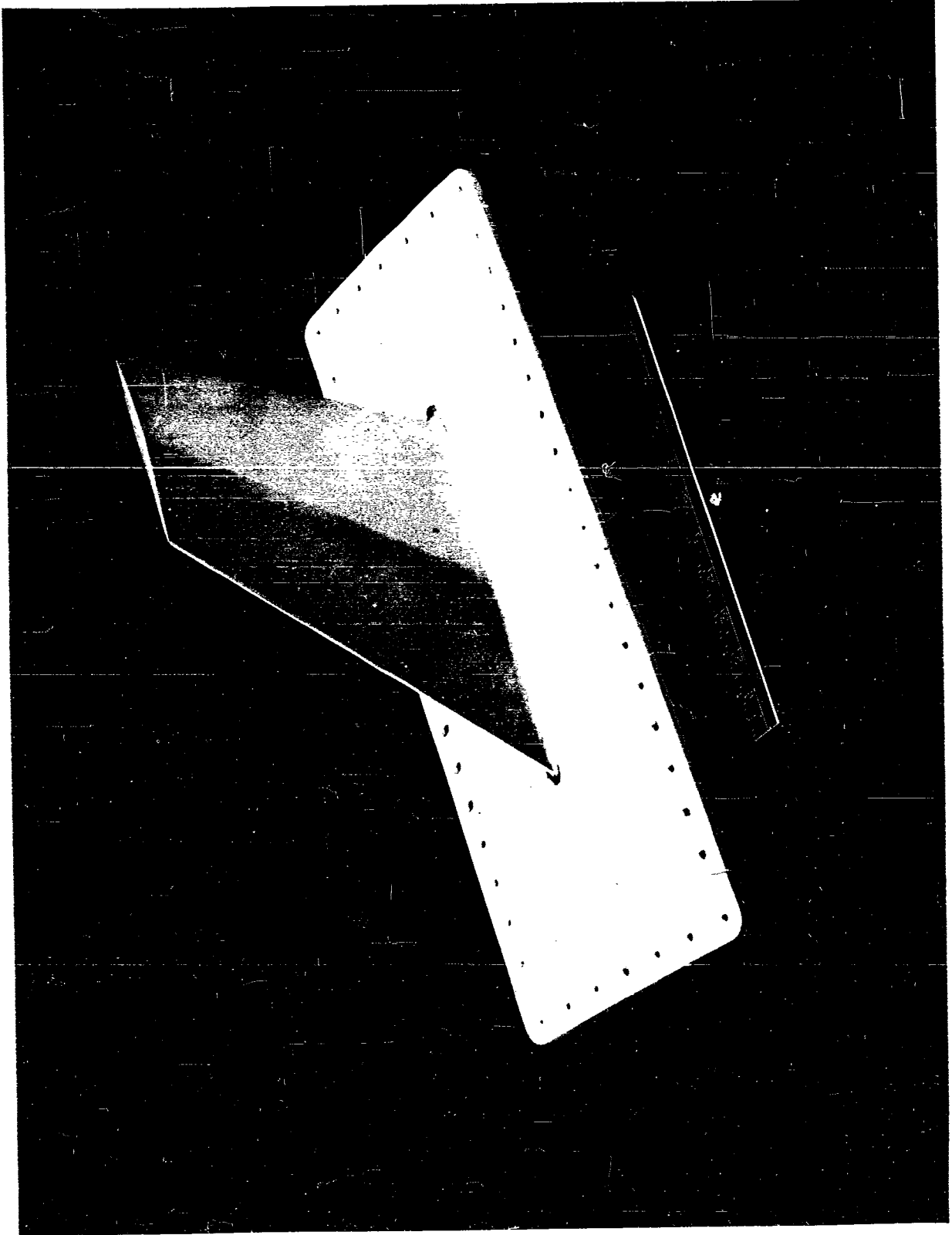


Figure 2. UHF Antenna

The electrical performance requirements for these antennas were similar to those required of the standard AT-740 and AT-741 antennas. Meeting these requirements under the environmental conditions of temperature and altitude of the B-70 did pose some problem, however. As in the instance of the UHF antenna design approach, a flush-type annular slot antenna design was initially considered. However, here also, later analyses indicated a low profile slot excited blade (similar to the UHF antenna) being developed for the Navy approached the B-70 requirements. In this application also, the high-temperature aluminum was replaced by stainless steel. The pressure leak problem experienced with the UHF antenna did not present itself here however, presumably because of the slight difference in mechanical attachment caused by the size relationship to the mounting radius of curvature.

Environmental tests to validate the antenna performance showed that voltage breakdown, observed at the blade tips and across the dielectric filled slots, occurred at power levels, temperatures, and pressure altitudes much in excess of those required in the B-70 application. These tests qualified both the UHF and the L-band blade antennas.

The resulting antenna, shown in figure 3, incorporates a test probe for system checkout. Transmission lines from the probes are routed to a test panel in the vehicle electronic equipment bay.

LANDING AIDS ANTENNA SYSTEM

This system includes antennas for Marker Beacon, Glide Slope, and Localizer functions.

NA-63-917

Because the Marker Beacon antenna is a narrow band tuned cavity, it was recognized that some problems in design for the extreme thermal band requirement of the B-70 would be realized if conventional cavity dimensions were imposed. A cavity volume of approximately four times that of the standard AT-134 antenna was permitted to accommodate a larger antenna element and offset the dielectric losses expected from a thick, structurally sound, dielectric cover.

The compensation required to keep the antenna tuned over the thermal band width and the sealing of the dielectric cover presented significant developmental problems. However, mechanical rather than electrical difficulties proved to be the more difficult to solve.

A thermal compensating, printed circuit capacitive element keeps the antenna within a 2.5:1 VSWR at 75 mc \pm 300 kc throughout a temperature range of -65°F to $+500^{\circ}\text{F}$.

Two significant problems were associated with the dielectric cover: that of sealing the cover itself, and that of sealing the cover to the cavity case. Several dielectric laminate companies tried to solve the problem of cover leakage. Although sound thin laminates could be easily achieved, thicker, structurally acceptable laminates, wicked and/or became porous as sections were temperature cycled. Finally, a structurally acceptable dielectric cover was fabricated by Laminar of Gardena, California, using a proprietary resin to high-pressure laminate a Specification MIL-R-9300 material. This cover darkened after repeated temperature cycling and, therefore, did effect the antenna performance to a minor degree because of this carbonization, but the cover did not leak during or after

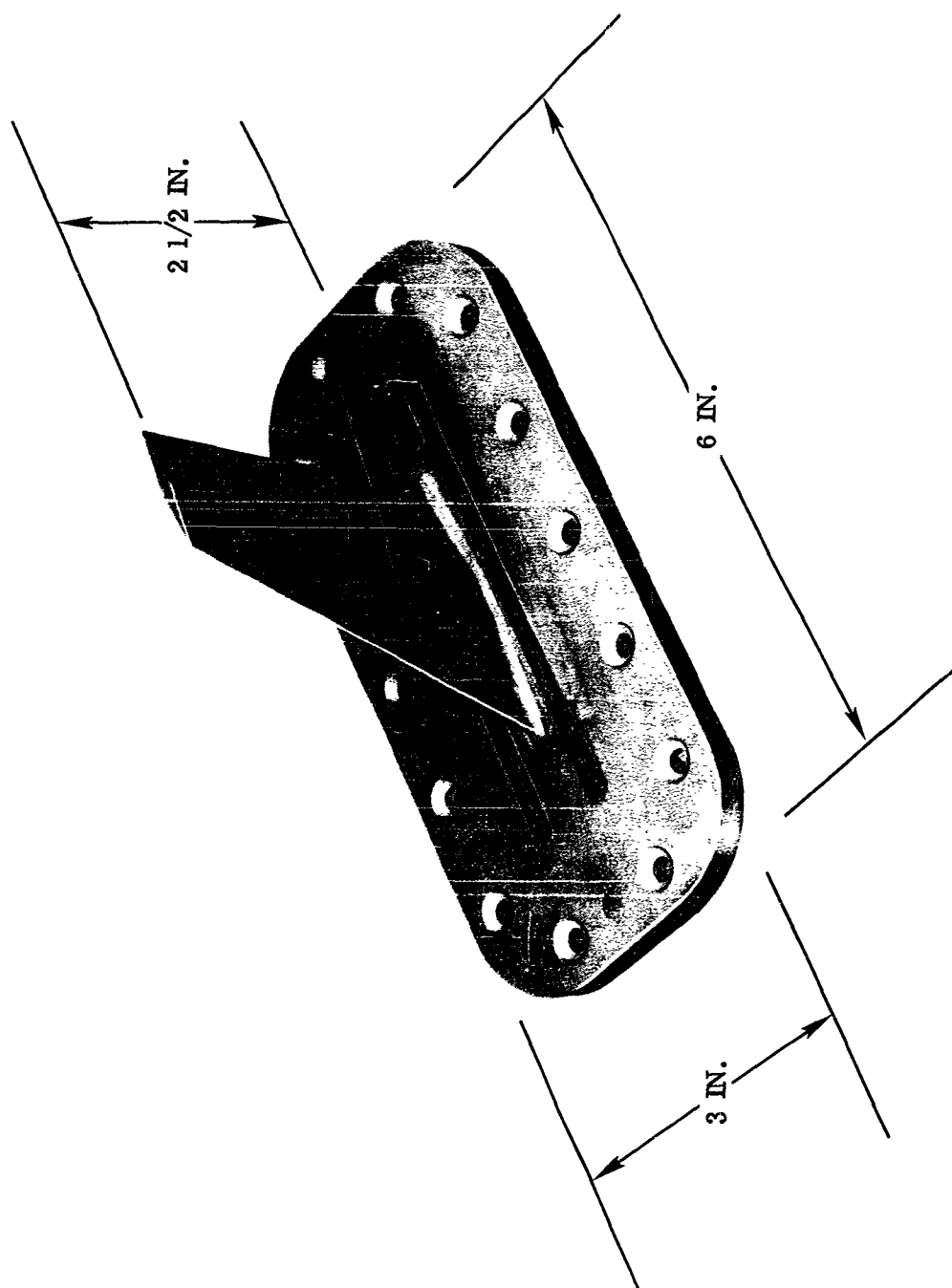


Figure 3. L Band Antenna

environmental exposure. The material was later accepted for this cover as well as the UHF slot windows.

In a joint effort, Transco Products and NAA/LAD investigated many techniques of bonding the cover to the cavity case after mechanical fasteners were found unacceptable because of their damaging effect on the laminate. Room-temperature vulcanizing compounds (RTV) and various film adhesives were investigated, with varying results. After considerable experimentation and testing, an AF-31 film adhesive, qualified to Specification MIL-A-5090, was used to bond the dielectric cover to the Marker Beacon case. This provided both a structurally sound adhesive bond throughout the temperature range and a leakproof seal. This film adhesive was not applicable on the UHF antenna because of bonding surface discontinuities. However, a technique was developed using a RTV compound which was successful in sealing the UHF antenna.

The Marker Beacon antenna finally developed is shown in figure 4, and is located as shown in figure 1. Although the gain of this antenna is low because of the composite effect of the element, high-temperature foam filler, dielectric cover, and cavity size, it does meet the performance requirements.

The harmonic relationship of the operating frequencies for the Glide Slope and Localizer equipments permitted the design of a single antenna. A bent dipole, balanced with a broadband coax balun, bonded to the inside surface of the nose radome was designed by NAA. A diplexer which separates the glide slope and localizer signals and provides isolation between the equipments is located in the electronic equipment bay.

NA-63-917

The antenna has less than a 2.5 to 1 VSWR in both frequency bands, and the pattern, although narrower in azimuth than military specification requirements, satisfies the requirement for the high performance B-70. The antenna is an integral part of the nose cavity and because of the cavity effect, the pattern was narrowed and forced downward. A photograph of this antenna on the XB-70A dielectric nose fairing is shown in figure 5.

SUMMARY

In conclusion, it can be said that the environmental conditions of the B-70 was the basis for the need of an antenna development effort. A program that analyzed the structural, thermal, aerodynamic, and electrical performance requirements to obtain a practical and economic balance of these requirements mitigated the magnitude of development effort required. A survey of state-of-the-art developments proved successful in several areas where existing technology was upgraded to produce a design which met the new XB-70 requirements. Use of both testing and analysis in combination allowed a reduction in the over-all test program.

The approach taken on this program has proved to be successful at NAA/LAD and is worthy of consideration for application on future programs.

NORTH AMERICAN AVIATION, INC.
INTERNATIONAL AIRPORT
LOS ANGELES 9, CALIFORNIA

NA-63-917

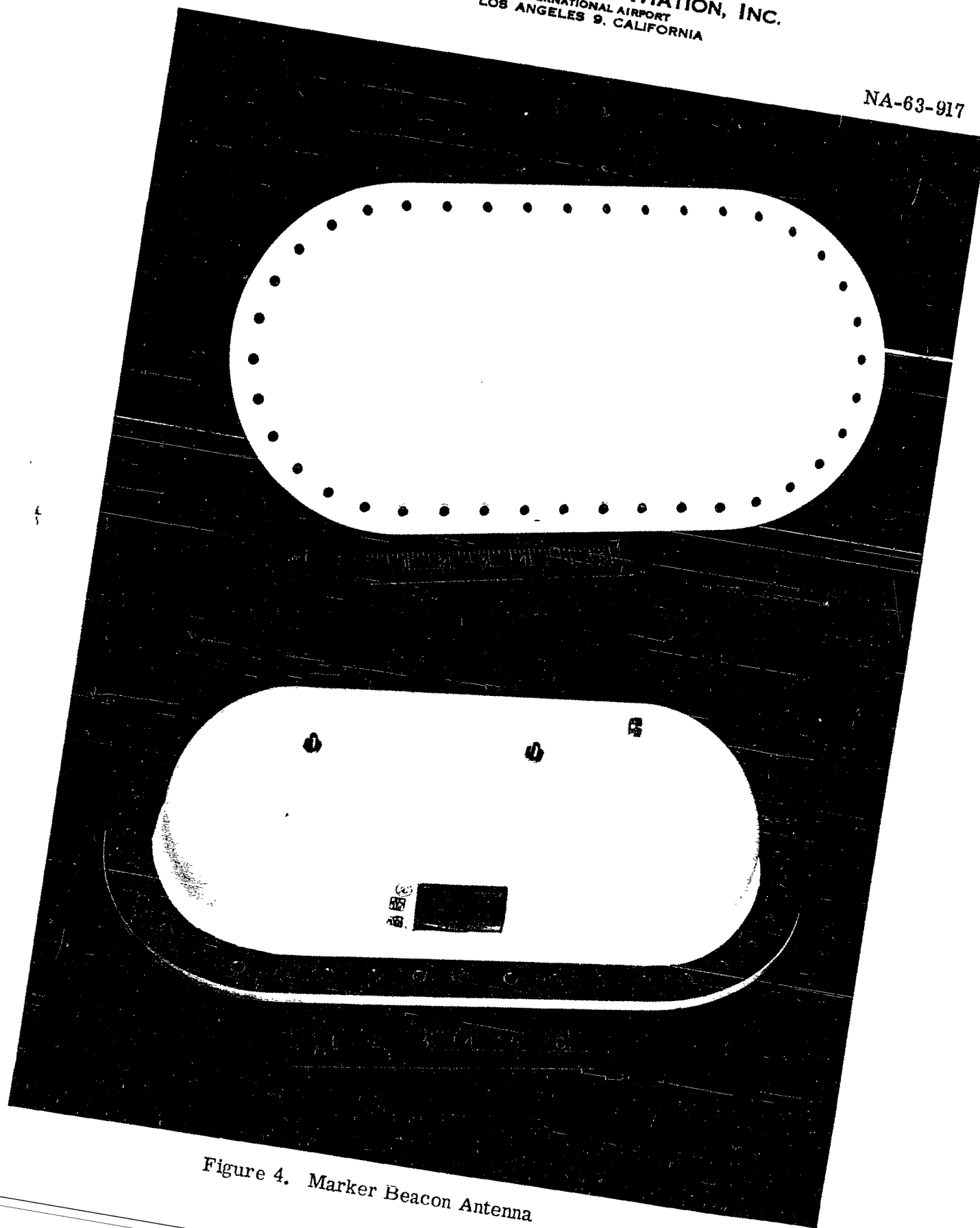


Figure 4. Marker Beacon Antenna

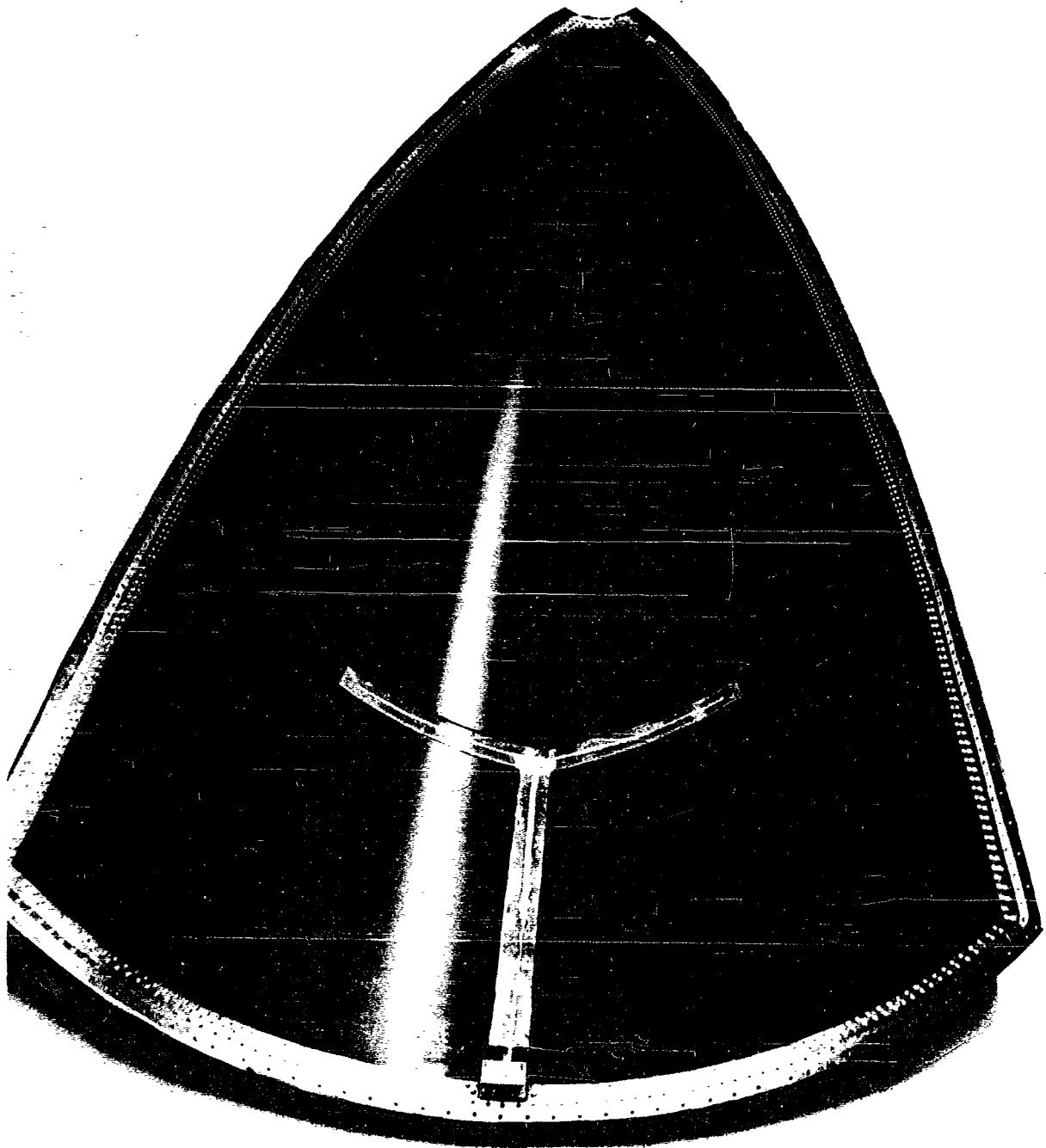


Figure 5. Glide Slope - Localizer Antenna

SUMMARY OF AIRCRAFT RADOME SHAPES AND ELECTRICAL
CHARACTERISTICS WITH MONOPULSE ANTENNAS

BY

GRANT M. RANDALL AND DONALD F. ZEMKE

AUTONETICS, A Division of North American Aviation, Inc.
3370 East Anaheim Road, Box X-1
Anaheim, California

ABSTRACT: During recent years, monopulse radar antennas have been used quite extensively in high performance aircrafts. The monopulse antennas have been incorporated on multimode airborne radars. Since the radome shape is more usually designed from the aerodynamic standpoint rather than from the radar, serious system problems may result. The radome shapes are usually quite different for each aircraft. The evaluation of the effect of each radome on the radar system performance is of extreme interest. Investigation has been made on several production radome shapes of the following items:

- A. Effect of the radome shape on antenna performance
- B. Radome construction methods and materials
- C. Effect of the presence or absence of a pitot nose boom on the antenna performance

The conclusions reached from this radome shape study and the measurement of the perturbations on the monopulse antenna radiation parameters are as follows:

- A. The high performance aircraft streamlined radome shape presents a difficult design problem for the radome, antenna, and radar system.
- B. Very good correlation between the angle of incidence for various antenna look angles and the transmission through the radome is obtained. Higher angles of incidence (more pointed radome) gives more transmission loss. Transmission through the nose area is further reduced by the presence of the pitot nose boom.
- C. The design of high performance radomes can be accomplished to meet rigid boresight requirements.

- D. Monopulse antenna radiation characteristics may be seriously effected by a severe radome shape.
- E. The radome transmission - one way is not all ohmic losses, but is predominantly antenna scattering loss. The antenna radiation pattern sidelobes are very seriously increased by extremes in radome shape and presence of the pitot nose boom.
- F. The development of future radar systems should not separate the radome and radar antenna designs. Close coordination and cooperation between the aircraft or missile airframe manufacturer and the radar/radome manufacture is a must.

AN S-BAND CONICAL SPIRAL ANTENNA

FOR SPACE VEHICLE APPLICATION

By

R. J. Eckstein

 **MOTOROLA INC.**
WESTERN CENTER
Military Electronics Division
8901 EAST MCDOWELL ROAD, SCOTTSDALE, ARIZONA

INTRODUCTION

The antenna to be described is a part of the Goddard Range and Range Rate Tracking System developed for NASA by the Military Electronics Division of Motorola. The Goddard System utilizes carrier and side-tone modulation measurements to determine the exact position of a spacecraft to within a few feet and its velocity to within fractions of a foot per second. The antenna was designed for use with the spaceborne transponder of the tracking system.

The antenna, shown in Figure 1, prior to the application of a thermal control coating, is a conical spiral radiator supported on a fiberglass cone. It is designed to perform at the widely separated operating frequencies of the Range and Range Rate System, near 1700 and 2300 megacycles. Over-all antenna height is less than 4.5 inches and antenna weight is less than 0.3 pounds. Circularly polarized pattern coverage is obtained throughout a 150-degree conical sector, which is sufficient to cover the earth when the satellite is at a 150 nautical mile perigee. A unique broadband feed structure was developed which maintains a well-matched antenna input impedance so that maximum possible system gain is realized for tracking at cislunar distances. Mechanical design is such that the antenna is capable of withstanding the extreme shock, vibration, and acceleration forces experienced during the launching period, and capable of performing satisfactorily in the space environment.

THE SPIRAL CONFIGURATION

Performance characteristics of the conical equiangular spiral antenna are uniquely suited to the requirements of the Range and Range Rate transponder antenna. This type of radiator falls in the general class of frequency independent antennas and its design is well documented in the literature.^{1, 2, 3}

The two arms of the balanced spiral antenna are based on the logarithmic spiral curve defined in a plane by

$$\rho = ke^{a\theta}.$$

The simple planar spiral is itself a useful antenna for some applications, radiating normal to the plane of the spiral in both hemispheres. However, radiation is confined to one hemisphere with the conical spiral configuration. The conical spiral curve is derived from an orthogonal projection of the planar curve on the surface of a cone, in which case the defining relationship becomes

$$\rho = \rho_0 e^{\frac{\sin \theta_0}{\tan \alpha} \phi}$$

as shown in Figure 2. In a practical situation, in order to obtain a spiral arm of finite width, the curve is rotated through an angle δ . Then expressions for the second arm may be obtained simply by rotating these two curves through 180 degrees.

Dependence of the antenna performance characteristics upon the spiral parameters has been thoroughly investigated.^{1, 2} Radiation is confined largely to a single lobe directed off the apex of the cone, and back lobe radiation decreases with decreasing cone angle, $2\theta_0$. Useful cone angles are generally less than 45 degrees. Major lobe beamwidths may be adjusted from 60 to 180° by suitable selection of the rate of spiral determined by the angle α . The useful bandwidth of the antenna is a function of the diameters of the truncated apex and base. Generally, the apex diameter should be less than $\frac{\lambda}{4}$ at the upper frequency limit, and the base diameter should be at least $\frac{3\lambda}{8}$ at the lower frequency limit.

The balanced spiral arms are fed at the apex of the cone. The impedance at this point is influenced by the cone angle and by the terminal geometry but is nominally between 130 and 150 ohms. It has been shown that the spiral antenna may be operated satisfactorily in free-space, in a cavity, or over a ground plane.

ANTENNA DESIGN AND PERFORMANCE

For the Range and Range Rate transponder antenna, an included cone angle of 30 degrees was chosen as a compromise between back lobe level and over-all antenna height. The angle α was taken as 60 degrees, producing the rapid rate of spiral necessary to obtain the broad, 150-degree pattern coverage. An arm width, δ , of 90 degrees was employed. The apex diameter was made approximately 0.2λ at the highest frequency of interest, and the base diameter is approximately 0.4λ at the lowest operating frequency.

The radiation pattern shown in Figure 3 is typical of the circularly polarized coverage obtained from the antenna at frequencies from 1700 to 2300 megacycles. Furthermore, the broad, null-free pattern is obtained in any plane through the axis of the cone.

THE BROADBAND FEED STRUCTURE

The feed system for a balanced spiral antenna must perform two functions. It must include a transition from unbalanced to balanced transmission line, and it must generally

provide an impedance transformation from approximately 50 to 140 ohms. In addition, if the bandwidth capabilities of the spiral radiator are to be realized, the feed circuitry must perform these operations across a wide band of frequencies. A number of broadband balanced-to-unbalanced transformers (baluns) have been developed in recent years. The feed system developed for the S-band spiral antenna employs a novel realization of a balun arrangement which was first proposed by Roberts in 1957⁴.

The general circuit arrangement as described by Roberts is illustrated in Figure 4. Z_a is the characteristic impedance of the input unbalanced line, Z_b is the characteristic impedance of an open-circuited unbalanced line of electrical length θ_b , and Z_{ab} is the characteristic impedance of a short-circuited balanced line of electrical length θ_{ab} . Line ab is formed from the outer conductors of lines a and b . R represents the resistive impedance of the balanced load.

It may be shown that if transmission line losses are neglected and $\theta_{ab} = \theta_b = \theta$, the following expression for Z is obtained,

$$Z = \frac{RZ_{ab}^2}{R^2 \cot^2 \theta + Z_{ab}^2} + j \frac{(\cot \theta) (R^2 Z_{ab} - R^2 Z_b \cot^2 \theta - Z_b Z_{ab}^2)}{R^2 \cot^2 \theta + Z_{ab}^2}.$$

The balun circuit will be impedance-matched when $Z = Z_a$. This condition is satisfied when $\cot \theta = 0$ and $R = Z_a$, but this is a narrow-band solution which is only of passing interest for this application. Roberts discusses a specific broadband solution, making $Z_{ab} = R$ and $Z_a = Z_b$ for which a perfect impedance match is obtained at two widely separated frequencies, f_1 and f_2 , where

$$\sin^2 \theta = \frac{Z_a}{R}.$$

The frequencies f_1 and f_2 are symmetrically related to a band center frequency, f_0 , as shown on the typical VSWR versus frequency curve of Figure 5. The theoretical maximum VSWR in the frequency band $f_2 - f_1 = \Delta f$ will occur at midband where $Z = R$ and, hence, is proportional to R/Z_a . Another solution of the same balun circuit,^{5, 6} which makes $Z_b = R^2/Z_{ab}$, provides increased bandwidth without the corresponding increase in midband VSWR. It is interesting to note that, in any case, the balun provides a step-up impedance transformation as a by-product since $R \geq Z_a$.

These specific solutions, while of considerable practical value, place some unnecessary restrictions on the circuit parameters. For this reason, a more general analysis has been developed. Referring again to the general expression for Z , the line impedances

are matched when the imaginary part is zero and the real part is equal to Z_a . If the narrow-band solution is rejected (i.e. $\cot \theta \neq 0$), the following relationships may be written,

$$R^2 Z_{ab}^2 - R^2 Z_b^2 \cot^2 \theta - Z_b Z_{ab}^2 = 0$$

$$\frac{R Z_{ab}^2}{R^2 \cot^2 \theta + Z_{ab}^2} = Z_a$$

Rearranging these equations and normalizing all impedances with respect to R such that

$$z_a = \frac{Z_a}{R}, z_b = \frac{Z_b}{R}, z_{ab} = \frac{Z_{ab}}{R}$$

the expressions obtained are,

$$z_b = \frac{z_{ab}}{\tan^2 \left(\frac{\Delta f}{f_0} \times \frac{\pi}{8} \right) + z_{ab}^2}$$

and

$$z_a = z_b z_{ab}$$

where $\cot \theta$ has been expressed in terms of the bandwidth, $\frac{\Delta f}{f_0}$. It may also be shown that, in general,

$$z_a \leq 1$$

$$z_b \leq \frac{1}{z_{ab}}$$

and that the midband VSWR is equal to $\frac{1}{z_a}$.

The relationships between the several circuit impedances have been plotted for various values of $\frac{\Delta f}{f_0}$, producing the families of curves shown in Figures 6 and 7. These curves permit the designer to make judicious impedance selections in order to obtain specified balun bandwidths and voltage standing-wave ratios. The particular solutions mentioned earlier are seen to be special cases of the general solution. Roberts' condition that

$Z_{ab} = R$ becomes $z_{ab} = 1$, and the second particular solution making $Z_b = \frac{R^2}{Z_{ab}}$ becomes $z_b = \frac{1}{z_{ab}}$.

FEED DESIGN AND PERFORMANCE

The bandwidth desired for the Range and Range Rate transponder antenna is approximately $\frac{\Delta f}{f_0} = 0.3$. Normalized balun impedances were chosen as $z_{ab} = 1.0$ and $z_a = z_b = 0.94$. In order to keep circuit impedances at practical levels, Z_a and Z_b were made 50 ohms and $Z_{ab} = R$ was made 53.4 ohms. A separate transformation was then provided from the 53.4 ohm balun terminal impedance to the spiral feed point impedance of approximately 140 ohms.

Mechanical features of the feed structure are shown in Figure 8. Lines *a* and *b* of the analysis are the short coaxial sections near the antenna base, and line *ab* is a parallel-strip line formed from a copper-clad fiberglass sheet. The 53.4-to-140 ohm impedance transformation is accomplished in the upper half of the structure by tapering the parallel-strip line.

† Typical values of antenna input VSWR are plotted versus frequency in Figure 9. As can be seen, the input impedance is well-controlled over the desired frequency range. The operating bandwidth of this particular antenna and balun is not, of course, indicative of any fundamental limitation of either the balun or spiral configuration. Both are capable of satisfactory performance over much wider bandwidths.

REFERENCES

1. Dyson, J. D., "The Non-Planar Equiangular Spiral Antenna," Abstracts of the Eighth Annual Symposium on the USAF Antenna Research and Development Program, Robert Allerton Park, Monticello, Illinois, October, 1958.
2. Dyson, J. D., "The Unidirectional Equiangular Spiral Antenna," IRE Transactions on Antennas and Propagation, Vol. AP - 7, pp 329-334, October, 1959.
3. Dyson, J. D. and Mayes, P. E., New Circularly Polarized Frequency Independent Antennas with Conical Beam or Omnidirectional Patterns, University of Illinois Antenna Laboratory, Technical Report No. 46, June 20, 1960.
4. Roberts, W. K., "A New Wide-Band Balun," Proceedings of the IRE, Vol. 45, pp 1628-1631, December, 1957.
5. McLaughlin, J. W., Dunn, D. A., and Grow, R. W., "A Wide-Band Balun," IRE Transactions on Microwave Theory and Techniques, Vol. MTT-6, pp 314-316, July, 1958.
6. Bawer, R. and Wolfe, J. J., "A Printed Circuit Balun for Use with Spiral Antennas," IRE Transactions on Microwave Theory and Techniques, Vol. MTT-8, pp 319-325, May, 1960.

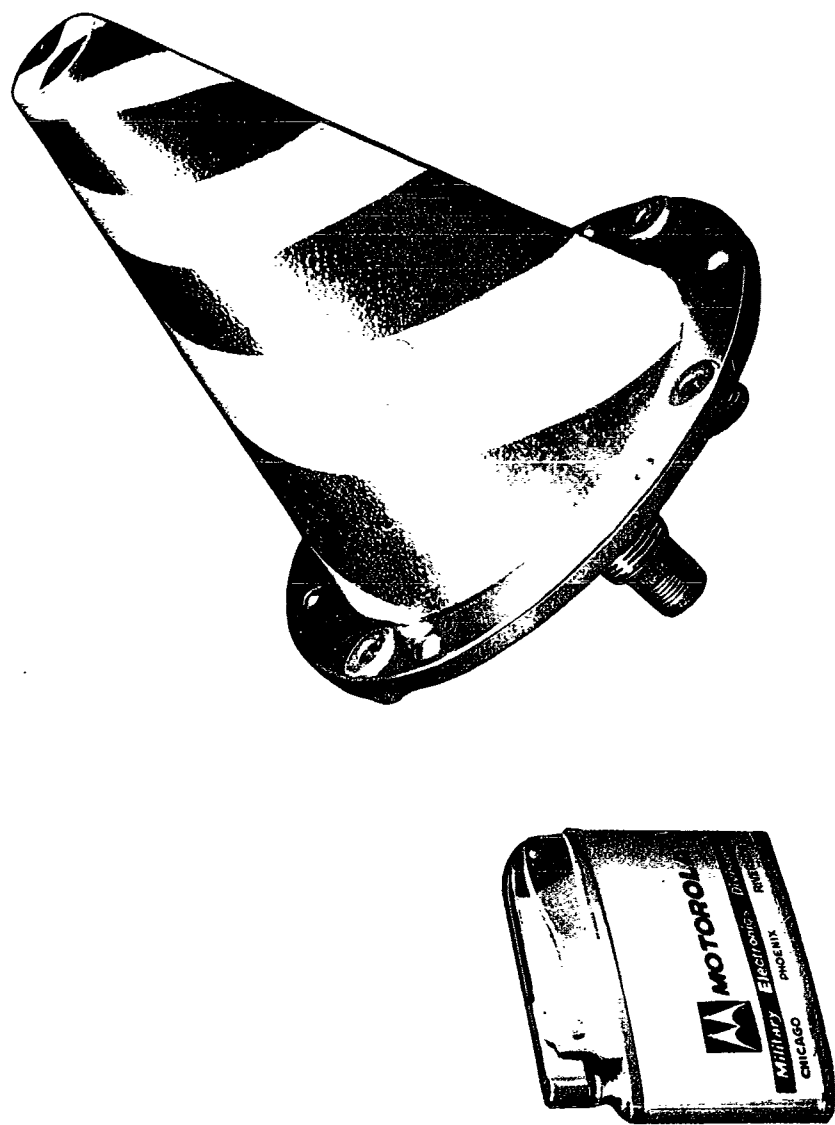


Figure 1. CONICAL SPIRAL TRANSPONDER ANTENNA.

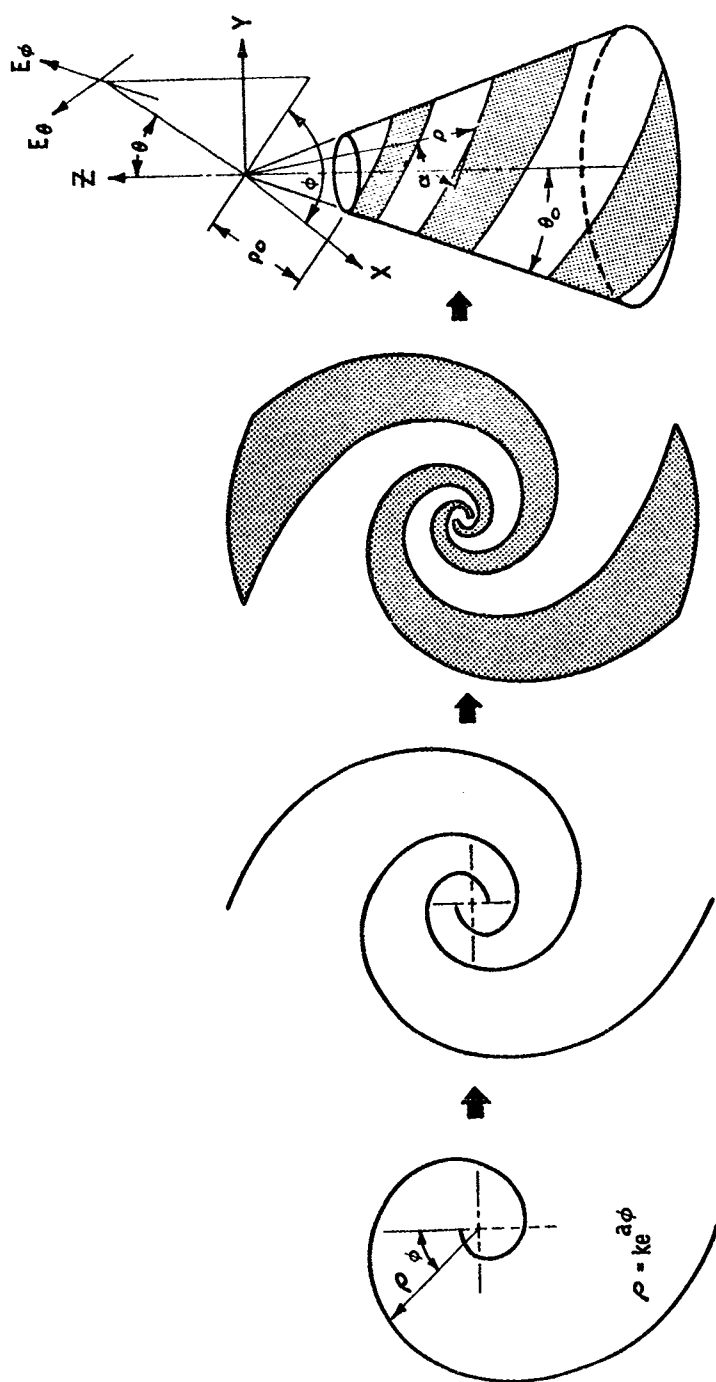


Figure 2. GENERATION OF THE CONICAL SPIRAL CONFIGURATION FROM THE PLANAR LOGARITHMIC SPIRAL

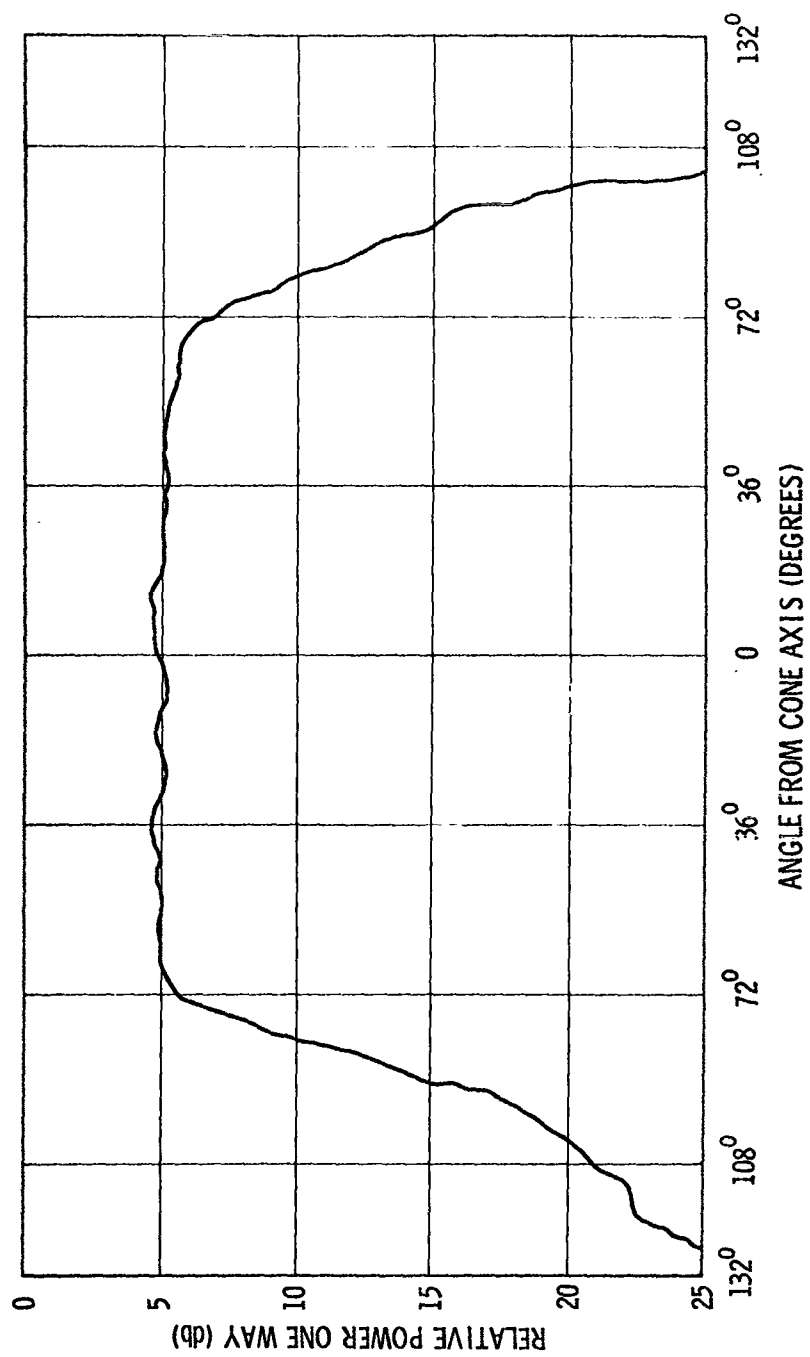
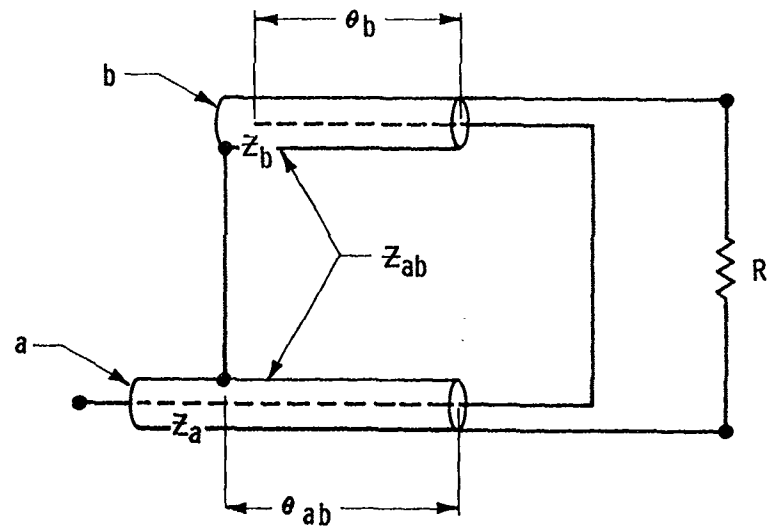
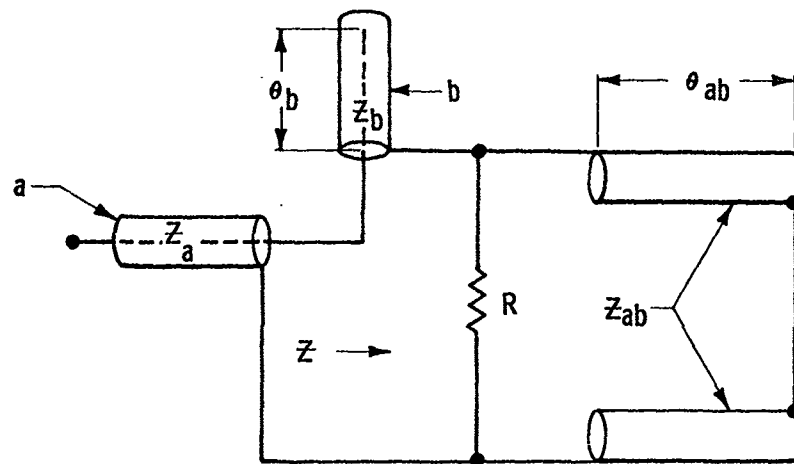


Figure-3. TYPICAL CIRCULARLY POLARIZED RADIATION PATTERN
OF THE RANGE & RANGE RATE TRANSPONDER ANTENNA



(a) BALUN CONFIGURATION



(b) EQUIVALENT CIRCUIT

Figure 4. WIDE BAND BALUN CIRCUIT ARRANGEMENT FROM ROBERTS⁴

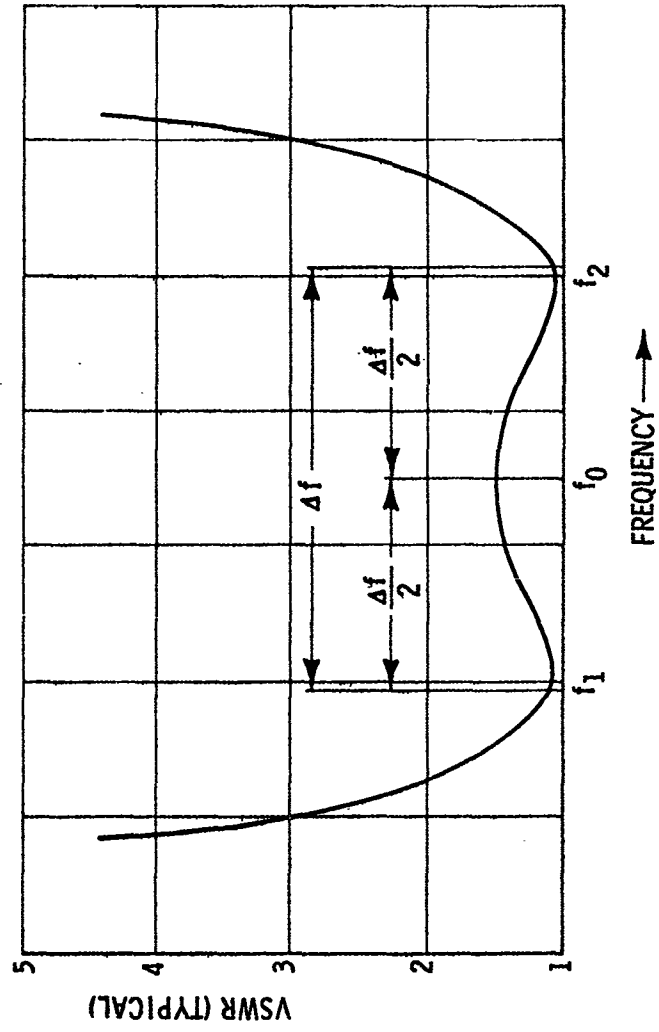


Figure 5. RELATIONSHIP BETWEEN THEORETICAL VSWR AND FREQUENCY FOR THE WIDEBAND BALUN CIRCUIT.

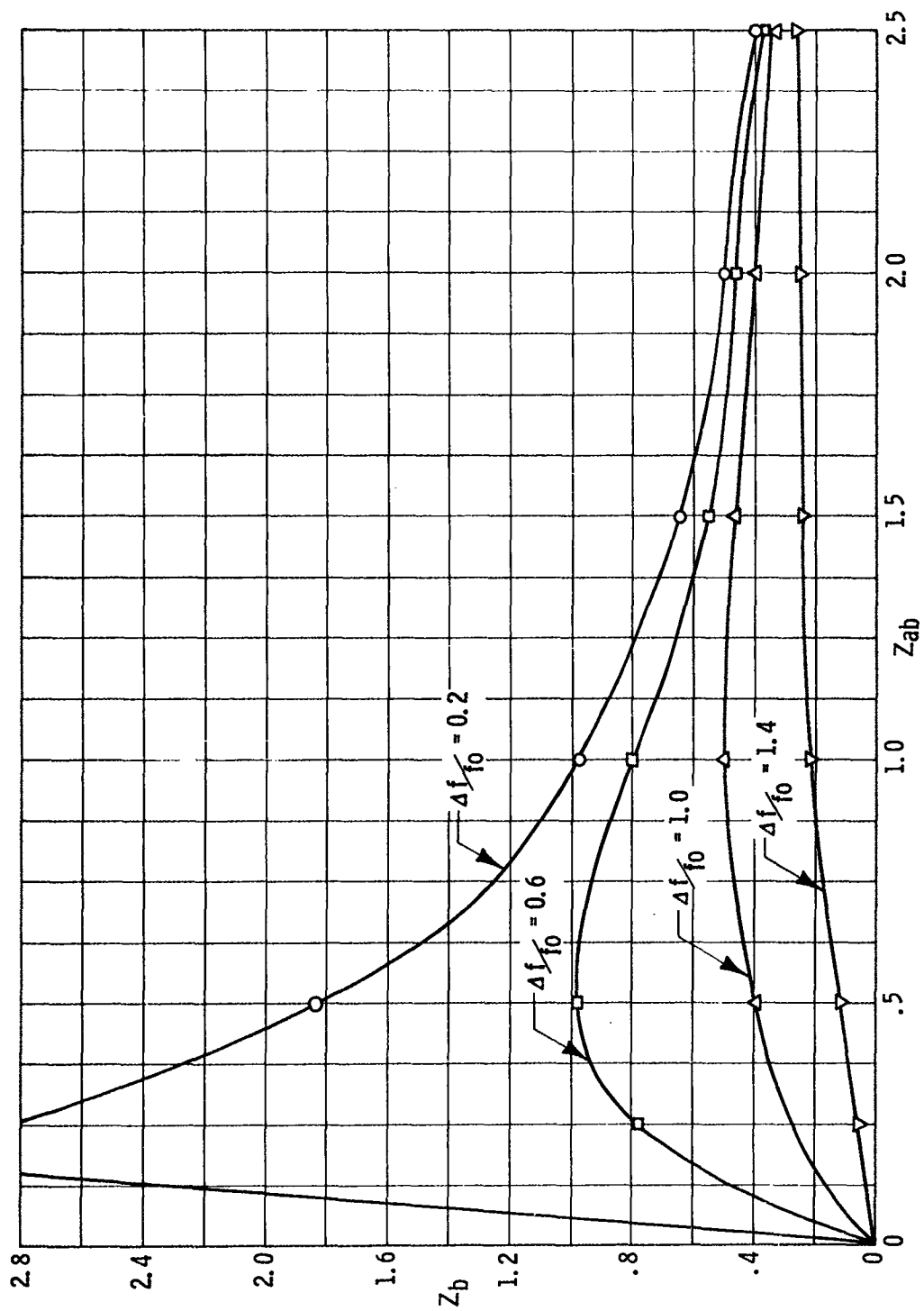


Figure 6. RELATIONSHIP BETWEEN NORMALIZED BALUN CIRCUIT IMPEDANCES FOR VARIOUS BANDWIDTHS.

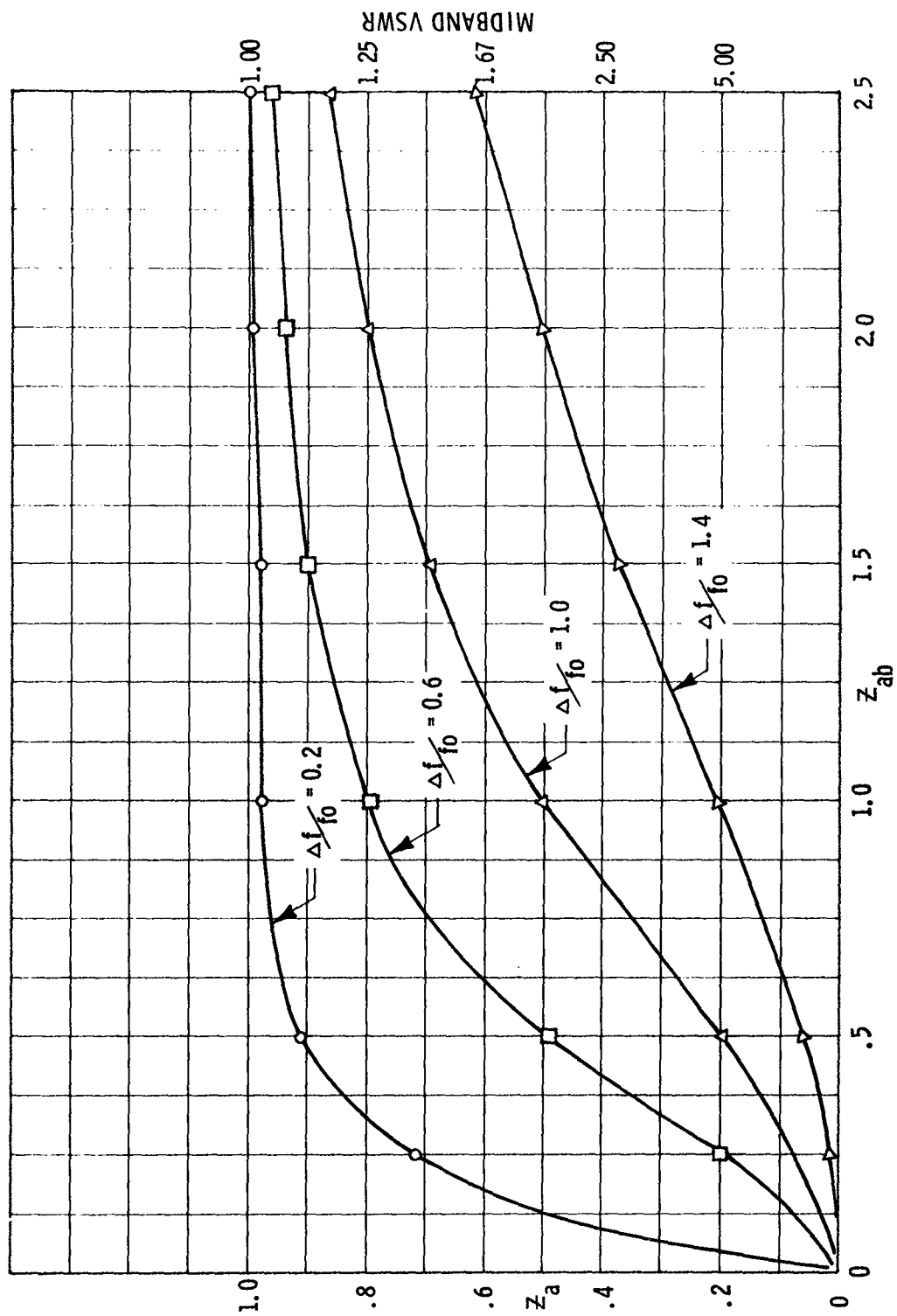


Figure 7. RELATIONSHIP BETWEEN NORMALIZED BALUN CIRCUIT IMPEDANCES FOR VARIOUS BANDWIDTHS

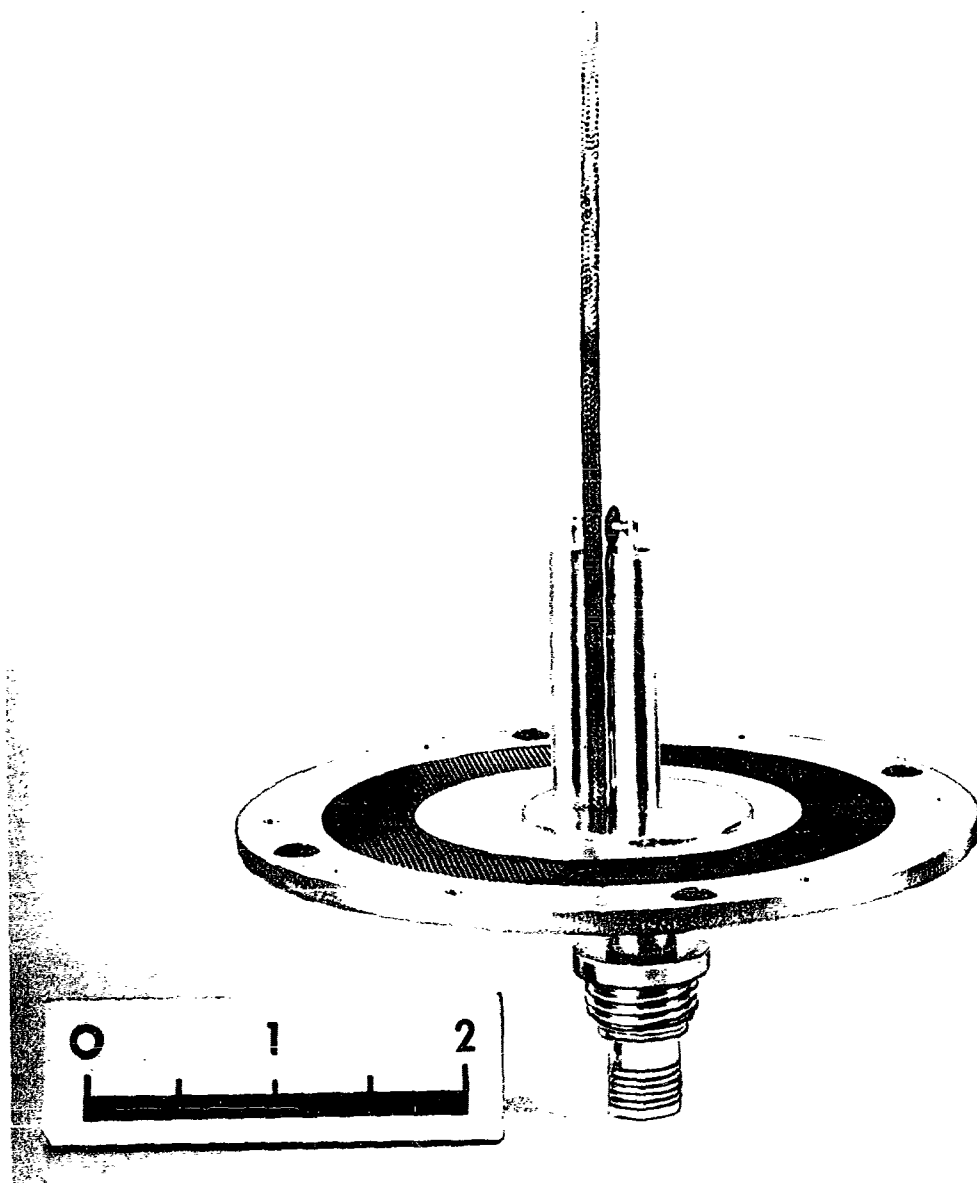


Figure 8. BROADBAND FEED SYSTEM FOR THE SPIRAL ANTENNA.

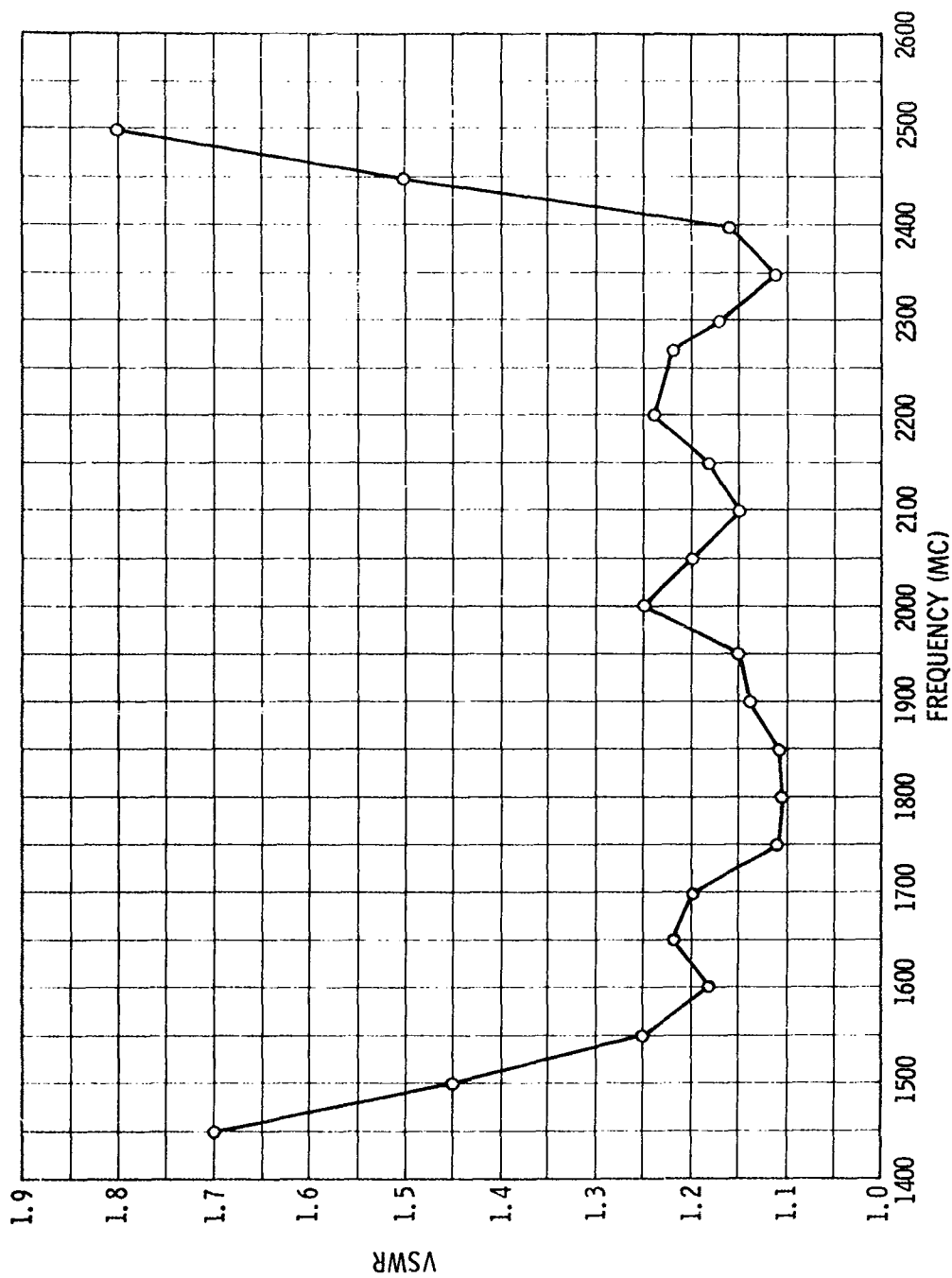


Figure 9. MEASURED INPUT VSWR OF THE CONICAL SPIRAL TRANSPONDER ANTENNA

AUTOMATIC CALIBRATION SYSTEMS
FOR
TRACKING RADARS

by
Leonard Blaisdell

SYLVANIA ELECTRONIC SYSTEMS – EAST
SYLVANIA ELECTRONIC SYSTEMS
A Division of Sylvania Electric Products Inc.
100 First Avenue, Waltham 54, Massachusetts

AUTOMATIC CALIBRATION SYSTEMS FOR TRACKING RADARS

by

Leonard Blaisdell

INTRODUCTION

Normally, calibrating the position of the electrical boresight axis of a tracking radar is at least straightforward, if not simple. However, when the calibration of the electrical axis is a function of the position of the beam in space, as can be the case if the radar antenna has a scanning capability, the problem can become complex. Under these conditions, hundreds of calibration points may be required as a function of the angle of scan.

The problem may be divided in two parts: 1) collecting the calibration data representing the error (difference) between the electrical and mechanical or read-out axes; 2) how to use the data in the dynamic situation to correct the indicated target position in real time. This paper describes an automatic calibration system which represents a practical solution to both parts of the problem.

ANTENNA MODEL

One type of antenna with which the automatic calibration system described in this paper can be effectively used is the phased array. A monopulse tracking capability can be incorporated in the phased array by grouping the elements to form four beams which are, in turn, combined in a monopulse comparator in the usual way. The complex pre-comparator corporate feed and phasing system in a steerable array of this type can result in system tracking errors due to pre-comparator amplitude and phase asymmetries.

Another antenna system which perhaps illustrates the application of the auto-calibration system more fully than the array, is the organ pipe scanner-lens configuration shown in Figure 1. For this reason, the calibration system operation will be explained in terms of this model.

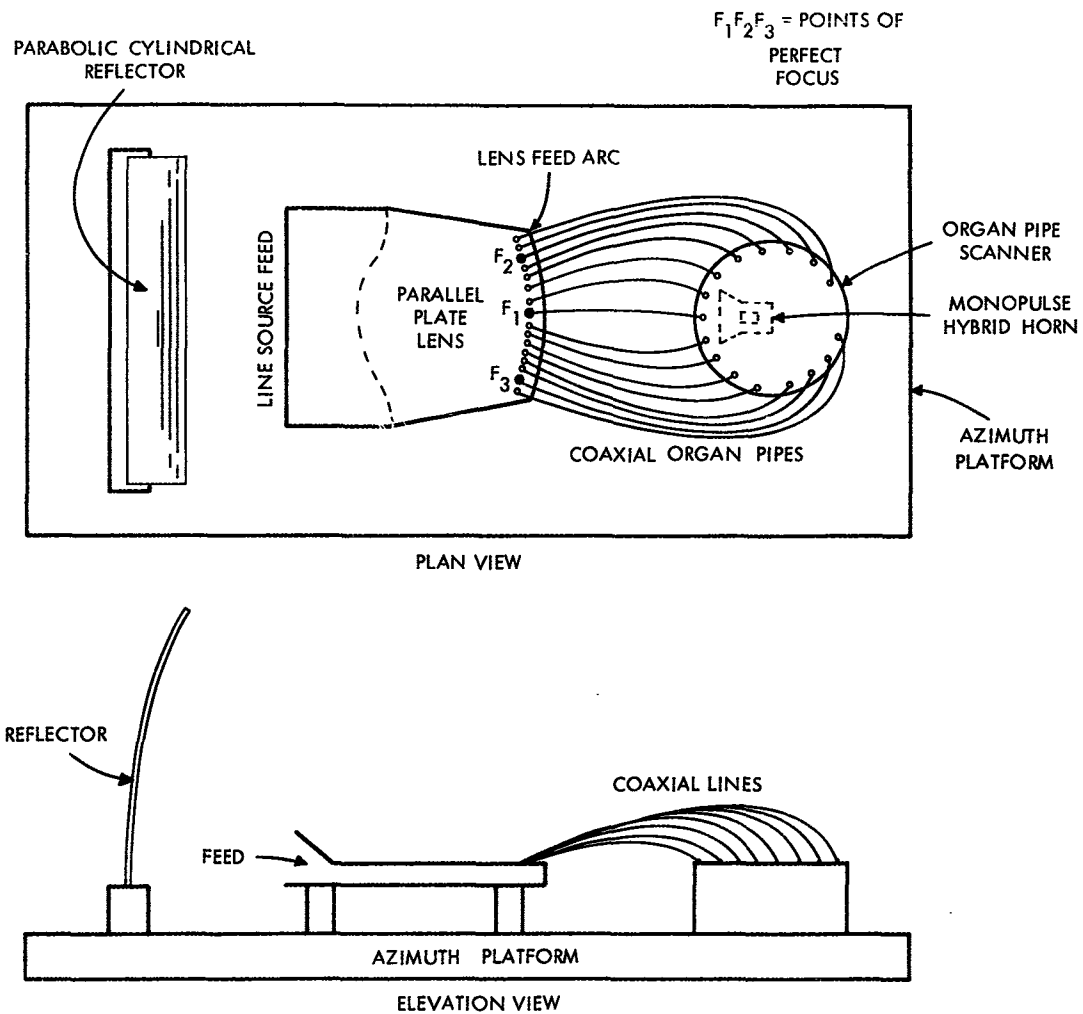


Figure 1. Electro-mechanical Scanning Antenna System Model

As the sketch shows, the antenna contains a parabolic cylindrical reflector fed from a line source feed. A coaxial organ pipe scanner containing a monopulse sum and difference hybrid horn is used to move a radiating phase center along the focal arc of a parallel plate lens which, in turn, excites the feed. This whole assembly is mounted on a rotatable platform so that the antenna can be readily positioned to search a given sector of space. Actually, an elevation plane monopulse capability can be included in the system by stacking two of these configurations, one on top of the other. However, elevation scan is unnecessary to explain the operation of the "auto-calibration" system. Suffice it to say that the same technique applies equally well to such an elevation plane tracking system whose electrical axis also varies as a function of the azimuth scan angle.

SOURCES OF TRACKING ERROR

In any monopulse tracking radar, the indicated position of the electrical tracking axis can be in error for many reasons — pre-comparator electrical asymmetries in both amplitude and phase, defocusing within the antenna system. Mechanical distortions in the reflector or other parts of the antenna structure can cause beam pointing error.

In this antenna configuration, all these sources of error can vary in magnitude as a function of scan angle. In the relatively complex pre-comparator systems, the amplitude and phase of the "equivalent" electrical paths seen by the monopulse horns in the scanner depend upon which organ pipes are in the paths, as well as the particular region of the lens seen by each horn. The degree of defocusing in the parallel plate lens also varies as a function of position between the points of perfect focus along the lens feed arc. The auto-calibration system is designed to correct these and other errors listed at the end of this paper.

DATA COLLECT MODE

In the antenna system depicted in Figure 1, we can define three axes:

- 1) The Electrical Tracking Axis. In any tracking system this axis defines the target position because only when the electrical axis is on the target does the tracking error voltage ideally go to zero (neglecting the servo positioning error required to maintain dynamic control). In operation, therefore, the position of the electrical axis is the true reference.
- 2) The Optical Axis of The Antenna Reflector-feed System. This axis, determined by a theodolite or other optical instrument mounted on the antenna, is the reference during the calibration data collect mode.
- 3) The Mechanical or Read-out Axis. An encoder on the scanner shaft in the above described system defines this axis.

The required calibration data consists of the angular difference between the actual position of the electrical tracing axis defined by the optical axis during the data collect mode, and its position as indicated by the mechanical axis read-out device.

Before describing the data collect mode of operation, it should be pointed out that there is a definite relation between the motion of the beam in space and the motion of the scanner called the "microwave ratio, N ". This ratio determines the mechanical angle through which the scanner must rotate to move the beam in space through a specified angle. In an ideal tracking radar of the type described, this ratio is maintained a constant at every increment of scan. It is fundamentally system defects, which upset this ratio from point to point in the scan of a real radar, that the auto-calibration system (ACS) is designed to correct.

Normally, to calibrate the organ pipe scanner-lens system, a zero scan angle reference position is established by optically aligning the antenna system to a marker located in the far field. This marker may be a pair of crosshairs on a corner reflector.

Next, the tracking loop is closed and the scanner allowed to come to rest on the target (the corner reflector). At this point, the electrical and optical axes are coincident. The mechanical axis encoder is then set to zero, and the zero scan angle reference is determined.

When the antenna platform on which the antenna is mounted is rotated through an angle θ , the scanner in an ideal system moves through an angle $N \theta$ (in the opposite direction) to keep the electrical axis on the target (where N is the microwave ratio, previously defined).

However, due to system defects, the scanner in a practical system actually moves through an angle $N \theta + e$, where e is the error in the scanner angle relative to the beam angle. Therefore, to get the angular error in the encoder reading, the platform angle θ must be multiplied by the microwave ratio N and subtracted from the indicated encoder reading. This procedure can be continued at as small increments of θ as required throughout the whole scan range of the system to obtain a set of calibration data.

The relationship between the target (or mount) angular position and the scanner angle for two cases is shown in Figure 2: (1) the ideal system; (2) the real system.

For the ideal system the target position and scanner angle are linearly related by a straight line, the slope of which is $1/N$. For simplicity the relationship for the real system is assumed to be sinusoidal, though it need not be mathematically definable as long as it is continuous, as it must be in the real system.

To automate this operation a precision motor drive and encoder to read the angle θ on the azimuth platform must be incorporated. A simple computer (part of the antenna system) can be used to perform the indicated calculations. The calibration data is then stored on a memory drum as a digital word representing the angular error, e . The drum address is $N \theta$, the correct scanner angle representing the true target position.

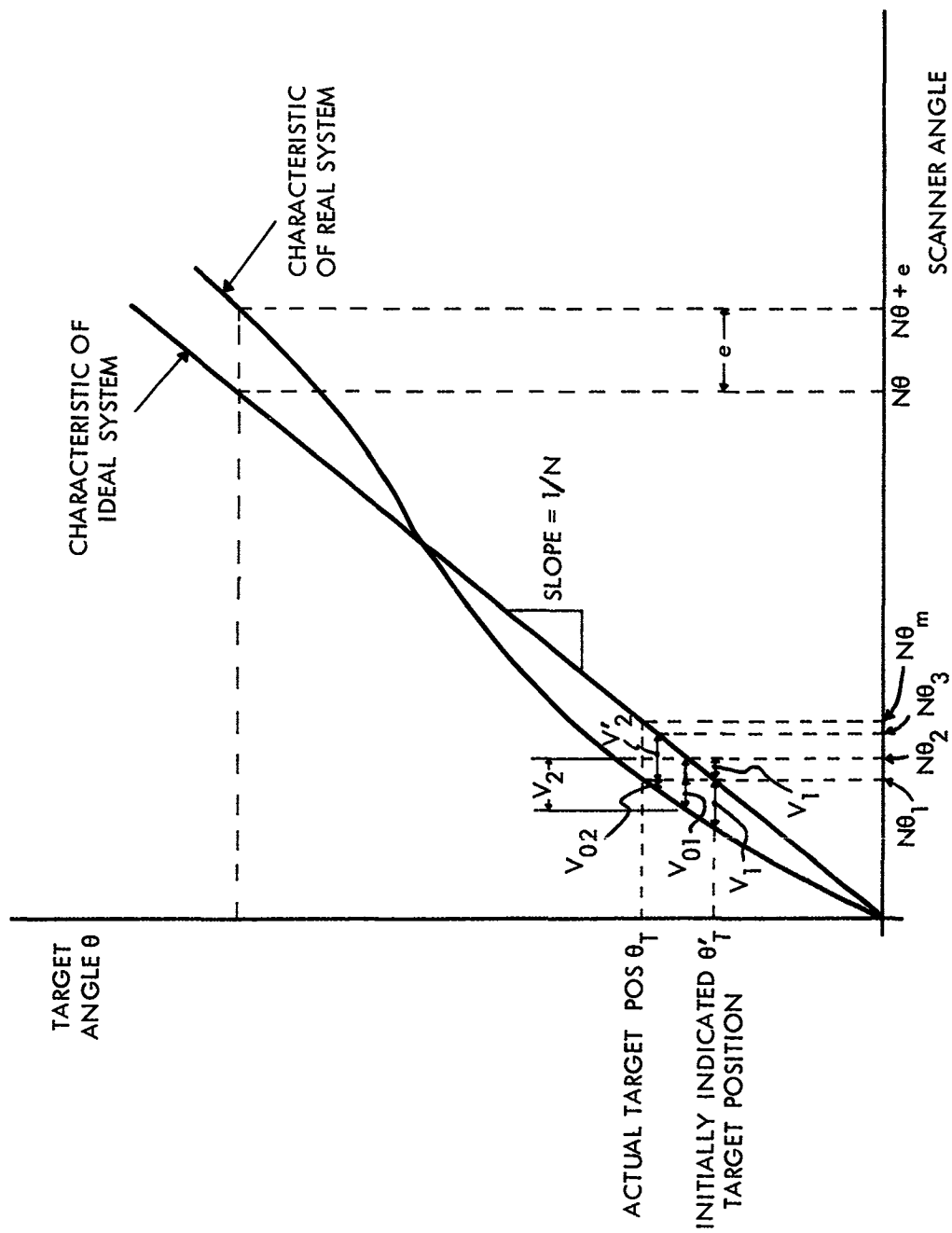


Figure 2. Target Angle Versus Scanner Angle

One method for implementing the data collect mode is shown in Figure 3. The mount encoder (1) angle θ is fed to a digital computer (2) where it is multiplied by the microwave ratio N . Into this computer is also fed two other inputs: The scanner encoder (3) angle $N\theta + e'$; the monopulse angle $N\psi + e''$. The symbol e' represents that part of the total error e which occurs in the encoder reading; e'' is the error in the voltage at the output of the monopulse system (4) error detector. This voltage represents a specific angle in terms of the known transfer function of the system. It is converted to digital form in the A-D converter (5). The sum of $N\phi + e'$ and $N\psi + e''$ is $N\theta + e$, previously defined. Subtracting from this sum, the mount angle $N\theta$ gives the total error e subject to ACS correction. This error is stored on the magnetic drum (6) under the address of the true target angle.

It should be noted that were the data collection operation performed slowly enough, the scanner would come to rest before each calibration point is obtained. In this case, the total error e would exist in the encoder reading and the residual error voltage would be essentially zero, with only the servo positioning error, which ACS does not correct, remaining. However, so that the minimum data collect operation time is not limited by this requirement, data is collected and stored as fast as the drum storage rate allows. Several hundred points can be collected and stored in approximately one minute. Under these conditions, the scanner does not come to rest. Consequently, a residual error voltage which must be included in the data is present.

CORRECTION MODE

The calibration data having been obtained, it is now necessary to use it in an appropriate manner to correct the indicated target position in real time.

One obvious approach is to use the stored data to correct the azimuth encoder reading. However, it can be shown that in some cases this removes the error, and in others it adds it in part or in total.

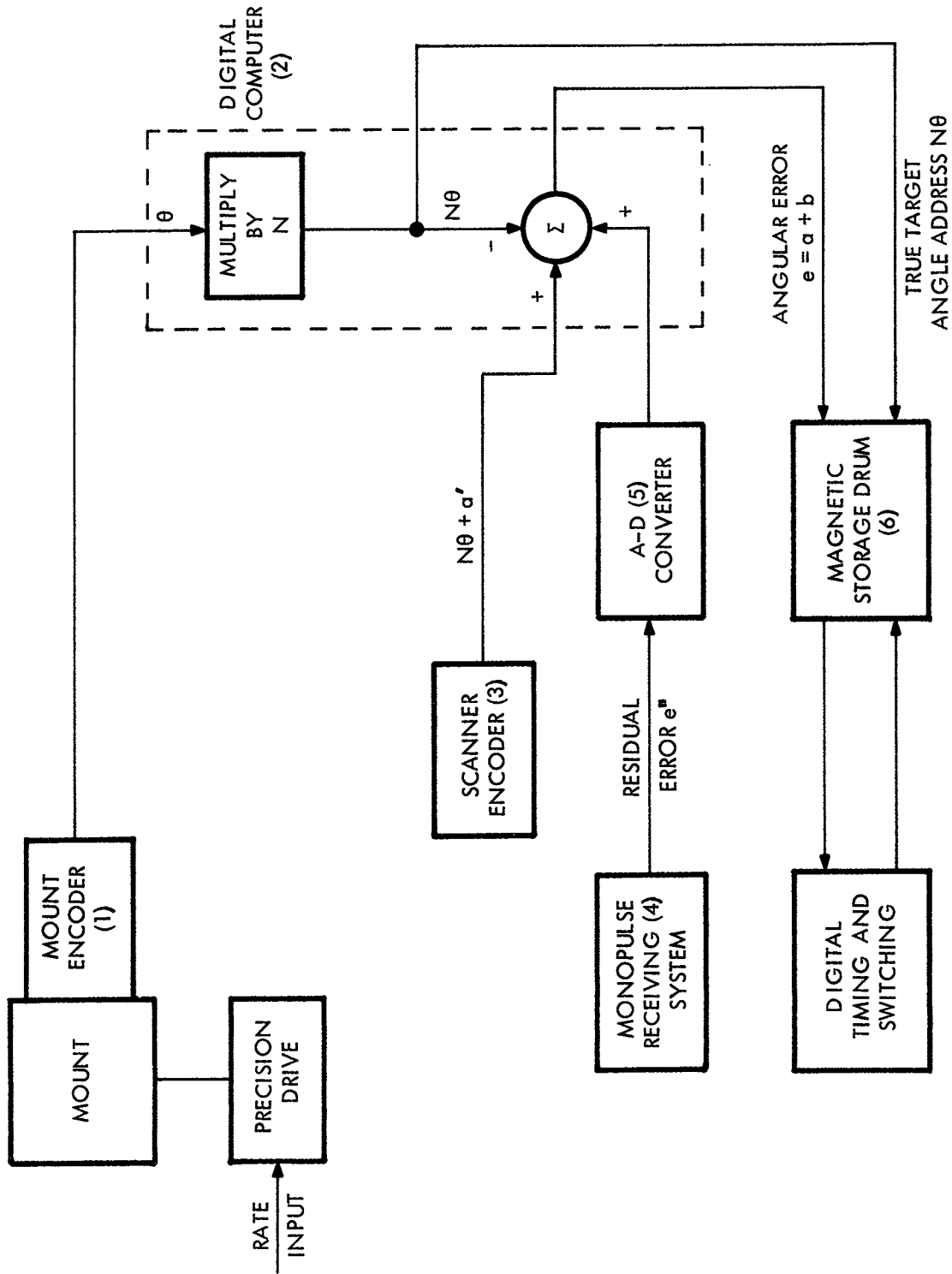


Figure 3. Data Collect Mode Block Diagram

For example, consider a target coming in along the system boresight. The scanner is essentially in one position and the total system error will show up in the encoder reading. The scanner is "at rest". Using the stored data to correct the scanner encoder reading in this case removes the error.

A second operational situation is one in which a target is moving tangentially to the system boresight at a relatively short range. Under these conditions, the scanner is rotating rapidly. Due to system defects in the organ pipes and other parts of the antenna system, the error voltage at the input to the scanner servo system (at the receiver output) can fluctuate at a high rate.

However, since the servo bandwidth is generally of the order of a few cps as determined by the lowest resonant frequency in the structure, this high frequency error will not pass through the servo. Since it is filtered out, it will not show up in the scanner encoder reading. The encoder reading is incorrect only by the bias or average error. Thus, if the stored data is used to correct the encoder reading in this case, a large part of the system error will be added to the indicated target position.

To avoid this problem the correction scheme shown in Figure 4 is used. The stored data from the magnetic drum (1) is converted in a D-A converter (2) to a voltage which, in terms of the known receiver system transfer function, represents the angular error e . This voltage is then summed at the scanner servo (3) input with the error voltage from the monopulse receiver (4) error detector. The output of the monopulse receiver is an error voltage representing the angle $N\theta + e$ previously defined. (Note that the servo positioning error δ is neglected since ACS does not correct this quantity.) The drive voltage actually applied to the input terminals of the servo is that required to obtain the correct angular position of the target in the scanner encoder (5) reading. In substance, the beam has been forced off the target the amount of the angular error so that the scanner encoder always reads the correct angle. This angle can then be used to address the magnetic drum, since the true target angle is the required address, as explained previously.

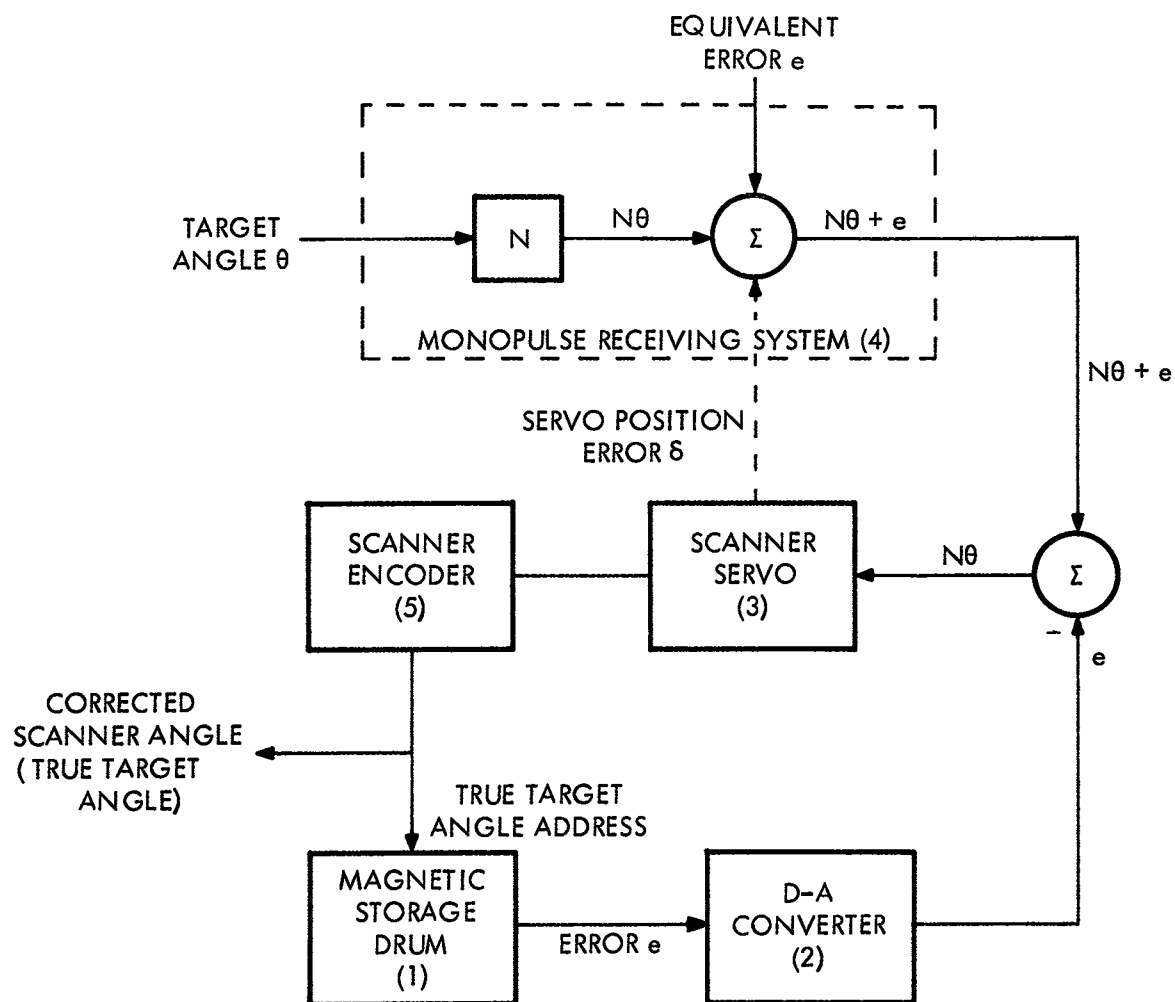


Figure 4. Correction Mode Block Diagram

In the steady state, the scanner encoder does in fact, read the correct angular position of the target. Referring again to Figure 2, let us assume that the scanner angle is $N \theta_1$, when the radar initially locks-on the target and before any correction is applied. This scanner angle corresponds to an indicated target position θ'_T . However, due to the system defects, this initial reading is in error. The true target position is θ_T in Figure 2.

Before any correction is made, the electrical axis (beam) is on the target, and the servo driving voltage from the monopulse receiver is, therefore, zero (neglecting the servo positioning error δ required for dynamic control).

Addressing the magnetic drum containing the calibration data with the scanner angle reading $N \theta_1$, (assumed to be the true target angle) we obtain an angular correction e_1 . The voltage V_1 corresponding to the angular correction e_1 is applied to the servo input as explained previously, moving the scanner to $N \theta_2$.

Since the beam has been forced off the target by the driving voltage V_1 , a voltage V'_1 from the monopulse receiver now exists at the input to the servo in addition to the correction voltage V_2 corresponding to the encoder error e_2 at $N \theta_2$. The voltage V'_1 acts to drive the scanner back toward the original $N \theta_2$ reading. Hence, V'_1 subtracts from V_2 leaving the net driving voltage V_{D1} in Figure 2. This process is repeated until the correction voltage V_n from the drum and the voltage V'_m from the monopulse receiver are arbitrarily close in magnitude as well as opposite in phase.

From Figure 2, the desired condition in which the scanner encoder reading represents the true target position occurs when $|V_n|$ and $|V'_m|$ are equal. The difference between these two in the steady-state condition is determined by the rate at which the correction is made. It may, therefore, be made arbitrarily small.

As long as the slope in the error curve of Figure 2 does not reverse (go negative), there is no ambiguity or instability in the ACS operation. If the slope does reverse, a given target position then corresponds to two different scanner angles. In this case, an ambiguity does clearly exist, and oscillation can occur.

However, a slope reversal means that the scanner (of any type) can move in the direction opposite to the normal direction for the beam motion. For example if the beam (target) moves toward the zero scan angle, the scanning mechanism indicates an increase in the beam scan angle. For this to happen, system defects would have to generate an error in the scanner reading which is larger in magnitude (as well as opposite in direction) than the beam motion itself. In any real system which is properly designed, an error characteristic of this magnitude is not very likely. For the original application this possibility was investigated and found not to be a problem. Clearly, a slope reversal in the error characteristic of any system is a serious problem which should be corrected whether or not auto-calibration is to be used.

It should be noted that a false crossover with a sidelobe is not a consideration in this case since the second null it produces is sufficiently far away that, once the radar has locked-on properly, it is not a source of ambiguity. The concern here is with slope reversals that occur within fractions of a mil of beam motion. The false crossover presents a problem in initially locking-on properly.

CONCLUSION

The auto-calibration system is designed to remove the effects on the indicated target position of a tracking radar of electrical and mechanical defects in the system. Since the data collection operation can be performed in approximately one minute after referencing the encoder at zero scan angle, ACS can be used to correct not only initial system defects, but also changes in the system that occur over a period of time such as temperature and aging effects.

The following items represent some of the general types of errors that can be corrected by the auto-calibration system:

- 1) Pre-comparator RF asymmetries in the organ pipe scanner and lens system (or the corporate feed and phasing system of an array)
- 2) Post-comparator electrical asymmetries
- 3) Monopulse comparator defects
- 4) Antenna aperture defocusing errors in both the distributed aperture and array
- 5) Mechanical defects in the reflector over which the beam is scanned (or the array elements are mounted) as well as other structural deformations in the antenna system
- 6) Changes in the above due to temperature gradient changes
- 7) Changes due to equipment aging
- 8) Changes due to a new operating frequency

While ACS has been described in terms of a particular antenna configuration for clarity, it is by no means limited to this system. As pointed out, the array is another example of an antenna system in which ACS can be effectively used. The technique is generally applicable to any tracking radar antenna system where the degree of sophistication makes it either impossible or prohibitively costly to build the required accuracy into the antenna system.

ACKNOWLEDGEMENT

The writer expresses his appreciation to Mr. William Humphrey of the Servo Department who was instrumental in detailing the block diagrams in that area.

- 1) Pre-comparator RF asymmetries in the organ pipe scanner and lens system (or the corporate feed and phasing system of an array)
- 2) Post-comparator electrical asymmetries
- 3) Monopulse comparator defects
- 4) Antenna aperture defocusing errors in both the distributed aperture and array
- 5) Mechanical defects in the reflector over which the beam is scanned (or the array elements are mounted) as well as other structural deformations in the antenna system
- 6) Changes in the above due to temperature gradient changes
- 7) Changes due to equipment aging
- 8) Changes due to a new operating frequency

While ACS has been described in terms of a particular antenna configuration for clarity, it is by no means limited to this system. As pointed out, the array is another example of an antenna system in which ACS can be effectively used. The technique is generally applicable to any tracking radar antenna system where the degree of sophistication makes it either impossible or prohibitively costly to build the required accuracy into the antenna system.

ACKNOWLEDGEMENT

The writer expresses his appreciation to Mr. William Humphrey of the Servo Department who was instrumental in detailing the block diagrams in that area.

**BORESIGHT ERRORS IN THE NEAR
FIELD OF A MONOPULSE ANTENNA**

(RAC 1725)

by

**Peter R. Zuzolo
Stanley J. Jurczak
and
Joseph A. Castrigno**

prepared for

**The Thirteenth Annular Symposium on
U. S. A. F. Antenna Research and Development
University of Illinois
Monticello, Illinois
15 to 18 October 1963**

**Republic Aviation Corporation
Engineering Division
Farmingdale, New York**

ABSTRACT

A requirement for the order of magnitude of boresight errors in the near field of a monopulse antenna indicated that this data was not available. All previous near field work uncovered was related to amplitude, phase or pattern type measurements. Therefore, measurements were made on a four horn phase comparison monopulse X-band antenna. This permitted accurate determination of the apparent shift in the elevation channel null as a function of test antenna separation.

These boresight errors were determined at the 125 foot free space boresight range of Republic Aviation Corporation. Antenna separation was successively reduced from the 125 foot maximum (far field) to 6 feet (near field). Therefore, the monopulse antenna was checked in the Fraunhofer, Fresnel and near field regions. The accepted far field distance criteria for boresight measurements is $D^2 \lambda^{-1}$ which in this case is 38.4 feet. Similar data was taken utilizing an anechoic chamber with a maximum antenna separation of 50 feet. The test measurement accuracy varied from 0.08 milliradians at 125 feet to 0.8 milliradians at 6 feet.

The data indicates that boresight errors increase with decreasing antenna separation and with increasing elevation angle. The data from the anechoic chamber relative to the free space range also indicates that the boresight errors increase with increased reflections. The measured boresight error variation is compared to calculated values. The actual far field requirement is a function of the boresight error accuracy required for the particular test being conducted. The $D^2 \lambda^{-1}$ criteria has been correlated to a boresight error in the order of 1.0 milliradian.

A. INTRODUCTION

Monopulse radar antennas utilize phase and amplitude information to determine the direction of arrival of target data. When the target is in the far field, a plane electromagnetic wave is incident on the antenna. In conducting various tests, however, it is often difficult or impossible to illuminate the antenna with a plane wave. Various criteria have been established setting acceptable test antenna separations to insure accuracy of results. Boresight error tests were conducted in order to obtain data within the established antenna separation criteria.

These tests were performed in support of an engineering program to develop a radar tester suitable for flight line use. Space limitations prohibit the use of such a tester in the far field of the monopulse radar antenna. Since any testing must be conducted in the near field, knowledge of the boresight errors which may be encountered is essential. The tests conducted were basically to determine the boresight errors as the test distance was reduced from the far field region into the near field region. This report describes the results and analysis of these minimum distance tests conducted on both a free space range and in an anechoic chamber. Work was done under contract number AF 33(600)-40838.

B. EXPERIMENTAL PROCEDURE

The evaluation of boresight error was accomplished by measuring the elevation channel null shift of the monopulse antenna on both a free space range and in an anechoic chamber. The azimuth channel null was continuously monitored to assure alignment in the azimuth plane. The free space tests were conducted on Republic's fifteen hundred inch boresight range. This range, instrumented to perform various tests on antennas and radomes, is located at the Antenna/Radome Laboratory in an area free of obstructions. The anechoic chamber tests were conducted in a sixteen foot by sixteen foot by

forty foot microwave absorbent material lined chamber located in the Engineering Research Laboratory. Boresight error was measured as the distance between the monopulse and test antennas was reduced from the far field to a six-foot separation, well within the near field.

1. Free Space Range

Tests conducted on the fifteen hundred inch boresight range utilized a C. T. I. three-axis fixture adjustable to within one milliradian on each axis for holding the monopulse antenna. A Craigg Systems portable tower adjustable in elevation and azimuth was used to hold the test antenna. A standard gain horn was used on the tower. Transmission could not be accomplished from the test antenna due to large cable length losses and the unwieldiness of moving the transmission equipment with the portable tower. The monopulse antenna was used for transmission through the elevation difference channel. In normal radar system operation, this channel is used only as a reception channel. However, since bilateral components are used in the antenna feed system and the theorem of reciprocity insures identical results, transmission through the elevation channel is valid. Figure 1 illustrates how the sidewall couplers, topwall couplers and phase shifters deliver equal power to the four horn feed system (A, B, C, D) with 180 degree phase difference between the two top (B, C) and bottom horns (A, D). This is required to produce the two oppositely phased elevation channel lobes and central null on a transmission basis.

To insure a minimum effect of ground reflections, antenna elevation angles (θ) were varied from the horizontal boresight axis in an upward direction. Data was taken every one-half degree for elevation angles from zero to six degrees. At low angles, ground reflections were minimized by a triangular scattering mound of earth between the laboratory building and the tower.

The monopulse radar antenna was first calibrated and adjusted at a distance of 125 feet from the test antenna until the indicated boresight error was less than 0.1 milliradians. This is within the accuracy of the CTI

Boresight System. The location of the elevation null was tracked by moving the test horn on the tower in a vertical plane. This method was utilized since it is a standard boresight test practice to check errors in a vertical plane. The errors introduced by not moving on a sphere are less than the errors introduced by system inaccuracies (reference 11). The test instrumentation is shown in figure 2. Data was taken for antenna separations (R) of 125, 50, 30, 20, 15, 12, 10, and 6 feet. The distance of 125 feet falls between the range of $2D^2/\lambda$ and $4D^2/\lambda$ which is well within the far field. The distance of 50 feet falls between the range of D^2/λ and $2D^2/\lambda$ which is well within the boresight test distance criteria. The distances of 20 and 30 feet fall between the D^2/λ and $D^2/2\lambda$ range. The distances of 15, 12, and 10 feet fall between the $D^2/2\lambda$ and $D^2/4\lambda$ range. These last five distances can be considered as being within the transition region (defined in section D). The distance of 6 feet is well within the $D^2/4\lambda$ criteria of the Fresnal region. Therefore, a well represented sampling was tested for all regions.

2. Anechoic Chamber

The same procedures described above were utilized for the anechoic chamber tests. The standard gain horn was mounted on a smaller tower in order to position it in the center of the chamber. The first test, conducted at a separation (R) of 50 feet, was performed with the monopulse antenna placed 20 feet away from the mouth of the chamber. Subsequent tests, at distances of 30, 20, 15, 12, 10, and 6 feet were performed with the monopulse antenna at the mouth of the chamber. The standard gain horn and its supporting tower were moved forward from the rear wall of the chamber.

The anechoic chamber is lined with ECCOSORB type FR-340 absorbent material. At X-band frequencies, the maximum reflected power is 0.035 percent which is greater than or equal to -35 DB. However, more reflections were encountered in the chamber than on the free space range. This effect, visible as increased boresight error, is evident in the data.

C. EXPERIMENTAL RESULTS

Boresight error is defined as the angular difference between the expected location of the elevation null as determined by geometrical considerations and the actual null location as detected in the standard gain horn. The motion of the horn in tracking the null was measured to within one-eighth of an inch. This corresponds to a test accuracy of 0.08 milliradians at 125 feet and 0.8 milliradians at 6 feet. The angular location of the null was found by a trigonometric calculation knowing the antenna separation and the displacement of the test horn from a horizontal reference. The reference was set at that height of the test antenna when the monopulse antenna was at zero degrees elevation. The data is presented as boresight error versus separation as a function of elevation angle:

In general, boresight errors increased with increasing elevation angle (θ) and decreasing separation (R). The free space data shows a variation of error at 6 feet separation from +0.75 milliradians at θ equals zero to +25.5 milliradians at θ equals six degrees. At R equals 50 feet, the maximum variation is from -1.0 to +0.3 milliradians. This variation may be attributed primarily to measurement inaccuracies. The anechoic chamber data shows corresponding variations of 30.5 milliradians and 7.0 milliradians, a combined effect of measurement inaccuracies and reflection variations.

Free space data is plotted in figures 3, 4, and 5. Those curves which varied in an identical fashion are grouped together for ease of interpretation. Anechoic chamber data is plotted in figures 6 and 7.

D. THEORETICAL ANALYSIS

The monopulse antenna tested utilizes both amplitude and phase information to obtain target data. Therefore, the following analysis will consider both phase and amplitude effects as related to the test distance criteria.

The horizontally polarized antenna tested is a linearly polarized electric field system. Therefore, the electric field components can be described in the

spherical coordinate system (R, θ, φ) with the origin $(0, 0, 0)$ at the antenna aperture vertex. For the main pencil beam transmitting lobe the radial component is represented by the following relationship.

$$E_R = \frac{P}{2\pi\epsilon} f(\cos \theta, \sin \varphi) e^{-j\beta R} \left(\frac{1}{R^3} + \frac{j\beta}{R^2} \right)$$

The normally polarized azimuthal component is then given by

$$E_\varphi = \frac{P}{2\pi\epsilon} f(\sin \theta, \cos \varphi) e^{-j\beta R} \left(\frac{1}{R^3} + \frac{j\beta}{R^2} - \frac{\beta^2}{R} \right)$$

and the cross-polarized elevation component is given by

$$E_\theta = \frac{PK}{2\pi\epsilon} f(\sin 2\theta, \sin 2\varphi) e^{-j\beta R} \left(\frac{j\beta}{R^2} - \frac{\beta^2}{R} \right)$$

where ϵ is the permittivity of the propagating medium (in this case free space)

β - is the propagation constant and equal to $2\pi/\lambda$

p - is the electric dipole moment

R - is the radial distance from the aperture

θ - is the elevation angle from the aperture

φ - is the azimuth angle from the aperture

f - is the antenna aperture distribution function

K - is a constant with a value less than unity

These components can be divided into three regions as a mathematical function of the distance R .

a) The static field - This field is composed of the inverse cube law terms (R^{-3}). They are familiar quantities of electrostatics and DC theory.

b) The induction field - This field is composed of the inverse squared law terms (R^{-2}). They are the quasi-stationary state values encountered in AC theory. In this region the velocity of propagation of electromagnetic energy is assumed to have an infinite value.

c) The radiation field - This field is composed of the inverse first power law termed (R^{-1}). This is the area of retarded electromagnetic action where the velocity of propagation is a finite constant quantity.

At large distances, where the (R^{-3}) and (R^{-2}) terms become negligible so that the (R^{-1}) term predominates, the radiation field is defined as the far field of the far zone. In optical terms, this region is called the Fraunhofer region where the field is a quasi-point source field characterized by a cone of divergent rays. In the vicinity of the antenna aperture, all three terms are present and defined as the near fields of the near zone. In optical terms, this is the Fresnel region where a column of parallel rays propagate geometrically from the aperture.

1. Phase Errors

Utilizing a geometrical-optical approach, the Fresnel region is also defined as the region where the aperture can be divided into half-wavelength annular Fresnel zones. The distance at which the entire aperture appears as one Fresnel zone occurs at

$$R = \frac{D^2}{4\lambda}$$

where D is the maximum physical aperture dimension and λ is the wavelength of the operating frequency.

But this limit of the Fresnel region can not be taken as the beginning of the far field or Fraunhofer region. For at this distance, the contributions from the edge of the aperture are 180 degrees out of phase with that from the center. The Fraunhofer region assumes that the path differences between points on the aperture to the distant point are negligible. This region separating the Fresnel and Fraunhofer region is known as the Transition region or optically the shadow region.

This region is not however, just the superposition of the induction and radiation fields. The two contradictory interpretations of finite and infinite velocities of propagation cannot be combined rationally. The instantaneous induction field action and the retarded action of the radiation field are inconsistent. The intermediate Transition region contains a single field that obeys a complicated law.

In the Fresnal and Transition regions, all the electric field components are present. They are mutually perpendicular and differ in phase. The resultant electric vector is, therefore, neither linear nor a plane wave. It is, generally, elliptically or circularly polarized in a changing plane.

The beginning of the Fraunhofer region for test purposes is dependent upon the value of allowable errors and the type of antenna being tested. Listed in Table I are the quadratic phase errors for various values of test antenna separation (R). The generally accepted criteria for boresight measurements is at distances of (reference 1).

$$R \geq \frac{D^2}{\lambda}$$

for pattern measurements (references 4 to 12) the criteria is

$$R \geq \frac{2D^2}{\lambda}$$

for backscattering or reflectivity measurements the criteria accepted (reference 4) is

$$R \geq \frac{4D^2}{\lambda}$$

2. Amplitude Variation

The near field errors due to amplitude variations are not as pronounced as those of the phase errors. The amplitude decrease at $2D^2/\lambda$ is approximately 0.086 to 0.100 decibels (DB) at the point of maximum gain.

Across the entire aperture this variation is generally in the order of 0.25 DB. For a defocused paraboloid or antenna which has a large phase curvature, such as a horn, the error in measured maximum gain can be as great as 0.03 DB.

At a distance of D^2/λ the amplitude is decreased by 0.506 DB at the point of maximum gain. This decrease in gain is also accompanied by an increase in the minima of the side lobe structure and an increase of the side lobe maxima. Within the Fresnel zone the gain decreases from 2.5 DB at $D^2/4\lambda$ to 13 DB at $D^2/10\lambda$ the main beam bifurcates up to the region of $D^2/16\lambda$ where the gain is reduced to 17 DB.

In Table I are listed the theoretical gain reduction at the point of maximum gain as compared to the theoretical gain at infinity (references 2 to 11). In general, however, for test conducted beyond D^2/λ , the amplitude errors are not the limiting test criteria. The range of test system accuracy falls between the ± 0.1 to ± 0.5 DB tolerances (reference 1).

TABLE I. THEORETICAL AMPLITUDE AND PHASE ERROR

Distance (R)	Quadratic Phase Error (degrees)	Amplitude Error (DB)
$D^2/4\lambda$	180	-2.50
$D^2/2\lambda$	90	- .80
D^2/λ	45	- .51
$2D^2/\lambda$	22.5	- .09
$4D^2/\lambda$	11.25	- .01

E. CONCLUSIONS

Monopulse radar operation is dependent upon the amplitude and phase of both the sum and difference channels. The amplitude variations for either channel are of the order of system and testing accuracy. The phase errors are the more predominate criteria. In the sum channel the one main lobe is

essentially of the same phase until the first side lobe minima. In system operation the information is generally confined to the region of the main lobe within the -3 DB points. In this area the phase errors, as well as amplitude errors are very small.

In the elevation difference channel, the two main lobes are of opposite phase with one being of the same phase as the sum channel main lobe. The crossover phase point for the elevation channel occurs at the central null region. Since boresight is defined as the position of the elevation null, any phase errors in this critical area appear as BSE. This is the quantity measured and presented, BSE due to null position shift.

Test conducted on both ranges displayed general characteristics that were common to both. As the distance was decreased from the far field into the near field, the BSE increased from zero to larger values in an exponential type curve that was modified by a sinusoidal variation. Also, except for a few random cases, the BSE increased for increased elevation angle. The errors encountered in the anechoic chamber are also generally, greater than those taken on the free-space range. This is directly related to the increased reflections encountered in the anechoic chamber. A general mathematical relationship can be expressed in the form:

$$\text{BSE} = K \sin t e^{t^1}$$

where (t) and (t^1) are functions of elevation angle (θ) , distance (r) and range reflection characteristics (Γ) , i.e.

$$t = f(\theta, \Gamma, r^{-1})$$

and

$$t^1 = f^1(\theta, \Gamma, r^{-1})$$

The data obtained at fifty feet on the free space range verifies the generally accepted boresight criteria of an antenna separation greater than $D^2 \lambda^{-1}$. The errors encountered at this distance varied from +0.3 to -1.0 milliradians which

are generally in the order of magnitude of overall system inaccuracies. The data obtained at fifty feet in the anechoic chamber indicate that the $D^2\lambda^{-1}$ criteria is insufficient when reflections are present. The boresight errors in the chamber varied a total of 7 milliradians which is entirely unsatisfactory for boresight testing.

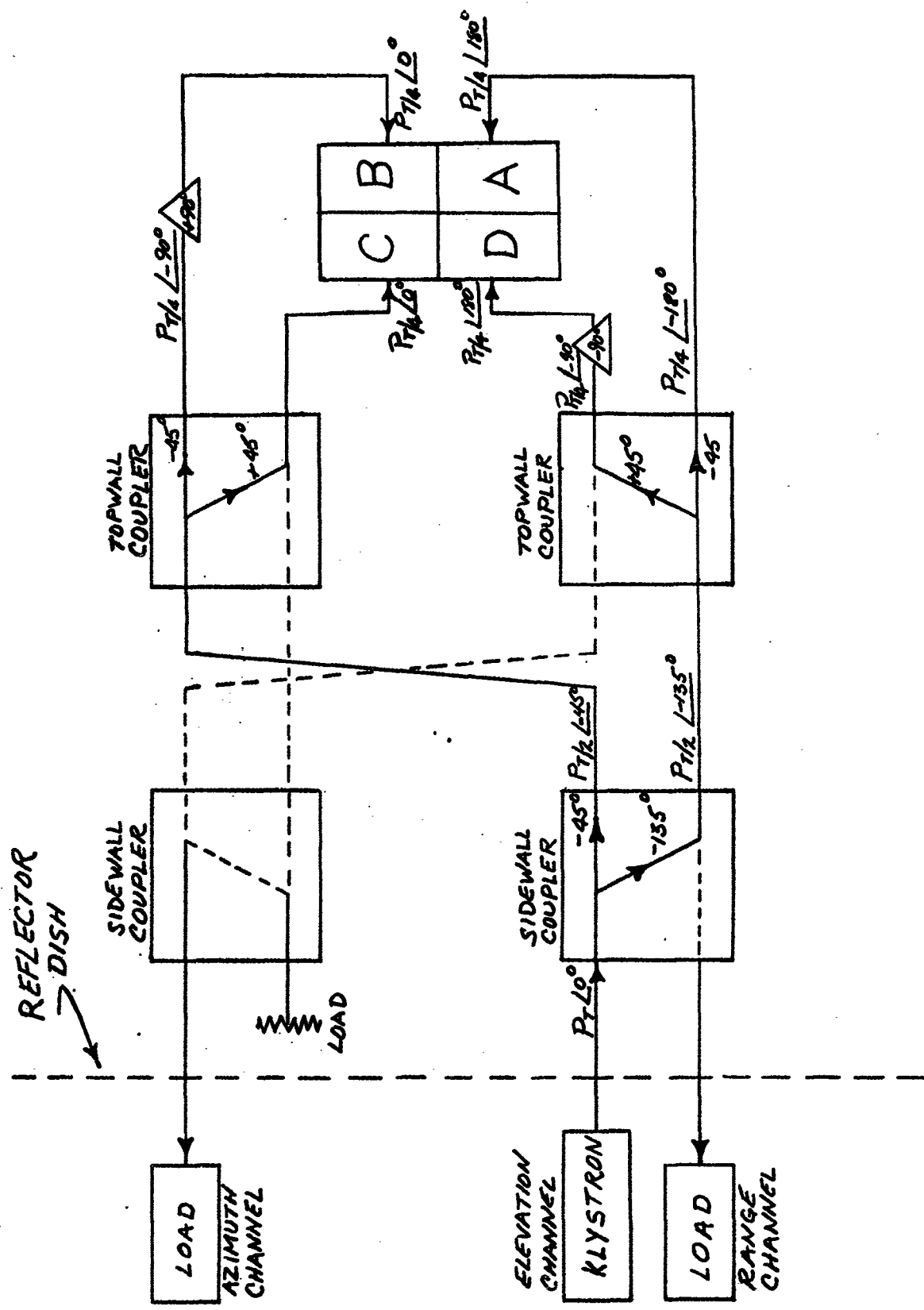
The results of the data also indicate that boresight errors in the near field of an antenna are very significant. Unless these errors are known and calibrated, radar checkout equipment operated in the near field is very impractical. Some means must be utilized to compensate for these errors. Phase correcting microwave lens are one approach that may be feasible for radar testing in the near field of an antenna.

ACKNOWLEDGEMENT

The aid of the personnel of the Republic Antenna/Radome facility proved invaluable. Special acknowledgement is given to Mr. F. Fallacaro for obtaining the data utilized in this report.

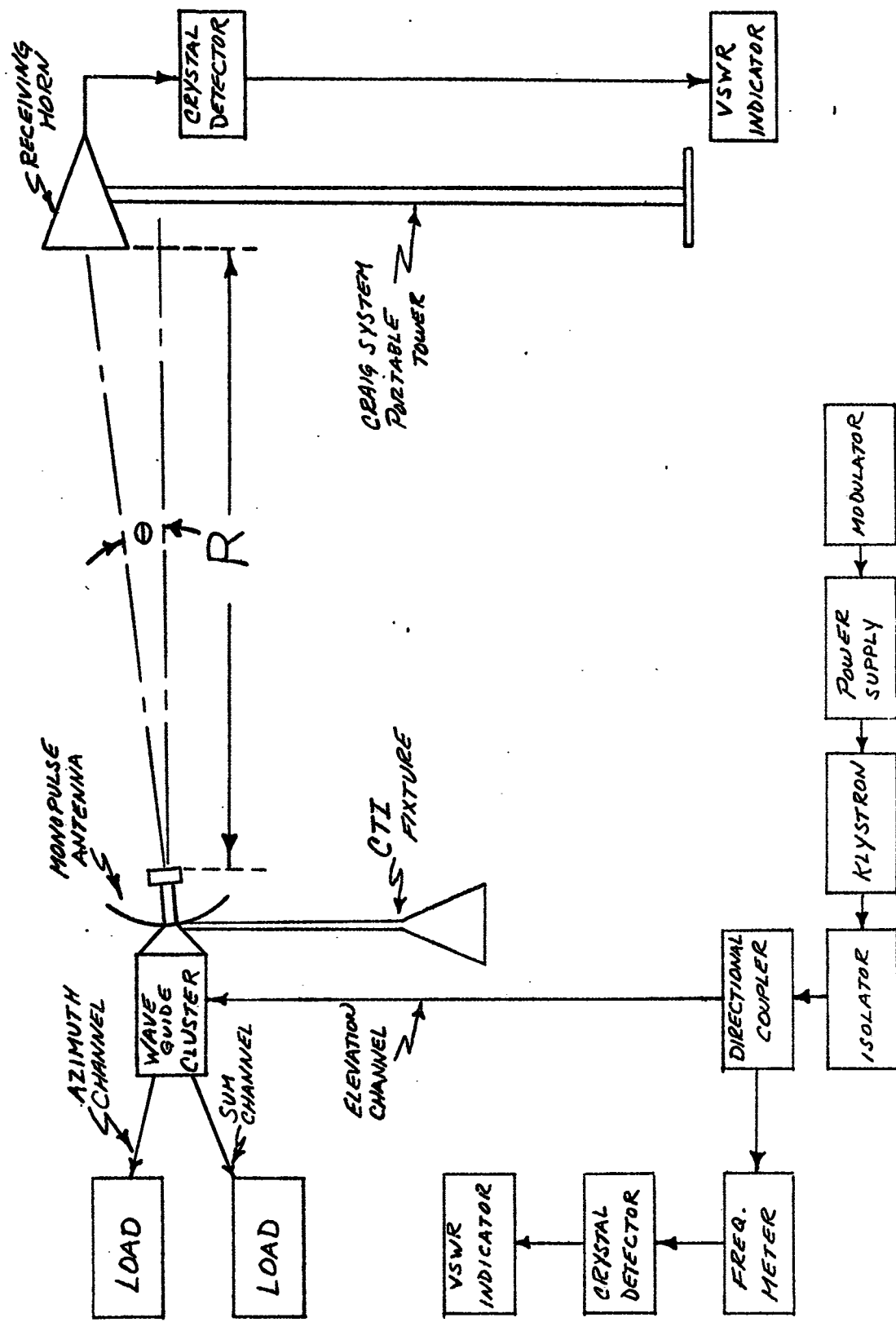
REFERENCES

1. CTI "Instruction Manual for Model 150C Boresight-Error Measuring System" dated November 1960.
2. MIT Radiation Laboratory Series Vol. 12, "Microwave Antenna Theory and Design" S. Silver dated 1949.
3. Cutler, King and Kock, "Microwave Antenna Measurements" Proceedings of IRE Vol. 35 No. 12 dated December 1947.
4. Rhodes, D.R. "On Minimum Range For Radiation Patterns," Proceedings of IRE Vol. 42 No. 9 dated September 1954.
5. Hollis, J.S. "Antenna Measurements", The Microwave Journal Vol. 3. No. 2 dated February 1960.
6. Cohen and Maltese, "The Lincoln Laboratory Antenna Test Range" The Microwave Journal, Vol. 4, No. 4, dated April 1961.
7. Hollis and Moseley, "Sitting Considerations in Microwave Antenna Measurements," Scientific-Atlanta Essay No. 3 dated August 1961.
8. Saad, T. "The Microwave Engineer's Handbook" 1961-1962 and 1963.
9. Jasik, H. "Antenna Engineering Handbook" dated 1961.
10. Sherman, John "Properties of Focused Apertures in the Fresnel Region" IRE Transactions July 1962, Vol. AP-10 No. 4.
11. McClellan, C.E., "Error Factors in the Design of Boresight-Error Measuring Equipment" Carco Electronics, 1 January 1962.



ELEVATION CHANNEL TRANSMISSION BLOCK DIAGRAM

Fig. 1



BORE SIGHT ERROR MEASUREMENTS TEST SET UP

FIG. 2

PREPARED _____

CHECKED _____

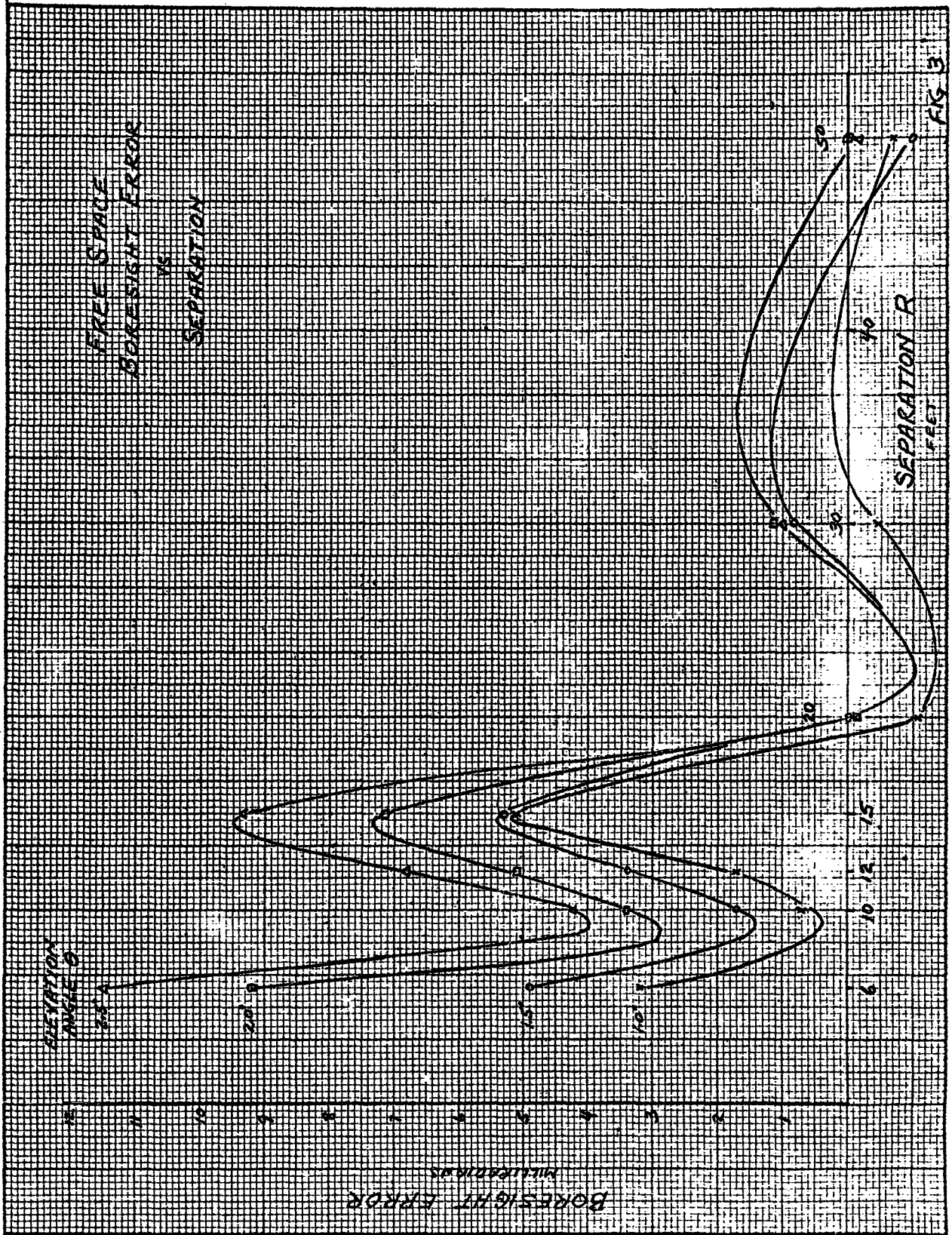
REVISED _____



PAGE _____

REPORT NO. _____

MODEL _____



PREPARED _____

CHECKED _____

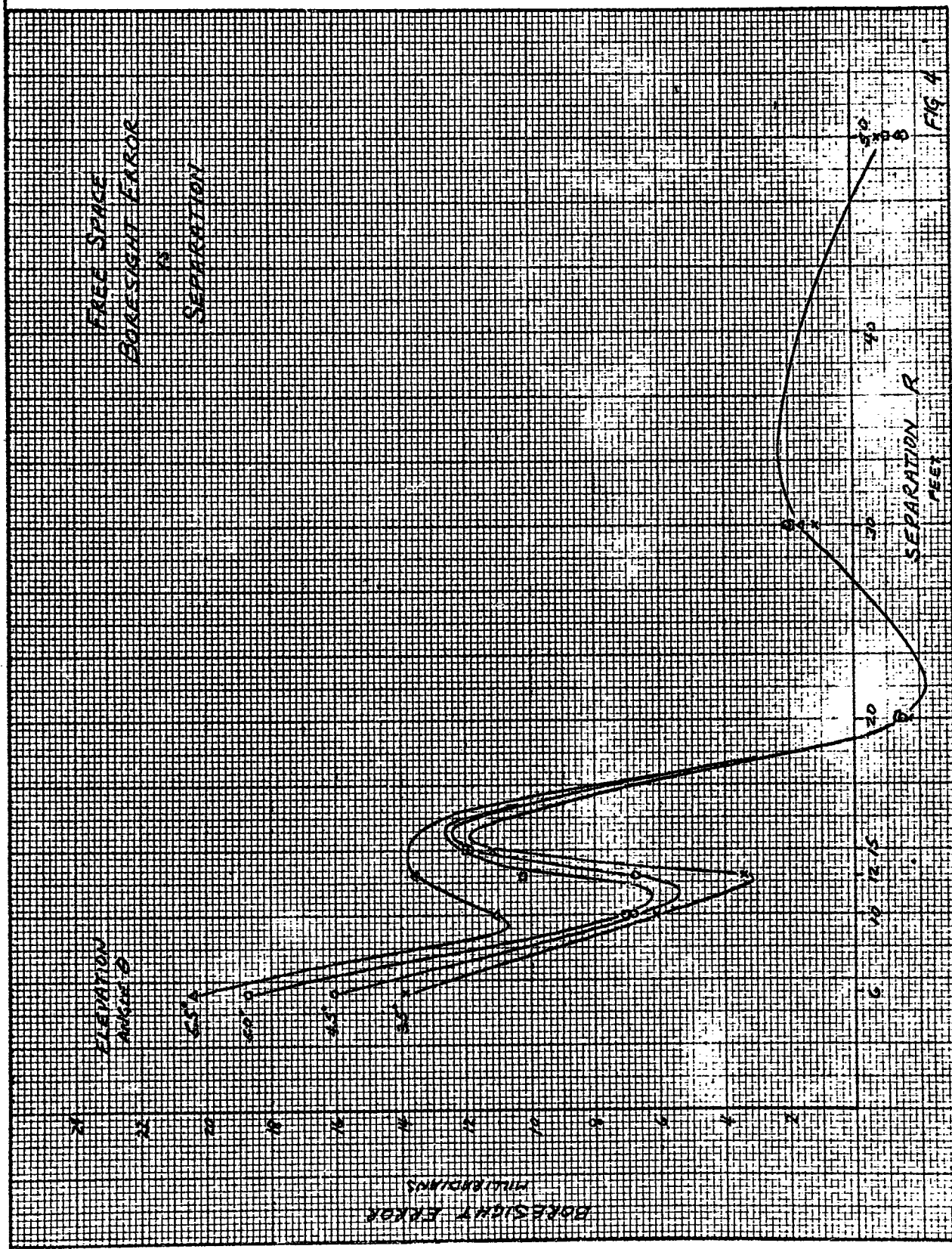
REVISED _____



PAGE _____

REPORT NO. _____

MODEL _____



PREPARED _____

CHECKED _____

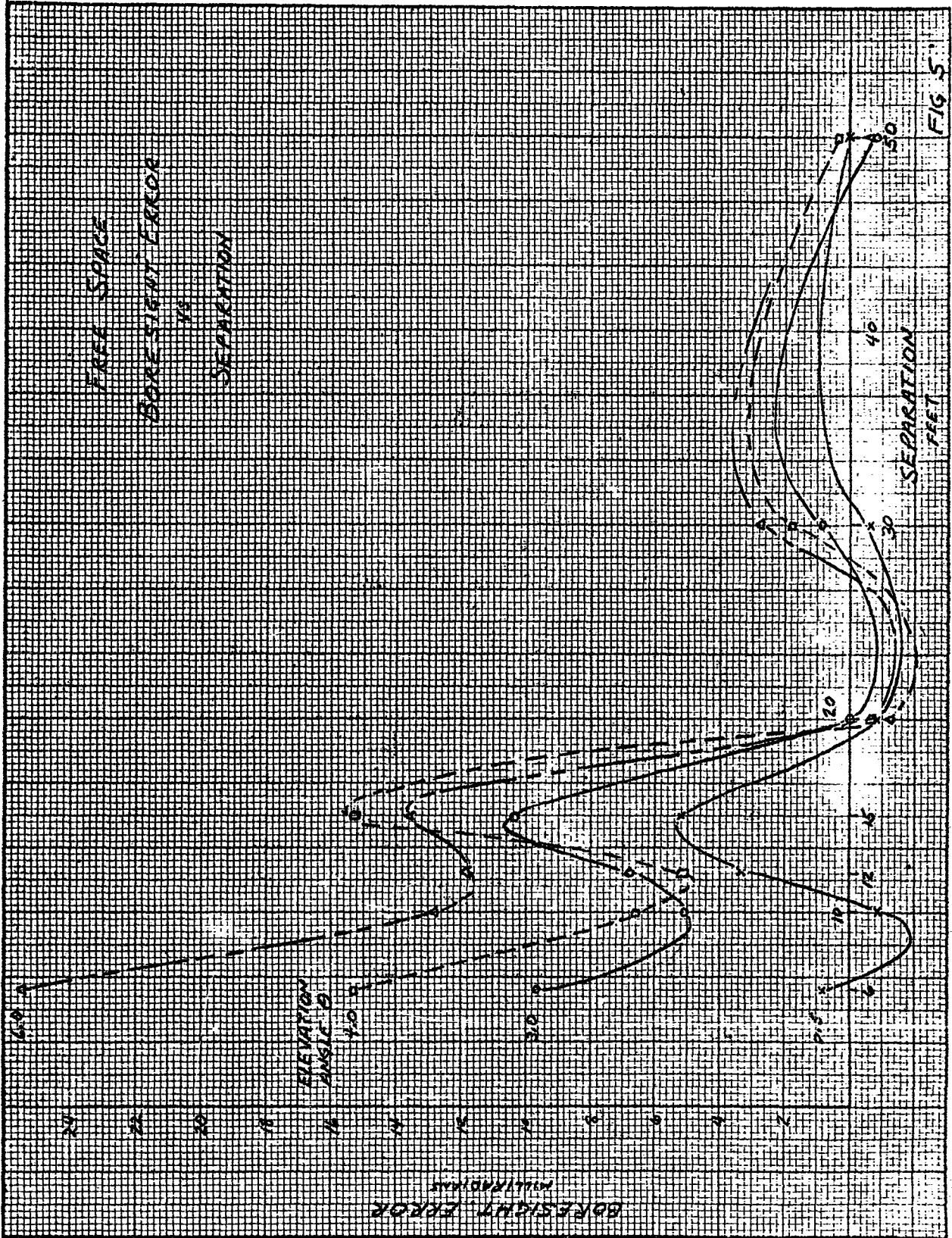
REVISED _____



PAGE _____

REPORT NO. _____

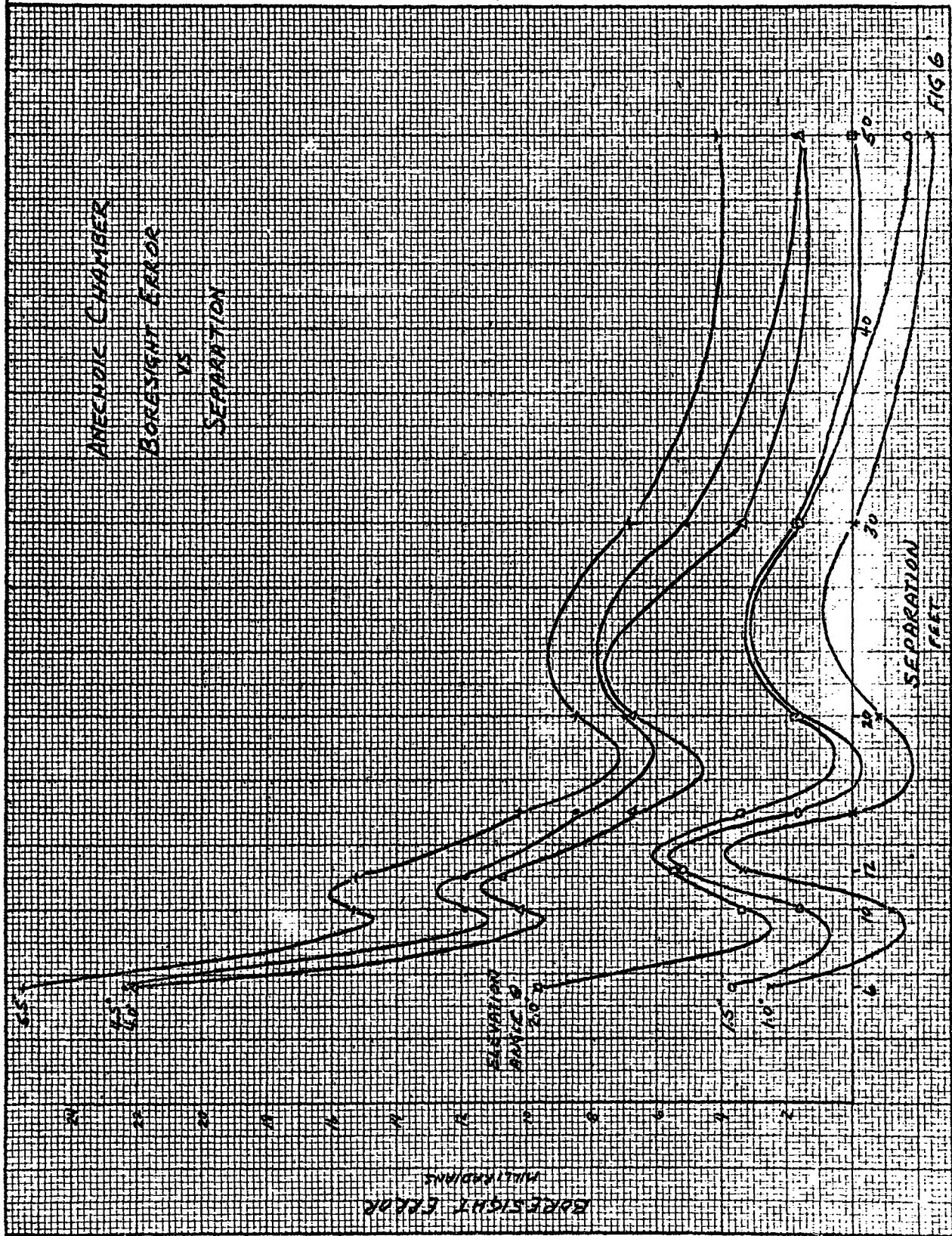
MODEL _____



PREPARED _____
 CHECKED _____
 REVISED _____



PAGE _____
 REPORT NO. _____
 MODEL _____



PREPARED _____
 CHECKED _____
 REVISED _____



PAGE _____
 REPORT NO. _____
 MODEL _____

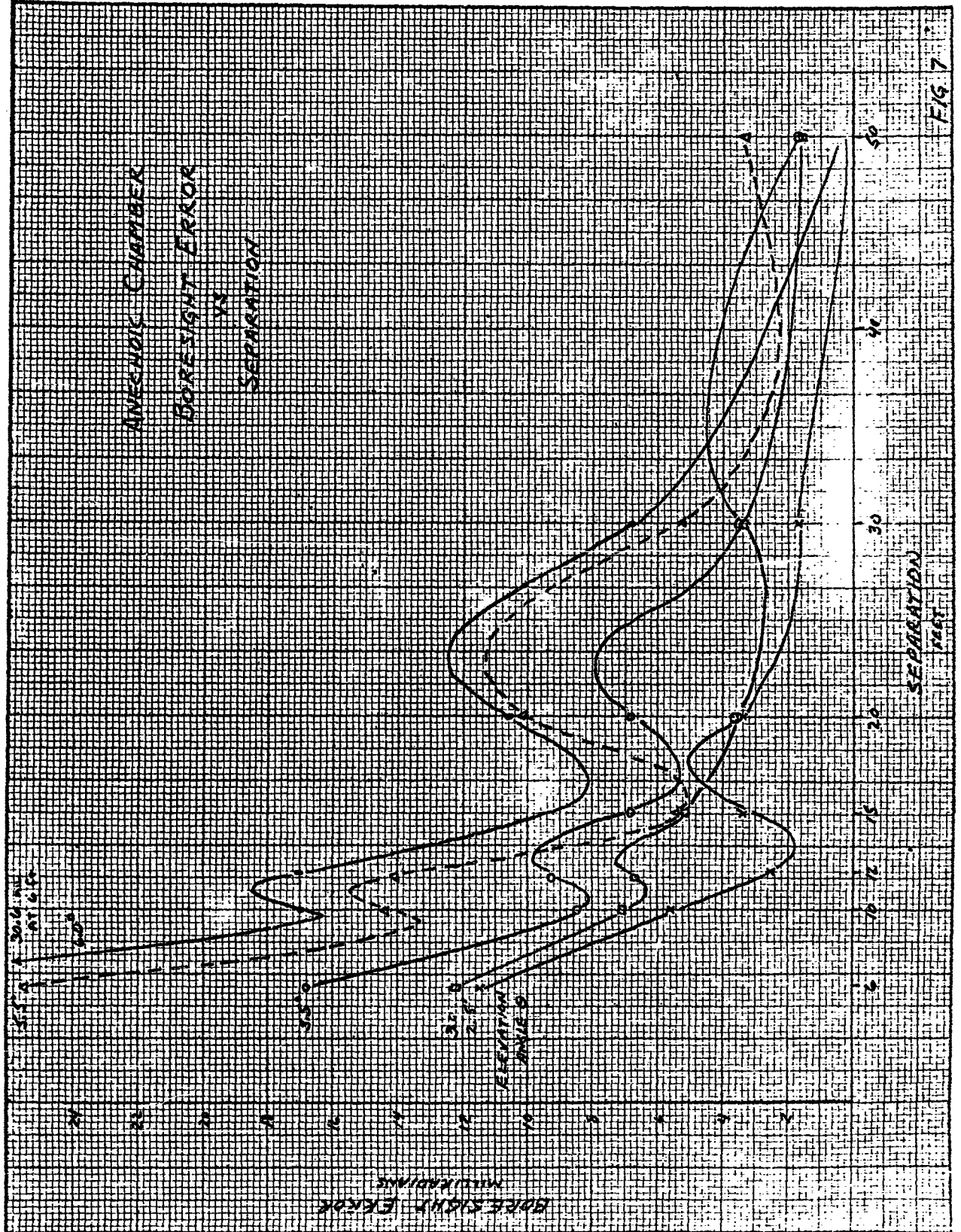


FIG 7

THE SOLUTION FOR ANTENNA ARRAY
INPUT IMPEDANCE BY THE METHOD OF
SYMMETRICAL COMPONENTS AND AN
ALTERNATING CURRENT NETWORK CALCULATOR

By
Jack W. Pool



INTRODUCTION

When two or more antennas are used in an array, the feed point impedance of each element depends upon the mutual coupling between that element and the others plus the effect of its self-impedance. Equation for finding the self-and mutual impedance of antennas in an array have been derived.¹ A set of equations that describes the terminal characteristics of antennas in an array has also been derived.² The feed point impedance may be calculated from these equations. It will be shown later that the number of equations for a given array is the same as the number of antennas used in that array, and that each equation has the same number of terms as the number of antenna elements. As the number of equations increases, the more laborious the solution becomes. There is, then, a need for some type of model or analog to represent the antenna array so that measurements may be made that yield the feed point, or input impedance, to each element.

The general forms of the equations lend themselves to a solution using the superposition theorem as applied to polyphase systems or, as it is commonly termed, the method of symmetrical components.

It is the purpose of this paper to represent the equations of arrays of thin linear antennas by an equivalent electrical network and to solve for the input impedance of each antenna in the array using the method of symmetrical components. The solution of these equations involves the use of a special purpose analog computer (a-c network calculator or analyzer) which has been used extensively in the solution of electrical power system problems involving the use of symmetrical components.

Equivalent Circuit of the Antenna Array

In order to measure the feed point impedance of an antenna in an array it is necessary to make measurements at its terminals.¹

In general, the self-impedance, Z_{ii} , of antenna is defined as $Z_{ii} = \frac{V_i}{I_i}$ when $V_a = V_b = V_c = V_j \dots = V_n = 0$. (See Figure 1)

The mutual impedance of antenna in an array is defined as $Z_{ij} = \frac{V_{ij}}{I_i}$, where V_{ij} is the open circuit voltage produced at the terminals of antenna j due to a circuit in antenna i. Since the antennas are linear and bilateral, $Z_{ij} = Z_{ji}$.³ The self-and mutual impedance of these linear antennas in an array may be calculated.

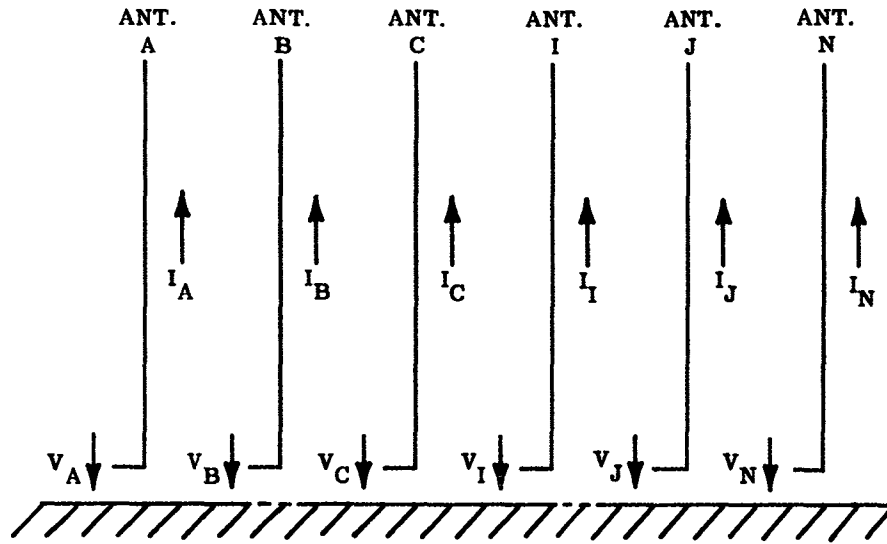


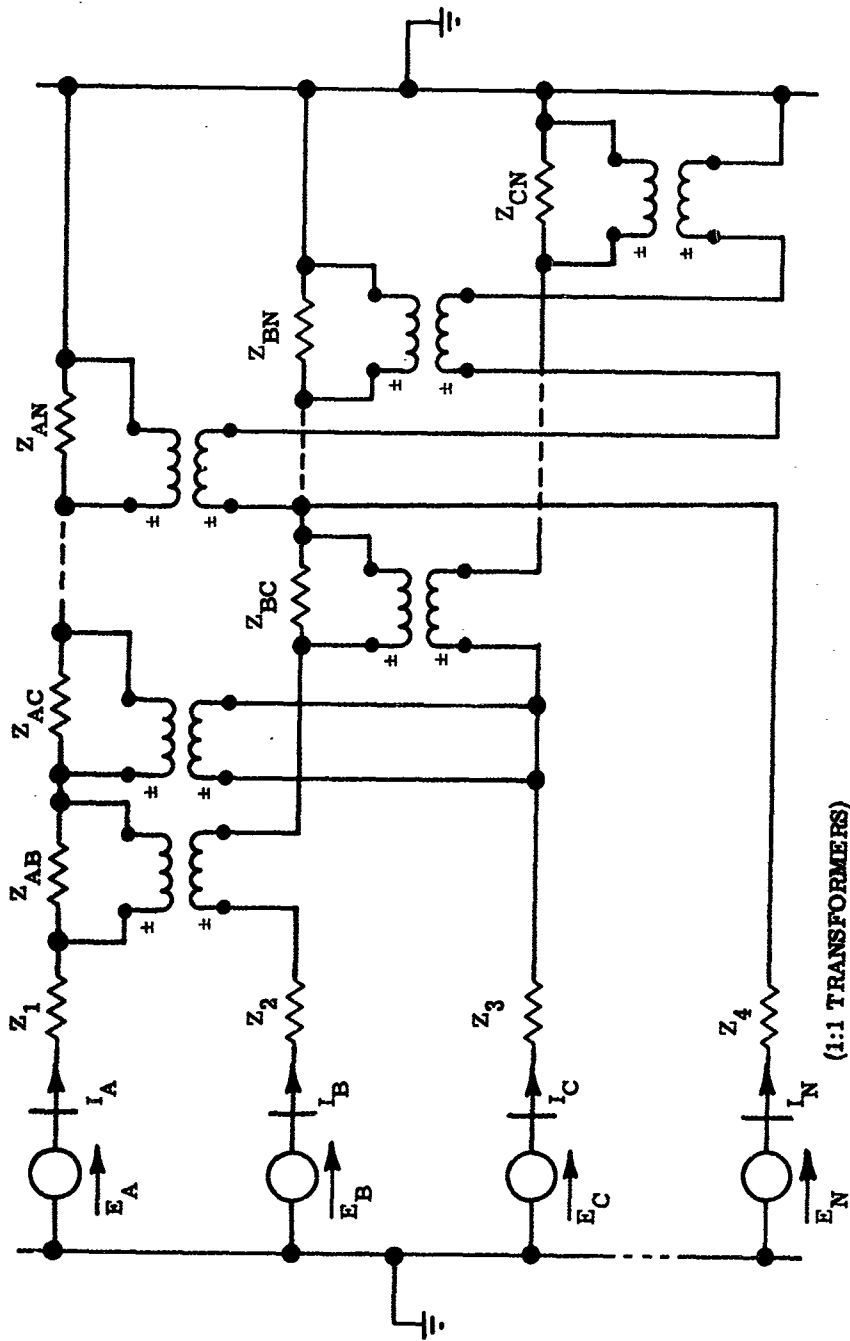
Figure 1. Array of n Antennas

It has been shown that the equations of n antennas in an array are,¹

$$\begin{aligned}
 (1) \quad E_a &= I_a Z_{aa} + I_b Z_{ab} + I_c Z_{ac} + \dots + I_n Z_{an} \\
 E_b &= I_a Z_{ba} + I_b Z_{bb} + I_c Z_{bc} + \dots + I_n Z_{bn} \\
 E_c &= I_a Z_{ca} + I_b Z_{cb} + I_c Z_{cc} + \dots + I_n Z_{cn} \\
 &\vdots \\
 E_n &= I_a Z_{na} + I_b Z_{nb} + I_c Z_{nc} + \dots + I_n Z_{nn}
 \end{aligned}$$

The above equations are identical to Kirchhoff's second law equations for linear bilateral networks. Therefore it is possible to find an electrical network where Kirchhoff's law equations are analogous to equation 1.⁴ Such a circuit is pictured in Figure 2. This network is, then, the equivalent circuit of an n element array of antennas as far as the terminal characteristics of the array are concerned.

Once the dimensions of the antennas and their spacing in the array are determined, the self- and mutual impedances may be found. Knowing these impedances and spacings, an analogous network similar to the general network (Figure 2) may be derived.



(1:1 TRANSFORMERS)

WHERE,

$$Z_1 = Z_{AA} - (Z_{AB} + Z_{AC} + \dots + Z_{AN})$$

$$Z_2 = Z_{BB} - (Z_{BA} + Z_{BC} + \dots + Z_{BN})$$

$$Z_3 = Z_{CC} - (Z_{CA} + Z_{CB} + \dots + Z_{CN})$$

$$Z_N = Z_{NN} - (Z_{NA} + Z_{NB} + Z_{NC} + \dots)$$

Figure 2. Equivalent Circuit of n Element Array of Antennas

The networks may then be programmed on a network calculator and measurements of feed point voltages may be obtained for various current distributions on the antennas. From these measurements the input impedance may be calculated since

$$Z_{\text{input}} = \frac{E_a}{I_a} = \text{input impedance to antenna a} \quad (2)$$

This calculation may be made by conventional mathematical means but, if there are more than a few antennas, the calculation becomes very laborious.

THE USE OF SYMMETRICAL COMPONENTS

There are two reasons for using symmetrical components in the solution of Equations (1). First, the method of symmetrical components is a method by which unbalanced currents may be broken into components such that these components may be arranged to form balanced systems. This greatly simplifies the operation of a network calculator. The solution for each balanced system of components may then be found and combined for the complete solution. Second, in the case of a symmetrical array the solution of the equations is simplified to such an extent that it is actually easier to solve the equations by symmetrical components alone rather than using a network calculator.

To explain the use of symmetrical components as it applies to this problem, assume an n element array of the type shown in Figure 1. Unbalanced currents $I_a, I_b, I_c, \dots, I_n$ are applied to antennas a, b, c, \dots, n , respectively. For a multiphase system, it has been shown that the currents and voltages may be broken into components as shown below.

$$I_a = I_{a0} + I_{a1} + I_{a2} + \dots + I_{a(n-1)} \quad (3)$$

$$I_b = I_{b0} + I_{b1} + I_{b2} + \dots + I_{b(n-1)}$$

$$\vdots$$

$$I_n = I_{n0} + I_{n1} + I_{n2} + \dots + I_{n(n-1)}$$

and

$$E_a = E_{a0} + E_{a1} + E_{a2} + \dots + E_{a(n-1)} \quad (4)$$

$$E_b = E_{b0} + E_{b1} + E_{b2} + \dots + E_{b(n-1)}$$

$$\vdots$$

$$E_n = E_{n0} + E_{n1} + E_{n2} + \dots + E_{n(n-1)}$$

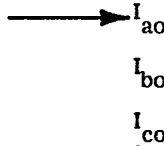
where the first subscript indicates the antenna and the second indicates the set (or sequence) of components. In each sequence, each antenna current or voltage is related to the other antenna quantities by the x power of an operator, p , that causes a progressive phase shift of $\theta = \frac{360}{n}$, where $p = 1e^{jx\theta}$, n is the number of antennas in the array, and x is the order of the sequence. For example, in a three-element array of antennas,

$$\theta = \frac{360}{3} = 120^\circ$$

Zero Sequence

$$p = e^{j0} = 1 + j0$$

$$I_{ao} = I_{bo} = I_{co}$$

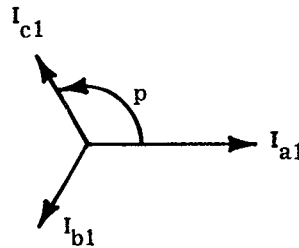


First Sequence

$$p = e^{j120 (\pi/180)}$$

$$I_{b1} = p^2 I_{a1}$$

$$I_{c1} = p I_{a1}$$

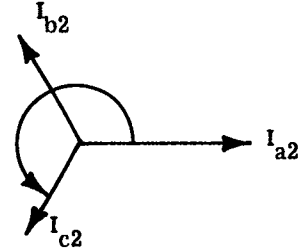


Second Sequence

$$p = e^{j240 (\pi/180)}$$

$$I_{b2} = p I_{a2}$$

$$I_{c2} = p^2 I_{a2}$$



It can also be shown, by solving equations (3) for the sequence components I_{ao} , I_{a1} , I_{a2} and considering a three-element array, (i.e., $n = 3$) that,

$$I_{ao} = 1/3 (I_a + I_b + I_c) \quad (5)$$

$$I_{a1} = 1/3 (I_a + p I_b + p^2 I_c)$$

$$I_{a2} = 1/3 (I_a + p^2 I_b + p^4 I_c).$$

By substituting the sequence currents into equations (3), equations (1) for a three-element array becomes,

$$E_a = \begin{bmatrix} I_{ao} + I_{a1} + I_{a2} \end{bmatrix} Z_{aa} + \begin{bmatrix} I_{bo} + I_{b1} + I_{b2} \end{bmatrix} Z_{ab} + \begin{bmatrix} I_{co} + I_{c1} + I_{c2} \end{bmatrix} Z_{ac} \quad (6)$$

$$E_b = \begin{bmatrix} I_{ao} + I_{a1} + I_{a2} \end{bmatrix} Z_{ba} + \begin{bmatrix} I_{bo} + I_{b1} + I_{b2} \end{bmatrix} Z_{bb} + \begin{bmatrix} I_{co} + I_{c1} + I_{c2} \end{bmatrix} Z_{bc}$$

$$E_c = \left[I_{ao} + I_{a1} + I_{a2} \right] Z_{ca} + \left[I_{bo} + I_{b1} + I_{b2} \right] Z_{cb} \\ + \left[I_{co} + I_{c1} + I_{c2} \right] Z_{cc}.$$

By definition, let the voltages due to the zero sequence currents be,

$$E)_{ao} = I_{ao} Z_{aa} + I_{bo} Z_{ab} + I_{co} Z_{ac} \quad (7)$$

$$E)_{bo} = I_{ao} Z_{ba} + I_{bo} Z_{bb} + I_{co} Z_{bc}$$

$$E)_{co} = I_{ao} Z_{ca} + I_{bo} Z_{cb} + I_{co} Z_{cc}.$$

Similar sets of equations can be written for each sequence and $E)_{a1}$, $E)_{a2}$, $E)_{b1}$ and $E)_{b2}$ are defined as the voltage due to the first and second sequence currents, respectively. Then,

$$E_a = E)_{ao} + E)_{a1} + E)_{a2} \quad (8)$$

$$E_b = E)_{bo} + E)_{b1} + E)_{b2}$$

$$E_c = E)_{co} + E)_{c1} + E)_{c2}.$$

The input impedance for antenna C for example is

$$Z_{ant C} = \frac{E_c}{I_c} \quad (9)$$

of course this procedure may be extended for any number of antennas in an array.

By programming the equivalent circuit of the array on a network calculator and impressing the sequence currents, the sequence voltages may be measured and then combined to give the total feed point voltages, E_a , E_b , $E_c \dots E_n$, respectively. Once these are known, the input impedance can be found.

SYMMETRICAL RING ARRAYS

The mathematical solution is greatly simplified, if the antenna array is a symmetrical ring array.

Consider a symmetrical ring array of three antennas, a, b, and c spaced as shown in Figure 3. In this case, it can be shown that $Z_{aa} = Z_{bb} = Z_{cc}$, $Z_{ab} = Z_{bc} = Z_{ac}$.

The equations for the voltages, due to the zero sequence currents, remembering that $I_{ao} = I_{bo} = I_{co}$, can be written as follows,

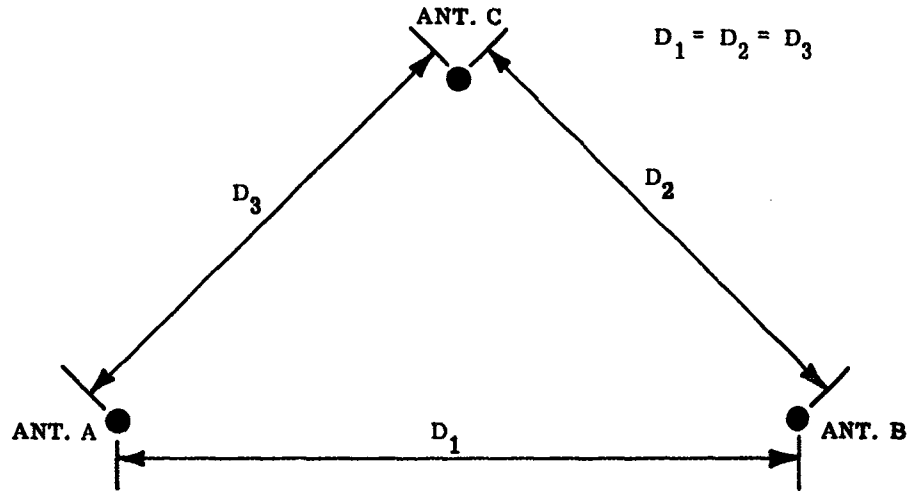


Figure 3. Symmetrical Ring Array of Three Antennas

$$E)_{ao} = I_{ao} (Z_{aa} + Z_{ab} + Z_{ac}) \quad (10)$$

$$E)_{bo} = I_{bo} (Z_{ba} + Z_{bb} + Z_{bc})$$

$$E)_{co} = I_{co} (Z_{ca} + Z_{cb} + Z_{cc})$$

Since this is a symmetrical Ring Array,

$$Z_o = Z_{aa} + Z_{ab} + Z_{ac} \quad (11)$$

$$= Z_{ba} + Z_{bb} + Z_{bc}$$

$$= Z_{ca} + Z_{cb} + Z_{cc}$$

where Z_o is the impedance offered to zero sequence current. Substituting Z_o in equations (10) they become,

$$E)_{ao} = I_{ao} Z_o = E_{ao} \quad (12)$$

$$E)_{bo} = I_{bo} Z_o = E_{bo}$$

$$E)_{co} = I_{co} Z_o = E_{co},$$

which are the zero sequence voltages.

The equations for the voltages due to the first sequence currents, remembering that $I_{b_1} = p^2 I_{a_1}$, $I_{c_1} = p I_{a_1}$, are

$$E)_{a_1} = I_{a_1} (Z_{aa} + p^2 Z_{ab} + p Z_{ac}) \quad (13)$$

$$E)_{b_1} = I_{b_1} (p Z_{ba} + Z_{bb} + p^2 Z_{bc})$$

$$E)_{c_1} = I_{c_1} (p^2 Z_{ca} + p Z_{cb} + Z_{cc})$$

and as before,

$$\begin{aligned} Z_1 &= Z_{aa} + p^2 Z_{ab} + p Z_{ac} \\ &= p Z_{ba} + Z_{bb} + p^2 Z_{bc} \\ &= p^2 Z_{ca} + p Z_{cb} + Z_{cc}, \end{aligned} \quad (14)$$

where Z_1 is the impedance offered to the first sequence currents. Substituting Z_1 in equations 10, they become

$$E)_{a_1} = I_{a_1} Z_1 = E_{a_1} \quad (15)$$

$$E)_{b_1} = I_{b_1} Z_1 = E_{b_1} = p^2 E_{a_1}$$

$$E)_{c_1} = I_{c_1} Z_1 = E_{c_1} = p E_{a_1}$$

E_{a_1} , E_{b_1} and E_{c_1} are the first sequence voltages. In a similar manner the impedance offered

to the second sequence currents is

$$Z_2 = Z_{aa} + p Z_{ab} + p^2 Z_{ac} \quad (16)$$

and

$$E)_{a_2} = I_{a_2} Z_2 = E_{a_2} \quad (17)$$

$$E)_{b_2} = I_{b_2} Z_2 = E_{b_2} = p E_{a_2}$$

$$E)_{c_2} = I_{c_2} Z_2 = E_{c_2} = p^2 E_{a_2}$$

where E_{a_2} , E_{b_2} , and E_{c_2} are the second sequence voltages.

As before, the input impedance to antenna c is

$$Z_{\text{input ant C}} = \frac{E_c}{I_c} = \frac{E_{c_0} + E_{c_1} + E_{c_2}}{I_c} \quad (18)$$

It should be noted that, once the sequence impedances are found, they do not change with excitation. The sequence impedances are strictly a function of antenna construction and spacing in a symmetrical ring array. Thus, the calculation of sequence voltages is greatly simplified. Case I shows the results of this method of calculation.

PRESENTATION OF THE DATA

The data obtained in this investigation will be presented in the following manner:

- (1) The number, half-length, and spacing of the antennas in the array
- (2) The self and mutual impedances of the antennas
- (3) The equations of the array
- (4) The assumed antenna currents
- (5) The equivalent circuit of the antenna array
- (6) The tabulated data for the case. This includes a comparison of the measured and calculated input impedances.

The number, half-length, and spacing of the antennas were assumed and their corresponding impedances determined³. The equations for the array were written and an equivalent circuit was devised to represent these equations. The equivalent circuit was then programed on an a-c network calculator. The assumed currents were analyzed for their symmetrical components. Each set of sequence currents, respectively, was then impressed on the circuit and the voltages due to that set of sequence currents were measured at those points on the equivalent circuit which would correspond to the feed points of the antennas. The impressed currents and measured voltages were then tabulated.

The equivalent circuit shown in each case is the circuit that was programed on the network calculator. Conductive coupling was used in all cases to eliminate the use of 1:1 transformers. Since the transformers are not without loss, they would have introduced some error.

A symmetrical array is shown in Case I, so Table I shows the calculated sequence voltage in addition to the total voltage which was calculated by solving the original equations of the antenna array.

CASE I

Input Impedance of a Symmetrical Ring Array of Four Antennas

- (1) Four antennas of half-length $H = \frac{\lambda}{4}$ and with their spacing as shown in Figure 4.

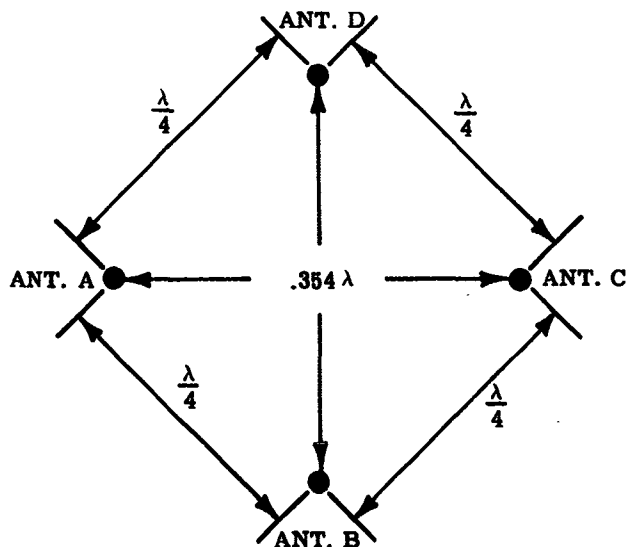


Figure 4
Symmetrical Ring Array of Four Antennas

- (2) From the above information it was found,

$$Z_{aa} = Z_{bb} = Z_{cc} = Z_{dd} = 37.4 + j 21$$

$$Z_{ab} = Z_{bc} = Z_{cd} = Z_{da} = 20.4 - j 14.2$$

$$Z_{ac} = Z_{bd} = 8.3 - j 18.8$$

- (3) The equations for a four antenna array are,

$$E_a = I_a Z_{aa} + I_b Z_{ab} + I_c Z_{ac} + I_d Z_{ad}$$

$$E_b = I_a Z_{ba} + I_b Z_{bb} + I_c Z_{bc} + I_d Z_{bd}$$

$$E_c = I_a Z_{ca} + I_b Z_{cb} + I_c Z_{cc} + I_d Z_{cd}$$

$$E_d = I_a Z_{da} + I_b Z_{db} + I_c Z_{dc} + I_d Z_{dd}$$

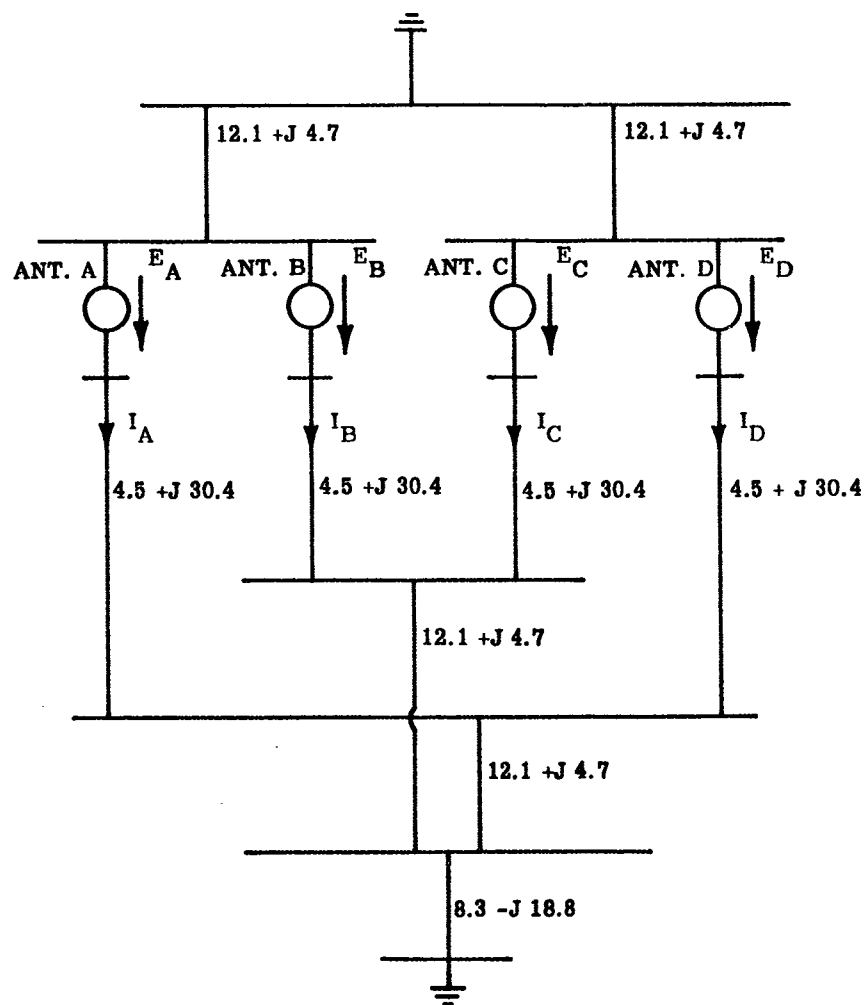


Figure 5. Equivalent Circuit of an Array of Four Antennas

TABLE I

	Antenna a	Antenna b	Antenna c	Antenna d	Units
I_0	.87 /38.5	.87 /38.5	.87 /38.5	.87 /38.5	amps
I_1	.415 /11.7	.415 /281.7	.415 /191.7	.415 /101.7	amps
I_2	.87 /38.5	.87 /218.5	.87 /38.5	.87 /218.5	amps
I_3	.625 /222	.625 /312	.625 /42	.625 /132	amps
I_{total}	1.5 /30	1.0 /-60	2.0 /45	1.0 /120	amps
Measured					
$E_0 = E_0$	74 + j25	74 + j25	74 + j25	74 + j25	volts
$E_1 = E_1$	9 + j18	18 + j 9	-9 - j18	-18 + j 9	volts
$E_2 = E_2$	-12 + j25	12 - j24	-12 + j25	12 - j24	volts
$E_3 = E_3$	0 - j31	31 + j 0	0 + j30	-31 + j 0	volts
E_{total}	71 + j37	135 - j 8	53 + j62	37 + j10	volts
Calculated using Symmetrical Components *					
$E_0 = E_0$	73 + j28.8	73 + j28.8	73 + j28.8	73 + j28.8	volts
$E_1 = E_1$	11.8 + j18.5	18.5 - j 8.5	-11.5 - j18.5	-18.5 - j 8.5	volts
$E_2 = E_2$	-14 + j24.2	14 - j24.2	-14 + j24.2	14 - j24.2	volts
$E_3 = E_3$	0 - j30.8	30.8 + j 0	0 + j30.8	-30.8 - j 0	volts
E_{total}	70.8 + j4-.7	136.0 - j 3.9	47.5 + j65.3	37.7 - j13.1	volts
Calculated					
E_{total}	70.3 + j40.3	134.5 + j 8	46.8 + j62	37.7 + j10.6	volts
Input Impedance					
Z_{input} (measured)	52 /-2.4	135 /60	40.6 /4.5	38.2 /-104	ohms
Z_{input} (calc. by sym. comp.)	54 /-.1	135 /60	34.4 /9	38.8 /-100	ohms
Z_{input} (calc. from Eq. 1)	54 /-.4	135 /60	34.4 /8	38 /-103	ohms

* $Z_0 = 90.0 /-16.9$, $Z_1 = Z_3 = 49.4 /53.8$, $Z_2 = 30.8 /80.95$

- (4) The currents for each of the antennas were assumed to be as follows,

$$I_a = 1.5 \angle 30^\circ$$

$$I_b = 1.0 \angle -60^\circ$$

$$I_c = 2.0 \angle 45^\circ$$

$$I_d = 1.0 \angle 120^\circ$$

- (5) The equivalent circuit for a four antenna array is shown in Figure 5.
 (6) Tabulated data for a four antenna array is shown in Table I.

CASE II

Input Impedance of an Array of Five Antennas

- (1) Five antennas of half-length $H = \frac{\lambda}{4}$ and with their spacing as shown in Figure 6.

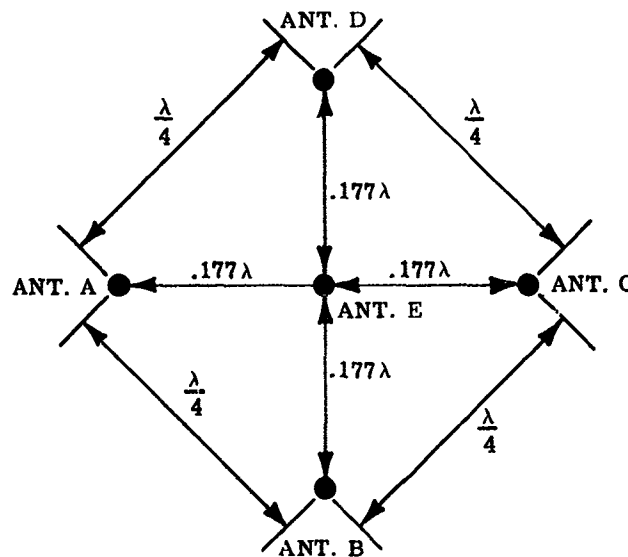


Figure 6. An Array of Five Antennas

(2) From the above information it was found,

$$Z_{aa} = Z_{bb} = Z_{cc} = Z_{dd} = Z_{ee} = 37.7 + j21$$

$$Z_{ab} = Z_{bc} = Z_{cd} = Z_{da} = 20.4 - j14.2$$

$$Z_{ac} = Z_{bd} = 8.3 - j18.8$$

$$Z_{ae} = Z_{be} = Z_{ce} = Z_{de} = 27.9 - j7.0$$

(3) The equations for a five antenna array are,

$$E_a = I_a Z_{aa} + I_b Z_{ab} + I_c Z_{ac} + I_d Z_{ad} + I_e Z_{ae}$$

$$E_b = I_a Z_{ba} + I_b Z_{bb} + I_c Z_{bc} + I_d Z_{bd} + I_e Z_{be}$$

$$E_c = I_a Z_{ca} + I_b Z_{cb} + I_c Z_{cc} + I_d Z_{cd} + I_e Z_{ce}$$

$$E_d = I_a Z_{da} + I_b Z_{db} + I_c Z_{dc} + I_d Z_{dd} + I_e Z_{de}$$

$$E_e = I_a Z_{ea} + I_b Z_{eb} + I_c Z_{ec} + I_d Z_{ed} + I_e Z_{ee}$$

(4) The currents for each of the antennas were assumed to be as follows,

$$I_a = 1.0 \angle 0^\circ$$

$$I_b = 3.0 \angle -60^\circ$$

$$I_c = 2.0 \angle 45^\circ$$

$$I_d = 1.5 \angle 120^\circ$$

$$I_e = 1.0 \angle 90^\circ$$

(5) The equivalent circuit for a five antenna array is shown in Figure 7.

(6) Tabulated data for a five antenna array is shown in Table II.

CONCLUSIONS

A small difference is seen, in some instances, between the measured and calculated values of input impedance. The main cause of this is the fact that a pure inductance cannot be obtained on a network calculator and, while in some cases compensation may be made for the resistance that is present in the coil, in other cases it was quite impossible. In cases where a negative resistance occurred a special circuit was used to represent it. This circuit is shown in Appendix I.

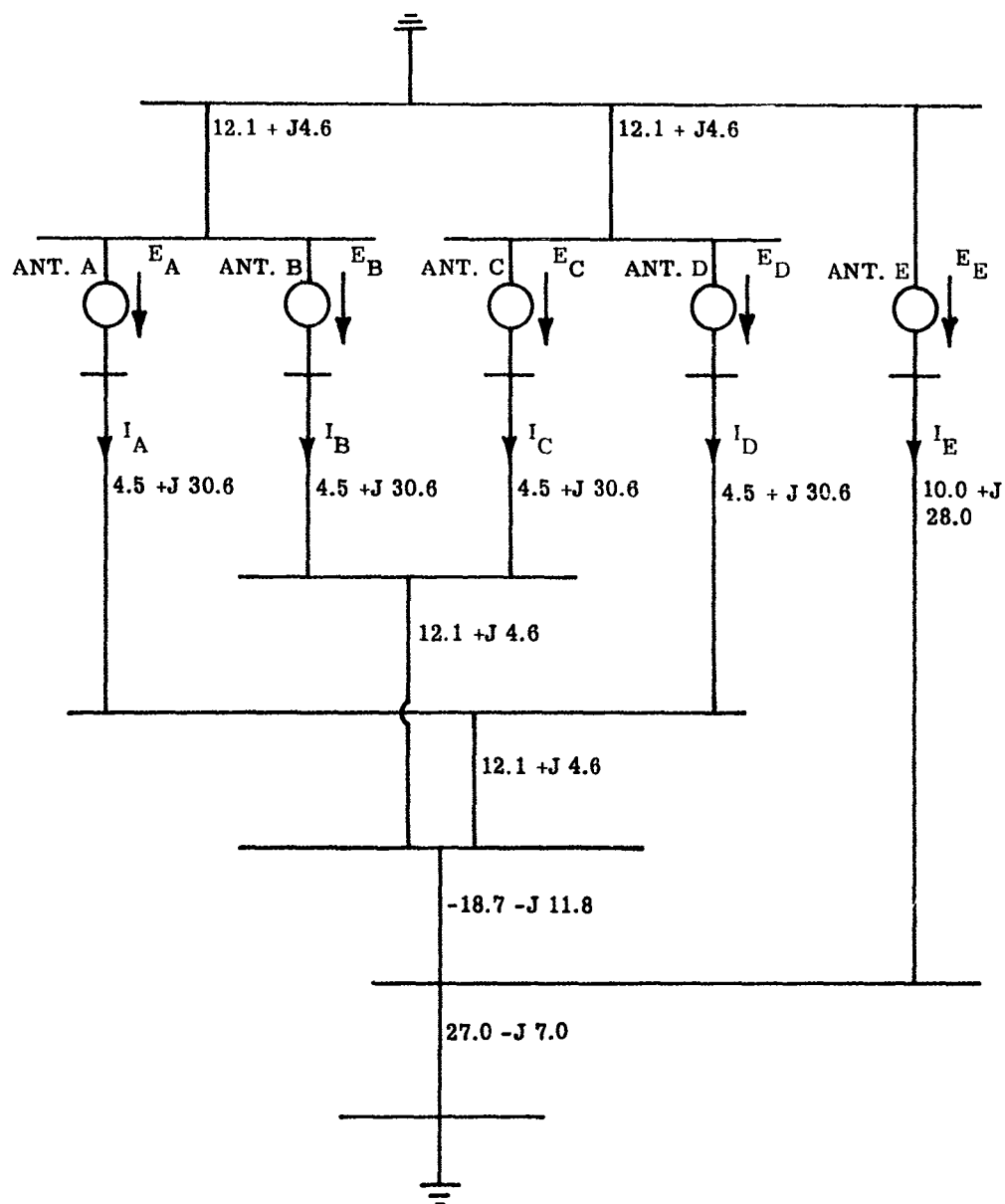


Figure 7. Equivalent Circuit of an Array of Five Antennas

TABLE II

	Antenna a	Antenna b	Antenna c	Antenna d	Antenna e	Units
I_{n0}	.7 \angle -25.3	.7 \angle -25.3	.7 \angle -25.3	.7 \angle -25.3	.7 \angle -25.3	amps
I_{n1}	.7 \angle 37	.7 \angle 325	.7 \angle 253	.7 \angle 181	.7 \angle 109	amps
I_{n2}	.94 \angle 1.86	.94 \angle 218	.94 \angle 73.8	.94 \angle 290	.94 \angle 146	amps
I_{n3}	1.07 \angle 152	1.07 \angle 296	1.07 \angle 90	1.07 \angle 234	1.07 \angle 18	amps
I_{n4}	.67 \angle 254.4	.67 \angle 326.4	.67 \angle 38.4	.67 \angle 110.4	.67 \angle 82.4	amps
I_{total}	1.0 \angle 0	3.0 \angle -60	2.0 \angle 45	1.5 \angle -120	1.0 \angle 90	amps
Measured						
E_{n0}	64 -j54	64 -j54	64 -j54	64 -j54	64 -j54	volts
E_{n1}	-13 +j37.5	25 +j17	8 -j25	-35 -j22	-23 +j 0	volts
E_{n2}	8 -j26	-6 -j30	-44 +j17	35 +j 6	-23 +j 0	volts
E_{n3}	-25 -j26	45 +j29	-23 +j31	8 -j14	-3 +j35	volts
E_{n4}	11 -j30	26 +j 6	-6 +j32	-44 +j 0	-5 -j14	volts
E_{total} (measured)	45 -j52.5	154 -j32	-1.0 +j 1.0	28 -j84	43 -j49	volts
E_{total} (calculated)	42.3 -j55.7	155 -j39	-2.1 +j 1.2	25.8 -j90.3	47 -j90.3	volts
Z_{input} (measured)	69.2 \angle -49.4	52.3 \angle 48.3	.707 \angle 90	59.2 \angle 48.4	65.6 \angle 138.8	ohms
Z_{input} (calculated from Eq. 1)	70.0 \angle -52.8	53.4 \angle 45.8	1.21 \angle 74.8	62.4 \angle 46	71.8 \angle 139.2	ohms

The adjustment or balancing of the equivalent circuit programmed on the network calculator is an iterative process. The rate of obtaining a balanced system increased as techniques were developed and solutions for the problem could be obtained quite rapidly.

In general, the values of input impedance obtained by using the a-c network calculator were the same as those calculated by conventional means. Except for antenna arrays with a low number of elements, and except for symmetrical ring arrays, the calculator solution is less laborious.

APPENDIX I

EQUIVALENT CIRCUIT FOR REPRESENTING NEGATIVE RESISTANCES

Where negative resistances were necessary in this investigation, a circuit such as that shown in Figure 8 was used.⁵

By connecting the primaries of two 1:1 transformers in series and the secondaries in parallel and by adjusting the generator to the proper voltage and phase to give a zero current in the jumper across the primaries, a negative resistance appears between points A and B. When $I_{\text{jumper}} = 0$, the primary and secondary currents are equal in magnitude and opposite in phase. This requires that the generator supply be $2I$ at point B and the voltage drop between points A and B becomes,

$$V_{ab} = -IR$$

or,

$$V_{ab} = I(-R).$$

The resistance represented between points A and B becomes,

$$\frac{V_{ab}}{I} = (-R).$$

A generator could have been used to represent a negative resistance; however, adjustments are difficult to make.

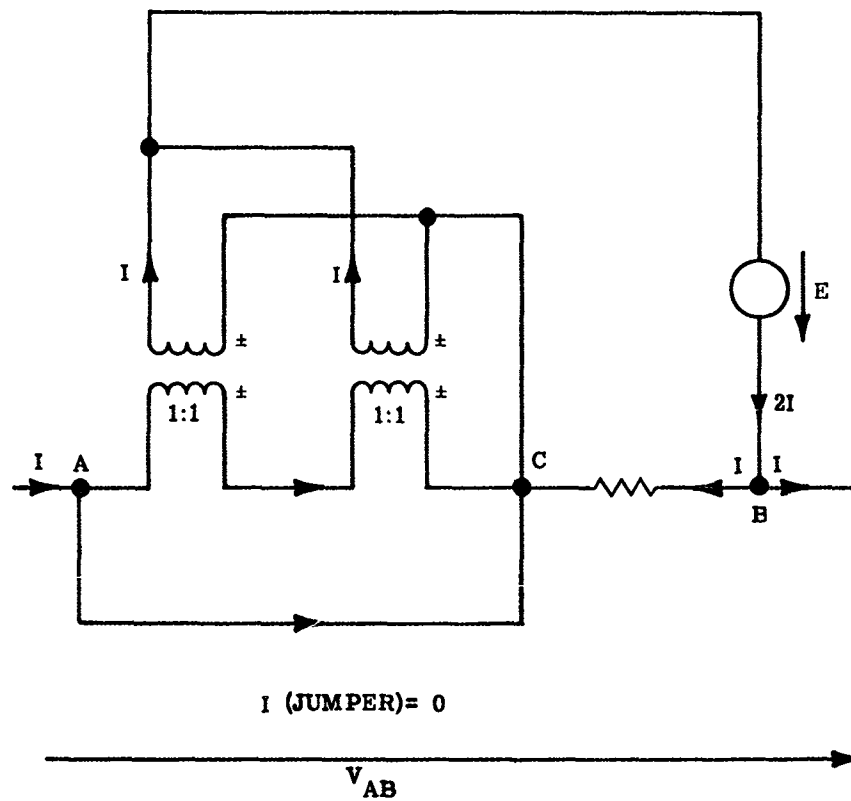


Figure 8. Equivalent Circuit for Representing Negative Resistance

BIBLIOGRAPHY

1. P. S. Carter, "Circuit Relations in Radiating Systems," *PROC. I. R. E.*, 20, p. 1004; June, 1932.
2. E. C. Jordan, "Electromagnetic Waves and Radiating Systems," Prentice-Hall, Inc., Englewood Cliffs, N. J., 1950.
3. J. P. German, "A program for Finding the Self and Mutual Impedance of Thin Linear Antennas of Equal Height, H, and d Distance Apart," Programed for the I. B. M. 709 Digital Computer, Agricultural and Mechanical College of Texas, Unpublished and Private.
4. L. M. Haupt, "Solutions of Simultaneous Equations Through Use of the A. C. Network Calculator," *THE REVIEW OF SCIENTIFIC INSTRUMENTS*, Vol. 21, No. 8, pp. 683-686; August, 1950.
5. General Electric Company, "G-E Network Analyzers Manual," 1950.
6. L. Thorel, "The Antenna," John Wiley and Sons, Inc., New York, N. Y., 1960.
7. Westinghouse Electric Corporation, "Alternating Current Network Calculator Manual," January, 1947.
8. L. M. Haupt, "Water Distribution Problems Solved by Network Calculators," *Journal of the Pipeline Division, PROC. A. S. C. E.*, Vol. 84, paper 1577, pp. 1-6; March, 1958.
9. R. Blumberg, "Introduction to Structural Solutions by Electrical Analogies Using an Alternating Current Network Calculator," Thesis, Agricultural and Mechanical College of Texas; June, 1950.
10. J. D. Kraus, "Antennas," McGraw-Hill Book Company, Inc., New York, N. Y., 1950.
11. C. F. Wagner and R. D. Evans, "Symmetrical Components," McGraw-Hill Book Company, Inc., New York, N. Y., 1933.

Hydroacoustic Simulation of Antenna Radiation Characteristics¹

by

M. L. Parker, Jr., W. A. Meyer, and H. J. Hewitt²

1. INTRODUCTION

Measurement techniques that describe the characteristics of electromagnetic radiators have long been of interest to the antenna engineer. The radiation and propagation of acoustic energy in water is, in many ways, analogous to the radiation and propagation of radio-frequency energy. The propagation velocity of hydroacoustic energy ($\approx 1.45 \times 10^3$ meters/second) results in millimeter wavelengths in the low and medium frequency range. Consequently, relatively small scale antenna models are possible at frequencies where instrumentation is simplified. A theoretical and experimental investigation of techniques to simulate the radiation characteristics of antennas using acoustic radiators propagating into a water medium has been conducted. The first phase of the investigation involved a feasibility study employing, primarily, empirical methods. During this phase it has demonstrated that the radiation pattern of a large reflector antenna could be simulated, hydroacoustically. This paper reports on the second phase of the investigation which dealt with the development of facilities and techniques employed in the hydroacoustic simulation of

1. The work described in this paper was supported by the Rome Air Development Center under Contracts AF 30(602)-2295 and AF 30(602)-2735.

2. M. L. Parker and W. A. Meyer, Melpar, Inc., Falls Church, Va.;
H. J. Hewitt, Rome Air Development Center, Rome, N. Y.

antenna radiation characteristics. A large (40 ft. x 30 ft. x 6 ft.) hydro-acoustic test tank was constructed, and considerable effort expended in making the tank essentially anechoic. Fabrication techniques for transducers, and methods of controlling their radiation pattern were developed. Pattern control techniques included the use of masks, horns and arrays.

2. TEST FACILITIES

A fundamental requirement for any successful program of measuring antenna or antenna system characteristics is an adequate test facility. The characteristics desired for the hydroacoustic modeling facility are essentially the same as those of an antenna test range, and the propagation medium characteristics would, ideally, be those of free space. A choice of a practical hydroacoustic test facility must be based, primarily, on the ability of the facility to minimize reflections. There are three techniques available to achieve this goal: (1) control of the configuration of the water boundary, (2) use of absorbing material at the boundaries, and (3) the use of specialized instrumentation to exclude undesired reflection signals from the measuring instruments.

Range requirements are a function of frequency and antenna size just as in r-f antenna measurements. A minimum range of d^2/λ is desirable where d is the maximum dimension of the antenna model under test, and λ is the hydroacoustic wavelength. Instrumentation requirements are similar to those of an enclosed anechoic antenna range. Some specialized equipment may be required to reduce reflection problems. Certain minimum range

requirements are deemed necessary for the successful employment of hydro-acoustic modeling techniques. These are:

- a. A homogenous water medium with reflection levels at least -30 db below the main signal.
- b. A tank size capable of providing a range of at least d^2/λ for the modeling frequencies and antenna sizes to be employed.
- c. A system, linear, dynamic range of 30 db with sufficient power to reduce system noise influence to a minimum.

A review of the available literature and consultation with hydroacoustic authorities revealed that construction of an essentially anechoic test facility capable of operating over a broad band of frequencies (10 to 1), is a difficult, costly, and somewhat empirical procedure. An added hindrance encountered in the design of hydroacoustic test facilities for modeling antenna characteristics was the limited information on practical methods and materials for the development of an anechoic, hydroacoustic tank in the 100 kc - 1 mc frequency range deemed suitable for antenna modeling techniques. A detailed study was made of available information pertaining to hydroacoustic tank designs to facilitate the determination of the most feasible tank shape and construction materials from both economic and technical viewpoints. Several techniques for reducing the effects of reflections in hydroacoustic test tanks were experimentally explored in an effort to provide a reliable test range. There are three general techniques that can be employed: (1) pulse techniques, (2) the complete lining of the medium boundaries with hydroacoustic absorbers,

and (3) the use of baffles of hydroacoustic absorber which, when properly placed, will reduce reflections. The latter two techniques were rather extensively examined during the study which this paper describes.

As the result of an investigation of hydroacoustic absorbing material, it was concluded that Insulcrete,³ a porous absorber developed in 1953 at the U.S. Navy's Underwater Sound Reference Laboratory in Orlando, Florida, was best suited for the test tank facilities to be used at Melpar. Insulcrete consists of a mixture of four parts by volume of loose, pine sawdust to one part of Portland cement. The sawdust-cement mixture is formed into a wedge shape, and installed with adjacent wedge dihedrals orthogonal to each other. A baffle of Insulcrete installed in a small (6 ft. x 6 ft. x 6 ft.) test tank used at Melpar is shown in Figure 1. A second, larger, test tank (40 ft. x 30 ft. x 6 ft.) was constructed at Melpar for use in the study of modeling techniques. Several baffles of Insulcrete wedges were placed at strategic points along the sides and on the bottom and top surfaces of the tank. Figure 2 shows a portion of this tank with the baffles installed. As a result of the use of Insulcrete in both the small and large test tanks, range conditions approaching those deemed desirable were obtained.

3. TRANSDUCER DESIGN

The transducer is a basic element of any hydroacoustic modeling technique. It was, therefore, necessary to have a thorough knowledge of

3. Darver, C. L., "An Underwater Sound Absorber for an Anechoic Tank," USNUSRL, Orlando, Florida, ASTIA No. AD 36133 (1953)



Figure 1. Baffle of Insulcrete Wedges in Small Test Tank

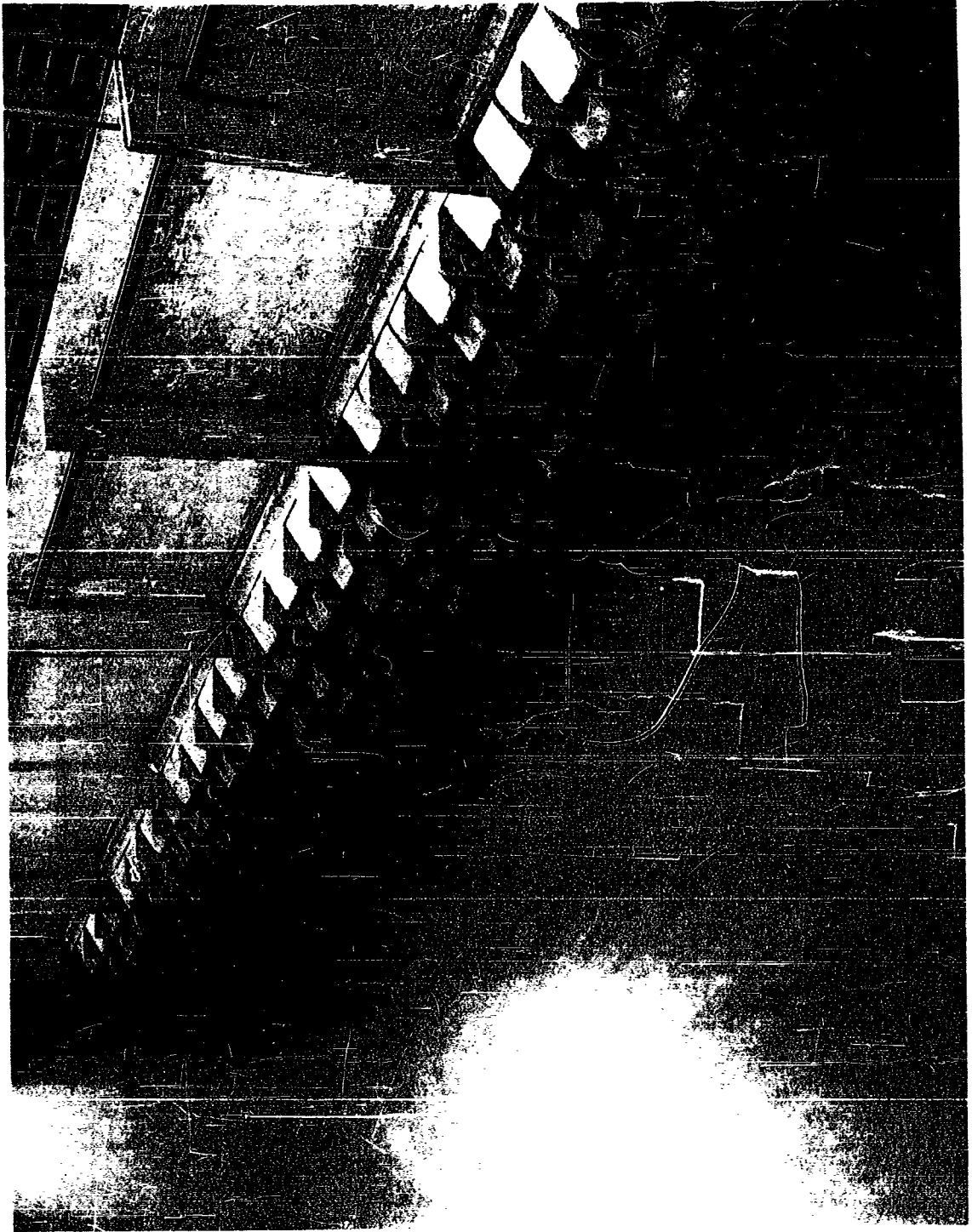


Figure 2. Portion of Insulcrete Installation in Large Test Tank

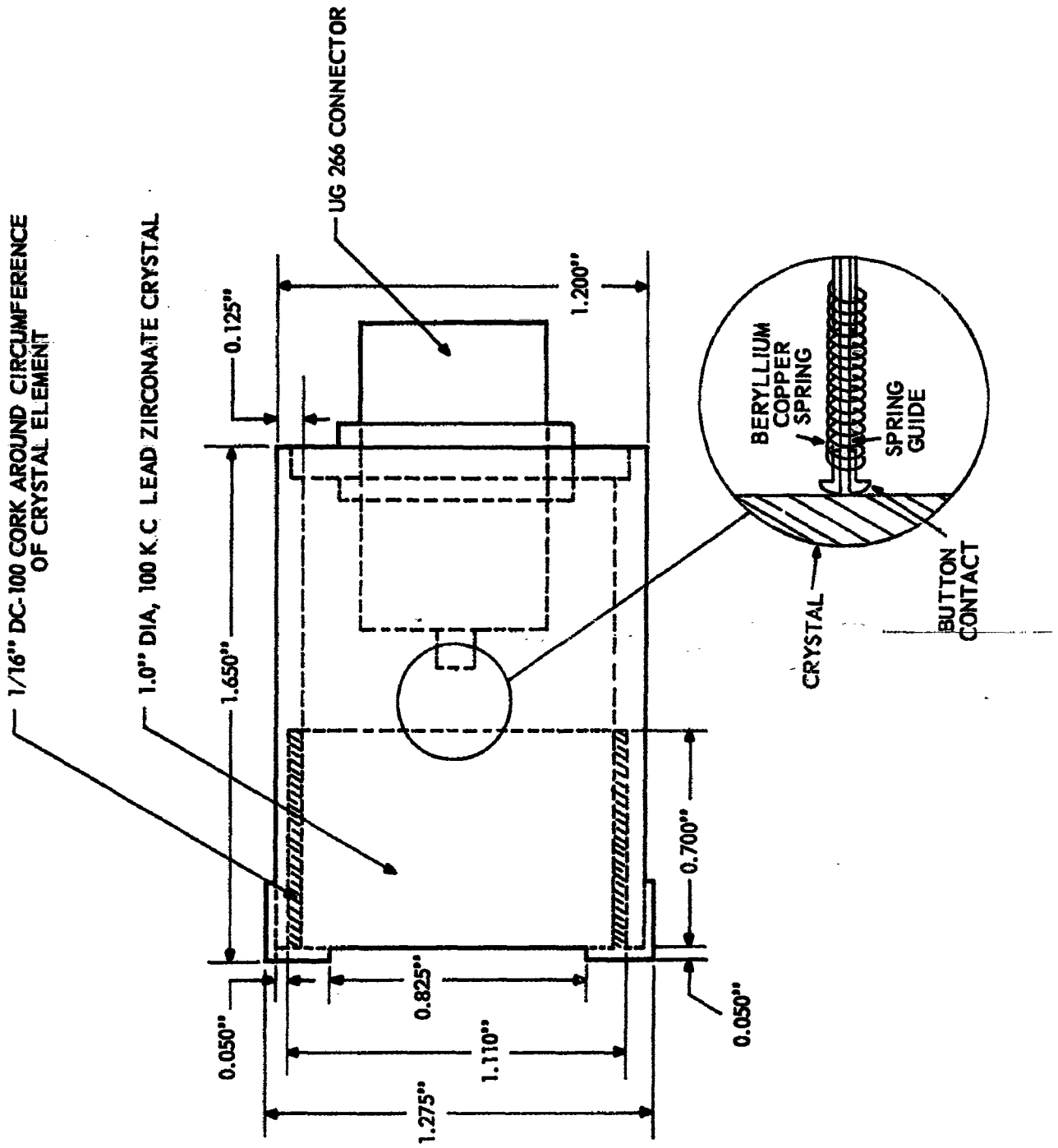


Figure 3. Typical Melpar Transducer Design

degrades the pattern of the transducer. The beryllium wire spring and button provide a flexible contact between the connector and the crystal. This minimizes the clamping effect on the element and improves the transducer efficiency. While not having ideal pattern characteristics, pairs of transducers of this type showed great improvement over commercial transducers.

Investigation of horns and waveguide techniques, and of array techniques requires the use of transducers which have broad radiation patterns. In addition, a transducer design was desired which would allow for quick changes of element size and configuration without the necessity of fabricating a new case and feed each time. To accomplish these ends, another transducer configuration was designed and fabricated (Figure 4). The advantage of this design is the replaceable cork disks and threaded cap. The cork disks were cut from sheet stock to the proper diameter. Holes were then drilled or cut in the blanks to the shape of the crystal element or elements to be used. The desired cork disk and crystals were the positioned in the case and the cap was screwed on to hold them in place. The cap aperture is large and does not contact crystal elements. The elements are held in the cork by friction. Electrical contact is made by painting a lead of conducting silver paint between the element and the cap.

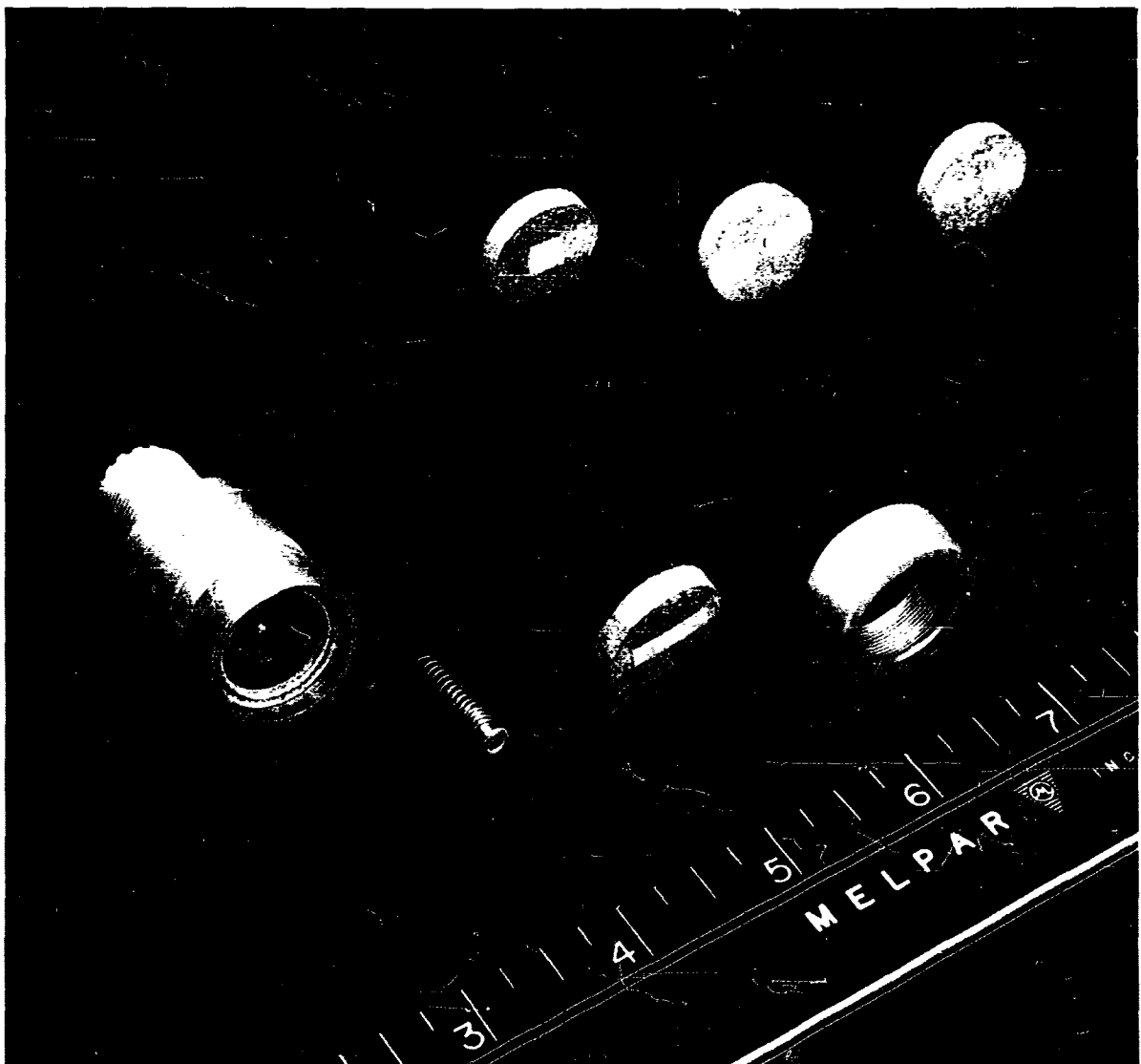


Figure 4. Exchangeable Element Transducer

4. PATTERN SYNTHESIS TECHNIQUES

From a theoretical consideration, it would seem that one of the most obvious techniques for controlling a transducer pattern is through the variation of the aperture size and shape. Thus, a masking material may be placed over the transducer aperture to alter its aperture size and shape. Such a method of altering the aperture size has been investigated, utilizing cork and metal masks over the transducer aperture. From a practical viewpoint, there are, in general, three major handicaps encountered in using the masking technique for transducer pattern control:

- 1) Patterns produced by the masking technique are a function of the transducer patterns.
- 2) A sharp decrease in transducer sensitivity is produced by the damping effect of masking material.
- 3) The theoretical prediction of the sidelobes is quite difficult because of the high amplitude taper of the clamped aperture and the sensitivity of the sidelobes to crystal surface variation and variations in the clamping of the mask.

Because of some of the inherent handicaps encountered in utilizing the masking techniques for controlling transducer patterns, it was decided that an experimental investigation should be pursued to determine the feasibility of using hydroacoustic horns. In general, a hydroacoustic horn could be used to modify the characteristics of a transducer and improve the impedance match between the transducer and the medium of propagation. In an effort to explore the practicality of using hydroacoustic horns for pattern synthesis, a number of rectangular aperture

horns were fabricated so that their characteristics could be determined over the frequency range of interest, (Figure 5).

From the experimental investigation of hydroacoustic horns, it has been determined that (1) approximately the same directivity pattern is produced by hydroacoustic horn as predicted by theory, provided the feed transducer produces a broad cosine-type pattern, (2) a relative gain can be realized from a hydroacoustic horn as with r-f horns, and (3) the throat dimension of the hydroacoustic horn determines the lower cutoff frequency.

A great many antennas utilize ground planes or shaped reflectors to produce the radiation characteristics desired. The reflector used in the hydroacoustic medium must produce effects similar to the electromagnetic reflector. During this study, a hydroacoustic model of a radar antenna having a shaped reflector fabricated from fiberglass was used. It was noted that the secondary pattern of the fiberglass reflector was extremely frequency-sensitive, and, at certain frequencies, produced nulls on the axis of the antenna reflector because of the phase cancellation produced by the thickness of the fiberglass. To reproduce, in water, single-surface reflecting characteristics of an electromagnetic reflector, it was necessary to produce an air-water interface of perfect reflectivity for hydroacoustic waves. A reflector was fabricated with Isocyanate foam to produce a smooth surface with enclosed unicellular air bubbles (Figure 6). Pattern measurements taken over the same frequency range with this reflector revealed that there was no bifurcation of the beam as was noted with the fiberglass reflector antenna.

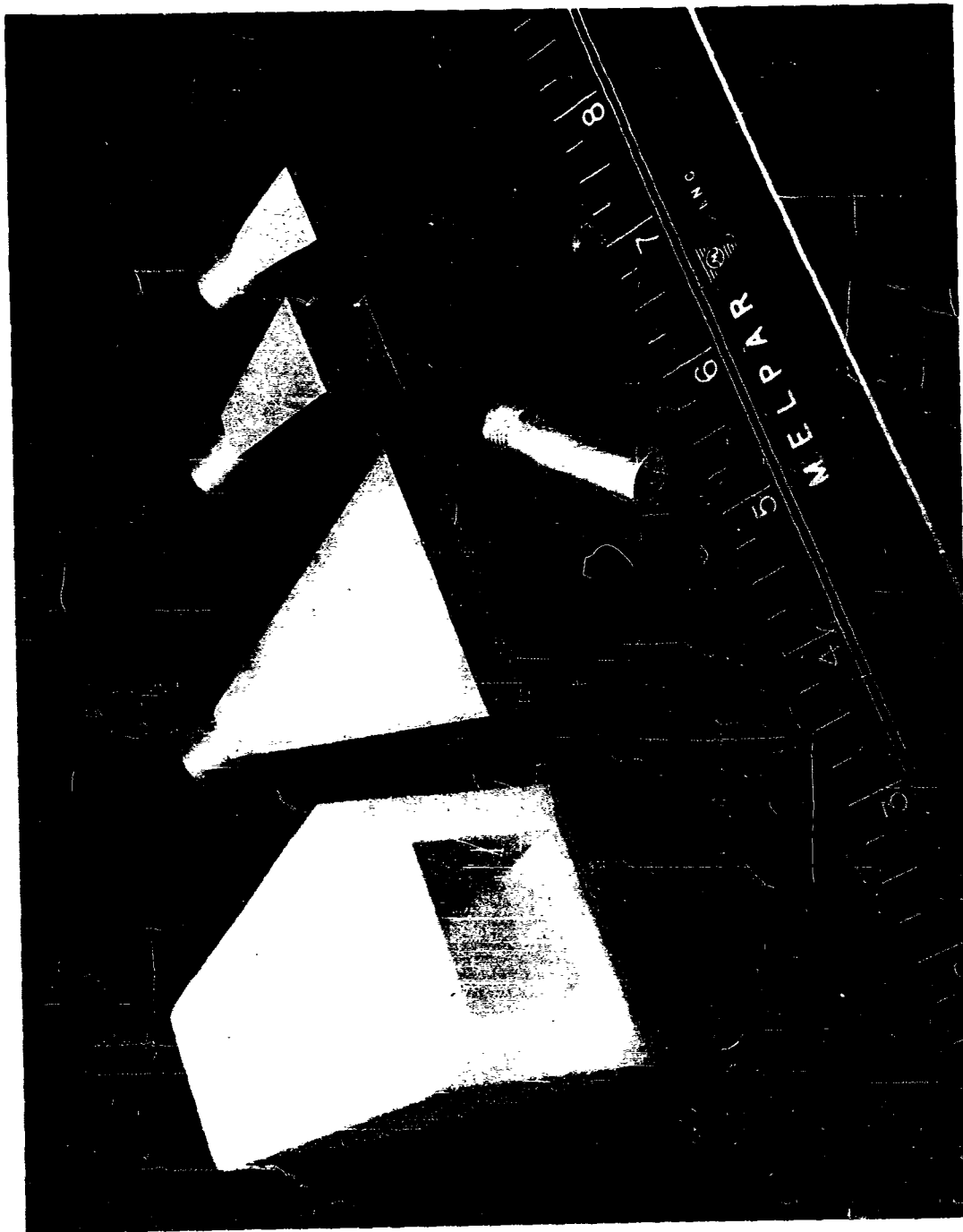


Figure 5. Hydroacoustic Horns and Transducer Feed

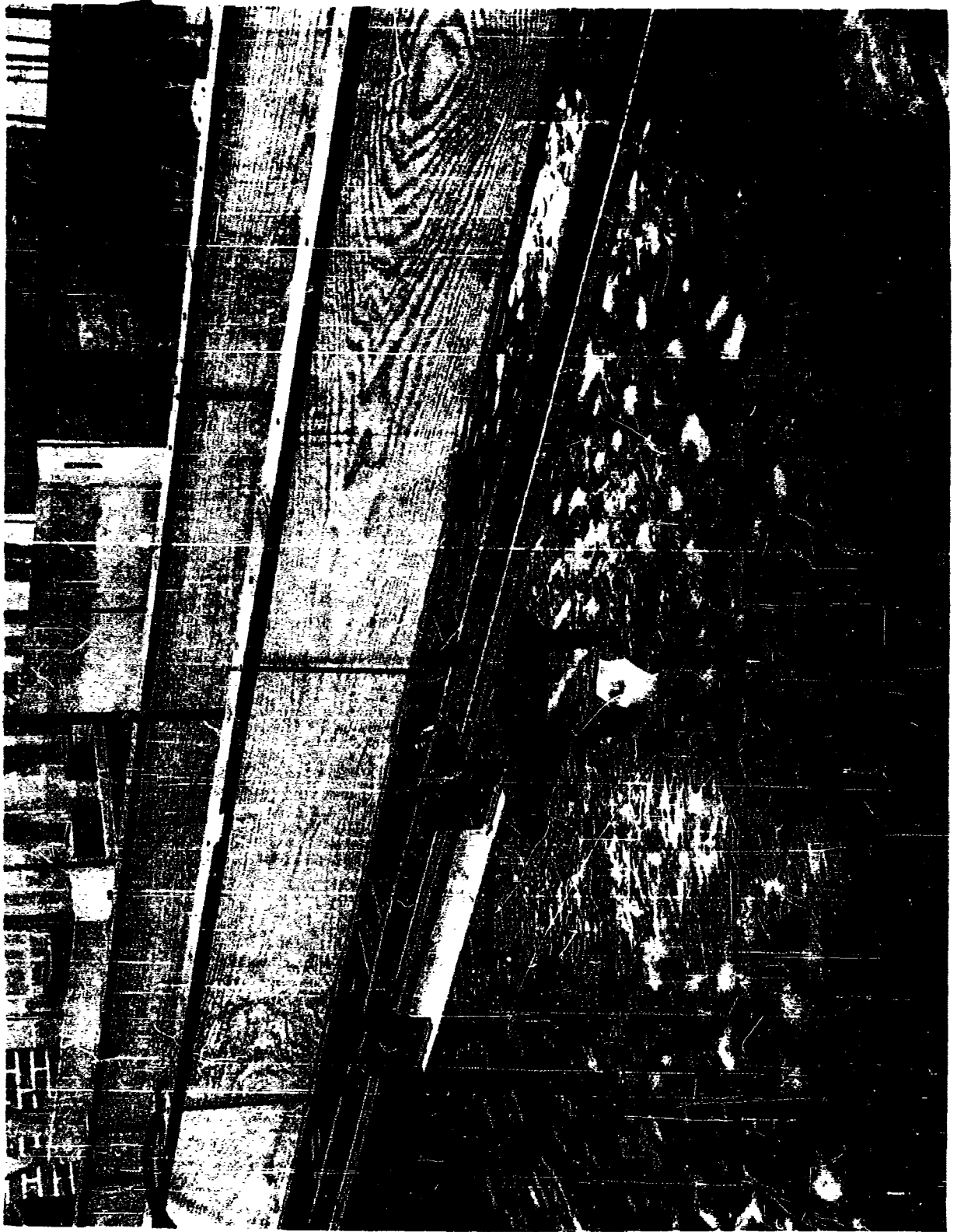


Figure 6. AN/FPS-8 Hydroacoustic Foam Model and Large Tank

Investigation of array techniques in the synthesis of antenna radiation patterns was undertaken during this study. Transducer arrays could be used to simulate the characteristics of r-f arrays. In addition, the arrangement of transducer elements of the proper size with the proper orientation to each other would provide a more versatile and reliable pattern control technique over that of masking. Finally, the development of array techniques offered a method of simulating the characteristics of more sophisticated antenna types, and of synthesizing the characteristics of large aperture antennas. A nine-element array of square piezoelectric elements was fed from a common line through spring finger contacts to the individual piezoelectric elements, resulting in a uniform amplitude, in-phase array. Patterns produced by the nine-element array were generally symmetrical and grating lobes were generated at the higher frequencies in agreement with array theory. To provide a more versatile experimental array, a six-element array was fabricated with each element fed individually by its own coaxial line (Figure 7). With this array, it was possible to examine not only the array pattern, but also the individual element patterns. The measurement of the individual element signal levels indicated a slight amplitude taper from the center elements to the end elements of about 2 db. This is attributed to the asymmetry of the end element environment as opposed to that of the center element. The patterns of the six elements, when fed by a simple power divider of coaxial tees, were exceptionally good in the range from 150 to 250 kc. A typical pattern is shown in Figure 8. A comparison of theoretical and measured beamwidth characteristics of the multielement arrays showed excellent

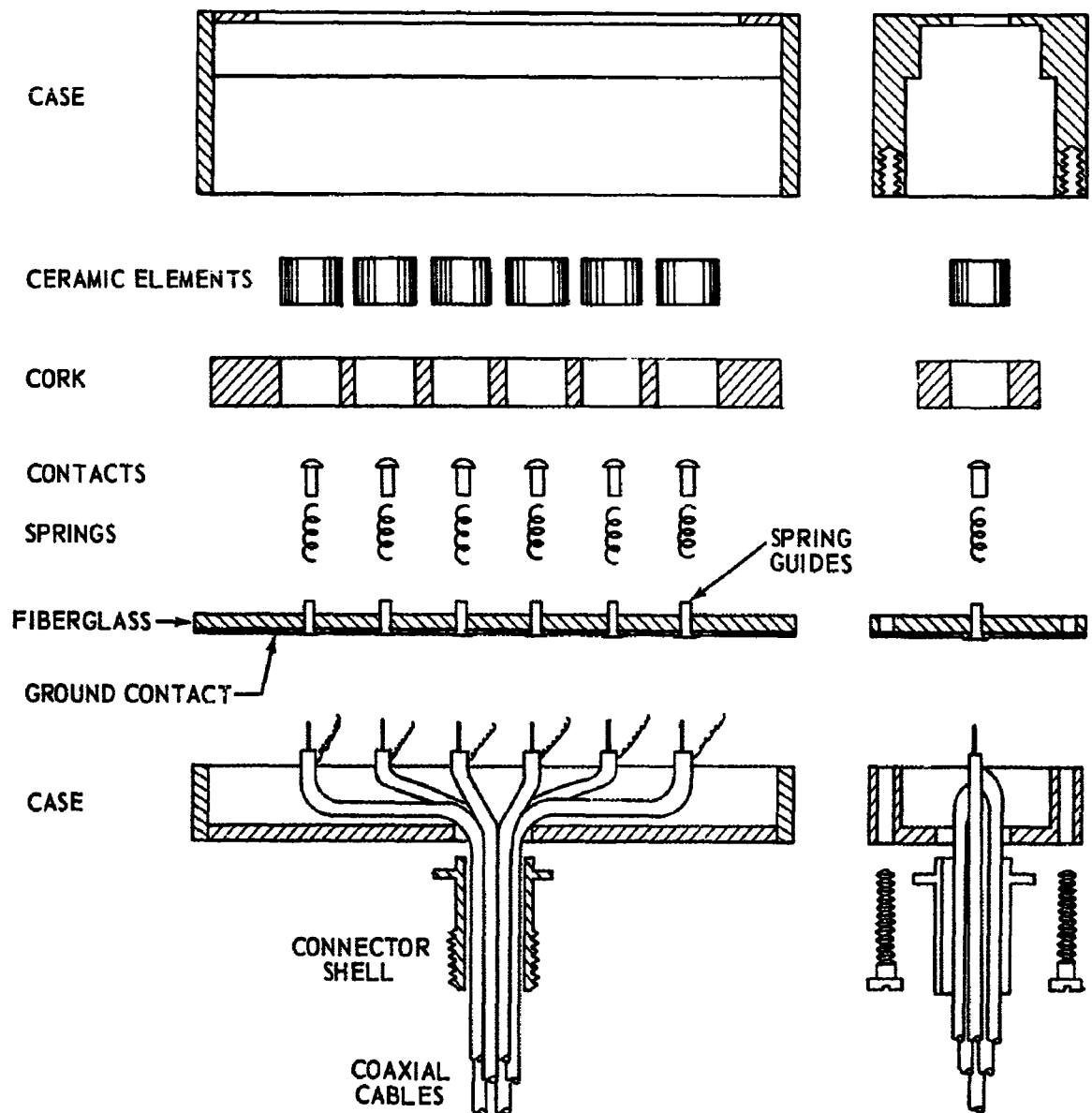


Figure 7. Design Features of Six-Element Crystal Array

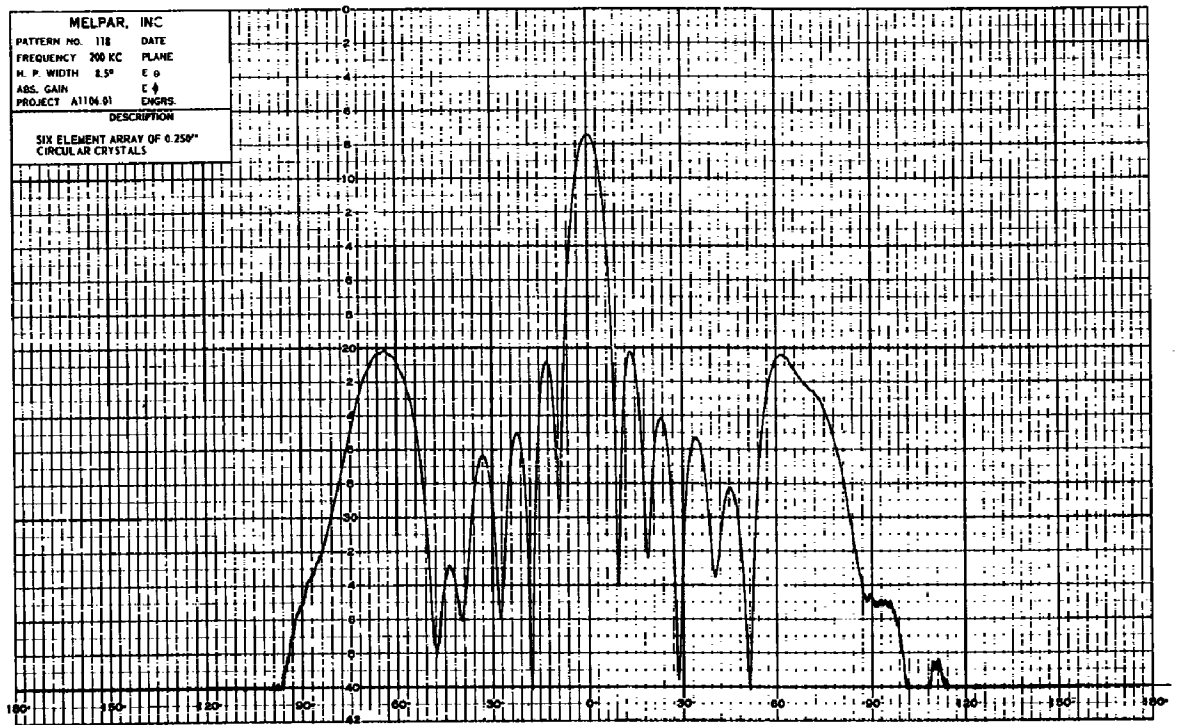


Figure 8. Pattern of Six-Element Array at 200KC

agreement in all cases. In addition, there is good correlation between the theoretical and measured sidelobe characteristics including grating lobe position.

5. SUMMARY

The results of the investigation of hydroacoustic modeling indicate that hydroacoustic techniques can be used successfully to simulate the radiation patterns of antennas using small scale models at frequencies where instrumentation is simplified. Methods for the construction of useful and reliable test facilities and transducers have been developed. A number of techniques for the synthesis of antenna radiation patterns have been investigated. Since this paper is in the form of an abstract, it is impossible to discuss thoroughly the complex aspects of this subject. For a more detailed discussion, interested persons are referred to the final reports issued in conjunction with the two contracts involved.^{4 5}

4. Pullara, J. C., "Model Techniques for Interference Measurements," final report, Melpar, Inc., Falls Church, Va., RADG-TR-61-191 (July 1961)
5. Meyer, W. A. et al., "Final Report Model Techniques for Interference Measurements," final report, Melpar, Inc., Falls Church, Va., RADG-TDR-63-281 (June 1963)

UNCLASSIFIED

UNCLASSIFIED